



EC Cluster 3
"Oxidation
Processes"
EUROTRAC-2
"Chemical
Mechanism
Development
(CMD)"



EC / EUROTRAC-2 Joint Workshop

"Shaping the Future of Atmospheric Chemistry
Research in Europe"

9-11 September, Paris
PROCEEDINGS



EC / EUROTRAC-2 Joint Workshop

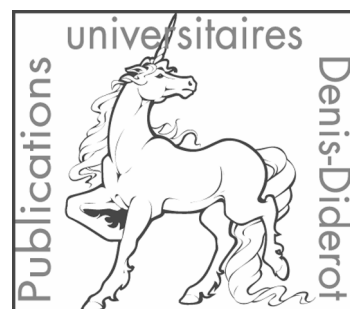
**"Shaping the Future of Atmospheric Chemistry
Research in Europe"**

**9-11 September, Paris
PROCEEDINGS**

Congrès annuel EC / EUROTRAC-2

**"Définir la poursuite de la recherche européenne en
chimie de l'atmosphère"**

**9-11 Septembre, Paris
ACTES DE CONGRES**



Remerciements: Bénédicte Picquet-Varrault, Jean François Doussin, Isabelle Rosetsky, Martin Schwell, Karine Desboeufs, Marlène Edwards, Sylvie Costes, Ministère de la Recherche, Université Paris 7, CNRS pour l'aide à l'organisation du congrès. Ulrich Schurath pour sa force de conviction au service de CMD.

Editions Paris 7 Denis Diderot, publié avec le concours du CNRS, septembre 2003

R. Losno, LISA, Universités Paris7-Paris12, CNRS

61 av. du Gal de Gaulle, 94010 Créteil Cedex

losno@lisa.univ-paris12.fr

ISBN: 2 -7442-0069-7

Couverture: crédits J.F. Doussin

15 €

Table of Contents

AUTHOR INDEX	7
PREFACE: EC / EUROTRAC-2 JOINT WORKSHOP “SHAPING THE FUTURE OF ATMOSPHERIC CHEMISTRY RESEARCH IN EUROPE”	9
MASS SPECTROMETRIC STUDIES RELATED TO IN-SITU MEASUREMENTS AND HETEROGENEOUS PROCESSES OF OVOCs IN THE UT-LS (GUEST)	13
CHEMICAL ACTIVATION IN TROPOSPHERIC OH-OXIDATION OF 1-N-ALKENES (GPP-GUEST)	17
MECHANISTIC DETAILS OF AROMATIC PHOTOOXIDATION DERIVED FROM THE CHARACTERIZATION OF SECONDARY AEROSOL FORMATION (EC – OSOA) (GUEST)	21
DEVELOPMENT OF EXPLICIT CHEMICAL SCHEMES FOR TROPOSPHERIC VOC OXIDATION – A SELF GENERATING APPROACH- (GUEST)	27
IS THE ACETYLPEROXY RADICAL $\text{CH}_3\text{C}(\text{O})\text{O}_2$ A GOOD MODEL FOR $\text{RC}(\text{O})\text{O}_2 + \text{HO}_2$ REACTIONS ? (GPP-GUEST)	33
FT-IR INVESTIGATIONS ON THE GAS-PHASE REACTIONS OF THE NO_3 AND OH RADICALS WITH A SERIES OF BENZENEDIOL COMPOUNDS (GPP1)	37
REACTION OF OH + ACETONE: DIRECT TIME RESOLVED DETERMINATION OF THE BRANCHING AT 298K (GPP3)	43
A KINETIC AND MECHANISTIC STUDY OF THE OH AND NO_2 INITIATED OXIDATION OF 2,4-HEXADIENE IN THE GAS PHASE (GPP6)	49
THEORETICAL STUDY OF THE MECHANISM OF THE OXIDATION OF BENZENE IN THE TROPOSPHERE. PATHWAYS REGENERATING OH (GPP7)	55
LOW PRESSURE KINETIC STUDY OF THE BRO REACTION WITH METHANETHIOL (GPP9)	57
A PLP-RF KINETIC STUDY OF THE ATMOSPHERIC REACTIVITY OF PROPENE AND A SERIES OF 3-HALOPROPENES WITH CL ATOMS (GPP9)	61
REACTIVITY OF THIOPHENE AND METHYLTHIOPHENES IN THE ATMOSPHERE: KINETICS STUDY OF NO_3 REACTIONS (GPP9)	67
THE UV-VISIBLE SPECTRA AND ATMOSPHERIC PHOTOLYSIS OF AROMATIC ALDEHYDES (GPP10)	73

THE ATMOSPHERIC FATE OF METHYL ISOPROPYL KETONE (GPP10)	79
OZONOLYSIS OF ALKENES: INFLUENCE OF THE STRUCTURE OF THE CRIEGEE INTERMEDIATE ON CARBOXYLIC ACID AND ORGANIC AEROSOL FORMATION (GPP11)	83
GENERALIZED STRUCTURE-ACTIVITY RELATIONSHIPS FOR THE DECOMPOSITION AND ISOMERISATION OF (SUBSTITUTED) ALKOXY RADICALS. THEORY-BASED VALIDATION (GPP13)	89
ISOMERIZATION OF 1-BUTOXY RADICALS (GPP22)	95
NITRATE FORMATION IN THE REACTION OF 1-NONYLPEROXY RADICALS WITH NO (GPP22)	103
ABSOLUTE RATE CONSTANTS FOR THE GAS-PHASE OZONOLYSIS OF ISOPRENE AND METHYLBUTENOL (GPP25)	109
COMPETITION BETWEEN VARIOUS ALKOXY EVOLUTION PROCESS IN THE ATMOSPHERE (GPP 25).	111
INFLUENCE OF PH ON KINETICS OF S(IV) AUTOXIDATION IN THE PRESENCE OF MN(II) (APP3)	119
LASER-BASED STUDIES OF OH WITH OXYGENATED ORGANICS IN AQUEOUS SOLUTION (APP4)	123
CONCENTRATION PROFILES USING A LOGNORMAL DISTRIBUTION REGARDING AEROSOLS WITH CAPRAM 2.4 (MODAC MECHANISM) (APP4)	129
EXPERIMENTAL SIMULATION OF IRON CYCLING (APP7)	135
AEROSOL DISSOLUTION ENHANCEMENT BY LIGHT IRRADIATION (APP7).	141
INTERACTION BETWEEN MINERAL COMPONENTS OF SEA AEROSOLS AND SULPHOXY RADICALS (APP8).	145
DEGRADATION OF ISOPRENE DURING AQUEOUS AUTOXIDATION OF SO₂ UNDER VARIOUS CONDITIONS OF INITIATION (APP8).	151
FE-CATALYSED AUTOXIDATION OF S(IV) INHIBITED BY ALIPHATIC ALCOHOLS, NONTERPENIC AND SUBSTITUTED WITH α-PINENE SKELETAL STRUCTURE (APP8)	157
KINETICS OF THE MN-CATALYSED AUTOXIDATION OF S(IV) INHIBITED BY CAFFEIC ACID AS A REPRESENTATIVE OF POLYPHENOLS (APP8)	161

AQUEOUS PHASE RADICAL CHEMISTRY OF NEW OXYGENATED SOLVENTS EXPERIMENTAL DEVELOPMENTS (APP15)	167
APPLICATION OF HOMOGENEOUS AND HETEROGENEOUS METHODS IN THE STUDY OF THE REACTION OF HOBR AND BR₂ WITH SULPHUR SPECIES (APP16)	173
AQUEOUS PHASE REACTIVITY OF ACETONE AND ITS PARENT COMPOUNDS IN THE TROPOSPHERE (APP17)	179
TROPOSPHERIC REACTIVITY OF ORGANIC HYDROPEROXIDES (APP17)	183
INTERACTION OF TRACE GAS SPECIES OF ATMOSPHERIC INTEREST WITH ICE SURFACES (ADSORPTION ENTHALPY OF ACETONE) (HEP1)	193
REACTION OF HNO₃ WITH MINERAL DUST PARTICLES. PRELIMINARY RESULTS (HEP1).	197
THE INTERACTION BETWEEN SEA-SALT AEROSOL AND MARINE GASEOUS CHEMISTRY (HEP2)	203
INTERACTION OF TRACE GASES WITH WATER-ICE SURFACES (HEP4)	207
AEROSOL FLOW TUBE STUDIES OF TRACE GAS UPTAKE TO MINERAL DUST (HEP4)	211
MECHANISM LEADING TO SOA-PARTICLE FORMATION IN THE OXIDATION OF BIOGENIC ALKENES (HEP7)	215
THE CHARACTERIZATION OF SURFACE FUNCTIONAL GROUPS OF SECONDARY ORGANICS AEROSOLS (SOA) GENERATED UNDER LABORATORY CONDITIONS (HEP9)	219
THE AIDA SOOT COATING CAMPAIGN: INFLUENCE OF COATINGS ON STRUCTURE AND OPTICS OF SOOT AEROSOL (HEP10).	225
AEROSOL OPTICAL PROPERTIES AS A TOOL FOR STUDYING MULTI-PHASE PROCESSES OVER A WIDE RANGE OF ATMOSPHERIC CONDITIONS (HEP10)	229
CHARACTERIZATION OF DIESEL AND SYNTHETIC SOOT: A SINGLE PARTICLE MASS SPECTROMETRY INVESTIGATION (HEP13)	235
HETEROGENEOUS CONVERSION OF NO₂ ON SECONDARY ORGANIC AEROSOL SURFACES: A POSSIBLE HONO SOURCE? (HEP15)	241
UPTAKE KINETICS OF OXYGENATED ORGANICS ON ICE SURFACES (HEP16)	247

CHEMICAL REACTIVITY AND TRANSFORMATION OF AEROSOL PARTICLES: MECHANISTIC DESCRIPTION OF SURFACE PROCESSES INVOLVING REVERSIBLE ADSORPTION AND LANGMUIR-HINSHELWOOD REACTIONS (HEP20)	253
A NEW CHEMICAL MODULE FOR TROPOSPHERIC ISOPRENE DEGRADATION APPLIED TO THE RACM MECHANISM (MPM2)	259
SIMULATION OF ATMOSPHERIC PHOTOCHEMISTRY IN A LARGE REACTION CHAMBER (SAPHIR): DESIGN OF CHAMBER EXPERIMENTS USING SENSITIVITY ANALYSIS (MPM6).	265
NUMERICAL SIMULATIONS OF NITROUS ACID IN THE PLANETARY BOUNDARY LAYER – RATE CONSTANTS AND UNKNOWN SOURCES (MPM10)	271
SENSITIVITY STUDY ON THE INFLUENCE OF NEW KINETIC DATA AND OF SPECIES LUMPING ON THE SIMULATION RESULTS (MPM11)	275

Author index

- Albaladejo, 61
 Ammann, 193, 197, 253
 Aranda, 57
 Aumont, 27
 Baeza, 67
 Barcellos da Rosa, 173
 Barnes, 37, 259
 Bartels-Rausch, 193
 Behnke, 173, 203
 Behr, 247
 Bejan, 37, 259
 Benter, 37, 259
 Bercic, 119
 Bonn, 83, 215
 Bronikowski, 145
 Bröske, 241
 Cabañas, 67
 Caralp, 17
 Carlier, 109, 111, 183
 Catoire, 13
 Chakir, 73
 Chevallier, 183
 Clappier, 275
 Colin, 135, 141
 Coninck, 211
 Crowley, 207, 211
 Cuevas, 61
 Daumont, 73
 Delbos, 43
 Demiral, 247
 Demirdjian, 219
 Desboeufs, 135, 141
 Devolder, 43
 Díaz de Mera, 57
 Dorn, 265
 Doussin, 109, 111
 Durand Jolibois, 183
 Durand-jolibois, 111
 Elend, 203
 Fantechi, 89
 Fittschen, 43
 Forst, 17
 Gaeggeler, 197
 Geiger, 259
 George, 167
 Gligorovski, 123
 Grgic, 119
 Guimbaud, 193, 197
 Hanisch, 211
 Herrmann, 123, 129
 Holmes, 207
 Hurley, 49
 Jenkin, 49
 Junier, 275
 Kabir, 103
 Karl, 265
 Kirchner, 235, 275
 Klawatsch-Carrasco, 109
 Kleffmann, 241, 271
 Krajewska, 161
 Krolik, 151
 Krüger, 203
 Kurtenbach, 271
 Laval-Szopa, 27
 Laverdet, 79
 Le Bras, 73, 79
 Le Crâne, 33
 Lesclaux, 55
 Linke, 225, 229
 Losno, 135, 141
 Madronich, 27
 Magneron, 79
 Majdik, 129
 Martín, 67
 Martínez, 57, 61, 67
 Martín-Reviejo, 21
 Mellouki, 73, 79
 meunier, 111
 Michel, 13
 Möhler, 225, 229
 Monod, 179, 183
 Moortgat, 83, 215
 Naumann, 225, 229
 Notario, 61
 Olariu, 37
 Palm, 203
 Pasiuk-Bronikowska, 145, 151, 157, 161
 Paulus, 95
 Peeters, 89
 Picquet-Varrault, 111, 183
 Podkrajšek, 119
 Poppe, 265
 Pöschl, 253
 Poulain, 179
 Poulet, 13
 Raoult, 55
 Rayez (JC), 55
 Rayez (MT), 55
 Rossi, 219
 Roulet, 275
 Rousse, 167
 Rudich, 253
 Rudzinski, 151
 Saathoff, 225, 229
 Sadezky, 83
 Salgado, 57, 67
 Scharfenort, 247
 Schnaiter, 225, 229
 Schöck, 225, 229
 Schurath, 9, 225, 229
 Sofikitis, 135
 Sokolowski, 145
 Sokolowski-Gomez, 73
 Sørensen, 49
 Sowka, 179
 Spittler, 259
 Strekowski, 167
 Terziyski, 247
 Thiault, 73
 Thirkell, 13
 Tomas, 33
 Turpin, 43
 Uherek, 83
 Ulejczyk, 145
 van den Bergh, 275
 Velay, 141
 Vereecken, 89
 Villenave, 33
 Vlasenko, 197
 Vogel (B), 271
 Vogel (H), 271
 Vogt, 235
 Volkamer, 73
 Wagner, 225, 229
 Wallington, 49
 Wiesen, 241
 Winkler, 207
 Wirtz, 21, 37, 73
 Wortham, 179
 Zabel, 95, 103
 Zellner, 247
 Zetzsch, 173, 203
 Ziajka, 157

PREFACE: EC / EUROTRAC-2 Joint Workshop “Shaping the Future of Atmospheric Chemistry Research in Europe”

Ulrich Schurath

Institut fuer Meteorologie und Klimaforschung, IMK-AAF

POBox 3640 - Building 326

D-76021 KARLSRUHE

e-mail schurath@imk.fzk.de, <http://imk-aida.fzk.de>

Climate change and health effects of pollutants are intimately related with on-going changes in emission pattern and with emissions of new chemicals, which give rise to new and complex chemistry in the multiphase atmospheric system. Clearly, laboratory investigations, chemical model development and theoretical studies are needed to elucidate the new chemistry which occurs in a changing atmosphere.

It is in this spirit that the 6th and last Annual Workshop of the “Chemical Mechanism Development (CMD)” subproject of EUROTRAC-2 was termed “Shaping the future of Atmospheric Chemistry Research in Europe”. Like most previous ones, the workshop was organised as a joint EC / EUROTRAC-2 meeting. Contributions from other researchers, if relevant to the motto of the workshop, were explicitly welcomed.

The workshop took place from 9th to 11th September in Paris, hosted on the first and second day by the French Ministry of Research in the large “Poincaré” lecture hall of the “Carré des Sciences”. This facility is located in the middle of the historic area “Quartier Latin”, right in the centre of the city, within walking distance of the Sorbonne University, the Seine River and the “Notre Dame” cathedral. The meeting attracted more than 90 European scientists who presented over 60 scientific contributions. The meeting was organised by Rémi Losno and his colleagues from LISA Université Marne-La-Vallée and Université Paris 7 Denis Diderot, in particular Bénédicte Piquet-Varrault and Jean-François Doussin who was also in charge of the excellent web presentation: <http://www.lisa.univ-paris12.fr/CMD2002/>. It is due to the dedicated care of these people that the workshop was a great success, both scientifically and as a social event amongst good old friends.

We are indebted to the French Ministry of Science, the CNRS, and the Université Paris 7 Denis Diderot who provided the excellent meeting places free of charge, generously supported the workshop, and sponsored a number of invited speakers.

The workshop started on Monday morning with an invited lecture which was presented by Prof. Howard Sidebottom from the University College Dublin, Ireland. His talk with the unpretentious title “Gas phase oxidation of oxygenated compounds” turned out to be a carefully prepared, comprehensive, and extremely well presented review on structure-activity relationships for the atmospheric degradation of this important class of environmental pollutants. Structure-activity relationships have been in the focus of CMD because they are powerful tools for the development of more accurate chemical mechanisms in a rapidly changing environment. The theoretical considerations of Prof. Sidebottom were based on experimental work which had predominantly been funded by the European Commission.

The next invited speaker was Professor Benoît Nemery from the Katholieke Universiteit Leuven. He is head of the Unit of Lung Toxicology, Department of Occupational Medicine and Laboratory of Pneumology, and member of the Health Council of the Ministry of Health and Environment in Belgium. He talked about “Human health effects of urban air pollution: observations and mechanisms”. After a brief historical review of air pollution events in Europe he focussed on the problem of relating human health effects with specific atmospheric pollutants. Methods of eliminating biases from cohort studies and other epidemiological data were convincingly discussed, with particular emphasis on health effects by ozone and - more timely - small particles. It should be mentioned that Prof. Nemery and his collaborators have recently presented experimental evidence that nm-sized insoluble soot particles can pass directly from the human lungs into the blood circulation system (CIRCULATION 105 (4) (2002) 411-414), which may explain the association of

PM₁₀ exposure with increased morbidity and mortality from cardiovascular diseases. Clearly, the chemistry of small particles under atmospheric conditions is a new direction of atmospheric research.

Monday was the evening of the conference dinner which had been organised „A la Bonne Franquette“. This is a pretty old-fashioned restaurant in the historic area of Montmartre, very close to the last and only vineyard in the city of Paris. I will always remember the beautiful evening and the breath-taking view over Paris, shed with gold by the setting sun! – But this was nothing compared with the excellent dinner and a most colourful entertainment programme, guided by two wild-looking musicians who covered the whole spectrum from Johnny Halliday's songs to old chansons which clearly belong to the cultural heritage of the French people. The evening culminated in the breath-taking performance of three cancan dancers who obviously had a weakness for famous scientists.

The programme on Tuesday morning started with an invited lecture by Prof. Tim Wallington who is scientist at Ford Research Laboratories in Dearborn, Michigan, USA, on „The effect of atmospheric aerosols on the OH radical initiated oxidation of organic compounds“. Tim Wallington has pioneered numerous studies of the degradation rates and mechanisms of novel anthropogenic pollutants, e.g. fuel additives and other oxygenated compounds. He was now able to prove, on the basis of aerosol chamber experiments, that the OH-initiated atmospheric degradation of alcohols is unaffected by the presence of particulate matter. It was shown that this result, which contrasted with previous work reported in the literature, agreed well with theoretical considerations.

Space does not allow us to quote all the other excellent contributions to the workshop, except for two other overview lectures, the first one on "Generalised structure activity relationships for the decomposition and isomerisation of (substituted) alkoxy radicals. Theory-based validation", presented by Luc Vereecken from Jozef Peeters' group. A second overview on "Chemical reactivity and transformation of aerosol particles: experimental investigation and mechanistic description" was presented by Uli Pöschl. Being chief executive editor of the web-based EGS-Journal „Atmospheric Chemistry and Physics“ he took the opportunity to draw attention to this new way of publishing scientific results, see <http://www.atmos-chem-phys.org> for details.

On Wednesday 11th September the workshop was moved to a large lecture hall at the Université Paris VII which is within walking distance of the "Carré des Sciences". The scientific part of the workshop ended with presentations of two large chamber facilities: the brand new photochemical chamber "SAPHIR" in Juelich, and the coolable aerosol chamber AIDA in Karlsruhe. These and a few other chambers – not to forget the large EUPHORE double-chamber in Valencia – may become important tools of future atmospheric research in Europe. The final discussion was reserved to upcoming matters, in particular to the prospect of the expressions of interest for Integrated Projects and Networks of Excellence which had been submitted to the EC, and which were still in the dark at the time of the meeting. Christian George reported on a Scientific Programme proposal focussing on Atmospheric Chemistry, which upon his initiative had been prepared jointly by a group of scientists from many European countries, and submitted to the European Science Foundation in May of this year. This project holds promise of becoming a new umbrella for the community of atmospheric chemistry researchers in Europe after EUROTRAC-2. In anticipation of a successful outcome of the ESF proposal it was decided that a follow-up workshop should be organised in September 2003, either in Cologne jointly by Forschungszentrum Juelich and the University of Wuppertal, or by Ole John Nielsen and his collaborators at the University of Copenhagen. With this optimistic outlook into the future the conference adjourned.

Ulrich Schurath, Forschungszentrum Karlsruhe



Figure 1: Global change – a perhaps not too serious view of the problem in Paris, rue de Seine (credits: W. Schöck)



Figure 2: Cancan dancer at Richard Wayne's table (credits: J.F. Doussin)



Figure 3: Prof. B. Nemery presenting his invited talk on “Human health effects of urban air pollution: observations and mechanisms” in the lecture hall “Poincaré” (credit: J.F. Doussin)

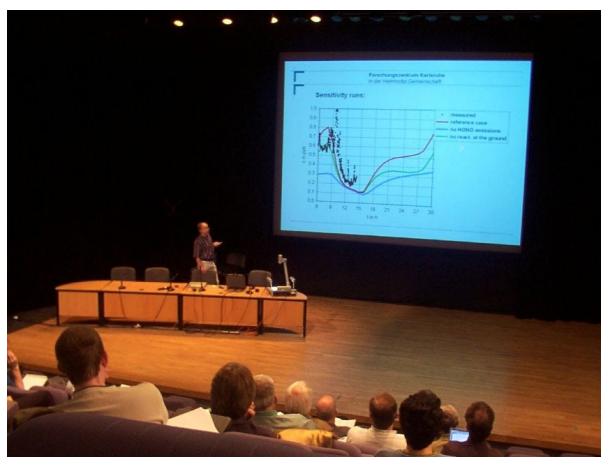


Figure 4: Bernhard Vogel lecturing in amphitheatre at the Université Paris VII (credit: J.F. Doussin)

Mass Spectrometric Studies Related to In-situ Measurements and Heterogeneous Processes of OVOCs in the UT-LS (Guest)

Elodie Michel, Valéry Catoire, Laurent Thirkell, Gilles Poulet
*Laboratoire de Physique et Chimie de l'Environnement,
 UMR CNRS – Université d'Orléans, 45071 Orléans cedex 2, France
 e-mail: Valery.Catoire@univ-orleans.fr*

Introduction

The upper troposphere–lower stratosphere (UT-LS) has attracted recently increasing attention because of persistent disagreement between the measurements and modelling of OH and NO_x/NO_y ratio concentrations [Wennberg et al., 1998; Jaeglé et al., 1998]. The formation and destruction of ozone depend on the concentrations of these species, and must be better understood as ozone plays a major chemical and radiative role in this region. The emissions of particles, H₂O and NO_x from commercial aircraft, the transport of oxygenated volatile organic compounds (OVOCs) and of NO_x from the lower troposphere, and the presence of cirrus clouds are among the factors that influence the OH, NO_x and NO_y concentrations in the UT-LS.

As an important example, acetone photooxidation in the UT-LS acts as the principal source of odd hydrogen radicals (HO_x = OH + HO₂) [Singh et al., 1995; Folkins et al., 1998], since water vapor is typically low in this part of the atmosphere, limiting the reaction: O(¹D) + H₂O → 2 OH. Other OVOCs are suspected to be additional sources of HO_x radicals and their simultaneous measurements with these radicals are needed. Chemical ionisation mass spectrometry (CIMS) is one successful method enabling OVOC in-situ measurements, based on reactions of proton hydrates:



with $0 \leq m \leq n \leq 5$ [Arnold et al., 1997]. The OVOC concentration is derived from the knowledge of the rate constants and product ions of the reactions involved. Some rate constants and product ions have been already determined in laboratory studies performed at room temperature and low pressure (< 1 mbar; see, for example, Spanel et al. [1997] and Lovejoy [1999]). However, these data required to be measured at the lower temperatures and higher pressures of the UT-LS, since different mechanisms may occur, as it is the case for formaldehyde [Midey et al., 2000]. Studies under these conditions have been undertaken in our laboratory, using a variable temperature and pressure (i.e. in the turbulent flow regime) CIMS apparatus.

In parallel to in-situ measurements, the interactions of OVOCs with the ice of cirrus clouds must be clarified, in order to assess the partitioning of OVOCs between the gas phase and the condensed phase, and their possible participation to heterogeneous reactions. The development of a method for studying the adsorption and diffusion of OVOCs in ice single crystals using a time-of-flight secondary ion mass spectrometer (TOF-SIMS) is under progress in our laboratory. TOF-SIMS capabilities (sensitivity and depth resolution) are known to be excellent for analysis of solid material at room temperature, but have not been tested for ice, except in one recent study [Donsig et al., 1999].

Laboratory CIMS experiments applied to measurements of OVOCs

An ion flow tube apparatus [Catoire et al., 2001] has been modified to allow studies of ion/molecule reactions over wide ranges of temperature and pressure. The ion flow reactor is a triple jacketed stainless steel tube: ion/molecule reactions take place in the inner tube (2.3 cm i.d., 87 cm long), a thermostated fluid circulates through the intermediate jacket, and vacuum is maintained in the third jacket for thermal isolation. Proton hydrates are generated from traces of water vapour in argon flow < 1 SLM (standard liter per minute) using a corona discharge. Controlled flows of diluted acetone (< 0.010 SLM) are injected through a movable concentric line. The flow of the main carrier

gas N₂ (2-100 SLM) results in pressures of 1-100 mbar. The temperature in the flow tube ranges from 220 to 370 K by using precooling or preheating of all the gases injected. At the downstream end of the tube, a fraction of the reactant and product ions are sampled and focused by ion optics through two differentially pumped chambers, one of which containing a quadrupole guide (in the radio-frequency mode only). Ions are selected in a third differentially pumped chamber by a quadrupole mass analyzer and detected by a secondary electron multiplier. The new experimental setup (shown in Figure 1) has been validated at room temperature and low pressure (1.7-5.3 mbar) from the kinetic and mechanistic results obtained for the reactions of acetone with proton hydrates, H₃O⁺(H₂O)_n with n =0-2, in agreement with other studies [Spanel et al., 1997; Lovejoy, 1999]. Studies at higher pressure and variable temperature are planned for the same series of reactions, which should not have significant dependencies on these parameters in the case of acetone.

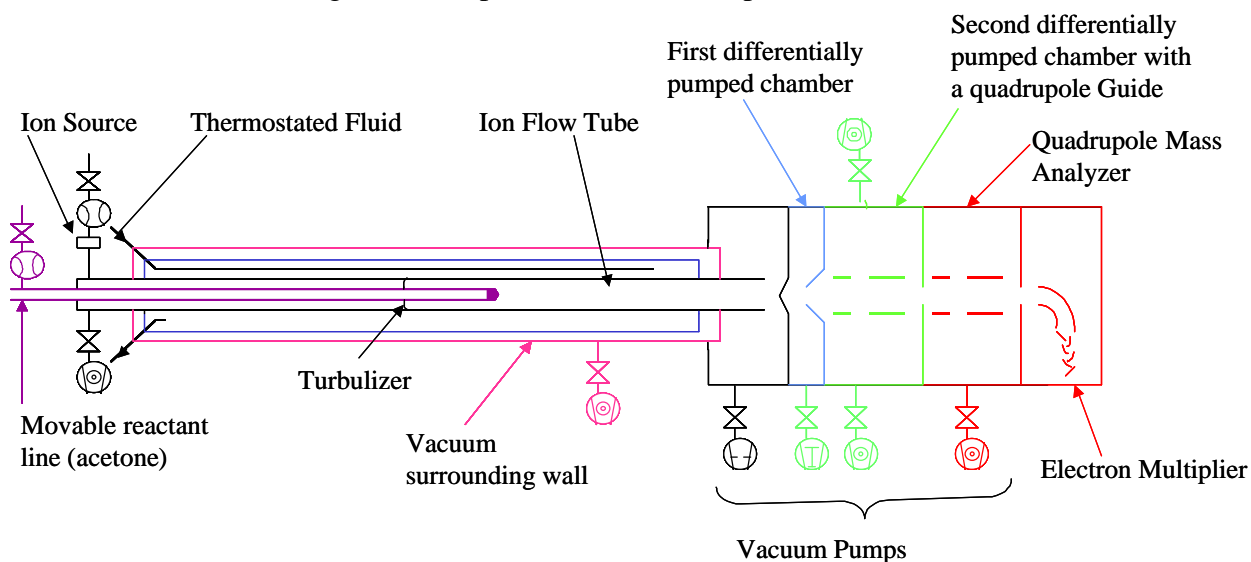


Figure 1: Schematic of the ion flow tube coupled to CIMS detection

Laboratory TOF-SIMS experiments applied to heterogeneous processes of OVOCs

A time-of-flight secondary ion mass spectrometer (TOF-SIMS) is being adapted for the laboratory analysis of OVOC-doped ice under very low pressure ($< 10^{-8}$ mbar). The primary ion beam, working at an energy of 8 kV, is extracted from a liquid source of mono-isotopical indium ($\text{amu} = 112.90$). The pulse duration is 2-3 ns with a repetition rate of 1 kHz and the spot diameter is about 25 μm . The mass resolution is 1500 at $\text{amu} 28$. In the present state of development, the apparatus (shown in Figure 2) is able to give spectra from bulk ice sample. Some improvements are under progress to reach the primary objective of measuring diffusion coefficients of trace gases in ice. In particular, chemical contamination is being reduced by adding a new pumping system, resulting in a better vacuum and limiting therefore the condensation of the residual gas at the sample surface. In addition, a charge compensation method is being tested using an electron flood gun in order to increase the instrument sensitivity. The TOF-SIMS method will then be tested by the analysis of ice single crystals doped with known HCHO concentrations, prepared at the Laboratoire de Glaciologie et Géochimie de l'Environnement (CNRS, Grenoble).

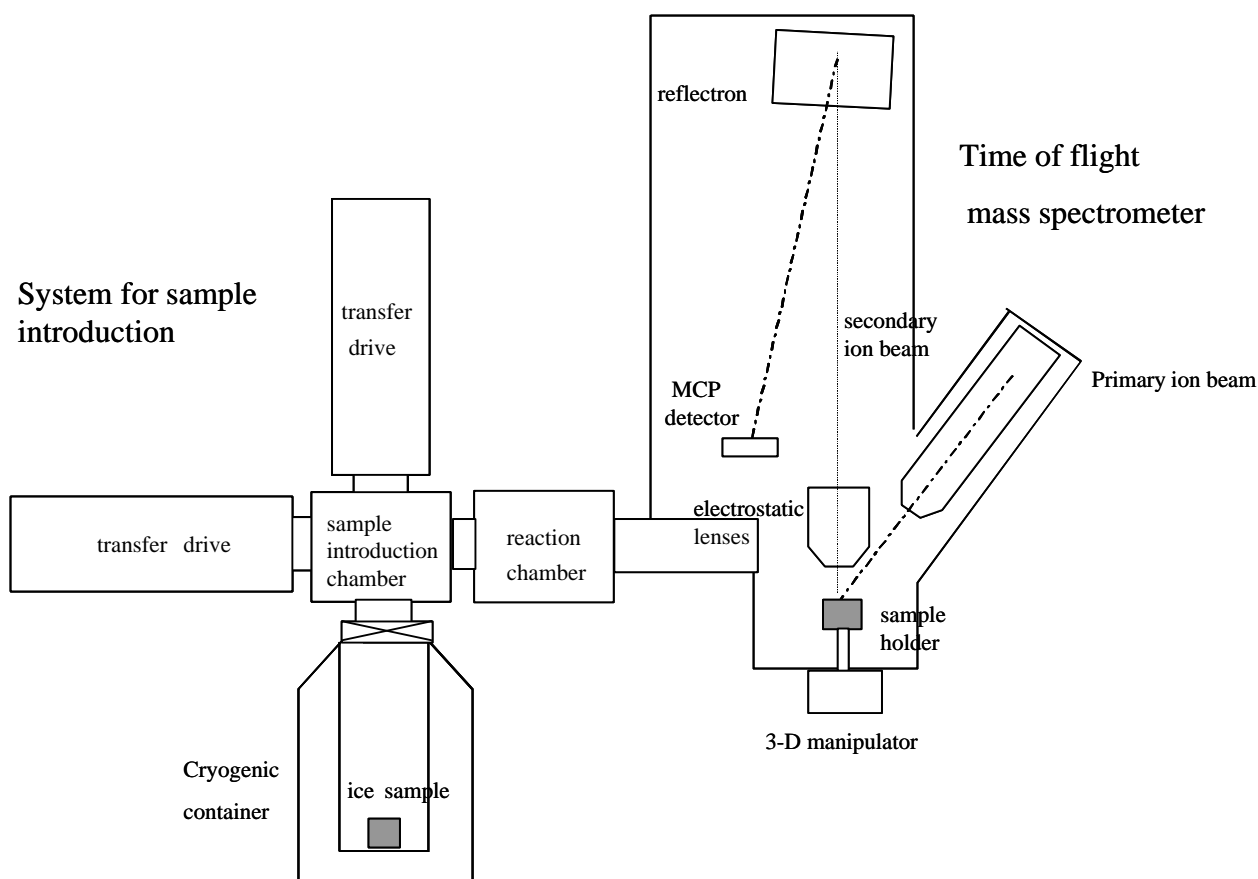


Figure 2: Schematic of the TOF-SIMS apparatus for ice surface analysis

References

- Arnold F., Bürger V., Droste-Fanke B., Grimm F., Krieger A., Schneider J. and Stilp T., *Geophys. Res. Lett.*, 1997, 24(23), 3017-3020.
- Catoire V., Stépien C., Labonnette D., Rayez J.-C., Rayez M.-T. and Poulet G., *Phys. Chem. Chem. Phys.*, 2001, 3, 193-197.
- Donsig H.A., Herridge D. and Vickerman J.C., *J. Phys. Chem. A*, 1999, 103, 9211-9220.
- Folkins I., Chatfield R., Singh H., Chen Y. and Heikes B., *Geophys. Res. Lett.*, 1998, 25(9), 1305-1308.
- Jaeglé L., Jacob D.J., Wang Y., Weinheimer A.J. et al., *Geophys. Res. Lett.*, 1998, 25, 1705-1708.
- Lovejoy E. R., *Int. J. Mass Spectrom.*, 1999, 190/191, 231-241.
- Midey A.J., Arnold S.T. and Viggiano A.A., *J. Phys. Chem. A*, 2000, 104, 2706-2709.
- Singh H.B., Kanakidou M., Crutzen P.J. and Jacob D.J., *Nature*, 1995, 378, 50-54.
- Spanel P., Yufeng J. and Smith D., *Int. J. Mass Spectrom. Ion Proc.*, 1997, 165/166, 25-37.
- Wennberg P.O., Hanisco T.F., Jaeglé L., Jacob D.J., Hintsä E.J., Lanzendorf E.J., Anderson J.G., Gao R.S., Keim E.R. and Donnelly S.G., *Science*, 1998, 279, 49-53.

Chemical Activation in Tropospheric OH-Oxidation of 1-n-alkenes (GPP-Guest)

Françoise Caralp and Wendell Forst

Laboratoire de Physico-chimie Moléculaire, UMR 5803 CNRS,

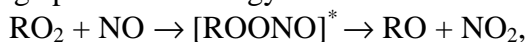
Université Bordeaux I, 33405 Talence Cedex, France.

E-mail: fcaralp@cribdx1.u-bordeaux.fr; wforst@waol.com

The mechanism of oxidation of alkenes (general formula $\text{RC}=\text{CR}$), mainly initiated by OH-radical addition to the double bond, gives rise to β -hydroxy-alkoxy radicals HORC-CRO^\bullet , essentially by reaction (3):



A large part of the energy available from the exothermic reaction (3),



is deposited on the nascent alkoxy radical, and a significant fraction of this radical is formed with sufficient internal energy to decompose “promptly”. It was recently shown⁽¹⁾ that the reaction of $\text{HOCH}_2\text{CH}_2\text{O}_2$ with NO produces chemically activated β -hydroxy-ethoxy radicals ($\text{HOCH}_2\text{CH}_2\text{O}^\bullet$), of which about 25 % decomposes on a time-scale that is rapid compared with collisions. The prompt dissociation of β -hydroxy-ethoxy and β -hydroxy-2-propoxy were then theoretically quantified.⁽²⁻³⁾ However, while the behaviour of the hydroxy-alkoxy radicals derived from the two first 1-alkenes has been extensively studied, the importance of chemical activation in the atmospheric chemistry of larger alkenes and in the decomposition of the hydroxy-alkoxy radical in particular is unknown.

The aim in this work is to evaluate the fraction of chemically activated β -hydroxy-1-alkoxy radicals formed by the OH-radical initiated oxidation of a series of 1-n-alkenes from 1-butene to 1-hexene and the importance of such a phenomena on the tropospheric fate of these alkoxy radicals.

A four-steps procedure based on RRKM-Master Equation (RRKM-ME) analysis was developed (illustrated by the schematic energy profile of figure 1):

1. Reaction of RO_2 with NO to form vibrationally excited peroxyxynitrite ROONO^* ;
2. Collisional energy loss during the lifetime of this intermediate, quantified by RRKM-ME;
3. Dissociation of ROONO^* into RO and NO_2 with partitioning of the available energy between the two products calculated using Phase Space Theory;
4. Prompt dissociation of the chemically activated nascent alkoxy radical in competition with thermalisation, quantified by a second RRKM-ME analysis.

The results of these calculations are presented in Table I and Table II for lower and upper tropospheric conditions respectively

For evaluating the impact of such a chemical activation, the thermal fall-off behaviour of these alkoxy radicals was obtained by applying the RRKM theory. The resulting calculated values of the thermal rate constants, for lower and upper tropospheric conditions, are listed in Table III and Table IV for the dissociation and isomerisation reactions respectively. For quantifying the competition between these unimolecular reactions and the reaction with oxygen, the pseudo-first-order rate constant of this last reaction, obtained from the expression $k_{(\text{RCH}_2\text{O} + \text{O}_2)} = 6.0 \times 10^{-14} \exp(-550 / T) \text{ cm}^3 \text{ molecule}^{-1} \text{ s}^{-1}$ and for 20 % O_2 are also reported in Table III.

The totality of these results allows us to evaluate the importance of chemical activation in the subsequent evolution of β -hydroxy-1-alkoxy radicals produced in the atmospheric oxidation of 1-

alkenes, by predicting the proportion of each competitive way of reaction of the radical (reaction with O_2 , dissociation, isomerisation). Results of calculations are presented in Table V.

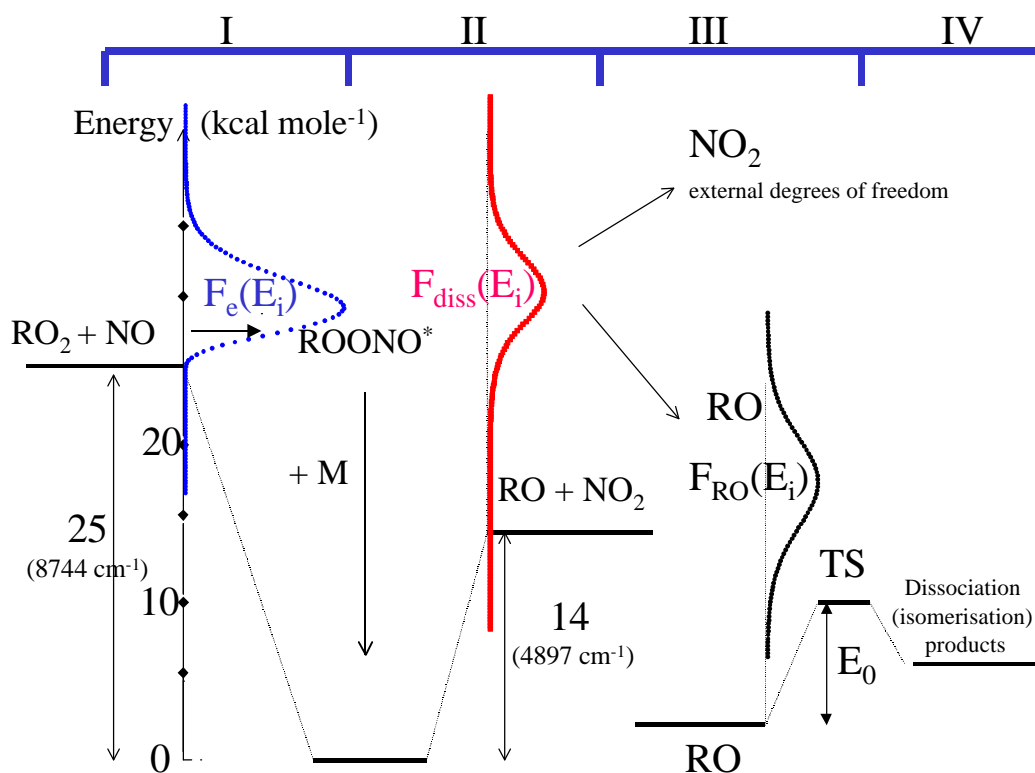


Figure 1

Table I. Calculated prompt unimolecular reaction fractions for β -hydroxy-alkoxy radicals formed in the reaction $\text{RO}_2 + \text{NO}$ at P=1 atm and T = 298 K. (Lower troposphere conditions).

	% prompt dissociation	% prompt isomerisation
β -hydroxy-ethoxy	30	—
β -hydroxy-2-propoxy	75	—
β -hydroxy-1-propoxy	75	—
β -hydroxy-1-butoxy	40	0.03
β -hydroxy-1-pentoxy	19.5	12
β -hydroxy-1-hexoxy	13	7.4

Table II. Calculated prompt unimolecular reaction fractions for β -hydroxy-alkoxy radicals formed in the reaction $\text{RO}_2 + \text{NO}$ at P=0.2 atm and T = 220 K (upper troposphere conditions)

	% prompt dissociation	% prompt isomerisation
β -hydroxy-ethoxy	23	—
β -hydroxy-2-propoxy	73	—
β -hydroxy-1-propoxy	75	—
β -hydroxy-1-butoxy	38	0.005
β -hydroxy-1-pentoxy	16.6	16.8
β -hydroxy-1-hexoxy	11.1	9.8

Table III: Thermal dissociation rate constants of β -hydroxy-alkoxy radicals obtained from RRKM calculations of the fall-off curves. Pseudo-first-order rate constant for reaction with O_2 under troposphere conditions assuming $k_{(RCH_2O + O_2)} = 6.0 \times 10^{-14} \exp(-550 / T)^{(8)}$ and 20% O_2 .

Dissociation Rate constants	298 K			220 K		
	k_∞ (s^{-1})	k_{1atm}^a (s^{-1})	k_{1atm} / k_∞	k_∞ (s^{-1})	$k_{0.2atm}^a$ (s^{-1})	k_{1atm} / k_∞
β -hydroxy-ethoxy	5.5×10^5	1.4×10^{5b}	0.25	9.1×10^2	1.6×10^2	0.62
β -hydroxy-2-propoxy	6.2×10^7	1.1×10^7	0.17	5.3×10^5	9.3×10^4	0.42
β -hydroxy-1-propoxy	7.4×10^7	1.3×10^7	0.17	6.6×10^5	1.1×10^5	0.42
β -hydroxy-1-butoxy	5.5×10^6	2.6×10^6	0.47	1.9×10^4	9.8×10^3	0.79
β -hydroxy-1-pentoxo	5.1×10^6	2.5×10^6	0.49	1.7×10^4	9.4×10^3	0.82
β -hydroxy-1-hexoxo	4.9×10^6	3.0×10^6	0.62	1.7×10^4	1.2×10^4	0.96
$k_{(RCH_2O + O_2)} \times [O_2]^c$		4.7×10^4			6.6×10^3	

^a fall-off calculations performed with $\beta_c = 0.2 \times (300/T)$. ^b Experimental value: $1.3 \times 10^5 s^{-1}$ ref.1. ^c with: $k_{(RCH_2O + O_2)} = 6.0 \times 10^{-14} \exp(-550 / T) cm^3 molecule^{-1} s^{-1}$ and for 20 % O_2 .

Table IV: Thermal isomerisation rate constants of β -hydroxy-alkoxy radicals obtained from RRKM calculations of the fall-off curves.

Isomerisation Rate constants	298 K			220 K		
	k_∞ (s^{-1})	k_{1atm}^a (s^{-1})	k_{1atm} / k_∞	k_∞ (s^{-1})	$k_{0.2atm}^a$ (s^{-1})	k_{1atm} / k_∞
β -hydroxy-1-butoxy	6.3×10^3	1.8×10^2	0.03	3.9	0.06	0.07
β -hydroxy-1-pentoxo	5.5×10^6	3.8×10^6	0.69	4.5×10^4	3.5×10^4	0.93
β -hydroxy-1-hexoxo	4.9×10^6	3.7×10^6	0.75	4.0×10^4	3.4×10^4	0.96

^a fall-off calculations performed with $\beta_c = 0.2 \times (300/T)$.

Table V: Fraction of unimolecular reactions of hydroxy-alkoxy radicals compared with reaction with O₂ for thermalised alkoxy and for chemically activated alkoxy produced by the RO₂+NO reaction (combining prompt and thermal reactions), assuming:

$$k_{(\text{RCH}_2\text{O}+\text{O}_2)} = 6.0 \times 10^{-14} \exp(-550/T) \text{ cm}^3 \text{ molecule}^{-1} \text{ s}^{-1}.$$

	Percentage of dissociation, <i>isomerisation</i> (italic characters) and reaction with O₂ (bold characters)							
	Lower troposphere conditions (P = 1 atm ; T = 298K; 20 % O ₂)				Upper troposphere conditions (P = 0.2 atm ; T = 220K; 20 % O ₂)			
	Thermal Activation		Chemical activation		Thermal activation		Chemical activation	
β-hydroxy-ethoxy	74.0	26.0	81.0	19.0	2.5	97.5	25.0	75.0
β-hydroxy-2-propoxy	99.6	0.4	99.9	0.1	92.0	8.0	98.0	2.0
β-hydroxy-1-propoxy	99.7	0.3	99.9	0.1	93.2	6.8	98.3	1.7
β-hydroxy-1-butoxy	98.2	(a) 1.8	98.9	(a) 1.1	59.7	(a) 40.2	75.2	(a) 24.8
β-hydroxy-1-pentoxy	39.4	9.9 0.7	39.2	60.3 0.5	18.4	68.6 12.9	29.0	62.3 8.6
β-hydroxy-1-hexoxy	44.4	4.9 0.7	46.2	53.2 0.5	22.2	65.1 12.6	28.6	61.3 9.9

(a): isomerisation reaction by 1,5-H-atom abstraction from a –CH₃–group is negligible.

From these calculations we conclude that:

- i) the fraction of peroxyxynitrite ROONO* decomposing before thermalisation decreases when the chain-length increases: an increase of the chain-length by one carbon results in a decrease of about 15 % of this fraction (which is 96 % for C₃ radical); at 298 K and 1 atm, still 45 % of C₆ chain-length peroxyxynitrite decomposes before thermalisation.
- ii) under these same pressure and temperature conditions, the fraction of hydroxy-alkoxy radicals which reacts before thermalisation decreases from 75 % for C₃-radical to 20 % for C₆-radical. The C₂ hydroxy-ethoxy with higher dissociation barrier is a particular case with only 30 % of prompt dissociation. iii) tropospheric impact of chemical activation is likely to be important for this last radical specially at the upper troposphere temperature (220 K): the chemically activated radical is predicted to undergo 25 % of dissociation compared with reaction with O₂, instead of 2.5 % for a thermalised radical.
- iii) for ≥ C₃ chain-length hydroxy-alkoxy radicals, the thermal dissociation rate constant, (at 298 K and 1 atm), is two or three orders of magnitude higher than the pseudo-first order rate constant of the reaction with O₂ and thus the impact of a chemical activation is negligible. On the contrary, at 220 K, owing to the higher activation energy for the unimolecular reactions than for the O₂ reaction, the importance of this last reaction is largely enhanced. Therefore, the impact of a chemical activation must be taken into account: by favouring the unimolecular reactions it will decrease the fraction of O₂ reaction, the major effect being predicted for the C₄ radical. For all radicals except the C₂ radical, at low temperature, the unimolecular reactions are predicted to be preponderant, the isomerisation, when possible from a –CH₂– group, being the major way of reaction.

References

- (1) J. J. Orlando, G. S. Tyndall, M. Bilde, C. Ferronato, T. J. Wallington, L. Vereecken, and J. Peeters, *J. Phys. Chem.*, **102**, (1998), 8116.
- (2) L. Vereecken, and J. Peeters, *J. Phys. Chem.*, **103**, (1999), 1768.
- (3) L. Vereecken, J. Peeters, J. J. Orlando, and G. S. Tyndall, C. Ferronato, *J. Phys. Chem.*, **103**, (1999), 4693.

Mechanistic Details of Aromatic Photooxidation derived from the Characterization of Secondary Aerosol Formation (EC – OSA) (Guest)

Montserrat Martín-Reviejo and Klaus Wirtz

Fundación Centro de Estudios Ambientales del Mediterráneo. EUPHORE Laboratories

Charles R. Darwin, 14; 46980 Paterna, Valencia, Spain. montse@ceam.es

Introduction

Aromatic hydrocarbons are known to produce particles during their oxidation in the presence of NO_x . In classical smog chamber experiments a “latent” toluene consumption has been observed previous to the particle formation and dependent on the initial toluene concentration. This behaviour occurs when an intermediate product other than toluene is responsible for the aerosol formation (Izumi and Fukuyama, 1990; Hurley et al., 2001).

This work presents recent studies on secondary aerosol formation during the photooxidation of toluene in smog chamber experiments under realistic conditions. Experiments were performed in the EUPHORE environmental chamber (Spain) with the objective of investigating the reaction channels responsible for aerosol formation during toluene oxidation and the parameters that may control the total amount of aerosols formed in the aromatic system. Thus, aerosol yields were calculated and the values of the toluene threshold for aerosol formation were analysed for experiments in different toluene/ NO_x regimes together with the gas-phase concentrations of primary oxidation products.

Experimental

Experiments were carried out in the atmospheric simulation chamber EUPHORE B that consists of a half-spherical FEP Teflon cover with a volume of 200 m^3 . The chamber is equipped with state-of-the-art analytical instrumentation in order to obtain the concentration-time profiles of reactants and products during the photooxidation of the organic precursor compound, as well as other parameters like the solar light intensity, temperature and pressure in the chamber. A SMPS (Scanning Mobility Particle Sizer) system was used to measure particle size distribution and particle number and volume concentrations. The system consists of a particle counter TSI 3022A CPC and a differential mobility analyser TSI 3081 DMA. Sheath and aerosol sampling flows were 4 L/min and 0.34 L/min , respectively. Aerosol concentrations in $\mu\text{g/m}^3$ were calculated assuming a particle density of 1 g/cm^3 . A new method to perform photosmog experiments was developed and applied to study the oxidation of toluene under very low NO_x concentrations (Martín-Reviejo et al., 1997). The system maintains the NO_x concentration at low, constant levels throughout the experiment by using an active feedback system. The output of a nitrogen-oxides analyser is fed into a control unit which activates a magnetic valve to inject a mixture of HONO, NO_2 and NO 1:1:1 if the concentration of NO_x in the environmental chamber drops below a given set point. This system prevents the strong variations in the VOC/ NO_x and NO/ NO_2 ratios, found during the course of the experimental runs in classic smog chambers.

Results and discussion

The study consisted in carrying out experiments in the presence of NO_x , in very low NO_x concentrations (NO_x -free conditions) and under atmospheric NO_x conditions prevalent in real atmospheres.

The performed experiments fall into three groups (Table 1):

- toluene photooxidation in the absence of NO_x (OH generated by H_2O_2 photolysis),
- toluene photooxidation with a continuous HONO/ NO_x emission (OH generated by HONO photolysis; the NO_x concentration is maintained constant during the irradiation), and

c) classic smog chamber experiments where toluene and NO_x are initially in the chamber.

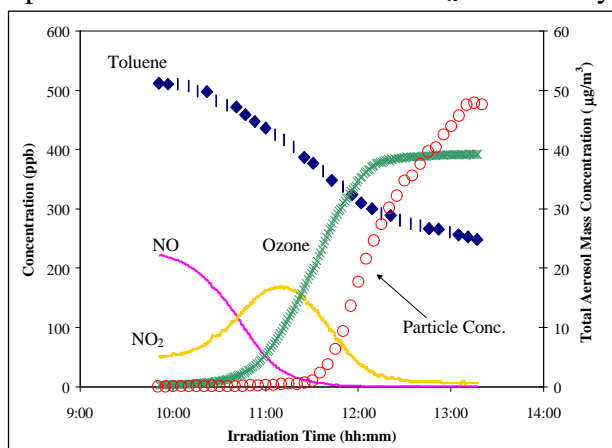


Figure 1: Concentration time profiles of toluene, NO, NO_2 , ozone and total aerosol mass concentration from the irradiation of 500 ppb toluene in the presence of 300 ppb NO_x . The photochemical oxidation of aromatic compounds in the presence of NO_x produces condensable material. This experiment reported an aerosol yield of 13.2 %.

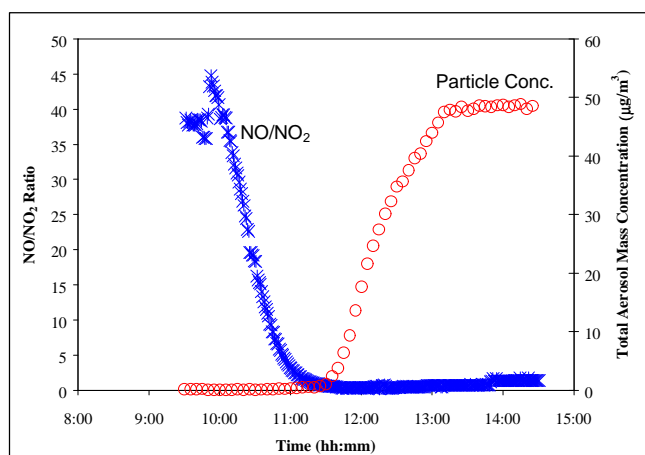


Figure 2: The start of aerosol formation during toluene photooxidation is observed when the conversion of NO into NO_2 is nearly completed (NO/NO_2 below 1). With the control NO_x technique we reduce the NO/NO_2 ratio to the same value where the formation of particles starts in experiments with initial NO_x .

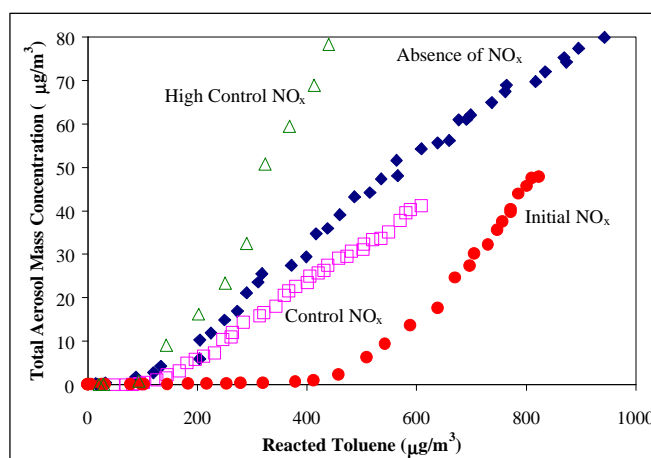


Figure 3: The aerosol mass concentration *versus* the amount of reacted toluene is plotted for different NO_x -regimes. High initial NO concentrations produce a delay in the particle formation and create a pseudo-toluene threshold for aerosol formation with respect to the NO_x -free system. On the

other hand, aerosol yields in the absence of NO_x are slightly higher than the standard control NO_x (5-7 ppb of NO_x), but lower than the high control NO_x (15-17 ppb of NO_x).

The formation of condensable material during the irradiation of toluene in the presence of initial NO_x is observed when NO is nearly completely converted into NO₂ and ozone presents the maximum formation rate (Figure 1). Classical smog chamber experiments are characterized by the strong variation in the experimental conditions during the experiment with respect to the toluene concentration and the NO/NO₂ ratio as can be seen in Figure 2. On the other hand, the photooxidation of toluene in the absence of both NO_x and ozone produces particles in significant yields. The aerosol formation is affected by the initial conditions which, in the case of toluene, produce the scattering of aerosol yields over a wide range (6-14 %) depending on the initial toluene and NO_x concentrations (see Table 1).

Experiment	Toluene/NO _x ppb/ppb	Aerosol Yield %	Toluene Threshold μg.m ⁻³	Product Molar Yields			
				Glyoxal	Methylglyoxal	o-Cresol	CO
Initial NO _x	514/ 55	12.7	270	0.38	0.35	0.15	-
	481/ 150	11.7	300	-	0.33	-	1.5
	500/ 150	13.6	310	-	0.31	-	1.77
	518/ 162	12.0	280	-	0.32	-	2.15
	512/ 300	13.2	410	-	0.31	0.10	3.77
	514/ 509	7.3	590	0.42	0.28	0.13	2.43
Absence of initial NO _x	1056/ + O ₃	10.6	90	-	0.08	-	-
	1042/ + O ₃	10.5	60	-	0.09	-	0.94
	1039	9.7	60	0.15	0.09	0.17	0.90
	2150	23.5	120	0.13	0.09	0.15	0.90
	2100	24.4	112	0.10	0.10	-	-
Control NO _x	500/ 5-7	9.4	100	-	-	-	1.47
	549/5-7 + O ₃	5.7	110	-	0.22	-	-
	517/ 5-7	10.7	160	0.33	0.24	0.13	1.44
	521/ 15-17	26.1	130	-	0.29	-	2.41
	188/ 5-7	8.6	110	-	0.29	-	-
	1910/ 5-7	14.7	160	-	0.22	-	1.17
	2150/ 15-17	18.9	150	0.30	0.22	0.12	1.20

Table 1: Experiments performed in the atmospheric simulation chamber EUPHORE

In all experiments a toluene threshold for aerosol formation (reacted toluene before start of particle formation) is observed depending on the initial NO_x (Figure 3). The experiments with initial NO_x show a high toluene threshold for aerosol formation, which increases with increasing amounts of initial NO_x (see Table 1). The toluene threshold is significantly lower in experiments where the NO/NO₂ ratio is held constant and in the experiments without NO_x. During control NO_x experiments the start of particle formation is not affected by the presence of NO because the NO_x concentration is maintained constant and low throughout the experiment (atmospheric relevant). Gas-phase oxidation products typically coming from the fragmentation of the ring, such as glyoxal and methylglyoxal, show lower molar yields under NO_x-free conditions than in the presence of NO_x. CO presents significantly lower molar yields under NO_x-free conditions.

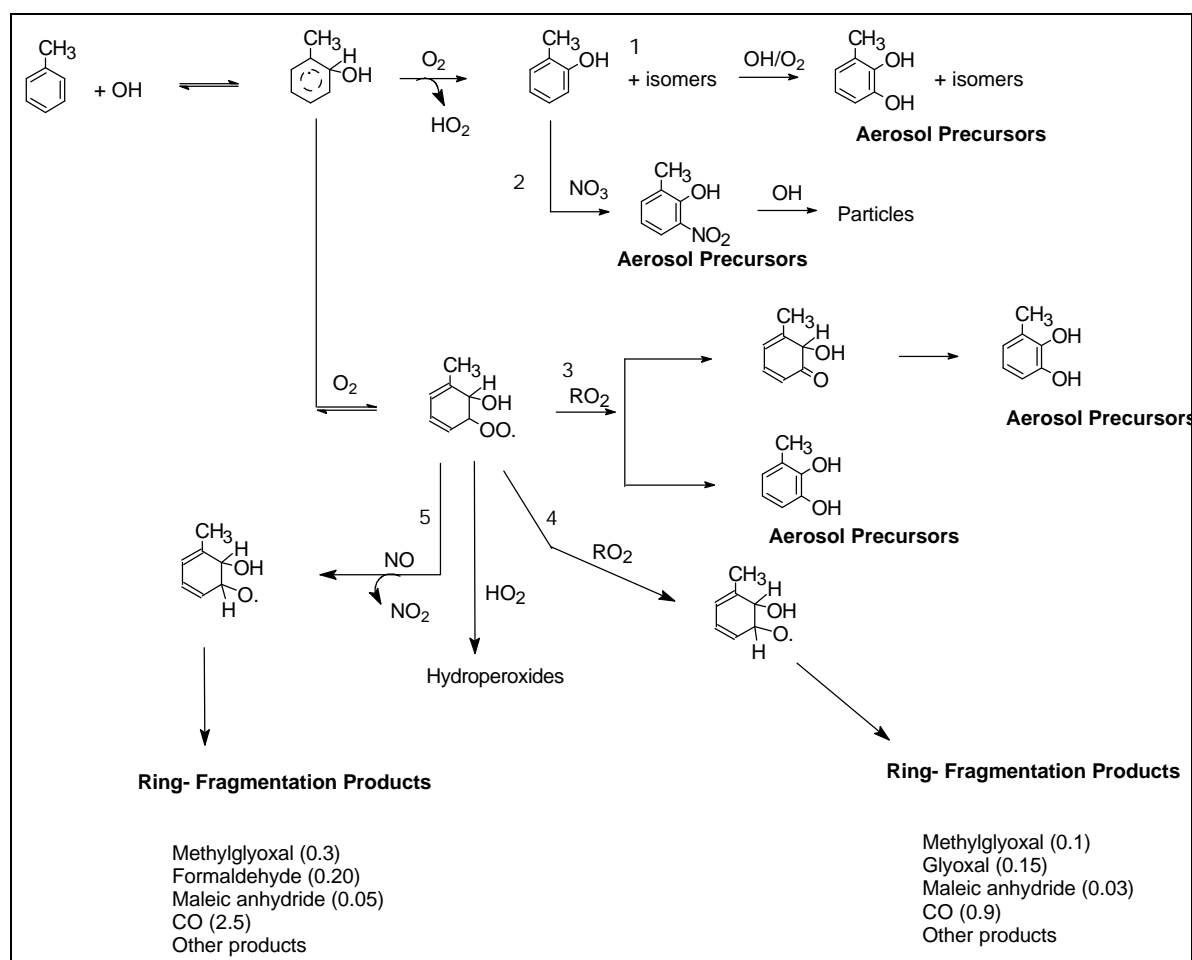


Figure 4: Simplified tentative mechanistic channel to explain the aerosol formation during the photochemical oxidation of toluene.

Figure 4 shows the proposed mechanism to explain the aerosol formation during the photochemical oxidation of toluene in the presence and in the absence of NO_x.

In the absence of NO_x, channels 1, 3 and 4 will determine the oxidation pathways. Particle formation in the NO_x-free system is observed with aerosol yields of 10 %. Lower molar yields of the ring-fragmentation products than in the presence of NO_x means that channel 4 is not favoured under NO_x-free conditions. Hence, the reaction of the peroxy radical with itself or with other RO₂ via channel 3 will cause the formation of methyl-dihydroxybenzenes, which can act as aerosol precursors. The oxidation of cresols via channel 1 also produces methyl-dihydroxybenzenes in very high yields (Olariu et al., 2002). Methyl-dihydroxybenzenes can produce particles by reactions with OH and O₃ (when there is ozone formation). This last reaction does not affect the aerosol yields significantly.

In the presence of initial NO_x, the peroxy radical will react with NO via channel 5 without particle formation, producing the fragmentation of the ring. This channel is favoured under these conditions because the ring-cleavage products show higher molar yields in the presence of NO_x than in the absence of NO_x. At this stage of the oxidation, channel 1 will not contribute to the aerosol formation because the condensable product does not reach the saturation concentration. The presence or absence of NO_x does not affect significantly the o-cresol molar yields (see Table 1). The start of particle formation will depend on the presence of NO in the system. The formation of a significant amount of particles coincides with the complete conversion of NO into NO₂ as well as with the maximum ozone formation. These conditions favour the formation of the nitrate radical NO₃ and the possible reaction of this radical with cresols initiating a reaction channel that may be

responsible for the initial aerosol formation during the photochemical oxidation of toluene in the presence of NO_x . The direct reaction of cresol with NO_3 does not produce particles, but the oxidation products, nitrocresols, can act as aerosol precursors.

Conclusions

- Nitrogen oxides, and in particular NO , are key species controlling particle formation during the photochemical oxidation of toluene.
- There is a competition between OH and NO_3 radicals to form secondary products that act as aerosol precursors, and therefore a dependence of aerosol formation on the NO_x content in the system is observed. The presence of ozone does not affect the aerosol yields.
- Ring-retaining products are major contributors to aerosol formation in the toluene system. Methyl-dihydroxybenzenes and nitro-cresols are likely the major aerosol precursors for particle formation by reactions with OH /ozone and NO_3 . Without a complete characterization of the aerosol chemical composition it is not possible to exclude the contribution from ring-fragmentation products to the total aerosol mass.

Acknowledgement

This work has been partially funded by the European Commission, DG Research, within contract EVK2-1999-00016 "OSOA" and by the Ministerio de Medio Ambiente within project REN2000-3277-CE/CLI. The CEAM Foundation is supported by the Generalitat Valenciana and BANCAIXA.

References

- Hurley, M. D., O. Sokolov, T. J. Wallington, H. Takekawa, M. Karasawa, B. G. Klotz, I. Barnes and K. H. Becker; Organic aerosol formation during the atmospheric degradation of toluene, *Environ.Sci.Technol.* 35 (2001) 1358-1366.
- Izumi, K. and T. Fukuyama; Photochemical aerosol formation from aromatic hydrocarbons in the presence of NO_x , *Atmos.Environ.* 24A (1990) 1433-1441.
- Martin-Reviejo M., M. Pons Nicolau, K. Wirtz, T. Etzkorn and J. Senzing; An outdoor smog chamber study of the gas-phase chemistry of toluene and xylenes in the NO_x /air systems, in: B. Larsen, B. Versino, and G. Angeletti (eds.), *Proc. of the seventh European Symposium on Physico-Chemical Behaviour of Atmospheric Pollutants, Air Pollution Res. Rep. EUR 17482 EN*, CEC, Brussels (1997) 350-354.
- Olariu R.I., B. Klotz, I. Barnes, K.H. Becker, R. Mocanu; FT-IR study of the ring-retaining products from the reaction of OH radicals with phenol, o-, m-, and p-cresol; *Atmos. Environ.* 36 (2002) 3685-3697.

Development of explicit chemical schemes for tropospheric VOC oxidation – a self generating approach- (Guest)

Laval-Szopa S. (1), Aumont B. (1), Madronich S.(2)

(1) Laboratoire Interuniversitaire des Systèmes Atmosphériques LISA,UMR CNRS 7583 Universités ParisVII - Paris XII, Créteil

(2) NCAR, Boulder Colorado USA

laval@lisa.univ-paris12.fr

General frame

VOCs emitted into the atmosphere are oxidized in complex reaction sequences that produce a much larger number of intermediates (e.g. oxy, peroxy, and Criegee radicals; ketones, aldehydes, alcohols, nitrates, peroxides, carboxylic acids and peracids – often multifunctional). These intermediates play a key role in the formation of tropospheric ozone and in the HOx and NOx budgets on regional and global scales. Most of secondary VOC are multifunctional species having low vapor pressure and high Henry's law coefficient. These secondary VOC probably play an important role in cloud chemistry and microphysics and in the formation of organic aerosols. Although the cumulative importance of these intermediates is widely acknowledged, their estimated number far exceeds that for which direct laboratory measurements are available. However, reasonable estimates for their reaction kinetics and pathways can be made by analogy to known reactions, with the aid of several structure-activity relations (SARs). The main goal of the generator is to codify the various estimation methods to generate explicit reaction pathways, and the associated kinetics, for the oxidation of specified VOCs down to one carbon species (for which direct laboratory data are then available).

The generator

The generator is simply a computer program that mimic the steps by which chemists develop chemical schemes (i.e. the list of the reactions involved in the oxidation of a given species and their associated rate constants). These steps can be summarized as follow. First the generator analyses the chemical structure of the molecule to identify all its possible reaction pathways. For each identified reactions, the generator then “searches” if laboratory measurements are available for the rate constant and/or the distribution of the reaction products. If not (as it is usually the case), estimation of the rate constant and the reaction products is made based on structure/activity relationships. The reaction (reactants, products, stoichiometry and rate constant) is then written in a file and, if new, the reaction products added to a “stack” for further reactions. These steps are repeated as long as species are added to stack. The process stops when the stack is empty, meaning that the full oxidation scheme has been written for the parent compounds. A flow diagram of the chemical generator is given figure 1.

The chemical schemes given as output are in fact very similar to schemes “handwritten” by chemists. However, the self generating approach has significant advantages, namely:

- its speed: explicit chemical schemes usually contains thousands of reactions and handwriting such schemes requires months of work. In fact, fully explicit chemical schemes are extremely large (see examples below) and far exceed what can reasonably be done by hand. A self-generating approach is probably the only realistic approach to develop such fully explicit schemes.
- accuracy: it is almost impossible to write large schemes without introducing “errors” (for example in setting the rate constants or simply typographical errors in naming the species).
- maintenance: updating chemical scheme can be a very tedious task. This is particularly true when the scheme must be updated as a result of a change in a SAR. Updating problems can be very easily resolved with the generator approach.

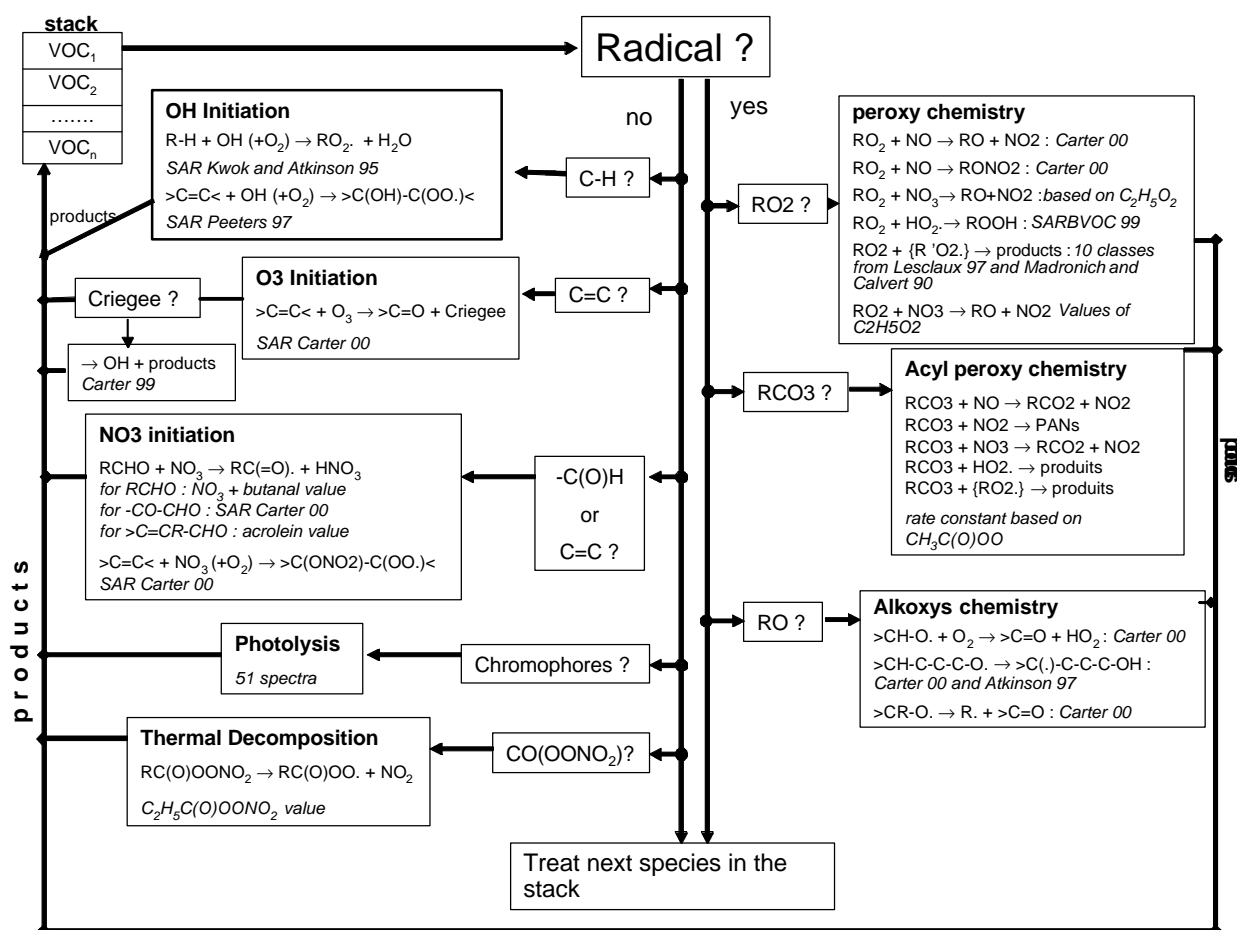


Figure 1: Flow diagram for the generator

The generator can therefore be viewed as an expert system, assimilating physico-chemical data coming out from laboratory experiments (rate constants, vapor pressure, products yields, ...) and estimating all the missing information. It is a very natural link between fundamental laboratory studies and the chemical models.

The current version of the generator (version 1.0) treats the chemistry of every species (C, H, O, N) except cyclic molecules. The chemistry of cyclic molecules (up to ring-opening) is actually read in a file and corresponding mechanisms are added to the generator output file. The version 1.0 is based on up-to-date data for the rate constants, photolysis, and structure/activity relationships.

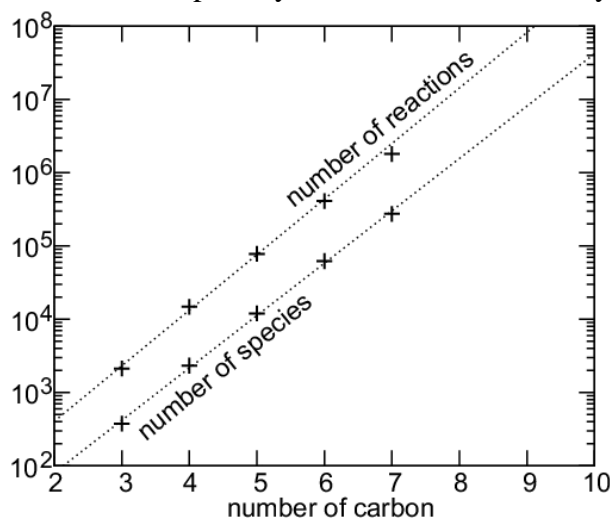


Figure 2: Number of species and reactions created by the generator for the n-alkane series.

Output examples and first tests

Figure 2 shows the number of species and reactions generated for the n-alkane series as a function of the number of carbon atoms. The number of species generated is extremely large, growing from a few hundred for propane to about 1 million for octane. Number of reactions is typically five times larger than the number of species.

To test the relevance of the schemes made by the generator, some comparisons were made with well-established chemical schemes: the SAPRC99 schemes developed by Carter [1] and the Leeds scheme developed by Jenkin and co-workers [2][3]. The simulations were made using a 2 layers box model for typical urban summertime conditions and in which the emissions were only expressed in term of alkanes and alkenes (to avoid any confusion linked to the aromatic schemes not truly “generated” by the generator). A fairly good agreement between the 3 chemical schemes was found, at least for those species represented in the smaller mechanisms.

A second set of comparisons was made for high latitude conditions (“TOPSE” conditions) with the NCAR master mechanism. The 2 schemes were integrated using 2 different solvers, a “Gear” solver for the NCAR master mechanism and the solver “2step” for the generator scheme. In this comparison, the 2 sets of results are thus fully independent. Results are given figure 3 for some species.

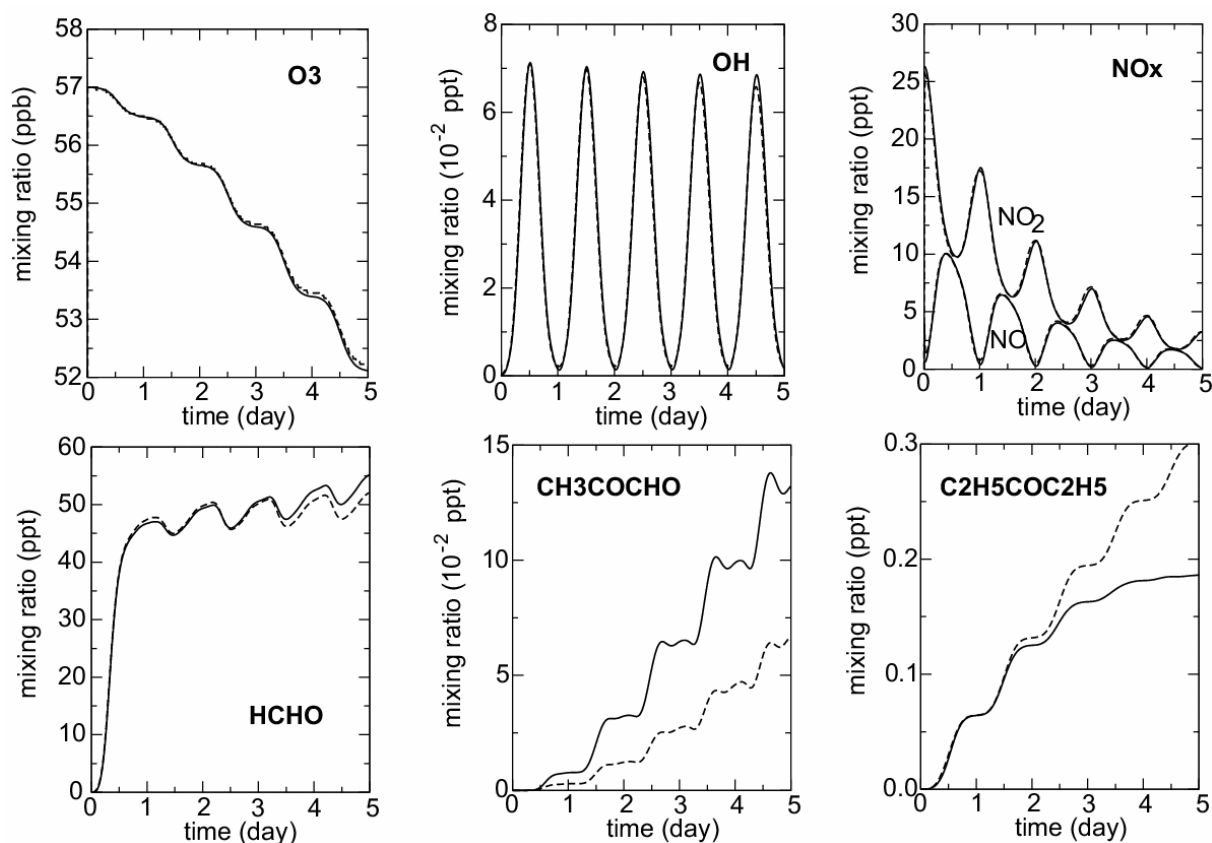


Figure 3: Comparison of the NCAR master mechanism (dotted line) and the generator scheme (solid line) for high latitude free tropospheric conditions.

The 2 schemes reproduce almost identical concentrations for NO_x, OH, O₃ and HCHO but significant discrepancies in some secondary VOC was found.

All the tests performed so far did not highlight “bugs” in the schemes produced by the generator nor major skews induced by the time integration of huge numbers of reactions and species.

Some very preliminary simulations were also performed to figure out the oxidation pathway of large VOC. Figure 4 shows the time concentration profiles simulated for an initial load of 7 ppbC heptane under fixed T and NO_x (here 1ppb) conditions. Figure 4 shows only very little carbon loss (a few ppt); this result is satisfying since the numerical method implemented in 2step is not mass conserving. For the heptane scheme, we solved the chemistry of about 2.7×10⁵ species and 1.6×10⁶

reactions. For these conditions, heptane is almost totally removed in about 1 day but the fraction of organic carbon actually remains significant even after 2 days. This organic fraction is dominated by species holding 7 carbons, i.e. of same size than the parent compound. Figure 4 shows how these C7 species are distributed as a function of the number of functional group borne by the molecule. Organics appear to have typically 2 or more functional groups. The most abundant functionalities found were carbonyl, nitrate and alcohol functions with a predominance of the ketone function. Two functional group species are expected to have a Henry's law coefficient high enough to be almost totally dissolved in aqueous droplets during a cloud events. Furthermore, a non-negligible fraction is found to bear at least 4 functional groups. Vapor pressure for these kinds of species are very small, so that these compounds may be precursors for the formation of Secondary Organic Aerosols (SOA).

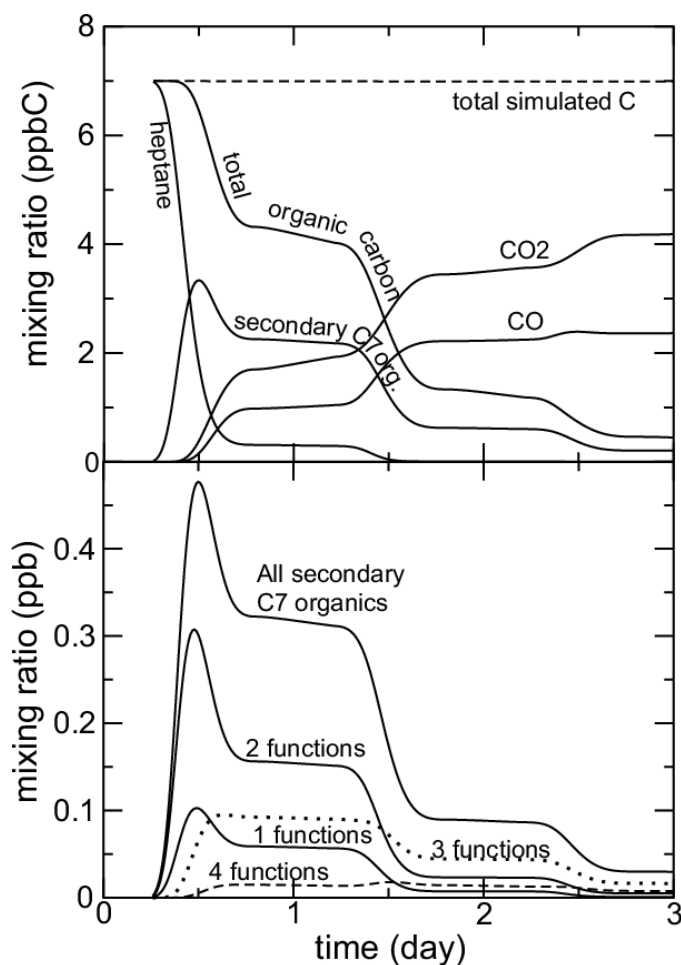


Figure 4: Evolution of carbonaceous species during the oxidation of heptane. Top panel : distribution of the carbon. Bottom panel : distribution of secondary organic C7 species as a function of the number of functional group borne by the molecule.

For the n-alkane series (up to C8), some crude estimates of SOA formation yield were made by assuming that all the 4 functional groups species are SOA precursors. The orders of magnitude as well as the trend in the series were found to agree pretty well with smog chamber results. Although very preliminary, these results are very promising and show the potential of the self-generating approach for the development of multiphase organic chemical schemes.

Future developments

A very promising application of the generator is to model SOA formation. Current models describing SOA formation are developed on a fully empirical basis (based on yields measured in smog chambers) and may not be always relevant for atmospheric applications. The fundamental

processes leading to SOA formation in the atmosphere still need to be clarified. The main difficulties lie in describing the sources and sinks of the myriad of VOC expected to contribute to SOA, as well as their thermodynamic equilibrium with condensed phases. The generator is clearly a powerful tool to study SOA formation by its ability to explicitly describe the chemical dynamics of the various precursors. A thermodynamical “module” still has to be developed. This requires the estimation of few physico-chemical parameters for each organic precursor, especially its vapor pressure and its chemical activity in a given condensed phase. Methods are available to estimate these parameters using group contribution methods (e.g. the UNIFAC method) and could “easily” be implemented in the generator.

Furthermore, organic chemistry inside cloud droplets raises many questions, including, without order of priority:

- Does organic oxidation inside cloud significantly contribute to the formation of organic acids ?
- Does organic oxidation inside cloud play a role in the Ox/HOx budget ?
- What fraction of the organic carbon is removed by a rain event ?
- Is organic oxidation inside cloud a significant sink for the volatile organic matter ?
- Is organic oxidation inside cloud a source of organic aerosol after the evaporation of the cloud droplet ?

Answering this kind of questions by a modeling approach clearly requires the development of chemical schemes describing the organic oxidation in the aqueous phase. Currently, laboratory studies dealing with the oxidation in atmospheric aqueous phases receive a growing interest and the available kinetic database for these processes is becoming substantial. The self-generating approach will be extended to the aqueous phase chemistry.

References :

- [1] **Carter W.P.L.** (2000), Report to California air resources board, contract 92-329 and 95-305.
- [2] **Jenkin M.J., Saunders S.M., Pilling M.J.** (1997), “The tropospheric degradation of volatile organic compounds: A protocol for mechanism development” *Atmospheric Environment* Vol.31, N°1 p81-104
- [3] **Saunders S.M.** et al. (1997), “World wide web site of master chemical mechanism (MCM) for use in tropospheric chemistry models”. *Atmospheric Environment* Vol.31, N°8 p1249 [Mechanism available on <http://chmlin9.leeds.ac.uk/MCMframe.html>]

Is the Acetylperoxy Radical $\text{CH}_3\text{C}(\text{O})\text{O}_2$ a Good Model for $\text{RC}(\text{O})\text{O}_2 + \text{HO}_2$ Reactions ? (GPP-Guest)

¹Jean Paul Le Crâne, ^{1,2}Alexandre Tomas and ¹Eric Villenave*

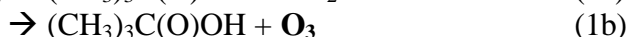
¹Laboratoire de Physico-Chimie Moléculaire, UMR 5803 CNRS, Université Bordeaux I, 33405 Talence Cedex France

²Ecole des Mines de Douai, BP 898, 59508 Douai Cedex France
e-mail :eric.villenave@lpcm.u-bordeaux.fr

Introduction

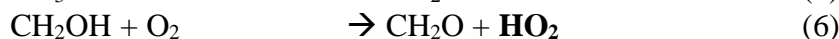
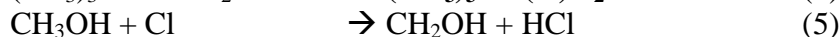
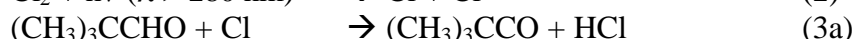
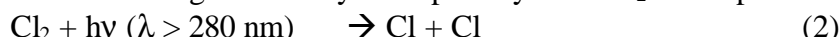
In the atmosphere, acylperoxy radicals are formed by hydrogen abstraction from aldehydes and combination with O_2 . Firstly, they may undergo fast reactions with other peroxy radicals and with nitrogen oxides which have a significant influence on ozone formation. Secondly, in polluted atmospheres, the association reaction with NO_2 may form peroxyacylnitrates $\text{RC}(\text{O})\text{O}_2\text{NO}_2$ which are recognized as severe irritants of photochemical smog. Moreover, due to their high stability in polluted atmospheres, compared to other peroxy nitrates, they are efficient reservoirs of NO_x in troposphere and they contribute to the transport of NO_x species far away from sources.

The objective of this study was to investigate the kinetics of $\text{RC}(\text{O})\text{O}_2 + \text{HO}_2$ reactions as these reactions are important termination reactions as they may lead to the formation of ozone. We have first started to study the $(\text{CH}_3)_3\text{CC}(\text{O})\text{O}_2 + \text{HO}_2$ reaction to evaluate the effect of substitution of H atoms by methyl groups on the reactivity of the acetylperoxy radical $\text{CH}_3\text{C}(\text{O})\text{O}_2$ which is used to now as a model for all acylperoxy radicals in chemical models of the tropospheric chemistry.



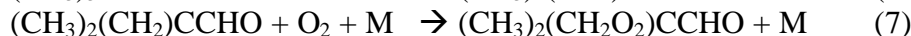
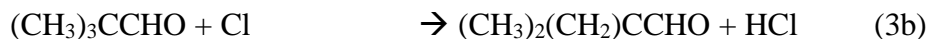
Experimental

Experiments were performed at room temperature and atmospheric pressure. Flash photolysis technique coupled to UV absorption spectrometry was used for real time radical monitoring in order to measure the branching ratio of the $(\text{CH}_3)_3\text{CCHO} + \text{Cl}$ reaction, the rate constant of $(\text{CH}_3)_3\text{CC}(\text{O})\text{O}_2 + \text{HO}_2$ reaction and the branching ratio leading to the formation of ozone. The experimental set-up was already described in details in preceding publications (Lightfoot et al. (1990)). Radicals were generated by flash photolysis of Cl_2 in the presence of appropriate precursor:



Results

In their study of the atmospheric degradation mechanism of acetaldehyde, Beukes et al. (2000) suggest that the attack of chlorine atoms on hydrogens atoms from the methyl group (CH_3CHO) represents less than 5% of the total $\text{CH}_3\text{CHO} + \text{Cl}$ reaction pathways (the other way being the chlorine attack on the aldehydic hydrogen (CH_3CHO) to form the acetyl radical). In this work (for $(\text{CH}_3)_3\text{CCHO}$), experimental curves could never be well simulated without taking into account 12% of initial formation of the $(\text{CH}_3)_2(\text{CH}_2)\text{CCHO}$ radical (see Figure 1 below)



Decay traces, systematically recorded at 207 and 240 nm (corresponding to the maximum absorption of $(\text{CH}_3)_3\text{CC}(\text{O})\text{O}_2$ and $(\text{CH}_3)_3\text{CCO}_2$ radicals respectively), were simulated by taking the complete chemical mechanism into account. The main kinetic information was derived from traces recorded at 207 nm where the concentration and the absorption cross sections of $(\text{CH}_3)_3\text{CC}(\text{O})\text{O}_2$ were larger than those of other absorbing species in the system. Experimental traces recorded at 240 nm were flat because $(\text{CH}_3)_3\text{CC}(\text{O})\text{O}_2$ is principally converted during the reaction into $(\text{CH}_3)_3\text{CCO}_2$, both radicals presenting a similar absorption cross section at 240 nm. Therefore, no kinetic information could be deduced from those experimental decays, even if such traces provide additional information on the mechanism (Figure 1).

Self-Reaction rate constant of $(\text{CH}_3)_3\text{CC}(\text{O})\text{O}_2$ has also been measured in this study:

$$k((\text{CH}_3)_3\text{CC}(\text{O})\text{O}_2 + (\text{CH}_3)_3\text{CC}(\text{O})\text{O}_2) = (1.46 \pm 0.32) \times 10^{-11} \text{ cm}^3 \text{ molecule}^{-1} \text{ s}^{-1}$$

This value is in good agreement with that previously measured by Tomas et al. (2000) using Br atoms as initiators ($k = 1.41 \times 10^{-11} \text{ cm}^3 \text{ molecule}^{-1} \text{ s}^{-1}$).

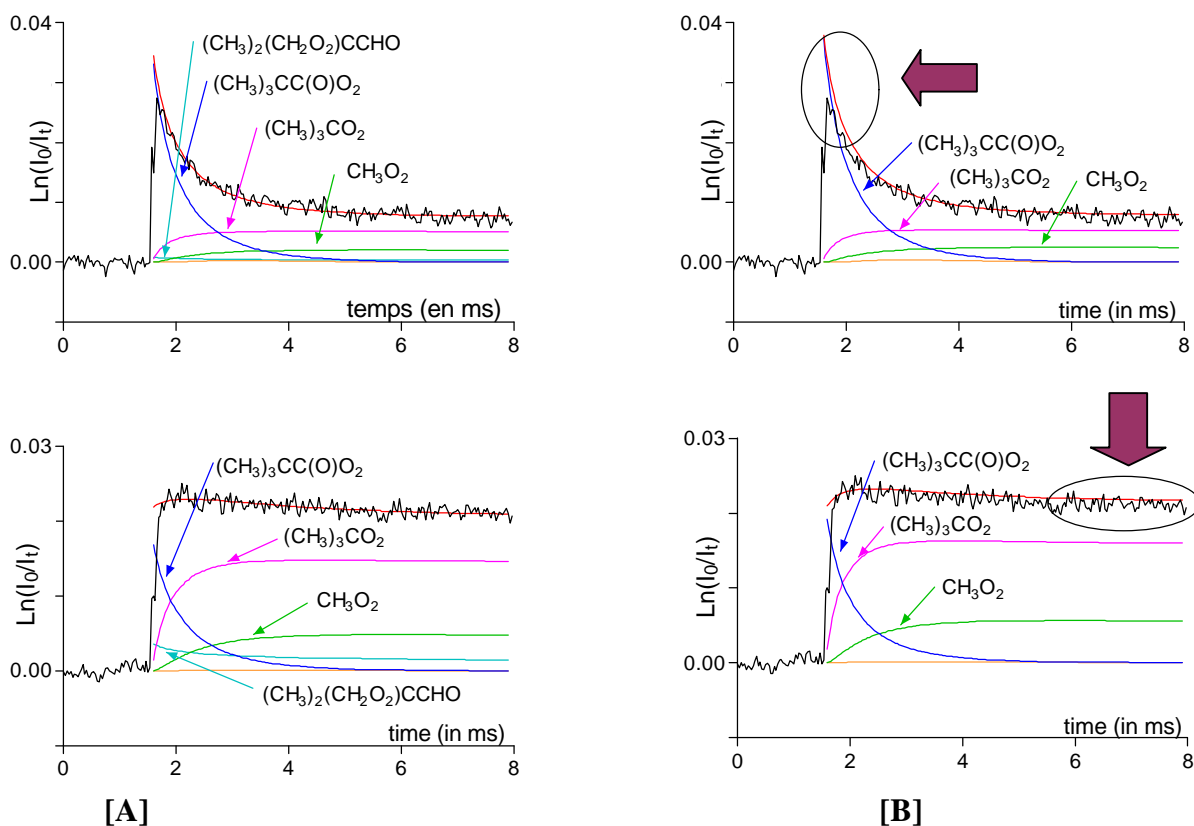


Figure 1. Experimental decays at 207 nm (top) and 240 nm (bottom) of trimethylacetylperoxy radical self reaction [A] : with 12% of $(\text{CH}_3)_2(\text{CH}_2\text{O}_2)\text{CCHO}$ radical formation [B] : With no formation of $(\text{CH}_3)_2(\text{CH}_2\text{O}_2)\text{CCHO}$

In order to investigate the kinetics of the $((\text{CH}_3)_3\text{CC}(\text{O})\text{O}_2 + \text{HO}_2)$ reaction, concentrations of precursor ($(\text{CH}_3)_3\text{CCHO}$ and CH_3OH) and the rate constant ratio k_3/k_5 have to be accurately known to measure the initial concentrations of $(\text{CH}_3)_3\text{CC}(\text{O})\text{O}_2$ and HO_2 radicals, according to :

$$\frac{[(\text{CH}_3)_3\text{CC}(\text{O})\text{O}_2]_{\text{ini}} + [(\text{CH}_3)_2(\text{CH}_2\text{O}_2)\text{CCHO}]_{\text{ini}}}{[\text{HO}_2]_{\text{ini}}} = \frac{k_3 \times [(\text{CH}_3)_3\text{CCHO}]}{k_5 \times [\text{CH}_3\text{OH}]}$$

As in the case of $(\text{CH}_3)_3\text{CC}(\text{O})\text{O}_2$ radical self reaction, traces recorded at 240 nm are fairly flat whereas traces recorded at 207 nm are representative of the kinetics of the $(\text{CH}_3)_3\text{CC}(\text{O})\text{O}_2 + \text{HO}_2$ reaction. The rate constant was measured at 207 nm and the branching ratio $\beta = k_{1b}/k_1$, leading

to the formation of ozone was measured at 240 nm, where ozone absorbs significantly (see Figure 2.).

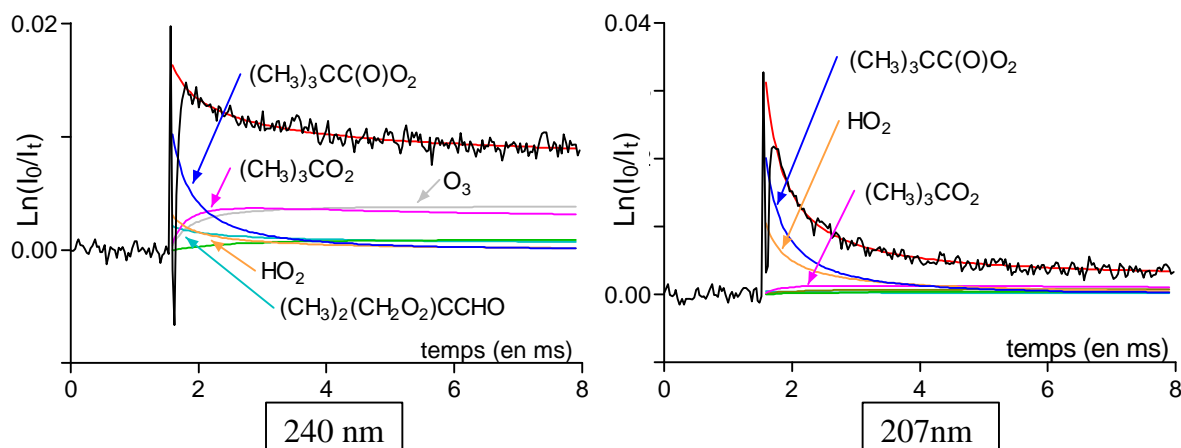


Figure 2. Experimental decays recorded at 207 nm and 240 nm for the $(\text{CH}_3)_3\text{CC}(\text{O})\text{O}_2 + \text{HO}_2$ reaction

Measurements of the $(\text{CH}_3)_3\text{CCHO} + \text{HO}_2 \rightleftharpoons (\text{CH}_3)_3\text{CCH}(\text{OH})\text{O}_2$ equilibrium constant show that the equilibrium is totally shifted to the aldehyde and the hydroperoxy radical. Therefore this reaction will not interfere in the mechanism, unlike the case of CH_3CHO where it was previously observed. Results for the rate constant of the $(\text{CH}_3)_3\text{CC}(\text{O})\text{O}_2 + \text{HO}_2$ reaction and the branching ratio β at 298 K are :

$$k_1 = (4,62 \pm 0,52) \times 10^{-11} \text{ cm}^3 \text{ molécule}^{-1} \text{ s}^{-1} \text{ with } \beta = (0,25 \pm 0,02)$$

This rate constant is three time larger than the rate constant of the $\text{CH}_3\text{C}(\text{O})\text{O}_2 + \text{HO}_2$ reaction (Tomas et al. (2001)) ($k = 1,4 \times 10^{-11} \text{ cm}^3 \text{ molécule}^{-1} \text{ s}^{-1}$). This suggests that the rate constant of the reactions of acylperoxy radicals with HO_2 is increasing with the radical substitution. The next step will be the study of isobutyraldehyde to check the trend observed in this work.

References

- Lightfoot, P.D., R. Lesclaux, B. Veyret; Flash photolysis study of the $\text{CH}_3\text{O}_2 + \text{CH}_3\text{O}_2$ reaction: Rate constant and branching ratio from 248 to 573 K, *J. Phys. Chem.* **94** (1990) 700.
- Beukes, J.A., B. D'Anna, V. Bakken, C.J. Nielsen; Experimental and theoretical study of the F, Cl and Br reactions with formaldehyde and acetaldehyde, *Phys. Chem. Chem. Phys.* **2**(18) (2000) 4049-4060.
- Tomas, A., R. Lesclaux, Self reaction kinetics of the $(\text{CH}_3)_2\text{CHC}(\text{O})\text{O}_2$ and $(\text{CH}_3)_3\text{CC}(\text{O})\text{O}_2$ acylperoxy radicals between 275 and 363 K, *Chemical Physics Letters* **319** (2000) 521-528.
- Tomas, A., E. Villenave, R. Lesclaux, Reaction of the HO_2 Radical with CH_3CHO and $\text{CH}_3\text{C}(\text{O})\text{O}_2$ in the Gas Phase, *J. Phys. Chem. A* **105** (2001) 3505.

FT-IR Investigations on the Gas-Phase Reactions of the NO₃ and OH Radicals with a Series of Benzenediol Compounds (GPP1)

Iustinian Bejan^{1,2}, Romeo I. Olariu^{1,2}, Ian Barnes¹, Thorsten Benter¹ and Klaus Wirtz³

¹*Bergische Universität Wuppertal, FB 9 - Physikalische Chemie, Gaußstraße 20, D-42097 Wuppertal, Germany*

²*“Alexandru Ioan Cuza” University of Iasi, Faculty of Chemistry, Department of Analytical Chemistry, Carol I Boulevard 11, 6600 Iasi, Romania*

³*Centro de Estudios Ambientales del Mediterraneo (CEAM), Parque Tecnológico, Calle 4, Sector Oeste, E - 46980 Paterna, Valencia, Spain*
barnes@uni-wuppertal.de

Summary

As parts of a systematic study of the gas phase atmospheric chemistry of dihydroxybenzenes (catechols), we present here preliminary results from studies on their reactions with NO₃ and OH radicals.

The kinetics of the reaction of NO₃ with the aromatic vicinal diols 1,2-benzenediol, 3-methyl-1,2-benzenediol and 4-methyl-1,2-benzenediol have been investigated in 2 different reactors using a relative rate technique. The rate coefficients obtained using 2,3-dimethyl-2-butene as reference hydrocarbon are:

$$k_{\text{NO}_3}(1,2\text{-dihydroxybenzene}) = (9.84 \pm 4.0) \times 10^{-11} \text{ cm}^3 \text{ s}^{-1},$$

$$k_{\text{NO}_3}(1,2\text{-dihydroxy-3-methylbenzene}) = (17.05 \pm 5.3) \times 10^{-11} \text{ cm}^3 \text{ s}^{-1}$$

$$k_{\text{NO}_3}(1,2\text{-dihydroxy-4-methylbenzene}) = (14.7 \pm 5.6) \times 10^{-11} \text{ cm}^3 \text{ s}^{-1}.$$

Product studies on the reaction of the benzenediols with OH using the FT-IR technique for product detection indicate the formation of maleic anhydride (2,4-furandione), an unknown ketene product and also possibly organic nitrates in the reaction system.

Introduction

Phenols are produced in atmosphere in the reactions of OH with BTX (benzene, toluene, xylene isomers) in substantial yields, benzene producing phenol (Atkinson, 1994; Calvert et al., 2001; Volkamer et al., 2002), toluene a mixture of *o*-, *m*- and *p*-cresols (Atkinson et al., 1989; Klotz et al., 1998; Smith et al., 1998) and the xylene isomers a series of hydroxydimethylbenzenes (Smith et al., 1999). Recent studies in Wuppertal have shown that the major products in the OH-radical initiated oxidation of phenols are benzenediols (also known as dihydroxybenzenes or catechols) (Olariu et al., 2002).

Catechols have also many industrial applications, i.e. in dyes and drugs production, production of antioxidants in rubber and oil industries, photographic and ink industry (Flickinger et al., 1976). Significant amounts of catechols have also been found in the particulate phase from both the wounding and burning of wood (Fine et al., 2002). Catechol is a strong mutagenic and carcinogenic aromatic compound (Li et al., 1997).

Benzenediols have been shown to react rapidly with OH radicals (Olariu et al., 2000) and in a recent study from the present work group, it has been shown that benzenediols also react significantly fast with O₃. (Tomas et al., 2002). It is expected that benzenediols will also be extremely reactive towards NO₃ radicals. The nitrate radical is the most important night-time oxidizing species, removing, for example, hydrocarbons, which would otherwise be available for daytime ozone formation. In the case of phenolic aromatic compounds, which have rate constants for reaction with NO₃ radicals comparable to those for OH, the NO₃ radical is probably an important oxidant even during daytime (Calvert et al., 2002).

Apart for rate constants for the reaction of OH radicals and O₃ with these compounds (Olariu et al., 2000, Tomas et al., 2002), nothing is presently known about the atmospheric

chemistry of 1,2-benzenediols. Here, investigations on the kinetics of the reaction of NO₃ radicals with three benzenediols are presented along with preliminary results from product studies of their reaction with OH radicals.

Experimental

EUPHORE Chamber. NO₃ kinetic experiments were performed using the European Photoreactor (EUPHORE) located on top of the building of the Centro de Estudios Ambientales del Mediterraneo (CEAM) near Valencia, Spain (Becker, 1996). Chamber A, used for the experiments presented here, consists of a 200 m³ hemispherical FEP bag and contains a White mirror system, operated at an optical path of 326.8 m, for *in situ* measurement of the reaction mixtures by FTIR spectroscopy. Additional analytical techniques included an NOx analyzer (ECO-Physics CLD 770 AL NO-analyzer with photolytic NO₂ converter PLC 760) and an ozone monitor.

The benzenediolic compounds were added to the chamber using a spray inlet system and 2,3-dimethyl-2-butene and NO₂ were injected by means of a syringe into a glass tube (impinger) connected to the chamber by a Teflon line. The initial reactant concentrations were (in molecules cm⁻³ units): the reactant organics, (5 - 7.2) x 10¹² and NO₂, (0 - 7) 10¹². N₂O₅, was produced by titration of a flow of NO₂ with O₃.

Wuppertal chamber. Both the NO₃ kinetic and OH product experiments were performed in a darkened cylindrical quartz reactor with a volume of 1080 l (6.2 m length and 47 cm inner diameter) in 760±10 Torr of synthetic air at 298±2 K. A White mirror system located inside the chamber and operated at an optical path of (484.7 ± 0.8) m was used for *in situ* measurement of the reaction mixtures by FTIR spectroscopy (Barnes et al., 1994).

The aromatic compounds investigated being solid were transferred to the gas phase by gently heating weighed amounts in a low-pressure nitrogen flow. Other gaseous (NO₂) and liquid reagents (2,3-dimethyl-2-butene) were introduced using calibrated syringes with the reactor under reduced pressure. The initial reactant concentrations were (in molecules cm⁻³ units): the reactant organics, (1.2 - 4.8) x 10¹³ and NO₂, (0 - 2.4) 10¹⁴. N₂O₅ was added continuously to the reaction mixture through a glass inlet line by evaporating solid N₂O₅.

Kinetic method. In both chambers rate coefficients for the reaction of NO₃ radicals with 1,2-benzenediol, 3-methyl-1,2-benzenediol and 4-methyl-1,2-benzenediol were determined using a relative kinetic technique. NO₃ radicals were generated by thermal decomposition of N₂O₅:



2,3-Dimethyl-2-butene was employed as reference organic compound with a recommended rate coefficient of k(2,3-dimethyl-2-butene + NO₃) = 5.72 x 10⁻¹¹ (Atkinson, 1994).

In the presence of NO₃ radicals, both the aromatic and the reference compound will react:



The aromatic compounds are also lost to the surface of the reactor:



No wall deposition was observed for the reference hydrocarbon. Integrating and combining these two equations yields the following relationship:

$$\ln \frac{[\text{aromatic}]_{t_0}}{[\text{aromatic}]_t} - k_{\text{wall}}(t - t_0) = \frac{k_1}{k_2} \ln \frac{[\text{reference}]_{t_0}}{[\text{reference}]_t}$$

Results and observations

Kinetic results. Plots of the results according to eq (I) from the EUPHORE chamber are displayed in Figure 1. For each aromatic compound, at least three experiments were performed using different aromatic hydrocarbon and NO₂ concentrations. No effect on variation the initial NO₂ concentration was observed and good linear plots were obtained.

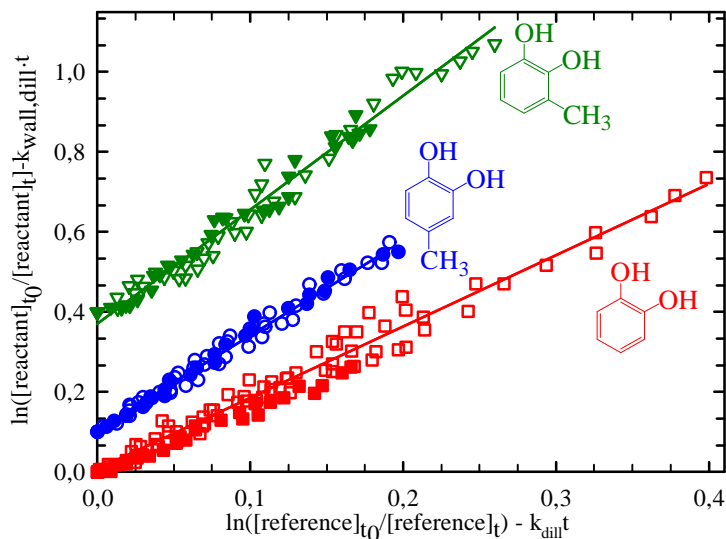


Figure 1: Plots of the EUPHORE chamber kinetic data according to eq. I for the gas-phase reaction of the NO₃ radical with **1,2-benzenediol**, **3-methyl-1,2-benzenediol** and **4-methyl-1,2-benzenediol** relative to **2,3-dimethyl-2-butene**. For clarity, the data for **3-methyl-1,2-benzenediol** and **4-methyl-1,2-benzenediol** have been displaced vertically by 0.4 and 0.125 units, respectively. The open symbols are for the low NO₂ concentration experiments and the full symbols are for high NO₂ concentration conditions.

The data obtained from the NO₃ kinetic investigations performed in the Wuppertal 1080 l quartz glass reactor are plotted in accordance with eq. I in Figure 2. For each aromatic compound, at least five experiments were performed using different aromatic hydrocarbon and NO₂ concentrations. Good straight-line plots were obtained and no effect was observed on varying the initial NO₂ concentration.

The rate constant ratios k_1/k_2 obtained from the least-square analyses of the data from both chambers are given in Table 1. The rate coefficient values k_1 for the various NO₃ + benzenediol reactions have been placed on an absolute basis using the recommended rate coefficient for k_2 . Table 1 lists the individual values of k_1 obtained from each chamber together with the overall averaged value from both data sets. Good agreement was found between the rate coefficients measured in each of the chambers. The errors quoted in Table 1 are a combination of the 2 σ statistical errors from the linear regression analysis, the errors given for k_2 in the literature and other method related errors such as the spectral subtraction procedure, wall deposition etc.

This study represents the first determination of rate coefficients for the reaction of NO₃ radicals with 1,2-benzenediol, 4-methyl-1,2-benzenediol and 3-methyl-1,2-benzenediol. As seen in Table 1, the reactivity of the 1,2-benzenediols takes the order k_{NO_3} (1,2-benzenediol) < k_{NO_3} (4-methyl-1,2-benzenediol) < k_{NO_3} (3-methyl-1,2-benzenediol). This order is expected from a consideration of the presence and position of the methyl group.

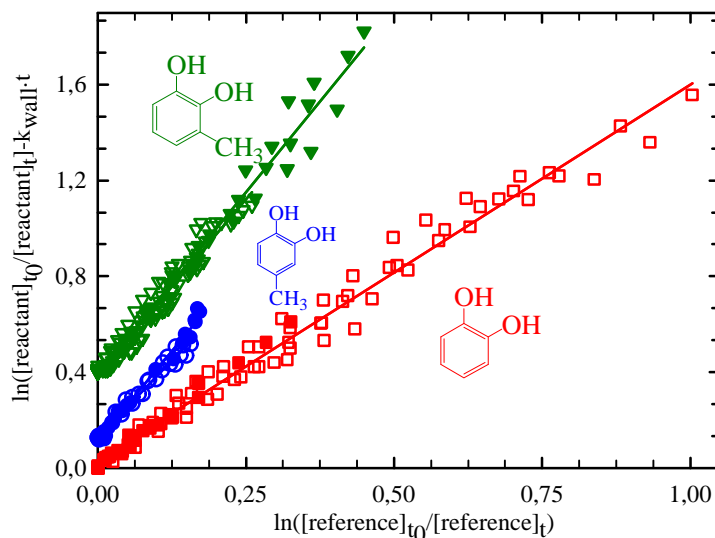
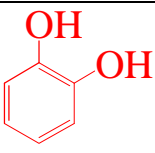
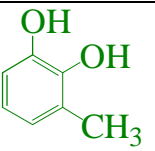
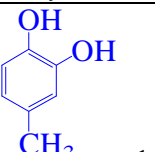


Figure 2: Plots of the kinetic data from the **Wuppertal** chamber according to eq. I for the gas-phase reaction of the NO_3 radical with **1,2-benzenediol**, **3-methyl-1,2-benzenediol** and **4-methyl-1,2-benzenediol** relative to **2,3-dimethyl-2-butene**. For clarity, the data for **3-methyl-1,2-benzenediol** and **4-methyl-1,2-benzenediol** have been displaced vertically by 0.4 and 0.125 units, respectively. The open symbols are for low NO_2 concentrations and the full symbols are for high NO_2 concentrations.

Using the kinetic data in combination with a nighttime average tropospheric nitrate concentration of $[\text{NO}_3] = 2.4 \times 10^8 \text{ cm}^{-3}$ (Geyer et al., 2001) an estimated atmospheric residence time τ_1 of a compound i due to reaction with NO_3 radicals can be calculated according to the relationship: $\tau_1 = (k_1 \times [\text{NO}_3])^{-1}$. The residence times thus obtained are presented in Table 1. The 1,2-benzenediols will have very short atmospheric nighttime lifetimes. Because of the fast reactions between NO_3 and benzenediols, reaction with NO_3 during the day is also a possibility in some regions. A daytime average tropospheric OH radical concentration of $1.6 \times 10^6 \text{ cm}^{-3}$ (Crutzen and Zimmermann, 1991) and NO_3 radical concentration of $3.1 \times 10^6 \text{ cm}^{-3}$ (Geyer et al., 2001) *for example* would imply that 1,2-benzenediols will react during the daytime about 60% with OH and about 40% with NO_3 radicals.

The reaction of NO_3 with 1,2-benzenediols and its methylated derivatives is expected to mainly result in the formation of products with low vapor pressure. Therefore, it is not improbable that products from the NO_3 -initiated oxidation of 1,2-benzenediols (or their further oxidation products) could contribute to the formation of secondary organic aerosol (SOA).

Table 1: Rate coefficients for the reaction of NO₃ radicals with **1,2-benzenediol**, **3-methyl-1,2-benzenediol** and **4-methyl-1,2-benzenediol**.

compound	1080 l reactor		EUPHORE		k _(average) (10 ⁻¹¹ cm ³ s ⁻¹)	τ _i =1/k _i [NO ₃]
	k ₁ /k ₂	k ₁ (10 ⁻¹¹ cm ³ s ⁻¹)	k ₁ /k ₂	k ₁ (10 ⁻¹¹ cm ³ s ⁻¹)		
 1,2-dihydroxybenzene	1.58±0.07	9.09 ± 3.7	1.88±0.11	10.60 ± 4.3	9.84 ± 4.0	44s
 1,2-dihydroxy-3-methylbenzene	3.01±0.10	17.3 ± 5.6	2.93±0.06	16.8 ± 4.8	17.05 ± 5.3	24 s
 1,2-dihydroxy-4-methylbenzene	2.80±0.10	16.0 ± 5.2	2.36±0.06	13.4 ± 5.00	14.7 ± 5.6	28s

Products OH + benzenediols. The mechanisms of the OH radical reaction initiated oxidation of 1,2-benzenediols are currently under investigation using the photolysis of CH₃ONO as OH radical source in 1000 mbar of synthetic air at 298 K. Figure 3 shows a typical example of the FT-IR spectral data obtained for reaction of OH with 1,2-dihydroxybenzene. Formation of maleic acid anhydride and an unknown ketene-type product is observed in the reaction system. Spectral features tentatively attributed to unidentified organic nitrates are also observed. Maleic acid anhydride and the ketene-type compound are both ring fragmentation products. The yield of maleic acid anhydride is low and that of the ketene is presently unknown. The ketene product has also been observed in studies of the reaction of Cl atoms with 1,2-benzenediol where abstraction of an H-atom from an OH group is expected to be the main pathway. The results are still very preliminary and further work is in progress using GC-MS to further elucidate the nature and yields of the reaction products.

Acknowledgement

Financial support of this work from the EU within the 5th Framework Programme EXACT project is gratefully acknowledged.

Literature

- Atkinson, R., 1994 Gas-Phase Tropospheric Chemistry of Organic Compounds. *J. Phys. Chem. Ref. Data, Monograph 2*, 156
- Atkinson, R., 1989, Kinetics and Mechanisms of the Gas-Phase Reactions of the Hydroxyl Radical with Organic Compounds, *J. Phys. Chem. Ref. Data, Monograph 1*, 239
- Barnes, I., K. H. Becker, N. Mihalopoulos, 1994, An FT-IR Product Study of the Photooxidation of Dimethyl Disulfide, *J. Atmos. Chem.*, 18, 267-289.
- Becker, K. H., (Ed), The European Photoreactor EUPHORE, 1996, EC Final Report EV5V-CT92-0059.
- Calvert, J. G., R. Atkinson, K. H. Becker, R. M. Kamens, J. H. Seinfeld, T. J. Wallington, and G. Yarwood, 2002: Mechanisms of Atmospheric Oxidation of Aromatic Hydrocarbons, Oxford University Press.

- Crutzen, P. J., and P. H. Zimmermann, 1991, The changing photochemistry in the troposphere, *Tellus*, 43AB, 136-151.
- Fine, P. M., G. R. Cass, and B. R. Simoneit, 2002, Chemical Characterization of Fine Particle Emissions from the Fireplace Combustion of Woods Grown in the Southern United States, *Environ. Sci. Technol.*, 36, 1442-1451.
- Flickinger, C. W., 1976, The benzenediols: catechol, resorcinol and hydroquinone - a review of the industrial toxicology and current industrial exposure limits, *Am. Ind. Hyg. Assoc. J.*, 37, 596-606.
- Geyer A., B. Alicke, S. Konrad, T. Schmitz, J. Stutz, and U. Platt, 2001, Chemistry and oxidation capacity of the nitrate radical in the continental boundary layer near Berlin, *J. Geophys. Res.*, 106, 8013-8025.
- Klotz, B., S. Sorensen, I. Barnes, and K.H. Becker, 1998, Atmospheric Oxidation of Toluene in a Large-Volume Outdoor Photoreactor: In Situ Determination of Ring-Retaining Product Yields, *J. Phys. Chem. A*, 102, 10289-10299.
- Li, Q., M. T. Aubrey, T. Christian, and B. M. Freed, 1997, Differential Inhibition of DNA Synthesis in Human T Cells by the Cigarette Tar Components Hydroquinone and Catechol, *Fundamental and Applied Toxicology*, 38, 158-165.
- Olariu, R., I. Barnes, K. H. Becker, and B. Klotz, 2000, Rate Coefficients for the Gas-Phase Reaction of OH Radicals with Selected Dihydroxybenzenes and Benzoquinones, *Int. J. Chem. Kinet.*, 32, 696-702.
- Olariu, R., B. Klotz, I. Barnes, K.H.Becker, and R. Mocanu, 2002, FT-IR study of the ring-retaining products from the reaction of OH radicals with phenol *o*-, *m*-, and *p*-cresol, *Atmospheric Environment*, 36, 3685-3697.
- Smith, D. F., C. D. McIver and T. E. Kleindienst, 1998, Primary Product Distribution from the Reaction of Hydroxyl Radicals with Toluene at ppb NO_x Mixing Ratios, *Journal of Atmospheric Chemistry*, 30, 209-228.
- Smith, D. F., T. E. Kleindienst, and C. D. McIver, 1999, Primary Product Distribution from the Reaction of OH with *m*-, *p*-Xylene, 1,2,4- and 1,3,5-Trimethylbenzene, *Journal of Atmospheric Chemistry*, 34, 339-364.
- Tomas, A., R. Olariu, I. Barnes, K.H. Becker, 2002, Kinetics of the Reaction of O₃ with Selected Benzenediols, submitted to *Int. J. Chem. Kinet. in press*.
- Volkamer, R., B. Klotz, I. Barnes, T. Imamura, K. Wirtz, N. Washida, K. H. Becker, and U. Platt, 2002, OH-initiated oxidation of benzene. Part I. Phenol formation under atmospheric conditions, *Phys. Chem. Chem. Phys.*, 4, 1598-1610.

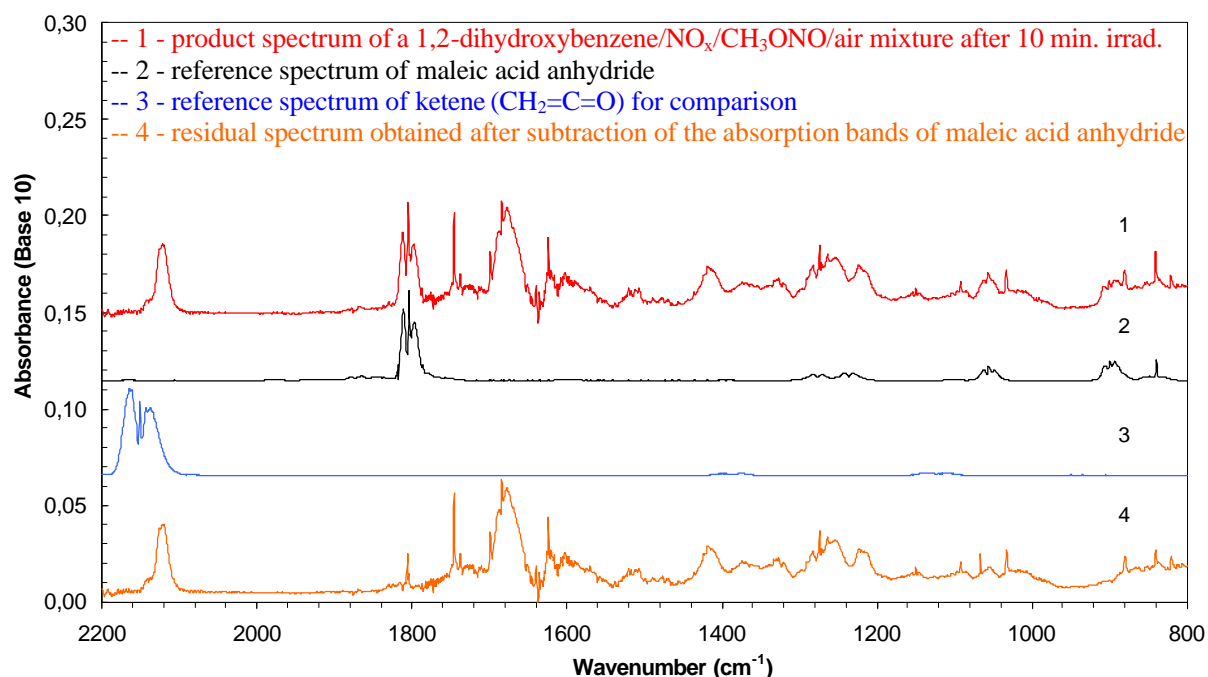


Figure 3: Infrared spectra from the OH-radical initiated photo-oxidation of 1,2-dihydroxybenzene

Reaction of OH + acetone: direct time resolved determination of the branching at 298K (GPP3)

Estelle Turpin, Eric Delbos, Christa Fittschen, and Pascal Devolder

Physico-Chimie des Processus de Combustion et de l'Atmosphère (PC2A),

UMR CNRS 8522 and Fédération de Recherche CERLA CNRS FR 2416

Université de Sciences et Technologies de Lille, 59655 Villeneuve d'Ascq Cedex, France

Abstract

We have determined the 1-methylvinoxy ($\text{CH}_3\text{C}(\text{O})\text{CH}_2$) radical yield for the reaction of acetone with OH radical relative to the 1-methylvinoxy yields for the reactions of F- and Cl atoms with acetone using the Discharge Flow technique. The 1-methylvinoxy radical has been monitored by LIF at short reaction times in the systems: OH + acetone (R1), F + acetone (R2), and Cl + acetone (R3). From these measurements we have deduced the branching ratio for the 1-methyl vinoxy radical formation in the title reaction to be in the range $0.85 \leq R \leq 1$.

Introduction

Recent results (Folkins and Chatfield, 2000) have highlighted the importance of various oxygenated COV (including acetone, formic and acetic acids) for the mixing ratio of OH + HO₂ in the upper troposphere / lower stratosphere (UTLS). Concerning the fate of acetone, two main sinks are involved: solar photolysis and reaction with OH. Until recently, the role of OH reaction was believed negligible for acetone degradation at UTLS temperatures since available data above room temperature indicated that its rate constant was decreasing monotonically with temperature; however, two recent series of observations have increased the expected importance of this reaction for two reasons:

(i) its rate constant with OH exhibits a negative temperature coefficient below 298K, with a possible increase below 250K [Wollenhaupt et al, 2000], [Gierczak and Ravishankara, 2000].

(ii) two experimental studies [Vasvari et al, 2001], [Wollenhaupt and Crowley, 2000] concluded that the reaction proceeds at room temperature via two different pathways of equal importance:

Abstraction: $\text{OH} + \text{CH}_3\text{C}(\text{O})\text{CH}_3 \rightarrow \text{CH}_3\text{C}(\text{O})\text{CH}_2 + \text{H}_2\text{O}$ k_{1a}

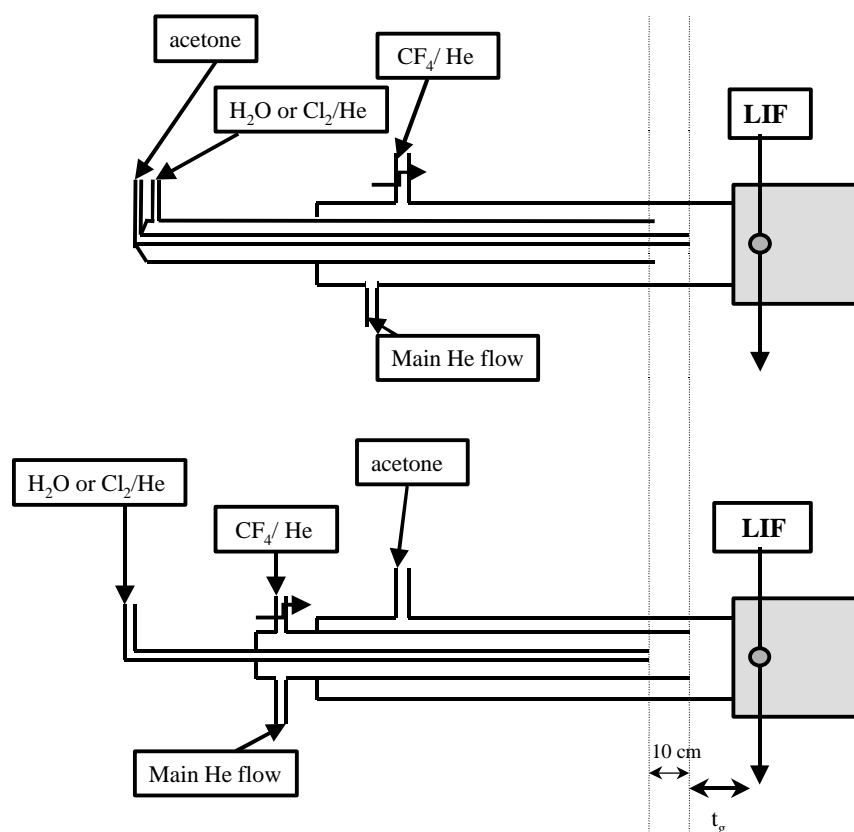
Addition-elimination: $\text{OH} + \text{CH}_3\text{C}(\text{O})\text{CH}_3 \rightarrow \text{HOC}(\text{CH}_3)_2\text{O}^\circ \rightarrow \text{CH}_3 + \text{CH}_3\text{C}(\text{O})\text{OH}$ k_{1b}

Both observations have been tentatively assigned to a change in the reaction mechanism though calculations by the same authors [Vasvari et al, 2001] and by [Vandenberk et al, 2002] show that the barrier for the abstraction pathway is much lower than the addition-elimination one. On the other hand, the importance of pathway (R_{1b}) has been questioned in two very recent experimental studies by [Tyndall et al, 2002] and [Vandenberk et al, 2002], which failed to detect any acetic acid. Furthermore, the observation of a large primary isotope effect [Smith and Ravishankara, 2002] is in better agreement with a major, if not unique contribution of pathway (1a). At last, a negative temperature coefficient has been associated with the formation of H-bonded complexes in the entrance channel [Vasvari et al, 2001], [Smith and Ravishankara, 2002].

We have thus decided to investigate this reaction and determine the branching ratio by the fast flow technique coupled to a detection of 1-methylvinoxy radicals by Laser Induced Fluorescence (LIF).

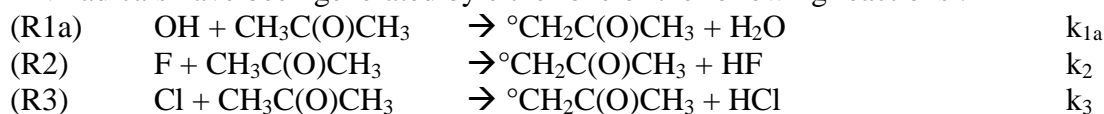
Experiment

Experiments have been performed using two different configurations of the discharge flow technique (figure 1):

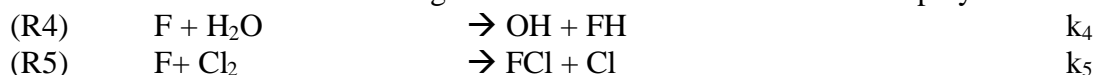


coupled to a detection of 1-methylvinloxy radicals (noted MV in the following) by laser induced fluorescence LIF ($\lambda_{\text{exc}}=342.9\text{nm}$, $\lambda_{\text{det}}>360\text{nm}$). The pressure in the flow tube is measured at the LIF detection cell and an average “corrected” pressure is calculated using the Poiseuille law in the middle of the reaction distance z_g . The flow velocity v_c was typically around 5000 cm s^{-1} . Acetone is directly pumped from degassed liquid immersed in a thermostated bath and its flowrate is regulated by a needle valve. Flow rates for Acetone, H_2O and Cl_2/He mixtures are determined by diverting the flow to a calibrated volume and measuring the rate of pressure increase. All other flows (CF_4/He mixture, He as bath gas) are measured with mass flow controllers.

MV radicals have been generated by either one of the following reactions :



F atoms are generated by a microwave discharge in the CF_4/He mixtures; for generation of OH radicals or Cl atoms the following fast titration reactions have been employed:



Rate constants for these reactions are $k_4=1.3\times 10^{-11}\text{ cm}^3\text{ s}^{-1}$ [Frost et al, 1986] and $k_5=1.6\times 10^{-10}\text{ cm}^3\text{ s}^{-1}$ [Appelman and Clyne, 1975]. To estimate the influence of the mixing time between acetone and reactive species (F or OH), we have used two different configurations (figure 1):

(i) fixed discharge: the microwave discharge is fixed to the main flow tube, which contains a movable double injector fitted with a smaller central injector 10 cm longer than the main injector: Cl_2/He or H_2O flows run within the main injector, while acetone is added downstream through the longer central one. In this configuration, the small flow of acetone exits along the central axis while the large F/He flow is concentric.

(ii) movable discharge: the microwave discharge is fixed to a movable main injector (external diameter 16 mm) in which was inserted a second smaller injector (external diameter 6mm), ending 10 cm before the main injector. F-atoms are generated in the discharge, traveling along the main

injector. Cl₂/He or water vapor is added through the small central injector, allowing (R4) or (R5) to take place along the last 10cm of the main injector before mixing with acetone which was flown in the main flow tube. Since the entire He bath gas is flown inside the main injector, mixing occurs between a large central flow of F (or OH or Cl)/He mixture with a small concentric slow flow of acetone.

Principle of the method

The determination of the branching ratio R:

$$R = k_{1a} / (k_{1a} + k_{1b})$$

is based on the measurements of the ratio r of two MV signals at the same fixed reaction time and generated by two equal concentrations of respectively OH and F:

$$r = [MV_{OH}] / [MV_F].$$

Experimental conditions are such that (R1) is not completed and [MV] depends on both acetone concentration [Ac] and reaction time t_r . As a consequence, our data derivation protocol, which is detailed in the following paragraph, is not so straightforward as in classical flow tube studies. The advantage is that the importance of possible secondary reactions, i.e. radical-radical, is reduced.

Establishment of the basic relationships

With the injector in a fixed position, i.e. fixed reaction time t_r , and constant acetone concentration [Ac], MV is generated by either (R1a) (with excess H₂O added) or (R2) (no H₂O) and the resulting LIF intensities are alternatively measured. Since acetone is in large excess (pseudo-first order conditions), these fluorescence intensities are proportional to the respective MV concentrations at t_r :

$$[MV_{OH}]_{t_r} = R [OH]_0 (1 - \exp(-k_1[Ac] t_r)) \quad (1)$$

$$[MV_F]_{t_r} = R_F [F]_0 (1 - \exp(-k_2[Ac] t_r)) \quad (2)$$

[F]₀ and [OH]₀ are the initial concentrations of F atoms and OH radicals, respectively.

Since (R2) is very fast ($k_2 \approx 10^{-10} \text{ cm}^3 \text{ s}^{-1}$, [Smith et al, 1977]), it can be considered as completed under our experimental conditions: ([Ac] > $5 \times 10^{13} \text{ molecule cm}^{-3}$, $t_r \geq 1 \text{ ms}$); it is also easily checked that [MV_F] is indeed on a plateau by varying the reaction distance in preliminary experiments. Provided moreover that the titration reaction is stoichiometric, one obtains

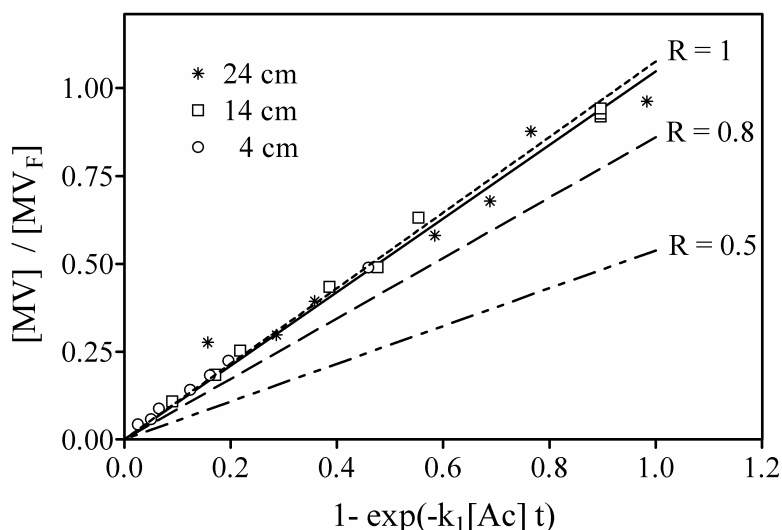
$$[OH]_0 = [F]_0 \text{ and } [MV_F] = R_F \times [F]_0$$

$$\text{and thus : } [MV_{OH}]_{t_r} / [MV_F] = R/R_F \times (1 - \exp(-k_1[Ac] t_r)) \quad (3)$$

$$r = R/R_F \times (1 - \exp(-k_1[Ac] t_r)) \quad (3)$$

with $r = [MV_{OH}]_{t_r} / [MV_F]$

Since k_1 is well known and both [Ac] and t_r are measured, equation (3) allows the determination of R/R_F from a simple ratio r of two signals: by varying [Ac] at a fixed reaction time, $[MV_{OH}]_{t_r}$, and thus r , should increase linearly with $(1 - \exp(-k_1[Ac] t_r))$, the slope being the ratio R/R_F . This value corresponds to a lower limit of the branching ratio for (R1a), since a MV yield in (R2) of $R_F = 0.93$ increases R . The value of k_1 has been measured several times, we have adopted for the interpretation of our experiments the average of various recent room temperature determinations [Wollenhaupt et al, 2000], [Le Calvé et.al., 1998], [Vasvari et.al., 2001]]: $k_1 = 1.8 \times 10^{-13} \text{ cm}^3 \text{ s}^{-1}$.



This is the basis of our method, which is illustrated by an example of a plot of equation (3) in figure 2. To estimate systematic errors, especially those linked to the reaction time and to possible radical-radical reactions, experiments have been performed at several reaction distances (4, 14, 24 and 34cm). Before presenting and discussing our results, a few tests have been performed to demonstrate the validity of our approach.

In the example (figure 2) the linear regression has been forced through zero since no LIF signal should be present at zero reaction time. Also displayed in this figure are the theoretical lines corresponding to branching ratios of $R = 1$, 0.8 and 0.5 (since $R_F = 0.93$, the line corresponding to $R=1$ ends for $(1-\exp(-k_1[Ac]t_r) = 1$ at $[MV_{OH}]_{t_r}/[MV_F] = 1.07$ and not at 1, same for the others). The slope for the experiment displayed in figure 2 is (1.04 ± 0.02) and taking into account $R_F=0.93$ we obtain $R = 0.97 \pm 0.02$. The given uncertainty is statistical only, an estimation of the other classical uncertainties usually admitted in flow tube experiments, in this case mainly deduction of the absolute reaction time, induces an uncertainty range of ± 0.07 . The average value obtained by all our experiments is

$$R = (0.93 \pm 0.07).$$

As can be seen in figure 2, a value of $R = 0.5$ can never be reconciled with our experimental data. And this is true for all our experiments, in the entire range of experimental conditions. This is rather puzzling since our experimental technique is the same than the one used by [Vasvari et al, 2001] who certainly performed the measurements very carefully. The difference is that we worked at short reaction times (a few milliseconds), allowing the reaction to progress only partially, while [Vasvari et al, 2001] measured the signal intensities after reaction is completed. They also performed kinetic experiments and observed the OH-consumption and MV-formation simultaneously and deduced the same low branching ratio from modeling these signals. [Tyndall et al, 2002] and [Vandenberck et al, 2002] suggested that secondary reactions (MV self reaction or with OH) could play a role, this is apparently supported by our results. We have not performed experiments in the conditions of [Vasvari et al, 2001] to further check this hypothesis.

[Wollenhaupt and Crowley 2000] also deduced a value of $R=(0.5 \pm 0.1)$ for the abstraction pathway. These authors did not monitor MV, but one of the products of the addition-elimination pathway (R1b), CH_3 radical. This radical has been detected indirectly by LIF monitoring of CH_3O after transformation through the fast titration reaction $CH_3 + NO_2 \rightarrow CH_3O + NO$. Though various checks have been performed by the authors, it is obvious that their chemical system is more complex and that their technique is not as straightforward as the present one.

Conclusion

We have determined the branching ratio for the formation of MV in the reaction of OH radical with acetone at (298 ± 3) K and a pressure of 1 Torr. Under the assumption of a branching ratio of 1 (for the same radical) for the reaction $\text{Cl} + \text{acetone}$, the average of all our experiments gives $R = 0.93 \pm 0.07$. The global uncertainty is the result of uncertainties for the reaction time t_r (the main source of error) and usual uncertainties in classical discharge flow kinetic measurements (pressure, flow rates). Our result is clearly in contradiction with the “low” value of $R \approx 0.50$ reported in [Vasvari et.al., 2001] and [Wollenhaupt and Crowley, 2000] and favors the “high” value of $R \approx 1$ determined in two recent studies [Vandenberk et.al. 2002], [Tyndall et.al., 2002]. It is worth reminding that the two studies favoring a value of R close to 1 are indirect since based on measuring the yield of the expected product of the other pathway: acetic acid. From the absence of any signal, an upper limit for the yield of acetic acid has been proposed by these authors: $R \leq 0.05$ [Vandenberk et.al. 2002], $R \leq 0.1$ [Tyndall et.al., 2002].

References

- Appelman, E.H. and Clyne, M.A.A., *J.Chem.Soc.Faraday Trans. 1*, **71**, 2072-2085 (1975)
 Folkins, I. and Chatfield, R., *J. Geophys. Res.*, **105**, D9, 11585-11599 (2000)
 Frost, R.J., Green, D.S., Osborn, M.K., Smith, I.W.M., *Int.J.Chem.Kinet*, **18**, 885 (1986)
 Gierczak, T. and Ravishankara, A.R., *16th International Symposium on Gas Kinetics*, Poster PB13, July 23rd-27th, Cambridge (UK) (2000)
 Le Calvé, S., Hitier, D., Le Bras G., Mellouki, A., *J.Phys. Chem. A*, **102**, 4579-4584 (1998)
 Nielsen, O.J., Johnson, M.S., Wallington, T.J., Christensen, L.K., Platz, J., *Int.J.Chem.Kinet.*, **34**, 283-291 (2002)
 Olsson, B.E.R., Hallquist, M., Ljungstrom, E., Davidsson, I., *Int. J. Chem. Kinet.* **29**, 195-201 (1997)
 Smith, D.J., Setser, D.W., Kim, K.C., Bogan, D.J., *J. Phys. Chem.* **81**, 898 (1977)
 Smith I.W.M. and Ravishankara, A.R., *J.Phys. Chem. A.*, **106**, 4798-4807 (2002)
 Tyndall, G.S., Orlando, J.J., Wallington, T.J., Hurley, M.D., Goto, M. and Kawasaki, M. *Phys.Chem.Chem.Phys.*, **4**, 2189-2193 (2002)
 Vandenberk, S., Vereecken, L. and Peeters, J., *Phys.Chem.Chem.Phys.*, **4**, 461-466 (2002)
 Vasvari, G., Szilayi, I., Bencsura, A., Dobè, S., Berces, T., Henon, E., Canneaux S. and Bohr, F., *Phys.Chem.Chem.Phys.*, **3**, 551-555 (2001)
 Wallington, T.J., Kurylo, M.J., *J.Phys. Chem.*, **91**, 5050-5054 (1987)
 Wallington, T.J., Andino, J.M., Ball, J.C., Japar, S.M., *J. Atmos. Chem*, **10**, 301 (1990)
 Wollenhaupt, M. Crowley, J.N., *J.Phys. Chem. A*, **104**, 6429-6438 (2000)
 Wollenhaupt, M., Carl, S.A., Horowitz, A. Crowley J.N., *J. Phys. Chem. A*, **104**, 2698-2705 (2000)

A kinetic and mechanistic study of the OH and NO₂ initiated oxidation of 2,4-hexadiene in the gas phase (GPP6)

Michael E. Jenkin¹, Malene Sørensen², Michael D. Hurley² and Timothy J. Wallington²

¹Imperial College, Ascot, UK; ²Ford Motor Company, Dearborn, USA

m.jenkin@ic.ac.uk

Introduction

Conjugated dienes play a significant role in the chemistry of the atmosphere. Isoprene (mainly emitted from biogenic sources), is believed to have the highest global emissions of all non-methane hydrocarbons (Guenther et al., 1995), and a number of conjugated dienes are emitted as highly reactive components of vehicle exhaust or fuel vapour (e.g., Jemma et al., 1995; Smith et al., 2002). In addition, the detection of several conjugated dienes (including 2,4-hexadiene) in the urban environment has been reported (Ciccioli et al., 1994).

The dominant atmospheric sink for conjugated dienes tends to be reaction with the OH radical. However, the reactions with NO₂ have also received attention due to their possible role in thermal initiation of free radical catalysed NO-to-NO₂ conversion during urban winter pollution episodes (Shi and Harrison, 1997; Harrison et al., 1998; King et al., 2002). Whereas kinetic data are available for reactions of OH and NO₂ with a number of conjugated dienes (e.g. Calvert et al., 2000; King et al., 2002), OH product studies appear to be limited to 1,3-butadiene and isoprene. There are no reported studies of the products of NO₂-initiated oxidation, although Shi and Harrison (1997) have demonstrated that the chemistry involving 1,3-cyclohexadiene and 1-methyl-1,3-cyclopentadiene leads to oxidation of NO to NO₂.

To extend the available database on the atmospheric chemistry of conjugated dienes, the reactions of OH and NO₂ with 2,4-hexadiene at 296(±2)K have been investigated using long-path FTIR spectroscopy.

Experimental

All experiments were performed in the Ford 140 L Pyrex chamber, interfaced with a Mattson Sirius 100 FTIR spectrometer, which is described in detail elsewhere (Wallington and Japar, 1989). The chamber is equipped with 22 fluorescent blacklamps (GE F40BLB), emitting near UV radiation in the range 300-450 nm. OH radicals were thus generated by the photolysis of CH₃ONO in the presence of NO and O₂, by the well-established mechanism:

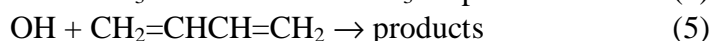


Infra-red spectra were derived from 32 co-added interferograms with a spectral resolution of 0.25 cm⁻¹, and an analytical path length of 27.1 m. Hexadiene was obtained from Aldrich Chemical Co. as a mixture of isomers (isomeric distribution unknown).

Results and discussion

Kinetics of OH + 2,4-hexadiene

The rate coefficient for the reaction with OH was determined using the relative rate technique, with 1,3-butadiene as the reference reagent:



The results confirmed that reaction (4) is rapid, and a rate coefficient ratio $k_4/k_5 = 2.47 \pm 0.10$ was determined from the initial relative decays of the two reagents. Using $k_5 = (6.66 \pm 1.33) \times 10^{-11}$

(Calvert et al., 2000) gives $k_4 = (1.65 \pm 0.34) \times 10^{-10} \text{ cm}^3 \text{ molecule}^{-1} \text{ s}^{-1}$, consistent with the only previously reported determination (Ohta, 1983). At longer extents of photolysis, accelerated decay of 2,4-hexadiene was observed, resulting from its preferential additional removal by reaction with NO_2 accumulating in the system.

Products of OH + 2,4-hexadiene

Acetaldehyde, crotonaldehyde and 2,5-dimethylfuran were observed as oxidation products, with molar yields of 30.6%, 13.6% and 5.6%, respectively. This is broadly consistent with the mechanism expected following addition of OH, as illustrated schematically in Figure 1. However, the observed yields do not preclude the possibility of partial reaction by abstraction of the 'superallyl' hydrogens on the terminal CH_3 groups, which might be expected to make a minor contribution on the basis of experimental and theoretical studies of related systems (Peeters et al., 1999). The mechanism in Figure 1, defined by analogy with those generally accepted for 1,3-butadiene and isoprene (e.g., Jenkin et al., 1998), qualitatively explains the observed products. However, the non-equivalence of the yields of acetaldehyde and crotonaldehyde (as predicted by this mechanism) is not fully understood, and is under further investigation.

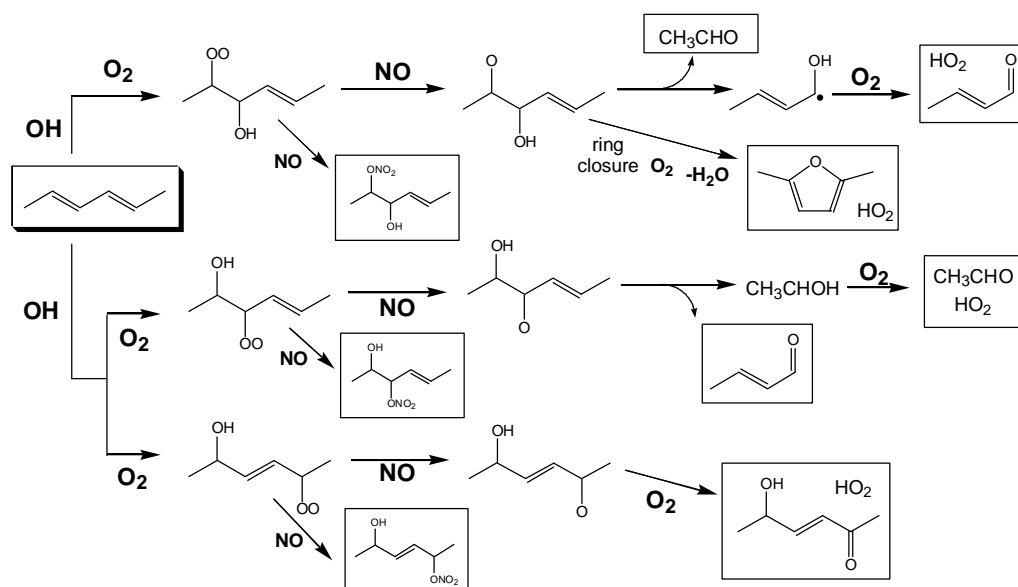


Figure 1: Schematic representation of the likely mechanism of the OH initiated oxidation of 2,4-hexadiene, leading to the observed products.

Kinetics of NO_2 + 2,4-hexadiene

The rate coefficient, k_6 , was determined directly from the pseudo-first order decay of 2,4-hexadiene over a tenfold range of $[\text{NO}_2]$, as shown in Figure 2.



A value of $k_6 = (3.0 \pm 0.1) \times 10^{-19} \text{ cm}^3 \text{ molecule}^{-1} \text{ s}^{-1}$ was derived, independent of whether the diluent was O_2 or N_2 . This is consistent with the relative rate determination reported by Ohta et al. (1984), provided the rate coefficient for the reference reaction (isoprene + NO_2), reported by Atkinson et al. (1984), is used.

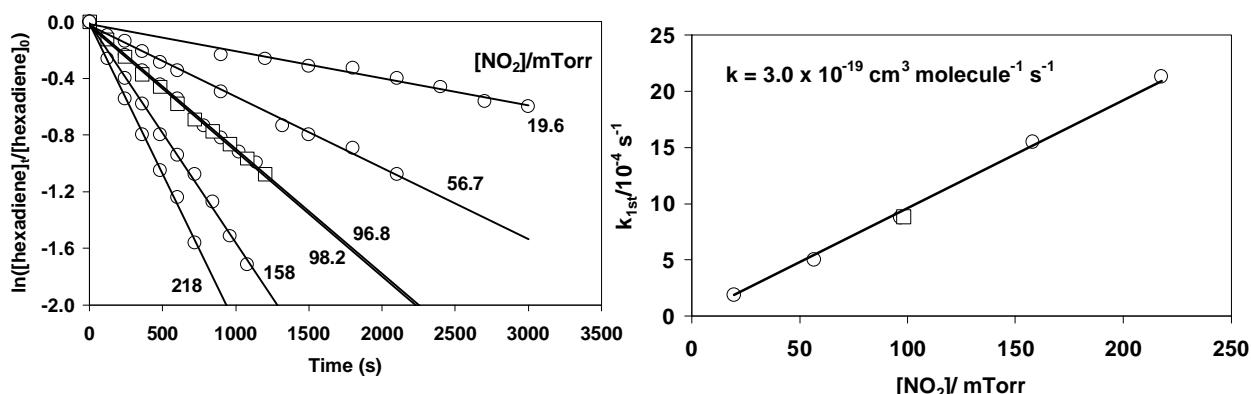


Figure 2: Log-linear (first order) decays of 2,4-hexadiene in the presence of a tenfold variation of $[NO_2]$, and the variation of the corresponding pseudo first order coefficients with $[NO_2]$. Experiment with 98.2 mTorr NO_2 (square points) performed in N_2 diluent: all other experiments with O_2 diluent.

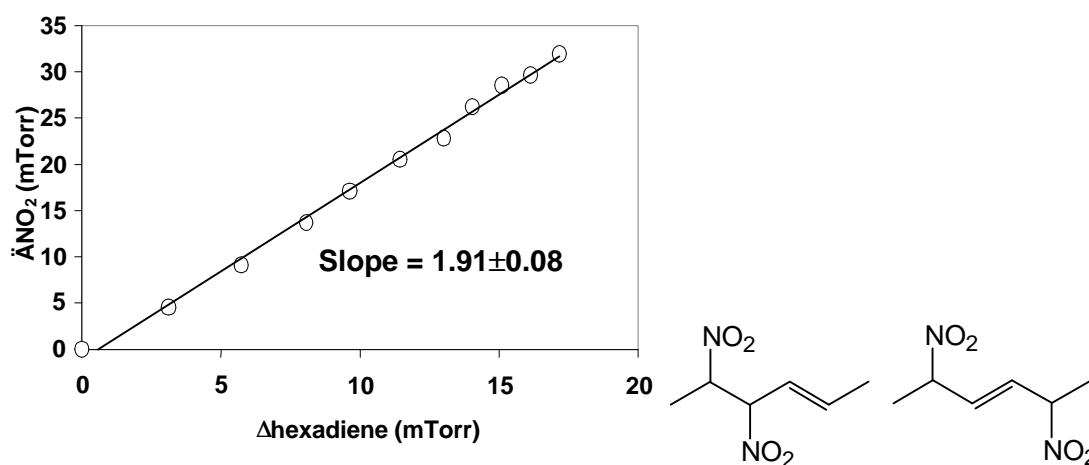
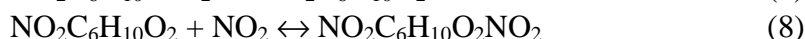
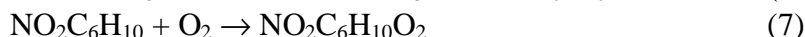


Figure 3: Removal stoichiometry of 2,4-hexadiene and NO_2 during reaction in N_2 diluent, and the likely structures of the reaction products.

Stoichiometry of $NO_2 + 2,4\text{-hexadiene}$

The observed stoichiometry, $\Delta[NO_2]/\Delta[hexadiene]$, for a series of experiments performed with N_2 diluent (Figure 3) is consistent with sequential addition of 2 NO_2 molecules to 2,4-hexadiene to yield the isomeric dinitrohexenes also shown in the figure. In O_2 diluent, a stoichiometry of ca. 2 was also observed in the early stages of the reaction, consistent with formation of isomeric nitrohexenyl peroxy nitrates as follows:



At longer reaction times, the stoichiometry decreased, which is consistent with back decomposition of the peroxy nitrates and partial removal of $NO_2C_6H_{10}O_2$ by self and cross reaction to form mononitro products (e.g., nitrohexenone and nitrohexenyl alcohol isomers).

Mechanism of the NO_2 -initiated oxidation in the presence of NO : HO_x formation

Additional experiments were performed in the presence of NO . The observed time dependence of 2,4-hexadiene and the NO_x species (Figure 4), and the formation of acetaldehyde, crotonaldehyde and 2,5-dimethylfuran, could be explained by the NO_2 -initiated chemistry, propagated by peroxy radical + NO reactions, yielding HO_x radicals with further 2,4-hexadiene loss via reaction with OH . The main features of the probable mechanism are illustrated in Figure 5. This demonstrates the

autocatalytic removal of 2,4-hexadiene due to the generation of NO_2 by the mechanism, with the chain mainly terminated by the formation of organic nitrates from the alternative channels of the reactions of peroxy radicals with NO . During this phase of the reaction observed stoichiometry, $\Delta[\text{NO}_x]/\Delta[\text{hexadiene}]$, is significantly lower than in the absence of NO (ca. 0.5, as shown in Figure 4). Once NO is totally consumed, however, the NO_2 concentration declines and the stoichiometry increases to values comparable with those indicated above.

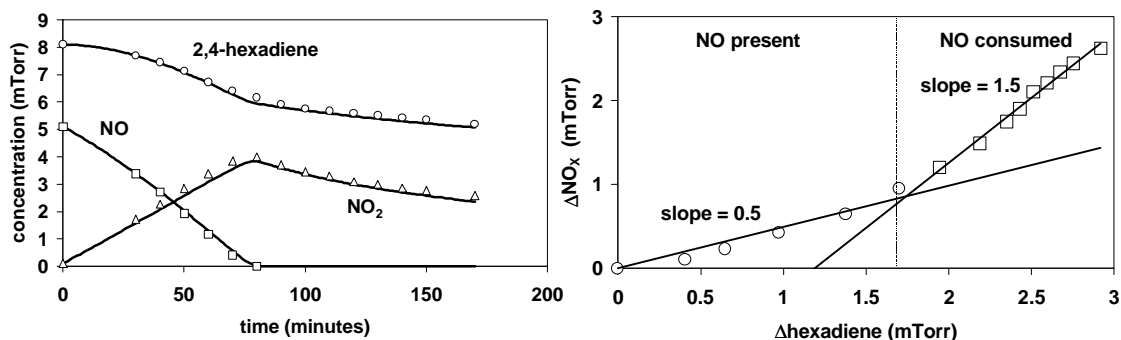


Figure 4 : Species time dependence and observed stoichiometry during NO_2 -initiated oxidation of 2,4-hexadiene in the presence of NO . The lines in the concentration-time plot were simulated using a chemical mechanism based on the schematic chemistry in Figure 5 (see text).

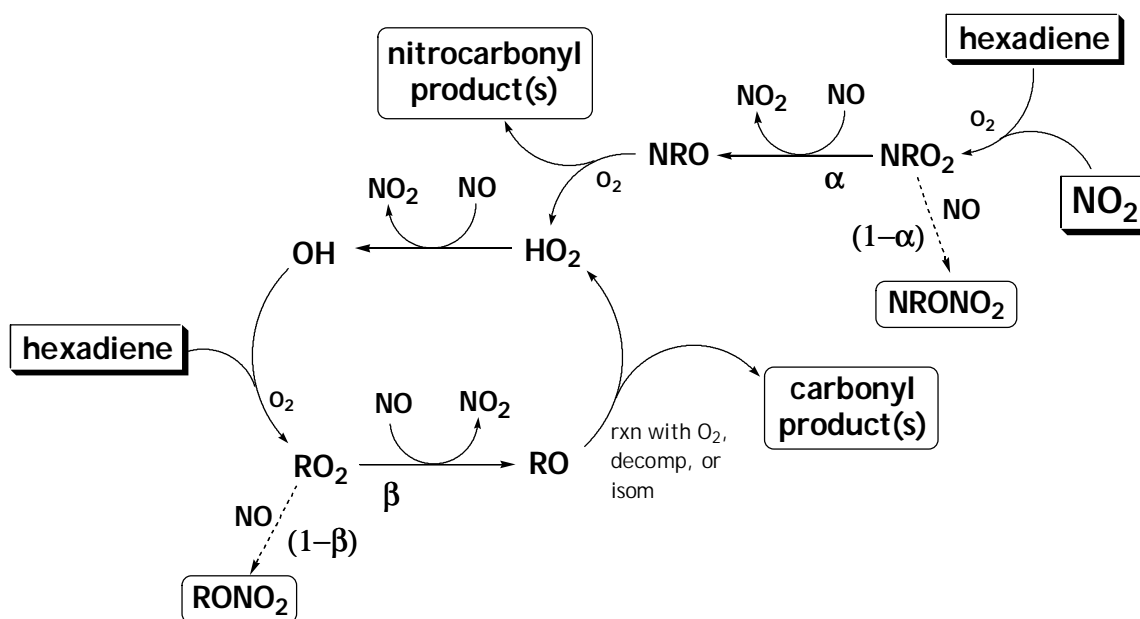


Figure 5 : Schematic representation of the main features of the NO_2 -initiated oxidation of 2,4-hexadiene in the presence of NO ('NR' is used as shorthand for ' $\text{NO}_2\text{C}_6\text{H}_{10}$ ', and 'R' is used as shorthand for ' $\text{HOC}_6\text{H}_{10}$ ').

On the basis of the mechanism in Figure 5 (assuming dominant radical removal by organic nitrate formation), the stoichiometry when NO is present can be shown to be $\Delta[\text{NO}_x]/\Delta[\text{hexadiene}] = 2(1-\beta)/(1-\beta+\alpha)$. Further assuming that the branching ratio of the reactions of the nitro- and hydroxy-substituted peroxy radicals with NO is equivalent, the observed stoichiometry of ca. 0.5 is consistent with $\alpha = \beta = 0.75$. This suggests a yield of ca. 0.75 HO_x from the NO_2 initiated chemistry. The system was also simulated using a more detailed version of the chemistry, i.e. based on that shown in Figure 5, but with relevant alternative reactions included for OH , HO_2 and the peroxy and oxy radicals. The mechanism clearly provides a good description of the time dependence of 2,4-hexadiene and NO_x .

Conclusions

The results of the present study suggest that the OH-initiated oxidation of 2,4-hexadiene proceeds, at least partially, by an analogous mechanism to those reported for 1,3-butadiene and isoprene. The NO₂-initiated oxidation in the presence of NO leads to NO-to-NO₂ conversion, and the formation of HO_x radicals in significant yield. The present work thus supports the general features of the mechanism postulated by Shi and Harrison (1997) for 1,3-cyclohexadiene and 1-methyl-1,3-cyclopentadiene, and the potential of conjugated diene/NO₂ reactions to promote NO to NO₂ oxidation in the urban environment. However, the significance of these reactions clearly depends on the levels of reactive conjugated dienes, and further ambient measurements are required for the impact of this chemistry to be fully assessed.

References

- Atkinson, R. Aschmann, S. M. Winer, A. M., Pitts, Jr., J. N. 1984: Gas phase reaction of NO₂ with alkenes and dialkenes. *International Journal of Chemical Kinetics*, **16**, 697-706.
- Calvert, J.G., Atkinson, R. Kerr, J.A., Madronich, S., Moortgat, G.K., Wallington, T.J., and Yarwood, G. 2000: The mechanisms of atmospheric oxidation of alkenes. Oxford University Press, New York. ISBN 0-19-513177-0.
- Ciccioli P., Cecinato A., Brancaleoni E., Brachetti A., Frattoni M. and Sparapani R. 1994: Composition and distribution of polar and non-polar VOCs in urban, rural, forest and remote areas. Proceedings of the 6th European symposium on the physico-chemical behaviour of atmospheric pollutants, Varese, 18-22 October 1993, pp 549-568. Report EUR 15609/1 EN. ISBN 92-826-7922-5.
- Guenther A., Hewitt C.N., Erickson D., Fall R., Geron C., Graedel T., Harley P., Klinger L., Lerdau M., McKay W.A., Pierce T., Scholes B., Steinbrecher R., Tallamraju R., Taylor J., Zimmerman P., 1995: A global model of natural volatile organic compound emissions. *Journal of Geophysical Research*, **100**, 8873 - 8892.
- Harrison, R.M., Shi, J.P., Grenfell J.L., 1998: Novel nighttime free radical chemistry in severe nitrogen dioxide pollution episodes. *Atmospheric Environment*, **32**, 2769-2774.
- Jemma C.A., Shore P.R., Widdicombe K.A., 1995: Analysis of C₁-C₁₆ hydrocarbons using dual-column capillary GC – application to exhaust emissions from passenger car and motorcycle engines. *Journal of Chromatographic Science*, **33**, 34-48.
- Jenkin M.E., Boyd A.A. and Lesclaux R. 1998: Peroxy radical kinetics resulting from the OH-initiated oxidation of 1,3-butadiene, 2,3-dimethyl-1,3-butadiene and isoprene. *Journal of Atmospheric Chemistry*, **29**, 267-298
- King M.D., Canosa-Mas C.E., Wayne R.P., 2002: A structure-activity relationship (SAR) for predicting rate constants for the reaction of nitrogen dioxide (NO₂) with alkenes. *Physical Chemistry Chemical Physics*, **4**, 295-303.
- Ohta T. 1983: Rate constants for the reactions of diolefins with OH radicals in the gas phase. Estimate of the rate constants from those of monoolefins. *Journal of Physical Chemistry*, **87**, 1209-1213.
- Ohta T., Nagura H., Suzuki S., 1986: Rate constants for the reactions of conjugated olefins with NO₂ in the gas phase. *International Journal of Chemical Kinetics*, **18**, 1-11.
- Peeters J., Vereecken L. and Vandenberg S. 1999: Experimental and theoretical studies of the oxidation of VOC: OH-initiated oxidation of alkenes and biogenics. 1998 annual report of the EUROTRAC-2 subproject Chemical Mechanism Development (CMD), pp 78-82. International Scientific Secretariat, GSF-Forschungszentrum für Umwelt und Gesundheit GmbH München, September 1999.
- Shi, J.P., Harrison, R.M., 1997: Rapid NO₂ formation in diluted petrol-fuelled engine exhaust - a source of NO₂ in winter smog episodes. *Atmospheric Environment*, **31**, 3857-3866.
- Smith D., Cheng P. and Špan P. 2002: Analysis of petrol and diesel vapour and vehicle engine exhaust gases using selected ion flow tube mass spectrometry. *Rapid Communications in Mass Spectrometry*, **16**, 1124-1134.
- Wallington T.J. and Japar S.M. 1989: Fourier-transform infrared kinetic-studies of the reaction of HONO with HNO₃, NO₃ and N₂O₅ at 295K. *Journal of Atmospheric Chemistry*, **9**, 399-409.

Theoretical study of the mechanism of the oxidation of benzene in the troposphere. Pathways regenerating OH (GPP7)

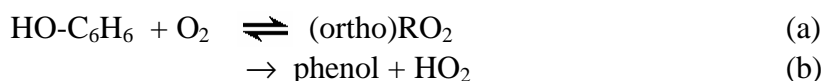
S  verine Raoult, Marie-Th  r  se Rayez, Robert Lesclaux and Jean-Claude Rayez
*Laboratoire de Physicochimie Mol  culaire – UMR5803 CNRS,
 Universit   Bordeaux 1, 351, cours de la Lib  ration – 33405 Talence Cedex – France*

The presence of aromatic compounds in the troposphere is strongly associated with the urban environment and the emission of volatile organic compounds as a result of anthropogenic activity, it has been estimated that their oxidation reactions may be responsible for 30% or so of photochemically produced tropospheric ozone. However, complete degradation mechanisms for aromatic species are still uncertain. In particular, the amount of OH predicted by the kinetic models is lower than observed experiment.

The first step of the oxidation of benzene is known to be the addition of OH onto the ring to form the hydroxycyclohexadienyl radical (C₆H₆-OH).

A theoretical work was carried out to provide information on the reactions of the adduct C₆H₆-OH with O₂. The calculations have been performed using DFT-B3LYP/6-31G(d) method.

Reactions of the OH-adduct with O₂



Arrhenius parameters have been calculated for reaction (1) in order to estimate the branching ratios of channels (a) and (b). The results are : $A_a = 2.6 \times 10^{-14} \text{ cm}^3 \text{ molecule}^{-1} \text{ s}^{-1}$; $E_{a_a} = 3.8 \text{ kcal mol}^{-1}$ and $A_b = 1.5 \times 10^{-14} \text{ cm}^3 \text{ molecule}^{-1} \text{ s}^{-1}$; $E_{a_b} = 3.2 \text{ kcal mol}^{-1}$. This corresponds to about 0.4 and 0.6 for the branching ratios of channel (a) and (b), respectively, in reasonable agreement with experimental observations. In addition, the low pre-exponential factor and the presence of a small activation energy explain why the reactions of such radicals (OH-adducts) with O₂ are slow.

Reactions of the peroxy radical

OH regeneration: In order to rationalize the experimental results from the Valencia chamber which show more OH radicals than predicted by the existing models, and according to a suggestion of Mike Jenkins, the rate constants of two reaction channels of the peroxy radical (I) RO₂ have been investigated : cyclisation (yielding the bicyclic radical) and the H-atom transfer from the OH group to the O-O group (yealding RO radical), leading to ring opening and formation of muconaldehyde.

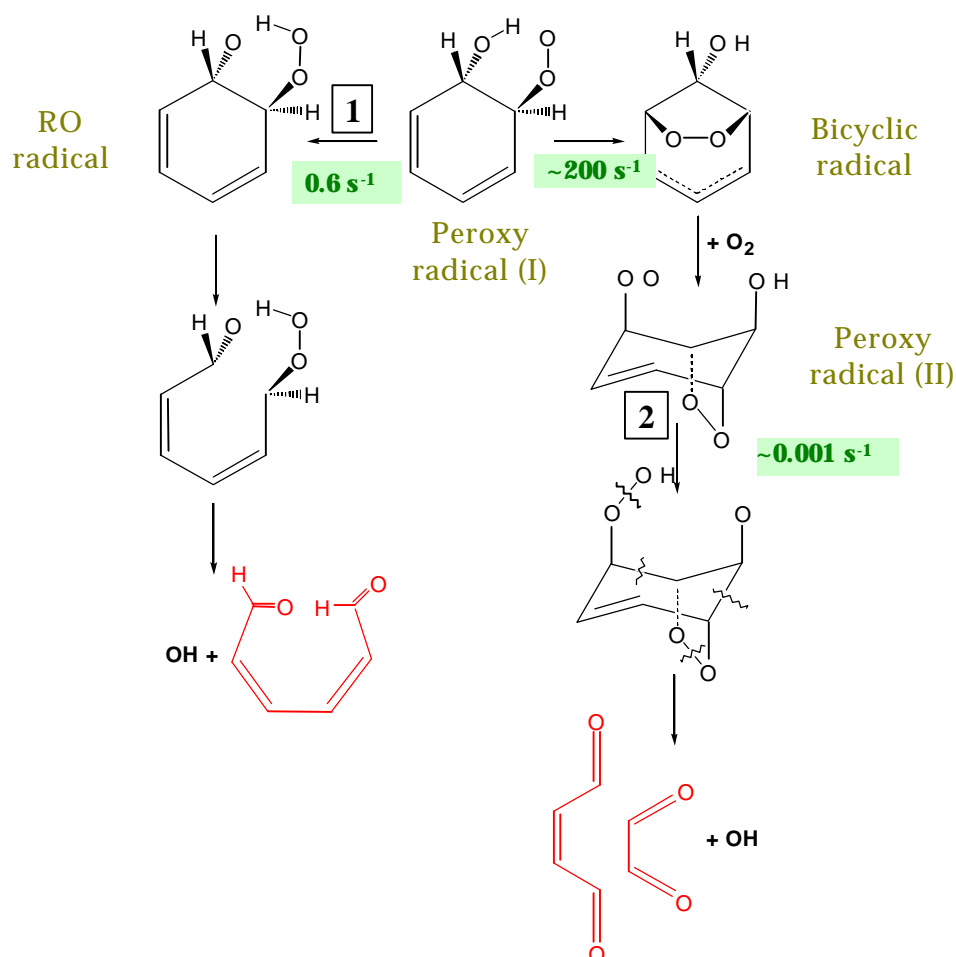


Figure 1 : Are there any competitive pathways able to regenerate OH radical ?

The results show that the cyclisation is preferred to the H-atom transfer and competes with the phenol formation. Moreover, the reaction pathways shown in figure 1 are not likely to occur as a result of significant barriers for steps (1) and (2) corresponding to internal H-transfer.

As can be seen, the H-transfer reactions are the limiting processes of the two pathways investigated and these pathways should be of negligible importance and cannot account for the regeneration of OH.

Reference

D. Johnson, S. Raoult, MT Rayez, JC Rayez and R. Lesclaux, Phys. Chem. Chem. Phys., 2002, **4**, 4678

Low pressure kinetic study of the BrO reaction with methanethiol (GPP9)

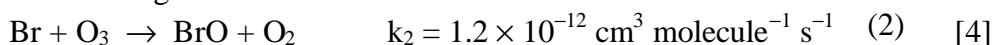
Alfonso Aranda, Yolanda Díaz de Mera, Diana Rodríguez, Sagrario Salgado, Ernesto Martínez
Departamento de Química Física, Facultad de Ciencias Químicas, Universidad de Castilla-La Mancha, Avenida Camilo José Cela, nº 10, 13071 - Ciudad Real, Spain.

Introduction

Methyl mercaptan (CH_3SH) is among the major trace reduced sulfur compounds emitted into the atmosphere. Natural biogenic emissions are the primary sources for this reduced compound [1]. The primary agents responsible for the gas phase oxidation of CH_3SH in the troposphere are OH radicals ($k_{298\text{K}} = 3.27 \times 10^{-11} \text{ cm}^3 \text{ molecule}^{-1} \text{ s}^{-1}$) and NO_3 radicals ($k = 8.9 \times 10^{-13} \text{ cm}^3 \text{ molecule}^{-1} \text{ s}^{-1}$) [2]. Under specific conditions, like in the marine boundary layer, initiation by different halogen compounds may also be important. Several reactions of CH_3SH with halogen compounds have been studied. For the reactions with F, Cl and Br, the obtained values for the rate constant at 298 K are 2.4×10^{-10} , 1.97×10^{-10} and $2.53 \times 10^{-12} \text{ cm}^3 \text{ molecule}^{-1} \text{ s}^{-1}$, respectively. Halogen oxides in tropospheric air have been measured with the DOAS technique. For BrO, levels range from 5 to $60 \times 10^8 \text{ molecule cm}^{-3}$ [3] showing that their reaction towards methyl mercaptan ought to be measured in order to evaluate the potential contribution to the removal of CH_3SH . So, in this work we report the first absolute kinetic study of the reaction $\text{BrO} + \text{CH}_3\text{SH} \rightarrow \text{Products}$ (1), its temperature and pressure dependences, the observation of the products of reaction with the possible mechanism and its atmospheric implication.

Experimental

The kinetic experiments were carried out using the discharge flow-mass spectrometry technique (DF-MS) over the temperature range 259-333 K and at low total pressure between 0.5 and 3 Torr. BrO radicals were generated inside a movable injector by reaction of bromine atoms with ozone before being introduced into the main reactor:



with $[\text{O}_3] \gg [\text{Br}]$ to ensure complete consumption of the Br atoms in order to avoid the interference of $\text{Br} + \text{CH}_3\text{SH}$ reaction.

Typical concentrations for Br_2 and O_3 were $(0.7\text{-}2) \times 10^{12}$ and $(0.6\text{-}1) \times 10^{14} \text{ molecule cm}^{-3}$.

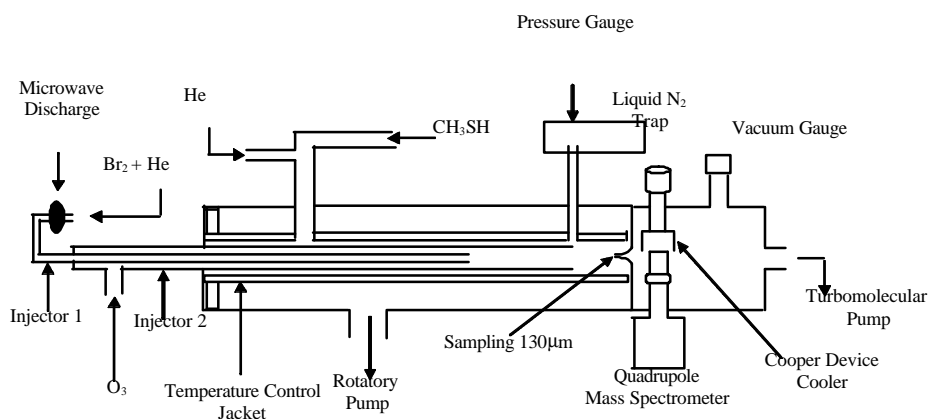


Figure 1. Schematic diagram of the experimental apparatus.

Results

In the absence of CH_3SH , BrO was expected to be lost through wall heterogeneous reactions and homogeneous recombination. In most cases, for the relatively low BrO concentrations used in this work, the homogeneous losses were negligible. The obtained rate constants for the wall losses were also low, $k_w = (1-3) \text{ s}^{-1}$.

All the experimental kinetics were carried out under pseudo-first-order conditions: $[\text{CH}_3\text{SH}]/[\text{BrO}] = 200 - 2000$.

The kinetic expression applying to such experiments was

$$\ln([\text{BrO}]_0/[\text{BrO}]_t) = (k' + k_w)t \quad \text{where } k' = k_1 [\text{CH}_3\text{SH}] \quad (\text{I})$$

Typical logarithmic decays of the intensity of BrO signal as a function of reaction time are shown in figure 2.

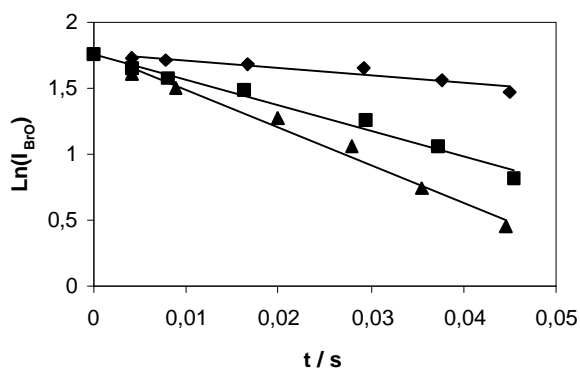


Figure 2: Examples of pseudo-first order plots for reaction $\text{BrO} + \text{CH}_3\text{SH}$ with $[\text{CH}_3\text{SH}]/(10^{14} \text{ molecule cm}^{-3}) = 0.71$ (\blacklozenge), 5.34 (\blacksquare), 8.65 (\blacktriangle) at 298 K and 1 Torr.

The bimolecular rate coefficient of interest, $k_1(p, T)$, is evaluated from the slope of k' versus $[\text{CH}_3\text{SH}]$ plot applying weighted least squares fittings. Some examples of these plots are given in figure 3.

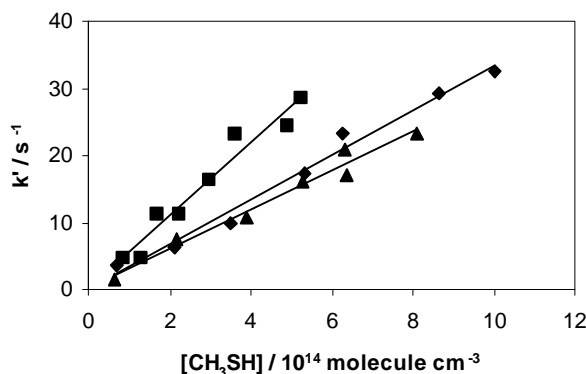


Figure 3: Pseudo-first order rate coefficients k' versus $[\text{CH}_3\text{SH}]$ for the $\text{BrO} + \text{CH}_3\text{SH}$ reaction at different temperatures. $T(\text{K}) = 259$ (\blacktriangle), 298 (\blacklozenge), 333 (\blacksquare) at $p = 1$ Torr.

The obtained results for k_1 in all experimental conditions are shown in table 1, where errors are one standard deviation.

T / K	P / Torr	$k_1 / \text{cm}^3 \text{molecule}^{-1} \text{s}^{-1}$
259	1.0	$(5.71 \pm 0.44) \times 10^{-14}$
278	1.0	$(5.25 \pm 0.70) \times 10^{-14}$
298	0.5	$(2.69 \pm 0.53) \times 10^{-14}$
	1.0	$(3.21 \pm 0.15) \times 10^{-14}$
	3.0	$(4.85 \pm 0.36) \times 10^{-14}$
333	1.0	$(2.93 \pm 0.20) \times 10^{-14}$

Table 1: Second order rate constants k_1 for reaction (1): $\text{BrO} + \text{CH}_3\text{SH} \rightarrow \text{P}$ at different temperatures and pressures. Errors are σ .

Conclusions

Experiments were carried out at four different temperatures and 1 Torr of total pressure of helium. The reaction rate was found to increase with decreasing temperature. The data obtained are shown plotted in Arrhenius form in figure 4.

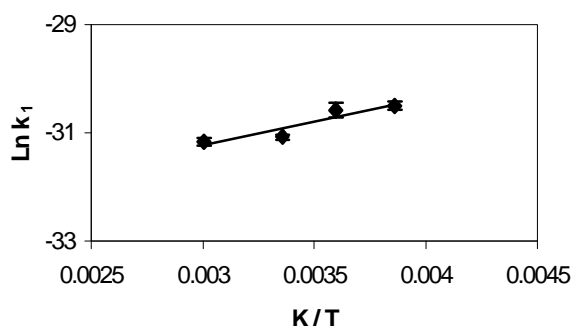


Figure 4: Arrhenius plot for the $\text{BrO} + \text{CH}_3\text{SH}$ reaction at 1 Torr

The following Arrhenius expression, derived from the figure, was obtained:

$$k = (2.2 \pm 1.9) \cdot 10^{-15} \exp[(827 \pm 254)/T] \text{ cm}^3 \text{ molecule}^{-1} \text{ s}^{-1} \quad (3)$$

with $k = (3.21 \pm 0.15) \cdot 10^{-14} \text{ cm}^3 \text{ molecule}^{-1} \text{ s}^{-1}$ at 298 K.

Concerning the pressure range studied, we have found a linear pressure dependence for k_1 . The rate coefficient increased when pressure was increased as it is shown in figure 5:

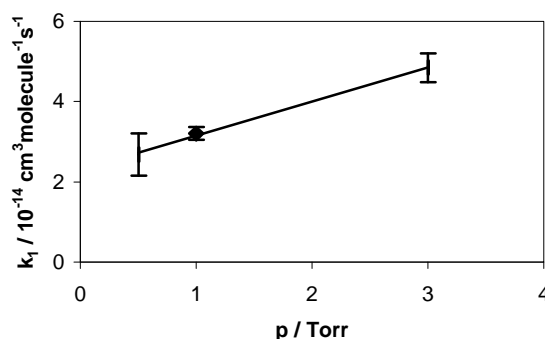


Figure 5. Rate coefficients for the $\text{BrO} + \text{CH}_3\text{SH}$ reaction as a function of pressure. Diluent gas: He

Discussion

Some additional experiments increasing the concentration of the reactants were conducted to identify the products and intermediates of reaction (1). The peaks observed by mass spectrometry

show the presence of HOBr as product. The relative low value of the pre-exponential factor, the negative temperature dependence observed for k_1 , and the increase of this constant with higher pressures clearly suggest the formation of an association complex, which can then decompose either back to reactant or to give products



In the experiments designed to identify products, where concentrations are considerably higher than in the kinetic runs, CH_3S may undergo self-recombination giving DMDS, reaction with Br_2 giving CH_3SBr , and with ozone in excess originating CH_3SO , what would explain all the minor mass spectrometric peaks observed:



$$k_4 = 4 \times 10^{-11} \text{ cm}^3 \text{ molecule}^{-1} \text{ s}^{-1} \quad [5]$$



$$k_5 = (1.7 \pm 0.5) \times 10^{-10} \text{ cm}^3 \text{ molecule}^{-1} \text{ s}^{-1} \quad [6]$$



$$k_6 = 5.29 \times 10^{-12} \text{ cm}^3 \text{ molecule}^{-1} \text{ s}^{-1} \quad [4]$$

Concerning the atmospheric implications in the removal of CH_3SH by BrO, the high [BrO] tropospheric concentrations and the measured rate constant of this reaction shows reaction (1) as a potentially important sink in the marine atmosphere. Although BrO- CH_3SH rate constant is three orders of magnitude lower than the OH- CH_3SH rate constant, the measured BrO concentration is in the range $(5\text{-}60) \times 10^8 \text{ molecule cm}^{-3}$, much higher than the [OH] concentration $(9.7 \times 10^5 \text{ molecule cm}^{-3})$ [7]. From the previous data, the room temperature gas phase lifetime of methyl-mercaptan may be calculated as 8.7 hours for OH radicals, and from 15.6 to 1.3 hours, for BrO. Thus, it may be concluded that CH_3SH would be scavenged efficiently by BrO and so our results should be taken into account in the chemical box models to evaluate the impact of the removal of CH_3SH in the marine boundary layer.

References

- 1.- Atkinson, R., D.L. Baulch, R.A. Cox, R.F. Jr. Hampson, J.A. Kerr, M.J. Rossi, J. Troe, *J. Phys. Chem. Ref. Data* 26 (1997) 1329.
- 2.- Urbanski, S.P., R.H. Wine, in Z.B. Alfassi (Ed.), S-Centered Radicals, *John Wiley & Sons*, Chichester, 1999.
- 3.- Hausmann, M., U. Platt, *J. Geophys. Res.* 99 (1994) 25399.
- 4.- DeMore, W. B.; Sander, S. P.; Golden, D.M.; Hampson, R. F.; Kurylo M. J.; Howard, C. J.; Ravishankara, A. R.; Kolb, C. E.; Molina, M. J. *Chemical kinetics and photochemical data for use in stratospheric modelling. Evaluation number 12, JPL Publication 97-4*, 1-266 (1997).
- 5.- C. Anastasi, M. Broomfield, O.J. Nielsen, P. Pagsberg, *Chem. Phys. Lett.* 182 (1991) 643.
- 6.- J.M. Nicovich, K.D. Kreutter, C.A. Van Dijk, P.H. Wine, *J. Phys. Chem.* 96 (1992) 2518.
- 7.- R. Prinn, R. Weiss, B. Miller, J. Huang, F. Alyea, D. Cunnold, P. Fraser, D. Hartley, D. Simmons, *Science*. 269 (1995) 187.

A PLP-RF Kinetic Study of the Atmospheric Reactivity of Propene and a Series of 3-Halopropenes with Cl Atoms (GPP9)

José Albaladejo, Alberto Notario, Carlos A. Cuevas and Ernesto Martínez

Departamento de Química Física, Facultad de CC Químicas, Universidad de Castilla-La Mancha, Avenida Camilo José Cela, nº 10, 13071 - Ciudad Real, Spain.

E-mail: Jose.Albaladejo@uclm.es

Introduction

Chlorine atoms in the troposphere may play a more important role in the oxidation of volatile organic compounds (VOCs) and in the production of ozone than previously thought. Atomic Cl reactions are now considered of potential importance in the marine boundary layer and in coastal regions where significant Cl concentrations may be present (10^4 - 10^5 atom cm^{-3}) (Spicer *et al.*, 1998). Atomic chlorine is highly reactive with a variety of organic and inorganic compounds, so that relatively small concentrations can compete with OH, O_3 and NO_3 in determining the tropospheric fate of such compounds. These Cl atoms, in polluted coastal regions, may initiate organic oxidation in a manner analogous to that of OH radicals, which is believed to be the dominant loss process of most organic compounds (Finlayson-Pitts, 1993). Hence, measuring accurately the rate coefficients of the reactions involving Cl atoms is very important in order to assess the role of these reactions in atmospheric chemistry at global or regional scales.

We report in this work room-temperature absolute rate constant determined in the pressure range 20 - 200 Torr, for the reactions of atomic Cl with propene and the following series of halopropenes: 3-fluoropropene, 3-chloropropene, 3-bromopropene and 3-iodopropene. These rate coefficients have been measured, using a newly constructed pulsed laser photolysis-resonance fluorescence (PLP-RF) system.

In order to check this new system in a wide range of Cl rate constants, the reactions of Cl with acetone and isoprene were also investigated. The rate coefficients of these two reactions at 298 K, which extend from $\sim 3 \times 10^{-12}$ to 4×10^{-10} $\text{cm}^3 \text{ molecule}^{-1} \text{ s}^{-1}$, have been recently measured using the same technique (PLP-RF) in a different laboratory (Notario *et al.*, 1997; Notario *et al.*, 2000) and will be compared with our results.

There have been relatively few studies of the Cl + propene reaction, being the study of Stutz *et al.* (1998) the only reported absolute measurements carried out in a fast flow discharge system at 1 Torr of total pressure. Thus, the present work provides the first absolute determination of the rate constant value for this reaction at higher pressures. As far as we know, this work also provides the first measurements for the reactions of Cl with the above mentioned series of 3-halopropenes.

Experimental System

The experimental technique of Pulsed Laser Photolysis-Resonance Fluorescence (PLP-RF) was used in this study (Figure 1). Cl atoms were produced in a excess of the VOC and He, by photolyzing Cl_2 at 308 nm using a pulsed excimer XeCl laser. The radiation ($\lambda \approx 135$ nm) from a microwave-driven lamp, through which He containing a low concentration of Cl_2 was flowed, was used to excite the resonance fluorescence from Cl in the cell. Signals were obtained using photon-counting techniques in conjunction with multichannel scaling. The fluorescence signal from the PMT was processed by a preamplifier and sent to an multichannel scaler to collect the time-resolved signal. The multichannel scaler was coupled to a microcomputer for further kinetics analysis.

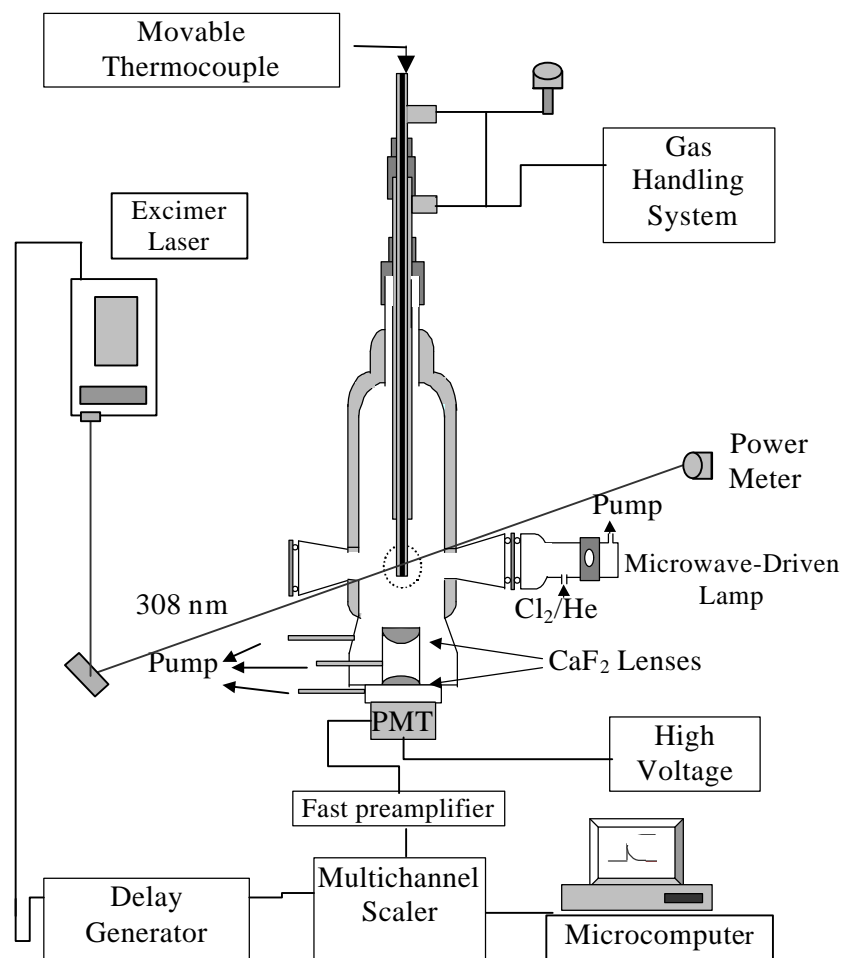


Figure 1: Schematic diagram of the experimental setup used in the present study

Results

With a reaction mixture containing Cl_2 , the VOC, helium, and in the absence of secondary reactions, the temporal profile of Cl is governed by the following processes:

$\text{Cl} + \text{VOC} \rightarrow \text{products}$ k (bimolecular rate constant)

$\text{Cl} \rightarrow \text{loss by diffusion}$ k_{dif} (first order decay rate for the loss of Cl in absence of VOC)

Under first order conditions and in the absence of secondary reactions, the Cl atom concentration profile should follow a simple exponential rate law:

$$[\text{Cl}]_t = [\text{Cl}]_0 \exp(-k't) \quad (\text{I})$$

$$k' = k[\text{VOC}] + k_{\text{dif}} \quad (\text{II})$$

The values of k' (pseudo-first-order rate constant) were determined in experiments at different concentrations of the VOC studied. Then, the k' vs. $[\text{VOC}]$ data, according to eq. (II), were also subjected to weighted linear least-squares analyses to obtain k . Examples of the k' vs. $[\text{VOC}]$ plots are presented in Figure 2, showing in all cases a good linearity.

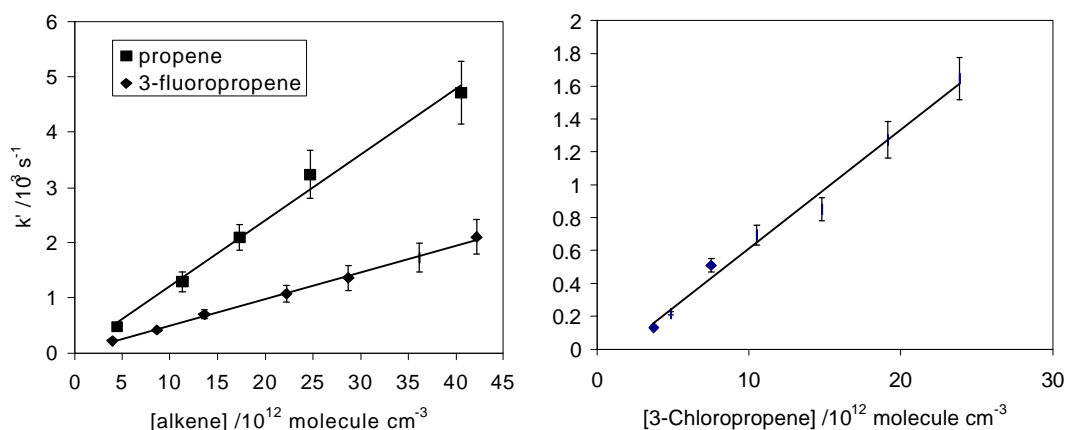


Figure 2. Examples of plots of k' vs. the concentration of some VOC studied in this work. $T = 298 \text{ K}$ and $p = 60 \text{ Torr}$. Solid lines are obtained from the weighted least-squares analysis of the data and give the corresponding rate constants ($\pm 2\sigma$) which are summarised in Table 1.

The experimental conditions and the values obtained for the rate coefficients $k_1 - k_7$ are listed in Table 1. As it can be seen in this table, no clear pressure dependence of the rate coefficients was observed in the pressure range studied (20 - 200 Torr) and the value reported is the weighted average of the measurements at three different pressures. The quoted errors are 2σ from the statistical analysis.

In the other hand and concerning the reactivity of the studied VOCs with Cl atoms is compared with their reactivity with OH, NO_3 and O_3 in Table 2. The rate constants summarised in this Table can be used to calculate the atmospheric lifetimes ($\tau = 1/\kappa[\Xi]$, where $\Xi = \text{X}\lambda$, OH, NO_3 or O_3). Using $[\text{Cl}] = 10^5$, $[\text{OH}] = 5 \times 10^5$, $[\text{NO}_3] = 5 \times 10^7$ and $[\text{O}_3] = 7 \times 10^{11}$ (in units of molecule cm^{-3}), the lifetimes of the compounds studied with Cl, OH, NO_3 and O_3 (when data are available) can be estimated and they are presented in Table 2 expressed in hours.

Conclusions

From the present work we can extract the following conclusions:

1.- The rate constants measured in this work for acetone and isoprene at room temperature ($(2.93 \pm 0.20) \times 10^{-12}$ and $(3.64 \pm 0.20) \times 10^{-10} \text{ cm}^3 \text{ molecule}^{-1} \text{ s}^{-1}$ respectively) are in excellent agreement with previous values obtained by the same technique, $(3.06 \pm 0.38) \times 10^{-12} \text{ cm}^3 \text{ molecule}^{-1} \text{ s}^{-1}$ (Notario *et al.*, 2000) for acetone, and $(3.61 \pm 0.10) \times 10^{-10} \text{ cm}^3 \text{ molecule}^{-1} \text{ s}^{-1}$ (Notario *et al.*, 1997) for isoprene. These rate coefficients permit to validate the newly built PLP-RF apparatus and to check its ability for measuring reactions rate constants in a large range, indicating that is a selective and sensitive technique to follow the reactions of Cl or halogen atoms in general.

2.- As it can be seen in Table 1, no clear dependence of the rate coefficients was observed in the pressure range studied (20 – 200 Torr).

3.- The comparison of the reactivity of propene and 3-halopropenes with Cl atoms shows that the rate constant of $\text{Cl} + \text{propene}$ ($k_3 = (1.40 \pm 0.24) \times 10^{-12} \text{ cm}^3 \text{ molecule}^{-1} \text{ s}^{-1}$) is reduced when an H atom is substituted by a halogen atom (see Table 1).

4.- In general, it is observed a reduction in the reactivity of the halopropene compounds when the electronegativity of the halogen atom in allylic position is increased (from iodine to fluorine) as corresponds with a parallel increase in the negative inductive effect (see Table 1):

$$k_{3\text{-fluoropropene}} < k_{3\text{-chloropropene}} < k_{3\text{-bromopropene}} \approx k_{3\text{-iodopropene}} < k_{\text{propene}}$$

5.- As can be seen in Table 2, on the basis of the rate constants obtained in the range 20 - 200 Torr, the reaction of alkenes and 3-halopropenes with chlorine atoms can provide effective tropospheric loss pathways for such compounds, and, it is expected to play a significant role in the

tropospheric chemistry of the marine boundary layer and in coastal regions where the chlorine atom concentration peak at dawn, much earlier than OH. These processes can compete with the effective loss pathway by O₃, by OH during the day and by NO₃ radical during the night.

6.- Finally, this kinetic study may contribute to extend the database for the reactions of Cl atoms with VOCs, and to clarify the influence of the different halogen atom substituents on the reactivity of Cl with alkenes and haloalkenes.

References

- Atkinson, R., Baulch, D.L., Cox, R.A., Hampson, R.F.Jr, Kerr J.A., Rossi, M.J., Troe, J., 1997: Evaluated kinetic, photochemical and heterogeneous data for atmospheric chemistry: supplement V, IUPAC subcommittee on gas kinetic data evaluation for atmospheric chemistry, *J. Phys. Chem. Ref. Data* **26**, 521-1011.
- DeMore, W.B., Sander, S.P., Golden, D.M., Hampson, R.F., Kurylo, M.J., Howard, C.J., Ravishankara, A.R., Kolb, C.E., Molina, M.J., 1997: *Chemical Kinetics and Photochemical Data for Use in Stratospheric Modeling*. Evaluation No. 12, JPL Publication No. **97-4**; Jet propulsion Laboratory: Pasadena, CA.
- Finlayson-Pitts, B. J., 1993: Chlorine atoms as a potential tropospheric oxidant in the marine boundary layer, *Research on Chemical Intermediates*, **19**, 235-249. Grosjean, E. and Grosjean, D., 1996: Rate constants for the gas-phase reaction of ozone with 1, 1-disubstituted alkenes: *Int. J. Chem. Kinet*, **28**, 911-918.
- Le Calve, S., Hitier, D., Le Bras, G., Mellouki, A., 1998: Kinetic studies of OH reactions with a series of ketones, *J. Phys. Chem. A* **102(24)**, 4579-4584. Marston, G., Monks, P.S., Canosa-Mas, C.E., Wayne, R.P., 1993: Correlations between rate parameters and calculated molecular properties in the reactions of the nitrate radical with alkenes, *J. Chem. Soc. Faraday Trans.* **89**, 3899-3905.
- Martínez, E., Cabañas, B., Aranda, A., Martin, P., Wayne, R.P., 1996: Kinetic study of the reactions of NO₃ with 3-chloropropene, 3-bromopropene and 3-iodopropene using LIF detection, *J. Chem. Soc. Faraday Trans.* **92**, 4385-4389.
- Martínez, E., Cabañas, B., Aranda A., Martin, P., Salgado, S., 1997: A temperature dependence study of the gas-phase reaction of the nitrate radical with 3-fluoropropene followed by laser induced fluorescence detection, *Int. J. Chem. Kinet.* **29**, 927-932.
- Notario, A., Mellouki, A., Le Bras, G., 1997: Kinetic of Cl atom reactions with butadienes including isoprene, *Chem. Phys. Lett.* **281**, 421-425.
- Notario, A., Mellouki, A., Le Bras, G., 2000: Rate constants for the gas-phase reactions of chlorine atoms with a series of ketones, *Int. J. Chem. Kinet.* **32**, 62-66.
- Spicer, C.W., Chapman, E.G., Finlayson-Pitts, B.J., Plastringe, R.A., Hubbe, J.M., Fast, J.D. and Berkowitz, C.M., 1998: Unexpectedly high concentrations of molecular chlorine in coastal air, *Nature* **394**, 353-356. Stutz, J., Ezell, M.J., Ezell, A.A., Finlayson-Pitts, B.J., 1998: Rate constants and kinetic isotope effects in the reactions of atomic chlorine with n-butane and simple alkenes at room temperature, *J. Phys. Chem. A* **102(44)**, 8510-8519. Tsang, W., 1991: Chemical kinetic data base for combustion chemistry. Part V. Propene, *J. Phys. Chem. Ref. Data* **20**, 221-273.
- Tuazon, E.C., Atkinson, R. and Aschmann, S.M., 1990: Kinetics and products of the gas-phase reactions of the OH radical and O₃ with allyl chloride and benzyl chloride at room temperature: *Int. J. Chem. Kinet.* **22**, 981-986. Wayne, R.P., Barnes, I., Biggs, P., Burrows, J.P., Canosa-Mas, C.E., Hjorth, J., Le Bras, G., Moortgat, G.K., Perner, D., Poulet, G., Restelli, G., Sidebottom, H., 1991: The nitrate radical: physics, chemistry and the atmosphere, *Atmos. Environ.* **25A**, 1-206.

Table 1: Summary of experimental conditions and the obtained rate coefficients for the reaction of Cl with the studied compounds at room temperature. The final results, k_1 - k_7 , are obtained from the combination of the results at 20 - 200 Torr since no pressure dependence of the rate coefficients was observed in this pressure range.

Compound	P (torr)	[VOC] (10^{12} molecule cm^{-3})	$(k \pm 2\sigma)^a$ (cm^3 molecule $^{-1}$ s $^{-1}$)
Acetone	20	34.3-136	$(2.5 \pm 0.5) \times 10^{-12}$
	60	33.2-182	$(3.03 \pm 0.30) \times 10^{-12}$
	200	45.5-460	$(2.94 \pm 0.10) \times 10^{-12}$
			$k_1 = (2.93 \pm 0.20) \times 10^{-12}$
Isoprene	30	2.5-20.2	$(3.59 \pm 0.18) \times 10^{-10}$
	60	2.3-13.2	$(3.74 \pm 0.21) \times 10^{-10}$
	200	4.1-12	$(3.47 \pm 0.62) \times 10^{-10}$
			$k_2 = (3.64 \pm 0.20) \times 10^{-10}$
Propene	20	4.5-29.6	$(1.51 \pm 0.10) \times 10^{-10}$
	60	4.5-40.5	$(1.39 \pm 0.12) \times 10^{-10}$
	200	8.9-78	$(1.29 \pm 0.10) \times 10^{-10}$
			$k_3 = (1.40 \pm 0.24) \times 10^{-10}$
3-fluoropropene	29	4.5-35.3	$(5.70 \pm 0.41) \times 10^{-11}$
	60	4-42.1	$(4.64 \pm 0.26) \times 10^{-11}$
	200	11.3-114	$(4.56 \pm 0.80) \times 10^{-11}$
			$k_4 = (4.92 \pm 0.42) \times 10^{-11}$
3-chloropropene	20	5.5-21.2	$(7.27 \pm 1.46) \times 10^{-11}$
	60	3.7-23.9	$(7.61 \pm 0.96) \times 10^{-11}$
	200	9.9-52.7	$(7.29 \pm 2.36) \times 10^{-11}$
			$k_5 = (7.47 \pm 1.50) \times 10^{-11}$
3-bromopropene	20	2.4-23.7	$(1.17 \pm 0.10) \times 10^{-10}$
	60	5.6-54.4	$(1.26 \pm 0.10) \times 10^{-10}$
	200	6.5-48.4	$(1.26 \pm 0.10) \times 10^{-10}$
			$k_6 = (1.23 \pm 0.14) \times 10^{-10}$
3-iodopropene	20	2.3-13.8	$(1.56 \pm 0.14) \times 10^{-10}$
	60	3.6-44.5	$(1.31 \pm 0.14) \times 10^{-10}$
	200	7.1-61.7	$(1.19 \pm 0.10) \times 10^{-10}$
			$k_7 = (1.29 \pm 0.15) \times 10^{-10}$

^aThe quoted errors in the final results are 2σ from the weighted statistical analysis.

Table 2: Comparison of the rate constants at room temperature for the reactions of Cl, OH, NO₃ and O₃ with the studied compounds (in cm³ molecule⁻¹ s⁻¹) and the corresponding atmospheric lifetimes, τ (in hours).

Compound	k (Cl) ^a	k (OH)	k (NO ₃)	k (O ₃)	$\tau_{\text{Cl}}/\text{h}$	$\tau_{\text{OH}}/\text{h}$	$\tau_{\text{NO}_3}/\text{h}$	$\tau_{\text{O}_3}/\text{h}$
Isoprene	3.64×10^{-10}	1.01×10^{-10} ^b	8×10^{-13} ^g	1.27×10^{-17} ⁱ	7.6	5.4	6.9	44.3
Acetone	2.93×10^{-12}	1.9×10^{-13} ^c	$<3 \times 10^{-17}$ ^b	—	948	2924	$>1.85 \times 10^5$	—
Propene	1.40×10^{-10}	2.64×10^{-11} ^d	9.3×10^{-15} ^h	1.11×10^{-17} ^j	20	21	597.5	39
3-fluoropropene	4.92×10^{-11}	1.42×10^{-11} ^e	3.9×10^{-15} ^e	—	56.5	39	1424.5	—
3-chloropropene	7.47×10^{-11}	1.53×10^{-11} ^f	4.95×10^{-15} ^f	1.6×10^{-18} ^k	37	36	1122	248
3-bromopropene	1.23×10^{-10}	1.41×10^{-11} ^f	3.85×10^{-15} ^f	—	22.5	39.5	1443	—
3-iodopropene	1.29×10^{-10}	$\leq 2.85 \times 10^{-11}$ ^f	$\leq 3.91 \times 10^{-14}$ ^f	—	21.5	≥ 19	≥ 142	—

^aThis work; ^bAtkinson *et al.*, 1997; ^cLe Calvé *et al.*, 1998; ^dTsang 1991; ^eMartínez *et al.*, 1997; ^fMartínez *et al.*, 1996; ^gWayne *et al.*, 1991; ^hMarston *et al.*, 1993. ⁱGrosjean *et al.*, 1996; ^jDeMore *et al.*, 1997; ^kTuazon *et al.*, 1990.

Reactivity of Thiophene and Methylthiophenes in the Atmosphere: Kinetics Study of NO₃ Reactions (GPP9)

B. Cabañas*, S. Salgado, P. Martín, M. T. Baeza and E. Martínez.

Facultad de Químicas, Universidad de Castilla-La Mancha. Campus Universitario s/n, 13071, Ciudad-Real, Spain.

E-mail: Ernesto.Martinez@uclm.es <<mailto:Martinez@uclm.es>>

**Author to whom correspondence should be addressed.*

Introduction.

A multitude of oxygen and sulphur containing organic compounds are released into the atmosphere as a result of fossil fuel refining and combustion. In recent years, a large body of kinetic and mechanistic data concerning reactions of atmospherically relevant oxygen or sulfur containing carbohydrates with OH, O₃ and NO₃ have been determined [1-4] in order to analyse the principal degradation pathways and to assess the potential significance of these compounds for the chemistry of the atmosphere. The OH radical reaction is normally the main sink for numerous compounds during daytime. However, the NO₃ radical, that undergoes photolysis by sunlight, is mainly involved in night-time atmospheric chemistry, when photochemically generated radicals, like OH, are present in very low concentrations. The high concentration of NO₃ under dark conditions makes the removal by NO₃ a competitive process. Thus, night time reaction with NO₃ is essential in atmospheric chemistry.

The reactions of some heterocycles with OH and O₃ have been the subject of different studies. However, the investigation about the reactivity of these compounds with the NO₃ radical is specially scarce, and more kinetic data for the NO₃ reaction with heterocycles compounds are needed to get a better understanding on its role in the atmospheric chemistry. The reaction of thiophene with OH and O₃ has been reported in several works [5-8]. But the reaction with NO₃ has been less investigated [4,9], and no kinetic data are available for substituted thiophenes.

Thiophene is a five-member heterocycle ring that is emitted in processes of energy production such as coal gasification, fuel oil, natural gas and coal combustion and also it is detected over seaweed fields [8]. The 2-and 3- methylthiophenes have been used as possible precursors of the sulfur componente of the fluid catalytic cracking (FCC) gasoline, desulfurization was not observed with methylthiophenes [9] and lower sulphur levels in gasoline would help to reduce tail-pipe emissions of NO_x gases and unburned hydrocarbons .

In this work, we report the first absolute kinetic study of the reaction of NO₃ radical with some methylthiophenes (2-methylthiophene, 3-methylthiophene and 2,5-dimethylthiophene) continuing the systematic investigation of the NO₃ reaction with heterocycles developed in our laboratory and completing the previous work on the reactivity of NO₃ radical with thiophene [10]. We have investigated the influence of alkylation around the double bond on reactivity of heterocyclic aromatics. A relative study of the reactions of the three compounds with NO₃ at 298 K using trans-2-butene as reference compound have also been reported, in order to compare the results obtained by both absolute and relative methods.

Experimental and results.

Absolute Method.

All the kinetic measurements of absolute rate constants were carried out using a discharge-flow tube reactor with LIF detection for the nitrate radical excited at 662 nm. The experimental setup has been described elsewhere [11] ([figure 1](#)) and only relevant details are given here. Nitrate radicals were generated in a side-arm tube by the reaction $F + HNO_3 \rightarrow NO_3 + HF$. Fluorine atoms

were obtained by passing F₂/He mixtures through a microwave discharge. Anhydrous gaseous HNO₃ in a He carrier was prepared by bubbling He through a mixture of H₂SO₄/HNO₃. The NO₃ radical was admitted from the cell through a fixed port. The initial NO₃ concentration ranged from (3.23-9.36) × 10¹² molecule cm⁻³. The reactants were added to the flow through a sliding injector, obtaining contact times between the NO₃ radical and the reactant ranged from 0 to 80 ms. Reactants concentrations varied between 1.68 × 10¹³ and 9.07 × 10¹³ molecule cm⁻³. The temperature flow tube was set between 260 and 433 (±1) K. The flow tube was cooled and heated at the desired temperature by circulating liquid silicone through a cooling jacket connected by viton tubes to a thermostatic bath, where the temperature was controlled. The internal temperature was previously calibrated and the external value was corrected adequately.

It was not possible to perform the experiments with a large excess of reactant over NO₃, due to the low volatility of these heterocycles. The ratio [reactant]/[NO₃] was varied between 3 and 10, so the data for the reaction of NO₃ with the compounds were analysed, using the second-order integrated rate expression [12], assuming 1:1 stoichiometry:

$$\ln \frac{(M - X_a)}{[M(1 - X_a)]} = (B_0 - A_0) kt \quad (1)$$

Where M = [reactant]₀/[NO₃]₀, B₀ = [reactant]₀, A₀ = [NO₃]₀ and

$$X_a = \frac{[\text{NO}_3]_0 - [\text{NO}_3]_t}{[\text{NO}_3]_0} \quad (2)$$

Then, second order rate constant may be obtained as the slope of plots of 1/(B₀ - A₀) ln[(M - X_a)/M(1 - X_a)] vs time. Figure 2 shows plots of 1/(B₀ - A₀) ln[(M - X_a)/M(1 - X_a)] vs time for the reaction of the nitrate radical with 3-methylthiophene at different temperatures. Figure 3 is an Arrhenius plot of the data obtained for the reaction of NO₃ with 2-methylthiophene, where ln k have been plotted vs 1/T. A linear least-squares analysis of the data yields the activation energy and the preexponential factor.

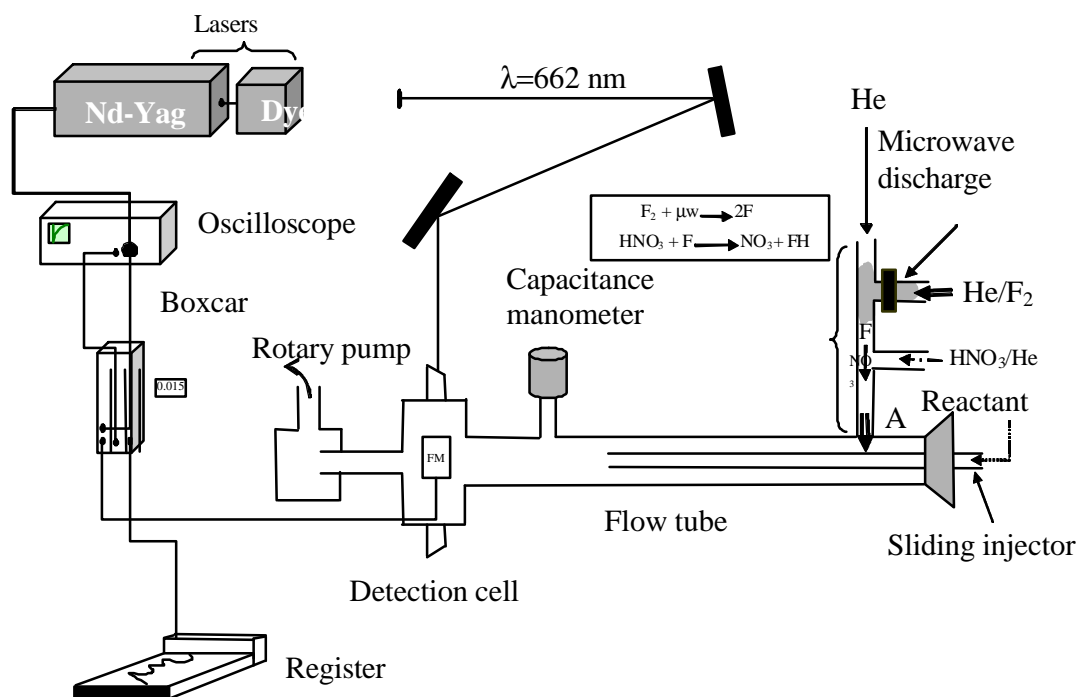
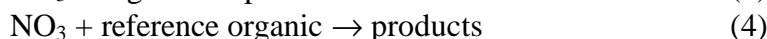


Figure 1: Absolute System: schematic diagram of apparatus

Relative Method.

The relative rate experiments were carried out in a ca. 80 l collapsible Teflon bag (Alltech). The bag was housed in a dark cabinet, and operated at atmospheric pressure (720 ± 10 torr) and 296 ± 2 K. Known quantities of each component of the reaction mixture were introduced separately into the chamber from pirex bulbs by a stream of ultrahigh purity N_2 . Concentration of heterocycle compound, reference organic and internal standard were measured by sampling the bag to a gas chromatograph (SRI 8610C) with flame ionisation detection (GC-FID) via a 1 cm^3 sample loop. Separation of individual compounds in the sample was achieved using a stainless steel (SS) column packet Chromosorb 102 80-100 MT 250. The temperature for the column was programmed from 313 to 493 K. The reference organic compound used in our case was trans-2-butene, with a known rate coefficient for its NO_3 -reaction, $k_{\text{trans-2-butene}} = 3.9 \times 10^{-13} \text{ cm}^3 \text{ molecule}^{-1} \text{ s}^{-1}$ [4]. Typical incremental amounts of N_2O_5 in the range of $(1.3\text{-}2.6) \times 10^{14} \text{ molecule cm}^{-3}$, were added to the bag during an experiment.

This experimental technique is based upon monitoring the relative decay rates of a series of organics, including at least one compound whose NO_3 radical reaction rate constant is reliably known, in the presence of NO_3 radicals. NO_3 radicals are generated by thermal decomposition of N_2O_5 . Since the organics studied here react negligibly with N_2O_5 and NO_2 , then under our experimental conditions, the sole chemical loss process of these compounds is due to reaction with NO_3 radicals:



Additionally, small amounts of dilution occurred as a result of the incremental additions of N_2O_5 to the reactant mixture. A standard internal, in this case ethane, which reaction with NO_3 is negligible ($k \leq 4 \times 10^{-18} \text{ cm}^3 \text{ molecule}^{-1} \text{ s}^{-1}$) [4], has been added to the system to quantify dilution effects. The rate coefficient k , with this correction of dilution, is defined by equation (5):

$$\ln \left(\frac{[\text{organic}]_0}{[\text{organic}]_t} \right) - D_t = \frac{k}{k_{\text{ref}}} \left(\frac{[\text{reference}]_0}{[\text{reference}]_t} \right) - D_t \quad (5)$$

Where D_t is the dilution factor at time t . Hence Plots of $[\ln([\text{reactant}]_0/[\text{reactant}]_t)]$ against $[\ln([\text{reference}]_0/[\text{reference}]_t)]$ should yield straight lines of slope $k/k_{\text{reference}}$. The slope combined with the rate constant of the reaction of reference, $k_{\text{reference}}$, gives the rate coefficient. Figure 4 shows the data obtained for the reaction of 3-methylthiophene with NO_3 .

Table 1 summarizes the rate coefficients obtained by both the absolute and relative techniques for the reactions of NO_3 radical with the studied heterocycles compounds. Activation energies and preexponential factor obtained are also summarized in table 1.

Table 1.- Rate constant determined in the present work by both absolute and relative methods, for the gas-phase reactions of thiophene and methylthiophenes with NO_3 radical at 298 K.

Compound	$K_{NO_3} / 10^{-13} \text{ cm}^3 \text{ molecule}^{-1} \text{ s}^{-1}$ Absolute technique	Ea/kJ mol ⁻¹	$K_{NO_3} / 10^{-13} \text{ cm}^3 \text{ molecule}^{-1} \text{ s}^{-1}$ Relative technique
thiophene	0.40 ± 0.02	18.4 (260-277K) - 4.2 (298-433K)	0.32 ± 0.03
2-methylthiophene	9.3 ± 0.6	-18.7 \pm 1.0	8.9 ± 2.7
3-methylthiophene	10.0 ± 1.7	-14.3 \pm 1.5	9.9 ± 2.2
2,5-dimethylthiophene	40.1 ± 3.0	-----	29.9 ± 17.1

Discussion.

The results obtained for the studied reactions by both relative and absolute methods, lead to similar rate coefficients. Similar rate constant values corresponding to both methods indicate that no pressure dependence is observed and results can be extrapolated to atmospheric conditions. No conclusive results were obtained for the reaction of 2,5-dimethylthiophene which indicates special difficulties in the absolute experiments for such NO_3 reaction, then a more careful kinetic study of the 2,5-dimethylthiophene- NO_3 reaction is needed.

The reactivity of NO_3 with thiophene has an anomalous temperature dependence as we have described previously [10]. For low temperatures (260-277), a slight decrease of the rate constant when the temperature increases is observed and when the temperature changes from 298 to 433 K, the rate constant increase. The rate constant appears to be essentially independent on temperatures between 272 and 296 K. This result could be due to two parallel mechanisms. At room and higher temperatures the dominant mechanism possibly is H-abstraction mechanism and an addition mechanism could be the important at lower temperatures.

The rate constant for 2-methylthiophene, 3-methylthiophene and 2,5-dimethylthiophene are higher than that for thiophene. The positive inductive effect of the CH_3 group enhances the electron density of the ring and so the electrophilic attack from NO_3 radicals will be favoured. A negative temperature dependence for the reactions of methylthiophenes is observed. Additionally, the magnitude of the rate constant is clearly dependent on the number of alkyl groups. Data analysis indicates an increase of the rate constant with increasing degree of alkylation. The measured rate coefficients for the reactions of methylthiophenes studied are in the range of the rate constants obtained for the reactions of NO_3 radical with alkenes, terpenes and others sulfur-containing organic compounds [4]. Our results are entirely consistent with a radical addition process. The positive inductive effect of the CH_3 group enhances the electron density of the ring and so the electrophilic attack from NO_3 radicals will be favoured.

References

- (1) B. R. Bandy. The Chemistry of the Atmosphere: Oxidants and oxidation in the Earth's Atmosphere. The Royal Society job Chemistry, Cambridge, 1998.
- (2) Wayne, R. P. Chemistry of Atmospheres. 3 Ed. Oxford University Press, 2000.
- (3) Finlayson-Pitts, Pitts, J.N. Chemistry of the Upper and lower Atmospheres. 2Ed. Academic Press, New York, 1999.
- (4) Atkinson, J. Phys. Chem. Ref Data (1991) 459.
- (5) Atkinson, R; Aschmann, S.M; Carter, W. P. L; Int. J. Chem, 15 (1983) 51.
- (6) Wine, P.H; Thompton, R.J. Int. J. Chem. Kinet, 16 (1984) 867.
- (7) Atkinson, R; J. Phys. Chem. Ref. Data Monogr. 1 (1989).
- (8) Atkinson, R; J. Phys. Chem. Ref. Data Monogr. 2 (1994).
- (9) Atkinson, R. Aschmann, S. M. Winer, A.M; Carter, W.P.L. Environ. Sci. Tech, 19, 90, 1985.
- (8) Berndt, T; Böge, O and Rolle, W; Environ. Sci. Tech. 31(4) 1997, 1157-1162.
- (9) Kirton, P.J; Ellis, J; Grips, P.T. Fuel 70 (1991) 1383.
- (10) Cabañas, B; Martín, P; Baeza, M.T; López, R; Martínez, E. Chem. Phys. Lett.358,5-6, 401-406, 2002.
- (11) E. Martínez, B. Cabañas, A. Aranda, P. Martín and R.P. Wayne J. Chem. Soc. Faraday Trans. 92, 4385-4391. 1996.
- (12) Laidler, J. K. Chemical Kinetics, 3rd edn, Harper Collins Publisher, Inc, 1987.

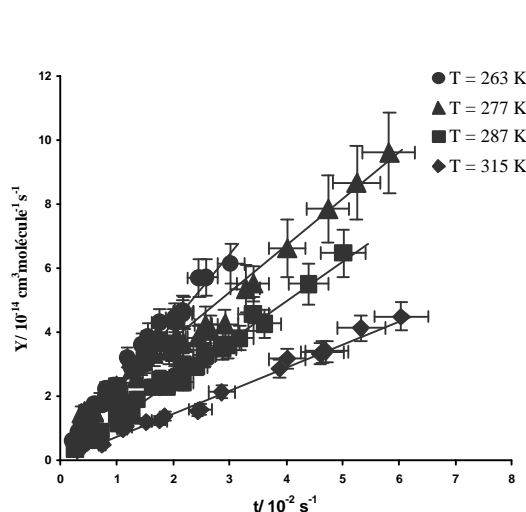


Figure 2.- Plots of $1/(B_0 - A_0) \ln[(M - X_a)/M(1 - X_a)]$ vs time or the reaction of the nitrate radical with 3-methylthiophene at different temperatures

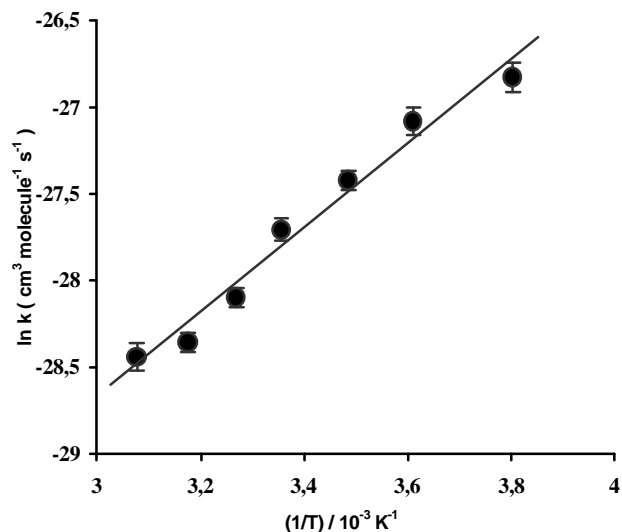


Figure 3 Arrhenius plots for the reactions of NO_3 with 2-methylthiophene

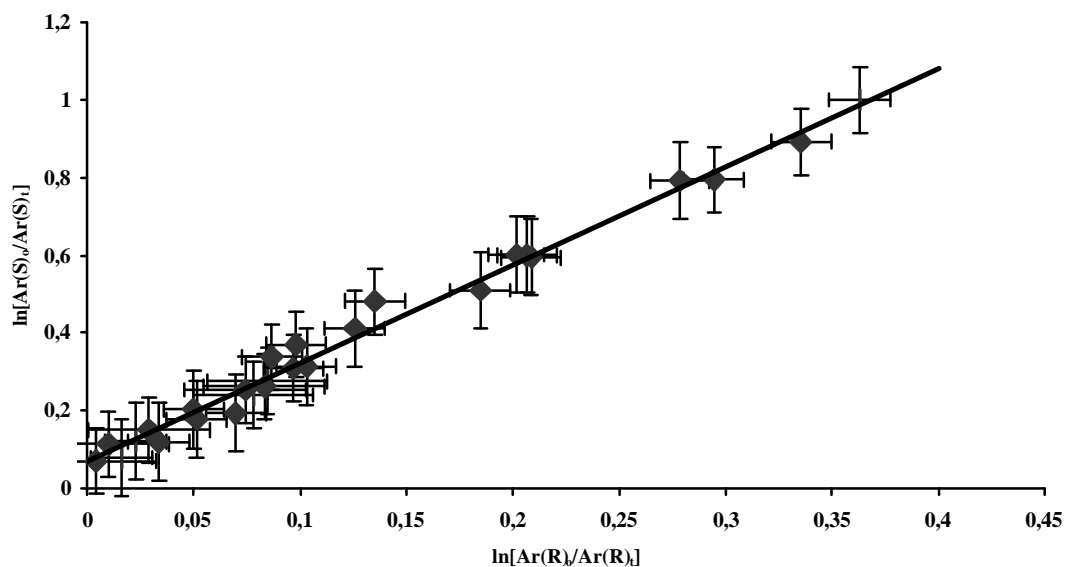


Figure 4. Plots of the experimental data according to eq (5) for 3-methylthiophene with z-2-butene as the reference organic.

The UV-Visible Spectra and Atmospheric Photolysis of Aromatic Aldehydes (GPP10)

G.Thiault⁽¹⁾, A.Mellouki⁽¹⁾, G. Le Bras⁽¹⁾, A.Chakir⁽²⁾, N.Sokolowski-Gomez⁽²⁾, D. Daumont⁽²⁾, R. Volkamer⁽³⁾, K. Wirtz⁽⁴⁾.

⁽¹⁾LCSR/CNRS, 1C avenue de la recherche scientifique 45071 Orléans cedex 02-France

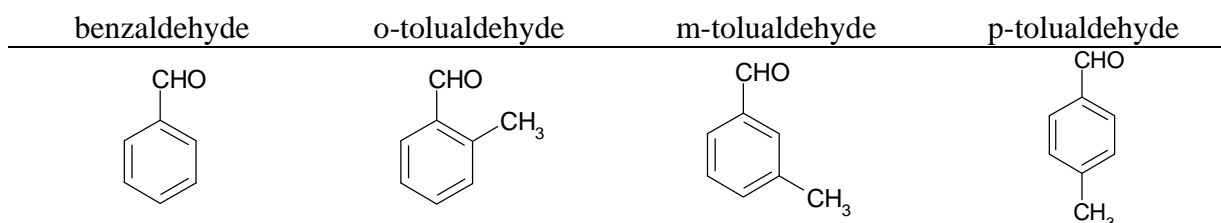
⁽²⁾GSMA/CNRS-UMR 6089, Faculté des Sciences, BP 1039, 51687 Reims cedex 02-France

⁽³⁾Universität d'Heidelberg, Im Neuenheimer Feld 229, 69120 Heidelberg-Germany

⁽⁴⁾Fundacion CEAM, Parque Tecnológico, E-46980 Paterna (Valencia)-Spain

Introduction

Simple aromatic aldehydes, benzaldehyde, o-tolualdehyde, m-tolualdehyde and p-tolualdehyde, are emitted into the atmosphere as primary pollutants from motor vehicles and through evaporation since they are used as soil fumigants and in the manufacturing of deodorants/air fresheners and loose mineral wool fiber.^{1,2} They are also produced in the atmosphere from the oxidation of species such as toluene and xylenes. The atmospheric fate of the aromatic aldehydes may be controlled in the gas phase by chemical reaction with OH, NO₃, O₃ and Cl or by photolysis. Therefore, in order to assess the contribution of these aromatic aldehydes to the photochemical reactions in urban and rural areas, it is necessary to know the relative importance of the above loss processes. In this respect, we have determined the UV-visible spectra of benzaldehyde, o-tolualdehyde, m-tolualdehyde and p-tolualdehyde using two different experimental systems and studied their photolysis at the EUPHORE facility. The obtained data are presented and discussed in terms of the importance of the photolysis as loss process of the aromatic aldehydes in the atmosphere compared to other gas phase loss processes.



Experimental

(i) UV absorption cross sections measurements

The UV-visible spectra have been determined using two different experimental systems: D₂ lamp-diode array system at LCSR-Orléans and D₂ lamp-monochromator at GSMA-Reims.

- **D₂ lamp-diode array system**: the experimental set up consists of a UV-visible spectrophotometer (1800 grooves/nm grating) - 1024 element diode array detector and a 100 cm long (2.5 cm id) absorption cell made of Pyrex (equipped with quartz windows). The collimated output of deuterium lamp passed through the absorption cell and focused onto the entrance slit of the spectrometer. Heated water was circulated through the cell jacket to regulate temperature.

- **D₂ lamp-monochromator**: In these experiments the diode array was replaced by a monochromator. The experimental set-up is similar to that described above, the only difference between the two systems is the length of the cell (here 49.6 cm).

Absorption cross sections were derived using the Beer-Lambert's law:

$$\sigma(\lambda) = -\ln [I(\lambda) / I_0(\lambda)] / LC$$

where $\sigma(\lambda)$ is the absorption cross section ($\text{cm}^2 \text{ molecule}^{-1}$) at wavelength λ , L is the pathlength in cm and C is the concentration in molecule cm^{-3} . I and I_0 are respectively the light intensities with and without aromatic aldehydes in the absorption cell.

(ii) Photolysis experiments

The experiments were conducted at EUPHORE (200 m^3 half spherical reactor irradiated by sun, made of FEP foil with more than 80% light transmission in the UV-visible region (280-640 nm))^{4, 5}. Analysis of reactants and products were performed using in-situ FTIR (553.5 m optical path-length), O_3 and CO monitors, GC-FID, MS and HPLC.

Results and discussion

UV-visible spectra

- ***D₂ lamp-diode array system***: The measurements have been performed at different pressures (0.2-0.8 Torr) and temperatures (303-333 K) in static and dynamic conditions in the wavelength range 252-368 nm. The results obtained by the two methods were in agreement. The precision of the experimental cross sections was calculated at each wavelength using the standard deviation. Between 252 and 340 nm, the standard deviation was found to be better than 10% while for wavelengths higher than 340 nm it was typically 20 to 30 %.

- ***D₂ lamp-monochromator***: The absorption cross sections were measured between 245 and 300 nm at different pressures (0.1-0.7 Torr) in the temperature range 353 - 373 K.

Figure 1 shows the spectra obtained in this work using the two systems along with those from the literature.

As shown in figure 1, the spectra of o- and m-tolualdehyde are similar in terms of peaks positions, values of cross sections and band widths. The p-tolualdehyde spectrum is close to that of benzaldehyde. The fine structures between 260 and 290 nm are characteristic of aromatic compounds while the absorption band between 320 and 360 nm results from a dipole forbidden $n-\pi^*$ electronic transition of C=O group. Furthermore, it has to be noticed that the four spectra show relatively high absorption cross sections for $\lambda > 290$ nm which could indicate that the atmospheric photolysis may not be a negligible loss process of these aromatic aldehydes.

The spectra obtained in both laboratories are in agreement except for o- and m-tolualdehyde in the range 254-268 nm where the disagreement is around 30 % which is not too high considering the difficulties of handling these compounds. Our results can be compared with literature values. For benzaldehyde, our results are in agreement with that of Etzkorn et al.⁶ despite a difference of 20% in the region 255-275 nm and are in disagreement with the spectra reported by Noziere et al.⁷ and Zhu et al.⁸. For the tolualdehydes, our results are 30% lower than those of Etzkorn et al. It has to be mentioned that this work reports the first measurements of the absorption cross sections for wavelengths higher than 300 nm for the four aldehydes.

The absorption cross sections from this study were used to calculate the photodissociation rate constants (k_{calc}) for the studied aromatic aldehydes using the following relationship:

$$k_{\text{calc}} = \int \sigma(\lambda) \phi(\lambda) I(\lambda) d\lambda$$

where $\sigma(\lambda)$ is the absorption cross section, $\phi(\lambda)$ is the primary quantum yield for photolysis and $I(\lambda)$ is the actinic flux of solar radiation. Rough calculations were made for specific conditions (at noontime on 1 July, cloudless and at sea level and at latitude of 40° N) and assuming $\phi(\lambda) = 1$ at all wavelengths. The data for the actinic flux at the Earth's surface and zenith angle ($\theta = 16.9^\circ$) are taken from Demerjian et al.⁹. The calculated photolysis rate for benzaldehyde, o-, m- and p-tolualdehyde are, respectively, 3.9×10^{-4} , 2.0×10^{-4} , 1.7×10^{-4} and $2.8 \times 10^{-4} \text{ s}^{-1}$. However, this calculation will be done for the specific dates of the experiments for the Euphore conditions.

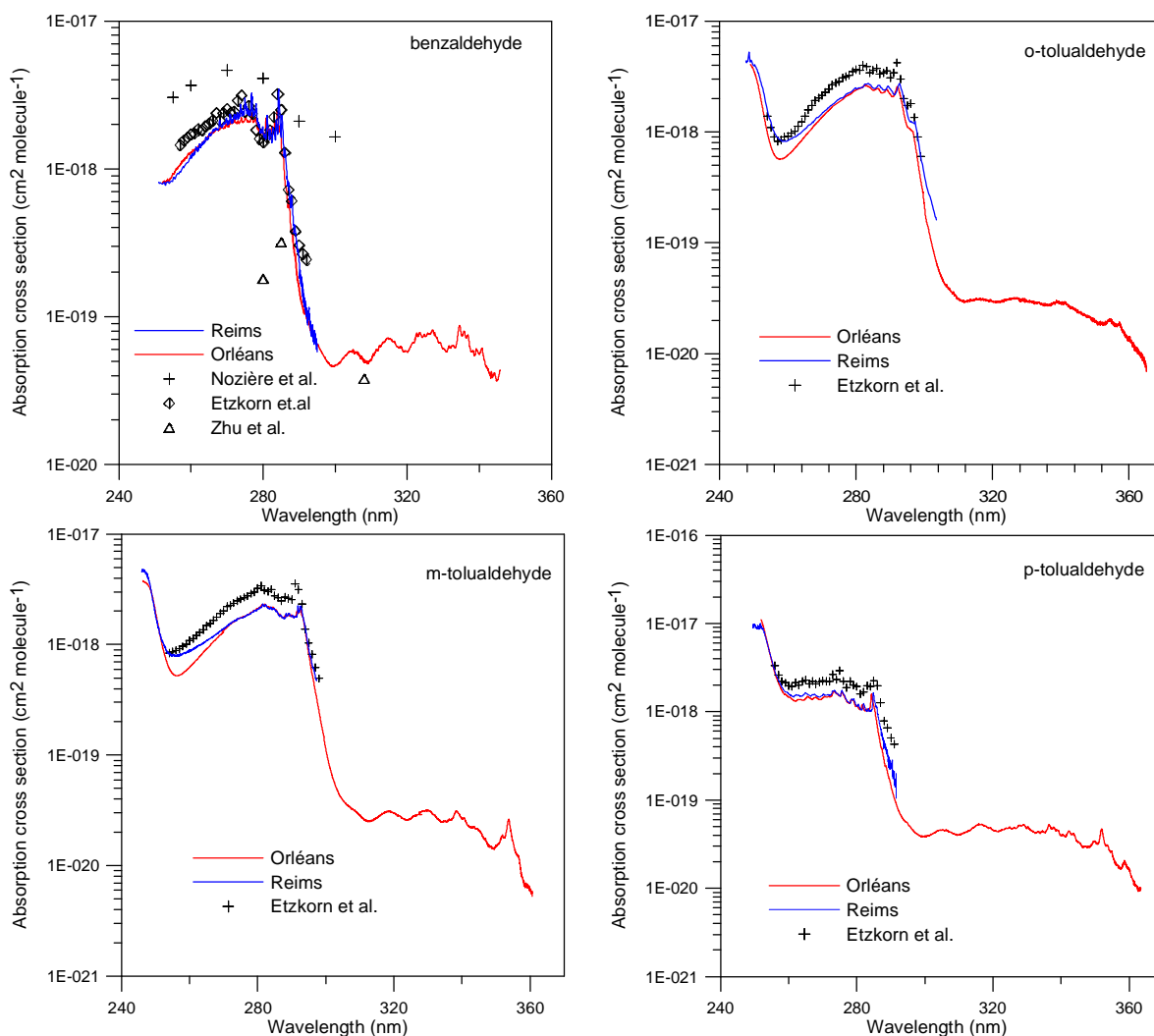


Figure 1: UV-vis spectra of benzaldehyde, o-tolualdehyde, m-tolualdehyde and p-tolualdehyde obtained in this work and those from the literature.

Photolysis experiments at EUPHORE

Experiments were performed at EUPHORE, with sunlight irradiation, in order to study the photolysis of benzaldehyde, o-, m- and p-tolualdehyde. Known amounts of aromatic aldehydes were introduced in the chamber along with SF₆ (to measure the dilution rate) and cyclohexane (to scavenge OH radicals) or di-n-butyl ether (as OH tracer).

For benzaldehyde and p-tolualdehyde, experiments have been conducted in the presence of 1 ppm of aldehyde, 30 ppb of SF₆ and large excess of cyclohexane (25 ppm). During 4 hours of sunlight irradiation, the decays of the aromatic aldehydes concentrations versus time were only due to the dilution (SF₆). This enables us to derive an upper limit for the photolysis rates of benzaldehyde and p-tolualdehyde: $J_{\text{meas}} < 6 \times 10^{-6} \text{ s}^{-1}$. For o-tolualdehyde, the experiment has been performed in the presence of 1 ppm of aldehyde, 186 ppb of di-n-butyl ether as OH tracer and 30 ppb of SF₆. During 2 hours of sunlight irradiation, we have observed a large decay of o-tolualdehyde (about 65%). Thus, we have derived a photolysis rate of $(1.1 \pm 0.2) \times 10^{-4} \text{ s}^{-1}$. Volkamer¹⁰ has measured the photolysis rate of m-tolualdehyde at EUPHORE and obtained: $J_{\text{meas}} = (1.1 \pm 0.8) \times 10^{-5} \text{ s}^{-1}$. Figure 2 shows two examples of the concentration-time profiles obtained during the photolysis experiments at Euphore.

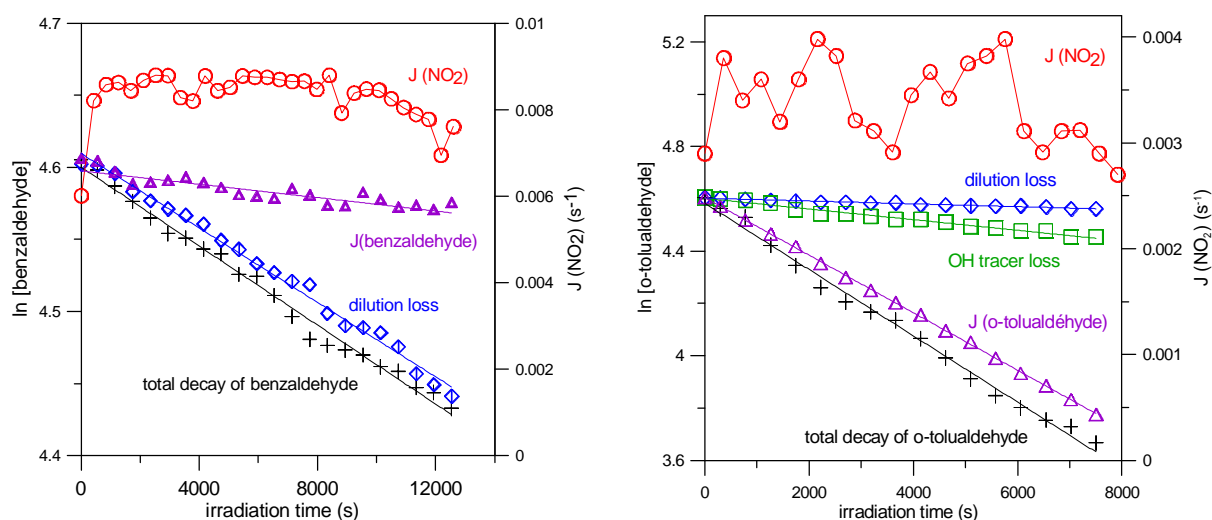


Figure 2: Concentration-time profiles obtained during the photolysis of benzaldehyde and o-tolualdehyde

The comparison between calculated and measured photolysis rates enables to derive an effective photolysis quantum yield for the studied aromatic aldehydes defined as: $\phi_{\text{eff}} = J_{\text{meas}}/J_{\text{calc}}$. The obtained values for benzaldehyde, o-tolualdehyde, m-tolualdehyde and p-tolualdehyde are, respectively, $\phi_{\text{eff}} < 0.15$, $\phi_{\text{eff}} = 0.6$, $\phi_{\text{eff}} = 0.06$ and $\phi_{\text{eff}} < 0.02$. These data indicate that in spite of high absorption cross sections for $\lambda > 290$ nm, the photolysis of benzaldehyde and p-tolualdehyde are not important loss processes in the troposphere. The photolysis of o-tolualdehyde seems to be an important atmospheric process. However, it has to be mentioned that J_{calc} was calculated for conditions which could be different from the real ones at Euphore. It is planned to re-evaluate these data using the real conditions.

Atmospheric implications

In the atmosphere, aromatic aldehydes are expected to be removed in the gas phase by chemical reactions with OH, NO₃, Cl and O₃ or by solar radiation photolysis. No data are available on the reactions of ozone with aromatic aldehydes but this process is expected to be negligible in the atmosphere². The lifetimes of the four aromatic aldehydes studied in this work with respect to different degradation processes are listed in Table 2.

Table 2: Lifetimes of benzaldehyde, o-tolualdehyde, m-tolualdehyde and p-tolualdehyde.

	τ_J	$\tau_{\text{OH}}^{(11)}$	$\tau_{\text{NO}_3}^{(2)}$	$\tau_{\text{Cl}}^{(11)}$
benzaldehyde	> 6 days	11 hours	2 days	4 months
o-tolualdehyde	2.5 hours	7 hours	-	2 months
m-tolualdehyde	1 day	8 hours	-	2 months
p-tolualdehyde	> 6 days	10 hours	-	3 months

These lifetimes indicate that the aromatic aldehydes are likely to be removed rapidly in the gas phase. For benzaldehyde and p-tolualdehyde, the reaction with OH is the major degradation pathway and as shown in this work, photolysis is negligible in spite of high absorption cross sections. For o-tolualdehyde, reaction with OH and photolysis are competitive. Finally, m-tolualdehyde will be removed essentially by reaction with OH but photolysis is not negligible especially in conditions where OH concentrations are low.

References

1. R. Atkinson, *J. Phys. Chem. Ref. Data.*, Monograph 2, 1994
2. <http://www.scorecard.org> (Environmental Defense, New York)
3. T. Wagner, M. L. Wyszynski, *Proc. Inst. Mech. Eng.*, 1996, 210, 109
4. *The European Photoreactor EUPHORE, Final report of the EC-Project Cpntract EV5VCT92-0059*, ed. K. H. Becker, Wuppertal, Germany, 1996
5. B. Klotz, S. Sorensen, I. Barnes, K. H. Becker, T. Etzkorn., T. Volkamer, U. Platt, K. Wirtz and M. J. Martin-Reviejo, *Phys. Chem. A.*, 1998, 102, 10289
6. T. Etzkorn, B. Klotz, S. Sorensen, I. V. Patroescu, I. Barnes, K. H. Becker, U. Platt, *Atmos. Environ.*, 1999, 33, 525
7. B. Nozière, R. Lesclaux, M. D. Hurley, M. A. Dearth, T. J. Wallington, *J. Phys. Chem.*, 1994, 98, 2864
8. L. Zhu, T. J. Cronin, *Chem. Phys. Letters*, 2000, 317, 227
9. K. L. Demerjian, K. L. Schere, J. T. Peterson, *Adv. Environ. Sci. Tech.*, 1980, 10, 369
10. R. Volkamer, *Thesis*, 2001
11. G. Thiault, A. Mellouki, G. Le Bras, *Phys. Chem. Chem. Phys.*, 2002, 4, 2194

The Atmospheric Fate of Methyl IsoPropyl Ketone (GPP10)

X. Lun, I. Magneron, G. Laverdet, A. Mellouki and G. Le Bras

LCSR/CNRS, 1C Avenue de la Recherche Scientifique 45071 Orléans cedex 02

Introduction

Methyl IsoPropyl Ketone (MIPK, $(\text{CH}_3)_2\text{CHC}(\text{O})\text{CH}_3$) is a raw material for a number of organic synthesis, primary used in the manufacture of dyes, herbicides and pharmaceuticals (1). Therefore, it can escape to the atmosphere through evaporation where it can play a role in photochemical processes. MIPK is also an intermediate product of the atmospheric degradation of other VOCs. Similarly to other saturated ketones, the atmospheric fate of MIPK in the gas phase is mainly controlled by reaction with OH radicals and photolysis.

We have conducted a kinetic and mechanistic study on the OH-initiated oxidation of MIPK using two different photoreactors, 200 L Teflon bag irradiated by lamps at LCSR-Orléans and the EUPHORE facility. In addition, we have determined its UV-visible absorption spectrum and studied its photolysis under sunlight conditions at EUPHORE.

UV-absorption spectrum and photolysis

Absorption cross-sections measurements, in the wavelength range 240-350 nm and (298 ± 2) K, were conducted using a 100 cm long cell and a D₂ lamp-diode array spectrophotometer system. Figure 1 shows the obtained UV-absorption spectrum.

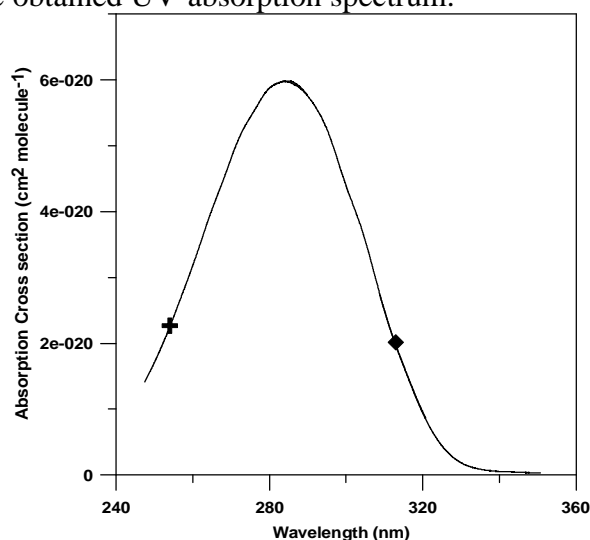


Figure 1 : UV-absorption spectrum of Methyl IsoPropyl Ketone

Independent measurements were also performed at 254 and 313 nm using a pen-ray Hg lamp-photodiode system. The obtained cross sections were in good agreement with those obtained using the D₂ lamp-diode array:

λ (nm)	UV-cross section ($\text{cm}^2 \text{ molecule}^{-1}$)	
	D ₂ lamp	Hg lamp
254	2.26×10^{-20}	2.27×10^{-20}
313	1.97×10^{-20}	2.01×10^{-20}

As presented in Figure 1, the spectrum of MIPK shows a significant absorption at $\lambda > 290$ nm indicating a possible photolysis in the troposphere.

A photolysis experiment of MIPK was conducted at EUPHORE in the presence of di-*n*-butyl ether as OH tracer. The obtained data showed that the total decay of MIPK is only due to the dilution rate, therefore, only an upper limit could be derived for the photolysis rate: $J_{\text{exp.}} < 2 \times 10^{-6} \text{ s}^{-1}$. The effective photolysis quantum yield defined as $\phi_{\text{eff}} = J_{\text{exp.}}/J_{\text{calc.}}$ (where $J_{\text{calc.}}$ is the calculated photolysis rate using the measured UV cross sections and assuming a quantum yield of unity, $J_{\text{calc.}} \approx 2.45 \times 10^{-5} \text{ s}^{-1}$) was estimated to be: $\phi_{\text{eff}} < 0.08$. These data indicate that the photolysis is a negligible loss process of MIPK in the lower troposphere.

OH-initiated oxidation of MIPK

OH rate constant measurements

The rate constant of OH reaction with MIPK was measured using the relative rate method (using two reference compounds: hexane ($k_{\text{OH}} = (5.45 \pm 0.16) \times 10^{-12} \text{ cm}^3 \text{ molecule}^{-1} \text{ s}^{-1}$) and *n*-butyl formate ($k_{\text{OH}} = (3.54 \pm 0.52) \times 10^{-12} \text{ cm}^3 \text{ molecule}^{-1} \text{ s}^{-1}$)). The experiments were performed in a 200 L Teflon bag and the photolysis of H_2O_2 at 254 nm in air was used as OH source at atmospheric pressure and $(298 \pm 2) \text{ K}$. At least two measurements were performed with each reference to check the reproducibility of the results. The analysis was performed using GC-FID and FTIR (10 m pathlength).

The average value derived from different experiments is $(2.6 \pm 0.4) \times 10^{-12} \text{ cm}^3 \text{ molecule}^{-1} \text{ s}^{-1}$. Figure 2 shows an example of the obtained relative loss of MIPK versus that of the reference compounds in the presence of OH.

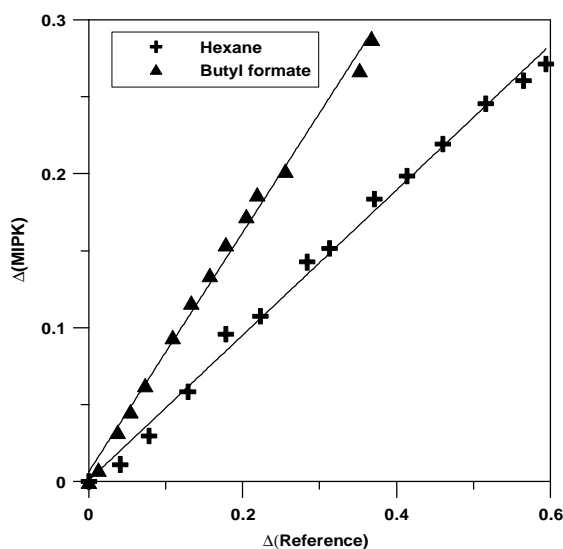


Figure 2: Examples of relative consumption of MIPK and the reference compounds in the presence of OH radicals.

The measured value of the rate constant for the reaction of MIPK with OH is in good agreement with that reported earlier from our laboratory using the absolute technique (PLP-LIF): $k_{\text{OH}} = (2.87 \pm 0.29) \times 10^{-12} \text{ cm}^3 \text{ molecule}^{-1} \text{ s}^{-1}$ (2).

Mechanistic study

Experiments were conducted at Orléans and EUPHORE. Figure 3 shows typical experimental concentration-time profiles and the derived yields from the reaction of OH with MIPK in the presence of NO_x .

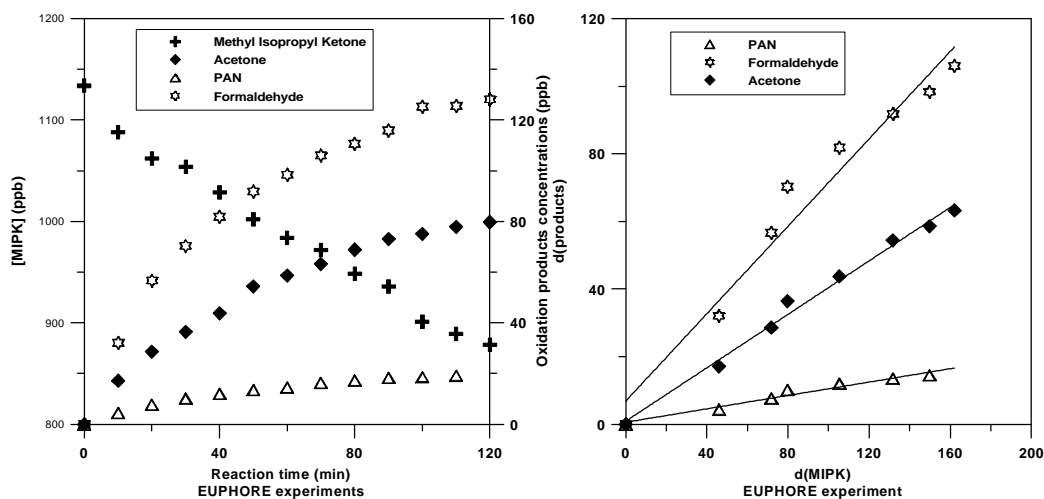


Figure 3: Typical concentration-time profiles of MIPK and its OH-initiated oxidation products obtained at EUPHORE.

The main reaction products are: acetone (55 ± 15 %), formaldehyde (49 ± 9 %) and PAN (11 ± 3 %). However, the carbon balance is only about 50 % (some products are still not identified). The observed products indicate that the OH reaction with MIPK proceeds at least partly by H-atom abstraction from the $>\text{CH}-$ group (Figure 4). According to the SAR estimation, this channel represents 55 % of the reaction which is in very good agreement with our experimental data (yield of acetone $\approx (55 \pm 15)$ %). This indicates that the decomposition of $(\text{CH}_3)_2\text{C}(\text{O}^\bullet)\text{C}(\text{O})\text{CH}_3$ (Figure 4) leads almost exclusively to acetone and that 2,3-butanedione ($\text{CH}_3\text{C}(\text{O})\text{C}(\text{O})\text{CH}_3$) is not produced (we did not observe it in our experiments).

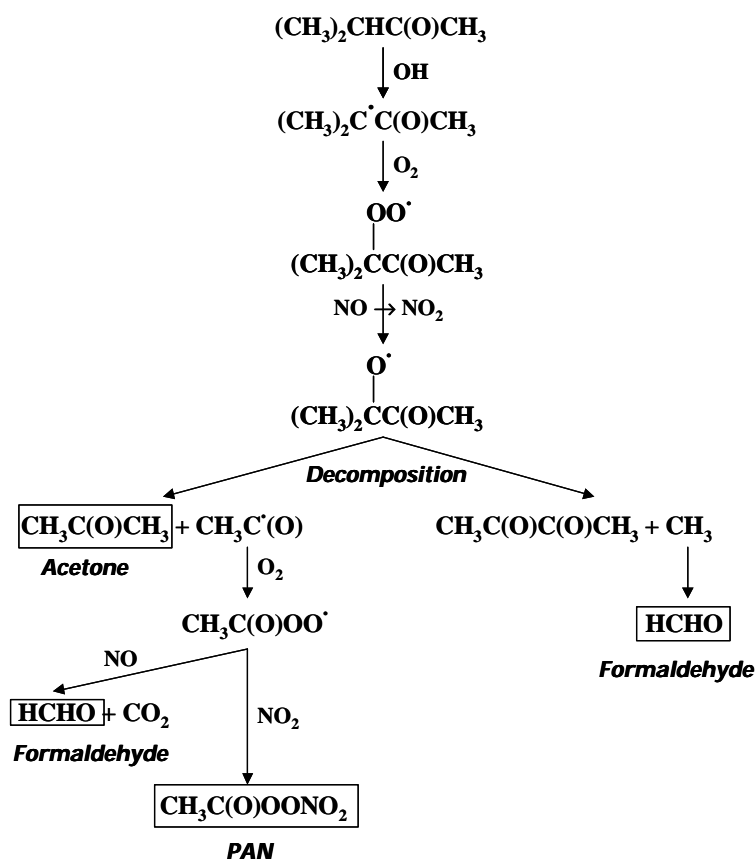


Figure 4: The OH-initiated degradation scheme of MIPK (channel proceeding through abstraction from the $>\text{CH}-$ group).

Conclusion

This work shows that, in the gas phase, the loss process of MIPK in the atmosphere is mainly controlled by reaction with OH (photolysis, reactions with O₃ and NO₃ being negligible). The derived tropospheric lifetime of MIPK is around 4 days, hence its role on ozone and photooxidant formation should be moderate at local scale. Also, its ozone forming potential may be reduced as a result of the lower reactivity of some of its oxidation products (acetone and PAN). Furthermore, the production of acetone (lifetime \approx 1 month) and PAN with relatively high yields is of importance since acetone is recognised to be a significant source of HO_x radicals in the upper troposphere while PAN can transport NO_x to remote areas.

Acknowledgements

CNRS through the PNCA programme, EC through the MOST project and ADEME for support.

References

- (1) Website: www.sasolchemie.com/products/fine-chemicals/MIPK.asp
- (2) Le Calvé S., Hitier D., Le Bras G., Mellouki A., J. Phys. Chem. A, 102, 4576-4584, 1998

Ozonolysis of Alkenes: Influence of the Structure of the Criegee Intermediate on Carboxylic Acid and Organic Aerosol Formation (GPP11)

Alexa Sadezky, Elmar Uherek, Boris Bonn and Geert K. Moortgat

Max-Planck-Institute for Chemistry, Atmospheric Chemistry Division, P.O. Box 3060, D-55020 Mainz, Germany

sadezky@mpch-mainz.mpg.de

Summary

Secondary organic aerosol (SOA) is formed in the troposphere by ozonolysis of biogenic volatile organic compounds (VOC). Laboratory investigations focusing on the analysis of formation and gas-to-particle partitioning of low-volatile ozonolysis reaction products and SOA formation might provide information about the nature of the species playing the key role in nucleation. In this work, SOA and carboxylic acid formation are studied during gas-phase ozonolysis of a variety of linear and cyclic alkenes, in order to elucidate the influences of certain structural features of the presumed Criegee intermediate on both processes, and to assess a possible participation of the carboxylic acids in the nucleation processes. SOA formation is observed by a scanning mobility particle sizer during ozonolysis reaction in a flow reactor. Carboxylic acids are analysed via ion chromatography in the particulate phase that is collected during ozonolysis experiments carried out in a 570 l spherical reactor. Some preliminary, qualitative conclusions can so far be drawn from the results. The SOA formation ability of the cyclic alkenes under study is observed to increase with the ring size, and so does the size of the highest-molecular-weight dicarboxylic acids identified in the particulate phase, which contain as many C-atoms as the ring of the educt alkene. As their vapour pressures decrease with increasing size, it has been suggested that dicarboxylic acids might be the ozonolysis reaction products which cause homogeneous nucleation (Koch et al., 2000). This appears to be consistent with the SOA formation behaviour observed for the cyclic alkenes. For linear alkenes, the SOA formation ability is observed to increase with increasing size of the expected energy-rich Criegee-Intermediate CI^* . Moreover, when forming CI^* with the same numbers of C-atoms, linear alkenes are observed to be significantly more efficient in new SOA particle formation than cyclic alkenes. As linear alkenes can only form monocarboxylic acids during ozonolysis, whose vapour pressures are significantly smaller than those of dicarboxylic acids formed by cyclic alkenes, homogeneous nucleation of these compounds cannot explain the observations, and different mechanisms need to be taken into consideration in the future.

Introduction

Secondary organic aerosol (SOA) formed by ozonolysis of biogenic volatile organic compounds (VOC) in the troposphere might influence the properties of global aerosol and therefore have an impact on the Earth's radiation budget. However, the gas phase processes leading to its formation are so far poorly understood. Mechanistic studies of the gas-phase ozonolysis of biogenic terpenes and simple alkenes as model compounds have been carried out in several laboratory investigations. A wide range of different primary or secondary reaction products has so far been suggested as potential precursor of nucleation, such as dicarboxylic acids (Koch et al., 2002), secondary ozonides (Bonn et al., 2002; Kamens et al., 1999) and peroxy compounds (Ziemann et al., 2002).

Objectives

Laboratory investigations aimed at studying SOA formation as well as identification and gas-to-particle partitioning of low-volatile reaction products during gas-phase alkene ozonolysis permit to gain knowledge about interactions between the gas-phase and the particulate phase. The combined

information might allow to draw conclusions on the likelihood of potential particle precursors, with sufficiently low vapour pressures for nucleation, to be formed. In this work, measurements of SOA formation and carboxylic acid yields in the particulate phase are described for ozonolysis reactions of a variety of alkenes. On the one hand, influences of structural features of the Criegee intermediate (such as its number of C-atoms, functional groups) are to be examined. On the other hand, possible correlations between the carboxylic acid yields and the nucleation threshold (here arbitrarily defined as the alkene conversion necessary to reach the particle number concentration of 1000 particles/cm³) are to be elucidated. Preliminary results are qualitatively discussed here.

Experimental

a) Analysis of SOA Particle Formation performed in a flow reactor

Ozonolysis experiments of *trans*-4-octene, *trans*-5-decene, linalool, 1-nonene, cyclohexene, cycloheptene, *cis*-cyclooctene, and 1-methyl-cyclohexene were performed in a cylindrical glass flow reactor of 120 cm length and 10 cm diameter at (755 ± 1) Torr total pressure of synthetic air at (295 ± 2) K (Bonn et al., 2002). Initial alkene concentrations were varied between 40 ppb and 6 ppm at an initial ozone concentration of 50 ppb and 50 s of reaction time (defined by the position of the mixing plunger). SOA particles are observed using a scanning mobility particle sizer (TSI 3936) with a L-DMA and an ultrafine particle counter (TSI 3025a).

b) Analysis of Carboxylic Acids in SOA Particles performed in a spherical reactor

Ozonolysis experiments of *trans*-4-octene, *trans*-5-decene, cyclohexene, and cycloheptene were carried out in a 570 l glass reactor at (295 ± 2) K and (730 ± 1) Torr total pressure of synthetic air. Initial concentrations were 4 ppm alkene and 2 ppm ozone. Particles were trapped in a hexanol driven supersaturation chamber, and the organic acids were analysed via ion chromatography (Uherek and Moortgat, 2002).

Results and Discussion

The initial step of the gas-phase ozonolysis of alkenes consists in the addition of O₃ to the >C=C< double bond, yielding an energy-rich primary ozonide (POZ). It rapidly decomposes to a primary carbonyl and an initially energy-rich Criegee-Intermediate (CI*) (Fig. 1). Carboxylic acids are formed by secondary gas-phase reactions of the CI* following the initial steps of the alkene ozonolysis (Fig. 1) (Uherek and Moortgat, 2002; Koch et al., 2000). The yields in the particulate phase of the respective highest-molecular-weight carboxylic acids formed, are given in Tab. 1. The SOA particle concentrations measured during alkene ozonolysis are shown in Fig. 2a) and 2b). The particle number concentrations are in this early stage of SOA formation essentially nucleation-controlled.

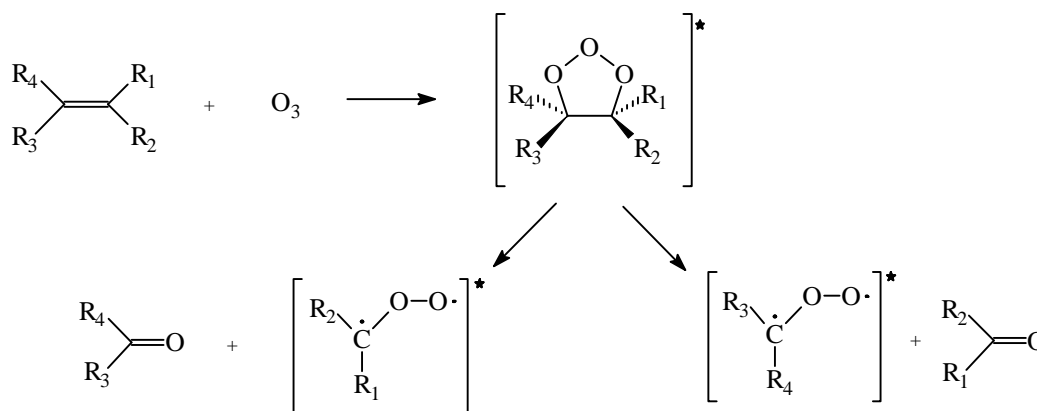
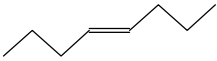
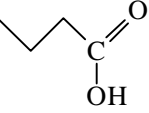
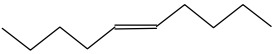
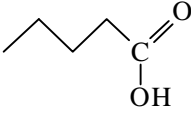
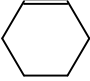
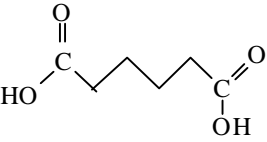
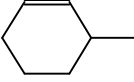
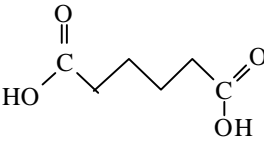
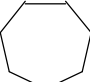
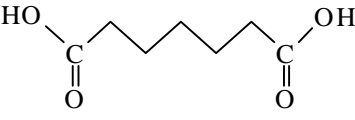


Figure 1: Initial steps of the alkene ozonolysis leading to the formation of the energy-rich Criegee-Intermediate.

Table 1: Yields of the highest-molecular-weight carboxylic acids in the particulate phase and bimolecular rate constants of the gas-phase alkene ozonolysis.

Alkene	k_{O_3} [$10^{-18} \text{ cm}^3 \text{ molecule}^{-1} \text{ s}^{-1}$]	Highest-Molecular-Weight Carboxylic Acid	Yields (Particulate Phase (mol %))
 <i>trans</i> -4-Octene	$(131 \pm 15)^{(5)}$	 Butyric Acid	< 0.5
 <i>Trans</i> -5-Decene	$\geq 130^{(5)}$	 Valeric Acid	< 0.5
 Cyclohexene	$(85 \pm 8)^{(5)}$	 Adipic Acid	0.7
 1-methyl-Cyclohexene	$(166 \pm 12)^{(5)}$	 Adipic Acid	1.9 ⁽¹⁾
 Cycloheptene	$(237 \pm 21)^{(5)}$	 Pimelic Acid	3.0

For cyclic alkenes, the ring size is observed to be decisive for their ability to form SOA. With increasing number of C-atoms as ring members, a lower alkene conversion is necessary for SOA formation, significantly decreasing from *cis*-cyclooctene to cyclohexene (Fig. 2a). 1-methyl-cyclohexene, although it forms a CI* with 7-C atoms in total, like cycloheptene, shows an SOA formation behaviour similar to that of cyclohexene, thus confirming the importance of the ring size. An explanation can be given by the assumption that dicarboxylic acids might play the key role in the nucleation process (Koch et al., 2000). Both cyclohexene and 1-methyl-cyclohexene form adipic acid as highest-molecular-weight carboxylic acid, which might be responsible for their similar SOA formation behaviour. (A detailed mechanism leading to the formation of adipic acid by the ozonolysis of 1-methyl-cyclohexene is presented by Koch et al. (2000).) Cycloheptene, however, forms the less volatile pimelic acid with the highest yields of carboxylic acids in the particulate phase. Therefore, lower concentrations of pimelic acid than of adipic acid, and consequently less alkene conversion by ozonolysis, are expected to be needed to initiate homogeneous nucleation. For linear alkenes, the amount of alkene conversion necessary for SOA formation decreases with increasing size of the CI*, thus from *trans*-4-octene, which forms a unique CI* of four C-atoms, to 1-nonene, which is expected to form a CI* of eight C-atoms with the branching ratio of unity (Atkinson, 1997) (Fig. 2b, Fig. 1). Moreover, SOA formation is observed to occur for linear alkenes generally after significantly less alkene conversion than for cyclic alkenes, which form CI* with respective same numbers of C-atoms. Thus, for 1-nonene and *cis*-cyclooctene, both of which are expected to form CI* with eight C-atoms, a particle number concentration of 1000 particles/cm³ is reached after an alkene conversion of around 0.3 ppb and 1.7 ppb, respectively (Fig. 2a) and 2b)).

Trans-4-octene is situated close to cycloheptene, with a particle number concentration of 1000 particles/cm³ being reached after 8 ppb of alkene conversion, and *trans*-5-octene is found to be close to *cis*-cyclooctene. These observations cannot be explained by assuming that SOA formation is controlled by carboxylic acids only. The highest-molecular-weight carboxylic acids formed by *trans*-4-octene and *trans*-5-decene, the monoacids butyric and valeric acid, respectively, both have a much higher vapour pressure than the dicarboxylic acids identified for cyclic alkenes, and are consequently present in the particulate phase in much lower yields. Thus, the clearly higher efficiency of the linear alkenes in new SOA particles' formation in comparison with cyclic alkenes cannot be not due to carboxylic acids formed by secondary gas-phase reactions, and other nucleating species must be taken into consideration.

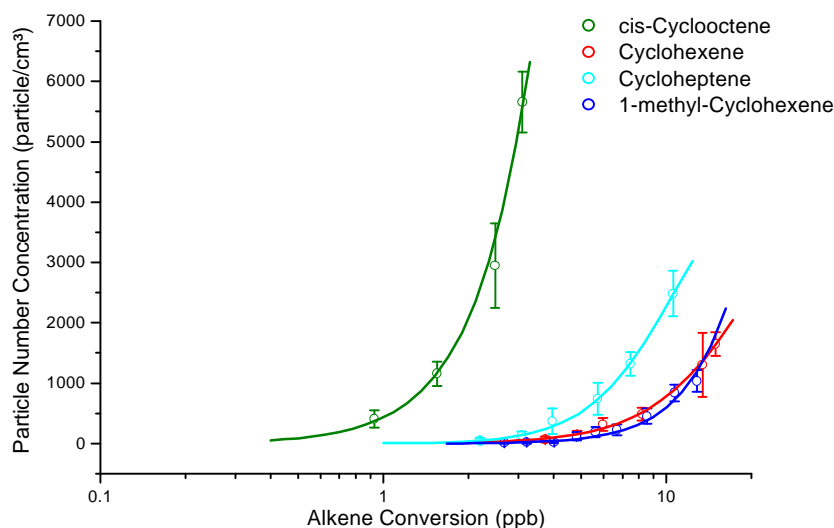


Figure. 2a: SOA particle number concentrations during ozonolysis of cyclic alkenes.

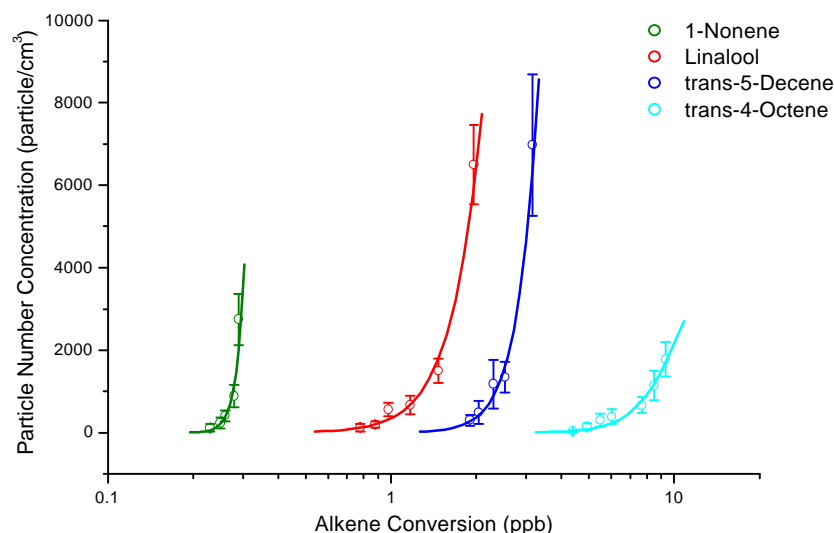


Figure 2b: SOA particle concentrations during ozonolysis of linear alkenes.

Conclusion

In this work, SOA and carboxylic acid formation have been investigated during gas-phase ozonolysis for a variety of alkenes. For the cyclic alkenes, their SOA formation ability increases with their ring size. This can be explained by assuming that dicarboxylic acids are those reaction

products of the gas-phase ozonolysis, which might play the key role in the nucleation process (Koch et al., 2000). For linear alkenes, the SOA formation ability is observed to increase with increasing size of the expected energy-rich Criegee-Intermediate CI*. Their particle formation behaviour is however not consistent with homogeneous nucleation of carboxylic acids which are formed as reaction products, like for cyclic alkenes. Linear alkenes are observed to be significantly more efficient in new SOA particle formation than cyclic alkenes for CI* with the same numbers of C-atoms. However, linear alkenes can only form monocarboxylic acids, which are more volatile than dicarboxylic acids formed by cyclic alkenes. Therefore, a different mechanism must be responsible for nucleation in their case.

Acknowledgements

A. S. gratefully thanks the collaboration partners within a binational PhD thesis, Dr. Georges Le Bras and Dr. Wahid Mellouki (LCSR, CNRS Orleans), and the French Ministry of Research and Technology for financial support.

This work was financially supported by the European Commission, project Origin of Secondary Organic Aerosol (OSOA, EVK2-1999-00016).

References

- Atkinson, R., *Journal of Physical and Chemical Reference Data* **1997**, 26, 215 – 290.
Bonn, B., G. Schuster, G. K. Moortgat, *J. Phys. Chem. A* **2002**, 106 (12), 2869-2881.
Grosjean, E., D. Grosjean, *Int. J. Chem. Kin.* **1998**, 30 (1), 21 – 29.
Kamens, R. M., M. Jang, C.-J. Chien, K. Leach, *Environ. Sci. Technol.* **1999**, 33, 1430 – 1438.
Koch, S., R. Winterhalter, E. Uherek, A. Koloff, P. Neeb, G. K. Moortgat, *Atmos. Environ.* **2000**, 34, 4031 – 4042.
Uherek, E., G. K. Moortgat, *Proceedings of the EUROTRAC Symposium 2002*, in press.
Ziemann, P. J., *J. Phys. Chem. A* **2002**, 106 (17), 4390 – 4402.

Generalized Structure-Activity Relationships for the Decomposition and Isomerisation of (Substituted) Alkoxy Radicals. Theory-based Validation (GPP13)

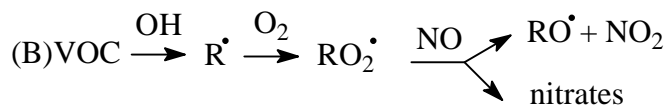
Luc Vereecken, Gaia Fantechi and Jozef Peeters

Katholieke Universiteit Leuven, Celestijnenlaan 200F, B-3001 Leuven

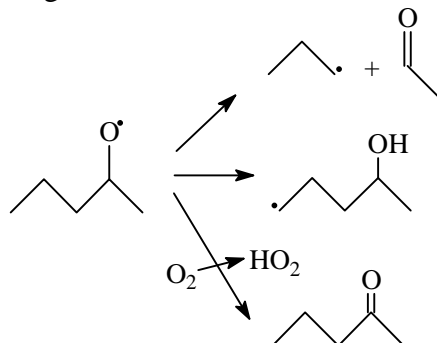
Jozef.Peeters@chem.kuleuven.ac.be

Introduction

Alkoxy radicals are important intermediates in the atmospheric oxidation of (biogenic) hydrocarbons, and are often formed in O₂ and NO reactions following an initiation step by OH or NO₃ radicals, or formed in mutual RO₂ reactions.



The fate of these oxy radicals is, in general, determined by the competition between decomposition reactions, isomerisations, and hydrogen abstraction reactions with O₂:



Depending on the structure of the alkoxy radical the rate of decomposition and/or isomerisation ranges from negligible to 10^{12} s^{-1} , whereas the rate of the reaction with O₂ at 298 K and 1 atm. of air tends to be in a fairly narrow range of $k_{O_2}[O_2] = 4\text{--}7 \times 10^4 \text{ s}^{-1}$ (Atkinson, 1997). Prediction of the fate of a specific oxy radical, or the analysis and verification of an experimentally obtained product distribution, requires that the relative rates of the different reactions are known. For a number of smaller, structurally less complex alkoxy radicals direct experimental data are available, but for the elucidation of the degradation mechanisms of more complex (biogenic) VOCs such measurements are very difficult. Quantum chemical calculations on the potential energy surface, followed by quantum statistical treatments, allow the *a priori* prediction of rate coefficients, but these calculations become tedious for larger molecules, such as isoprene, the ubiquitous terpenes, and the dozens of different alkoxy radicals formed in their degradation mechanisms.

We have developed generalized and readily applicable Structure-Activity Relationships for the decomposition and isomerisation reactions of substituted alkoxy radicals. The decomposition SAR predicts the barrier height E_b to β C–C fission in alkoxy radicals with alkyl, oxo- and/or hydroxy substituents. The isomerisation SAR predicts Arrhenius activation energies E_A for strain-free 1,5-H-shifts from alkane-, alcohol-, or aldehyde carbons.

Alkoxy radical decomposition SAR

Derivation of the SAR

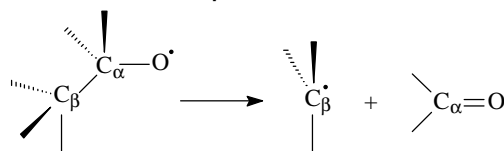
A number of SARs have already been published (Atkinson, 1997; Méreau et al., 2000; Somnitz and Zellner, 2000), some of which are difficult to use as they require knowledge of reaction enthalpies and/or ionization potentials, and none of which are applicable to oxo- or hydroxy-substituted alkoxy radicals. Inspired by these earlier SARs, we have developed a new microscopic SAR correlating the

rate of decomposition to the structure of the alkoxy radical, or, more precisely, to the substitution on the α - and β -carbons. It was already shown by Somnitz and Zellner (2000) that the barrier height to decomposition depends primarily on the substituents on these carbons.

The Transition State Theory pre-exponential factor $A^{\infty}_{\text{TST}}(298 \text{ K})$ is roughly the same for all cases ($\sim 2 \times 10^{13} \text{ s}^{-1}$), leaving the decomposition barrier height E_b as the critical parameter to be determined. Once known, the rate coefficient for the decomposition can be estimated from $k_{\text{diss}}(298 \text{ K}) = 2 \times 10^{13} \cdot \exp(-E_b/kT)$. For conversion of $A_{\text{TST}}(T)$ and E_b to Arrhenius parameters A and E_A , Fittschen et al. (2000) found that for these reactions, $E_A \approx E_b + 1 \text{ kcal/mol}$, and hence $A_{\text{Arr}} \approx 6 \times A_{\text{TST}}(298 \text{ K})$.

Direct experimental data on E_b is scarce, with measurements on ethoxy, propoxy, 2-butoxy and t-butoxy (Devolder et al., 1999; Caralp et al., 1999; Fittschen et al., 2000; Blitz et al., 1999). There is a larger body of quantum chemical data, mainly for alkoxy radicals from alkanes: Somnitz and Zellner, 2000 (G2(MP2,SVP) level of theory), Fittschen et al., 2000 (B3LYP-DFT/SVP), Méreau et al., 2000 (B3LYP-DFT/6-31G(d_{6d},p)), Jungkamp et al., 1997 (B3LYP-DFT/6-31G(d_{5d},p)). There are also calculations on hydroxy-substituted alkoxy radicals (Dibble, 2001, B3LYP-DFT/6-31G(d_{5d},p)) and oxo-substituted alkoxy radicals (Fenske et al. 2000, B3LYP-DFT/6-31G(d_{5d},p)). We have added data for all classes of substituents, mainly at the B3LYP-DFT/6-31G(d_{5d},p) level of theory but also at higher levels of theory (Peeters et al., 2002).

Correlation analysis on these data yielded the following expression for E_b , as a function of the number and type of substituents on the α - and β - carbons:



$$E_b(\text{SAR}) / \text{kcal/mol} = 17.5 - 2.1 N_{\alpha}(\text{alkyls}) - 3.1 N_{\beta}(\text{alkyls}) - 8.0 N_{\alpha,\beta}(\text{OH}) - 8.0 N_{\beta}(\text{O=}) - 12.0 N_{\alpha}(\text{O=})$$

where $N_{\alpha}(\text{alkyls})$ and $N_{\beta}(\text{alkyls})$ are the number of alkyl substituents on the α - and β - carbons, respectively, $N_{\alpha,\beta}(\text{OH})$ the number of OH substituents on the α - and/or β - carbons (with a maximum of 1 on either carbon), $N_{\beta}(\text{O=})$ the number of oxo functions on the β -carbon (0 or 1), and $N_{\alpha}(\text{O=})$ the number of oxo functions (0 or 1) on the α -carbon. Oxy radicals with low barriers to dissociation, below $\sim 7 \text{ kcal/mol}$, show a non-linear dependence on the substituents, with the barrier height decreasing asymptotically towards zero. For these cases, with $E_b(\text{SAR}) \leq 7 \text{ kcal/mol}$, the predicted barrier height should be corrected for this curvature with the following equation: $E'_b(\text{SAR}) = E_b(\text{SAR}) + 0.027 \times [9 \text{ kcal/mol} - E_b(\text{SAR})]^2$.

The average deviation between $E_b(\text{SAR})$ ($E'_b(\text{SAR})$ for low barriers) and the mean of the available data for each compound is about 0.5 kcal/mol (see Figure 1), with an average deviation of about 0.5 - 1 kcal/mol from each individual set of data. The B3LYP-DFT/6-31G(d_{5d},p) level of theory, as used by us for much of the data, is on average within 0.6 kcal/mol of the experimental data, and the average deviation from the results obtained at higher levels of theory is only 0.4 kcal/mol. This indicates that the SAR is able to predict the results from experiment and quantum chemical calculations within chemical accuracy.

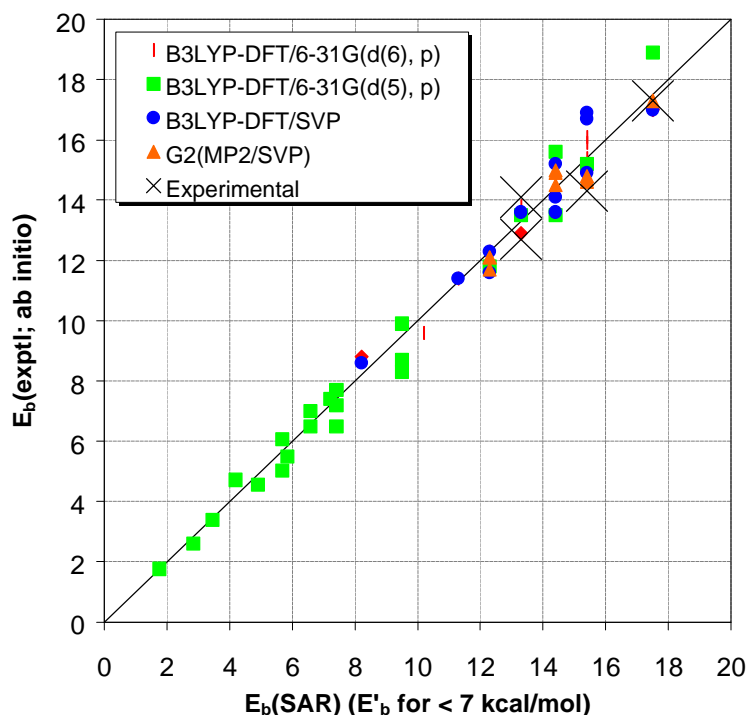
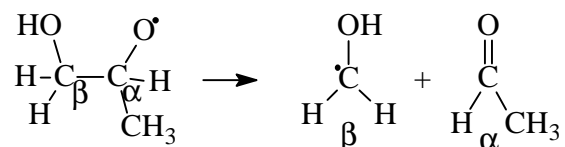


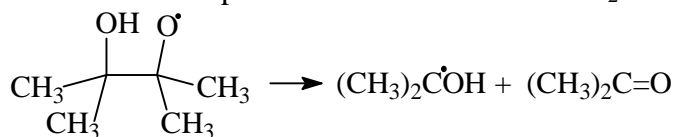
Figure 1: Correlation between SAR-predicted barrier heights $E_b(\text{SAR})$, and the available experimental and quantum chemical data.

Examples and exceptions

A few examples:

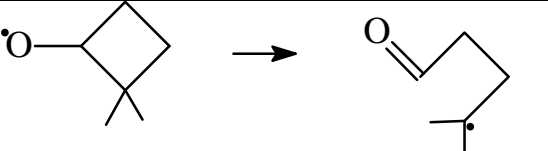
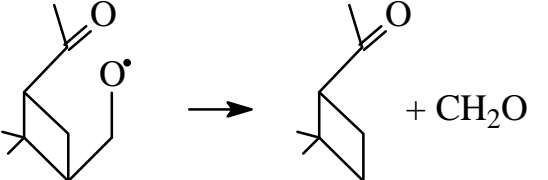
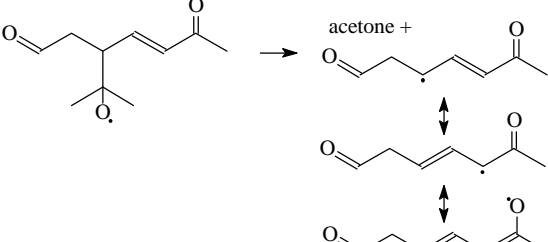


1-hydroxy-2-propoxy: On the α -carbon we find 1 CH_3 group, on the β carbon 1 OH function, so $N_{\alpha}(\text{alkyls}) = 1$ and $N_{\alpha\beta}(\text{OH}) = 1$, hence $E_b(\text{SAR}) = 17.5 - 2.1 \times 1 - 8.0 \times 1 = 7.4$ kcal/mol. This compares very well with our DFT value of 7.4 kcal/mol. If we would eliminate the CH_3 group instead, we would have 1 alkyl group (HOCH_2-) on the α -carbon, and no substituents on the β -carbon (i.e. a simple CH_3 group). $E_b(\text{SAR})$ then becomes $17.5 - 2.1 = 15.4$ kcal/mol. It is clear that in this case CH_3 elimination can not compete with the formation of $\text{CH}_2\text{OH} + \text{CH}_3\text{CHO}$.



2,3-di-Me-3-hydroxy-2-butoxy: $N_{\alpha}(\text{alkyls}) = 2$, $N_{\beta}(\text{alkyls}) = 2$, $N_{\alpha\beta}(\text{OH}) = 1$, so $E_b(\text{SAR}) = -0.9$ kcal/mol. This prediction is below 7 kcal/mol, so it must be corrected for curvature. Applying the formula for $E'_b(\text{SAR})$ we find $E'_b(\text{SAR}) = 1.7$ kcal/mol, which corresponds nearly exactly to a lengthy DFT calculation yielding 1.8 kcal/mol.

Some exceptions to our SAR are caused by (increasing of decreasing) ring strain, or by resonance stabilization of the radicals (see table below). Incorporating resonance stabilization effects into the SAR is currently under investigation.

	Release of the ring strain in the ring reduces the barrier from $E_b(\text{SAR})=6.1$ kcal/mol to a DFT value of essentially 0.
	The radical carbon in the ring switches to an sp^2 hybridization which increases the ring strain. DFT barrier = 15.5 kcal/mol, while $E_b(\text{SAR}) = 11.3$ kcal/mol.
	Resonance stabilization favors the product radical, such that the DFT barrier is 2.8 kcal/mol, significantly below the $E_b(\text{SAR})$ value of 7.1 kcal/mol.

Alkoxy radical isomerisation SAR

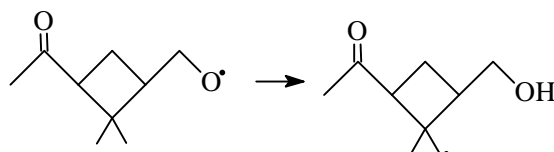
Derivation of the SAR

As far as we know, no SARs have been published to predict the rate of 1,5-H-shift isomerisation in (substituted) alkoxy radicals. Recent work by our group showed that hydrogen abstraction rate coefficients correlate well with C–H bond strengths; as a H-shift can be considered an intramolecular H-abstraction a similar correlation is expected. Using available experimental $D(\text{C–H})$ bond strengths, and recommended values for hydrogen shift rate coefficients, we were able to derive the following formula for alkanes, alcohols and aldehydes :

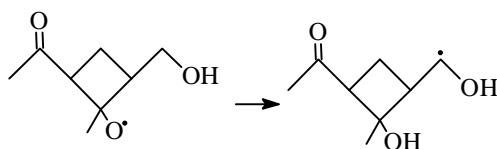
$$E_A(\text{SAR}) / \text{kcal/mol} = 8.4 - 0.65 \times [99 - D(\text{C–H})/\text{kcal mol}^{-1}]$$

Anchor values in this formula are the activation energy of 8.4 kcal/mol for the strain free 1,5-H-shift in the template molecule 1-butoxy, with a bond strength for the primary hydrogens of about 99 kcal/mol. Contrary to the alkoxy decomposition SAR discussed above, a hydrogen-shift SAR is better expressed in terms of Arrhenius activation energies E_A , as we can then include the important effects of tunneling and fall-off directly. For barriers of appr. 8 kcal/mol, the barrier height $E_b \approx E_A + 1$ kcal/mol, due to tunneling which enhances the rate of reaction by about a factor of 3 at 298K, and fall-off which slows down the reaction by appr. 20% at 1 atm. For other barrier heights the difference $E_b - E_A$ changes due to differences in tunneling and fall-off. The Arrhenius pre-exponential factor of $2.4 \times 10^{11} \text{ s}^{-1}$ for 1-butoxy can be used to derive the rate coefficient for isomerisation: $k_{\text{iso}}(298\text{K}, 1\text{atm}) = 2.4 \times 10^{11} \text{ s}^{-1} \cdot \exp(-E_A/kT)$.

Examples and exceptions



The hydrogen to be abstracted is a regular primary hydrogen, with a $D(\text{C–H})$ bond strength of about 99 kcal/mol, resulting in an Arrhenius activation energy of 8.4 kcal/mol. This compares favorable with the DFT barrier height $E_b = 9.5$ kcal/mol when taking into account the ~ 1 kcal/mol difference between E_b and E_A . Note that for this example, CH_2O elimination (see higher) cannot compete due to its barrier of 15.5 kcal/mol.



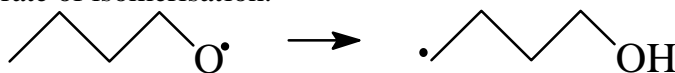
In this example $D(C-H)$ is reduced due to the presence of an α -OH substituent, which lowers the bond strength by about 6 kcal/mol. The predicted activation energy is therefore $E_A=4.5$ kcal/mol. DFT calculation on this type of H-shifts in a number of compounds all resulted in barrier height $E_b \approx 4.7$ -5.3 kcal/mol. As tunneling is less important for these lower barriers, the difference between E_A and E_b is roughly between 0.5 and 1 kcal/mol, bringing the SAR and the DFT calculations in close agreement.

As with the alkoxy decomposition, exceptions to the above SAR are often caused by changes in ring strain or by resonance stabilization of the radicals involved:

<p>H anti-position</p>	<p>Abstraction of the hydrogen in anti position gives rise to a very strained TS with a DFT barrier of 20 kcal/mol.</p>
	<p>Allyl resonance reduces the bond strength, but this stabilization is not yet fully active in the TS. This causes the SAR E_A of -0.7 kcal/mol to strongly underestimate the DFT barrier of 6.4 kcal/mol.</p>

Future work and improvements

For the derivation of the SAR as described above, we have used experimental bond strengths as tabulated in the literature (Wing Tsang, 1996). However, for many molecules the $D(C-H)$ bond strengths are not known, especially for the often complex intermediates found in the decomposition of large biogenic VOCs. It would therefore be interesting to use easily obtained bond strengths calculated using e.g. the B3LYP-DFT/6-31G(d,p) level of theory. This way, one could account for all effects altering the bond strength, including different classes of radical stabilization such as hyperconjugation stabilization, allyl-resonance, vinyloxy-resonance, etc., each of which has a different impact on the rate of isomerisation.



As a test case, we have done extensive quantum chemical and TST calculations on 1-butoxy, using the B3LYP-DFT/6-31G(d,p) level of theory, including all 9 low-lying rotamers, 2 transition state structures, Eckhart tunneling, and fall-off corrections. The predicted rate coefficient $k_{TST,DFT}(298\text{ K}) = 1.8 \times 10^5\text{ s}^{-1}$ is very close to the experimental results which are in the range of 1.1 - $1.8 \times 10^5\text{ s}^{-1}$. An Arrhenius fit yielded $k_{TST,DFT}(T) = 2.06 \times 10^{11}\text{ s}^{-1} \exp(-8.3\text{ kcal mol}^{-1} / RT)$ for $T = 280$ -320 K, in excellent agreement within chemical accuracy with the recommendation by Atkinson (1997) : $k_{TST,EXP}(T) = 2.4 \times 10^{11}\text{ s}^{-1} \exp(-8.4\text{ kcal mol}^{-1} / RT)$.

Conclusions

Two SARs were derived for the reactions of substituted alkoxy radicals, which allow the prediction of the dissociation and isomerisation rate coefficients of these alkoxy radicals. Combined with the literature data on the rate coefficients for the reaction with O_2 , these SARs can be used to predict the fate of a large set of alkoxy radicals and are therefore of direct use in the construction of chemical mechanisms, and in modeling of atmospheric processes. These SARs are generally applicable, such that a more detailed analysis is required only when two reactions are similar in rates, requiring an accurate case-by-case verification, or in the case of e.g. ring strain and resonance effects, which are not included in the SAR.

Acknowledgements

This work was carried out in part in the frame of the ongoing Belgian research program on Global Change and Sustainable Development, funded via the Federal Office for Scientific, Technical and Cultural Affairs. The authors are also indebted to the Fund for Scientific Research (FWO-Vlaanderen) and to the KULeuven Research Council (BOF) for continuing support.

References

- Atkinson, R. 1997: *J. Phys. Chem. Ref. Data* **26**, 215-290.
- Dibble, T. S. 2001, *J. Am. Chem. Soc.* **123**, 4228.
- Blitz, M.; Pilling, M.J.; Robertson, S.H.; and Seakins P.W. 1999, *Phys. Chem. Chem. Phys.* **1**, 73.
- Caralp, F.; Devolder, P.; Fittschen, Ch.; Gomez, N.; Hippler, H.; Mereau, R.; Rayez, M.-T.; Striebel, F., and Viskolcz, B. 1999, *Phys. Chem. Chem. Phys.* **1**, 2935-2944.
- Devolder, P.; Fittschen, Ch.; Frenzel, A.; Hippler, H.; Poskrebychev, G.; Striebel, F.; and Viskolcz, B. 1999, *Phys. Chem. Chem. Phys.* **1**, 675-681.
- Fenske, J. D. 2000, *J. Phys. Chem. A* **104**, 7821
- Fittschen, C.; Hippler, H.; and Viskolcz, B. 2000, *Phys. Chem. Chem. Phys.* **2**, 1677-1683.
- Jungkamp, T. P. W.; Smith, J.N.; and Seinfeld, J.H. 1997, *J. Phys. Chem. A* **101**, 4392-4401.
- Méreau, R.; Rayez, M.-T.; Caralp, F.; and Rayez, J.-C., 2000, *Phys. Chem. Chem. Phys.* **2**, 3765-3772.
- Somnitz, H. and Zellner, R., 2000, *Phys. Chem. Chem. Phys.* **2**, 4319-4325.
- Peeters, J.; Fantechi, G.; and Vereecken, L., 2002, Manuscript in preparation.
- Wing Tsang, in *Energetics of Organic Free Radicals*, eds. Simoes, J. ; Greenberg, A.; and Liebman, J. F., Search Series, Blackie, London, 1996, Vol. 4.

Isomerization of 1-Butoxy Radicals (GPP22)

M. Paulus and F. Zabel

*Institut für Physikalische Chemie, Universität Stuttgart, Pfaffenwaldring 55,
D-70569 Stuttgart; e-mail: f.zabel@ipc.uni-stuttgart.de*

Introduction

Alkoxy radicals are important reactive intermediates in the atmospheric degradation of volatile organic compounds. In the atmosphere, they undergo either unimolecular transformation (decomposition/isomerization, k_{uni}) or reaction with O_2 (k_{O_2}):

(1a) thermal decomposition ($k_{\text{uni}} = k_{\text{dis}}$, aldehyde/ketone + alkyl/H)

(1b) isomerization ($k_{\text{uni}} = k_{\text{iso}}$, hydroxyaldehyde/hydroxyketone)

(2) reaction with O_2 (k_{O_2} , aldehyde/ketone + HO_2)

Depending on the ratio $k_{\text{uni}}/(k_{\text{O}_2} \times [\text{O}_2])$, different products are formed with different effects on atmospheric chemistry.

The 1-butoxy radical is a model compound for large alkoxy radicals where isomerization via a six-membered transition state is possible (Carter et al., 1976; Niki et al., 1981; Kwok et al., 1996; Lendvay and Viscolcz, 1998). It was apparent from earlier work that, for 1-butoxy, $k_{1b} \gg k_{1a}$. It has been suggested that 4-hydroxybutanal is a stable product of the isomerization channel (Carter et al., 1979; Niki et al., 1981; Atkinson et al., 1996); the stable product of channel (2) is *n*-butanal. The rate constant ratio $k_{\text{iso}}/k_{\text{O}_2}$ can then be calculated from the product yields of reaction channels (1b) and (2):

$$\frac{k_{\text{uni}}}{k_{\text{O}_2}} \approx \frac{k_{\text{iso}}}{k_{\text{O}_2}} = \frac{\Delta[4\text{-hydroxybutanal}] \times [\text{O}_2]}{\Delta[n\text{-butanal}]}$$

However, identification of 4-hydroxybutanal (Niki et al., 1981; Atkinson et al., 1996) was not very straightforward so far.

The main aim of this work is

- (i) to identify 4-hydroxybutanal as a product;
- (ii) to determine the ratio $k_{\text{iso}}/k_{\text{O}_2}$ for 1-butoxy as a function of temperature.

Method

Experiments were performed in a temperature controlled photochemical reaction chamber from quartz ($v = 209$ L). 1-Butoxy radicals are prepared by stationary photolysis of mixtures of 1-iodobutane, O_2 , NO , and N_2 at 254 nm. Reaction mixtures are analyzed *in situ* by long path FT-IR spectrometry (optical pathlength = 29 m).

There are 3 sets of experiments:

- I. Low partial pressure of O_2 (1-10 mbar) \rightarrow no formation of *n*-butanal; the product spectrum is monitored after termination of photolysis \rightarrow no time resolution but long signal accumulation and good signal-to-noise ratio.
- II. Low partial pressure of O_2 (1-10 mbar) \rightarrow no formation of *n*-butanal; time resolution 7 s (1 spectrum every 7 s during and after photolysis); high conversion of 1-iodobutane \rightarrow acceptable signal-to-noise ratio.
- III. High partial pressures of O_2 (200 - 1000 mbar), no time resolution.

Results and Discussion

IR spectra obtained for set I conditions are shown in Figure 1. The residual spectrum (1d) is very similar to the product spectrum of the photolysis of 1-butyl nitrite in the presence of O_2 reported by

Niki et al. (1981). However, different from Niki et al., we assign most of the residual absorption, in particular the OH band at 3647 cm^{-1} , to a tautomer of 4-hydroxybutanal, viz. 2-hydroxytetrahydrofuran. This will be explained in the next section.

In order to identify 4-hydroxybutanal, an attempt was undertaken to synthesize this compound by acidic hydrolysis of 2,3-dihydrofuran. In solution, there exists an equilibrium between 4-hydroxybutanal and 2-hydroxytetrahydrofuran (Hurd and Saunders, 1952). After removal of the solvents and purification of the raw product by column chromatography, only 2-hydroxytetrahydrofuran was obtained. This compound was identified

- by comparison of its IR spectrum with that of a purchased sample of 3-hydroxytetrahydrofuran, and
- by comparison of its NMR spectrum with a literature spectrum (Ogata et al., 1980).

The absorption coefficients of 2-hydroxytetrahydrofuran were determined based on pressure measurements ($\sigma(3647\text{ cm}^{-1}) = 1.58 \times 10^{-19}\text{ cm}^2$). The IR absorption coefficient of 4-hydroxybutanal at 3674 cm^{-1} was estimated by mass balance in experiments at set I conditions. In Figure 2, the synthesized sample of 2-hydroxytetrahydrofuran is compared with the residual spectrum of the 1-iodobutane photolysis system, showing that the major part of the residual absorption may be assigned to 2-hydroxytetrahydrofuran. After subtraction of the absorption of 2-hydroxytetrahydrofuran (Figure 2b), a residual remains (Figure 2c) which can partly be assigned to 4-hydroxybutanal (O-H and C=O absorptions). We thus conclude that both 4-hydroxybutanal and 2-hydroxytetrahydrofuran are formed in our reaction chamber during the photolysis of 1-iodobutane in the presence of O_2 and NO. In order to support the preliminary identification of 4-hydroxybutanal (Figure 2c) and to check if there exists a thermal equilibrium between both tautomers, the time dependence of the product IR absorption was determined under set II conditions (see Figure 3). In the residual spectra (before the subtraction of absorptions from the tautomers 2-hydroxytetrahydrofuran and 4-hydroxybutanal), two OH absorption bands centered at 3647 and 3674 cm^{-1} with different time behaviour were observed. The 3647 cm^{-1} band was identified as originating from 2-hydroxytetrahydrofuran, the second band was assigned to 4-hydroxybutanal. After subtraction of the absorption of the synthesized sample of 2-hydroxytetrahydrofuran, the absorption from 4-hydroxybutanal could also be determined. In Figure 4, the time dependence of the concentrations of these tautomers is shown, both during and after termination of photolysis.

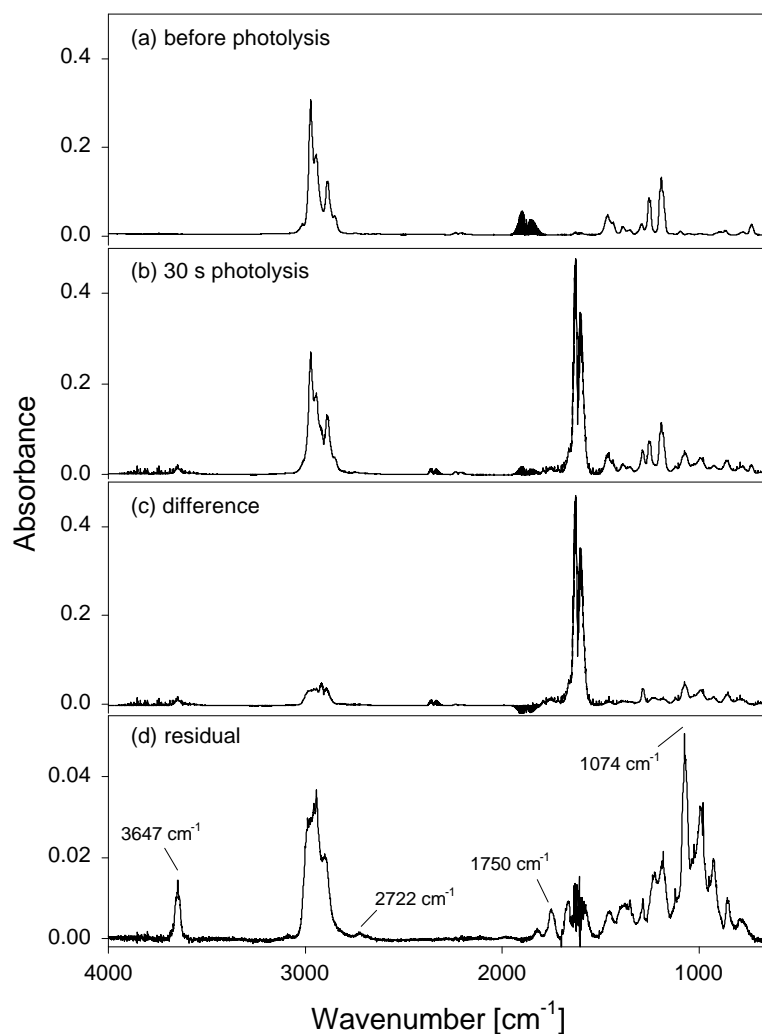


Figure 1: Photolysis of a mixture of 1-iodobutane, O_2 , NO , and N_2 at 254 nm (set I conditions). (a): educt spectrum; (b): product spectrum; (c): difference (b) - (a); (d): result of spectral subtraction/addition of NO , NO_2 , H_2O , H_2CO , HNO_3 , HONO , HC(O)OH , *n*-butanal, *n*-butyl nitrate, *n*-butyl nitrite, and 1-butyl iodide from/to spectrum (c).

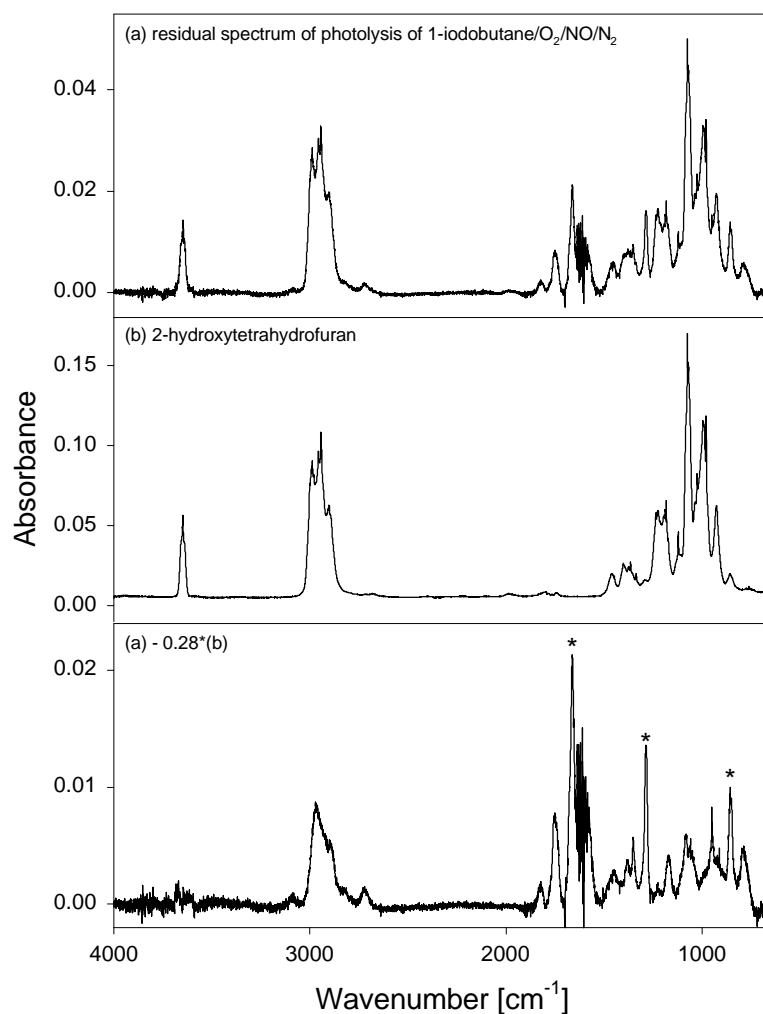


Figure 2: Photolysis of a mixture of 1-iodobutane, O₂, NO, and N₂ at 254 nm (set I conditions). Comparison of the residual absorption of the photolysis product spectrum and that of a synthesized sample of 2-hydroxytetrahydrofuran; *: typical nitrate bands (probably from 1-hydroxy-4-nitrato-butane).

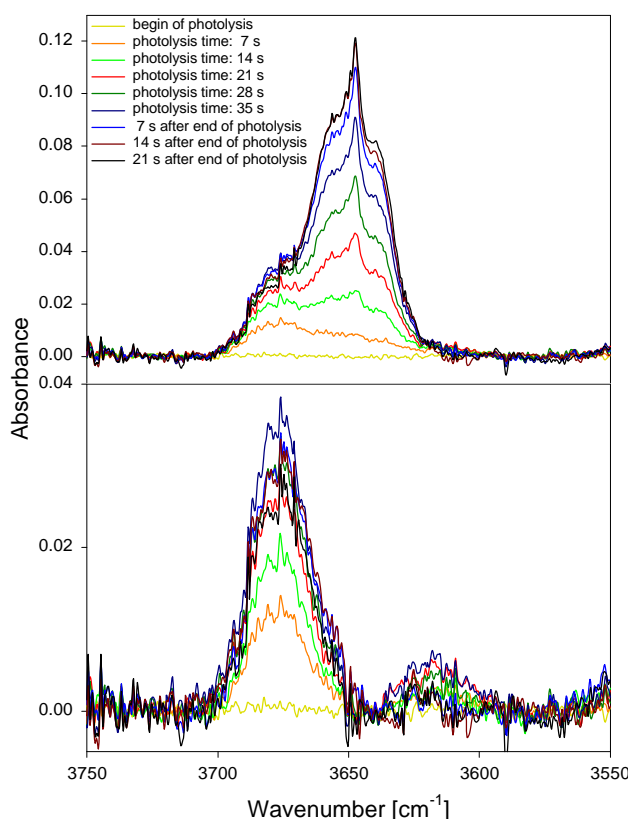


Figure 3: Photolysis of a mixture of 1-iodobutane, O₂, NO, and N₂ at 254 nm (set II conditions). OH-bands of the product spectra after subtraction of the IR-absorptions of educts and byproducts (top) and after spectral subtraction of 2-hydroxytetrahydrofuran (bottom).

From Figures 3 and 4 we conclude that

- 4-hydroxybutanal is probably the major gas phase product of the isomerization of 1-butoxy radicals;
- during photolysis, there is obviously a radiation or radical catalysed transformation of 4-hydroxybutanal to 2-hydroxytetrahydrofuran;
- in the dark, the concentration ratio of 4-hydroxybutanal and 2-hydroxytetrahydro-furan is frozen.

In order to check if, in the dark, both tautomers are in thermal equilibrium, the synthesized sample of 2-hydroxytetrahydrofuran was injected into the reaction chamber, and its IR absorption was monitored for about 24 hours. There was no conversion to 4-hydroxybutanal detected within this time. This is in agreement with DFT calculations performed with the GAUSSIAN 98 programme which suggest that the barrier for isomerization is too high to proceed at a measurable rate at room temperature.

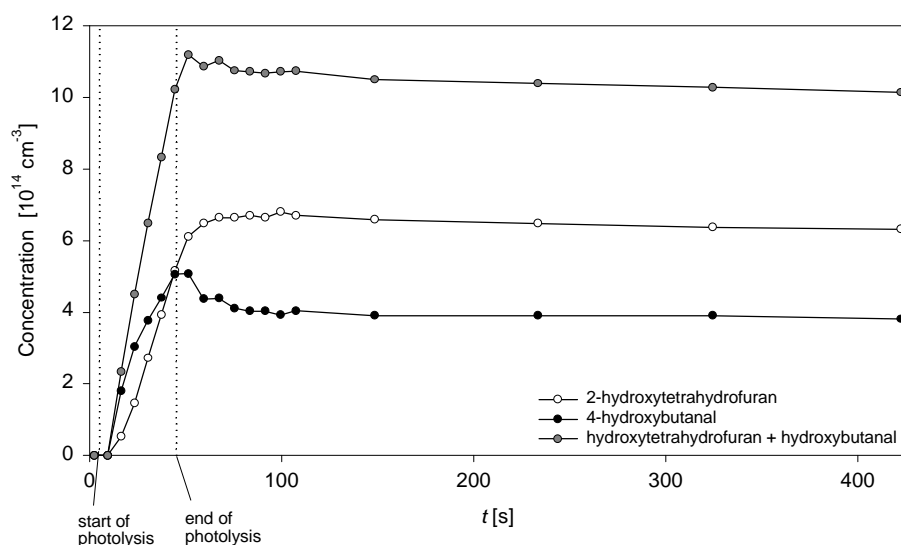


Figure 4: Photolysis of a mixture of 1-iodobutane, O₂, NO, and N₂ at 254 nm (set II conditions). OH-bands of the residual spectra after subtraction of the IR-absorptions of the educts and of the byproducts.

Kinetics of the 1-Butoxy Radical

$k_{\text{iso}}/k_{\text{O}_2}$ was estimated from set III experiments, using the equation

$$\frac{k_{\text{iso}}}{k_{\text{O}_2}} = \frac{\{\Delta[2\text{-hydroxytetrahydrofuran}] + \Delta[4\text{-hydroxybutanal}]\} \times [\text{O}_2]}{\Delta[n\text{-butanal}]}$$

Preliminary results are collected in Figure 5. Similar to our experiments on 2-butoxy radicals

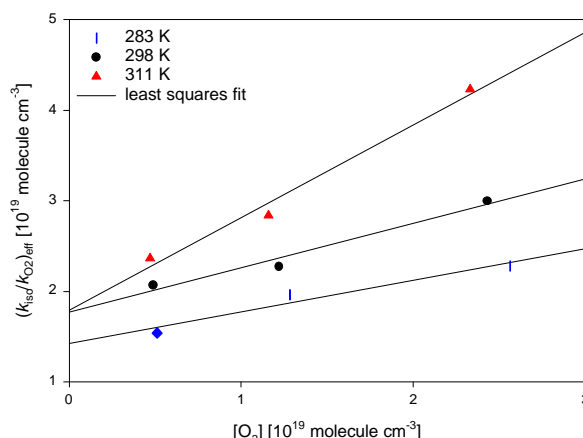


Figure 5: Preliminary results on the temperature dependence of $k_{\text{iso}}/k_{\text{O}_2}$ based on the yields of *n*-butanal (reaction 2) and 4-hydroxybutanal+2-hydroxytetrahydrofuran (reaction 1b). (Libuda et al., 2001) and other alkoxy radicals (Geiger et al., 2001), the effective $k_{\text{iso}}/k_{\text{O}_2}$ values depend on the partial pressure of O₂.

Experiments are under way to determine this rate constant ratio more accurately, based on an improved absorption coefficient of 4-hydroxybutanal and corrections for other C4 products from reaction (1b) (e.g. 1-hydroxy-4-nitrato-butane).

Acknowledgement

We thank S. Jagiella for doing the DFT calculations.

References

- Carter, W. P. L., K. R. Darnall, A. C. Lloyd, A. M. Winer and J. N. Pitts, Jr., 1976: Evidence for Alkoxy Radical Isomerization in Photooxidations of C4-C6 Alkanes under Simulated Atmospheric Conditions, *Chem. Phys. Letters*, **42**, 22-27.
- Carter, W. P. L., A. C. Lloyd, J. L. Sprung and J. N. Pitts Jr., 1979: Computer Modeling of Smog Chamber Data: Progress in Validation of a Detailed Mechanism for the Photooxidation of Propene and n-Butane in *Photochemical Smog*, *Int. J. Chem. Kinet.*, **11**, 45-101.
- Geiger, H. et al., 2002: Chemical Mechanism Development: Laboratory Studies and Model Applications, *J. Atm. Chem.*, **42**, 323-357, Table VIII.
- Kwok, E. S. C., J. Arey, and R. Atkinson, 1996: Alkoxy Radical Isomerization in the OH Radical-Initiated Reactions of C₄-C₈ n-Alkanes, *J. Phys. Chem.*, **100**, 214-219.
- Lendvay, G. and B. Viscoltz, 1998: Ab Initio Studies of the Isomerization and Decomposition Reactions of the 1-Butoxy Radical, *J. Phys. Chem.* **102**, 10777-10786.
- Niki, H., P. D. Maker, C. M. Savage, and L. P. Breitenbach, 1981: An FT-IR Study of the Isomerization and O₂ Reaction of n-Butoxy Radicals, *J. Phys. Chem.* **85**, 2698-2700.
- Hurd, C. D., W. H. Saunders, Jr., 1952: Ring-Chain Tautomerism of Hydroxy Aldehydes, *J. Am. Chem. Soc.*, **74**, 5324-5329.
- Ogata, Y., K. Tomizawa and T. Ikeda, 1980: Novel Oxidation of Tetrahydrofuran to γ -Butyrolactone with Peroxyphosphoric Acid, *J. Org. Chem.*, **45** (1980), 1320-1322.
- Libuda, H. G., O. Shestakov, J. Theloke, and F. Zabel, 2002: Relative-Rate Study of Thermal Decomposition of the 2-Butoxy Radical in the Temperature Range 280 - 313 K, *Phys. Chem. Chem. Phys.*, **4**, 2579-2586.

Nitrate Formation in the Reaction of 1-Nonylperoxy Radicals with NO (GPP22)

M. Kabir and F. Zabel

Institut für Physikalische Chemie, Universität Stuttgart,

Pfaffenwaldring 55, D-70569 Stuttgart, e-mail: f.zabel@ipc.uni-stuttgart.de

Introduction

Nonmethane volatile organic chemicals (VOCs) are introduced into the atmosphere from both anthropogenic and biogenic sources (Atkinson, 1997). The tropospheric oxidation of VOCs in the presence of NO_x leads to the production of O₃ and other secondary photochemical pollutants, including alkyl nitrates. Organic nitrates were often measured in tropospheric air masses on the ppb level (*e.g.* Atlas *et al.*, 1992; Bertman *et al.*, 1995; O'Brien *et al.*, 1995; Flocke *et al.*, 1998) but modelling of the observed mixing ratios is not yet satisfactory.

A major part of the organic nitrates in the troposphere are formed in one of two reaction channels of the RO₂ + NO reaction:



The yields of alkyl nitrates in reaction (1) were investigated mainly by Atkinson and coworkers (Atkinson *et al.*, 1982, 1984), showing that the yield increases from close to zero for R = CH₃ to ≈ 0.3 for R = heptyl and larger. In addition, the alkyl nitrate yields were observed to be markedly temperature and pressure dependent, increasing with increasing pressure and decreasing temperature (Atkinson *et al.*, 1983). In these experiments, alkanes were reacted with OH radicals, and the mixtures of isomeric nitrates formed in reaction (1b) were analysed by GC-FID analysis. In two recent papers, however, Atkinson and coworkers claimed that the yields for long-chain alkyl nitrates, using GC-MS analysis, are lower than the previously stated values (Arey *et al.*, 2001; Aschmann *et al.*, 2001).

In the present work, a different method was used to detect the products of reaction (1) for the *n*-nonoxy radical. The yield of 1-nonyl nitrate (channel 1b) has been measured by long-path IR absorption, and the relative yield of the nitrate (= $k_{1b}/(k_{1a}+k_{1b})$) was determined from this yield and the conversion of the precursor compound 1-nonyl iodide. Experiments were also performed above and below room temperature.

Experimental

The experiments were performed in a temperature controlled, evacuable photoreactor constructed of quartz (*v* = 209 L, see Figure 1). The photoreactor consists of two concentric quartz tubes being kept in their position by two rings of stainless steel which are pressed together by 12 steel rods. The reactor is closed by disks made of stainless steel which contain a number of openings for the inlet system, pumping line, etc. The space between the quartz tubes and cavities within the end flanges made of steel can be filled with heating/cooling agent being circulated from/to a cryostat (Haake KT 90W). 24 fluorescent lamps of different types can be positioned around the outer quartz tube to photolyse the gas mixtures within the reaction chamber. The reactor is equipped with 2 fans to support mixing of the gas mixtures and various temperature gauges to measure the temperature of the gas within the reaction volume and of the heating/cooling liquid. Gas mixtures are analysed by long-path IR absorption, using a White system (optical pathlength = 29.0 m) and an FT-IR spectrometer (Nicolet MAGNA 560). The pumping system consists of a turbo pump (Pfeiffer TMH 260SG) and a 35 m³/h forepump. Gaseous chemicals can be added to the chamber from bulbs of calibrated volume or via syringes.

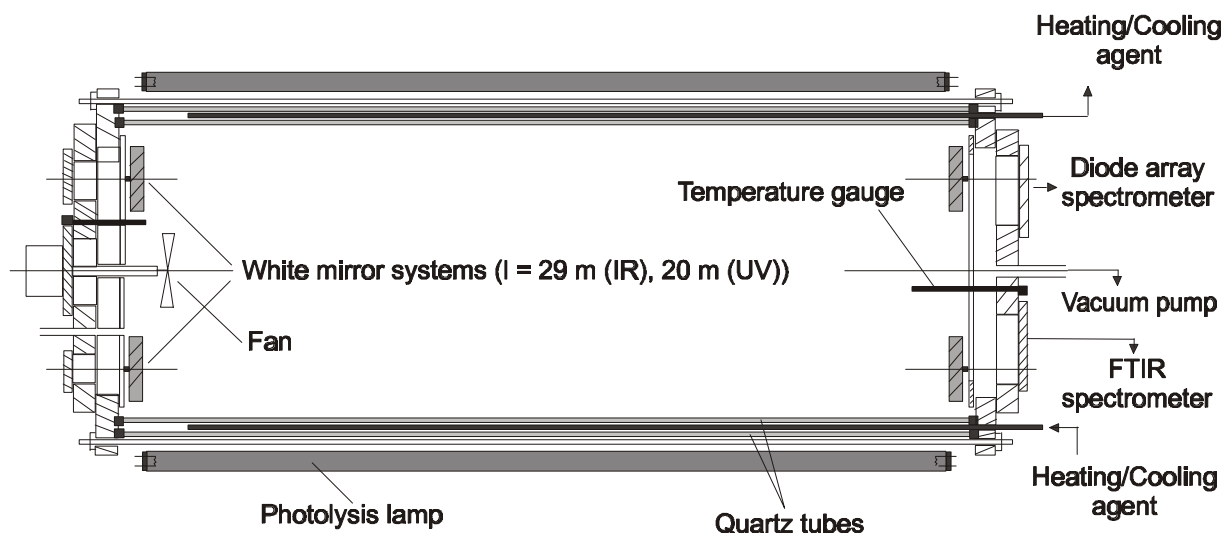
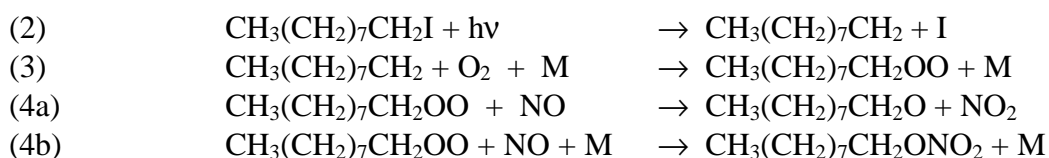
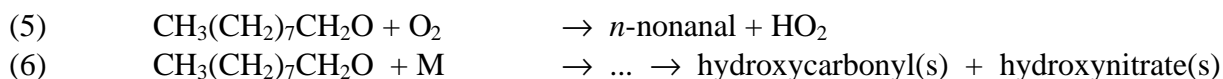


Figure 1: 209 L Photoreactor from Quartz

1-Nonylperoxy radicals were generated by stationary photolysis of 1-nonyl iodide/ $\text{NO}/\text{O}_2/\text{N}_2$ mixtures at 254 nm:



Reaction of 1-nonyloxy radicals formed in reaction (4a) will lead to different reaction products by two reaction pathways, reaction with O_2 or unimolecular transformation (decomposition and/or isomerization):



Reaction mixtures were analysed *in situ* by long-path FT-IR spectrometry. Photolysis experiments were performed at atmospheric pressure and 298 K in air. Standard photolysis times were 10, 30, 60 and 90 s. At these photolysis periods about 7 – 50 % of nonyl iodide was consumed.

Typical initial concentrations were (in units of molecule cm^{-3}): 1-nonyl iodide (1.5×10^{14}), NO (5×10^{14}), NO_2 (3×10^{13}). The initial NO_2 was formed when NO was added to the O_2/N_2 mixture. Typical product concentrations are (photolysis time 10 s, in units of molecule cm^{-3}): 1-nonyl nitrate (2.2×10^{12}), HONO (9.4×10^{11}), HNO_3 (7.8×10^{11}), HC(O)OH (1.1×10^{12}), HCHO (1.6×10^{11}), CO_2 (5.7×10^{11}). Concentrations were determined by spectral subtraction of reference IR spectra. 1-Nonyl nitrate was synthesised from 1-nonanol by nitration with a mixture of concentrated sulphuric acid and nitric acid at -10°C . The product was dried and distilled under vacuum. The purity of the nitrate was checked with GC, and reference infrared spectra were recorded.

Results and Discussion

1-Nonylnitrate is detected as one of the major products (bands marked with * in Residual 1, Figure 2) and the other (side) products identified are HCHO , HC(O)OH , HONO , and HNO_3 .

At 298 K,

$$k_{1b}/(k_{1a} + k_{1b}) = 0.23 \pm 0.02$$

has been derived from 12 experiments, based on the conversion of 1-nonyl iodide and the yield of 1-nonyl nitrate. This number is in very good agreement with the new results of Arey *et al.* (2001) and Aschmann *et al.* (2001). These authors studied the nitrate formation in reaction (1) for the series

R = *n*-butyl - *n*-decyl (leaving out, however, *n*-nonyl), where the authors observed that the alkyl nitrate yields increase monotonically with increasing carbon number in the *n*-alkane.

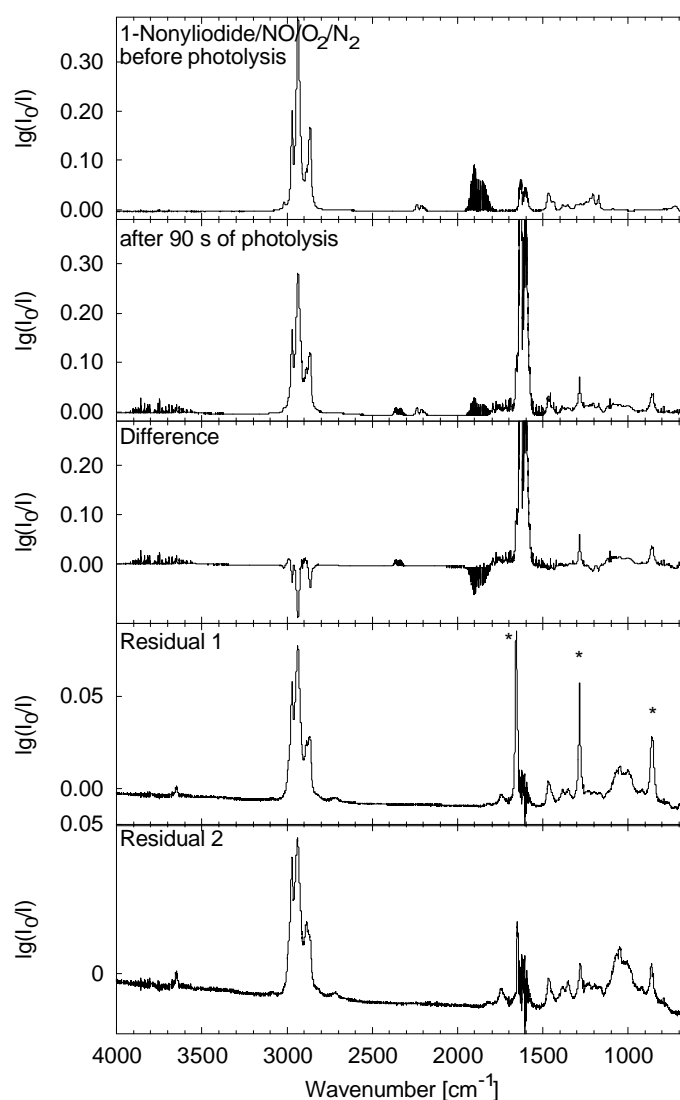


Figure 2: IR Spectra of a typical photolysis experiment. Residual 1: after subtracting the IR absorptions of 1-nonyl iodide, N₂O, NO, NO₂, CO₂, H₂O, HONO, HC(O)OH, HNO₃ and HCHO. Residual 2: after subtracting IR absorption of 1-nonyl nitrate from Residual 1.

Formation of the nitrates can be shown by the following mechanism:

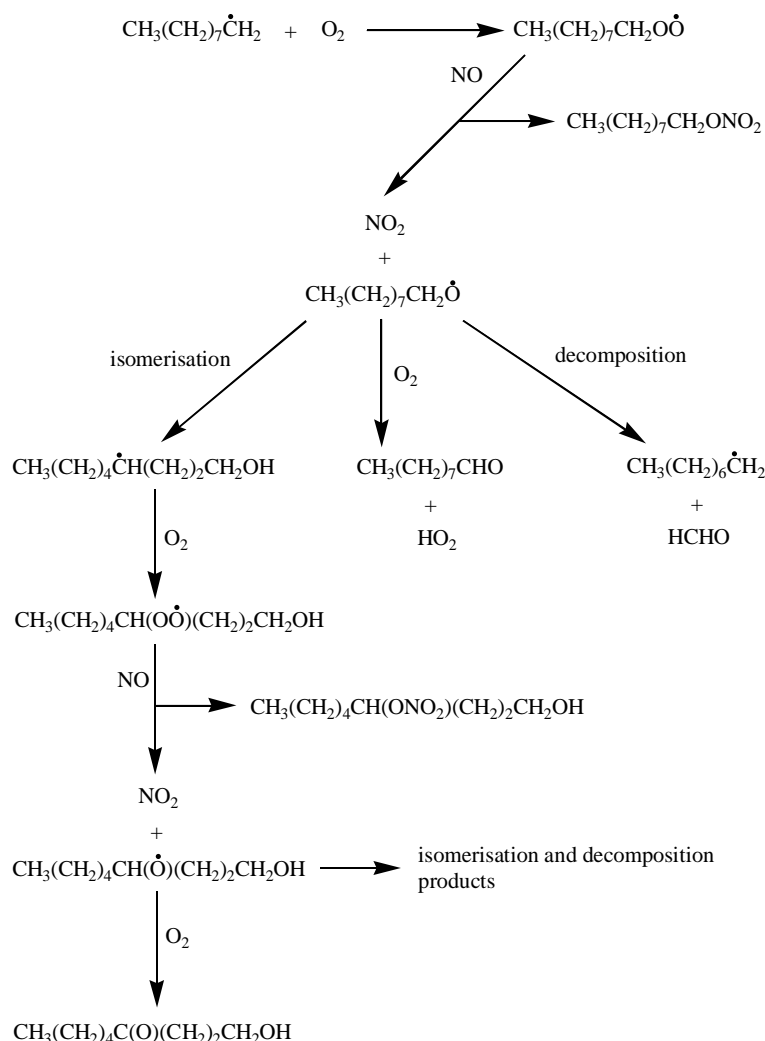


Figure 3: Simplified Reaction Mechanism

The mechanism and the residual IR spectra indicate that the products remaining to be identified are probably hydroxynitrates (nitrate bands at 1649, 1280 and 862 cm^{-1}), hydroxy-carbonyls (carbonyl bands at 2718, 1742 cm^{-1}) and their *hemi*-acetals (3647, 980-1120 cm^{-1}), formed following the isomerisation of the alkoxy radical. The position of the OH band in the residual spectra (3647 cm^{-1}) is shifted from that of alkanols and is identical to that of a hydroxytetrahydrofuran (see Paulus and Zabel (2002)).

Preliminary investigation on the temperature dependence indicates that the nitrate yield slightly decreases with the increase of temperature. The yields of isomerisation products also appear to be increased with temperature as expected. Further investigation on the temperature dependence is in progress.

References

- Arey, J., Aschmann, S.M., Kwok, E.S.C., Atkinson, R., 2001: Alkyl Nitrate, Hydroxyalkyl Nitrate, and Hydroxycarbonyl Formation from the NO_x – Air Photooxidation of C_5 – C_8 *n*-Alkanes, *J. Phys. Chem. A*, **105**, 1020-1027.
- Aschmann, S. M., J. Arey, and R. Atkinson, 2001: Atmospheric Chemistry of Three C_{10} Alkanes, *J. Phys. Chem. A*, **105**, 7598-7606.
- Atkinson R., 1997: Gas Phase Tropospheric Chemistry of Volatile Organic Compounds, *J. Phys. Chem. Ref. Data*, **26**, 215-290.
- Atkinson, R., Carter, W.P.L., Winer, A.M., 1983: Effects of Temperature and Pressure on Alkyl Nitrate Yields in the NO_x Photooxidations of *n*-Pentane and *n*-Heptane, *J. Phys. Chem.*, **87**, 2012-2018.

- Atkinson, R., Aschmann, S.M., Carter, W.P.L., Winer, A.M., Pitts, J.N. Jr., 1982: Alkyl Nitrate Formation from the NO_x – Air Photooxidations of $\text{C}_2 - \text{C}_8$ *n*-Alkanes, *J. Phys. Chem.*, **86**, 4563-4569.
- Atkinson, R., Aschmann, S.M., Carter, W.P.L., Winer, A.M., Pitts, J.N., Jr., 1984: Formation of Alkyl Nitrates from the Reaction of Branched and Cyclic Alkyl Peroxy Radicals with NO, *Int. J. Chem. Kinet.*, **16**, 1085-1101.
- Atlas, E.L., Ridley, B.A., Hübler, G., Walega, J.G., Carroll, M.A., Montzka, D.D., Huebert, B.J., Norton, R.B., Grahek, F.E., Schauffler, S., 1992: Partitioning and budget of NO_y species during the Mauna Loa Observatory Photochemistry Experiment, *J. Geophys. Res.*, **97**, 10,449-10,462.
- Bertman, S.B., Roberts, J.M., Parrish, D.D., Buhr, M.P., Goldan, P.D., Kuster, W.C., Fehsenfeld, F.C., Montzka, S.A., Westberg, H., 1995: Evolution of alkyl nitrates with air-mass age, *J. Geophys. Res.*, **100**, 22,805-22,813.
- Flocke, F., Volz-Thomas, A., Buers, H.J., Patz, W., Garthe, H.J., Kley, D., 1998: Long-term measurements of alkyl nitrates in southern Germany 1. General behaviour and seasonal and diurnal variation, *J. Geophys. Res.*, **103**, 5729-5746.
- O'Brien, J.M., Shepson, P.B., Muthuramu, K., Hao, C., Niki, H., Hastie, D.R., Taylor, R., Roussel, P.B., 1995. Measurements of alkyl and multifunctional organic nitrates at a rural site in Ontario, *J. Geophys. Res.*, **100**, 22,795-22,804.
- Paulus, M., Zabel, F., 2002: Isomerization of 1-Butoxy Radicals, this volume.

Absolute rate constants for the gas-phase ozonolysis of isoprene and methylbutenol (GPP25)

Klawatsch-Carrasco, N., Doussin, J.F., Carlier, P.

LISA, Université Paris 12, 61 avenue du Général de Gaulle, 94010 Créteil Cedex

klawatsch@lisa.univ-paris12.fr

The reactions of the biogenic organic compounds isoprene and 2-methyl-3-buten-2-ol (MBO) with ozone have been investigated under controlled conditions for pressure (atmospheric pressure) and temperature ($293 \pm 2\text{K}$), using FTIR spectrometry. CO was added to scavenge hydroxyl radical formation during the ozonolysis experiments. Reaction rate constants were determined by absolute rate technique by measuring both ozone and the organic compound concentrations. The measured values were $k_1 = (1.19 \pm 0.09) \cdot 10^{-17} \text{ cm}^3 \cdot \text{molec}^{-1} \cdot \text{s}^{-1}$ for the reaction between ozone and isoprene and $k_2 = (8.3 \pm 1.0) \cdot 10^{-18} \text{ cm}^3 \cdot \text{molec}^{-1} \cdot \text{s}^{-1}$ for the reaction between ozone and MBO.

Biogenic volatile organic compounds (BVOCs) account for around 90% of global hydrocarbon emissions into the Earth's atmosphere. Several thousand different compounds have been identified, including well-known unsaturated hydrocarbons such as isoprene, and mono- and sesquiterpenes. The gas-phase degradations of these reactive molecules contribute to produce photooxidants in the atmosphere. These reactions are liable to aggravate the situations of pollution events by increasing the background level of ozone in the troposphere. The details of the mechanisms and the rate constants are important when describing the impact of these processes on air quality.

One oxygenated BVOC recently detected, 2-methyl-3-buten-2-ol (MBO) seems to be emitted in large quantities by certain types of trees. The strong similarities with isoprene (structure, types of vegetation source and diurnal trend) suggest that both might come from the same kind of vegetative metabolism. Both isoprene and MBO are sensitive to the main oxidants in the atmosphere such as OH radicals, O_3 and NO_3 radicals. Isoprene has already been well-studied. The values reported in the literature for the room temperature rate constant of the reaction between ozone and isoprene (k_1) were quite dissimilar but they tend to converge to a nowadays well-admitted value. In the contrary, very little data is available about the reactivity of MBO.

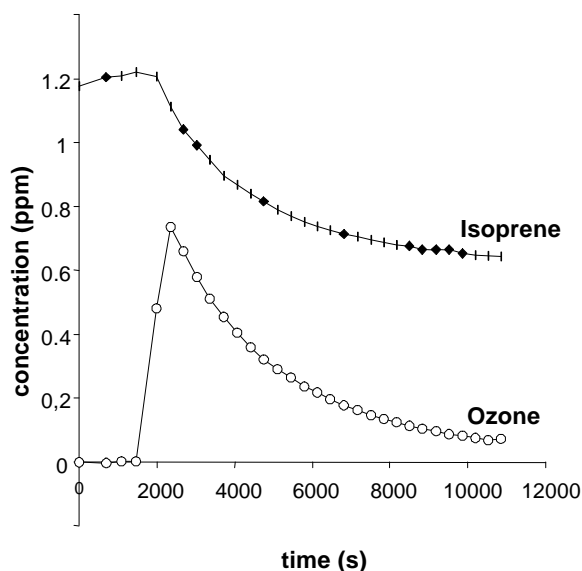


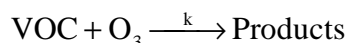
Figure 1: An experiment of ozonolysis of isoprene followed by infrared spectrometry

In this study we have measured the rate constant of the reaction of ozone with both biogenic compounds isoprene and MBO by absolute rate technique by monitoring both ozone and the biogenic compound concentrations using FTIR spectrometry under simulated atmospheric

conditions (atmospheric pressure, low concentration and $T=293\pm 2\text{K}$). The comparison of the results obtained with isoprene allowed us to confirm the validity of our method and to precise the value of k_1 . The determination of k_2 is decisive to evaluate the atmospheric persistence of the recently detected compound MBO. The experiments were performed in a 977L cylindrical pyrex evacuable reactor, containing a multiple-reflection optical system coupled to a Bomem DA8-ME FTIR spectrometer. The pathlength in the chamber was adjusted to 156m. The ozonolysis experiments were performed with CO as an OH-scavenger.

Figure 1 shows a typical plot of an experiment of ozonolysis, followed by infrared spectrometry.

Given the chemical equation:



Without injection of ozone, no VOC loss was observed with the timeframe of the experiment. On the other hand, it is well known that ozonolysis of olefins produce OH radicals in proportions that depend on the structure of the alkene [6-8]. To avoid the reaction of the OH radical with the organic compound, an OH scavenger was used (carbon monoxide). The only way of consuming the COV being the ozonolysis reaction, the decrease of the COV concentration was equal to the speed of the ozonolysis reaction. The kinetic law for this reaction was also:

$$\frac{-d[\text{VOC}]}{dt} = k \cdot [\text{VOC}] \cdot [\text{O}_3]$$

For each point we approximated this relationship with small variations of [VOC] and time and obtained a value of k for each point:

$$k = \frac{-\Delta[\text{VOC}]}{\Delta t \cdot [\text{VOC}] \cdot [\text{O}_3]}$$

The value of k was obtained by a statistical study of all the measurements for each scavenged experiment, (ie 313 measurements for MBO and 27 for isoprene). We observed that the scavenging was necessary for the kinetic study. CO was used in sufficient quantity to scavenge the reaction.

The average k-values for these experiments are:

$$k_1 = (1.19 \pm 0.09) \times 10^{-17} \text{ cm}^3 \text{ molec}^{-1} \cdot \text{s}^{-1}$$

$$k_2 = (0.83 \pm 0.10) \times 10^{-17} \text{ cm}^3 \text{ molec}^{-1} \cdot \text{s}^{-1}$$

The uncertainties on the rate constants take into account the uncertainties on the reactants calibrations and the statistic dispersion of the measurements (given by the product of the standard deviation with $t_{95\%}$, the Student coefficient).

In conclusion, the absolute determination method avoids the use of a reference compound. Nevertheless, it is important to underline that we had to use the variation of the organic compound, and not the variation of ozone, to precisely calculate the rate constant. Indeed we observed an additional consumption of ozone. In consequence, the precision of the values is given by the measurement of both ozone and VOC.

Our kinetics study of the ozonolysis of isoprene gives a value for k_1 that confirms the rate constants found in the literature, and therefore the validity of our method. As for the determination of k_2 , our measured value is in good agreement with the work of Fantechi et al. [1] but we were able to precise this value.

Reference

[1] Fantechi, G., et al., *Determination of the rate constants for the gas phase reactions of methylbutenol with OH radicals, ozone and NO₃ radicals*. Atmospheric Environment, 1998. **32**(20): p. 3547-3556.

Competition Between Various Alkoxy Evolution Process in the Atmosphere (GPP 25).

N. Meunier, J.F. Doussin, R. Durand-jolibois, B. Picquet-Varrault and P. Carlier.

L.I.S.A. 61 ave du general de Gaulle 94010 Créteil Cedex France

meunier@lisa.univ-paris12.fr

Abstract.

This work aims at studying the chemical evolution of several alkoxy radicals, to measure the ratio between each reaction way by quantification of products of each evolution process.

This experiment has been carried out in the evacuable simulation chamber of LISA. Alkoxy radicals has been generated by the photolysis near 420 nm of the corresponding alkyl nitrite. In order to detect minor process, the study was made at several partial pressures of O₂ completed at 1 bar by N₂. Reactants and products has been detected "in situ" by long path FTIR.

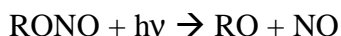
We measure for 1-propoxy, 2-propoxy, 2-butoxy, 3-pentoxy, 2 methyl 1-propoxy, the $k_{\text{isom}}/k_{\text{O}_2}$ ratio and find respectively $(3.8 \pm 0.4) \times 10^{16}$, $(2.9 \pm 0.3) \times 10^{16}$, $(2.9 \pm 0.3) \times 10^{18}$, $(4.1 \pm 0.8) \times 10^{18}$ and $(3.7 \pm 0.8) \times 10^{18} \text{ molec}^{-1} \cdot \text{cm}^3$. 1-butoxy radical have also been studied. We had to synthesise the product of the isomerization, the 4-hydroxy-butanal by ozonolysis of 4-penten-1-ol in gaseous phase and obtain its IR spectrum. And so, we determine the $k_{\text{isom}}/k_{\text{O}_2}$ ratio at $1.1(\pm 0.4) \times 10^{19} \text{ molec}^{-1} \cdot \text{cm}^3$.

Introduction.

Alkoxy radicals RO· are key intermediates in the atmospheric photooxidation of volatil organic compounds, which is leading to the formation of ozone and other oxidation products baneful for environment. In this mechanism, the evolution of alkoxy radicals determines the nature and the concentration of the secondary compounds. These radicals can, depending on the nature of the alkyl group, undergo a β-C-C decomposition, a reaction with O₂ and, for alkoxy radicals with a δ-carbon, a 1-5-H shift isomerization by a 6-member cyclic transition state.

Experimental.

It is necessary to perform a reliable and specific generation of alkoxy radicals. Among various sources (alkane + Cl, ROOR photolysis, ROCl photolysis ...) we choose to photolyse appropriate alkyl nitrite (RONO).



This chemical system allows us to generate directly the alkoxy radical needed and the NO_x side chemistry is fairly known. We photolyse alkyl nitrites with low energy radiation (around 420nm) to be able to minimise the potential formation of excited radicals.

The percentage of O₂ was adjusted to maintain the two reaction pathways compatible with the detection limit of the two monitored compounds.

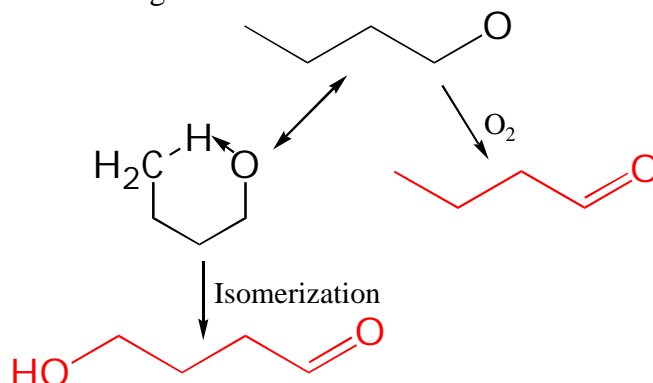
We use a scavenger of OH radicals (cyclohexane and CO) in such concentration to prevent reactions $\text{RONO} + \text{OH}$ and products + OH

Experiments were carried out in a 6 meters length Pyrex evacuable chamber of 977 litres. Near 420 nm fluorescent tube irradiation is used to prevent excitation and to work with slow photolysis. Products and reactants were detected by long path FTIR (~156m). Each alkoxy radical was studied at atmospheric pressure with several partials pressures of O₂ completed with N₂. Each experiment was performed with and without an OH-scavenger.

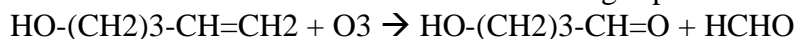
Results

Fate of 1-butoxy radical

The 1-butoxy radical react according to this scheme :



4 hydroxy butanal was calibrated from the carbon balance in gas phase reaction of :



The obtain infrared absorption spectrum is given in figure 1.

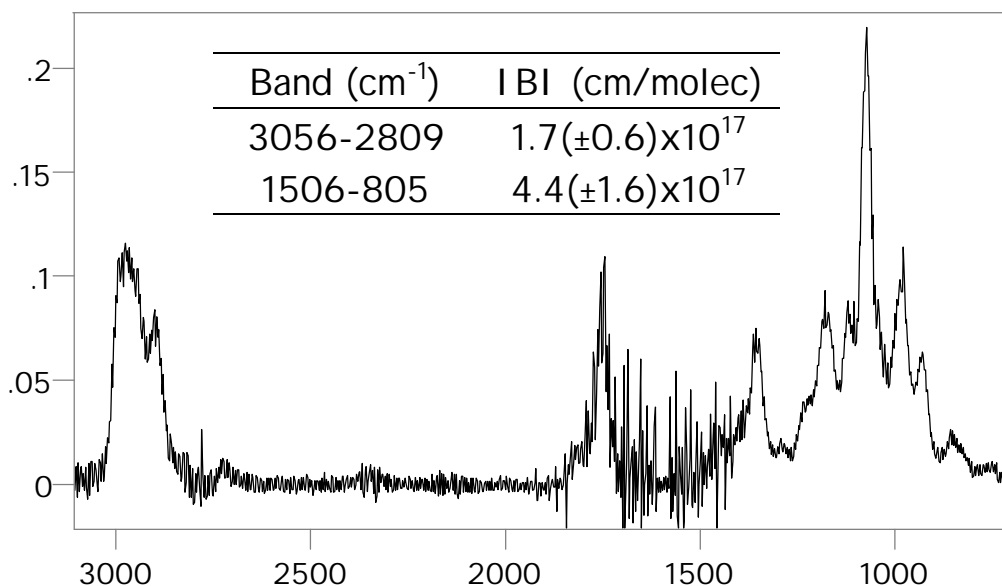


Figure 1: Spectrum of 4-hydroxy butanal, no band was detected between 3000 and 3500 cm⁻¹.

With the help of sequential infrared spectra acquired during the photolysis, concentrations of reactants and products versus time were followed. The branching ratio measured is $1.1(\pm 0.4) \times 10^{19}$ molec/cm³ obtained (figure 2).

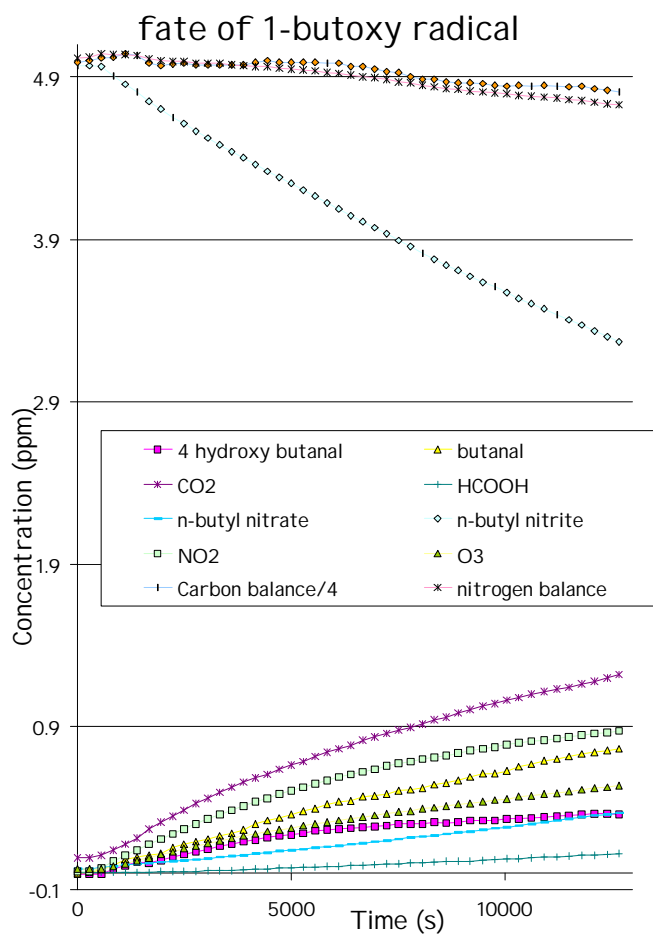
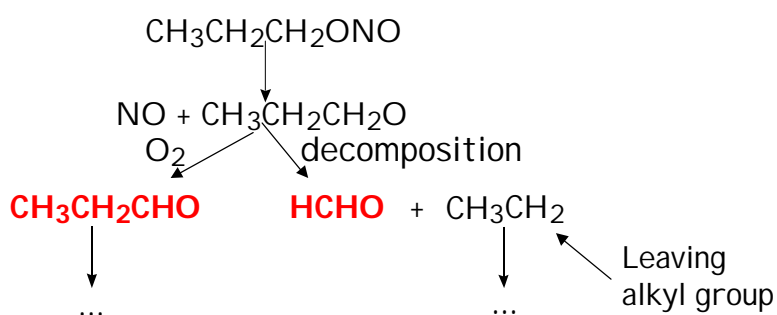


Figure 2: concentration of products vs. time for 1-butyl nitrite photolysis.

Fate of some branched alkoxy radical

Experiments were carried out for branched alkoxy, they react according to this example scheme :



From infrared spectra obtained during experiments, we obtain concentrations versus time plots (figure 3).

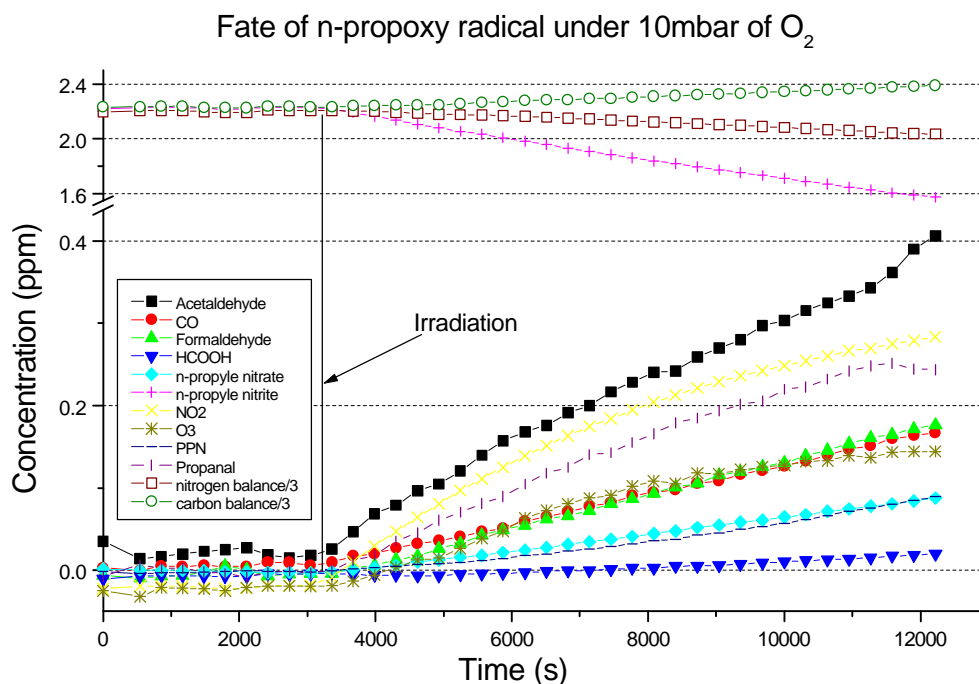


Figure 3 : concentration of products vs. time for 1-propyl nitrite photolysis.

By plotting the formation of product vs. loss of nitrite, normalised by initial nitrite concentration (Fig. 4), we observed the reproducibility of experiments. The plots are linear confirming that these carbonyl compounds do not further react. Hence, the yield of each product has been determined by linear regression. With ratio of yields of products from each way, the ratio $k_{\text{dec}}/k_{\text{O}_2}$ is calculated. The results of these experiments are given in table 1.

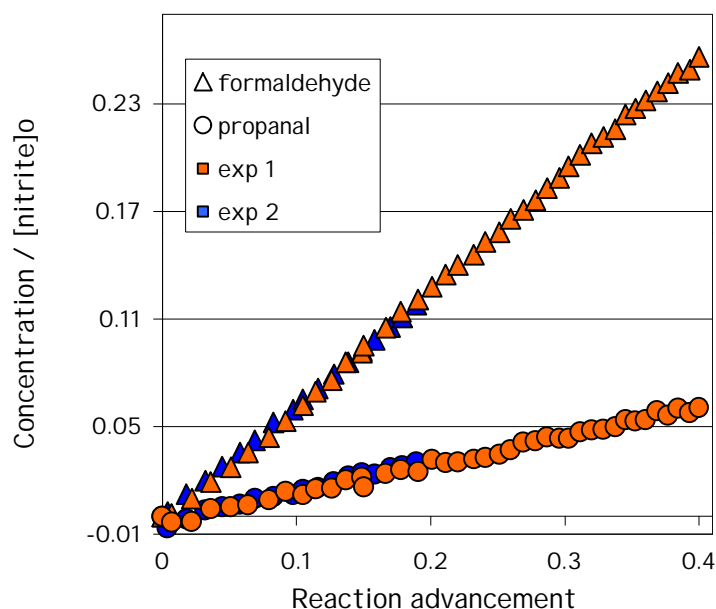


Figure 4 : reaction advancement of principal products of 1-propyl nitrite photolysis.


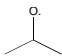
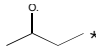
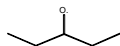
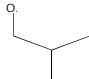
K _{dec} / K _{O2}						
	This Work	Zabel 2000	Carter 1979	Cox 1981	Fittschen 1999, 2000	Atkinson 1997
	(3.8±0.4)x10 ¹⁶					(3.4)x10 ¹⁶
	(2.9±0.3)x10 ¹⁶				(12.8)x10 ¹⁶	(0.18)x10 ¹⁶
	(2.9±0.3)x10 ¹⁸	(3.0±0.6)x10 ¹⁸	(3.1)x10 ¹⁸	(2.6±0.35)x10 ¹⁸		(2.8)x10 ¹⁸
	(3.8±0.7)x10 ¹⁸	(3.6±0.7)x10 ¹⁸				(1.9)x10 ¹⁸
	(4.0±0.6)x10 ¹⁸					
* décomposition	between 2 nd and 3 rd carbon					
K _{isom} / K _{O2}						

Table 1: Ratio obtained in this work compare with literature.

Moreover, theoretical chemistry has been studied especially by Méreau et al. (Méreau et al. 2000), who have established a structure reactivity relationship for the decomposition pathway. These relationships have been parameterised, using quantum chemistry ab initio BAC-MP4 and density functional theory calculated activation energies and reaction enthalpies on a set of linear and branched C₁ to C₅ alkoxy radical decomposition processes. In order to calculate k_{O_2} from our ratio, we use the rate constant k_{decomp} from Méreau 2000 (table 2).


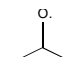
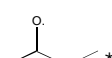
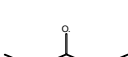
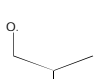
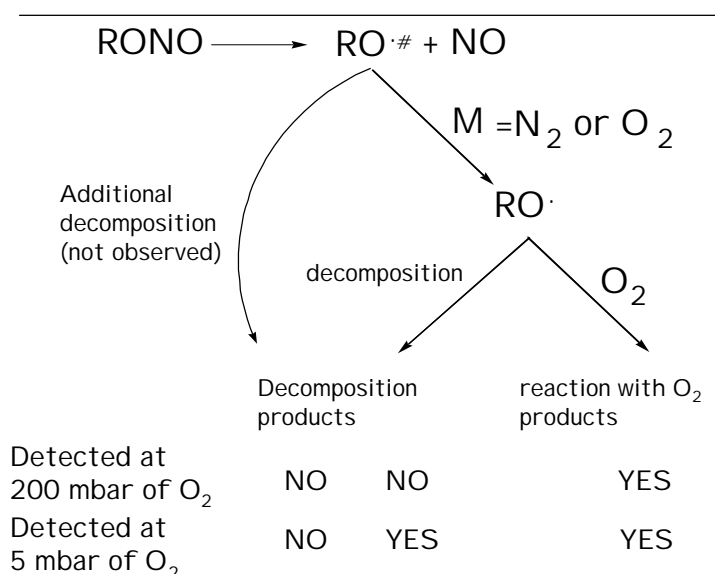
	This work	Méreau 2000	
	$k_{\text{dec}} / k_{\text{O}_2}$	$k_{\text{d}, 760}$	k_{O_2} deduced
	$(3.8 \pm 0.4) \times 10^{16}$	2.5×10^2	6.6×10^{-15}
	$(2.9 \pm 0.3) \times 10^{16}$	1.3×10^2	4.5×10^{-15}
	$(2.9 \pm 0.3) \times 10^{18}$	3.5×10^4	1.2×10^{-14}
	$(3.8 \pm 0.7) \times 10^{18}$	3.4×10^4	8.9×10^{-15}
	$(4.0 \pm 0.6) \times 10^{18}$	5.7×10^4	1.4×10^{-14}
* décomposition	between 2 nd and 3 rd carbon		

Table 2: k_{O_2} deduced from méreau et al. (Méreau 2000) and this work values.

Are alkoxy radicals Excited ?

No dependence of the $k_{\text{dec}}/k_{\text{O}_2}$ ratio with O₂ concentration have been found. Libuda et al.(2002) had shown that such dependence is the sign of radical excitation. Systematic study as a function of O₂

concentration have been done in order to verify the thermalisation of RO radicals following the method given by Wallington et al. 1996. No excitation has been found.



Typically, for $C \leq 3$, when O₂ reach 200mbar no decomposition is detected (furthermore no additional decomposition)

Conclusion.

We obtain the IR calibrated spectrum of 4 hydroxy butanal. Then, we measure the branching ratio of the fate of 1-butoxy radical. However, this calibration must be confirmed by HPLC analysis of samples taken from the simulation chamber.

We also measure the branching ratio for four alkoxy radicals. We can see the influence of the class of the alkoxy and the nature of the leaving alkyl group (Méreau 2000) on the branching ratio.

When we add one methyl group on the leaving alkyl group (1-propoxy \rightarrow 2 methyl 1-propoxy and 2-propoxy \rightarrow 2-butoxy) the ratio is growing by a factor 100 due in majority to the decomposition rate.

We have the same factor between the 1-propoxy (class I) and the 2-butoxy (class II).

We do not have this factor between the 2-butoxy and the 3-pentoxy because the class of the alkoxy and the leaving alkyl group is the same.

Outlook.

We have established a protocol to measure the branching ratios of the fate of alkoxy radicals, we have already measured six branching ratios, some other products are in studying.

We have measured these branching ratios for several branched alkoxy. With some others, we will be able to determine a structure reactivity relationship.

References

- Atkinson, R. (1997). "Atmospheric Reactions of Alkoxy and β -Hydroxyalkoxy Radicals." *International Journal of Chemical Kinetics* 29: 99-111.
- Carter, W. P. L., A. C. Lloyd, et al. (1979). "Computer Modeling of Smog Chamber Data : Progress in Validation of a Detailed Mechanism for the Photooxidation of Propene and n-Butane in Photochemical Smog." *Int. J. Chem. Kinet.* 11: 45-101.
- Cox, R. A., K. F. Patrick, et al. (1981). "Mechanism of Atmospheric Photooxidation of Organic Compounds. Reactions of Alkoxy Radicals in Oxidation of n-Butane and Simple Ketones." *Environ. Sci. Technol.* 15(5): 587-592.

- Fittschen, C., A. Frenzel, et al. (1999). "Rate Constante for the Reactions of C₂H₅O, i-C₃H₇O, and n-C₃H₇O with NO and O₂ as a function of Temperature." *Int. J. Chem. Kinet.* 31: 860-866.
- Fittschen, C., H. Hippler, et al. (2000). "The b C-C bond scission in alkoxy radicals: thermal unimolecular decomposition of t-butoxy radicals." *Phys. Chem. Chem. Phys.* 2: 1677-1683.
- Libuda, H. G., O. Shestakov, et al. (2002). "Relative-rate study of thermal decomposition of the 2-butoxyl radical in the temperature range 280-313 K." *Phys. Chem. Chem. Phys.* 4: 2579-2586.
- Méreau, R., M. T. Rayez, et al. (2000). "Theoretical study of alkoxy radical decomposition reactions: structure-activity relationships." *Phys. Chem. Chem. Phys.* 2: 3765-3772.
- Niki, H., P. D. Maker, et al. (1981). "An FT IR Study of the Isomerization and O₂ Reaction of n-Butoxy Radicals." *J. Phys. Chem.* 85: 2698-2700.
- Wallington, T. J., M. D. Hurley, et al. (1996). "Role of Excited CF₃CFHO Radicals in the Atmospheric Chemistry OF HFC-134a." *J. Phys. Chem.* 100: 18116-18122.
- Zabel, F. (2000). The atmospheric fate of long-chain alkoxy radicals. EC/eurotrac-2 Joint Workshop.

Influence of pH on Kinetics of S(IV) Autoxidation in the Presence of Mn(II) (APP3)

Boštjan Podkrajšek, Irena Grgic and Gorazd Bercic

National Institute of Chemistry (NIC), Hajdrihova 19, P.O.B. 660, SI-1001 Ljubljana, Slovenia,
(e-mail: irena.grgic@ki.si)

Introduction

Recent laboratory studies of chemical reactions involving S(IV) species in aqueous solution have greatly improved our understanding of the processes responsible for the oxidation of SO₂ in the aqueous phase (Warneck *et al.*, 1996). Since most laboratory experiments were carried out under conditions different from those in atmospheric liquid water, the laboratory data alone do not allow comparison of the individual contributions to the overall oxidation rates in the atmosphere. This problem may be overcome by means of computer model calculations (Warneck, 1999; Herrmann *et al.*, 2000), by which it is possible to identify the leading processes involved in the oxidation of SO₂ under different meteorological and atmospheric conditions. However, laboratory data (i.e., kinetic measurements) in combination with field data are very important and essential parameters.

Transition metal ions (TMI) and their complexes either present in atmospheric waters or in the liquid film of aerosol particles are considered to be potential catalysts in the autoxidation of S(IV) oxides (Brandt and van Eldik, 1995; Grgic and Bercic, 2001). Each species (i. e., dissolved S(IV) as well as TMI) shows a different reactivity and it is the chemistry of these species that is the basis for understanding the complex reaction mechanisms. In spite of many investigations on metal ion catalysis, there are still discrepancies, particularly for manganese catalysis at pH above 4.

This work presents new experimental results for aqueous S(IV) autoxidation catalyzed by Mn(II) in the pH range 3.0 – 5.0 under dark conditions. The results of a new numerically derived kinetic model based mainly on the formation of transient manganese-sulfito complexes are compared with the predictions obtained by a simple kinetics model evaluated by standard integral approach.

Experimental

Kinetic experiments were conducted in a semi-batch continuous stirred tank reactor (CSTR) protected from light and maintained at constant temperature. A pH adjusted aqueous solution of Mn(II) was saturated by air. To start a run, a small amount of aqueous S(IV) stock solution was added. To provide constant pH during the reaction course we used pH-stat (Metrohm) based on NaOH addition. The kinetics was followed by periodically withdrawing an aliquot of the reaction solution, immediately quenching any further S(IV) oxidation with the addition of formaldehyde, and determining the concentration of HSO₃⁻ and SO₄²⁻ by ion-exchange chromatography (DIONEX, IonPac AS4A anion separation column). The experiments were performed under the following conditions: [HSO₃⁻] = 0.1 – 0.4 mM, [Mn(II)] = 2 – 8 µM, pH = 3.0 – 5.0 and T = 15°C, 25°C and 35°C.

Results

The experiments showed that the reaction rate is proportional to [HSO₃⁻] up to 0.1 mM HSO₃⁻, while at higher concentrations the reaction rate becomes independent of [HSO₃⁻]. The reaction is autocatalytic, which is evident from the time dependence of the reaction rate (Fig. 1). With higher concentrations of HSO₃⁻, the maximum of the curve shifts to longer times. The results evaluated by standard integral approach show first-order dependance on both [HSO₃⁻] and [Mn(II)], but only for concentrations of HSO₃⁻ lower than 0.2 mM.

It should be pointed out that the first experimental points were not used for kinetic evaluation, because the reaction rate in the first minute is unusually high, most probably due to the mixing

equilibration, as it is evident from Fig. 1. The rate constant k is $1.2 \times 10^3 \text{ M}^{-1} \text{ s}^{-1}$ under the following experimental conditions: $[\text{Mn(II)}] = 2 - 8 \text{ } \mu\text{M}$, $[\text{HSO}_3^-] = 0.2 \text{ mM}$, $T = 25^\circ\text{C}$ and $\text{pH} = 4.5$. The activation energy determined from the slope of Arrhenius plot was found to be $E_a = 91.1 \text{ kJ mol}^{-1}$ at $\text{pH} = 4.5$.

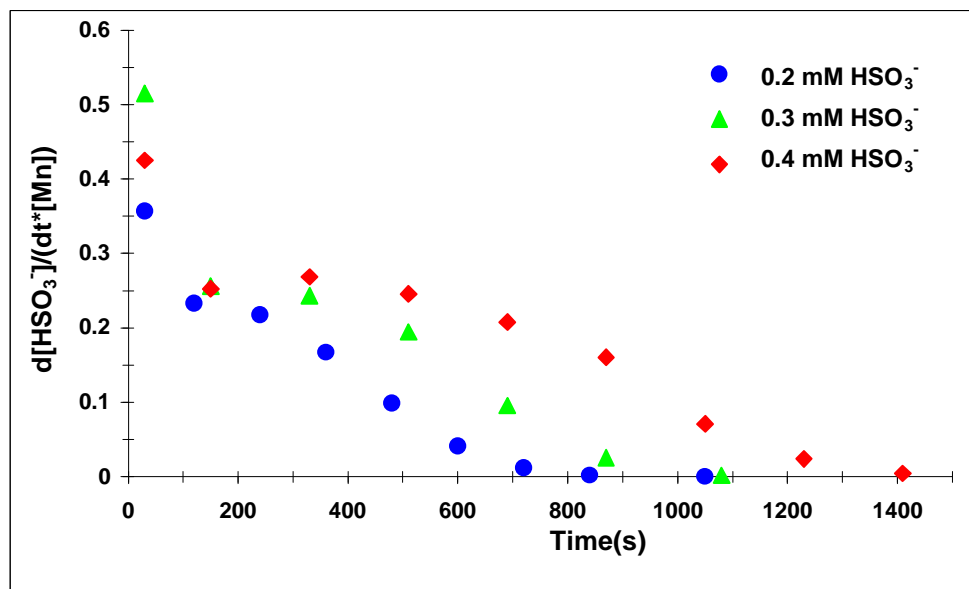


Figure 1: Reaction rate as a function of time. Experimental conditions: $[\text{HSO}_3^-]_0 = 0.2 - 0.4 \text{ mM}$, $[\text{Mn(II)}] = 6 \text{ } \mu\text{M}$, $\text{pH} = 4.5$, $T = 25^\circ\text{C}$.

In our kinetic model we assumed that the reaction rate of Mn(II)-catalyzed S(IV) autoxidation is proportional to the concentration of a transient manganese-sulfito complex formed in the initial step of a radical chain mechanism. The concentration of complex is a function of time and determined by the stability constant K . The equilibrium concentration of manganese-sulfito complex at time t ($[\text{MnHSO}_3^{(a-1)+}(t)]$) was obtained by solving quadratic Equation 1. The kinetics was determined using integral data analysis, which proved to be the most suitable for our experimental procedure. The unknown values for the stability constant, reaction order and rate constant were determined using the non-linear regression programme (Duggleby, 1984). The proposed power law kinetic model (Eq. 2) predicts very well the kinetics for the Mn(II)-catalyzed S(IV) autoxidation in the studied range ($[\text{Mn(II)}] = 2 - 8 \text{ } \mu\text{M}$, $[\text{HSO}_3^-] = 0.1 - 0.4 \text{ mM}$, $T = 15 - 35^\circ\text{C}$, $\text{pH} = 3.0 - 5.0$), especially in the pH range from 3.5 to 4.5 (Figs. 2, 3).

$$K_{\text{MnHSO}_3^{(a-1)+}} = \frac{[\text{MnHSO}_3^{(a-1)+}(t)]}{[\text{Mn}^{a+}_{t=0} - \text{MnHSO}_3^{(a-1)+}(t)] \cdot [\text{HSO}_3^-(t) - \text{MnHSO}_3^{(a-1)+}(t)]} \quad (1)$$

$$-r_{\text{S(IV)}} = k_{\text{S(IV)}} \cdot [\text{MnHSO}_3^{(a-1)+}]^2 \cdot \frac{1}{[\text{H}^+]^{0.4}}, \quad (2)$$

with the following predicted values for the rate constant $k_{\text{S(IV)}}$, activation energy E_a , stability constant K for manganese-sulfito complex and Gibbs free energy:

$$k_{\text{S(IV)}} = 2.05 \cdot 10^{11} \cdot e^{-\frac{E_a}{RT}}, \quad E_a = 56 \text{ kJ mol}^{-1};$$

$$K_{MnHSO_3^{(a-1)+}} = 4.37 \cdot 10^{16} \cdot e^{-\frac{\Delta G}{RT}}, \Delta G = 67 \text{ kJ mol}^{-1}.$$

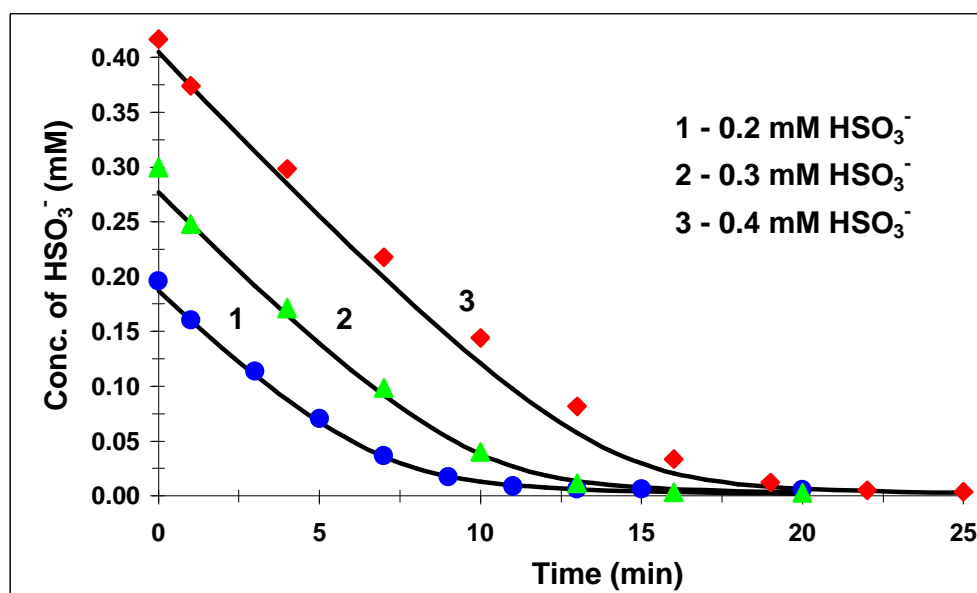


Figure 2: $[HSO_3^-]$ as a function of time for the Mn(II)-catalyzed S(IV) autoxidation at different initial concentrations of $[HSO_3^-]$. Symbols: experimentally measured concentrations. Solid lines: predicted concentration profiles. Experimental conditions: $[HSO_3^-]_0 = 0.2 - 0.4 \text{ mM}$, $[Mn(II)] = 6 \mu\text{M}$, $\text{pH} = 4.5$, $T = 25^\circ\text{C}$.

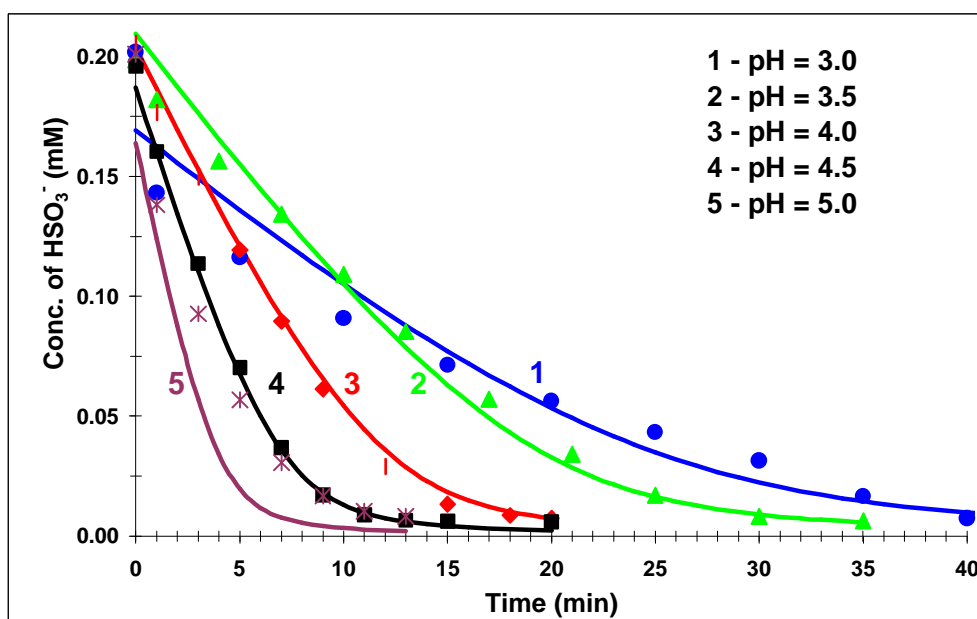


Figure 3: Effect of pH on the Mn(II)-catalyzed HSO_3^- autoxidation. Symbols: experimentally measured concentrations. Solid lines: predicted concentration profiles. Experimental conditions: $\text{pH} = 3.0 - 5.0$, $[Mn(II)] = 6 \mu\text{M}$, $[HSO_3^-]_0 = 0.2 \text{ mM}$, $T = 25^\circ\text{C}$.

Conclusions

- The reaction of S(IV) autoxidation catalyzed by Mn(II) is autocatalytic.
- The dependence of the reaction rate against the $[HSO_3^-]$ is linear up to $0.1 \text{ mM } HSO_3^-$, and the rate is independent of $[HSO_3^-]$ at higher concentrations.

- First experimental points were not used for kinetic evaluation, because the reaction rate in the first minute is unusually high, most probably due to the mixing equilibration.
- The results evaluated by standard integral approach show first-order dependance on both $[\text{HSO}_3^-]$ and $[\text{Mn(II)}]$.
- A simple power law kinetic model based on the Mn-sulfito complex formed in the first step of a radical chain mechanism can be used for predicting the reaction kinetics.
- The proposed power law rate equation predicts adequately the kinetics for Mn(II)-catalyzed HSO_3^- autoxidation in the studied range, especially in the pH range 3.5 – 4.5.

Acknowledgment

The financial support of the Ministry of Education, Science and Sport of Republic Slovenia (contract no. P1-0511-0104) is gratefully acknowledged.

References

- Brandt, Ch., and R. van Eldik, 1995: Transition metal-catalyzed oxidation of sulfur(IV)-oxides. Atmospheric-relevant processes and mechanisms, *Chem. Rev.* **95**, 119-190.
- Duggleby, R.G., 1984: Regression Analysis of Nonlinear Arrhenius Plots: An Empirical Model and Computer Program, *Comput. Biol.Med.* **14**, No.4, 447-455.
- Grgic I. and G. Bercic, 2001: A Simple Kinetic Model for Autoxidation of S(IV) Oxides Catalyzed by Iron and/or Manganese, *J. Atmos. Chem.* **39**, 155-170.
- Herrmann, H., B. Ervens, H.-W. Jacobi, R. Wolke, P. Nowacki, and R. Zellner, R., 2000: CAPRAM2.3: A chemical aqueous phase radical mechanism for tropospheric chemistry, *J. Atmos. Chem.* **36**, 231-284.
- Warneck, P., P. Mirabel, G.A. Salmon, R. van Eldik, C. Vinckier, K.J. Wannowius, and C. Zetzsch, 1996: in *Transport and chemical transformation of pollutants in the troposphere*, **Vol. 2, Heterogeneous and Liquid Phase Processes**, ed. P. Warneck, Springer-Verlag, Berlin. pp. 7-74.
- Warneck, P., 1999: The relative importance of various pathways for the oxidation of sulfur dioxide and nitrogen dioxide in sunlit continental fair weather clouds, *Phys. Chem. Chem. Phys.* **1**, 5471-5483.

Laser-based Studies of OH with Oxygenated Organics in Aqueous Solution (APP4)

Saso Gligorovski and Hartmut Herrmann
*Institut für Troposphärenforschung,
 Permoserstr. 15, 04318 Leipzig, Germany*

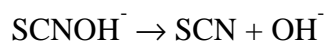
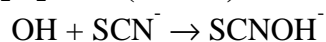
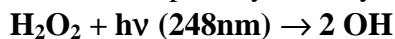
Motivation

Free radicals such as OH, NO₃, Cl/Cl₂⁻, Br/Br₂⁻, play an important role in the chemistry of the aqueous tropospheric particle phase (Zellner and Herrmann, 1995). The OH radical is the most important oxidant in both the tropospheric gas and aqueous phase i.e. in clouds droplets, fog, rain and the aqueous aerosols. Organic solvents are used in a large number of industrial processes (i.e. cleaning and degreasing processes, polymer disposal agents and adhesives). Due to their volatility, in many of these processes they are emitted either directly or indirectly into the atmosphere. A number of organic compounds employed as solvents at the present time has been shown to have adverse health effects (i.e., carcinogenic, mutagenic and reprotoxic properties).

In this study the rate constants of the OH radical reactions with such organic compounds have been investigated in aqueous solution, under different conditions as a contribution to the MOST project.

Experimental Methods

A laser-photolysis long path laser absorption (LP-LPLA) set-up (Fig.1) was used for kinetic studies of OH radical reactions. Due to the small extinction coefficient of OH and the overlapping of the stronger absorption of organic peroxy radicals formed in correspondence to the OH decay, kinetic measurements were carried out by competition kinetics using thiocyanate as reference substance. The OH radicals were formed by excimer laser photolysis of hydrogen peroxide at $\lambda=248$ nm, i. e.:



The kinetic investigations were performed following the absorption of the (SCN)₂⁻ radical anion at $\lambda = 473$ nm (10 mW) by means of a cw - diode laser detection system. The amplified electrical signal from the photodiode was fed to a digital oscilloscope connected to a PC controlling the experiment. The measurements were performed in a temperature range between 283 and 328 K. In this study the temperature dependence of the reference reaction as described by Chin and Wine (1992) was used as the reference data set.

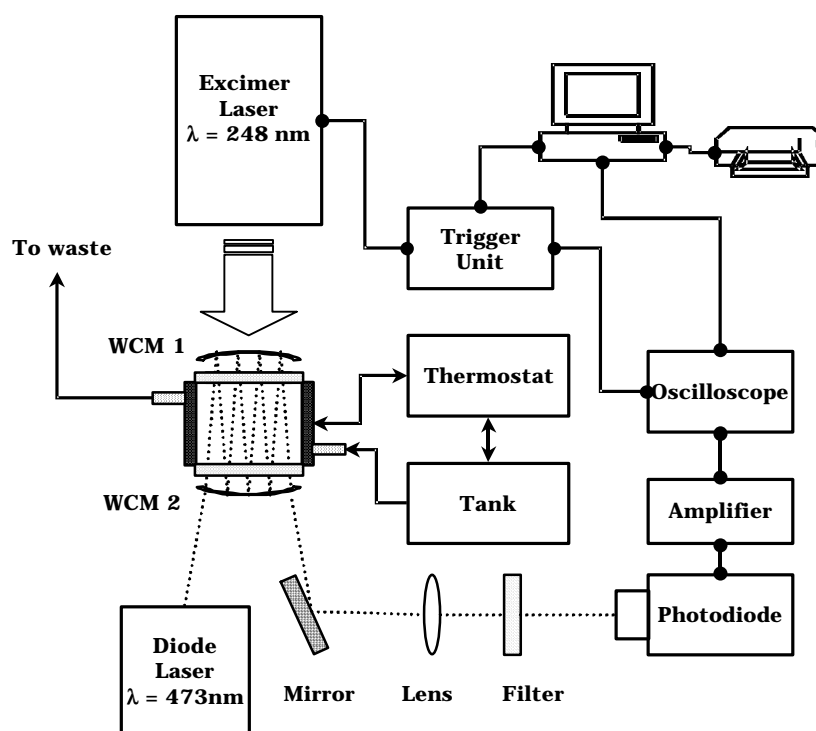


Figure 1: Laser-photolysis long path laser absorption (LP-LPLA) set up for kinetic investigation

Results and Discussion

Reaction of OH with Acetone, Methyl Ethyl Ketone, Acetonylacetone, Isobutyraldehyde, Ethyl Formate

Due to the low boiling point of acetone the rate constants for the reaction with the OH radical were investigated in a temperature range between 283 K and 318 K. Measured rate coefficients and Arrhenius parameters are reported in Table 1 and Table 2, respectively.

In the literature the very small rate coefficient for the reaction of acetone with OH was explained with an essential influence of the enol form on the reactivity of acetone. The authors suggested that the tautomeric form is affecting the inductive effects of the methyl group leading to a less reactivity toward the OH attack (Adams et al., 1967). This explanation is not consistent for two main reasons: (i) it is known that unsaturated alcohols are reacting faster with hydroxyl radicals (Simic et al., 1973) and (ii) in view of an H-abstraction mechanism the low reaction coefficient could be ascribed to the very high bond dissociation energy (BDE) (Figure 2) for the weakest extractable hydrogen atom in the acetone molecule. This last observation is also confirmed with the rate constants observed for 2-butanone and Acetonylacetone which have shown to proceed faster than acetone. Both compounds present a secondary hydrogen atom which has a low value of BDE and consequently it is easier to be abstract (Table 1 and Figure 2).

Compound	Formula	$k_{298\text{K}} (\text{M}^{-1}\text{s}^{-1})$
Acetone	CH_3COCH_3	$(2.1 \pm 0.6) \cdot 10^8$
2-Butanone	$\text{CH}_3\text{COCH}_2\text{CH}_3$	$(1.5 \pm 0.7) \cdot 10^9$
Acetonylacetone	$\text{CH}_3\text{COCH}_2\text{CH}_2\text{COCH}_3$	$(7.6 \pm 1.1) \cdot 10^8$
Isobutyraldehyde	$(\text{CH}_3)_2\text{CHCHO}$	$(2.9 \pm 1.0) \cdot 10^9$
Ethyl Formate	HCOOC_2H_5	$(3.2 \pm 0.8) \cdot 10^8$

Table 1: Observed rate constants for the reaction of OH with organic compounds

The reactivity of OH radical with 2-Butanone has been investigated in the temperature range from 278 to 328 K. The results are reported in Table 1 and Table 2. Diffusion rate constants k_D were

calculated and the results showed that k_{obs} is not controlled by diffusion processes, but in fact is reactivity-controlled ($k_{\text{obs}} = k_{\text{react}}$).

$$\frac{1}{k_{\text{obs}}} = \frac{1}{k_{\text{D}}} + \frac{1}{k_{\text{react}}} \quad (\text{Eq-1})$$

Diffusion-controlled reactions are those for which ($k_{\text{obs}} = k_{\text{D}}$) corresponding to Table 3. Isobutyraldehyde is very reactive as might be expected from the chemistry of the aldehydes. The tertiary hydrogen atom in α position to the carbonyl group is very weakly bonded (BDE = 313.3 kJ mol⁻¹) in the molecule because the resulting alkyl radical is stabilized by inductive and resonance effects.

For a given ester group, the rate constants increase with increasing chain length of the acid, i.e. butyrate > propionate > acetate. Ethyl Formate is more reactive than might be expected from the general trend, but this may be explained by the presence of an α hydrogen atom with its resultant effect on the reducing properties of the molecule (Adams et al., 1967). This behaviour is shown in Figure 2.

Compound	A l/mol s	E _a kJ/mol	ΔG^\ddagger kJ/mol	ΔH^\ddagger kJ/mol	ΔS^\ddagger J/K mol
Acetone	(2.8±0.5) 10 ¹¹	(18±11)	(26±20)	(16±10)	-(34±6)
2-Butanone	(1.2±0.2) 10 ¹³	(23±10)	(21±12)	(20±9)	-(3±0.4)
Acetonylacetone	(5.1±0.1) 10 ¹¹	(16±8)	(22±13)	(14±7)	-(29±3)
Isobutyraldehyde	(3.0±0.1) 10 ¹⁰	(6±3)	(19±10)	(3.3±1.7)	-(53±3)
Ethyl Formate	(1.8±0.1) 10 ¹⁰	(10±4)	(24±11)	(7±3)	-(57±4)

Table 2: Arrhenius and activation parameters for the reaction of OH with organic compounds.

T (K)	278	283	288	298	308	318	328
$\eta_{\text{H}_2\text{O}}$ (kg/m s)	0.15 10 ⁻²	0.13 10 ⁻²	0.15 10 ⁻²	0.89 10 ⁻³	0.71 10 ⁻³	0.57 10 ⁻³	0.46 10 ⁻³
k_{D} (mol/l s)	4.8 10 ⁹	5.7 10 ⁹	5.1 10 ⁹	8.7 10 ⁹	1.7 10 ¹⁰	1.5 10 ¹⁰	1.8 10 ¹⁰
k_{obs} (mol/l s)	6.5 10 ⁸	7.2 10 ⁸	1.4 10 ⁹	1.5 10 ⁹	1.5 10 ⁹	2.0 10 ⁹	3.5 10 ⁹
$k_{\text{obs}}/k_{\text{D}}$ (%)	13.6	12.6	27.4	17.2	8.8	13.3	19.4

Table 3: Viscosity of water and diffusion limiting and observed rate constants for the reaction of OH with 2-Butanone in aqueous solution.

According to the principle of Evans and Polanyi there is a correlation between the activation energy and the enthalpy for reactions that follow the same chemical mechanism (Evans and Polanyi, 1938): $E_a = A + B \Delta H_r$. The reaction enthalpy ΔH_r represents the difference between the standard formation energies of the products and the reactants. To test whether the reaction of OH with organic compounds do follow the same reaction mechanism (H-atom-abstraction), the activation energies for the reaction of OH with different organic compounds were measured and plotted against the bond dissociation energies (Fig.2).

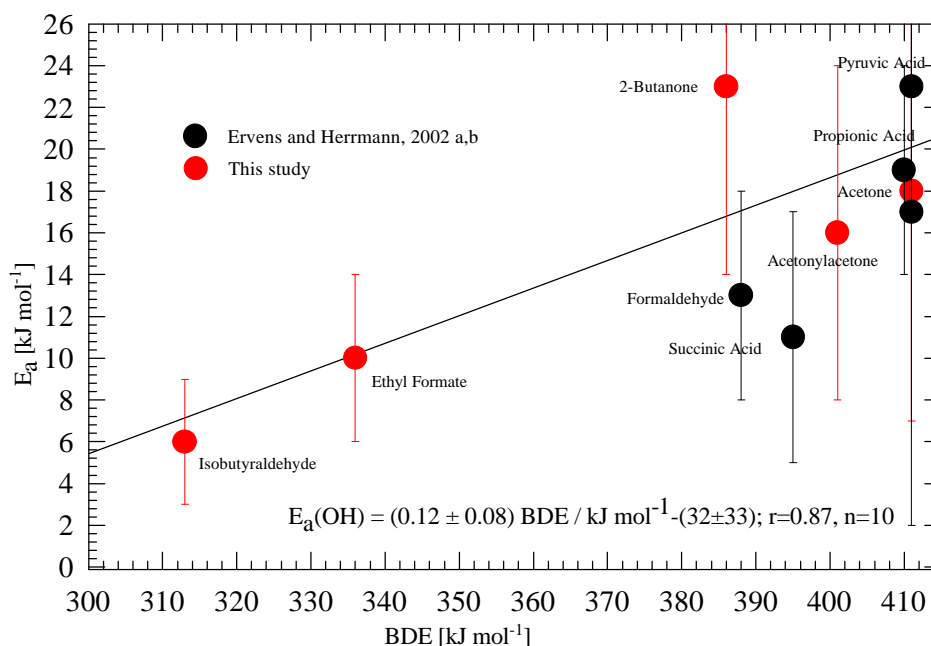


Figure 2: Bell-Evans-Polanyi plot for H-atom abstraction reactions of OH in aqueous solution

Summary and Conclusion

The kinetic investigations described here contribute to fill existing gaps with regard to OH radical reaction kinetics in aqueous solution. In contrast to most existing studies the reaction rates were investigated as a function of temperature. Considering available temperature dependent values both from literature studies and from the present study, it was shown that correlation exist between the activation energy and the bond dissociation energy. The kinetic data obtained from this study will be applied as input parameters for a tropospheric multiphase model (CAPRAM 2.4 (MODAC mechanism) clarifying the influence of cloud chemistry in the tropospheric multiphase system.

Acknowledgements

This research is supported by the EC within the project 'Multiphase chemistry of Oxygenated Species in the Troposphere' (MOST, coord. By C. George) under contract EVK2-CT-2001-00114.

References

- Adams, G.E., Boag, J.W., Currant, J. and Michael, B.D., 1965a, Absolute rate constants for the reaction of the hydroxyl radical with organic compounds, Pulse Radiolysis, Ebert, M., Keene, J.P., Swallow, A.J., Baxendale, J.H. (Ed.), Academic Press, New York, 131-143.
- Benson, S.W., 1976, Thermochemical Kinetics, 2nd ed., Wiley, New York.
- Buxton, G.V., Greenstock, C. L., Helman, W. P and Ross, A. B., 1988a, Critical Review of rate constants for reactions of hydrated electrons, hydrogen atoms and hydroxyl radicals, (OH, O₂⁻) in aqueous solution, J. Phys. Chem. Ref. Data 17, 513-886
- Chin, M. and Wine, P.H., 1992, A temperature - dependent kinetics study of the aqueous phase reactions OH + SCN⁻ → SCNOH⁻ and SCN + SCN⁻ → (SCN)₂⁻ J. Photochem. Photobiol. A 69, 17-25.
- Chin, M. and Wine, P.H., 1994, A temperature – dependent competitive kinetics study of the aqueous phase reactions of OH radicals with formate, formic acid, acetate, acetic acid and hydrated formaldehyde, in G.R. Helz, R.G. Zepp and D.G. Crosby (Eds.), Aquatic and Surface Photochemistry,, Lewis Publishers, Boca Raton, 85-96.
- Connors, K.A., 1990, Chemical Kinetics, Wiley, New York.

- Dogliotti, L. and Hayon, N., 1967, Flash photolysis study of sulfite, thiocyanate, and thiosulfate ions in solution, *J.Phys. Chem.*, 71, 2511.
- Elliot, A.J. and Simons, A.S., 1984, *Radiat. Phys. Chem.*, Rate Constants for reactions of hydroxyl radicals as a function of temperature, *Radiat. Phys. Chem.* 24, 229-231.
- Ervens, B., and Herrmann, H., 2002 a, A T-dependent study of OH reactions in aqueous solution. Part 1: Reference system and kinetic investigation of reactions with alcohols and carbonyl compounds, *Phys.Chem.Chem.Phys* accepted.
- Ervens, B., and Herrmann, H., 2002 b, A T-dependent study of OH reactions in aqueous solution. Part 2: Kinetic investigation of carboxylates and OH reactivity correlations, *Phys.Chem.Chem.Phys* accepted.
- Herrmann, H., 1997, Photochemische Bildung, Spektroskopie und Kinetik freier Radikale in wässriger Lösung, Habilitationsschrift, Universität Essen.
- Lide, D.R., 1995, Handbook of Chemistry and Physics, CRC Press, New York.
- Zellner, R. and Herrmann, H., 1994, Free Radical Chemistry of the Aqueous Atmospheric Phase, in Clark, R.J.H. and Hester, R.E. (Eds.), *Advances in Spectroscopy*, 24, Spectroscopy in Environmental Science, 381-451, Wiley, London.

Concentration Profiles Using a Lognormal Distribution Regarding Aerosols with CAPRAM 2.4 (MODAC Mechanism) (APP4)

Zoltan Majdik and Hartmut Herrmann

Institut für Troposphärenforschung, Permoserstr. 15, D-04318 Leipzig

Introduction

Box model studies were performed considering a size-segregated system in order to investigate the influence of size and liquid water distribution on the mass transport processes and on the multiphase chemistry in cloud droplets for three different scenarios. The detailed and extended chemical mechanism describing tropospheric aqueous phase chemistry (147 species and 438 reactions) CAPRAM 2.4 (MODAC mechanism) (Chemical Aqueous Phase Radical Mechanism, Model Development for Tropospheric Aerosol and Cloud Chemistry Herrmann *et al.*, 2000, Ervens *et al.*, 2002, <http://www.tropos.de/CHEMIE/multimod/CAPRAM/CAPRAM24.pdf>) was used coupled to the gas phase mechanism RACM (Regional Atmospheric Chemistry Mechanism) (Stockwell *et al.*, 1997). Uptake processes of soluble species are included in the mechanism following the approach by Schwartz (1986) considering gas phase diffusion, mass accommodation coefficients, Henry solubility and chemical reaction within the aqueous phase

Model description:

The calculations were performed considering a different number of size bins n with $n=1,2,3,4,5,10,20,30,50$ for the particle size range $1\text{ }\mu\text{m} < r_{\text{droplet}} < 64\text{ }\mu\text{m}$ assuming an idealized lognormal distribution. In the present study three different CAPRAM standard scenarios : urban, remote and marine are considered which differ only in the initial concentrations and in the emission/deposition fluxes. For the runs time constant microphysical values were considered. For temperature (T), pressure (p) and the total liquid water content (LWC) the following values were assumed: $T=288\text{ K}$, $p=1\text{ atm}$ and $\text{LWC}=3\cdot 10^{-7}\text{ vol}_{\text{aq}}\text{ vol}_{\text{g}}^{-1}$. The distribution of the number concentration as a function of radius is plotted in Figure 1.

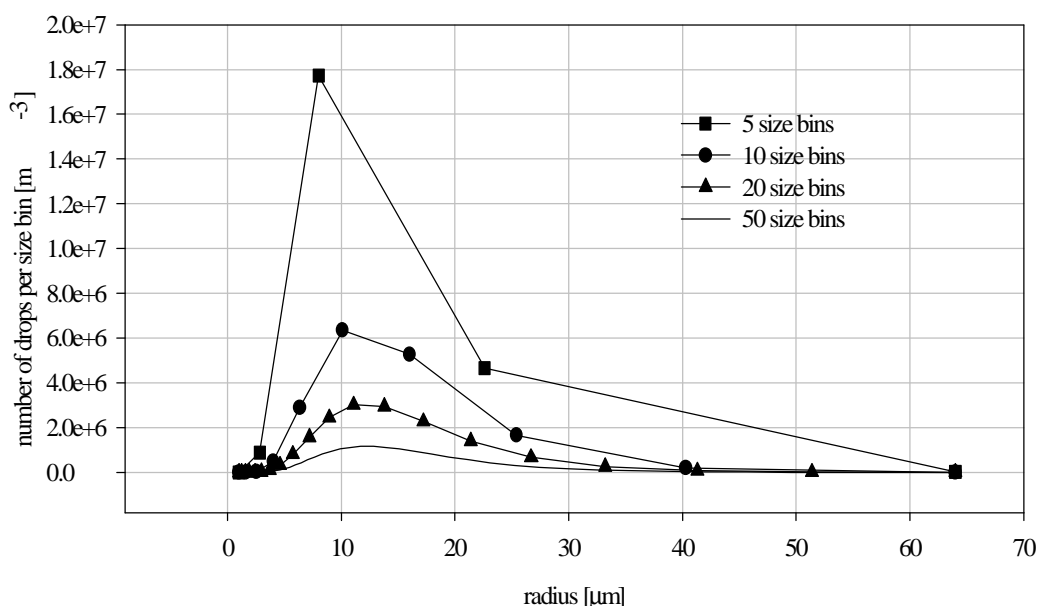


Figure 1: Number of drops per size bin in function of radius for different size resolutions.

Results

The iron redox system

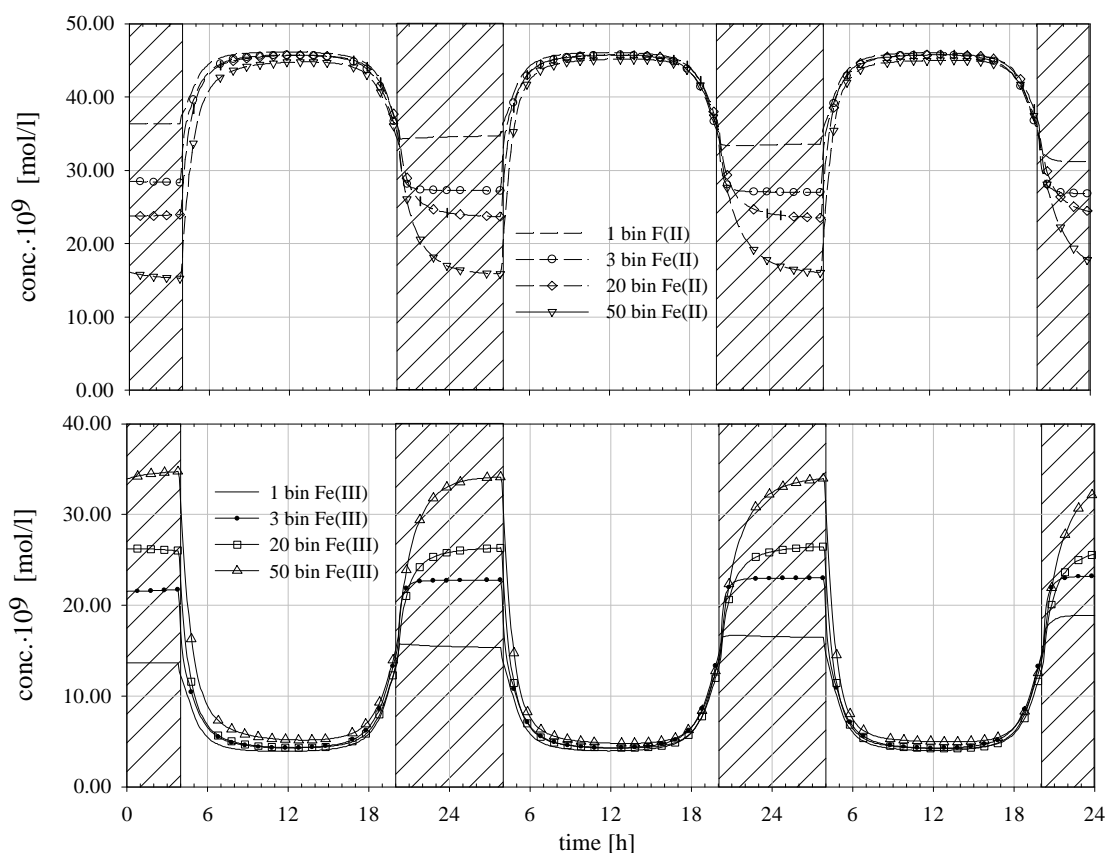


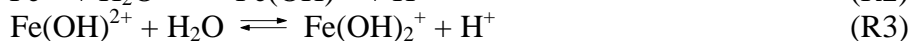
Figure 2: Size effect during the night in the iron redox system (marine scenario)

Table 1: From Figure 2 the following Fe(II) / Fe(III) ratios are obtained:

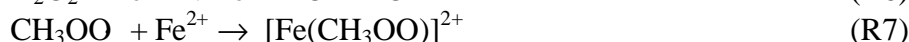
Time / h	Fe(II) / Fe(III) Ratio			
	Number of size bins			
	1	3	20	50
12	11.8	10.6	10.6	8.7
24	2.2	1.2	0.9	0.5

An interesting size effect can be observed in the case of Fe(III)-Fe(II) especially in the remote and marine cases (Figure 2). Considering different size resolutions the concentrations during the day reach approximately similar values, with the concentration of Fe(II) being higher than the one of Fe(III) at about $4 \cdot 10^{-8} \text{ mol l}^{-1}$, whereas during the night the concentration of Fe(III) is higher with approximately $2 \cdot 10^{-8} \text{ mol l}^{-1}$ than Fe(II) (considering 50 size bins), but considering only one size bins the concentration of Fe(II) is higher with about $2 \cdot 10^{-8} \text{ mol l}^{-1}$ than the concentration of Fe(III). From Table 1 it can be seen that considering more size bins the Fe(II) / Fe(III) ratio will decrease at noon from a value of 11.8 to 8.7, corresponding to a monodisperse and a size resolved system with 50 size bins, respectively. The same trend is also observed at midnight where the variation of the ratio is even greater from 2.2 to 0.51.

During the day the following reaction cycle reduces Fe(III) to Fe(II) leading to concentrations of about $4.5 \cdot 10^{-8} \text{ mol l}^{-1}$ and $0.5 \cdot 10^{-8} \text{ mol l}^{-1}$ for Fe(II) and Fe(III) respectively in all the size bins considered.



During the night the concentration of O_2^- is small. Hence, the oxidation of Fe(II) by H_2O_2 (R6) and by the methyl peroxy radical (R7) become the most important sink processes for Fe(II).



While the Fe^{2+} sink processes R6 and R7 are not influenced by size segregation, the reaction cycle R1-R5 is strongly size dependent. The smaller Fe(II) concentration during the night considering a size segregated system can be ascribed to a bigger contribution of R6 and R7 in the big droplets where the concentration of O_2^- is much smaller than in the small droplets. Considering a 1 μm radius droplet an O_2^- maximum concentration of about $3.4 \cdot 10^{-9} \text{ mol l}^{-1}$ will occur, while in a 64 μm radius droplet the maximum O_2^- concentration will be about $4 \cdot 10^{-10} \text{ mol l}^{-1}$. At midnight O_2^- concentrations of about $7.4 \cdot 10^{-11} \text{ mol l}^{-1}$ and $4.4 \cdot 10^{-12} \text{ mol l}^{-1}$ occur in a 1 μm and in a 64 μm radius droplet, respectively. The difference in the O_2^- concentration is occurring due to differences in the mass transport processes caused by the different surface areas. In the small droplets with big surface area the uptake of HO_2 at midnight represents about 46 % out of the total source of HO_2 in the aqueous phase, while in the big droplets just 1%.

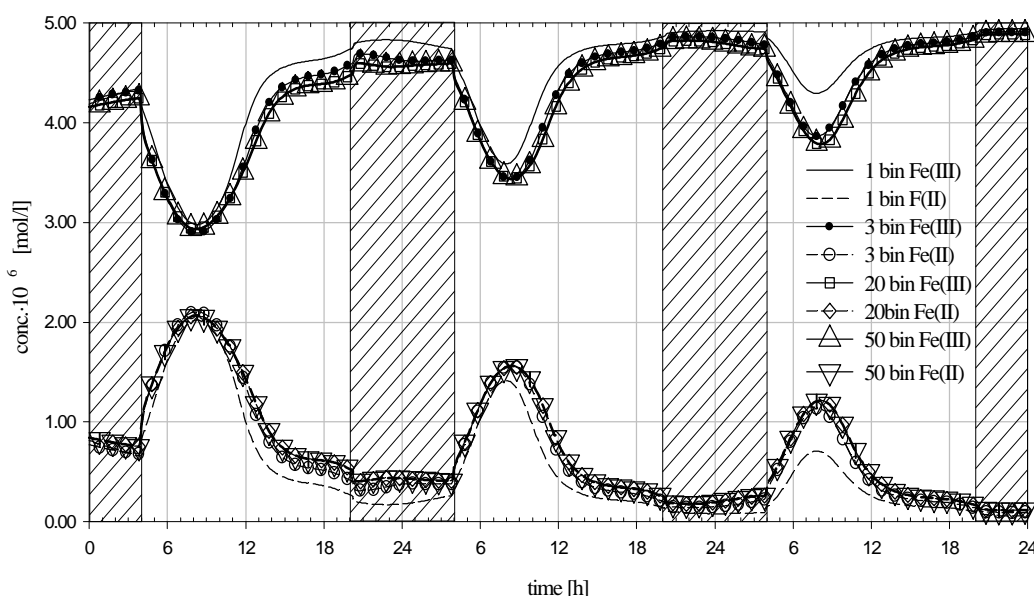


Figure 3: Diurnal concentration profile of Fe(II)-Fe(III) considering the urban scenario

In the case of urban clouds the size segregation has no great effect on the diurnal concentration profile (Figure 3). Fe(II) is peaking around eight o'clock in the morning reaching a concentration of about $2 \cdot 10^{-6} \text{ mol l}^{-1}$, when also Fe(III) has a minimum with a concentration of about $3 \cdot 10^{-6} \text{ mol l}^{-1}$. The most important sources for Fe^{2+} are the reactions of Fe^{3+} and FeOH^{2+} with Cu^+ . These source processes have a maximum around 8 a.m. reaching values about $1.5 \cdot 10^{-7} \text{ mol l}^{-1} \text{ s}^{-1}$ and $1.25 \cdot 10^{-7} \text{ mol l}^{-1} \text{ s}^{-1}$ respectively. The most important sink for Fe^{2+} is the reaction with HO_2 reaching a maximum of $2.5 \cdot 10^{-7} \text{ mol l}^{-1} \text{ s}^{-1}$ around 8 a.m. Investigating the sinks and sources of Cu^+ it becomes evident that the most important source is the reduction of Cu^{2+} by HO_2 . This process reaches a maximum through put of about $1.5 \cdot 10^{-5} \text{ mol l}^{-1} \text{ s}^{-1}$ around 12 a.m. As a conclusion at the beginning of the day the concentration of HO_2 is increasing, reducing Cu^{2+} to Cu^+ and the produced Cu^+ will

reduce Fe(III) to Fe²⁺. The increasing concentration of HO₂ also increases the rate of the reaction between HO₂ and Fe²⁺ yielding a maximum concentration for Fe²⁺ around eight o'clock in the morning.

Radical chemistry in the gas phase

In a size segregated system, considering marine conditions the concentration of OH radical (Figure 4) reach a maximum of about $1.25 \cdot 10^6 \text{ cm}^{-3}$, a value considerably smaller then the maximum considering a monodisperse system ($2.75 \cdot 10^6 \text{ cm}^{-3}$). The smaller concentration in the size-segregated system can be ascribed to the small droplets, where at noon the uptake into the small droplets represents about 39% out of the total sink of OH in the gas phase (OH_(g)). In the monodisperse case ($r = 10 \mu\text{m}$) the uptake represents about 7% from the total sink flux of OH_(g) at noon. Considering monodispersed droplets ($r = 64 \mu\text{m}$) the uptake into the particle phase is just about 0.23% from the total sink of OH_(g). In these conditions OH_(g) reaches a maximum concentration of about $4 \cdot 10^6 \text{ cm}^{-3}$.

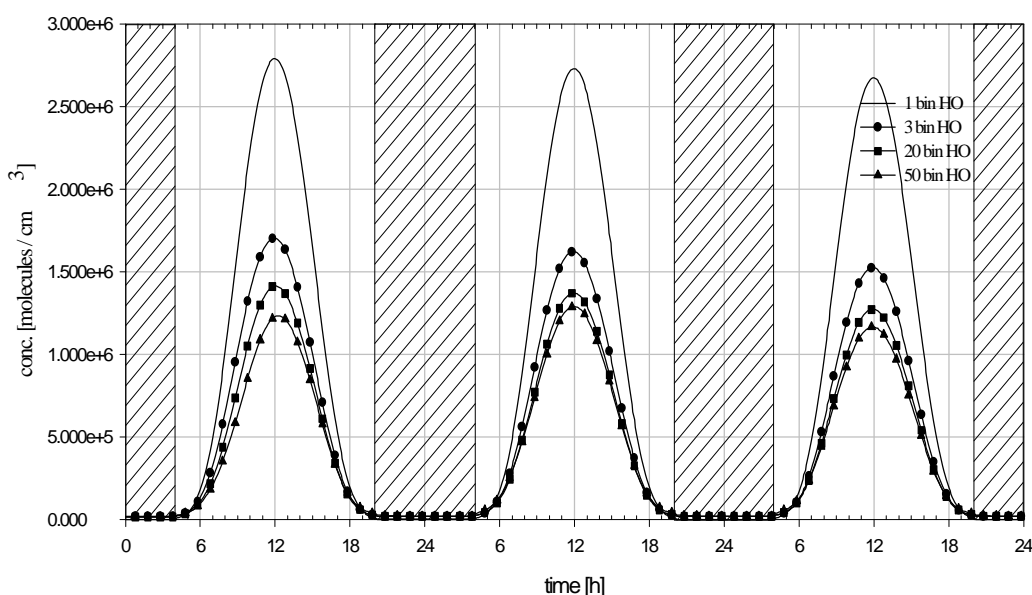


Figure 4: OH concentration profile over the simulation time (marine scenario)

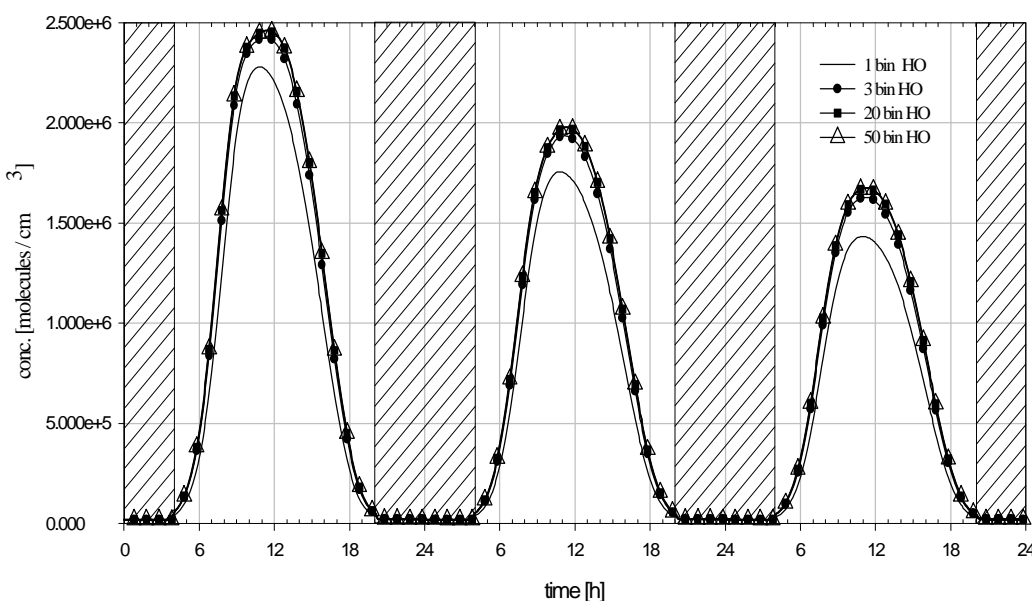


Figure 5: OH concentration profile over the simulation time (urban scenario)

In the case of the urban scenario the size effect is much smaller like shown in Figure 5. Considering multiple size bins the concentration of OH is higher compared to the monodisperse system with about $0.25 \cdot 10^6 \text{ cm}^{-3}$. The small difference in the concentrations compared to the marine case can be explained with the smaller contribution of the phase transfer processes in the urban scenario respect to the marine case. Considering a monodisperse distribution ($r = 10 \mu\text{m}$) and the urban scenario uptake represents 0.45% from the total sink of OH(g) at noon.

Overview on size effect on key species

Table 1 contains results obtained for three scenarios, considering a monodisperse distribution ($r = 10 \mu\text{m}$) and a size dependent distribution with 50 different size bins ($r = 1 \mu\text{m} - 64 \mu\text{m}$). The numbers in Table 1 represent maximum concentrations and are expressed in cm^{-3} for gas phase species and mol l^{-1} for aqueous phase species. For most species, the biggest differences between the two distributions are in the case of the marine scenario, due to the stronger contribution of phase transfer processes. In marine conditions a difference in the $\text{NO}_3(\text{g})$ concentration $[\text{NO}_3(\text{g})]$ of about two orders of magnitude occurs. In the case of the urban scenario the change in concentration is much smaller, $[\text{NO}_3(\text{g})] = 4 \cdot 10^7 \text{ cm}^{-3}$ in the monodisperse case and $[\text{NO}_3(\text{g})] = 6 \cdot 10^7 \text{ cm}^{-3}$ in the size segregated case. In the marine case direct uptake into the small droplets of NO_3 represents about 72% from the total sink of $\text{NO}_3(\text{g})$ while in the urban case direct uptake of $\text{NO}_3(\text{g})$ will not exceed 4% from the total sink of $\text{NO}_3(\text{g})$. In the case of $\text{NO}_2(\text{g})$ the same concentration levels are obtained both in the monodisperse and size dependent system. In this case phase transfer will have a much smaller contribution, between 0.035% and 0.05% from the total source of $\text{NO}_2(\text{g})$ depending on droplet size. During the night considering the marine scenario, phase transfer from the small droplets ($r = 1 \mu\text{m}$) to the gas phase will be almost the exclusive source of HONO(g). Under the same conditions, uptake into the bigger droplets will be the almost exclusive sink for HONO(g). In urban conditions phase transfer of HONO will be a source for HONO(g) in all the droplets considered, being more then 99% from the total source.

Summary and conclusions

The detailed and extended chemical mechanism CAPRAM 2.4 (MODAC mechanism) was applied to a size resolved system considering different number of size bins. In the present work up to 50 different size bins were considered with a radius between $1 \mu\text{m}$ and $64 \mu\text{m}$. The results showed that size segregation has a great effect on phase transfer processes and subsequently on diurnal concentration profiles. The biggest changes are encountered in the case of the marine scenario due to the bigger contribution of phase transfer processes.

Acknowledgement

This research is supported by the BMBF within the AFO 2000 atmospheric research program within the project MODMEP (07 ATF 40)

References

- Herrmann, H., B. Ervens, H.-W. Jacobi, R. Wolke and R. Zellner, 2000: CAPRAM2.3: A chemical aqueous phase radical mechanism for tropospheric chemistry. *J. Atmos. Chem.* 38, 231-284
- Ervens B., C. George, J. E. Williams, G. V. Buxton, , G. A. Salmon, M. Bydder, F. Wilkinson, F. Dentener, P. Mirabel, R. Wolke and H. Herrmann, 2002: CAPRAM 2.4 (MODAC mechanism): an extended and condensed tropospheric aqueous phase mechanism and its applications. *J. Geophys. Res.*, in press.
- Schwartz S., 1986: mass transport considerations pertinent to aqueous phase reactions of gases in liquid water clouds, in *Chemistry of Multiphase Atmospheric Systems*, W. Jaeschke (Ed.) NATO ASI Series, Springer (Berlin).
- Stockwell W. R., F. Kirchner, M. Kuhn and S. Seinfeld, 1997: a new mechanism for regional atmospheric chemistry modeling. *J. Geophys. Res.* 102 (D22), 25847-25879.

Table 2: Resulted maximum concentrations considering a monodisperse and a size segregated system with 50 size bins. All the gas and aqueous phase concentrations are expressed in cm^{-3} , and mol l^{-1} , respectively.

gas phase	Urban		remote		marine	
	1 size bins	50 size bins	1 size bins	50 size bins	1 size bins	50 size bins
O ₃	$3.5 \cdot 10^{12}$	$3.75 \cdot 10^{12}$	$5.8 \cdot 10^{11}$	$7 \cdot 10^{11}$	$6.4 \cdot 10^{11}$	$5.75 \cdot 10^{11}$
NO ₂	$6 \cdot 10^{10}$	$5.2 \cdot 10^{10}$	$8 \cdot 10^9$	$6 \cdot 10^9$	$1 \cdot 10^9$	$1 \cdot 10^9$
NO	$1.35 \cdot 10^{10}$	$1 \cdot 10^{10}$	$6 \cdot 10^{10}$	$4 \cdot 10^{10}$	$7 \cdot 10^8$	$8.4 \cdot 10^8$
NO ₃	$4 \cdot 10^7$	$6 \cdot 10^7$	$4.5 \cdot 10^6$	$7.5 \cdot 10^6$	$1.3 \cdot 10^6$	$1 \cdot 10^4$
OH	$1.75 \cdot 10^6$	$2 \cdot 10^6$	$3.25 \cdot 10^6$	$5 \cdot 10^6$	$2.75 \cdot 10^6$	$1.25 \cdot 10^6$
HONO	$1.8 \cdot 10^9$	$2.65 \cdot 10^9$	$4.7 \cdot 10^8$	$6 \cdot 10^8$	$7 \cdot 10^7$	$1 \cdot 10^4$
N ₂ O ₅	$5 \cdot 10^7$	$2 \cdot 10^8$	$1.75 \cdot 10^6$	$4.5 \cdot 10^6$	$7.5 \cdot 10^5$	$5 \cdot 10^0$
HO ₂ NO ₂	$2.25 \cdot 10^9$	$2.5 \cdot 10^9$	$1 \cdot 10^7$	$3 \cdot 10^7$	$1 \cdot 10^6$	$1 \cdot 10^1$
aqueous phase						
OH	$1 \cdot 10^{-13}$	$6 \cdot 10^{-14}$	$2 \cdot 10^{-13}$	$1.5 \cdot 10^{-13}$	$5 \cdot 10^{-13}$	$1.3 \cdot 10^{-12}$
NO ₂	$7 \cdot 10^{-11}$	$6 \cdot 10^{-11}$	$8 \cdot 10^{-12}$	$7 \cdot 10^{-12}$	$1 \cdot 10^{-12}$	$1 \cdot 10^{-12}$
Fe(II)	$1.5 \cdot 10^{-6}$	$1.5 \cdot 10^{-6}$	$4.5 \cdot 10^{-7}$	$4.5 \cdot 10^{-7}$	$4.5 \cdot 10^{-8}$	$4.5 \cdot 10^{-8}$
Fe(III)	$5 \cdot 10^{-6}$	$5 \cdot 10^{-6}$	$2 \cdot 10^{-7}$	$2.5 \cdot 10^{-7}$	$1.5 \cdot 10^{-8}$	$3.5 \cdot 10^{-8}$
Cu ²⁺	$2.5 \cdot 10^{-7}$	$2.5 \cdot 10^{-7}$	$5 \cdot 10^{-8}$	$5 \cdot 10^{-8}$	$1 \cdot 10^{-9}$	$1 \cdot 10^{-9}$
Cu ⁺	$2 \cdot 10^{-9}$	$1.6 \cdot 10^{-9}$	$1 \cdot 10^{-9}$	$1 \cdot 10^{-9}$	$1 \cdot 10^{-10}$	$1 \cdot 10^{-11}$
HO ₂	$6.2 \cdot 10^{-11}$	$4 \cdot 10^{-11}$	$2 \cdot 10^{-10}$	$2 \cdot 10^{-10}$	$2.9 \cdot 10^{-10}$	$3 \cdot 10^{-11}$
O ₂ ⁻	$1.4 \cdot 10^{-8}$	$1 \cdot 10^{-8}$	$7.8 \cdot 10^{-10}$	$6.4 \cdot 10^{-10}$	$4.5 \cdot 10^{-9}$	$1.8 \cdot 10^{-10}$
O ₃	$2 \cdot 10^{-9}$	$2.15 \cdot 10^{-9}$	$3.4 \cdot 10^{-9}$	$4 \cdot 10^{-9}$	$3.5 \cdot 10^{-10}$	$3 \cdot 10^{-10}$
HONO	$1.5 \cdot 10^{-9}$	$2.5 \cdot 10^{-9}$	$2 \cdot 10^{-9}$	$2.3 \cdot 10^{-9}$	$1 \cdot 10^{-10}$	$5 \cdot 10^{-14}$
NO ₂ ⁻	$1 \cdot 10^{-10}$	$1.1 \cdot 10^{-10}$	$7.5 \cdot 10^{-7}$	$7.5 \cdot 10^{-7}$	$7.5 \cdot 10^{-8}$	$5 \cdot 10^{-11}$
HO ₂ NO ₂	$2.5 \cdot 10^{-6}$	$2.5 \cdot 10^{-6}$	$1.075 \cdot 10^{-9}$	$2.5 \cdot 10^{-9}$	$5 \cdot 10^{-10}$	$1 \cdot 10^{-15}$
Oxalate	$6 \cdot 10^{-6}$	$5 \cdot 10^{-6}$	$3.75 \cdot 10^{-7}$	$2.5 \cdot 10^{-7}$	$4.75 \cdot 10^{-7}$	$4 \cdot 10^{-8}$
HSO ₃ ⁻	$7.5 \cdot 10^{-9}$	$1.1 \cdot 10^{-8}$	$1 \cdot 10^{-7}$	$1 \cdot 10^{-7}$	$1 \cdot 10^{-8}$	$5 \cdot 10^{-10}$
SO ₃ ²⁻	$1 \cdot 10^{-13}$	$2 \cdot 10^{-13}$	$8 \cdot 10^{-9}$	$8 \cdot 10^{-9}$	$1 \cdot 10^{-9}$	$5 \cdot 10^{-11}$

Experimental Simulation of Iron Cycling (APP7)

Alexandra Sofikitis, Jean Louis Colin, Karine V.Desboeufs et Rémi Losno

*Lisa, Universités Paris 7 et 12, UMR 7583 CNRS,
61, av. du Gal. de Gaulle F-94010 Créteil Cedex France
sofikitis@lisa.univ-paris12.fr -*

Summary

Transition metals are thought to play a major role in the redox cycle of sulphur and organic compounds in the troposphere, as well as controlling free radical production in cloud. Iron is the most abundant of trace metals in cloud, rain and fog water. As the only source of trace metals in aqueous phase is due to the solubilization of aerosol, we present here results of pure mineral phase dissolution rate of iron obtained by laboratory experiments with an open flow reactor. This includes goethite, hematite and vermiculite, which are typical mineral of dust particles. Comparisons are made with natural loess which is a blend of various crystalline and amorphous phases. The dissolution rate of iron strongly depends on the nature of the original solid phase. We will present results of crustal origin particles dissolution experiment where kinetic parameters are determined, including iron speciation. Major function of variation are pH and photochemistry in the aqueous weathering solution.

Introduction

Dissolved transition metal ions are common constituents of atmospheric liquid water. Iron is one of the most abundant chemically active trace metals found in fog water (Behra and Sigg, 1990), rainwater (Graedel et al., 1986; Hofmann et al., 1991) and aerosol particles (Dedik et al., 1992; Zhuang et al., 1992). In previous studies on the solubility of atmospheric Fe (Moore et al., 1984; Zhu et al., 1992), Fe(II)/Fe(III) partition was not well considered. However, several studies have shown that large proportions of iron could be present in the atmospheric water as soluble Fe(II) (Behra and Sigg, 1990; Sedlak et al., 1997; Zhuang et al., 1995). Fe is known to participate in a variety of redox reactions in natural waters. The photolysis of Fe(III) species as well as the Fenton reaction with Fe(II) are a significant source of OH radicals in rains, fogs and clouds (Jacob et al., 1989; Zhu et al., 1992; Zhuang et al., 1992; Faust and Hoigné, 1990; Graedel et al., 1986; Hoffmann and Jacob, 1984). Iron participates in redox and photochemical reactions with H_2O_2 and its associated species HO_2 and O_2^- . Several studies have investigated the iron speciation or reactivity of trace metals in cloud or fog water (Behra and Sigg, 1990; Erel et al., 1993) or in ambient aerosol (Siefert et al., 1996; Spokes et al., 1994; Zhu et al., 1993; Zhuang et al., 1992). Trace metals are also strongly involved in the catalytic cycles affecting the dissolved species from the gaseous phase (i.e. SO_2) and have also an influence on cloud chemistry (Graedel et al., 1986). Iron cycling strongly differs from other catalytic cycles (Cu, Mn) because the reduced form is much more stable for iron than for other metals and this stability increases with the acidity (Losno, 1998). This iron speciation which is dependent on the chemical composition of the cloud droplets and on the photochemistry within cloud is still poorly documented because of severe analytical conditions.

As the only source of trace metals in aqueous phase is due to the solubilization of aerosol, we present here results of pure mineral phase dissolution rate of iron obtained by laboratory experiments with an open flow reactor. This includes goethite, hematite and vermiculite, which are typical mineral of dust particles. As we discussed above, we have focused our study on the influence of solid phase in the soluble iron release process. We have taken pure natural goethite (FeOOH), hematite (Fe_2O_3), vermiculite (clay, $(\text{MgFeAl})_3(\text{AlSi})_4\text{O}_{10}(\text{OH})_2 \cdot 4\text{H}_2\text{O}$) and an eolian loess from Cape Verde. An analytical method operating at trace level will be used to follow dissolution processes and iron speciation.

Activity

Determination of Iron Speciation :

An open column fitted "on line " to the sampling device to prevent any evolution of the speciation. This open column filled with ferrozine which is a specific chelating agent for Fe(II). After separation, the samples are collected in a water-FZ (80%) methanol (20%) mixed matrix. The analysis of iron by GFAAS required the optimisation of a thermal program with the simplex method. Detection limit allows measurements of Fe(II) for concentration levels usually found in rain droplets.

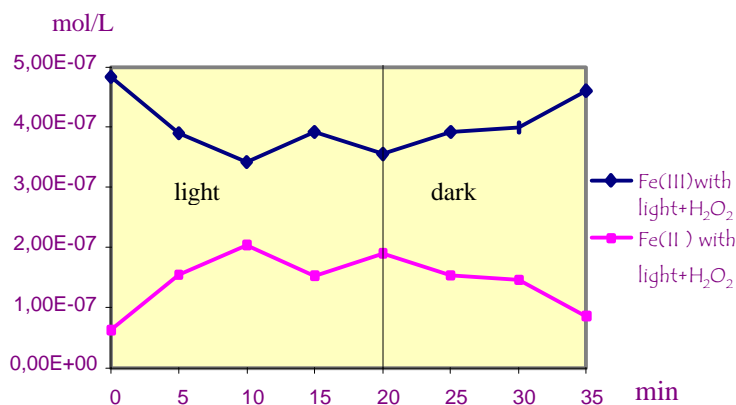
DL Fe(III)=0.3ppb (5.37×10^{-9} mol/L)

DL Fe(II) = 0.8ppb (1.43×10^{-8} mol/L)

We have thus a completely operationnal analytic method.

In order to simulate the photolysis of Fe(III), we started experiments into a closed homogeneous photoreactor. Preliminary results obtained clearly show a strong photochemical effect on iron speciation in presence of H_2O_2 . The Fe(II)/Fe(III) ratio seems to be related with the oxidising capacity of the atmosphere, supporting recent model's outputs.

HOMOGENEOUS RESULTS



Dissolution :

We have conducted experiments in an open-flow reactor system (Desboeufs et al., 1999) using 20 mg that was weathered with 1 L of fresh solution at pH 2 and 4.7 for about 1 hour. This reactor enables us to reproduce the dissolution of a particulate in aqueous atmospheric water.

$$R = FC + V \frac{dC}{dt} \quad (1)$$

where R is the rate of the reaction in moles per time unit ($\text{mol} \cdot \text{min}^{-1}$), F the flow rate ($\text{L} \cdot \text{min}^{-1}$), C the concentration of the solution in $\text{mol} \cdot \text{L}^{-1}$ and V the volume of the reactor cell (L). Using equation (1), we express the percentage of dissolved element X as

$$(X)\% = X / (m \cdot P_x) \quad (2)$$

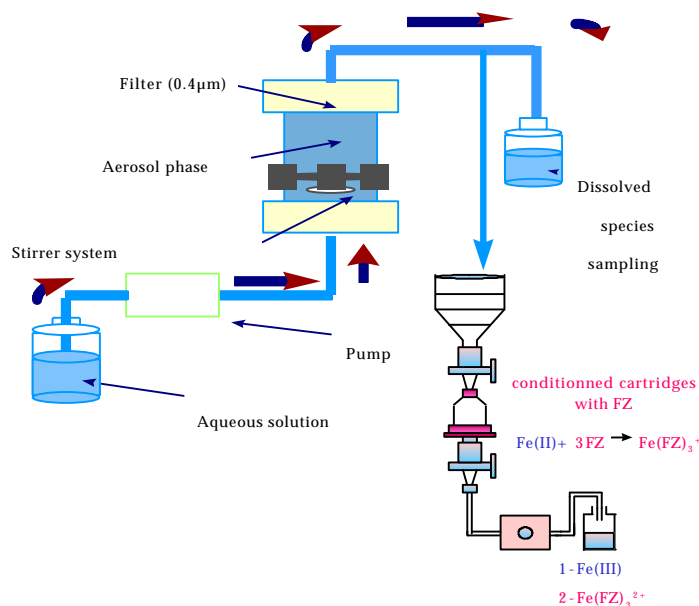
where X is the reaction progress expressed in mass of dissolved element, m the mass of raw dust introduced into the reactor cell for the experiment.

For all our work, m was constant and equal to 20 mg. P_x is the percentage of X in the dust.

To track the kinetic evolution of the system, solution containing the dissolved elements is collected at the outlet at regular intervals.

$$\text{Log } R = \text{Log } (k[X_f]) - kt \quad (3)$$

HETEROGENEOUS REACTOR



Results and discussion :

particulate influence :

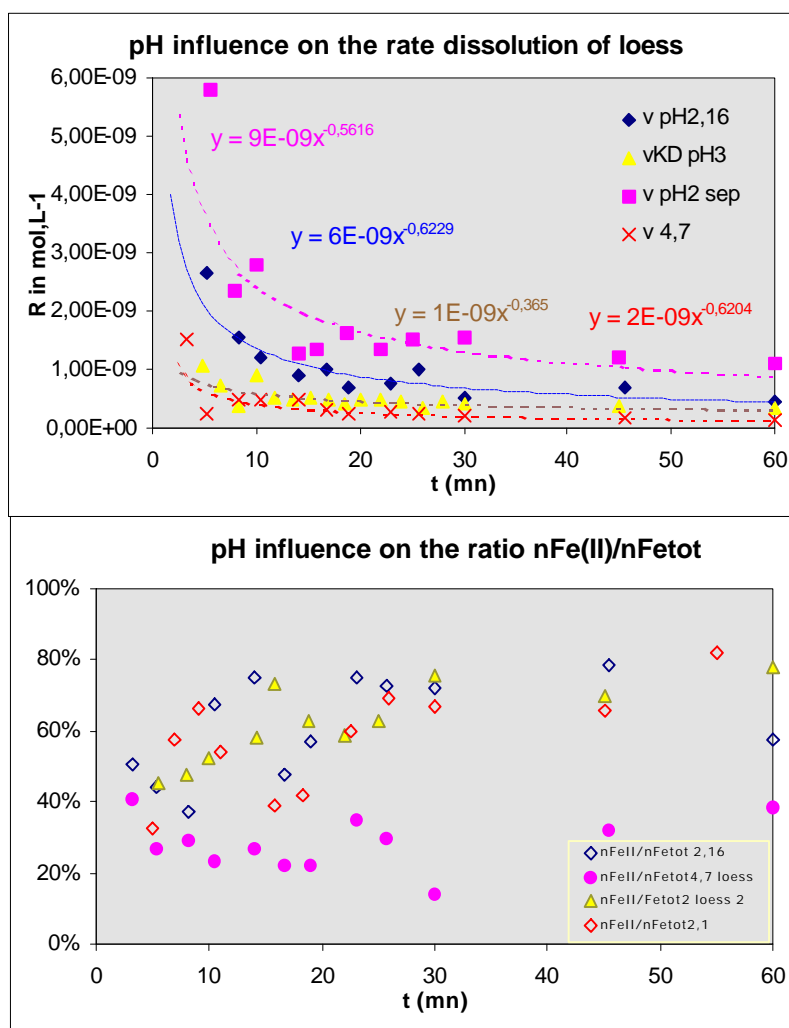
Fe(II)/Fetot showed us a ratio > 40% for loess dissolution, >70% for goethite and hematite, and 97% for vermiculite. Natural oxy-hydroxides is rarely stoichiometric and usually contains a number of substitutional cations isovalent or heterovalent to Fe(III). So an hypothesis is that mostly unstable Fe(II) were dissolved during the experiments and than a part of it was oxidised following this reaction:



We can show for loess dissolution experiments at pH≈2 an increase of Iron(II) / Fetot ratio during the first 20mn and then reached a high value of 70% Iron(II). We interpreted these data as a weathering layer of amorphous layer with disordered clay minerals on top of crystalline component of augite, Acmite and possible iron oxyhydroxides. A clay like vermiculite bring in the aqueous phase essentially iron(II).

pH influence :

pH is an essential parameter in dissolution experiments. With increasing pH, we decreased the dissolution rate of iron for all particulate. Results seem to show us big differences of solubility too. The ratio Iron(II) / Total soluble Iron is also very different for pH2 and pH4.7. According to the pH influence on the dissolution rate, we can interpreted these data as a weathering of an amorpheous layer only at pH 4.7. At pH2 we can see 2 steps. We can explain this particularity by a dissolution of the amorpheous surface for the 20 first minutes and a second step corresponding to the dissolution of the crystalline phase



	Loess	Goethite	Hematite	Vermiculite
$R_{\text{initial pH2}} (\text{mol.L}^{-1})$	$6.60\text{E-}9$	$1.92\text{E-}9$	$3.03\text{E-}9$	$2.29\text{E-}8$
$R_{\text{initial pH4.7}} (\text{mol.L}^{-1})$	$2.08\text{E-}10$	$1.20\text{E-}10$	$1.93\text{E-}10$	$4.16\text{E-}10$
$n\text{Fe(II)}/n\text{Fetot}$ pH2	60%	70%	72%	97%
solubility max pH2	0.350%	0.023%	0.019%	1.38%
solubility max pH4.7	0.130%	0.003%	0.005%	0.052%

Conclusion:

An open flow reactor was used to study solid phase dissolution. In this study 4 types of material were considered one blend of mineral and other pure phases. Results show that aerosol type and aqueous phase pH govern aerosol solubility in atmospheric water. Iron atmospheric chemistry is strongly controlled by the composition of the original aerosol. The $\text{Fe(II)} / \text{Fetot}$ ratio seems to be under pH and light dependence. The study reported here exposed solid phase to acid condition for one hour at ambient temperature. These preliminary results provided a first approach to understand iron cycling in cloud droplets. An analytical method is now operating and will be used to follow photolysis processes as well in heterogeneous as in homogeneous systems. We will further compare laboratory results with models. We also plan to test this method during field experiments at the ground level with a sampling collector already operational.

References

- Behra, P., and L. Sigg, Evidence for redox cycling of iron in atmospheric water droplets, *Nature*, 344, 419-421, 1990.
- Dedik, A.N., P. Hoffmann, and J. Ensling, Chemical characterization of iron in atmospheric aerosols., *Atmos. Environ.*, 26A, 2545-2548, 1992.
- Desboeufs, K.V., *Processus de Dissolution des Aérosols Atmosphériques au sein des Gouttes d'Eau Nuageuses*, Université Paris VII, Paris, 2001.
- Desboeufs, K.V., R. Losno, F. Vimeux, and S. Chobi, The pH-dependent dissolution of wind-transported Saharan dust, *J. of Geophysical Research*, 104 (D17), 21,287-21,299, 1999.
- Desboeufs K.V., R.Losno and J.L. Colin, Evolution of aerosol mineral solubility during cloud process and its impact on aerosol surface, IGAC conference, Bologna, Italy, 13-18 september 1999
- Erel, Y., S.O. Pehkonen, and M.R. Hoffmann, redox Chemistry of Iron in Fog and Stratus Clouds, *J. Geophys. Res.*, 98, 18,423-18,434, 1993.
- Faust, B.C., and J. Hoigné, Photolysis of Fe(III)-hydroxy complexes as sources of OH radicals in clouds, fog and rain., *Atmos. Environ.*, 24 A, 79-89, 1990.
- Graedel, T.E., M.L. Mandich, and C.J. Weschler, Kinetic model studies of atmospheric droplet chemistry, 2. Homogeneous transition metal chemistry in raindrops., *J. Geophys. Res.*, 91, 5225-5221, 1986.
- Hoffmann, M.R., and D.J. Jacob, Kinetics and mechanism of the catalytic oxidation of dissolved sulfur dioxide in aqueous solution: an application to nighttime fog water chemistry, in *Acid Precipitation Series*, edited by C. J.G., pp. 101-172, Butterworth, Boston, 1984.
- Jacob, D.J., E.W. Gottlieb, and M.J. Prather, Chemistry of a polluted cloudy boundary layer, *J. Geophys. Res.*, 94, 12,975-13,002, 1989.
- Losno R.; Trace Metals Acting as Catalysts in a Marine Cloud: a Box Model Study. *Phys. Chem. Earth (B)*, 24 N°3, 286-286, 1999.
- Moore, R.M., J.E. Milley, and A. Chatt, The potential for biological mobilization of trace elements from aeolian dust in the ocean and its importance in the case of Iron, *Oceanologica Acta*, 7, 221-228, 1984.
- Panias, D., M. Taxiarchou, I. Douni, I. Paspaliaris, and A. Kontopoulos, Dissolution of hematite in acidic oxalate solutions: the effect of ferrous ions addition, *Hydrometallurgy*, 43, 219-230, 1996.
- Sedlak, D.L., J. Hoigné, M.M. David, R.N. Colvile, E. Seyffer, K. Acker, W. Wiepercht, J.A. Lind, and S. Fuzzi, The cloudwater chemistry of iron and copper at Great Dun Fell, UK., *Atmos. Environ.*, 31, 2515-2526, 1997
- Spokes, L.J., T.D. Jickells, and B. Lim, Solubilisation of aerosol trace metals by cloud processing: a laboratory study., *Geochim. Cosmochim. Acta*, 58, 3281-3287, 1994.
- Zhu, X., J.M. Prospero, F.J. Millero, D.L. Savoie, and G.W. and Brass, The solubility of ferric ion in marine mineral aerosol solutions at ambient relative humidities, *Marine Chemistry*, 38, 91-107, 1992.
- Zhuang, G., Z. Yi, R.A. Duce, and B. P.R., Chemistry of iron in marine aerosol, *Global biogeochemical cycles*, 6 (2), 161-173, 1992.
- Zhuang, G., Z. Yi, and G. Wallace, Iron(II) in rainwater, snow, and surface seawater from a coastal environment., *Mar. Chem.*, 50, 41-50, 1995.

Aerosol dissolution enhancement by light irradiation (APP7).

Jean-Michel Velay, Karine Desboeufs, Rémi Losno and Jean-Louis Colin

*Lisa, Universités Paris 7 et 12, UMR 7583 CNRS,
61, av. du Gal. de Gaulle F-94010 Créteil Cedex France
losno@lisa.univ-paris12.fr -*

Introduction

Trace metals and especially transition metals strongly affect chemistry inside a cloud drop. Because of their availability through aerosol dissolution, we have investigated the effect of light irradiation on the dissolution rate of elements, including transition metals, from particulate matter in water. The first step of this work was to build and validate a device which can simulate in a laboratory the process occurring in a cloud. We have developed an open-flow reactor where a weathering solution flows continuously through a irradiated small Teflon cell (50 mL).

Method

This reactor cell (figure 1) is previously loaded with a small amount of particulate material and closed with a filter membrane (Sartorius™ cellulose-acetate, 0.45μ porosity) which prevent particle to flow out of the device. A silica window allows light to enter the system. Light is provided by a high pressure xenon discharge lamp and guided to the silica window by a liquid optical fibre.

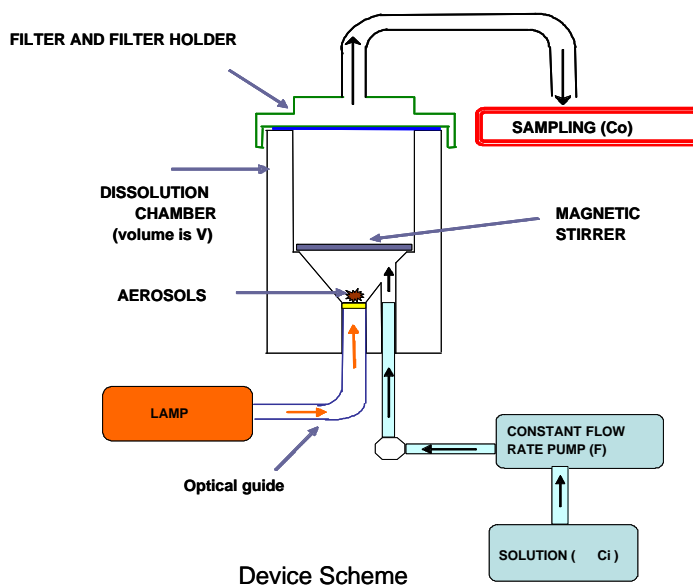


Figure 1: Schematic description of the dissolution cell

As the system is running in open flow, further precipitation of insoluble salts is avoided because the solution is constantly renewed. We can link the measured output concentrations and dissolution rate with the cell equation (Desboeufs, 1999):

$$R = dC_o/dt + F/V (C_o - C_i)$$

- R is the dissolution rate
- C_o is the measured output concentration
- C_i is the input concentration (0 if a pure acidic water)
- F is the flow rate
- V the reactor volume

The lamp spectra is quite continuous and close to sun spectra, but stronger in the blue and UV region (figure 2).

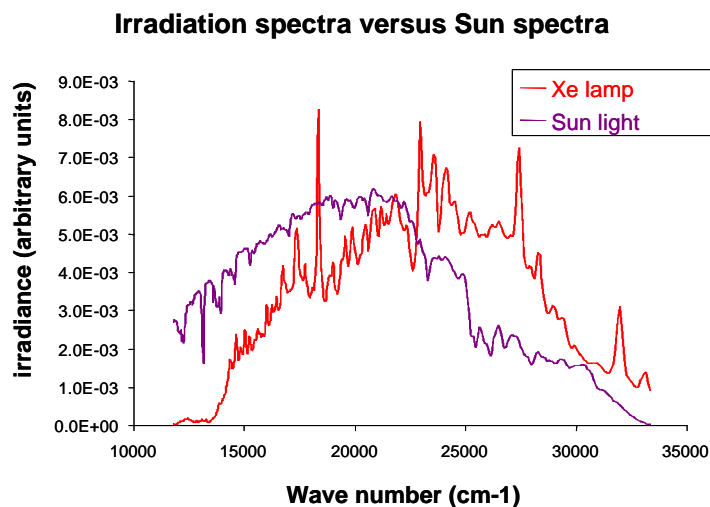


Figure 2: Irradiation spectra of the Xe discharge lamp at the end member of the optical fiber.

To calibrate the light intensity in the cell, we have made chemical actinometrical measurements on H_2O_2 photochemical decay. We have measured that for H_2O_2 photo-dissociation with the full power of the lamp, the light intensity is 50 times greater than we can expect in a summer clear sky.

We have chosen Capo Verde loess deposit to simulate a Saharan like aerosol. The weathering solution is diluted sulphuric acid (pH= 4.7). For quite soluble major elements (Na, Ca, Ca, Mg), no differences are observed whatever light is on or off (figure 3). But for poorly soluble transition metals (Mn and Fe), a strong effect is noticed (figure 4). For manganese, dissolution rate is 3 times faster under sunlight than in the dark. Further work will focus on the quantitative measurements of dissolution rate under various irradiation flux and various weathering solution composition, including radical photo-precursors (e.g. H_2O_2 , organic acids, ...).

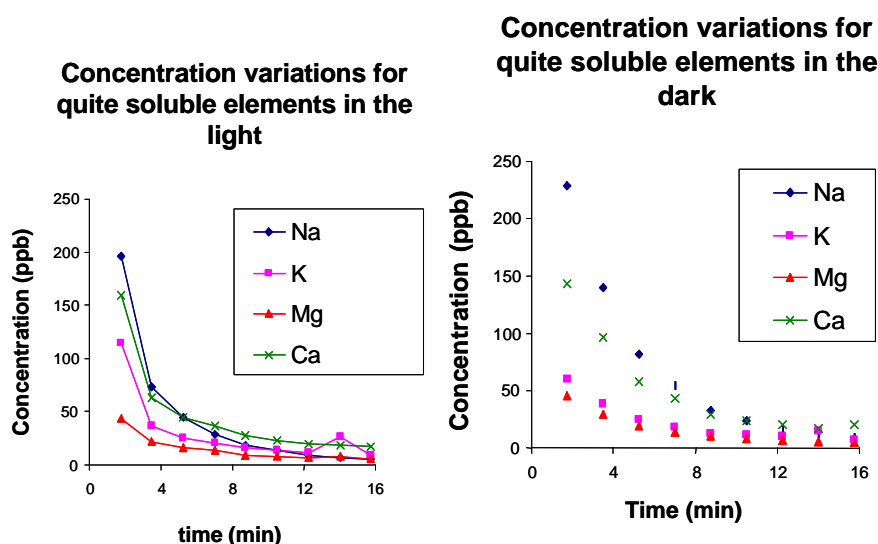


Figure 3: Variation of output elemental concentration for irradiated (left) and dark (right) conditions. No change can be noticed.

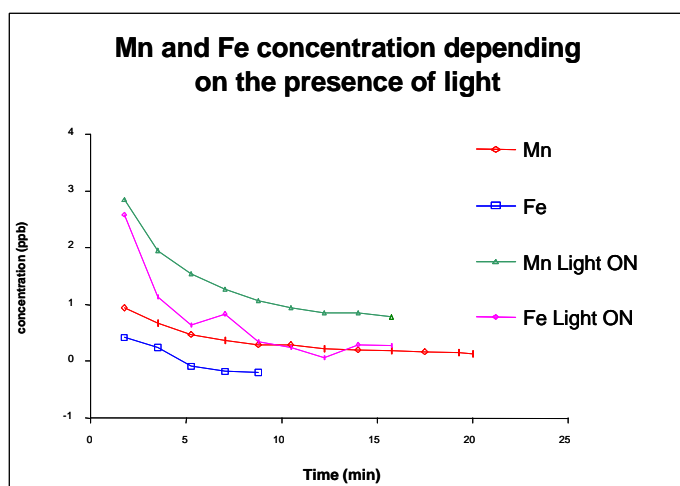


Figure 4: Influence of irradiation on transition metal Fe and Mn dissolution rate.

Conclusion

Comparisons of dissolution measurements with and without light clearly indicates a large influence of irradiation for iron and manganese dissolution rate, but no influence for sodium, calcium, potassium, and so on.... which is enhancing the conclusion given in Desboeufs et al. (2001). Two hypotheses are emitted concerning this dissolution rate enhancement:

- 1/ Irradiation acts directly on the surface of particles and help to extract the metals from its mineral lattice, probably by changing its redox state.
- 2/ Irradiation acts on the soluble species, creates radicals who react themselves on the surface of the particles, helping transition metal extraction.

References

- Desboeufs K., Losno R., Vimeux F. and Cholbi S. (1999), "pH dependent dissolution of wind transported Saharan dust", *J. GeoPhys. Res.*, 21287-21299.
- Desboeufs K.V., Losno, R. and Colin J.L. (2001), "Factors influencing aerosol solubility during cloud processes", *Atmos. Environ.*, 35, 3529-3537.

Interaction between Mineral Components of Sea Aerosols and Sulphoxy Radicals (APP8).

Wanda Pasiuk-Bronikowska, Tadeusz Bronikowski, Marek Ulejczyk and Ryszard Sokolowski
Institute of Physical Chemistry, Polish Academy of Sciences
Kasprzaka 44/52, 01-224 Warsaw, Poland
wpb@ichf.edu.pl

Introduction

To shed more light on the role of atmosphere components in the autoxidation of S(IV) we extended our interests on the main electrolytes in the aqueous phase of the sea aerosol: NaCl, NaNO₃ and Na₂SO₄. The autoxidation of S(IV) was carried out in a homogeneous (4 cm³ in volume) or heterogeneous reactor (150 cm³ in volume) under the following chemical conditions: initially 2x10⁻³ M S(IV), 2.5x10⁻⁴ M O₂ and 2x10⁻⁷ M sobrerol or steadily 5.6x10⁻⁴ M S(IV), 2.5x10⁻⁴ M O₂ and no organic inhibitor, respectively. The experiments were conducted at pH about 5.0 or 7.5 and temperature 25°C, both in the absence and presence of CoSO₄ as a catalyst. The reaction progress was followed by measuring the decrease in oxygen concentration (Clark type electrode) or the increase in conductivity due to sulphate formation (Orion conductivity cell).

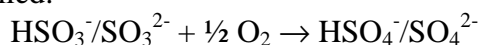
The measurements were performed for reacting solutions diluted or concentrated with respect to the selected mineral components. In the first case the solution composition was near to that of coastal precipitation (Table 1).

Table 1. Concentrations of main mineral species in precipitation in the Gdansk-Sopot-Gdynia Tricity at the coast of the Baltic Sea (Polkowska *et al.*, 2002)

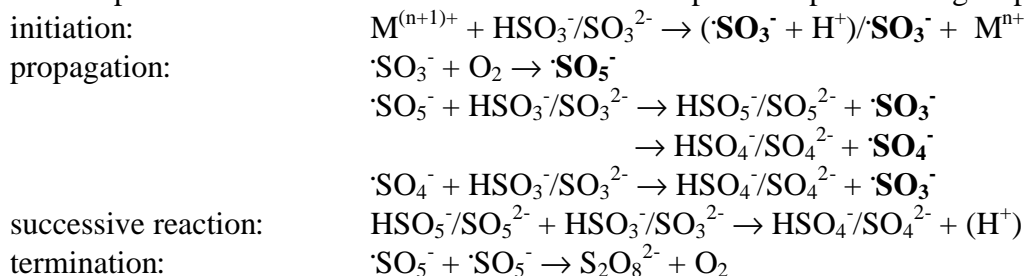
	SO ₄ ²⁻ M	NO ₃ ⁻ M	Cl ⁻ M	Ca ²⁺ M	Na ⁺ M
min.	4.16x10 ⁻⁵	6.45x10 ⁻⁸	2.82x10 ⁻⁶	1x10 ⁻⁶	2.72x10 ⁻⁵
max.	1.5x10 ⁻³	2.93x10 ⁻⁴	3.94x10 ⁻⁴	2.64x10 ⁻³	2.84x10 ⁻⁴

We took also into account the concentration values extracted from the CAPRAM model (Table 2). In the second case the high concentrations of mineral components reflected the situation in evaporating sea aerosols (consult Table 3). Comparative experiments were made for NaClO₄ commonly used to adjust the ionic strength (Cavalheiro *et al.*, 1987).

To study the interaction between mineral components of sea aerosols and sulphony radicals the following reaction was applied:



The simplified mechanism of this chain reaction comprises steps involving sulphony radicals:



A foreign substance may cause: catalyst activity change, change of the termination step, and development of new propagation steps.

Table 2. Concentrations of the above species assumed in the CAPRAM model for the atmospheric aqueous phase at marine conditions (Herrmann *et al.*, 2000)

SO_4^{2-} (M)	NO_3^- (M)	Cl^- (M)	Ca^{2+} (M)	Na^+ (M)
5.97×10^{-6}	3.15×10^{-5} *	5.6×10^{-4}		

*calculated from the gas-phase concentration and the Henry constant

Table 3. Concentrations of some mineral components at saturation, 25°C (Seidell, 1953)

Na_2SO_4 (M)	CaSO_4 (M)	NaNO_3 (M)	NaCl (M)
1.97	1.53×10^{-2}	7.80	6.42

Experimental results

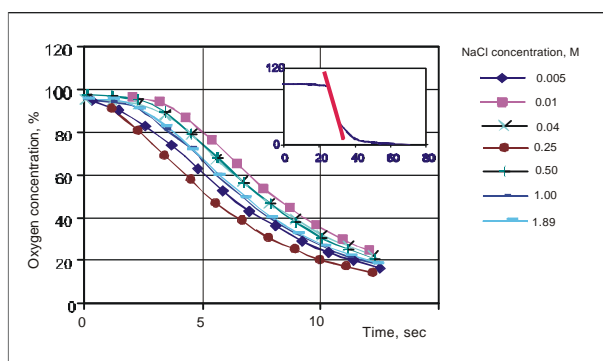
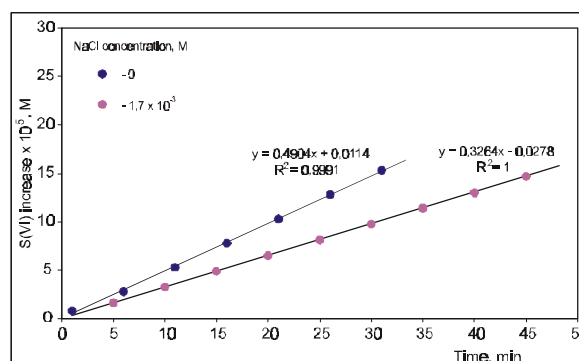
Laboratory techniques. To recognise the reactivity of the selected mineral electrolytes with respect to sulphydryl radicals the overall SO_2 oxidation rate in the presence of these electrolytes was determined. Typical experimental results obtained in a homogeneous reactor with a Clark - type sensor are shown in Fig.1. The results obtained in a heterogeneous reactor with a conductometric probe are given in Fig.2. The detailed operation conditions of the reactors were described earlier (Pasiuk-Bronikowska *et al.*, 1992; Pasiuk-Bronikowska *et al.*, 2001).

Influence of mineral components at low ionic strength. The effect of small amounts of the electrolytes: CaSO_4 , NaNO_3 or NaCl introduced to the aqueous solution containing S(IV), Co - catalyst and predissolved oxygen is shown in Fig. 3. Under these conditions the ionic strength effect could be neglected. No interaction between CaSO_4 and SO_2 oxidation transients is observed, whereas the inhibiting effect is visible for NaNO_3 and NaCl . To explain the peculiarities in the kinetic behaviour of the S(IV) oxidation in the presence of NaNO_3 and NaCl , it is instructive to distinguish some specific process regimes (Fig.4).

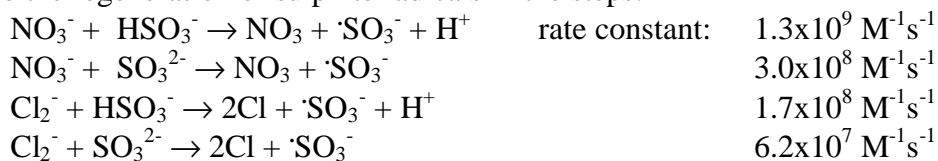
Regime I. In this regime characteristic by the steep decrease in the S(IV) oxidation rate sulphate radicals are scavenged in the steps:



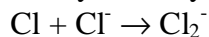
The concentration of foreign radicals NO_3 and Cl is sufficiently low, so that their kinetic contribution may be neglected.

**Figure 1.** Decay of O_2 at the S(IV) oxidation in time. The rate of S(VI) production is found as a doubled slope of the linear portion of the curve, see insert (homogeneous reactor).**Figure 2** Accumulation of S(VI) in the course of S(IV) oxidation. The rate of S(VI) production is found directly as a slope of the straight line (heterogeneous reactor).

Regime II. The decrease of the S(IV) oxidation rate in this regime becomes less pronounced. This is due to the regeneration of sulphite radicals in the steps:

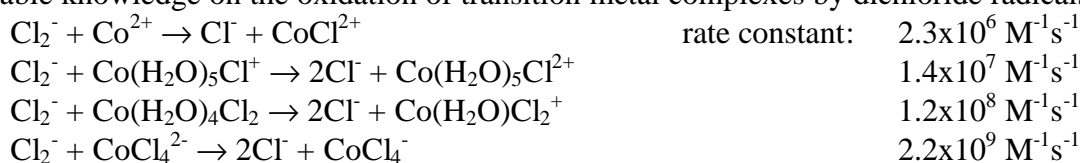


preceded by the very fast step:



In this regime the concentration of foreign radicals NO_3 and Cl_2^- is sufficiently high, so that the radicals enter the S(IV) oxidation chain and this effect is kinetically important.

Regime III. This regime is characterised by the non-monotonic variation of the S(IV) oxidation rate with the increasing concentration of chloride. To explain the nature of regime III we recall the available knowledge on the oxidation of transition metal complexes by dichloride radicals:



When the Cl to S(IV) concentration ratio increases, so that sulphite ions in the transition metal complexes constituting the real catalyst become gradually replaced by chloride ions, the oxidation catalyst in fact undergoes essential changes. In the new form of the catalyst the metal oxidation step to an initiator is faster.

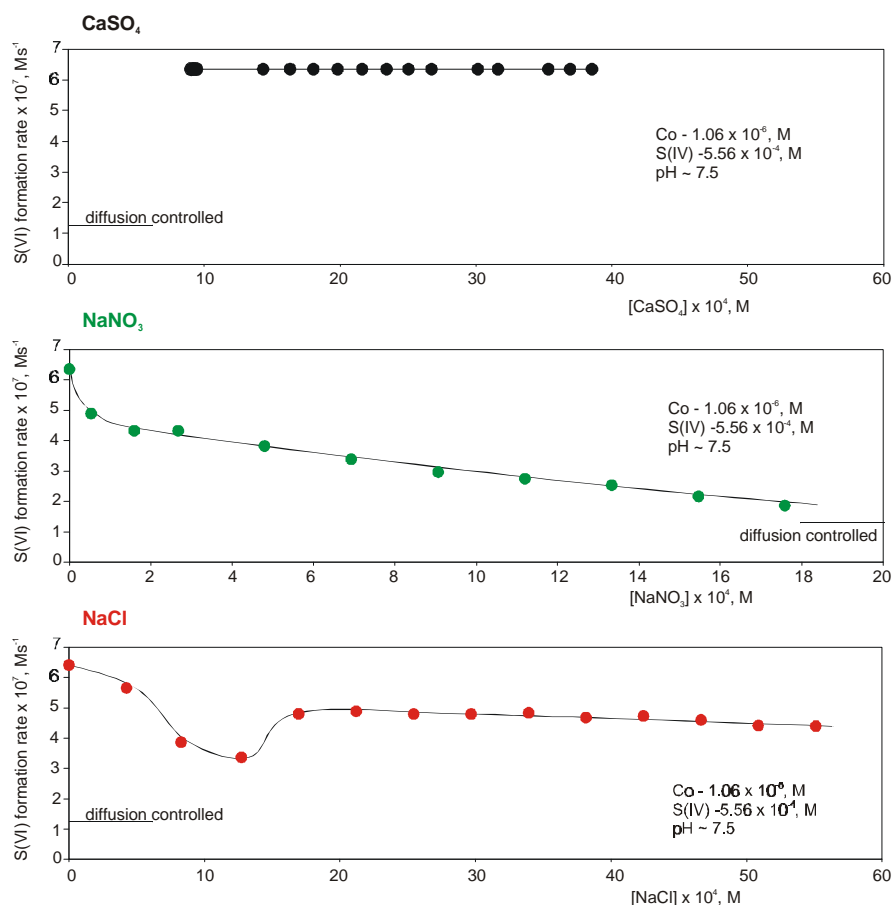


Figure 3: Salt concentration effects on the overall S(IV) oxidation rate at the low ionic strength for CaSO_4 , NaNO_3 and NaCl (heterogeneous reactor, fast reaction regime).

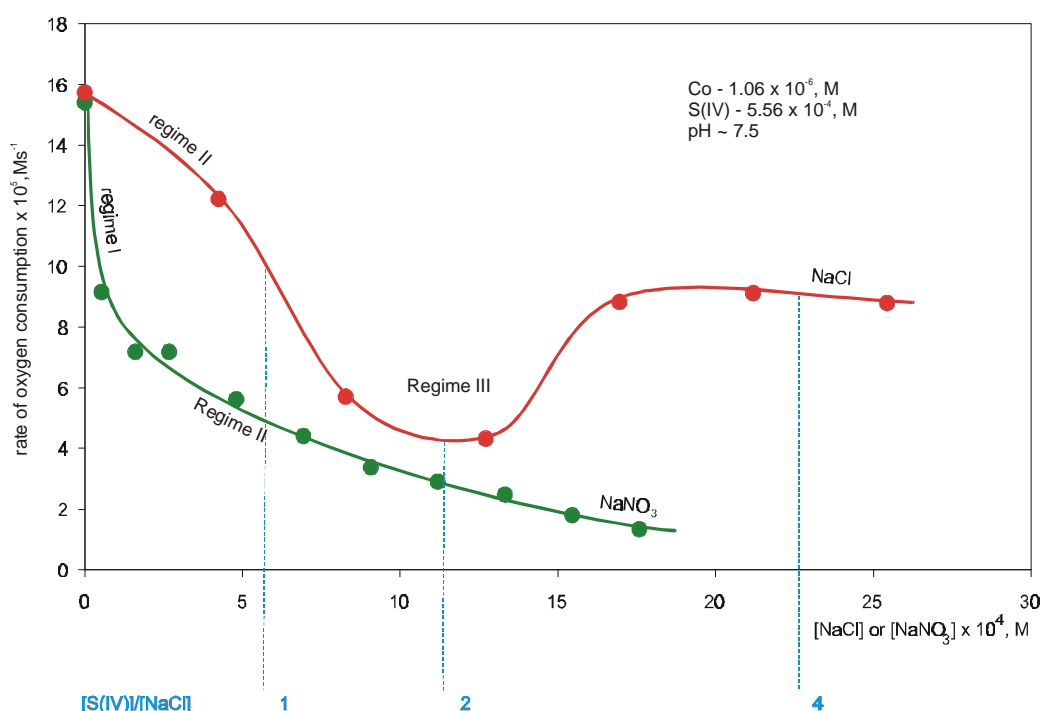


Figure 4: Regimes of S(IV) oxidation in the presence of NaNO₃ and NaCl (ionic strength negligible).

The above mentioned values of rate constant were taken after Neta *et al.*, 1988 and Herrmann *et al.*, 2000. As known atmospheric aerosols continuously exchange water with the gas phase, undergoing evaporation and gaining water by condensation. The question arose whether the drop of water content in aerosol particles causing the thickening of electrolytes exerts the effect on the rate of S(IV) oxidation.

Influence of mineral components at high ionic strength. The increasing concentration of chlorides or nitrates should, on one side, make the inhibiting effect deeper, but on the other side an increase of the S(IV) oxidation rate due to the effect of the ionic strength should be expected. The influence of NaCl at high concentrations on the rate of S(IV) oxidation to S(VI) is shown in Fig.5. It is characteristic that the rate of S(VI) formation attains values exceeding the rate value for this reaction in the absence of NaCl and the plots show maxima.

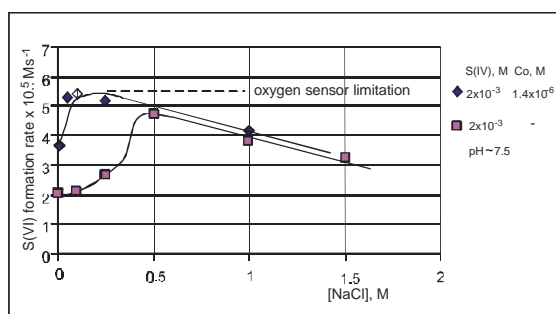


Figure 5: Effect of the ionic strength on the oxidation of S(IV) in the presence of NaCl.

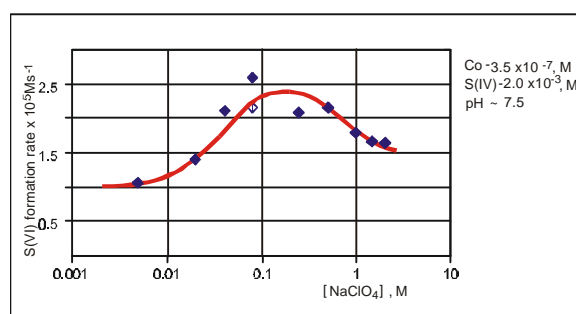


Figure 6: Effect of the ionic strength on the oxidation of S(IV) in the presence of NaClO₄.

A similar maximum is observed when NaCl is replaced by sodium perchlorate commonly used in laboratory practice as a background ion (Fig.6). So it seems that at sufficiently high concentrations of mineral components the effect of ionic strength becomes the dominating factor establishing the S(IV) oxidation rate at a pretty high level.

Influence of organic components. We performed experiments with NaCl and sobrerol, the terpenic compound of strong inhibiting properties proved by us earlier (Pasiuk-Bronikowska *et al.*, 2001; Pasiuk-Bronikowska *et al.*, 2002). Results of the experiments are shown in Fig. 7 as measured for the high ionic strength. Figure 8 gives the results recalculated for the ionic strength equal to zero.

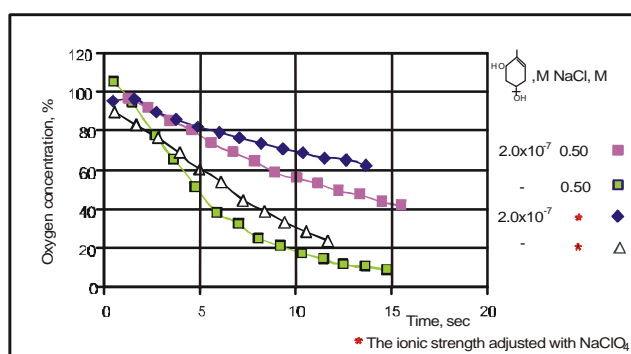


Figure 7: Effect of sobrerol on the oxidation of S(IV) at the ionic strength 0.5 M adjusted with NaCl or with NaClO₄ (experiments performed at Co-catalyst 1.4×10^{-6} M, S(IV) 2.0×10^{-3} M and pH ~ 7.5).

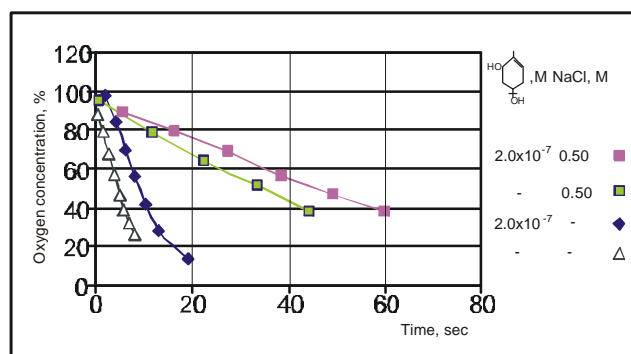


Figure 8: Effect of sobrerol on the oxidation of S(IV) as recalculated for the ionic strength zero (experiments performed at Co-catalyst 1.4×10^{-6} M, S(IV) 2.0×10^{-3} M and pH ~ 7.5).

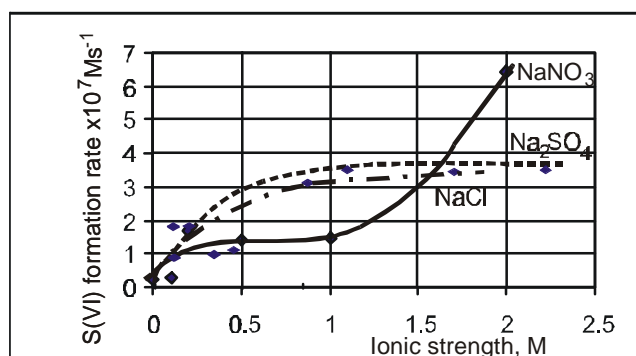


Figure 9: Salt concentration effect on the overall S(IV) oxidation rate in the presence of sobrerol (experiments performed at Co-catalyst 1.4×10^{-6} M, S(IV) 2.0×10^{-3} M, sobrerol 2.0×10^{-7} M and pH ~ 5.0).

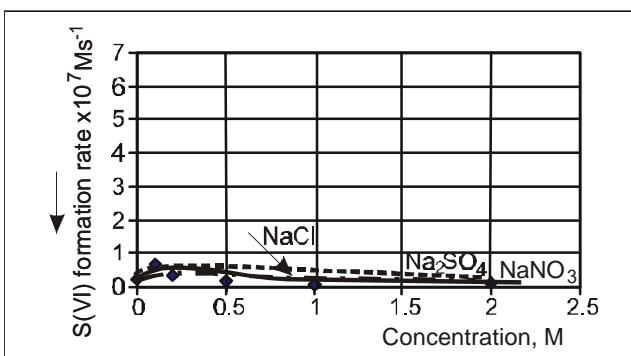


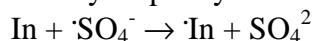
Figure 10: Salt concentration effect on the overall S(IV) oxidation rate in the presence of sobrerol as recalculated for the ionic strength zero (experiments performed at Co-catalyst 1.4×10^{-6} M, S(IV) 2.0×10^{-3} M, sobrerol 2.0×10^{-7} M and pH ~ 5.0).

From these figures it is clear that the inhibiting action of sobrerol is preserved also in solutions of NaCl to sobrerol concentration ratios over 1×10^6 . As results from Figs. 9 and 10 the strongly increased ionic strength becomes a decisive factor causing the S(IV) oxidation enhancement also in the presence of sobrerol.

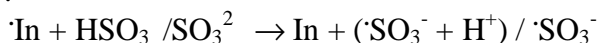
Conclusions

Mechanistic suggestions. It results from the kinetic arguments that the catalytic activity of transition metal ions in the oxidation of S(IV) changes in the presence of atmospheric components capable to form complexes with their ions, replacing sulphite/bisulphite anions.

We distinguish two types of the inhibition by sulphony radical scavenging:



(i) “hard” inhibition by increasing the rate of chain termination when In^\bullet behaves as an inert with respect to S(IV) and (ii) “soft” inhibition by inserting the additional propagation step when In^\bullet is capable to regenerate $\cdot\text{SO}_3^-$:



Both chlorides and nitrates belong to the “soft” inhibitors, whereas sobrerol behaves in our experiments as a “hard” inhibitor.

Since the inhibiting effect due to the simultaneous presence of NaCl and sobrerol seems additive, the interaction between sobrerol and chlorine atoms or dichlorine radicals may be neglected. However, it does not preclude the formation of sobrerol derivatives in non-rate-limiting radical steps.

Practical implications. At marine and coastal precipitation conditions the net result of the interaction between sulphony radicals and the mineral components of sea aerosols: nitrates or chlorides, is the decrease of the rate of sulphuric acid/sulphate production by the pathway involving molecular oxygen. Our results obtained at pH about 7 show this rate decreased even 16 times in the case of nitrate, but only about 4 times in the case of chloride.

At conditions of deliquescent salt aerosols the oxidation of S(IV) by molecular oxygen runs at a rate influenced by the two opposite factors: the increasing ionic strength responsible for the reaction enhancement and the increasing concentration of mineral components, active as inhibitors, accountable for the reaction slowing down. In acidic solutions the oxidation of S(IV) may be enhanced due to salt effects even by an order of magnitude, whereas in neutral solutions the rate of this reaction is less sensitive to the effect of ionic strength, which compensates only the inhibition.

This work should be treated as a signal on the problem of atmospheric aqueous phase as a source of exotic secondary products of poorly known toxicity (including sulfonated and halogenated derivatives).

Acknowledgement

The financial support for this work from the State Committee for Research in Poland is gratefully acknowledged.

References

- Cavalheiro E. T. G., de Guzzi Plepis A. M., Chierice G. O. and Neves E. F. A. (1987): The potentiometric determination of stability constants of sulfite and cobalt(II) in ionic strength 2.0 M (NaClO_4). Use of the matrix method, *Polyhedron* **6**, 1717-1719.
- Herrmann H., Ervens B., Jacobi H. W., Wolke R. and Zellner R. (2000): CAPRAM2.3: A chemical aqueous phase radical mechanism for tropospheric chemistry, *J. Atmos. Chem.* **36**, 231-284.
- Neta P., Huie E. and Ross A. B. (1988): Rate constants for reactions of inorganic radicals in aqueous solution, *J. Phys. Chem. Ref. Data* **17**, 1027-1284.
- Pasiuk-Bronikowska, W., Bronikowski, T. and Sokolowski, R., (2001): The autoxidation of S(IV) at low temperatures, in J. Hjorth, F. Raes, and G. Angeletti (Eds), *Proc. 8th European Symposium on the Physico-Chemical Behaviour of Atmospheric Pollutants: A Changing Atmosphere*, EC, Ispra, pp. 1-5.
- Pasiuk-Bronikowska, W., Bronikowski, T. and Ulejczyk, M. (1992): Mechanism and kinetics of autoxidation of calcium sulfite slurries, *Environ Sci. Technol.* **26**, 1976-1981.
- Pasiuk-Bronikowska, W., Bronikowski, T. and Ulejczyk, M. (2002): Inhibition of the S(IV) autoxidation in the atmosphere by secondary terpenic compounds, *J. Atmos. Chem.*, **44**, 97-111.
- Polkowska Z., Astel A., Gryniewicz M., Gorecki T. and Namiesnik J. (2002): Studies on intercorrelation between ions co-occurring in precipitation in the Gdansk-Sopot-Gdynia Tricity (Poland), *J. Atmos. Chem.* **41**, 239-264.
- Seidell A. (1953): *Solubilities of Inorganic and Metal Organic Compounds*, 3rd edition, vol. 1, D. Van Nostrand Company, New York.

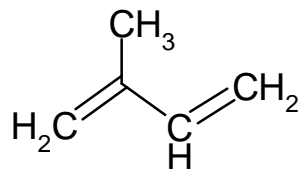
Degradation of Isoprene during Aqueous Autoxidation of SO₂ under Various Conditions of Initiation (APP8).

Krzysztof J. Rudzinski, Wanda Pasiuk-Bronikowska and Joanna Krolik

Institute of Physical Chemistry of the P.A.S., Kasprzaka str. 44/52, 01-224 Warsaw, Poland

kjrudz@ichf.edu.pl

Introduction



Isoprene, a major organic pollutant of biogenic and anthropogenic origin, was shown to slow down the aqueous autoxidation of SO₂ at the cost of undergoing degradation (Rudzinski *et al.*, 2002, and the references quoted therein). In that work two chemical mechanisms of isoprene degradation were proposed, assuming the chain oxidation of isoprene induced either by the sulphite or by the sulphate radicals generated within the autoxidation of SO₂. The mechanisms were tested against the experimental data obtained for the autoxidation of sulphite initiated by MnSO₄, i.e. by the generation of the sulphite radicals. Neither type of the sulphonyl radicals could be indicated as the prevailing species inducing the isoprene degradation.

In this work, we studied the degradation of isoprene during the autoxidation of SO₂ initiated via thermal decomposition of K₂S₂O₈, i.e. by direct generation of sulphate radicals, in alkaline solutions. The metal ions absent, we hoped to discriminate the roles of sulphite and sulphate radicals in the process.

Experimental

The reaction was followed in a perfectly stirred tank without the gas phase, thermostated at 25 °C. A solution of K₂S₂O₈ initiator in Milipore water, saturated with O₂ at the atmospheric pressure, was placed in the reactor. Then an aliquot of isoprene solution in water was added, prepared using the ultrasonic mixing. The reaction run was started by adding an aliquot of aqueous Na₂SO₃ solution. Initial concentrations of reactants were listed in Table 1. The concentration of O₂ in the reacting solution was measured electrochemically. The UV spectra of the solution were recorded with the spectrophotometer, using a closed external loop consisting of a flow-through micro-cuvette, a valve and a syringe. The spectra were later analysed to obtain the running concentrations of sulphite and isoprene. The reacting solutions were alkaline (initially pH ~8.5, at the end of reaction pH~7.6).

Table 1. Initial concentrations of reactants, approximate values in M

O ₂	2.5×10 ⁻⁴
Na ₂ SO ₃	5×10 ⁻⁴ , 6.5×10 ⁻⁴
isoprene	0, 1×10 ⁻⁶ , 5×10 ⁻⁶ , 1×10 ⁻⁵
K ₂ S ₂ O ₈	1×10 ⁻⁴ , 2×10 ⁻⁴ , 1×10 ⁻³

Kinetic analysis

Degradation of isoprene during autoxidation of sulphite initiated by K₂S₂O₈ followed the exponential-decay kinetics, without the induction period observed in the case of MnSO₄ initiator (Fig. 1). Isoprene significantly slowed down the consumption of sulphite, in some proportion to the amount present (Fig. 2).

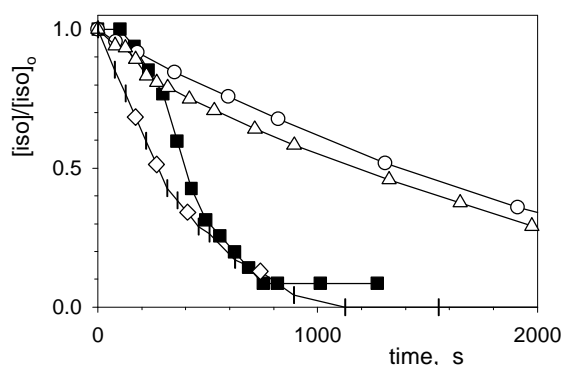


Figure 1: Degradation of isoprene during autoxidation of S(IV) initiated by: 1×10^{-5} M MnSO_4 (■) or $\text{K}_2\text{S}_2\text{O}_8$ at $\sim 1 \times 10^{-4}$ M (○), $\sim 2 \times 10^{-4}$ M (△) and $\sim 1 \times 10^{-3}$ M (◇); other initial concentrations: $\sim 6.3 \times 10^{-4}$ M Na_2SO_3 , $\sim 2.5 \times 10^{-4}$ M O_2 , $\sim 1 \times 10^{-6}$ M isoprene.

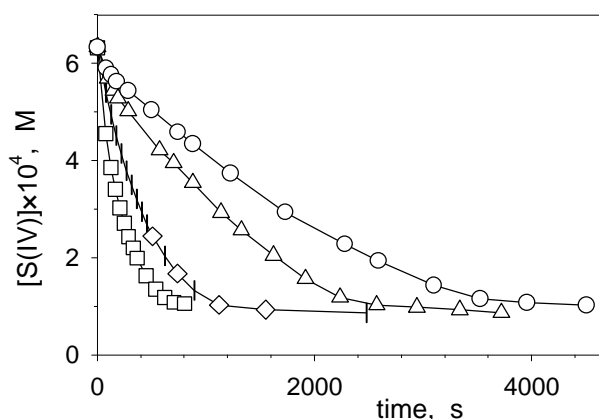


Figure 2: Autoxidation of S(IV) initiated by $\sim 1 \times 10^{-3}$ M $\text{K}_2\text{S}_2\text{O}_8$, with no isoprene (□) and with isoprene present at initial concentrations of $\sim 1 \times 10^{-6}$ M (◇), $\sim 5 \times 10^{-6}$ M (△), and $\sim 1 \times 10^{-5}$ M (○); other initial concentrations: $\sim 6.3 \times 10^{-4}$ M Na_2SO_3 , $\sim 2.5 \times 10^{-4}$ M O_2 .

Time profiles of the rates of the isoprene and sulphite consumption were compared for both initiators in Figs 3 and 4. In the case of $\text{K}_2\text{S}_2\text{O}_8$ initiator, the apparent first-order kinetics was observed. The pseudo-first-order rate constants k_{1a} and k_{1i} increased proportionally to the initial concentrations of $\text{K}_2\text{S}_2\text{O}_8$ and decreased hyperbolically with that of isoprene.

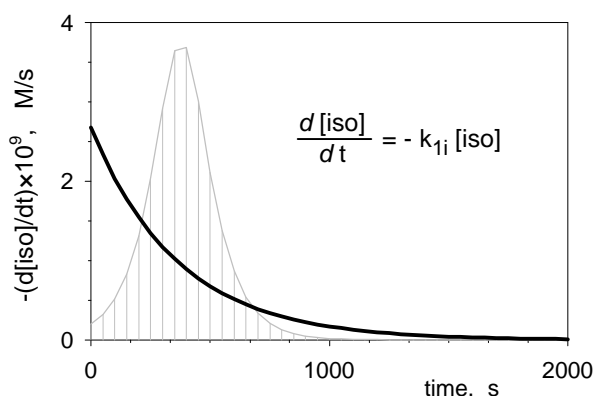


Figure 3: Rates of isoprene degradation during autoxidation of S(IV) initiated either by $\sim 1 \times 10^{-3}$ M $\text{K}_2\text{S}_2\text{O}_8$: (black solid line and equation) or by 1×10^{-5} M MnSO_4 (grey ghost shape); other initial concentrations are specified under Fig. 1.

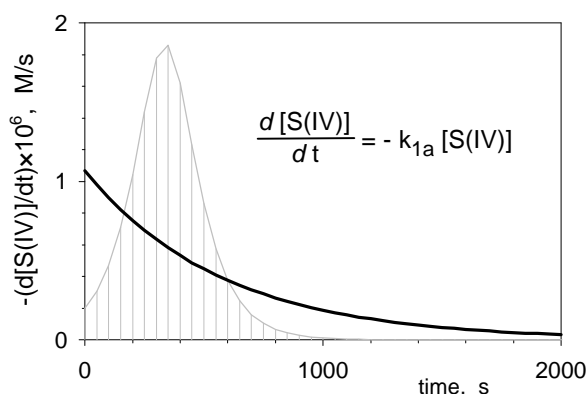
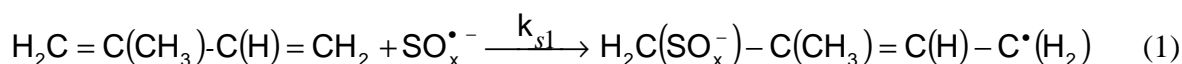


Figure 4: Rates of sulphite autoxidation initiated either by $\sim 1 \times 10^{-3}$ M $K_2S_2O_8$: (black solid line and equation) or by 1×10^{-5} M $MnSO_4$ (grey ghost shape); other initial concentrations are specified under Fig. 1.

The apparent first-order kinetics observed might result from the stationary states of some reaction transients. In conjunction with previous assumption (Rudzinski *et al.*, 2002), that isoprene reacted directly with one type of sulphony radicals only, either sulphite or sulphate, according to the equation:



The stationary concentrations of the $SO_x^{\bullet-}$ radicals (their type yet unspecified) were estimated for each experimental run from the pseudo-first-order rate constants k_{1i} , using the formula

$$[SO_x^{\bullet-}]_{stationary} = \frac{k_{1i}}{k_{s1}} \quad (2)$$

The values, obtained for $k_{s1} = 3.5 \times 10^9$ 1/(M s), increased proportionally to the initial concentration of $K_2S_2O_8$ and decreased hyperbolically with the initial concentration of isoprene (Fig. 5).

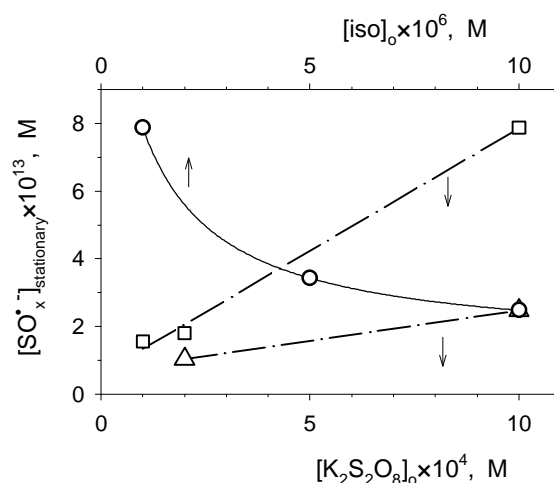
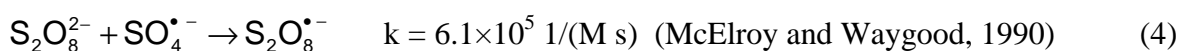
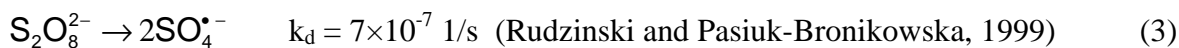


Figure 5: Influence of the initial concentration of peroxydisulphate or isoprene on the stationary concentrations of unspecified sulphony radicals assumed to exclusively react with isoprene; other initial concentrations of reactants: $\sim 2.5 \times 10^{-4}$ M O_2 , $\sim 6.3 \times 10^{-4}$ M Na_2SO_3 and $\sim 1 \times 10^{-3}$ M $K_2S_2O_8$ (O); $\sim 1 \times 10^{-6}$ M isoprene (□); $\sim 1 \times 10^{-5}$ M isoprene (Δ).

For further analysis, two previously suggested chemical mechanisms, A and B, of the S(IV) autoxidation in the presence of isoprene (Rudzinski *et al.*, 2002) were modified by replacing all steps incorporating transition metal species with two reactions of peroxydisulphate:



Other reaction steps as well as the rate constants remained unchanged, while the peroxydisulphate radicals formed in reaction (4) were assumed inactive towards other reactants. In the modified mechanism A the chain degradation of isoprene was induced by sulphite radicals, while in B – by sulphate radicals.

Each of the two mechanisms provided accurate approximation of experimental data by the way of computer simulation (Fig. 6), but at the cost of making the decomposition constant k_d a free parameter. This free parameter varied between the simulated experiments, increasing with the initial concentration of $\text{K}_2\text{S}_2\text{O}_8$ and decreasing with that of isoprene. For the runs without isoprene it appeared directly proportional to the initial concentration of $\text{K}_2\text{S}_2\text{O}_8$. The observed variations indicate the mechanism of the chain initiation by peroxydisulphate was more complicated than assumed in the mechanisms. Plausibly, the peroxydisulphate radicals were not inactive, but participated in the chain propagation.

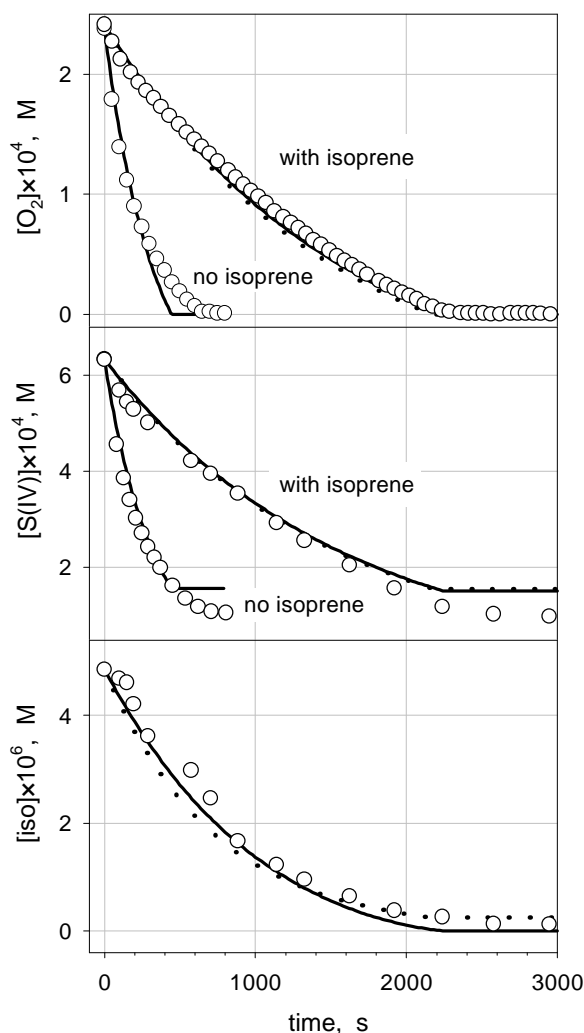


Figure 6: Simulation of S(IV) autoxidation initiated by $\sim 1 \times 10^{-3} \text{ M}$ $\text{K}_2\text{S}_2\text{O}_8$, in the absence and presence of isoprene: experimental data (○), mechanism A (—), mechanism B (·····); other initial concentrations of reactants were $\sim 6.3 \times 10^{-4} \text{ M}$ Na_2SO_3 , $\sim 2.5 \times 10^{-4} \text{ M}$ O_2 and $\sim 4.9 \times 10^{-6} \text{ M}$ isoprene.

However, within the computer-simulated experiments only the concentrations of sulphate radicals attained true stationary values, close to the values estimated from eqn (2) for the unspecified sulphonyl radicals exclusively reacting with isoprene. Thus, the degradation of isoprene was induced rather by the sulphate radicals than the sulphite ones. This conclusion is subject to the limitations of the present mechanism, which did not account for the pH changes observed experimentally and contained incomplete scheme of the chain initiation by $K_2S_2O_8$.

Conclusions

We showed that dissolved isoprene decayed in the course of autoxidation of S(IV) also in the absence of metal initiators, significantly slowing down the rates of oxygen and S(IV) consumption. Assuming the isoprene chain decay was initiated by one type of sulphonyl radicals only, the stationary concentrations of these radicals were estimated for a given rate constant of the initiating reaction (1), which increased proportionally to the $K_2S_2O_8$ concentration and decreased hyperbolically with the initial concentration of isoprene (Fig. 5). Simulations based on the presently suggested chemical mechanism indicated that the radicals in question were the sulphate radicals. This work provides stronger support to our claim, that the aqueous transformations of isoprene induced by the sulphonyl radicals should be taken into account by atmospheric experimentalists and modellers as a possible sink of isoprene and a source of secondary pollutants.

Acknowledgments

The authors are grateful to the State Committee for Scientific Research in Poland for the financial support of this work in the framework of Eureka/Eurotrac-2 project.

References

- McElroy, W.J. and S.J. Waygood, 1990. Kinetics of the reactions of the SO_4^- radical with SO_4^- , $S_2O_8^{2-}$, H_2O and Fe^{2+} . *J. Chem. Soc. Faraday Trans.* **86**, 2557.
- Rudzinski, K.J. and W. Pasiuk-Bronikowska, 1999. Consistency of rate constants for reactions of sulphonyl radicals with S(IV), in U. Schurath *et al.* (eds), *Proc. of Joint Workshop: Chemical Processes and Mechanisms-Chemical Mechanism Development*, Ford Forschungszentrum Aachen, Aachen, 199-202.
- Rudzinski, K.J., W. Pasiuk-Bronikowska and J. Krolik, 2002. Chemical interactions of precursors of tropospheric aerosols – SO_2 and isoprene, in P.M. Midgley, M. Reuther (eds), *Proc. from EUROTRAC-2 Symposium 2002*, Margraf Verlag, Werkheim, 1-4 (in print).

Fe-Catalysed Autoxidation of S(IV) Inhibited by Aliphatic Alcohols, Nonterpenic and Substituted with α -Pinene Skeletal Structure (APP8)

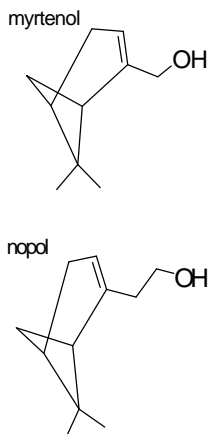
J. Ziajka and W. Pasiuk-Bronikowska

Institute of Physical Chemistry, Polish Academy of Sciences

Kasprzaka 44/52, 01-224, Warsaw, Poland

az@ichf.edu.pl

Introduction



Alcohols are common VOCs both in urban and in rural atmosphere (Isidorov, 2000). Since they belong to the group of organics rather well water soluble, the reactivity of alcohols with respect to intermediates in S(IV) autoxidation may have a bearing on acidity formation in clouds. The aim of this work is to elucidate the monoterpene alcohol inhibition of the S(IV) autoxidation by comparing the behaviour of myrtenol ($C_{10}H_{15}OH$) and nopol ($C_{11}H_{17}OH$) with that of ethanol (C_2H_5OH) and 2-propanol (C_3H_7OH). Results of laboratory experiments on the rate of S(IV) autoxidation in the presence of these alcohols are interpreted using the equation derived by Alyea and Bäckström, 1929, brought into relationship with the actual mechanistic knowledge on the reactivity of the inhibitors with respect to sulphate radicals (Clifton and Huie, 1989).

Experimental results

Laboratory investigations of the effect of aliphatic alcohols described previously (Warneck *et al.*, 1994, Ziajka and Pasiuk-Bronikowska, 2000) were continued to collect more data, particularly those related to the alcohols substituted with α -pinene skeletal structure.

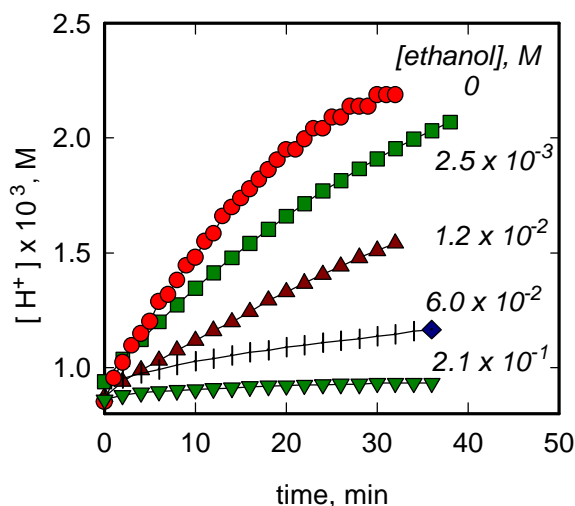


Figure 1: The hydrogen ion concentration-time plots for the autoxidation of S(IV) inhibited by ethanol (heterogeneous system, pH electrode). Initial experimental conditions were: S(IV) $2.0 \times 10^{-3} M$, Fe^{III} $1 \times 10^{-5} M$, pH 3.0, $25^\circ C$.

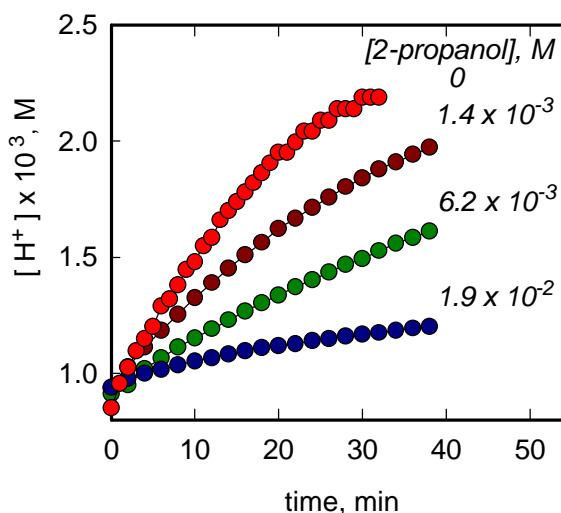


Figure 2: The hydrogen ion concentration-time plots for the autoxidation of S(IV) inhibited by 2-propanol (heterogeneous system, pH electrode). For experimental conditions see the caption to Fig. 1.

Figures 1 and 2 show the H^+ concentration, a measure of the extent of S(IV) autoxidation, increasing with reaction time, respectively, for ethanol and 2-propanol introduced to the reacting system. It is evident that in both cases initial rate of S(IV) autoxidation falls down with the rising concentration of alcohol (this rate is determined as a slope of the tangent to the experimental curve at time equal to zero).

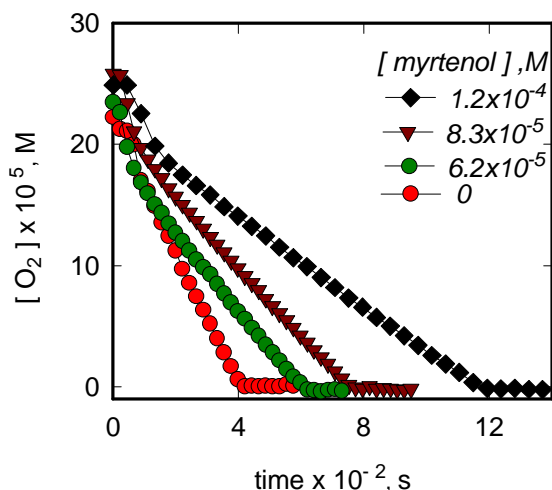


Figure 3. The oxygen concentration-time plots for the autoxidation of S(IV) inhibited by myrtenol (homogeneous system, oxygen sensor). For experimental conditions see the caption to Fig. 1.

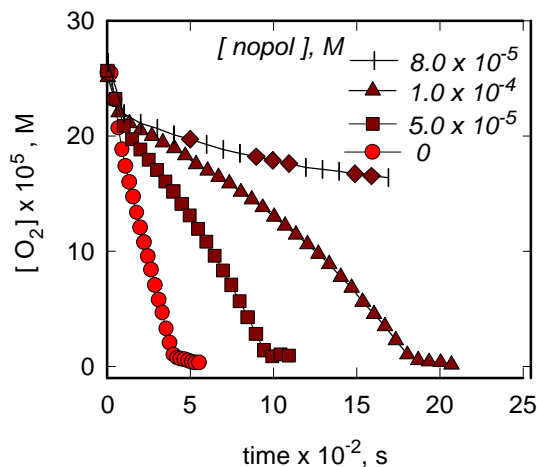


Figure 4. The oxygen concentration-time plots for the autoxidation of S(IV) inhibited by nopol (homogeneous system, oxygen sensor). For experimental conditions see the caption to Fig. 1.

Figures 3 and 4 show, respectively, the influence of myrtenol and nopol on the rate of S(IV) autoxidation (in this event we consider the rate of S(IV) autoxidation found as a doubled slope of the straight-line portion of the oxygen concentration-time curve, taken with a reversed sign). These figures also indicate that the higher concentration of an alcohol causes the deeper drop of the reaction rate. However, in the case of nopol the initial rate of oxygen consumption increases in time and, as results from sulphur and oxygen balances, exceeds that calculated from the stoichiometry of the overall reaction studied.

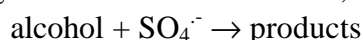
Discussion

As known, the inhibition of S(IV) autoxidation by such alcohols as ethanol and 2-propanol obeys the Alyea and Bäckström equation :

$$1/r = 1/r_0 + B[\text{alc}]$$

where r and r_0 are, respectively, the rate of S(IV) autoxidation in the presence of an inhibitor and the rate of uninhibited autoxidation of S(IV), B is a constant and alc denotes the inhibiting alcohol. In our case $r = r_H = d[H^+]/dt$ or $r = -2d[O_2]/dt = 2r_{O_2}$.

Attempts to confirm the validity of the Alyea and Bäckström equation with respect to our results are presented in Figs. 5 and 6. It immediately emerges that nopol behaves differently than other alcohols tested. These figures also give values of rate constant, k_{sc} for the step:



calculated using the kinetic model described previously (Ziajka and Pasiuk-Bronikowska, 2000).

As results from the comparison of the inhibition effectiveness exerted by the investigated alcohols (Fig. 7.), those with the substituted α -pinene skeletal structure are much stronger inhibitors than the non-terpenic ones. The rate constants found in this work for ethanol and 2-propanol roughly agree with those known from literature (Neta *et al.*, 1988).

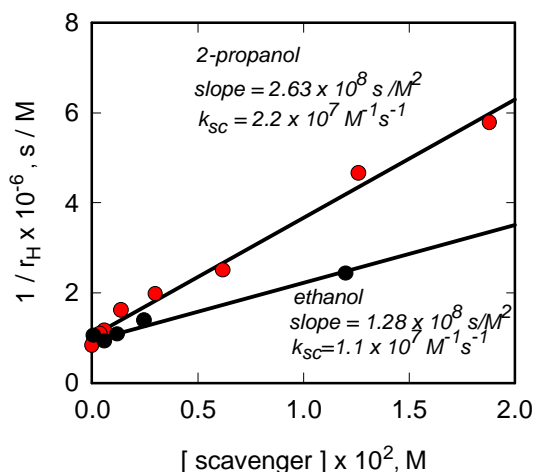


Figure 5: Consistency of the experimental results obtained for nonterpenic aliphatic alcohols: ethanol and 2-propanol with the equation derived by Alyea and Bäckström, 1929: r_H is the rate of hydrogen ion formation equivalent to the rate of S(IV) production, r . The figure indicates also values of k_{sc} afforded by the appropriate slopes.

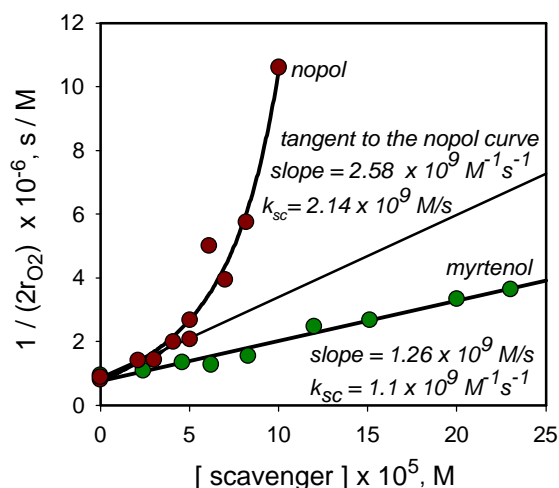


Figure 6: Consistency of the experimental results obtained for monoterpenic aliphatic alcohols: myrtenol and nopol, with the equation derived by Alyea and Bäckström, 1929 (r_{O_2} is the rate of oxygen consumption).

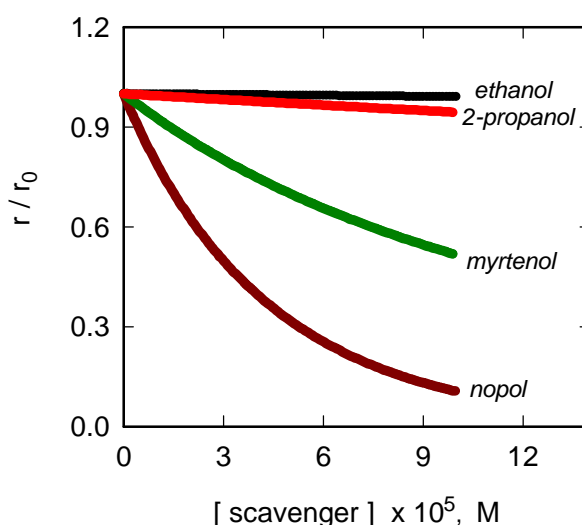
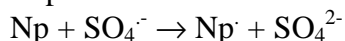


Figure 7: Comparison of the inhibition effectiveness by the monoterpenic alcohols with that by the nonterpenic ones (the curves approximate experimental data). The effectiveness is expressed as the doubled oxygen consumption or hydrogen ion production rate, r to the initial S(VI) production rate, r_0 ratio.

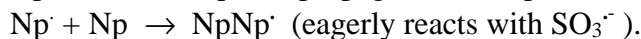
Conclusions

1. The substitution of alcohols with α -pinene skeletal structure drastically changes the activity of substituted alcohols with respect to sulphate radicals. We understand that the hydrogen abstraction mechanism characteristic for simple alcohols is no longer operative and its role is overtaken by the mechanism of radical addition to a double bond of the substituent.

2. It results from the behaviour of the S(IV) autoxidation in the presence of nopol (Np) that secondary competitive reactions occur kinetically important. We suggest that primary inhibiting step:



is followed by:



Aknowledgement

The authors gratefully acknowledge the financial support by the State Committee for Scientific Research in Poland.

References

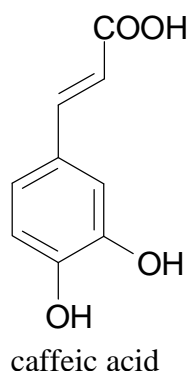
- Alyea, H. N. and H. I. J. Bäckström, 1929: The inhibitive action of alcohols on the oxidation of sodium sulfite. *J. Am. Chem. Soc.* **51**, 90-107.
- Clifton, C. L. and R. E. Huie, 1989: Rate constants for hydrogen abstraction reactions of the sulfate radical $\text{SO}_4^{\cdot-}$. Alcohols. *Int. J. Chem. Kinet.* **21**, 677-687.
- Isidorov, W. A. , 2001: *Organic Chemistry of the Atmosphere*. Khimizdat, St. Petersburg (Rus.).
- Ziajka, J. and W. Pasiuk-Bronikowska, 2000: Myrtenol as an inhibitor of S(IV) autoxidation, in: *Proc. of EUROTRAC-2 JOINT WORKSHOP : EC Cluster4: "Chemical Mechanism Development"*, Lausanne, pp. 152-155.
- Warneck, P., J. Ziajka, W. Pasiuk-Bronikowska, 1994: Scavenger of $\text{SO}_4^{\cdot-}$ in S(IV) autoxidation catalyzed by Fe, in: G. Ageletti, G. Restelli (eds), *Physico-chemical Behaviour of Atmospheric Pollutants. Proc. 6th European Symp. '93, vol. 2*, Brussels, pp. 901-906.

Kinetics of the Mn-Catalysed Autoxidation of S(IV) Inhibited by Caffeic Acid as a Representative of Polyphenols (APP8)

M. Krajewska and W. Pasiuk-Bronikowska

*Institute of Physical Chemistry, Polish Academy of Sciences,
Kasprzaka 44/52, 01-224 Warsaw, Poland
wpb@ichf.edu.pl*

Introduction



The characteristic feature of radical chain reactions is their susceptibility to even trace amounts of foreign substances that are capable to enter the net of chain steps. The kinetics of S(IV) autoxidation is very sensitive to the presence of such contaminants as transition metal ions (catalysts) and some organic substances (inhibitors). The role of transition metal ions is rather well understood, whereas the action of organic compounds may lead to a variety of effects not fully explored. In this work we study the effect of polyphenols. The term 'polyphenol' is understood as a substance which possesses an aromatic ring bearing more than one hydroxy functions and, moreover, functional derivatives such as esters, methyl ethers etc. These compounds, the main source of which are plants, can contribute to organic aerosols (Hoffmann, 2001). Caffeic acid (3-(3,4-dihydroxyphenyl)-2-

propenoic acid), chosen as a model polyphenolic compound, represents also carboxylic acids, compounds detected among secondary products of atmospheric degradation of biogenic and anthropogenic hydrocarbons (Chien *et al.*, 1998).

As shown in our previous communications, caffeic acid (CAF) may decrease the formation of S(VI) by scavenging sulphonyl radicals and by chelating and reducing transition metal ions (Pasiuk-Bronikowska *et al.*, 2001, Krajewska *et al.*, 2002). Now, we try to derive the rate law governing the S(IV) autoxidation at caffeic acid inhibition.

Experimental results

We performed laboratory experiments to determine the overall reaction orders with respect to oxygen, hydrogen sulphite, caffeic acid and manganese sulphate, the latter applied as a catalyst. The experiments were carried out in a gradientless reactor (4 ml volume) at 25°C and pH ≤ 5 in aqueous solutions. The extent of reaction was determined from the decrease in O₂ concentration measured with the Clark-type electrode (Fig.1). The experimental results were discussed with the view to bind them with the chain mechanism of the studied reaction. Figures 2-5 show subsequent steps in arranging the rate expression.

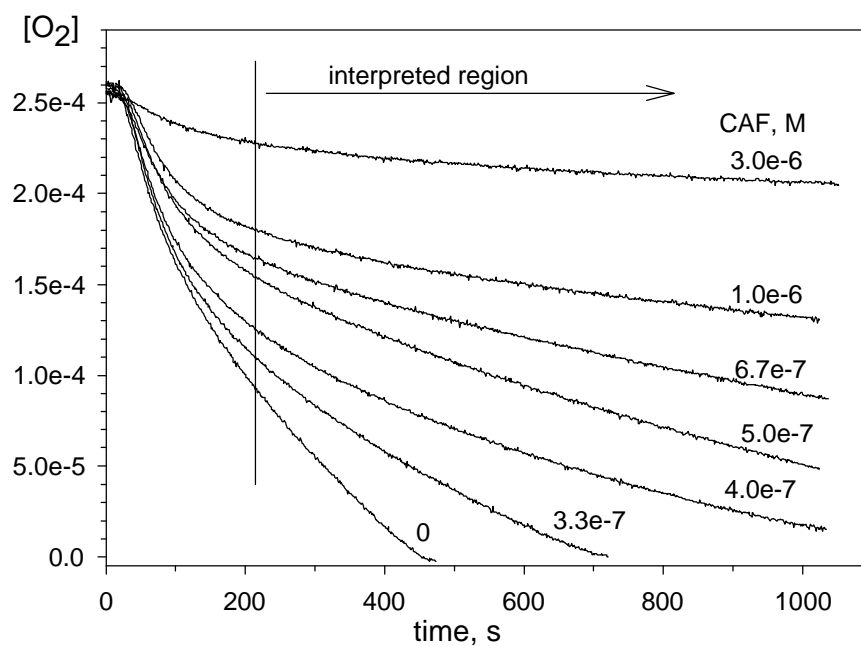


Figure 1. Kinetic plots for the autoxidation of S(IV) catalysed by Mn(II) at different CAF concentrations (all experiments at initial S(IV) 1.5×10^{-3} M and Mn(II) 3×10^{-5} M).

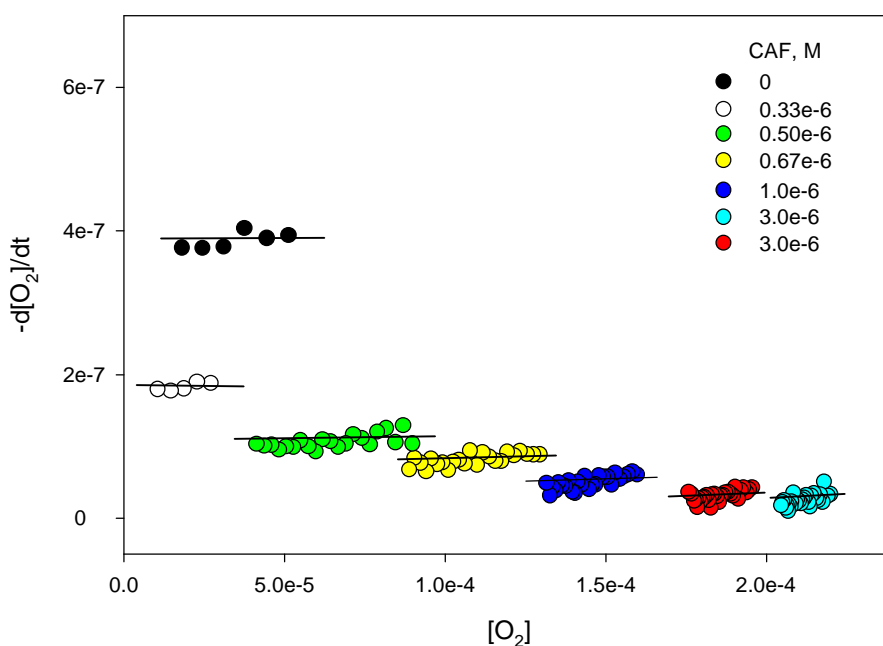


Figure 2. Experimental evidence for the zero-order reaction with respect to oxygen: Mn(II) catalysed autoxidation of S(IV) at different CAF concentrations, initial S(IV) 1.5×10^{-3} M and Mn(II) 3×10^{-5} M.

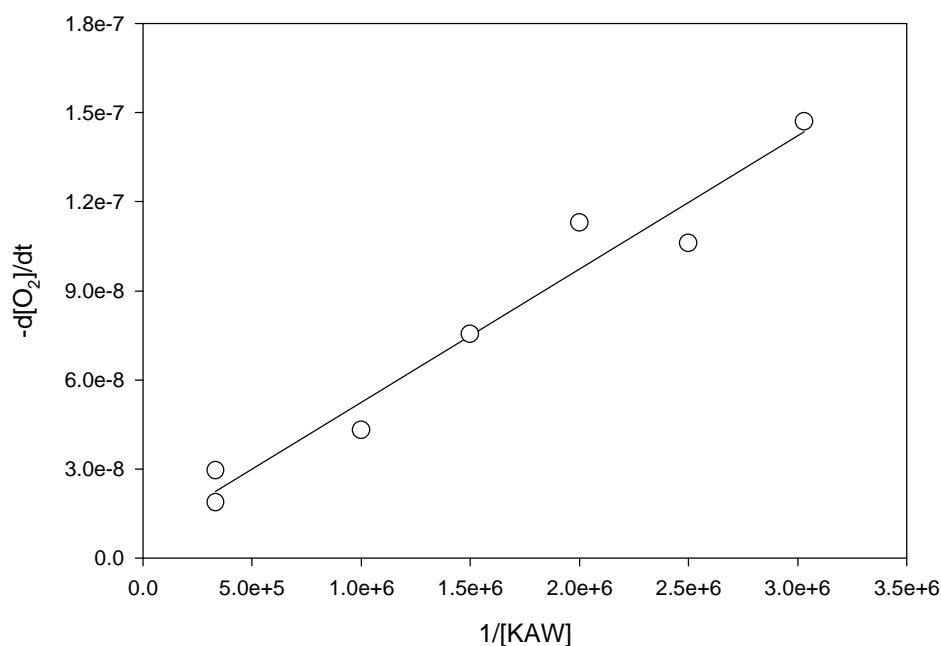


Figure 3. Experimental evidence for the reciprocal first-order dependence of the S(IV) autoxidation rate on the caffeic acid concentration (all experiments at initial S(IV) $1.5 \times 10^{-3}M$ and Mn(II) $3 \times 10^{-5}M$).

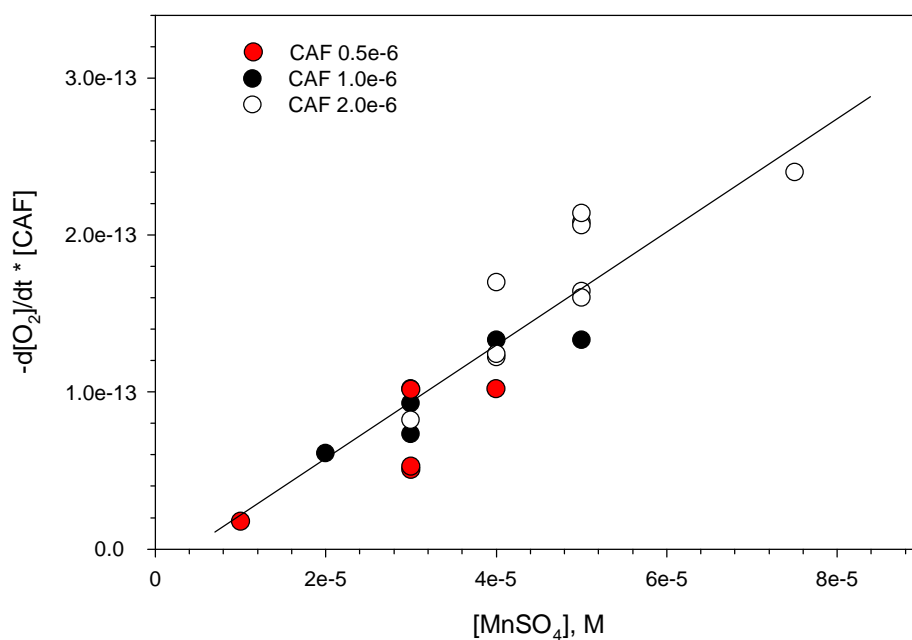


Figure 4. Experimental results showing the first-order reaction with respect to Mn(II) for different CAF concentrations (all experiments at initial S(IV) $1.5 \times 10^{-3}M$).

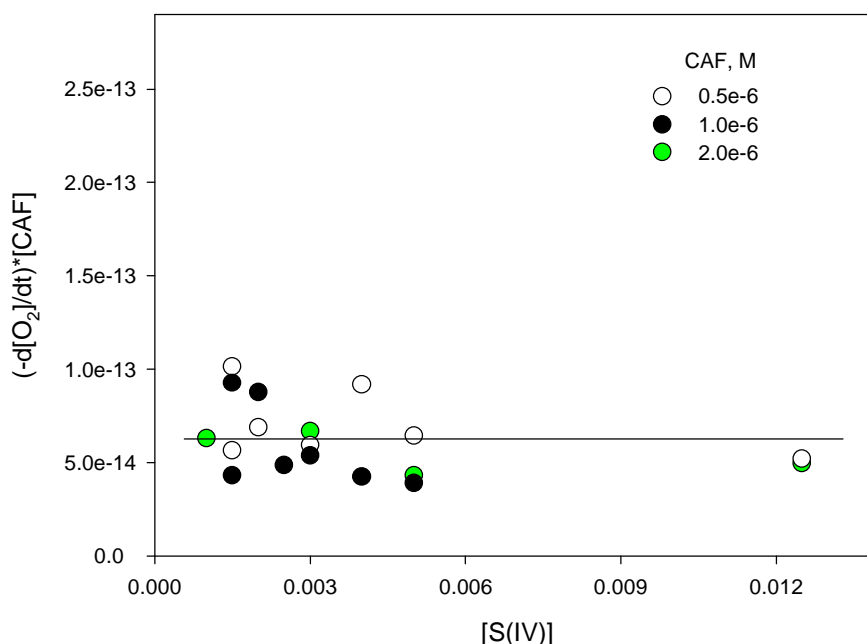


Figure 5. Results of measurements indicating zero-order dependence of S(IV) autoxidation rate on the concentration of S(IV): different CAF concentrations, all experiments at Mn(II) 3e-5M.

Reaction mechanism

The rate law was derived based on a chain mechanism under the following main assumptions:

- the rate of chain initiation depends on the rate of manganese-cafeic acid complex formation;
- the overall reaction rate is controlled by the propagation step involving SO_5^- and HSO_3^- ;
- the dominating termination route is by the reaction between SO_4^- and the radical of caffeic acid dimer.

The resulting rate law is:

$$r_{\text{aut}} = k_{\text{aut}} \frac{[\text{Mn(II)}]}{[\text{CAF}]}$$

where $k_{\text{aut}} = k_p \frac{k_i}{K_i k_t K_t}$ and the rate constants and equilibrium constants are related to

the appropriate steps: p – propagation, i – initiation, t – termination (for details see: Krajewska, 2002).

This rate law is compared to the broad family of kinetic expressions for the uninhibited Mn-catalysed autoxidation of S(IV) known from literature (Table 1).

Conclusions

1. The role of labile complexes formed by polyphenols with transition metal ions may be significant in the catalysis of atmospheric aqueous-phase processes involving S(IV).
2. Secondary organic radicals generated in the atmospheric aqueous phase by sulphony radical scavenging should be further examined as they may occur very active in subsequent radical reactions.
3. The variety of rate laws experimentally determined for the Mn(II)-catalysed autoxidation of S(IV) may suggest, that in the case of some of them the reaction was affected by trace impurities not recognised by experimenters.

Table 1. Review of rate laws determined for the Mn(II) catalysed autoxidation of sulphur (IV) in aqueous solution (Krajewska, 2002).

Rate law r_{aut} = right side of rate equation	Concentration		pH	Source
	Mn(II), $\text{M} \cdot 10^{-6}$	S(IV), $\text{M} \cdot 10^{-3}$		
12	700-6600	1.2-2.3	~2.5-3	Coughanowr <i>et al.</i> , 1965 ^e
$4.2 \times 10^{-5} [\text{Mn(II)}]^{0.5}$	0.1-5	1	3-5	Wilkoosz <i>et al.</i> , 1991
$0.41 [\text{Mn(II)}]^{1.25}$	5-10	1	3-5	Wilkoosz <i>et al.</i> , 1991
$6 \times 10^2 [\text{Mn(II)}]^{1.7-2.0}$	3-80	1-10	2.5-3.5	Hoather <i>et al.</i> , 1934 ^a
$420 [\text{Mn(II)}]^2$	40-100	1.2-2.3	~2.5-3	Coughanowr <i>et al.</i> , 1965 ^e
$5.1 \times 10^3 [\text{Mn(II)}][\text{S(IV)}]$	1-4	0.004-0.015	3-6	Ibusuki <i>et al.</i> , 1984
$2.5 \times 10^{-2} [\text{Mn(II)}][\text{S(IV)}]^{0.65}$	1.8-7	0.1	3-6	Grgiè <i>et al.</i> , 1991
$1.3 \times 10^{-5} [\text{Mn(II)}]/[\text{H}^+]$	231-414	0.13-1.9	1.4-2	Neytzell deWilde <i>et al.</i> , 1958
$4.7 [\text{Mn(II)}]^2/[\text{H}^+]$	10-1000	0.1-1	0-3	Martin, 1984
$1.34 \times 10^{-2} [\text{Mn(II)}]/[\text{H}_2\text{SO}_4]$	1000-3000	high	acidic	Hartley, 1973
$k_1 [\text{Mn(II)}]^2 + k_2 [\text{Mn(II)}][\text{HSO}_3^-]$	10-1000	1-150	0.5-4	Huss <i>et al.</i> , 1982 ^b
$[\text{Mn(II)}]^2/(2.67 \times 10^{-4} + 3.3 \times 10^{-3} [\text{H}_2\text{SO}_4])$	892-6370	high	acidic	Pasiuk-Bronikowska <i>et al.</i> , 1981
$25 [\text{Mn(II)}][\text{S(IV)}]/[\text{H}^+]$	10-1000	<0.001	0-3	Martin, 1984
$43 [\text{O}_2][\text{S(IV)}]^{0.5} [\text{Mn(II)}]^{0.5}$	10-75	0.4-5	5	Pasiuk-Bronikowska <i>et al.</i> , 2000
$[\text{Mn(II)}]^2[\text{O}_2]/(1.2 + 0.198 [\text{O}_2][\text{H}_2\text{SO}_4])$	892-6370	high	acidic	Pasiuk-Bronikowska <i>et al.</i> , 1981
$3.5 \times 10^{-3} [\text{HSO}_3^-]^2 + 1.23 [\text{HSO}_3^-][\text{Mn(II)}] + 89.6 [\text{Mn(II)}]^2$	1-140	1.5-12	4.5	Connick <i>et al.</i> , 1996
$C(\text{HSO}_3^-)(3.3 \times 10^{-2} ([\text{Mn(II)}] + 34 [\text{Mn(II)}]^2)/(5 \times 10^{-5} + [\text{Mn(II)}]))$	1-1500	0.023	4.0	Berglund <i>et al.</i> , 1993 ^c
$1.3 \times 10^6 [\text{Mn(II)}]C(\text{HSO}_3^-) ([\text{Mn(III)}]_0 + [\text{Fe(III)}]_0) / (0.33 \times 10^{-4} + [\text{HSO}_3^-] + [\text{Mn(II)}])$	1-1500	0.023	2.5	Berglund <i>et al.</i> , 1993 ^{c,d}
$1.6 \times 10^{-4} [\text{Mn(II)}]/[\text{H}^+] + 21 [\text{Mn(II)}]^2/(1 + 9.3 \times 10^4 [\text{S(IV)}][\text{H}^+]) + 9.8 \times 10^{-2} [\text{Mn(II)}][\text{H}^+][\text{S(IV)}]/(1 + 8.9 \times 10^3 [\text{S(IV)}])$	1-1000	0.05-4	0-2	Collins, 1987

a – the rate constants are taken from the compilation by Collins, 1987

b – k_1 , k_2 are the ionic strength functionsc – $C(\text{HSO}_3^-) = [\text{HSO}_3^-] + [\text{MnHSO}_3^+]$ d – $[\text{Mn(III)}]_0$, $[\text{Fe(III)}]_0$ – initial concentration of Mn(III) and Fe(III), respectively

e – calculated by the authors of this work

References

- Chien, C.J., M.J. Charles, K.G. Sexton, H.E. Jeffries, 1998: Analysis of airborne carboxylic acids and phenols as their pentafluorobenzyl derivatives: Gas chromatography ion trap mass spectrometry with a novel chemical ionization reagent, PFBOH. *Environ. Sci. Technol.* **32**, 299-309.
- Hoffmann, T., 2001: Organic aerosols: origin, composition and influence on tropospheric processes. In: P.M. Midgley, M. Reuther, M. Williams (eds.), *Proc. EUROTRAC-2 Symposium 2000*, Springer, Berlin, pp.132-142.
- Krajewska, M., W. Pasiuk-Bronikowska, 2002: Reactivity of secondary organic pollutants towards SO₂ by example of caffeic acid. In: P.M. Midgley, M. Reuther (eds.), *Proc. EUROTRAC-2 Symposium 2002*, Margraf Verlag, Wiesbaden 2002, enclosed CD, pp 1-5.
- Krajewska, M., 2002: Kinetics of the coupled autoxidation of S(IV) and polyphenol by example of caffeic acid. *PhD Thesis*, Warsaw (in Polish).
- Pasiuk-Bronikowska, W., M. Krajewska, T. Bronikowski and M. Ulejczyk, 2001: Interaction between secondary organic compounds and sulphony radicals. In: P.M. Midgley, M. Reuther, M. Williams (eds.), *Proc. EUROTRAC-2 Symposium 2000*, Springer, Berlin, pp. 1-4.

Aqueous phase radical chemistry of new oxygenated solvents Experimental developments (APP15)

Davy Rousse, Rafal Strekowski and Christian George

*Laboratoire d'Application de la Chimie à l'Environnement (UCBL-CNRS) 43 boulevard du 11
Novembre 1918, F-69622 Villeurbanne, France*

E-mail: christian.george@univ-lyon1.fr

Introduction

The Earth's atmosphere may be thought of as a homogeneous gas phase system with a very rich chemistry (Finlayson-Pitts and Pitts, 2000). In fact, one could speculate a very small impact of condensed matter on atmospheric chemistry just by considering the very small fractional volume it occupies (less than 10^{-6} !). However, it is now well known that the real atmospheric impact of heterogeneous (surface reactions) or multiphase (uptake by liquid and subsequent liquid phase reactions) chemistry is quite large (Ravishankara, 1997). This disproportionate impact is due to the rich atmospheric chemistry mentioned above that is different in many aspects to homogeneous gas phase chemical conversions.

Both, in the gas phase and in aqueous droplets such as those encountered in hydrometeors, the hydroxyl radical is the most important daytime oxidizing agent responsible for the atmospheric degradation of most of the volatile organic compounds (VOCs) (Huie, 1994). The kinetics of OH toward a large number of organic species have been reported (see for example the readily available solution kinetic data base (Ross et al., 1998)). Although many room temperature studies of the kinetics of the OH + C₁ to C₂ compounds or OH + long chain hydrocarbons (i.e., of biologic interest) reactions are reported in the literature⁵, very few reactions and temperature dependance studies have been performed for the reactions of OH with the intermediate sized aliphatic compounds (i.e., C₂ – C₁₀), and especially for the reactions of OH with organics containing oxygenated polyfunctional groups. The interest in the OH reactions mentioned above stems from the fact the intermediate length carbon chain and oxygenated hydrocarbon compounds are expected to be increasingly used in the industry in order to favour water based technology. To date, the atmospheric fate of these compounds is not known. In the atmosphere these compounds are likely to be involved in multiphase chemistry and be removed via the attack by OH.

Experimental

Teflon AF waveguides

Often when studying liquid phase reactions, when light passes through a reaction cell windows between two White cell mirrors, energy (or light) is lost on the windows. This problem may be overcome by using long-path cells without windows. This can be achieved by using a liquid core waveguide (henceforth called LCW). For practical reasons (discussed in the following section), the LCW must (1) have a relatively small diameter, (2) be flexible, (3) be transparent to UV radiation (used to produce OH radicals) and (4) have a refraction index lower than the one of water i.e., $n=1.33$. The latter condition is essential for the LCW in order to allow total internal reflection and therefore conduction of light.

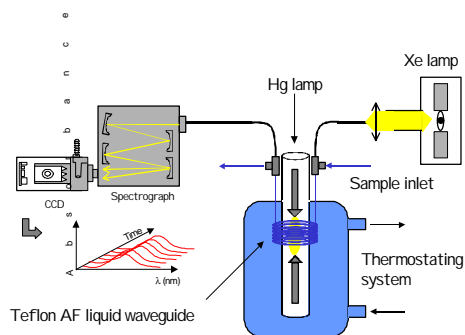


Fig. 1 Schematic drawing of the LCW micro-flowtube.

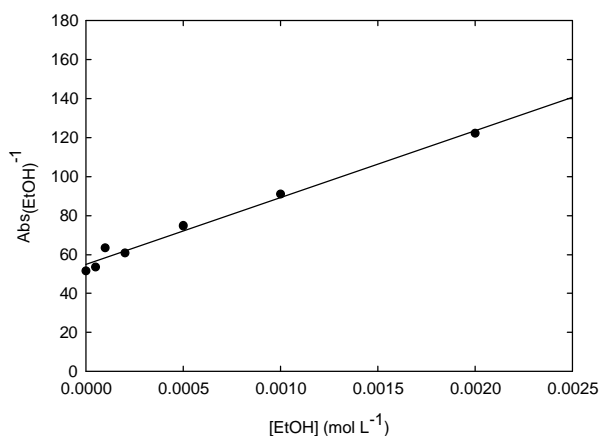


Fig. 2 A plot of the inverse of the absorbance of ethanol as a function of the ethanol concentration (according to equation 1). The slope of the fitted line is a measure of the ratio of the reference to ethanol rate constants.

Again, the centerpiece of the experimental set-up is a liquid core waveguide made of Teflon AF 2400 (from BioGeneral, San Diego, CA) with an inner and outer diameter of 200 μm and 800 μm , respectively. The length of the LCW was varied in the course of the study between 30 and 90 cm. In all cases, the internal volume was far less than 0.1 ml for a maximum optical path of 90 cm. This highlights already the first major benefit of using LCW compared to standard white cells for studying radical chemistry. A good white cell can achieve a maximum pathlength of a few meters (which requires already Lasers with a certain output at the wavelength of interest) in a volume of about 50-100 ml, which requires much larger flowrates to replenish the cell between the laser flashes. Briefly, LCW can achieve much longer optical pathlengths in much smaller volumes without requiring powerful light sources as those required in standard white cells for liquids. The application of these LCW for laser flash photolysis will be demonstrated in a forthcoming paper.

Experimental set-up

The Teflon waveguide photolysis system used for the reaction of OH with methanol, ethanol, tetrahydrofuran, dimethylmalonate, dimethylsuccinate, dimethylcarbonate and diethylcarbonate is shown schematically in Figure 1. The highly flexible Teflon AF 2400 tubing was loosely coiled (~ 4 cm diameter) around a 3 cm o.d. pyrex tube. The radiation from a medium pressure mercury UV lamp (Hereaus Noblelight, TQ150, 150W) located within the pyrex tube served as the photolytic light source. The cell was maintained at a constant temperature (± 0.5 K) by circulating water flowing from a thermostatically controlled Huber cc230 cryostat bath.

The OH radicals are generated within the LCW from the photodissociation of hydrogen peroxide (H_2O_2). The concentration of OH radicals in the aqueous phase was not directly measured but derived from the "titration" reaction used in the kinetic competition approach (see below). Typical OH concentrations were about 10^{-8} M.

The solution content of the LCW was analysed using UV-visible absorption spectroscopy simultaneously coupled with the photodissociation described above. Briefly, both ends of the Teflon AF capillary were connected to T-connectors which allowed the injection of both the white light and the solution (see Figure 1).

In order to probe the solution contents of the LCW tube, the output of a 75 W Xenon lamp (Lot-Oriel) was focused on the entry of a 100 μm diameter silicium optical fiber. The silicium optical fiber was held in the liquid content of the LCW tube. Then, the conducted light escaped the solid optical fiber but was then collected in the liquid core waveguide. The liquid core waveguide conducted the light up to its end where another silicium optical fiber (located in the liquid) collected most of this transmitted light. This second solid optical fiber then conducted the light to the entry of a spectrograph (Lot-Oriel, 127i) coupled to a CCD camera (Andor Technology). The CCD allowed

us to monitor the evolution of the uv-visible spectrum as a function of wavelength and residence time within the LCW. The $(\text{SCN})_2^-$ spectra were recorded in the wavelength range from 300 to 800 nm.

Using the experimental setup geometry listed above, the recorded spectra integrated the absorption of light over the entire length of the LCW (i.e., over time). However, computer simulations showed that the steady state is reached within a few milliseconds (i.e., a few millimeters of length of the LCW). This is beyond our sensitivity and will not affect our kinetic determination of the rate coefficient. We, therefore, believe that the integrated spectra can be safely attributed to the steady-state conditions.

The observed spectra were corrected by subtracting the mercury bands trapped in the LCW during the photolysis of H_2O_2 .

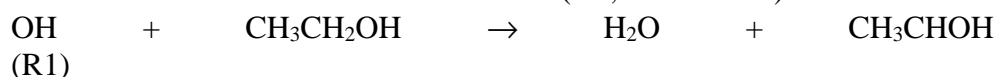
Competition kinetics

Since hydroxyl radical absorbs weakly in the visible, it cannot be directly measured (at least when other absorbing compounds are present). Therefore, the OH radical concentration (or its time evolution) has to be probed indirectly. This is commonly achieved using competition reaction kinetics. Among several potential competitors, the thiocyanate anion has been chosen because the product of its reaction with the OH radical (i.e., $(\text{SCN})_2^-$) exhibits the strongest extinction coefficient ($\epsilon(475\text{nm})=7600 \text{ M}^{-1} \text{ cm}^{-1}$) (Chin and Wine, 1992).

Results and discussion

OH+Ethanol

Many room temperature studies of the kinetics of the OH + ethanol reaction are reported in the literature. The absorbance of $(\text{SCN})_2^-$ as a function of ethanol concentration and wavelength was observed to decrease as a function of ethanol concentration. This is in agreement with the fundamentals of the competition kinetics. A plot of the inverse of the absorbance of $(\text{SCN})_2^-$ at 480 nm is shown in Figure 2. The fit is obtained from linear least squares analyses to equation (1). From the slope of a linear fit to equation (1), we can extract the ratio of the rate coefficients. Then, if we know the reference kinetic rate coefficient for the reaction of OH with thiocyanate, we can determine the rate coefficient for the reaction of OH with ethanol (i.e., reaction R5).



The measured rate coefficient for the reaction of OH with ethanol at 298 K is found to be $1.9 \cdot 10^9 \text{ M}^{-1} \text{ s}^{-1}$ which compares very well with the available literature data ranging from 1.8 to $2.2 \cdot 10^9 \text{ M}^{-1} \text{ s}^{-1}$.

Based on the results obtained in this work for the reaction of OH with ethanol we can state with confidence that the new experimental approach used in this study gives results that are in excellent agreement with the previously reported data using other well established techniques.

OH+Methanol

The kinetics of the reaction of OH with methanol (R6) have been studied before.



However, the agreement among the reported values for the rate coefficient for the reaction of OH with methanol is less clear than the reported values for the reaction of OH with ethanol. As a result, further investigations are warranted to better define the rate coefficient for the removal of OH by methanol.

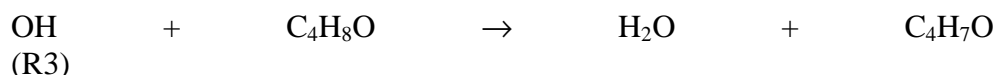
Similar to the procedure described for the reaction of OH with ethanol, the rate coefficient for the reaction of OH with methanol at 298 K is found to be $1.3 \times 10^9 \text{ M}^{-1} \text{ s}^{-1}$. Steady-state conditions applied when the methanol concentration was changed from 0 to 2 mM under typical experimental conditions applied. M. The reported room temperature rate coefficient for the reaction of OH with methanol falls within the upper limit of the previously reported room temperature data (ranging from 7 to $1.2 \cdot 10^9 \text{ M}^{-1} \text{ s}^{-1}$) but within the error limits of the individual studies. Also, certain room temperature studies failed to give specific experimental conditions or the specific experimental

conditions were impossible to extract. At least part of the variations among previously reported data for the rate coefficient for the reaction of OH with methanol can be attributed to temperature effects. A closer look to previously reported data also reveals that the highest reported values (for example $1.2 \cdot 10^9 \text{ M}^{-1}\text{s}^{-1}$ (Adams et al., 1965)) were obtained using SCN^- as the competitor (similar to our experimental conditions) and that higher values were measured at $\text{pH} < 7$. Under the experimental conditions employed, the temperature was monitored during each experiment and all reactions were carried out at $\text{pH} = 5$ in unbuffered solutions in order to minimise the number of chemical species in the cell. As a result, the rate coefficient for the reaction of OH with methanol reported here can only be compared with the work of Adams and coworkers. We find that the rate coefficient for the reaction of OH with methanol reported in this work is in excellent agreement with the previously reported value of $1.2 \cdot 10^9 \text{ M}^{-1}\text{s}^{-1}$ published by Adams *et al.* (Adams et al., 1965).

Again, based on the results obtained in this work for the reaction of OH with methanol we can report with confidence that the new experimental approach used in this study gives results that are in good agreement with the previously reported data using other well established and proven techniques.

OH+Tetrahydrofuran

The reaction of OH with tetrahydrofuran (R7) was the focus of only one previous investigation carried out by Eibenberger. (Eibenberger, 1980) These investigators reported a rate coefficient for (R3) of $3.8 \cdot 10^9 \text{ M}^{-1}\text{s}^{-1}$ at 298 K.

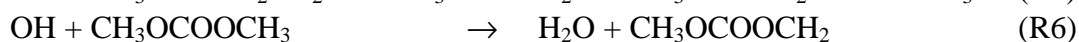


Similar to the experimental procedure described above for the reaction of OH with ethanol and methanol, the observed rate coefficient for the reaction of OH with THF at 298 K is found to be $4.0 \cdot 10^9 \text{ M}^{-1}\text{s}^{-1}$. This value is in excellent agreement with the data obtained by Eibenberger (Eibenberger, 1980). Under the experimental conditions employed, the tetrahydrofuran concentration was varied from 0 to 1 mM.

Since the reported rate coefficients for the reactions of OH with ethanol, methanol and THF show very good to excellent agreement with the literature data, we report with confidence that the new experimental approach used in this study is scientifically sound and reliable to be applied to carry out the following and any relative future liquid phase kinetic experiments.

Determination of new rate constants

The experimental approach described above was used to measure the bimolecular rate coefficients for the reactions of the OH radical with dimethylmalonate ($\text{CH}_3\text{OCOCH}_2\text{COOCH}_3$) (R4), dimethylsuccinate ($\text{CH}_3\text{OCOCH}_2\text{CH}_2\text{COOCH}_3$) (R5), dimethylcarbonate ($\text{CH}_3\text{OCOOCH}_3$) (R6) and diethylcarbonate ($\text{CH}_3\text{CH}_2\text{OCOOCH}_2\text{CH}_3$) (R7). Such atmospheric compounds are potentially formed as a byproduct in the gas phase degradation mechanism of various oxygenated species. The interest in the reactions of the OH radical with the four oxygenates listed above stems from the fact that these four particular compounds are possible end products resulting from fuel additive degradation mechanism. To date, the kinetic data is very sparse or nonexistent that helps in the evaluation of the chemical impact fuel additive degradation products will make on the environment. Quantification of the rates and mechanisms of even the minor sinks is important. In the atmosphere, the degradation of the dimethylmalonate, dimethylsuccinate, dimethylcarbonate and diethylcarbonate will most likely be governed by the attack by OH [i.e., reactions (R') – (R7)].



The rate coefficients for the reactions of OH with dimethylmalonate, dimethylsuccinate, dimethylcarbonate and diethylcarbonate carried out at T=295K are listed in Table 1. To our best knowledge, no kinetic data have been reported in the literature for the reactions (R4) – (R7) with which we can compare our results. However, it can be observed in Table 1, that the reactivity of the oxygenate toward the attack by OH may be linked to the steric environment of the –C(O)O– functional group.

Table 1 OH kinetics towards four oxygenates.

Organic species	Rate coefficients ^{a,b}
Dimethylcarbonate	$k_4 = 5.1 \pm 2.2 \times 10^7$
Diethylcarbonate	$k_5 = 7.9 \pm 3.2 \times 10^8$
Dimethylmalonate	$k_6 = 2.7 \pm 0.9 \times 10^8$
Dimethylsuccinate	$k_7 = 5.3 \pm 2.9 \times 10^8$

^a Rate coefficient unit is $M^{-1}s^{-1}$

^b Temperature=295 K

Conclusion

This work addressed the oxidation several oxygenated compounds by the hydroxyl radical using a newly developed experimental technique. The experimental approach described herein takes benefit of the novel liquid core waveguide technology of Teflon AF 2400. The physical nature of waveguides allow for the construction of photolysis reaction cells with extremely low volumes but potentially very long optical pathlengths. As a result, the Teflon waveguide photolysis system described here is potentially a very powerful cost-effective technique to study liquid phase chemistry with potentially very low detection limits of chemical transients in the aqueous phase.

Acknowledgments

Support of this work by the Programme National de Chimie Atmosphérique (PNCA) from the CNRS is gratefully acknowledged and the project PRIMEQUAL by the French Minister for Environment.

References

- Adams, G.E., J.W. Boag, J. Currant, and B.D. Michael, Absolute rate constants for the reaction of the hydroxyl radical with organic compounds, in *Pulse Radiolysis*, edited by M. Ebert, J.P. Keene, A.J. Swallow, and J.H. Baxendale, pp. 131-143, Academic Press, New-York, 1965.
- Chin, M., and P.H. Wine, 1992, A temperature-dependent kinetics study of the aqueous phase reactions $OH + SCN^- \rightarrow SCN + SCN^- \rightleftharpoons (SCN)_2^-$, *J. Photochem. Photobiol. A/ Chem.*, 69, 17-25.
- Eibenberger, J., Pulse radiolytic investigations concerning the formation and oxidation of organic radicals in aqueous solutions, Vienna, Vienna, 1980.
- Finlayson-Pitts, B.J., and J.N. Pitts, *Chemistry of the upper and lower atmosphere : theory, experiments, and applications*, xxii, 969 pp., Academic Press, San Diego, 2000.
- Huie, R.E., Free Radical Chemistry of the Atmospheric Aqueous Phase, in *Laboratory Studies of Atmospheric Heterogeneous Chemistry; Current Problems in Atmospheric Chemistry, Advances in Physical Chemistry Series*, edited by J.R. Barker, pp. 374-419, World Scientific, Singapore, 1994.
- Ravishankara, A.R., 1997, Heterogeneous and Multiphase Chemistry in the Troposphere, *Science*, 276 (5315), 1058-1065.
- Ross, A.B., W.G. Mallard, W.P. Helman, G.V. Buxton, R.E. Huie, and P. Neta, 1998, NDRL-NIST Solution Kinetics Database, National Institute of Standards and Technology (NIST), see all <http://www.rcdc.nd.edu>, Gaithersburg, MD.

Application of homogeneous and heterogeneous methods in the study of the reaction of HOBr and Br₂ with sulphur species (APP16)

Marcelo Barcellos da Rosa, Wolfgang Behnke and Cornelius Zetzsch

Fraunhofer Institut für Toxikologie und Aerosolforschung

Nikolai-Fuchs Str. 1, 30625, Hanover - Germany

e-mail: mbdarosa@ita.fhg.de and zetzsch@ita.fhg.de

Introduction

Heterogeneous (aqueous-phase) reactions of DMSO (CH₃SOCH₃), MSIA (CH₃SO₂H) and MSA (CH₃SO₃H) contribute to the oxidation of DMS (CH₃SCH₃) and decrease the yield of SO₂ (the relatively long-lived gaseous precursor of H₂SO₄ in the marine boundary layer) and increase the yield of non-sea-salt sulphate. Since DMS can suppress halogen activation in aerosol smog chamber experiments, information about reactions of sulphur species with bromine compounds in aqueous phase is required to explain the role of non-sea-salt sulphate in the Arctic during ozone depletion and to elucidate multiphase processes that govern the maintenance of the tropospheric aerosol (Behnke et al., 1998, Behnke et al., 1999, Campolongo et al., 1999, Katoshevski et al., 1999, Le Bras et al., 2000, Mozurkewich, 1995).

Objectives

1. To study the equilibrium of Br₂ as a function of pH in aqueous solution using UV spectroscopy;
2. To quantify the Henry's law coefficient of Br₂ on buffered aqueous solutions (pH ~ 3.0, 7.0 and 10.0) and on 1.0M and 5.0M NaCl using the wetted-wall flow tube (WWFT) technique;
3. To study the heterogeneous kinetics (uptake coefficient, γ) of Br₂ on solutions of sulphur compounds (DMS, DMSO, MSIA and MSA) at different temperatures using WWFT technique (note that MSIA and MSA dissociate to MSI⁻ and MS⁻ at pH > 2.0);
4. To observe the homogeneous kinetics of HOBr/BrO⁻ with DMS, DMSO, MSI⁻ and MS⁻ using the stopped-flow (SF) technique.

Equilibrium of Br₂ in aqueous solution

Bromine species in aqueous phase and the influence of pH were studied by UV spectroscopy in the pH-range between 0 and 12. The concentration of each species was obtained from linear combinations (Liu and Margerum, 2001)

$$A_j = \{\epsilon_{j1} \cdot c_1 + \epsilon_{j2} \cdot c_2 + \epsilon_{j3} \cdot c_3 \dots\}d = d \sum_{i=1}^n \epsilon_{ji} \cdot c_i$$

where the concentration of each bromine species was calculated from fits of reference spectra using: $\epsilon_{\text{Br}_2}(390\text{nm}) = 175 \text{ M}^{-1}\text{cm}^{-1}$ (Wang et al. 1994); $\epsilon_{\text{HOBr}}(265\text{nm}) = 87 \text{ M}^{-1}\text{cm}^{-1}$ (Soulard et al, 1981); $\epsilon_{\text{BrO}^-}(325\text{nm}) = 330 \text{ M}^{-1}\text{cm}^{-1}$ (Troy and Margerum, 1991); $\sigma_{\text{Br}_2}(415\text{nm}) = 6.9 \cdot 10^{-19} \text{ cm}^2 \text{ molecule}^{-1}$ (Maric et al.1994); $\epsilon_{\text{DMS}}(215\text{nm}) = 1,270 \text{ M}^{-1}\text{cm}^{-1}$ (Amels et al, 1997); $\epsilon_{\text{DMSO}}(215\text{nm}) = 530 \text{ M}^{-1}\text{cm}^{-1}$ (Amels et al, 1997); $\epsilon_{\text{MSI}^-}(210\text{nm}) = 3,700 \pm 500 \text{ M}^{-1}\text{cm}^{-1}$ (Barcellos da Rosa and Zetzsch, 2000); $\epsilon_{\text{MS}^-}(210\text{nm}) = 3.3 \pm 1.5 \text{ M}^{-1}\text{cm}^{-1}$ (Barcellos da Rosa and Zetzsch, 2000).

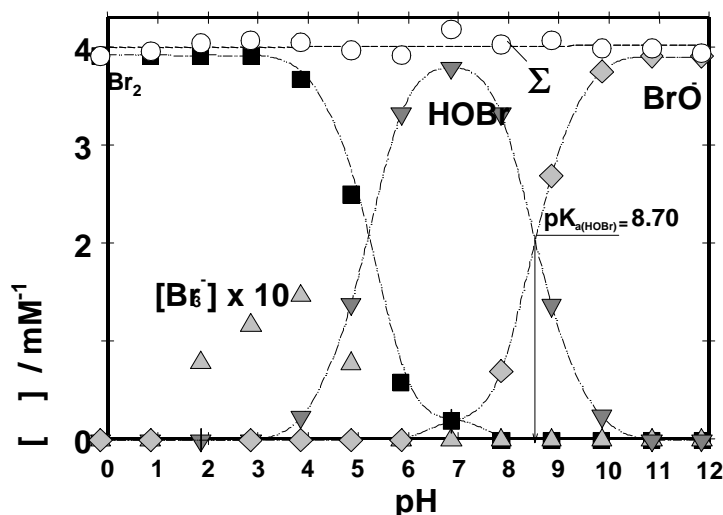


Figure 1. Bromine species in equilibrium at 293K in aqueous phase at various pH values

Wetted-Wall flow tube measurements

The EUROTRAC-HALIPP project (Warneck, 1996) reported on the wetted-wall flow tube technique (WWFT), described in detail by Danckwerts, 1970 for measurements of the uptake coefficient, g_g (the fraction of gas/liquid collisions that are effective in the uptake and/or chemical transformation, Katrib et al. 2001, Kulmala and Wagner, 2001, Vesala et al. 2001, Worsnop et al. 2001), to simulate chemical heterogeneous processes of the atmosphere experimentally in the laboratory (Behnke, et al. 1997, Frenzel et al. 1998, Fickert et al. 1999).

The Henry's law coefficient of Br_2 on aqueous solutions and on NaCl

The Henry's law coefficient of Br_2 was calculated from the equilibrium of a solution of Br_2 at several contact times of the liquid film in the WWFT with air, volatilising gaseous Br_2 in combination with the uptake of Br_2 on various aqueous solutions at different pH values (where a solution of (0.01-0.1M) Br_2 served as reservoir in a bubbler, passing the air through this solution directly into the WWFT). In the exit of the bubbler there is a faucet to alternatively monitor the level of Br_2 at the inlet or at the outlet of the WWFT. More details of the experimental set up are described in the **section 3** (heterogeneous reaction of Br_2 on sulphur compounds). The temperature dependence for the Henry's law coefficient was obtained from:

$$H = H^0 \exp(-\Delta H/R (1/T - 1/T^0)) / \text{M atm}^{-1}$$

and the principal results obtained for this measurements with the respectively temperature and pH dependence are presented in **Fig. 2**.

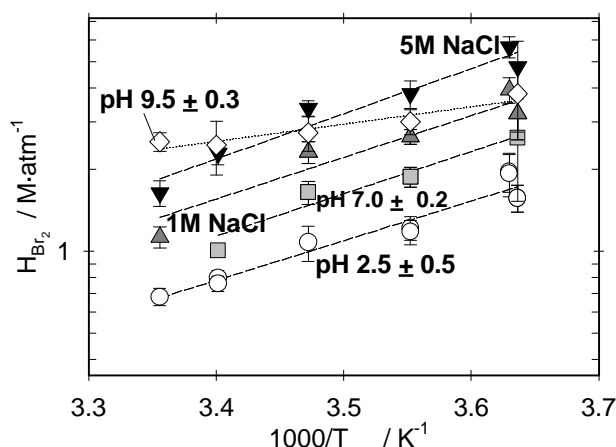


Figure 2: Temperature dependence and influence of pH on the Henry's law coefficient of Br₂ in buffered solutions.

Heterogeneous reaction (uptake coefficient) of Br₂ on DMS, DMSO, MSIA and MSA

The heterogeneous reactions Br₂ + sulphur compounds were studied measuring the uptake of Br₂ on various concentrations of sulphur compounds (see **Tab. 1**) at four temperatures obtaining the loss rate of Br₂ in air along a vertically aligned flow tube, the walls of which are conferred by a film of slowly flowing solutions of sulphur species, controlled by a peristaltic pump. The gas-phase inlet and outlet of the flow tube were made of PTFE tubing (outer diameter 0.6 cm, inner diameter 0.4 cm, length 140cm). The flow tube was made of Duran glass and had an inner diameter of 0.6 cm with a movable inlet to vary the contact time. The data analysis is based upon the assumption that the uptake rate is first order with respect to the gas phase concentration of the reacting species, i.e.,

$$C/C_0 = \exp [-k_{gas}t]$$

where **C**₀ and **C** are the concentrations at the entrance and outlet of the flow tube respectively, **t** is the average gas contact time, **k_{gas}** is the first-order loss rate constant from the gas to the liquid phase. For small uptake coefficients, the rate constant **k_{gas}**, obtained from such a plot is correlated to the uptake coefficient **γ** using simple gas kinetic theory:

$$k_{gas} = \gamma \cdot \langle c \rangle / 2r_{tube} \quad \text{where } r_{tube} \text{ is the flow tube radius } (r_{tube} = 3 \cdot 10^{-3} \text{ m})$$

The uptake coefficient, **γ**, of Br₂ with an average molecular speed, **<c>**, is given by the equation $\gamma = \frac{\text{molecules absorbed by the liquid layer}}{\text{molecules colliding with the liquid layer}} = \frac{4 \text{ HRT } (k^I D_{aq})^{1/2}}{\langle c \rangle}$ where $\langle c \rangle = (8 \text{ RT} / \pi \text{ M})^{1/2}$

It depends on the solubility of the gas, i.e. Henry's law constant, **H**, the temperature, **T**, the loss rate constant in the solution, **k^I** (**k^I** = **k^{II}** · **C**), the concentration of the dissolved molecule, **c**, and the diffusion coefficient of Br₂ in aqueous phase, **D_{aq}**. We adapted a calculated diffusion coefficient of Br₂ of **D_(aq)** = 1.27 · 10⁻⁵ cm²s⁻¹ at 291K (Reid et al., 1987) and the Henry's law constant to be **H** = 0.70 M atm⁻¹ at 298K (Mozurkewich, 1995).

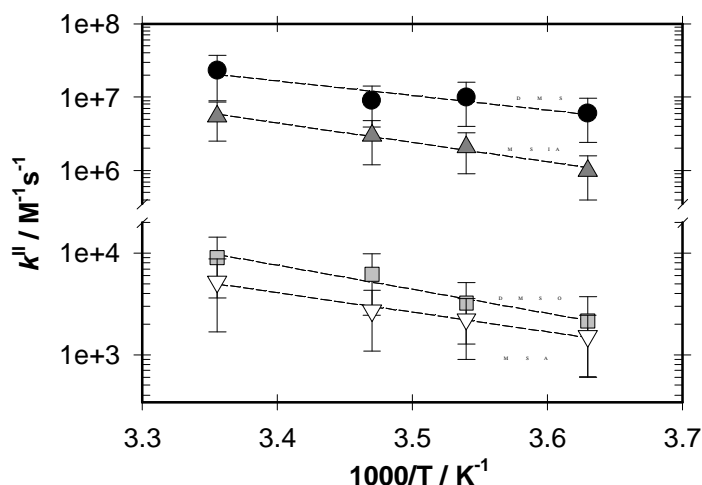


Figure 3: Temperature dependence of the second-order rate constant (k^{II}) for the reaction Br_2 + sulphur compounds

The homogeneous kinetics of HOBr/BrO^- with DMS, DMSO, MSIA and MSA

By stopped-flow measurements (SX18MV, Applied Photophysics) we determined the reaction rate of HOBr/BrO^- ($\text{pK}_a = 8.7$, Beckwith, et al, 1996) at different temperatures and concentrations of HOBr/BrO^- and sulphur compounds. The principal experimental conditions and results are presented in **Tab. 2**.

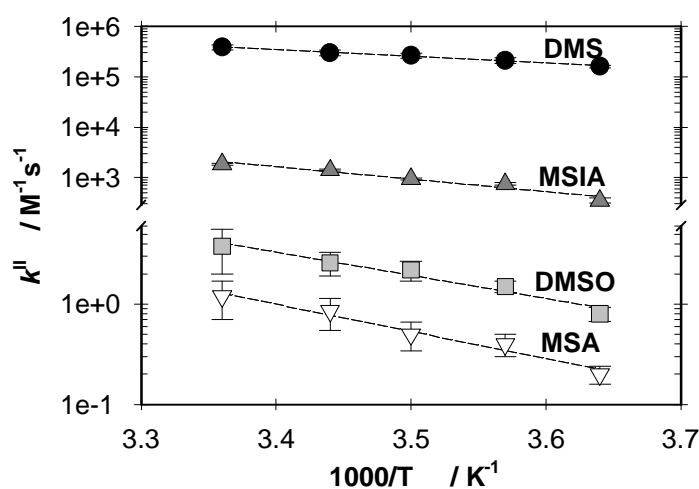


Figure 4: Arrhenius plot of k^{II} (HOBr/BrO^- + sulphur compounds)

Conclusions

- The equilibrium of Br_2 in aqueous phase was studied as a function of the pH, where the pH was observed to play an important role in the quantification of the Henry's law constant of Br_2 (**Fig. 1** and **Fig. 2**);
- The Henry's law constant was determined for Br_2 on pure water at various temperatures and the effect of pH and salt concentration is presented in **Fig. 2**;

- The heterogeneous kinetics (uptake) of Br₂ on DMS, DMSO, MSIA and MSA was obtained using WWFT and the principal results and experimental conditions are presented in **Fig. 3** and **Tab. 1**;
- Using stopped-flow measurements the reactions between HOBr/BrO⁻ and DMS, DMSO, MSIA and MSA were studied, where we observe that the reactions are dependent on pH (see **Tab. 2**) and also on temperature (Arrhenius plot of k^H) in **Fig. 4**.

References

- Amels, P., Elias, . H and Wannowius, K.-J. (1997) *J. Chem. Soc. Faraday Trans*, 93(15), 2537-2544.
- Barcellos da Rosa, M., Elend, M. and Zetzsch, C. (2000) Proceedings of the CMD Annual Report 2000 Lausanne, 131-135.
- Bartlett, W.P. and Margerum, D.W. (1999) *Environ. Sci. Technol.* 33, 3410-3014.
- Beckwith, R.C., Wang, T.H. and Margerum, D.W. (1996) *Inorg. Chem.* 35, 995-1003.
- Beckwith, R.C. and Margerum, D.W. (1997) *Inorg. Chem.* 36, 3754-3760.
- Behnke, W., George, C., Scheer, V. and Zetzsch, C. (1997) *J. Geophys. Res.*, 102, 3795-3804.
- Behnke, W., Elend, M., Frenzel, A., Krüger, H.U., Palm, W-U., Sikorski, R. and Zetzsch, C. (1998). CMD Annual report 1998, EUROTRAC-2, GSF-Forschungszentrum, München, pp.156-162.
- Behnke, W., Elend, M., Krüger, U. and Zetzsch, C. (1999) *J. Atmos. Chem.* 34, pp.87-99.
- Campolongo, F., Saltelli, A., Jensen, N.R., Wilson., J. and Hjorth, J. (1999) *J. Atmos. Chem.* 32, pp.327-356.
- Danckwerts, P.V., 1970: *Gas-liquid Reactions*, McGraw-Hill, New York.
- Fickert, S., Adams, J. and Crowley, J.N. (1999) *J. Geophys. Res.*, 104, 23,719-23,727.
- Frenzel, A., Scheer, V., Sikorski, R., George, C., Behnke, W. and Zetzsch, C. (1998) *J. Phys.Chem. A*, 102, pp.1329- 1337.
- Katoshevski, D., Athanasios, N. and Seinfeld, J.H. (1999) *J. Aerosol Sci.*, 30, 4, pp.503-532.
- Katrib, Y, Deiber, G., Schweitzer, F., Mirabel, P., George,C. (2001). *J. Aerosol Sci.* **32**, 893- 911.
- Kulmala, M., Wagner, P.E., 2001: *J. Aerosol Sci.* **32**, 833-841.
- Le Bras, G. Barnes, I., Hjorth, J., Zetzsch, C., Martinez, E. and Mihalopoulos, N. (2000) Final report ENV4-CT97-0410, EUR 19569 EN.
- Liu, Q. and Margerum, D.W. (2001) *Environ. Sci. Technol.* 35, 1127-1133.
- Maric, D., Burrows, J.P. and Moortgat, G.K. (1994) *J. Photochem. Photobiol. A: Chem*, 83, 179-192.
- Mozurkewich, M. (1995) *J. Geophys. Res.* D 100, 7, 14199-14207.
- Reid, R.C., Prausnitz, J.M. and Poling, B.E. (1987) McGraw-Hill, Inc. New York, 4th ed.
- Soulard, M., Block, F. and Hatterer, A. (1981) *J. Chem. Soc. Dalton Trans.*, 2300-2310.
- Troy, R.C. and Margerum, D.W. (1991) *Inorg. Chem.*, 30, 3538-3543.
- Vesala, T., Hannemann, A.U., Luo, B.P., Kulmala, M., Peter, Th., 2001: *J. Aerosol Sci.*, **32**, 7, 843-860.
- Wang, T.X., Kelley, M.D., Cooper, J.N., Beckwith, R.C. and Margerum, D.W. (1994) *Inorg. Chem.*, 33, 5872-5878.
- Warneck, P., 1996: *Heterogeneous and liquid phase processes - EUROTRAC, Vol. 2*, Springer, Berlin.
- Worsnop, D.R., Shi, Q., Jayne, J.T., Kolb, C.E., Swartz, E., Davidovits, 2001: *J. Aerosol Sci*, **32**, 7, 877-891.

Table 1. Principal results and experimental conditions of Br₂ + sulphur species (WWFT).

Experimental conditions	CH ₃ SCH ₃ (DMS)	CH ₃ SOCH ₃ (DMSO)	CH ₃ SO ₂ H (MSIA)	CH ₃ SO ₃ H (MSA)
[Sulphur] / M	1.0 – 30mM	100 – 500mM	1.0 – 50mM	50 – 500mM
pK _a	---	~ 11.3	2.0	~ 1.0
pH (buffered)	3.3 ± 0.2	3.3 ± 0.2	3.3 ± 0.2	3.3 ± 0.2
[Br ₂] / 10 ¹⁷ molecules cm ⁻³	0.05 – 5.0	0.1 – 5.0	0.05 – 3.0	0.1 – 3.0
k _{gas} (s ⁻¹) = 1/[Br ₂] · d[Br ₂]/dt	0.11 – 1.20	0.03 – 0.14	0.09 – 1.60	0.01 – 0.13
γ · 10 ⁻⁶ = k _{gas} · 2r / <c>	3.50 – 37.0	0.75 – 4.40	2.74 – 45.0	0.13 – 4.05
T(°C) / D _{aq} (m ² s ⁻¹) / H (M atm ⁻¹)	k ^{II} / 10 ⁷ M ⁻¹ s ⁻¹	k ^{II} / 10 ³ M ⁻¹ s ⁻¹	k ^{II} / 10 ⁶ M ⁻¹ s ⁻¹	k ^{II} / 10 ³ M ⁻¹ s ⁻¹
2.5±0.2 / 0.76 · 10 ⁻¹⁰ / 1.01	0.60 ± 0.36	2.10 ± 1.56	1.05 ± 0.60	1.52 ± 0.90
9.0±0.2 / 0.92 · 10 ⁻¹⁰ / 0.97	0.90 ± 0.51	3.20 ± 1.92	2.10 ± 1.20	2.23 ± 1.40
15.0±0.2 / 1.04 · 10 ⁻⁹ / 0.87	1.10 ± 0.60	6.15 ± 3.70	3.00 ± 1.80	2.70 ± 1.62
25.0±0.2 / 1.27 · 10 ⁻⁹ / 0.70	2.30 ± 0.71	9.03 ± 5.40	5.50 ± 3.00	5.23 ± 3.54

Table 2. Principal results and experimental conditions of HOBr/BrO⁻ + sulphur species (SF).

Experimental conditions	CH ₃ SCH ₃ (DMS)	CH ₃ SOCH ₃ (DMSO)	CH ₃ SO ₂ H (MSIA)	CH ₃ SO ₃ H (MSA)
[Sulphur]/M	0.05 – 5mM	5 – 500mM	0.25 – 25mM	5 – 700mM
pH _{SULPHUR}	4.0 ± 0.5	7.0 ± 0.5	6.5 ± 0.5	4.0 ± 0.3
pH _{HOBr/BrO⁻} (pK _a = 8.7)	10.0 ± 0.1	10.0 ± 0.1	7.5 ± 0.1	7.5 ± 0.1
[HOBr/BrO ⁻] / M	25 – 120μM	0.1 - 10mM	0.1 - 2mM	0.3 - 50mM
λ(nm) _{measurements}	325	325	265	265
Time (s)	10 – 100ms	10 - 200s	0.1 - 5s	0.2 - 2s
T(°C)	k ^{II} / 10 ⁵ M ⁻¹ s ⁻¹	k ^{II} / M ⁻¹ s ⁻¹	k ^{II} / 10 ³ M ⁻¹ s ⁻¹	k ^{II} / M ⁻¹ s ⁻¹
2.0 ± 0.2	1.60 ± 0.10	0.80 ± 0.10	0.35 ± 0.04	0.20 ± 0.04
7.0 ± 0.2	2.10 ± 0.20	1.50 ± 0.20	0.75 ± 0.04	0.40 ± 0.10
12.0 ± 0.2	2.70 ± 0.30	2.20 ± 0.50	0.95 ± 0.04	0.50 ± 0.16
17.0 ± 0.2	3.00 ± 0.40	2.60 ± 0.70	1.40 ± 0.06	0.85 ± 0.30
25.0 ± 0.2	3.90 ± 0.50	3.80 ± 1.80	1.85 ± 0.09	1.20 ± 0.50

Aqueous phase reactivity of acetone and its parent compounds in the troposphere (APP17)

Laurent Poulain, Izabela Sowka, Anne Monod, Henri Wortham

Laboratoire Chimie et Environnement, Université de Provence, case 29, 3 place Victor Hugo 13 331 Marseille Cedex 3, France

e-mail : laurent.poulain@voila.fr

Introduction

Acetone is both an intermediate and final product of OH-oxidation of VOCs. Because of its long atmospheric lifetime towards gas phase photolysis and OH-oxidation, acetone is one of the main HOx radicals precursors in the upper troposphere (Singh *et al.*, 2001). Although its water solubility is low, acetone was identified in clouds and rain samples (Snider and Dawson, 1985; Blando and Turpin, 2000), indicating that this compound can be either formed within the aqueous phase or directly transferred from the gas phase. The present study is aimed at exploring acetone's chemical behaviour in the aqueous phase of the troposphere. Aqueous phase OH-oxidation of acetone and its parent compounds under simulated tropospheric conditions were performed.

Experimental

The experiments took place in a static photoreactor, equipped with a continuous UV-visible irradiation (Figure 1).

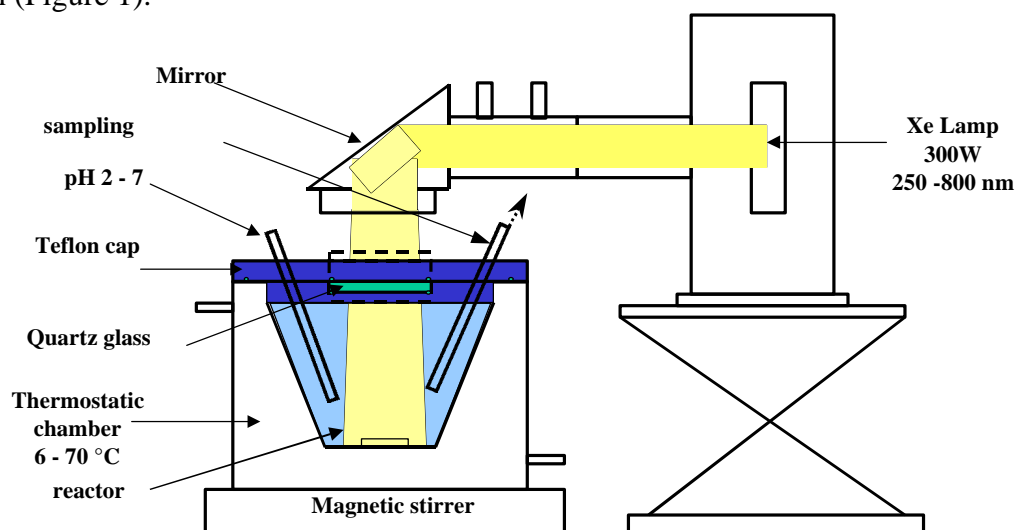


Figure 1: static photoreactor

Two different OH sources were tested: the photolysis of H_2O_2 (1), and the Fenton reaction (2).



Initial reagent concentrations varied over a wide range (10^{-4} – 10^{-2} M). To obtain the time profiles of stable reactants and products, analysis were performed periodically using conductimetry (dissolved O_2), gas chromatography, HPLC-UV and HPLC-fluorimetry.

Results

Relative kinetic experiments using methanol as the reference compound were performed in order to determine the rate constant of OH-oxidation of acetone. Two series of experiments were performed, and the obtained values at room temperature are in agreement with previous studies (within the

experimental uncertainties). The experiment was performed at three different temperatures in order to establish Arrhenius parameters (table 1).

OH source	pH	$k_{OH} (M^{-1}s^{-1})$ (298 K)	Ea (kJ)	Reference
H ₂ O ₂ + hv	2	$1,7 (\pm 0,5).10^8$		This work
Fenton	2	$1,3 (\pm 0,5).10^8$	15,4 ($\pm 3,7$)	This work
Pulse Radiolysis in water	6 - 7	$1,1.10^8$		Recommanded value by Buxton <i>et al.</i> , 1988

Table 1 : rate constant of OH oxidation of acetone in the aqueous phase.

These experiments allowed us to determine the photolysis frequency of acetone under our experimental conditions ($J = 9 (\pm 0,9).10^{-6} s^{-1}$).

Mechanistic studies of OH-oxidation of methyltetributylether (MTBE) in the aqueous phase have shown that together with formaldehyde, acetone is the main reaction product under atmospheric conditions (Monod *et al.*, 2001).

The chemical mechanism of OH oxidation of acetone in the aqueous phase has been studied at 298 K, at “free” pH under the following conditions:

OH source : H₂O₂ + hv \rightarrow 2 OH

Initial concentrations: [Acétone] = $1.10^{-3} M$; [H₂O₂] = $1.10^{-4} - 1.10^{-3} M$; [Fe(SO₄)] = $1.10^{-3} M$

Three primary reaction products have been detected: methylglyoxal, hydroxyacetone and formaldehyde (Figure 2). The pH value, initially at 6, decreased and stabilized at 4 after 1000 seconds, suggesting the formation of low acids in the solution.

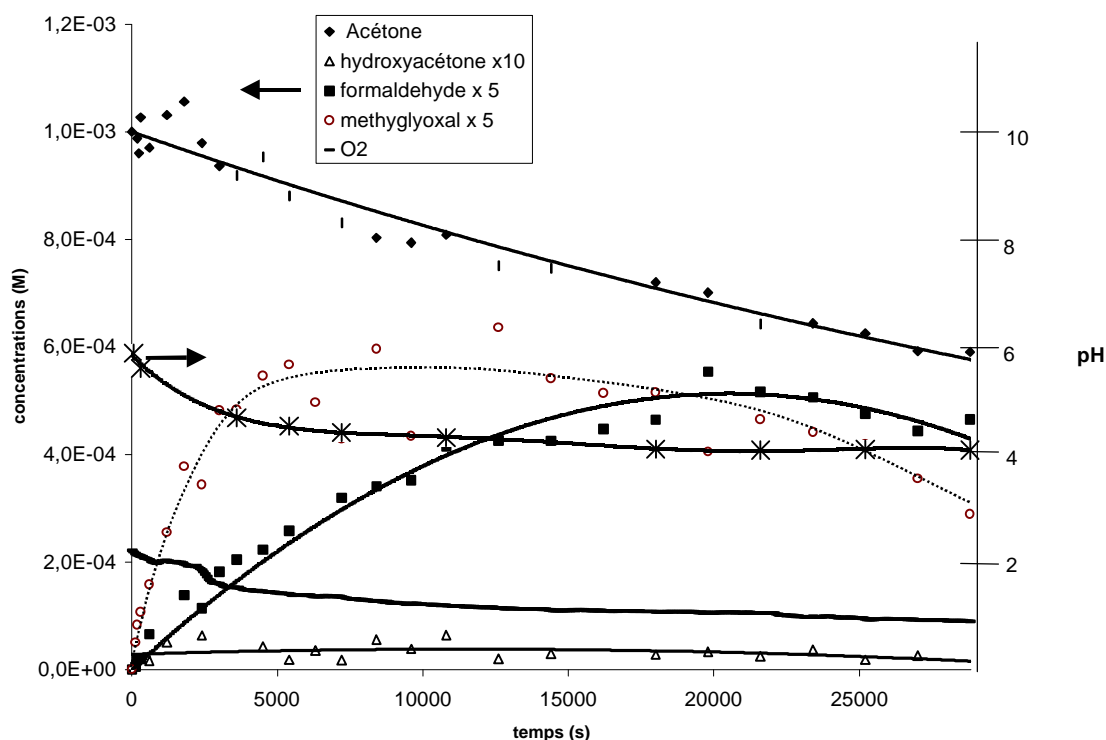


Figure 2: Time profiles of reactants and reaction products during OH oxidation of acetone in the aqueous phase

These experiments confirm the mechanism previously pointed out by Stefan and Bolton (1999) (Figure 3). Concerning the behaviour of tetroxide (3), our experiments have shown that pathways A and B are the two major pathways, with pathway A being around twice pathway B, in agreement with our previous investigation conducted on the tetroxide HOCH₂(O)₄CH₂OH formed during OH oxidation of methanol (Monod *et al.*, 2000)

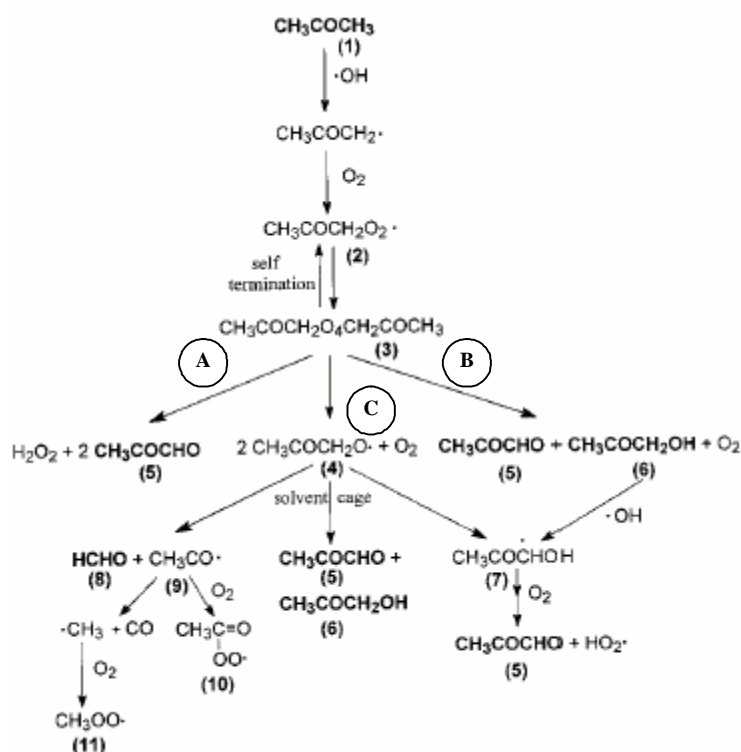


Figure 3 : Chemical mechanism of OH oxidation of acetone in the aqueous phase (Stefan and Bolton, 1999).

References

- Blando J.D., Turpin B.J., 2000. Secondary organic aerosol formation in cloud and fog droplets : a literature evaluation of plausibility, *Atmospheric Environment*, 34, 1623-1632.
- Buxton G, C.L. Greenstock, W.P Helman, and A.B. Ross, Critical review of rate constants for reactions of hydrated electrons, hydrogen atom and hydroxyl radicals (OH/O^\cdot) in aqueous solution, *J. Phys. Chem. ref. data* **17**, 2, 513-883, 1988
- Monod A., A Chebbi, R. Durand-Jolibois and P. Carlier : Oxidation of methanol by hydroxyl radicals in aqueous solution under simulated cloud droplet conditions. *Atmospheric Environment*, Vol. 34, 29-30, pp 5283-5294, 2000
- Monod A., S. Grubert, H. Wortham, P. Carlier : reactivity of oxygenated organic compounds in the atmospheric aqueous phase, *Journal of aerosol sciences* volume 32 supplement 1, 2001, S253, *European Aerosol Conference 2001*, 3-7 septembre 2001, Leipzig, Germany.
- Singh H., Chen Y., Staudt A., Jacob D., Blake D., Helkes B., Snows J., evidence from the Pacific troposphere for large global sources of oxygenated organic compounds, *Nature*, **410**, 1078-1081, 2001
- Snider J.R & G.A. Dawson Tropospheric light alcohols , carbonyls and acetonitrile : concentrations in the southwestern united states and Henry's law data *J. Geoph.; Res*, **90**, D2 , pp. 3797-3805, 1985.
- Stefan M.I., Bolton J.R., reinvestigation of the acetone degradation mechanism in dilute aqueous solution by the UV/ H_2O_2 process, *Environ. Sci. Technol.*, **33**, 870-873, 1999.

Tropospheric Reactivity of Organic Hydroperoxides (APP17)

E. Chevallier¹, R. Durand Jolibois¹, B. Picquet-Varrault¹, P. Carlier¹, and A. Monod²

¹ LISA, Université de Paris 7 et 12, Créteil (France) (e-mail: chevallier@lisa.univ-paris12.fr)

² Laboratoire de Chimie et Environnement, Université de Aix-Marseille I (France)

Abstract

For a better understanding of atmospheric multiphase chemistry, OH-oxidation of organic hydroperoxides are studied in both gaseous and liquid phases.

Kinetic results and hypothetical mechanism for the OH-induced oxidation of methylhydroperoxide (MHP) and ethylhydroperoxide (EHP) in aqueous and gas phase are presented. For gas phase, rate constants obtained are respectively $(4.2 \pm 0.1) \cdot 10^{-12} \text{ cm}^3 \text{ molecule}^{-1} \text{ s}^{-1}$ and $(1.4 \pm 0.3) \cdot 10^{-11} \text{ cm}^3 \text{ molecule}^{-1} \text{ s}^{-1}$, this study reveals that OH-oxidation is the major loss process and photolysis is of negligible importance. OH-oxidation leads mainly and respectively to the formation of formaldehyde and acetaldehyde. For aqueous phase, rate constant obtained at 6C° are respectively $(0.50 \pm 0.05) \cdot 10^9 \text{ M}^{-1} \text{ s}^{-1}$ and $(2.0 \pm 0.1) \cdot 10^9 \text{ M}^{-1} \text{ s}^{-1}$.

OH-oxidation of MHP produces formaldehyde, formic acid and hydroxymethylhydroperoxide (HMHP) whereas OH-oxidation of EHP produces acetaldehyde, acetic acid and hydroxyethylhydroperoxide (HEHP). The branching ratios of these products are dependent on pH.

Introduction

Organic hydroperoxides are key tropospheric secondary photochemical products. They are major oxidation products of VOCs at low levels of NO_x in the gas phase (Atkinson et al. 1997a) and they can be formed in liquid aerosols by peroxy-radicals recombinaison.

Consequently, these compounds play a significant role in tropospheric photochemistry. However, there is a lack of data concerning their tropospheric reactivity in both the gas and the aqueous phases. The aim of this work is to study the multiphase reactivity of two organic hydroperoxydes, methylhydroperoxyde (MHP) and ethylhydroperoxyde (EHP).

Experimental part

Aqueous phase experiments:

Aqueous phase reactions of organic hydroperoxides took place in a static photoreactor equipped with continuous photolysis. The apparatus consists of a Pyrex vessel of 500cm³. The irradiation source is a metal halide lamp, HMI 575W, OSRAM. Its spectrum is comparable with a standard solar spectrum. The volume of the aqueous solution medium was 220 cm³. This reaction medium was continuously stirred for the homogenization and maintained at 279.0±0.2 K. The surface of the solution was swept by a constant flow of ultra pure N_{2(g)} in order to avoid any contamination by ambient air. This procedure also allowed us to avoid dissolved O₂ saturation, thus enabling the monitoring of O_{2(aq)} concentrations as a function of time.

Aqueous phase OH radicals were generated using different methods:

- Continuous photolysis of H₂O₂, $\text{H}_2\text{O}_2 + h\nu \rightarrow 2\text{OH}$ $\lambda < 320 \text{ nm}$
- Continuous photolysis of Fe^{III}, $\text{Fe}^{\text{III}} + h\nu \rightarrow \text{Fe}^{\text{II}} + \text{OH}$ at pH = 2

Under continuous photolysis of H₂O₂, different pH values were tested: pH=2, pH=7 and “free” pH (non buffered solution). This range of pH values adequately covers the range typically encountered in atmospheric water droplets.

Products analysis were performed by gas-phase chromatography (GC-FID), ionic chromatography (IC-conductimetry), and two high-pressure liquid chromatography systems (HPLC-UV and HPLC-fluorimetry) devoted to the analysis of carbonyl compounds and hydroperoxydes respectively. The carbonyl compounds were quantified by UV absorption at 362 nm after precolumn derivatization using dinitro-2,4-phenylhydrazine. The hydroperoxydes were

quantified by fluorimetry ($\lambda_{\text{ext}}=320\text{nm}$ et $\lambda_{\text{emi}}=400\text{nm}$) after post-column derivatization using parahydroxyphenyl acetic acid (POPHA) in the presence of peroxidase (Hellpointner et al., 1989). Direct potentiometric measurements of dissolved O_2 were continuously performed in the reactor.

Gas phase experiments:

Gas phase photolysis and OH-oxidation of MHP and EHP were investigated in an atmospheric simulation chamber :

1- Indoor simulation chamber (L.I.S.A., University of Paris 7, France). Experiments were carried out in a 6 meters length evacuable chamber of 977 liters. OH radicals were generated by alkyl nitrite photolysis at 420 nm and 360 nm with fluorescent tubes. Products and reactants were detected by long path FTIR. MHP and EHP photolysis were studied at atmospheric pressure with and without OH-scavenger (cyclohexane).

2- Outdoor simulation chamber (Euphore, C.E.A.M., Spain). Experiments were carried out in a 200 m³ Teflon chamber under solar irradiation. Products and reactants were detected by long path FTIR. MHP was studied in purified air with and without an OH-scavenger (cyclohexane).

Reagents

Hydrogen peroxide and peroxyacetic acid are commercially available whereas MHP and EHP are not. Thus we performed synthesis of organic hydroperoxides based on previous studies (Rieche and Hitz, 1929; Rieche and Meister 1933 and 1935). Organic hydroperoxides are known to be very explosive thus, the synthesis was performed in a diluted solution (O'Sullivan 1996, Kok *et al.* 1995 and Lee 2000). Methyl hydroperoxide was synthesized from H_2O_2 and dimethyle sulfate by nucleophilic attack of HO_2^- anion on methyl group of dimethyl sulfate in the presence of strong base. The reaction is carried out in aqueous solution and the methylhydroperoxide was extracted by for final isolation from the excess of H_2O_2 . EHP was synthesised with approximately the same procedure by replacing dimethyle sulfate with diethyle sulfate. HMHP and HEHP were synthesised by reaction of H_2O_2 with respectively formaldehyde and acetaldehyde under anhydrous condition (Kok *et al.* 1995). The crude product was not purified further but diluted with ultrapure water .

The synthesised hydroperoxides solutions were standardized by $\text{Na}_2\text{S}_2\text{O}_3/\text{KI}$ titration and coupled by a HPLC-fluorimetry (as described above).

Results

Aqueous phase reactivity

A – Aqueous phase photooxidation of MHP :

Aqueous phase reactivity of MHP was studied under different conditions relevant to atmospheric droplets : direct photolysis in the presence and absence of OH-scavenger, OH-initiated oxidation at pH=2 and 7, OH-initiated oxidation at pH=2 in the presence of iron, and direct reactivity towards Fe^{II} . Figure 1 shows the obtained time profiles of reactants and products for OH-initiated oxidation of MHP at pH=2. The results (table 1) show that formaldehyde and formic acid are the main primary products. Hydroxymethylhydroperoxide (HMHP) and H_2O_2 were found as secondary products. In view of these results, a hypothetical mechanism is proposed in figure 2.

Photooxidation of MHP, $\text{H}_2\text{O}_2 + h\nu$ at pH=2 and 6°C

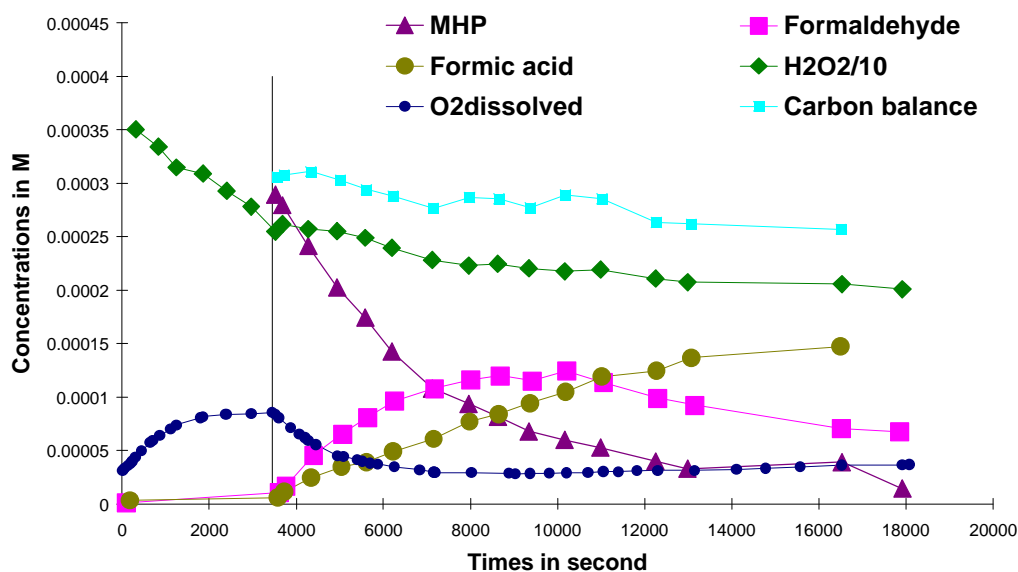


Figure 1:

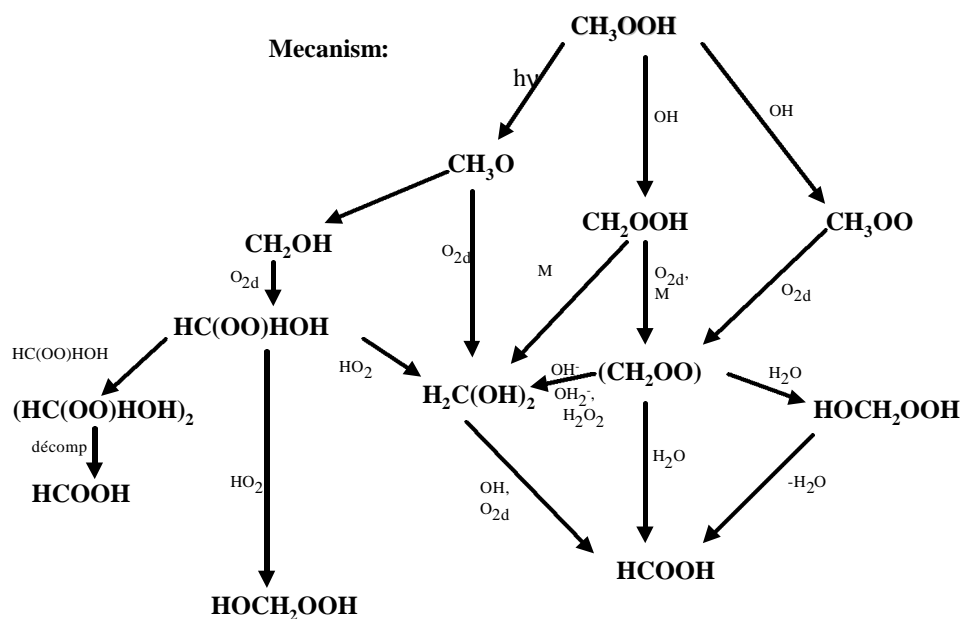


Figure 2:

Table 1: Yields of reaction products of aqueous phase reactivity of MHP

Products\Reaction	hn+scav(SCN-)	hn+H ₂ O ₂ (pH2)	hn+H ₂ O ₂ (pH7)	hn+Fe ^{III} (pH2)	Fe ^{II} +scav
Formaldehyde	77±2	62±1	90±4	87±2	86±2
Formic acid	7±1	40±4	*	6±1	7±1
HMHP	*	*	*	*	8±2
H ₂ O ₂	*	?	?	*	7±1

*= mainly secondary products.

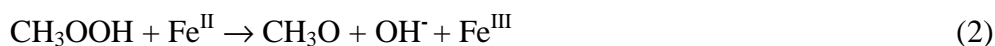
?= not determined.

Comparing OH-oxidation of MHP at pH=2 and 7 (under H₂O₂ photolysis), one can observe a pH effect on the primary reaction products: both formic acid and formaldehyde are formed at pH 2,

whereas only formaldehyde is formed at pH 7. This observation can be explained by reaction (1) which rate is pH dependent.



At pH 2, primary reaction products differ depending on the source of OH used: using H_2O_2 photolysis, both formic acid and formaldehyde are formed, whereas using Fe^{III} photolysis, only formaldehyde is formed. In addition to OH radicals, Fe^{III} photolysis produces Fe^{II} , which reacts directly towards MHP, producing only formaldehyde *via* reactions 2. In the Fe^{III} photolysis experiments, the competition between $\text{MHP} + \text{OH}$ and $\text{MHP} + \text{Fe}^{\text{II}}$ is probably in the favour of $\text{MHP} + \text{Fe}^{\text{II}}$ due to the high concentrations of Fe^{III} initially introduced.



B - Aqueous phase photooxidation of EHP :

Aqueous phase reactivity of EHP was studied under different conditions relevant to atmospheric droplets : direct photolysis in the presence and absence of OH-scavenger, OH-initiated oxidation at pH=2 and 7, and direct reactivity towards Fe^{II} . Figure 3 shows the obtained time profiles of reactants and products for OH-initiated oxidation of MHP at pH=7. The results (table 2) show that acetaldehyde and acetic acid are the main primary products. Hydroxyethylhydroperoxide (HEHP), H_2O_2 , formaldehyde, formic acid, peracetic acid and oxalic acid were found to be secondary products. In view of these results, an hypothetical mechanism is proposed in figure 4.

Photooxidation of EHP, $\text{H}_2\text{O}_2 + h\nu$ at pH=7, 6°C

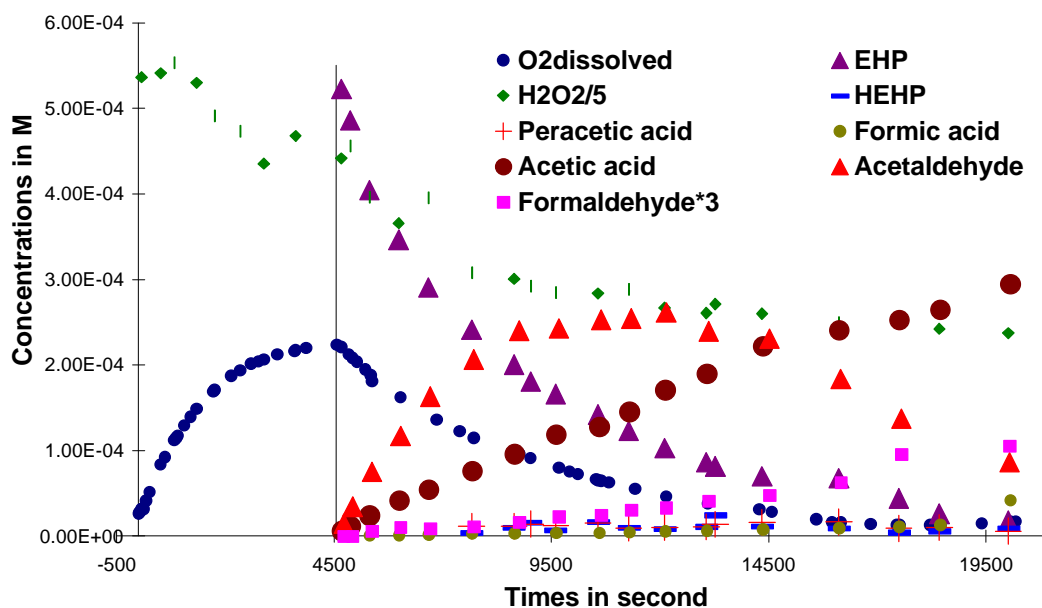


Figure 3:

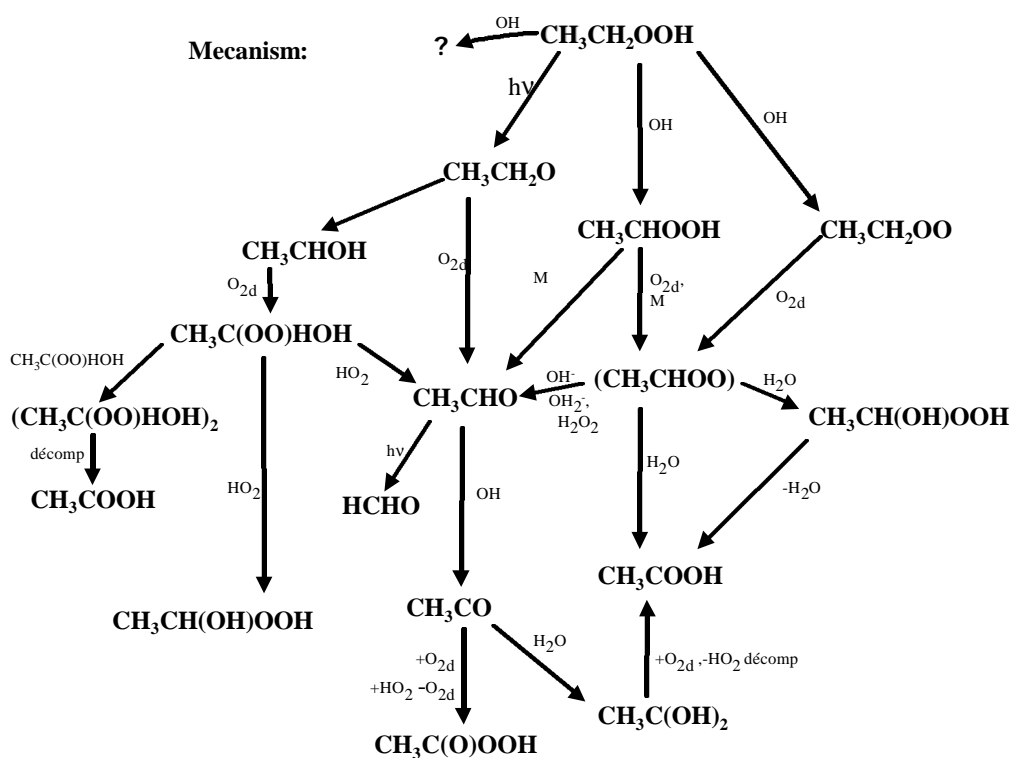


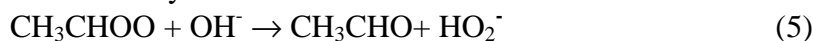
Table 2: Yields of reaction products of aqueous phase reactivity of EHP

Products\Reaction	hn+scav(SCN ⁻)	hn+H ₂ O ₂ (pH2)	hn+H ₂ O ₂ (pH7)	FeII(pH2)
Acetaldehyde	72±1	71±1	73±5	94±1
Acetic acid	*	29±3	22±2	7±4
Formaldehyde	*	*	*	*
Formic acid	*	*	*	*
HEHP	?	6±2	2±2	5±2
H ₂ O ₂	?	*	*	10±2
Peracetic acid	*	*	*	
Oxalic acid		*		

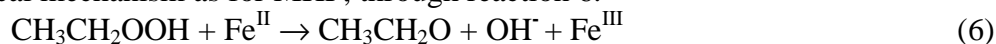
*= mainly of secondary product.

?= not determined

The branching ratios for EHP reactivity are different from those obtained for MHP. Comparing OH-oxidation of EHP at pH=2 and 7 (under H₂O₂ photolysis), no pH effect on the primary reaction products is observed. Because the rate of direct photolysis of EHP is of the same order as the rate of OH-oxidation, an important fraction of the yield of acetaldehyde observed for OH-oxidation of EHP can be due to direct photolysis. Therefore, reaction (5), which is pH dependent has a minor influence on the yield of acetaldehyde.



Direct reaction of EHP towards Fe^{II} produces 94% of acetaldehyde showing it follows the same chemical mechanism as for MHP, through reaction 6.



C – Aqueous phase kinetics

OH-initiated oxidation of MHP and EHP were studied using the relative kinetic method with known reference compounds. The results obtained in the kinetic study are summarized in table 3.

Table 3: Kinetic data of aqueous phase reactivity of EHP, MHP and the corresponding alcohols

Reaction ($T^{\circ}=6^{\circ}\text{C}$)	Reference compound	k ($\text{M}^{-1} \text{s}^{-1}$) or J (s^{-1})	Reference
MHP + OH	Ethanol and <i>i</i> -propanol	$0.50 (\pm 0.05) \cdot 10^9$	This study
$\text{CH}_3\text{OH} + \text{OH}$		$0.85 \cdot 10^9$	Buxton <i>et al.</i> 1988
MHP + $h\nu$		$J = 4.5 \cdot 10^{-5}$	This study
MHP + Fe^{II}		$16 (\pm 5)$	This study
EHP + OH	<i>i</i> -propanol	$2.0 (\pm 0.1) \cdot 10^9$	This study
$\text{CH}_3\text{CH}_2\text{OH} + \text{OH}$	methanol	$1.7 (\pm 0.1) \cdot 10^9$	Monod <i>et al.</i> 2001
EHP + $h\nu$		$J = 4.6 \cdot 10^{-5}$	This study
EHP + Fe^{II}		$24 (\pm 9)$	This study

The results show that the rate constants of OH-oxidation of the hydroperoxydes are comparable to the corresponding alcohols, indicating that the H-abstraction from the peroxide function is of minor importance compared to the one from the alkyl group. The results also show that aqueous phase photolysis is significant and the reaction of hydroperoxydes towards Fe^{II} is fast.

Gas-phase reactivity

A – Gas-phase photooxidation of MHP :

Direct photolysis and OH-oxidation of MHP were studied. The results show that (table 4) formaldehyde, formic acid, CO and methanol are primary products of OH-oxidation of MHP (figure 5), whereas only formaldehyde and methanol are primary products of its direct photolysis. A hypothetical mechanism is proposed in figure 6.

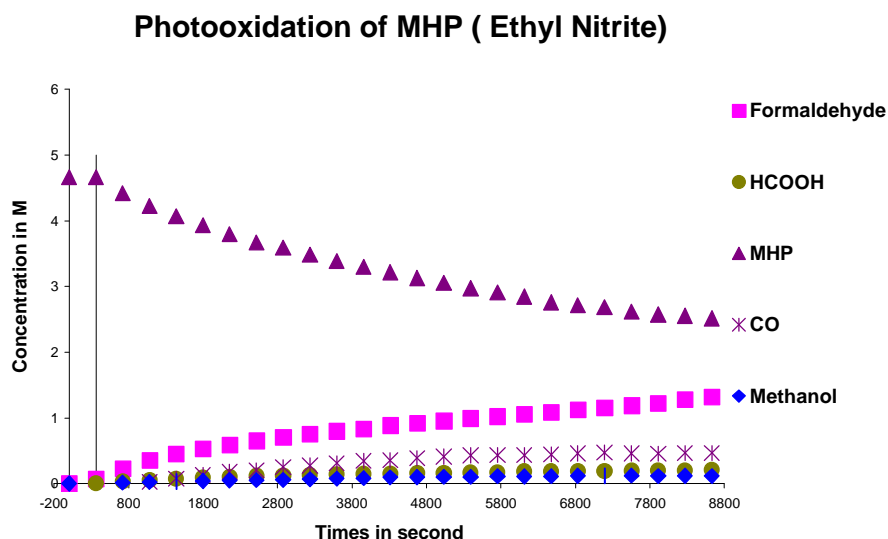


Figure 5:

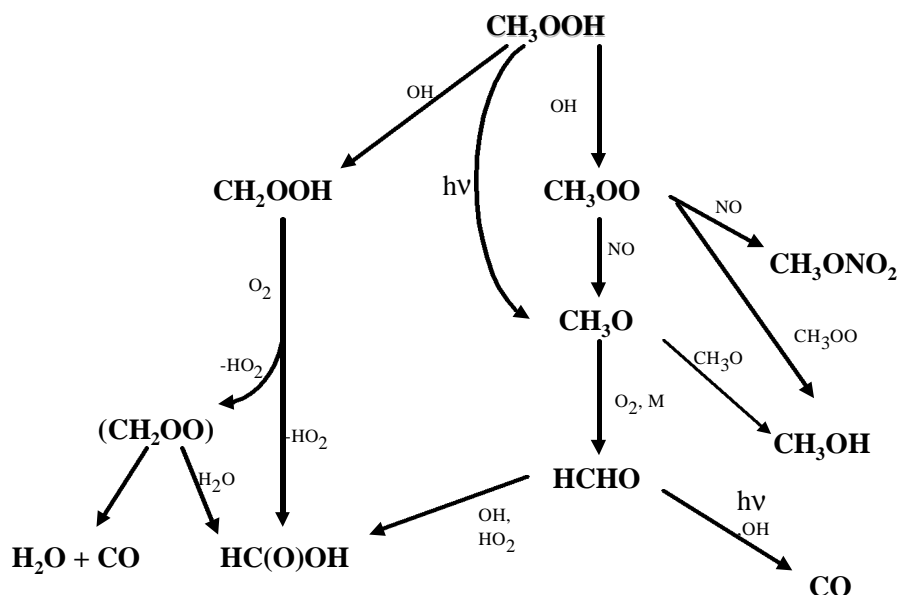


Figure 6: Mecanism

Table 4: Yields of reaction products of gas phase reactivity of MHP.

Products\Reaction	hn+scav	Ethyl or Isopropyl nitrite(OH)
Formaldehyde	88±4	65±2
Formic acid	*	11±2
CO	*	22±2
methanol	5±1	6.0±0.4

* = mainly secondary product

B – Gas phase photooxidation of EHP :

Direct photolysis and OH-oxidation of EHP were studied. The results show that (table 5) acetaldehyde, PAN, ethanol, and ethyl nitrate are primary products of OH-oxidation of EHP (figure 7), whereas only acetaldehyde and ethanol are primary products of its direct photolysis. A hypothetical mechanism is proposed in figure 8.

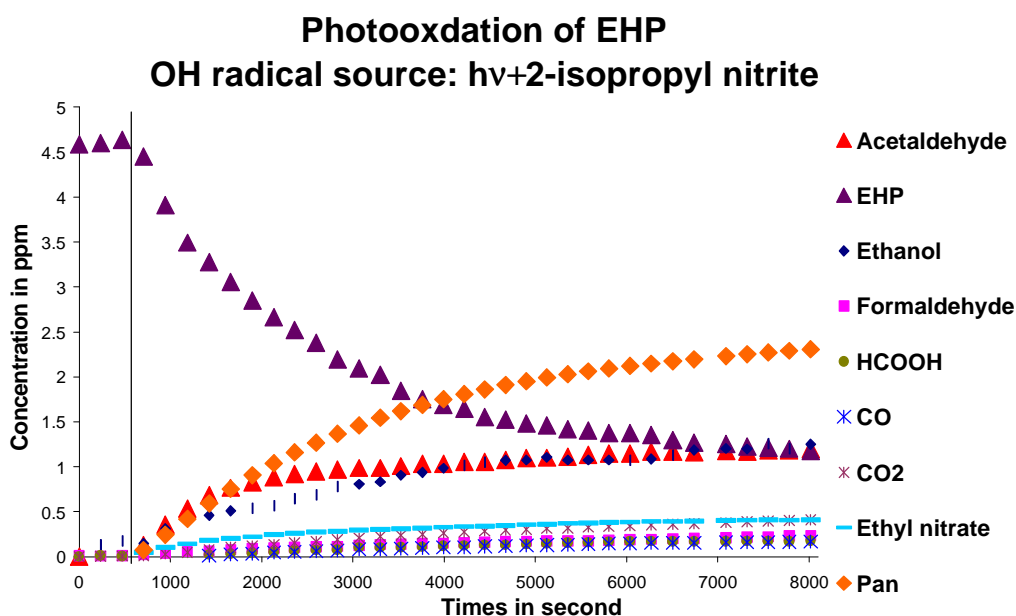


Figure 7:

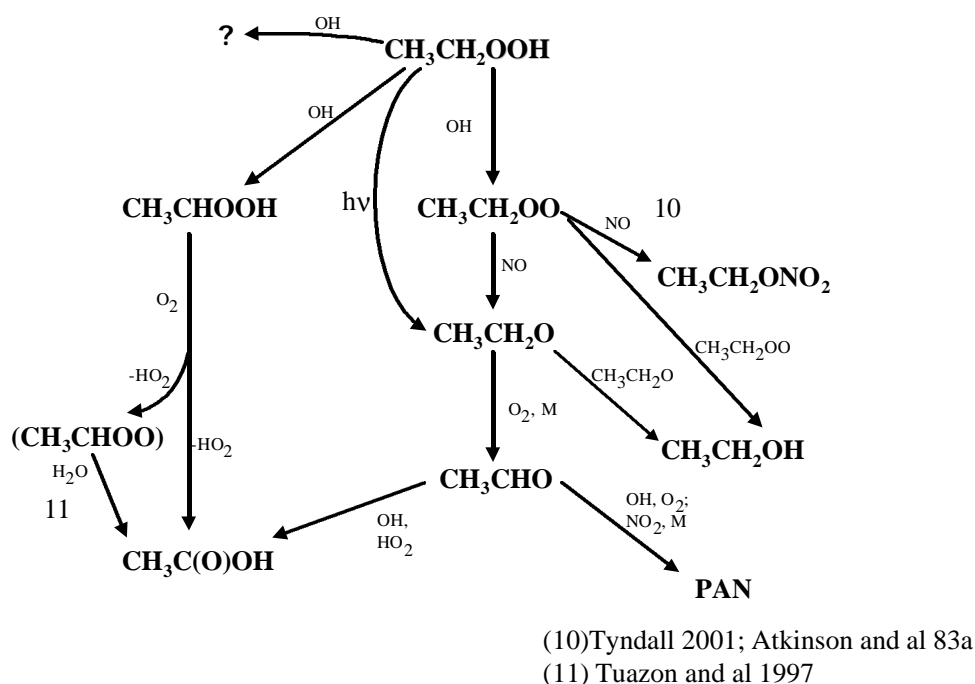


Figure 8: Mecanism

Table 5: Yields of reaction products of gas phase reactivity of EHP.

Products\Reaction	hn+scav (cycloexane, CO)	hn+Nitrite d'Isopropyl (OH)
Pan		75±1
Acetaldehyde	76±1	
ethanol	23±1	25±2
Acetic acid	*	8±1
Etyle nitrate	*	5±1
Formaldehyde	*	*
CO2	*	*
CO	*	*
Formic acid	*	*

* = mainly of secondary product

C – Gas phase kinetics

OH-initiated oxidation of MHP and EHP was studied using the relative kinetic method with known reference compounds. The results obtained in the kinetic study are summarized in table 6.

Table 6: Kinetic data of gas phase reactivity of EHP, MHP and the corresponding alcohols at 298K.

Reaction	Reference compound	k (molec ⁻¹ cm ³ .s ⁻¹) or J (s ⁻¹)	Reference
MHP + OH	Ethanol, propane, <i>i</i> -propanol	(4.2±0.1).10 ⁻¹² 7.4.10 ⁻¹² 5.5.10 ⁻¹²	This study Demore <i>et al.</i> 1997 Vaghjani <i>et al.</i> 1993
CH ₃ OH + OH	Recommanded value	0.91(±0.24) .10 ⁻¹²	Picquet <i>et al.</i> 1998
MHP + hν		J = 2.52.10 ⁻⁵	This study
EHP + OH	<i>i</i> -propanol	(1.4±0.1).10 ⁻¹¹	This study
CH ₃ CH ₂ OH + OH	Recommanded value	3.4 (±0.5).10 ⁻¹²	Picquet <i>et al.</i> 1998
EHP + hν		J = 4.77.10 ⁻⁵	This study

For Methylhydroperoxide (MHP) and et Ethylhydroperoxide (EHP), this study reveals that OH-oxidation is the major loss process and for MHP, photolysis is of negligible importance. The results also show that the rate constants of OH-oxidation of the hydroperoxydes are significantly higher than the corresponding alcohols, indicating that the H-abstraction from the peroxide function is more important than the one from the alcohol group.

Conclusion

Aqueous phase and gas phase reactivity of MHP et EHP were elucidated. In the aqueous phase, it was shown for the first time (to our knowledge) that the hydroperoxydes are highly reactive towards Fe^{II}. This reaction could compete with OH-oxidation within atmospheric droplets, thus influencing the iron photochemical cycles in the aqueous phase. In the gas phase, it was shown for the first time that OH-oxidation of EHP produces around 75% of acetaldehyde and secondary product PAN, thus providing a source of atmospheric PAN.

These data will be used to improve the multiphase photochemistry approach controlling the oxidising capacity of the atmosphere and in particular the photochemical formation and depletion of ozone (impact of clouds on the tropospheric ozone budget).

Acknowledgement :

The authors wish to thank the INSU-CNRS for financial support through the National Program on Atmospheric Chemistry (PNCA).

References.

- Atkinson, R., Baulch, D. L., Cox, R. A., R.F. Hampson, J., (Chairman), J. A. K., Rossi, M. J. and Troe, J., 1997: Evaluated Kinetic, Photochemical and Heterogeneous Data for Atmospheric Chemistry: *Supplement V. J. Phys. Chem. Ref. Data*, **26**, pp 521-1011.
- DeMore, W. B. and S. P. Sander, D. M. G., R. F. Hampson, R. E. Huie, M. J. Kurylo, C. J. Howard, A. R. Ravishankara, C. J. Kolb and M. J. Molina, 1997: Chemical kinetic and photochemical data for use in stratospheric modeling: *Evaluation N°12 of the NASA panel for data evaluation. JPL publication*, pp 170.
- Jacob, D. J., 1986: Chemistry of OH in remote clouds and its role in the production of formic acid and peroxymonosulfate. *J. Geophys. Res.*, **91**, pp 9807-9826.
- Kok, G. L., McLaren, S. E. and Staffelbach, T. A., 1995: HPLC Determination of Atmospheric Organic Hydroperoxides. *Journal of Atmospheric and Oceanic Technology*, **12**, pp 282-289.
- Lee, Y.-N. and Zhou, X., 1996: An aircraft measurement technique for formaldehyde and soluble carbonyl compounds. *Journal of Geophysical Research*, **101**, pp 29075-29080.
- Monod, A. and Carlier, P., 1999: Impact of clouds on the tropospheric ozone budget : direct effect of multiphase photochemistry of soluble organic compounds. *Atmospheric Environment*, **33**(27), pp 4431-4446.

- Monod, A., 1997: La réactivité troposphérique de composés organiques oxygénés en phase aqueuse : étude expérimentale et évaluation de son impact sur la capacité oxydante de l'atmosphère par une approche multiphasique, *Thèse Université Paris 7*.
- Neeb, P., Sauer, F., Horie, O. and K. Moortgat, G., 1997: Formation of hydroxymethyl hydroperoxide and formic acid in alkene ozonolysis in the presence of water vapour. *Atmospheric Environment*, **31**, pp 1417-1423.
- O'Sullivan, D. W., Lee, M., None, B. C. and Heikes, B. G., 1996: Henry's Law Constant Determinations for Hydrogen Peroxide, Methyl Hydroperoxide, Hydroxymethyl Hydroperoxide, Ethyl Hydroperoxide, and Peroxyacetic Acid. *J. Phys. Chem.*, **100**(8), pp 3241-3247.
- Sauer, F., Schuster, G., Schäfer, C. and Moortgat, G. K., 1996: Determination of H₂O₂ and organic peroxides in cloud and rain-water on the Kleiner Feldberg during FELDEX. *Geographical Research Letters*, **23**, pp 2605-2608.
- Sauer, F., Limbach, S. and Moortgat, G. K., 1997: Measurements of hydrogen peroxide and individual organic peroxides in the marine troposphere. *Atmospheric Environment*, **31**, pp 1173-1184.
- Vaghjiani, L. G. and Ravishankara, A. R., 1989: Kinetics and Mechanism of OH Reaction with CH₃OOH. *J. Phys. Chem.*, **93** (5), pp 1948-1959.
- Hellpointner, E. and Gäb, S., 1989: Detection of methyl, hydroxymethyl and hydroxyethyl hydroperoxides in air and precipitation. *Nature*, **337**, pp 631-634.
- Rieche, A. and Hitz, F., 1929: Über monomethyl-hydroperoxyd. *Ber. Dtsch. Chem. Ges.*, **62**, pp 12458-2472.
- Rieche, A. and Meister, R., 1933: Über peroxyde des formaldehyde: pertrioxymethylen und tetraoxymethylen diperoxyd. *Ber. Dtsch. Chem. Ges.*, **66**, pp 718-727.
- Rieche, A. and Meister, R., 1935: Über peroxyde des formaldehyde: oxymethyl-hydroperoxyd. *Ber. Dtsch. Chem. Ges.*, **68**, pp 1468-1472.

Interaction of trace gas species of atmospheric interest with ice surfaces (adsorption enthalpy of acetone) (HEP1)

Christophe Guimbaud*, Thorsten Bartels-Rausch, Markus Ammann

Paul Scherrer Institut, Labor für Radio- und Umweltchemie

5232 Villigen PSI, Switzerland

E-mail: christophe.guimbaud@psi.ch; Phone: (41) 56 310 4019; Fax: (41) 56 310 4435

Abstract

To investigate the adsorption enthalpy, ΔH_{ads} , of atmospheric trace gases on various ice surfaces, we developed a new instrument combining a chromatographic method and an Atmospheric Pressure Chemical Ionization Mass Spectrometer (APCI-MS). The adsorption enthalpy is obtained from the retention time measurement of the trace gas through a column packed with ice as function of temperature. The trace gas concentration is monitored at the end of the chromatographic column using Proton Transfer Reaction Mass Spectrometry (PTR-MS). As an example, we present the adsorption enthalpy of acetone on a snow sample.

Introduction

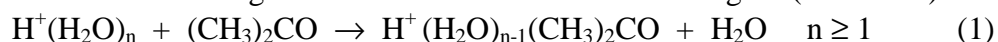
The adsorption enthalpy (ΔH_{ads}) of acetone on ice has recently been of great interest to the atmospheric chemistry community. In the upper troposphere, and under dry conditions ($\text{H}_2\text{O} < 100$ ppm), the photolysis of acetone is suggested to be the main source of HO_x , dominating the one from the reaction of $\text{O}(^1\text{D}) + \text{H}_2\text{O}$ [1]. Source and mainly sinks of acetone need to be quantified in order to simulate properly the concentration of the main atmospheric oxidant (HO_x). Partitioning to ice cirrus clouds is suggested to be one of the acetone sinks. Furthermore, snow-air and firn-air bi-directional fluxes of partially oxidized hydrocarbons such as carbonyl compounds and specifically acetone [2, 3] and their photochemical production in the upper snowpack [4-6] are significant enough to cause a strong impact on the carbonyl compounds concentrations in the planetary boundary layer, aging firns, and ice cores. However, the acetone mixing ratio between the gas and the solid phase is mainly determined by the value of its adsorption enthalpy. Thus, ΔH_{ads} adsorption enthalpy of acetone on ice has been investigated by many authors and further measurements to validate its existing value are desirable.

We developed an APCI-MS to investigate surface processes of atmospheric trace gases at the parts per billion by volume (ppbv) level. This instrument and a chromatographic technique similar to the one described in Bartels *et al.* [7] are combined to measure the adsorption enthalpy (ΔH_{ads}) of atmospheric species on ice surfaces.

The APCI-MS and the chromatographic method

The instrument is an Atmospheric Pressure Chemical Ionization Mass Spectrometer (APCI-MS, ABB Extrel, Merlin) housed in a two-stage differentially pumped vacuum chamber (Figure 1).

Proton Transfer Reaction Mass Spectrometry (PTR-MS) is used to monitor the acetone concentration in the gas phase. PTR-MS is a reliable analytical technique to monitor most of Oxygenated Volatile Organic Compounds (OVOCs), since they have higher proton affinity than H_2O . The APCI ion source is a corona discharge through which the acetone is carried by a 500 mL min^{-1} flow of N_2 buffer gas (quality 99.999 %). $\text{H}^+(\text{H}_2\text{O})_n$ clusters formed from the trace amount of H_2O present in the buffer gas react with acetone in the APCI region (reaction 1).



Ions and gases enter into an intermediate vacuum chamber through a $40 \text{ }\mu\text{m}$ diameter aperture held by a skimmer cone. Ions are focussed by two lenses constructed from cylindrical stainless steel mesh and are then directed to the rear vacuum chamber (housing the quadrupole mass

filter) through a second aperture of 350 μm diameter. Once the ions pass through the second stage aperture, they are focussed, deflected, and mass filtered (2-300 amu mass range) by a 90° angle off-axis quadrupole.

The adsorption enthalpy (ΔH_{ads}) of acetone (or any other non-reactive, non-diffusive, and non-dissociative atmospheric compounds) can be directly derived from the measurement of its retention time (t_R) through a column packed with ice as a function of the column temperature (T) [8].

$$\ln(t_R) = -\frac{\Delta C_{\text{ads}}}{R} \left(\frac{1}{T} \right) + \frac{\Delta S_{\text{ads}}}{R} - \ln \left(\frac{v}{a} \frac{A}{V} \frac{u}{l} \right) \quad (2)$$

l is the length of the column; u and v are the linear velocity and the volume of the gas in the column; a is the surface area of ice; A and V are the standard surface area and volume of ice.

A column 70 cm long and an 8 mm inlet diameter is filled with ice and introduced in a cooled jacket where the temperature can be varied from 200 K to 240 K (Figure 2). Introduction of acetone (and its concentration calibration) are performed using a permeation tube (VICI, DYNACAL), housed inside a thermostated oven maintained at 303 K. Using a 4 port valve setup, the total flow through the ice column and through the CI region remains constant (500 mL min⁻¹) whether if acetone is introduced or not through the column. The buffer gas is pre-humidified by flowing it over an ice water trap hold at the same temperature of the ice column in order to avoid co-condensation of water and acetone in the ice column.

Results and discussions

The retention time of acetone within the ice column t_R is derived from the difference between the measurement of the total retention time within the complete system (Figure 3; labelled plots with temperature values) and the measurement of the sum of the pre- and the post-column retention time ($\sim 2 \frac{1}{2}$ min) when the ice column is physically shortcut (Figure 3; thick plot on the left part of the panel). Figure 4 presents a plot of $\ln(t_R)$ versus inverse temperature measured from snow sampled in the top of Jungfraujoch (Switzerland, April 2002). The packed column is well characterized (inlet diameter: 0.6 cm; length: 66 cm; weight 7.5 g; Snow BET surface area: 206 cm².g⁻¹). An adsorption enthalpy (ΔH_{ads}) of $(-56 \pm 3, 2\sigma)$ kJ mol⁻¹ is derived according to Eq.(2). A comparable result is observed for polycrystalline ice spheres ($\sim \frac{1}{2}$ mm diameter) displaying a similar BET surface area. Since aging snow was used, its surface structure could be similar to that of the ice spheres and thus could lead to a similar ΔH_{ads} value. Indeed, it is suggested that defects on the ice surface have an effect on the calculated adsorption enthalpy of acetone on ice, implying higher ΔH_{ads} values for disordered ice surfaces than perfectly ordered ice surfaces [9, 10].

Our ΔH_{ads} measured on snow is in agreement with the ones derived within the same fractional coverage of one full monolayer ($0.01 \% < \theta < 3 \%$) and within the same temperature range [11-13] using ice films and other analytical approaches.

Conclusion and outlook

The APCI-MS system coupled with the new chromatographic method has been demonstrated to accurately measure the adsorption enthalpies (ΔH_{ads}) of acetone on an ice surface by measuring the retention time within a column packed with a snow sample as a function of temperature.

Experiments are under way to compare the adsorption enthalpy of acetone between polycrystalline structures such as fresh snow, which should display higher surface defects than

aging snow, ice spheres (poly-crystals), and single mono-crystal ice (no grain boundaries). Adsorption properties of other partially oxidized hydrocarbons could be also investigated.

Acknowledgements

We gratefully acknowledge the Laboratoire de Glaciologie et Géophysique de l'Environnement (Grenoble, France), and more particularly L. Legagneux and F. Dominé, who enabled and supervised T. Bartels-Rausch to perform at the LGGE the measurement of the BET surface areas of our ice spheres and snow sample. This work was supported by the Swiss National Science Foundation, the Swiss Federal Office of Education and Science and is integrated within the European Union project CUT-ICE n° EVK2-CT1999-00005.

References

1. L. Jaegle, D. J. Jacob, W. H. Brune, P. O. Wennberg, *Atmos. Environ.* 35 (2001) 469.
2. M. A. Hutterli, R. Rothlisberger, R. C. Bales, *Geophys. Res. Lett.* 26 (1999) 1691.
3. S. Houdier, S. Perrier, F. Domine, A. Cabanes, L. Legagneux, A. M. Grannas, C. Guimbaud, P. B. Shepson, H. Boudries, J. W. Bottenheim, *Atmos. Environ.* 36 (2002) 2609.
4. H. Boudries, J. W. Bottenheim, C. Guimbaud, A. M. Grannas, P. B. Shepson, S. Houdier, S. Perrier, F. Domine, *Atmos. Environ.* 36 (2002) 2573.
5. M. Grannas, P. B. Shepson, C. Guimbaud, A. L. Sumner, M. Albert, W. Simpson, F. Domine, H. Boudries, J. Bottenheim, H. J. Beine, R. Honrath, X. L. Zhou, *Atmos. Environ.* 36 (2002) 2733.
6. Guimbaud, A. M. Grannas, P. B. Shepson, J. D. Fuentes, H. Boudries, J. W. Bottenheim, F. Domine, S. Houdier, S. Perrier, T. B. Biesenthal, B. G. Splawn, *Atmos. Environ.* 36 (2002) 2743.
7. T. Bartels-Rausch, B. Eichler, P. Zimmermann, H. W. Gäggeler, M. Ammann, *Atmos. Chem. Phys.* 2 (2002) 235.
8. Guimbaud, T. Bartels-Rausch, M. Ammann, *Int. J. Mass Spectrom.* (2003).
9. S. Picaud, P. N. M. Hoang, *J. Chem. Phys.* 112 (2000) 9898.
10. F. Marinelli, A. Allouche, *Chem. Phys.* 272 (2001) 137.
11. F. Dominé, L. Rey-Hanot, *Geophys. Res. Lett.* 29 (2002).
12. K. Winkler, N. S. Holmes, J. N. Crowley, *Phys. Chem. Chem. Phys.* (2002).
13. N. Peybernès, C. Marchand, S. Le Calvé, P. Mirabel, *EC Cluster 3 (Oxidation Processes) /EUROTRAC-2 (Chemical Mechanism Development) Joint Workshop*, Paris, France, September 9-11, 2002.

Figures

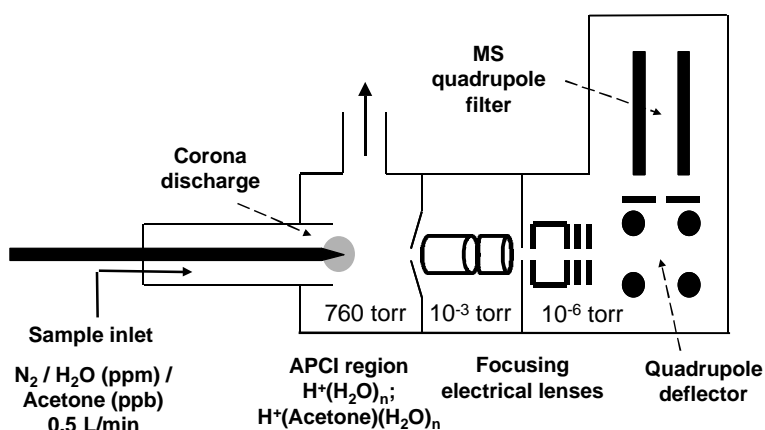


Figure 1. The Atmospheric Pressure Chemical Ionization Mass Spectrometer (APCI-MS).

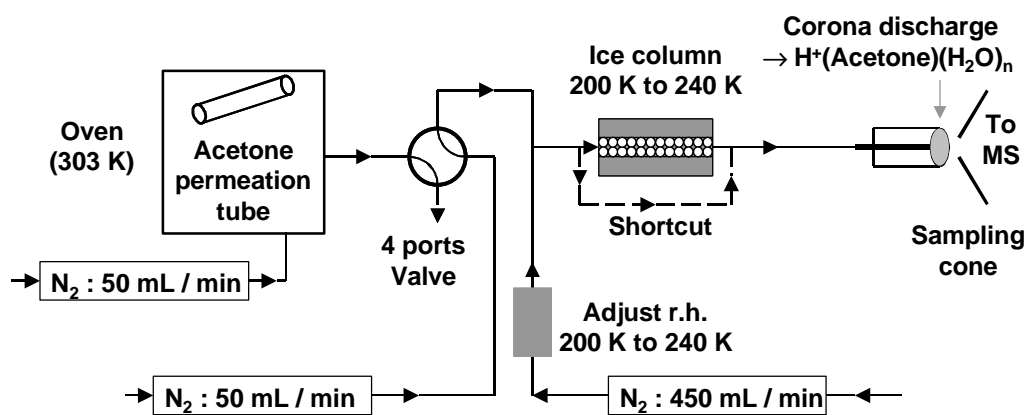


Figure 2. Schematic of the experimental set up (acetone flowing out of the ice column).

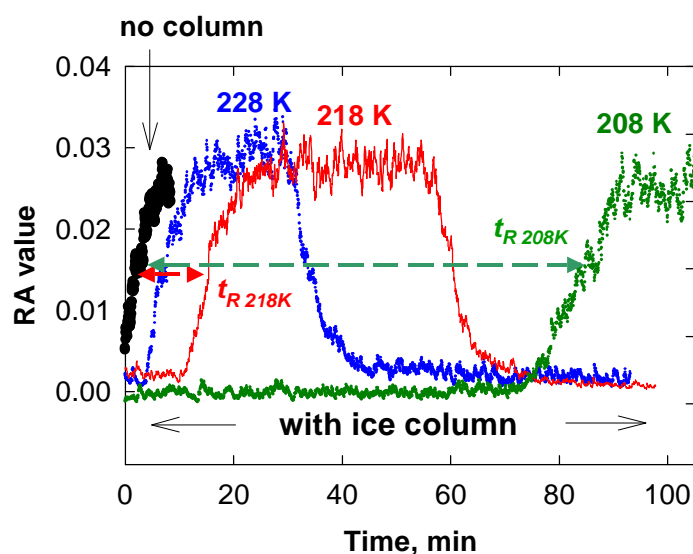


Figure 3. Retention time series (t_R) of the acetone within a column packed with a snow sample at various temperature. The reference time 0 is the moment when the acetone is introduced in the snow column following the $\frac{1}{4}$ turn of the 4 ports valve drawn in Figure 2.

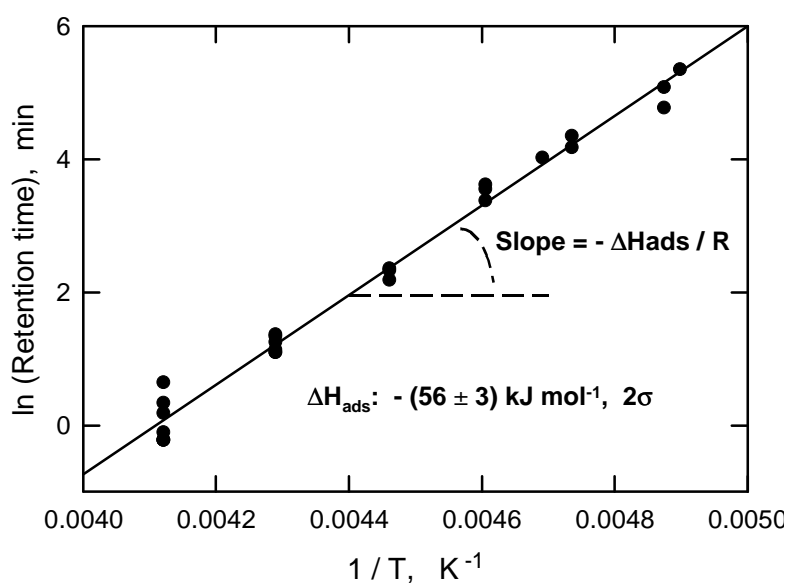


Figure 4. Plot of \ln (Retention time) versus inverse temperature for a column packed with snow.

Reaction of HNO_3 with Mineral Dust Particles. Preliminary Results (HEP1).

A. Vlasenko¹, C. Guimbaud², H.W. Gaeggeler^{1,2}, M. Ammann²

¹*Department of Chemistry and Biochemistry, University of Bern, CH-3012 Bern, Switzerland*

²*Paul Scherrer Institute, CH-5232, Villigen PSI, Switzerland*

Introduction

Nitric acid is an important acidic component in polluted air. It is formed in the troposphere by the oxidation of NO_x and is mainly removed by various heterogeneous processes such as rainout and uptake to aerosol particles. The concentration of HNO_3 in the troposphere varies from a few tenths of part per trillion in clean air to a few tenths of parts per billion by volume in industrial areas [1,2].

Several attempts were made to model the atmospheric behaviour of nitric acid in atmosphere. Singh et al. [3] compared the calculated ratio of HNO_3/NO_x with the observations made with aircraft over Western Pacific. Chatfield [4] did the same comparison for observations made over Mauna Loa in Hawaii. Both studies have shown a significant overestimation of HNO_3/NO_x ratio by the model. The possible explanation for this could be a poor understanding of HNO_3 removal processes, for example its heterogeneous uptake to ambient aerosol. Among various types of ambient particles, mineral dust was recently recognized as a strong sink of nitric acid in the atmosphere. The alkaline nature of mineral dust implies efficient reactivity with HNO_3 . Also, large arid areas of the planet provide a significant amount of mineral dust particles emission [5]. Dentener et al. [6] predicted a significant uptake of atmospheric gaseous nitric acid by mineral particles. According to this study, mineral dust nitrate represents 80-90% of the total nitrate budget in the atmosphere (gas phase HNO_3 + dust nitrate) in the regions of northern Africa, the Middle East and Asia.

Most laboratory studies of heterogeneous reaction between nitric acid and mineral dust were done in the Knudsen cell reactor with bulk samples [7,8]. The main disadvantage of this technique is that HNO_3 diffuses into the bulk sample. In this work, we measured the uptake of gaseous nitric acid to airborne mineral dust particles, which seems to be more relevant for atmospheric applications. The goal is to provide the essential parameters of the uptake coefficient for modeling the HNO_3 mineral dust chemistry.

Experimental

The experimental method used is similar to the ones reported previously [9,10]. Nitric acid labeled with a short-lived radioactive isotope ^{13}N is mixed with the aerosol particles in a flow tube reactor. After a certain reaction time gas phase and particulate phase products are trapped in a parallel-plate denuder and in a filter, respectively. The concentration of each species is measured by counting the number of ^{13}N decays in each trap. In this way, the loss of nitric acid from the gas phase and its consequent uptake by aerosol particle surface are measured simultaneously. A detailed description of the measurement procedure, the nitric acid generation and the detection system are given elsewhere [10] and are only briefly described hereafter. More detailed information is provided for the mineral particles generation since the sampling technique to generate sub-micron size particles is relatively new.

Production of HNO_3

Labeled ^{13}NO is carried in a main flow of He to the laboratory through a capillary. A fraction of this flow is mixed with nitrogen buffer gas. Additional amount of ^{14}NO can be added from a certified cylinder (10 ppm in N_2) to vary the total concentration of NO within a range of 1 ppb to 1 ppm. NO is oxidized to NO_2 by reaction with ozone in a 2 liters flow chamber. Ozone is generated by passing a mixture of synthetic air in nitrogen through a quartz tube irradiated by a UV light (172 nm

wavelength). HNO_3 is produced from the reaction of NO_2 with OH radicals; the flow containing NO_2 is humidified to 40 % relative humidity and irradiated by a second UV light to produce OH radicals [11].

Mineral dust particles generation

Mineral dust generation could be virtually divided in three steps: powder dispersion, particle size separation and control of aerosol size distribution. The setup is shown in Fig.1. In a first step, a sample powder (Arizona Test Dust, Fine Grade, Ellis Components, England) is dispersed by a solid aerosol generator (TOPAS GmbH, Germany). A special belt feeds the dust to the injector nozzle in order to provide a constant input. Shear forces created in the injector disperse and desagglomerate the powder to form particles. In a second step, the coarse particles ($> 5 \mu\text{m}$ diameter) are removed by passing the aerosol flow through a cyclone in order to avoid the sedimentation losses during aerosol transport through the tubes. The cyclone is immediately followed by a virtual impactor where a final particle separation is done. This impactor is built according to the design of Marple et al. [12] and has a cut-point of $0.8 \mu\text{m}$, removing particles above that size. During dust dispersion, particles acquire a high electrical charge [13]. This could cause an irreproducible particle loss to the walls. To avoid this problem the aerosol is passed through a neutralizer (^{85}Kr radioactive source) to reduce high particle charge. Then, the charged particles are removed by an electrical precipitator. In the last step, the aerosol size concentration and number distribution is controlled by Scanning Mobility Particle Sizer (SMPS), which consists of a ^{85}Kr neutralizer, a differential mobility analyzer DMA (model 3071, TSI®) and a condensation particle counter CPC (model 3025, TSI®). Aerosol humidity could be changed by passing the flow through a tube with H_2O permeable membrane (Goretex®) immersed in water. Temperature of the H_2O is adjusted to vary the relative humidity from 20 to 75%. The relative humidity is detected by capacitance sensors.

Flow tube reactor and detection

Mineral dust particles and nitric acid flows are mixed to react in the flow tube reactor. The reactor is a PFA Teflon tube of 8 mm inner diameter and 10 mm outer diameter. $\text{HNO}_3(\text{g})$ is introduced via a movable injector tube along the axis of the flow tube reactor (4 mm inner and 6 mm outer diameters). The movable injector position determines the reaction time between particles and gaseous nitric acid. The overall system is kept at room temperature.

The reaction products are directed to the parallel-plate denuder. The latter captures gaseous species $\text{HNO}_3(\text{g})$, $\text{HONO}(\text{g})$, $\text{NO}_2(\text{g})$ by different selective coatings due to the high diffusion mobility. Aerosol sub-micron particles have small diffusion mobility and pass through the denuder without being collected. Then, the particles are captured by a filter. Each trap is supplied with a γ -detector which measures the decay of ^{13}N atoms. The method to calculate the concentration of the species from this signal has been reported previously [9].

Results and discussion

Mineral dust particles production

Particles generated by the solid aerosol generator have a broad size distribution. The powder spray produces aerosol within a diameter range of 10 nm to 0.1 mm. Coarse particles ($> 1 \mu\text{m}$ diameter) are very difficult to transport through the tubing system due to gravimetric sedimentation and inertial losses on the walls. Despite the small number of coarse particles they contribute to the major part of the total aerosol surface to volume ratio of air. Thus, uncontrolled loss of fraction may cause a large uncertainty on the total aerosol surface. This explains the use of the two-stage separation described earlier. The performance of the separation with the cyclone and the virtual impactor is clearly shown by the measured size distribution of mineral dust aerosol (Fig. 2). The spectrum is mono-modal with a lognormal distribution. Particle concentration is around $5 \times 10^5 \text{ cm}^{-3}$ with a particle diameter mode of 200 nm. Total aerosol surface to volume ratio of air is about 10^{-3}

cm^2/cm^3 . We also studied the time stability of mineral dust aerosol generation. The system output was constant during 3 hours experiment with a 25 % variation (1σ) for the particle concentration and 4% (1σ) for the particle geometric mean diameter.

Observation of HNO_3 uptake by mineral dust

Fig. 3 represents the time series of the ^{13}N flux (count rate per second) of $\text{NO}_2(\text{g})$, $\text{HNO}_3(\text{g})$ and HNO_3 associated with particulates collected in their respective traps. The experiment starts with flowing NO_2 through the system (step A). Then part of NO_2 is transformed to HNO_3 by switching on the second UV lamp (step B). Nitric acid molecules are reversibly adsorbed by the inner surface of the flow tube. This retention process leads to a partial loss of radioactivity associated with $^{13}\text{HNO}_3$. To quantify the radioactivity loss of HNO_3 the movable injector is changed from a position with minimum HNO_3 -walls interaction time to maximum one (step C). Finally, the aerosol is introduced into the flow tube where mineral particles react with gaseous nitric acid. Step D shows how the concentration of HNO_3 associated with aerosol surface increases while the signal of nitric acid in the gas phase drops.

Uptake coefficient calculation

The derivation of the uptake coefficient is done according to Guimbaud et al. [10]. The observed depletion of nitric acid from the gas phase is considered as a combination of two first order loss rate processes (i) loss to the walls of the flow reactor and (ii) reaction with the particle surface (k_p). The wall loss rate is derived from steps B and C. k_p is calculated on the basis of the HNO_3 concentration partitioning between gaseous and particulate phases (step D). k_p is related to the net uptake coefficient (γ_{net}) as following:

$$k_p = \frac{1}{4} \omega \gamma_{\text{net}} S$$

where S is total particle surface to volume ratio and ω is mean thermal velocity of $\text{HNO}_3(\text{g})$. Using this approach, we calculated a net uptake coefficient of 0.09 ± 0.05 . The gaseous concentration of HNO_3 in the flow tube is 4 ppb. The uptake value observed is higher than the value of 0.057 ± 0.015 published by Hanisch and Crowley [8] who studied the reaction of HNO_3 with mineral dust in the Knudsen cell reactor. On the other hand our value is smaller than the uptake by CaCO_3 0.1-0.5 published by de Coninck [14] using another technique (aerosol flow reactor with chemiluminescence detection of nitric acid).

References

1. Neuman, J.A., et al., *Fast-response airborne in situ measurements of HNO_3 during the Texas 2000 Air Quality Study*. J. Geophys. Res., 2002. **107**: doi:10.1029/2001JD001437.
2. Huang, G., et al., *Measurements of atmospheric nitrous acid and nitric acid*. Atmos. Environ., 2002. **36**: 2225-2235.
3. Singh, H.B., et al., *Reactive nitrogen and ozone over the western Pacific: Distribution, partitioning, and sources*. J. Geophys. Res., 1996. **101**: 1793-1808.
4. Chatfield, R.B., *Anomalous HNO_3/NO_x ratio of remote tropospheric air: conversion of nitric acid to formic acid and NO_x* . Geophys. Res. Lett., 1994. **21**: 2705-2708.
5. Ginoux, P., et al., *Sources and distributions of dust aerosols simulated with the GOCART model*. J. Geophys. Res., 2001. **106**: 20255-20273.
6. Dentener, F.J., et al., *Role of mineral aerosol as a reactive surface in the global troposphere*. J. Geophys. Res., 1996. **101**: 22869-22889.
7. Underwood, G.M., et al., *Heterogeneous reactions of NO_2 and HNO_3 on oxides and mineral dust: A combined laboratory and modeling study*. J. Geophys. Res., 2001. **106**: 18055-18066.
8. Hanisch, F. and J.N. Crowley, *Heterogeneous reactivity of gaseous nitric acid on Al_2O_3 , CaCO_3 , and atmospheric dust samples: A Knudsen cell study*. J. Phys. Chem. A, 2001. **105**: 3096-3106.
9. Ammann, M., *Using ^{13}N as tracer in heterogeneous atmospheric chemistry experiments*. Radiochim. Acta, 2001. **89**: 831-838.
10. Guimbaud, C., et al., *Uptake of HNO_3 to deliquescent sea-salt particles: a study using the short-lived radioactive isotope tracer ^{13}N* . Atmos. Chem. Phys., 2002. **2**: 249-257.

11. Aschmutat, U., et al., *A tunable source of hydroxyl (OH) and hydroperoxy (HO₂) radicals: in the range between 106 and 109 cm⁻³*, in *Physico-chemical behaviour of atmospheric pollutants*, G. Angeletti and G. Restelli, Editors. 1994, European Commission: Luxembourg.
12. Marple, V.A., et al., *Diesel Exhaust Mine Dust Virtual Impactor Personal Aerosol Sampler - Design, Calibration and Field-Evaluation*. *Aerosol Sci Technol.*, 1995. **22**: 140-150.
13. Forsyth, B., et al., *Particle charge distribution measurement for commonly generated laboratory aerosols*. *Aerosol Sci Technol*, 1998. **28**: 489-501.
14. de Corninck, H.C., et al., *A potential role of mineral dust in tropospheric chemistry: Laboratory studies of trace gas uptake and reaction*. 8th European Symposium on the Physico-Chemical Behaviour of Atmospheric Pollutants, 2001.

Figures

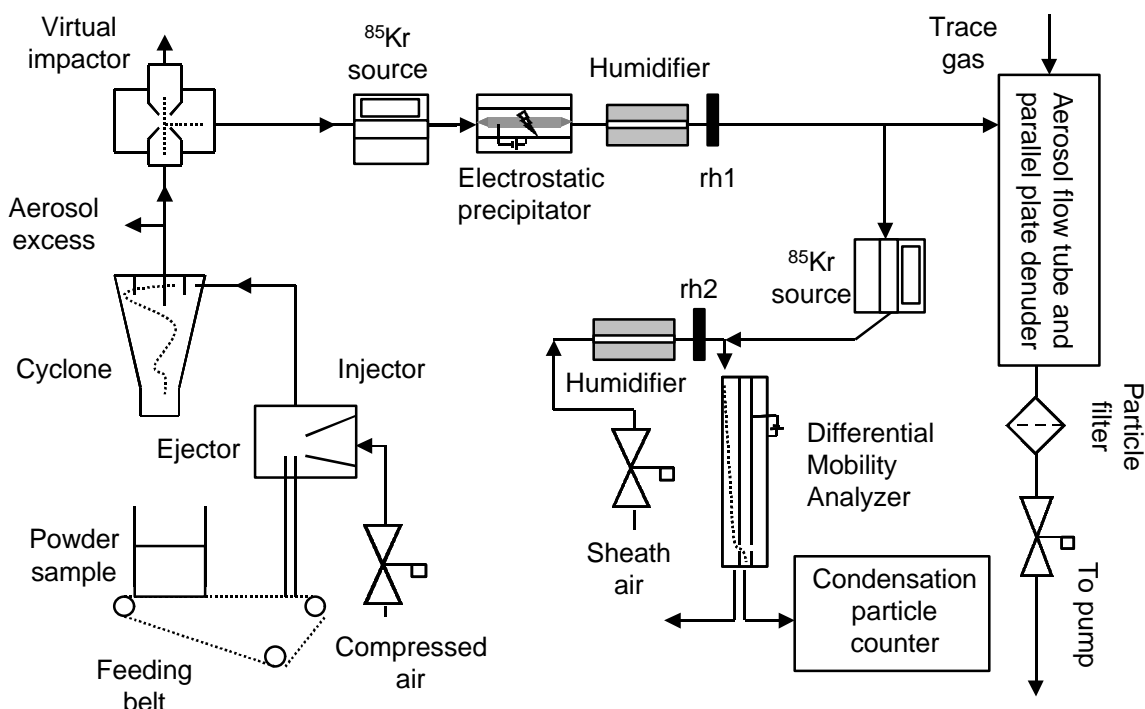


Figure 1. Experimental setup to generate mineral dust.

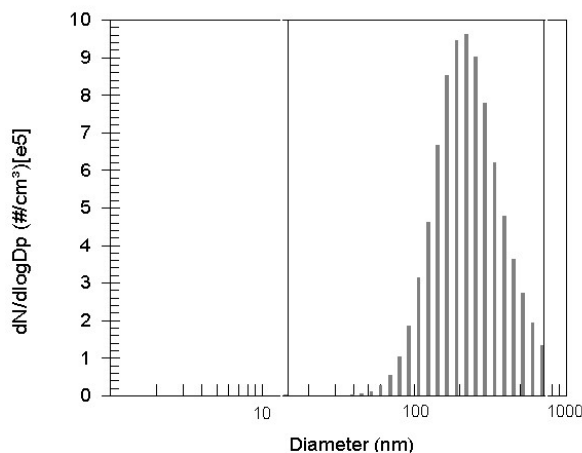


Figure 2. Particle size distribution of mineral dust

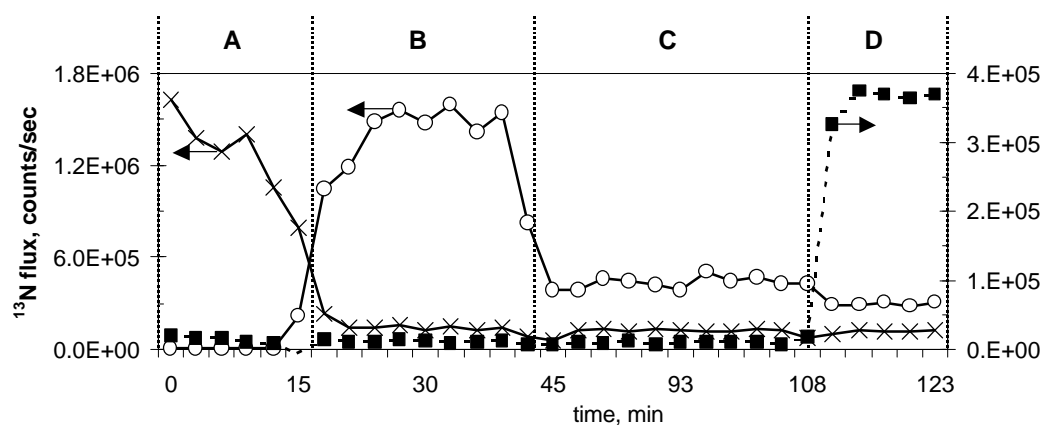


Figure 3. On line records of $\text{HNO}_3(\text{g})$ (open circles), HNO_3 associated with particles (solid squares), and $\text{NO}_2(\text{g})$ (crosses); see section 3.2 for more details.

The Interaction between Sea-Salt Aerosol and Marine Gaseous Chemistry (HEP2)

Wolfgang Behnke, Manfred Elend, Heinz-Ulrich Krüger, Wolf-Ulrich Palm* and Cornelius Zetzsch
Fraunhofer-Institut für Toxikologie und Aerosolforschung, Nikolai-Fuchs-Str. 1, D-30625 Hannover,

**Universität Lüneburg, Inst. f. Ökologie und Umweltforschung, D-21335 Lüneburg*

Introduction

Observations during the Arctic spring but even at mid-latitudes show that atomic Br and atomic Cl are produced in NO_x -poor periods (Pszenny et al., 1993; Jobson et al., 1994; Singh et al., 1996; Wingenter et al., 1996). Model calculations (Mozurkewich, 1995; Vogt et al., 1996, Sander and Crutzen, 1996) show that halogen-containing radicals are produced in the presence of sea-spray aerosol and ozone using Br^- as a catalysing species. Using an aerosol smog-chamber technique (Teflon bags), the activation of Br^- , I^- and Cl^- to atomic Br, I and Cl in sea-spray aerosol was investigated in laboratory experiments. Separate wetted-wall flow tube experiments observed the formation of BrCl from the uptake of Br_2 on NaCl solution to be independent of pH below 5 and to decrease at higher pH values.

The Activation of Chloride

Former unpublished experiments (performed in a flow tube, coated with teflon) show that in the presence of 80 ppm ozone, 80 ppm HCl, UV light and hydrocarbons nearly all HCl was transformed to Cl_2 within a few seconds. Similar results are achieved by Oum et al. (1998) at ozone concentrations above 10 ppm. But these conditions are not relevant to the environment. In the absence of Br^- we observed no production of atomic Cl if the ozone concentration was smaller than 500 ppb (the range of all our teflon bag experiments). Figure 1 shows an experiment, where ozone (300 ppb), hydrocarbons and pure NaCl aerosol are mixed together. To promote the chain reaction activating Cl^- , we injected 1.1 ppb Cl_2 additionally. But after the photolysis of Cl_2 no further production of atomic Cl was observed.

Figure 2 shows the influence of the aerosol water content on the production rate of atomic Cl in the presence of NaCl/NaBr aerosol. At higher relative humidities the rate of the activation is larger.

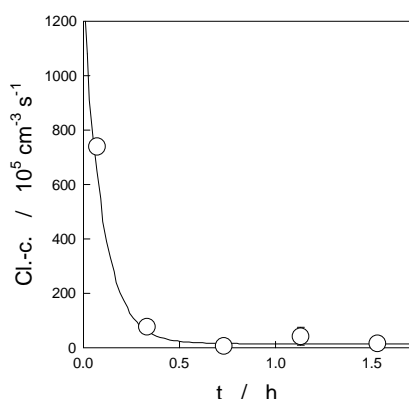


Fig. 1: Production rate of atomic Cl in the presence of pure NaCl aerosol and 350 ppb ozone (initial concentration) after the injection of 1.1 ppb Cl_2 .

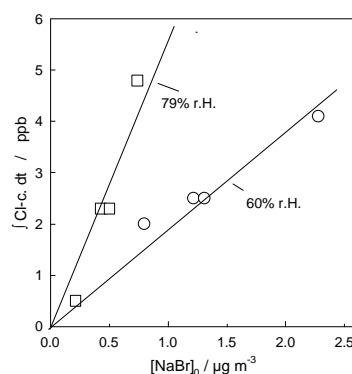


Fig. 2: Total degradation of hydrocarbons by atomic Cl after 4 hours vs. $[\text{NaBr}]_0$ at two different humidities. The lower humidity promotes Cl-production.

The Influence of Iodide on the Activation of Halogens from NaCl/NaBr-Aerosol

Replacing Br^- by I^- a constant but small production rate of atomic Cl is observed. Figures 3 and 4 show a summary of all experiments with Br^- or I^- or both (Br^- and I^-) for the influence of iodide on the production rate of atomic Cl and the decay of ozone. The influence of iodide on the production of atomic Cl is significant but smaller than that of bromide. Addition of iodide by more than one tenth of the bromide to the NaCl/NaBr aerosol leads to a saturation of the additional influence of iodide (upper curve in fig. 3).

In the absence of any iodide or bromide the ozone decay is generally observed to be exponential (depending on humidity mainly). Adding NaBr or NaI or NaBr+NaI to the aerosol accelerates the decay of ozone. Figure 4 shows this additional degradation rate of ozone, integrated over the first 4 hours of experimental time for each experiment. The circles in fig. 4 show experiments in the presence of NaCl/NaBr aerosol as a function of the initial Br^- -level, which was generated by various NaCl/NaBr ratios of the injected aerosol. The additional ozone decay shows almost quadratic behaviour (slope of 1.62 in this double logarithmic diagram):

$$\int_{0h}^{4h} O_{3-c} \cdot dt = 972 \cdot [\text{Br}^-]_0^{1.62} \quad (\text{equ. 1})$$

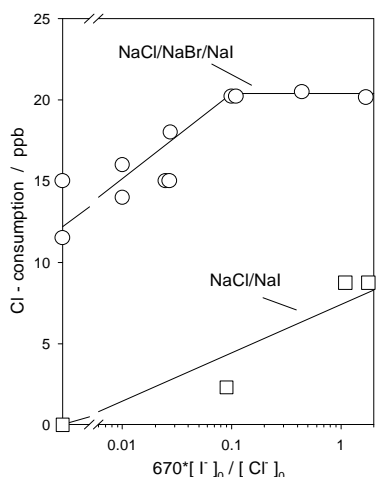


Fig. 3: Production of atomic Cl (integrated over 4 hours experimental time) in dependence of the initial I^-/Cl^- ratio. In experiments with NaBr the initial ratio of NaCl/NaBr was 670/1.

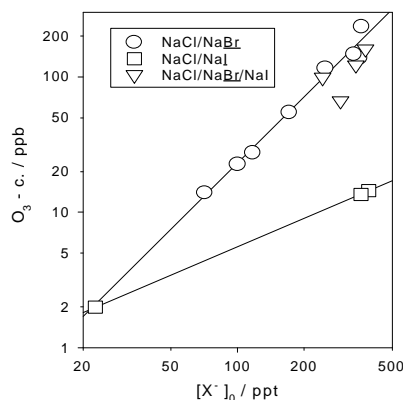


Fig. 4: Consumption of ozone by halogen reactions (integrated over 4 hours experimental time) in dependence of the initial $[\text{X}^-]$ (indicated by the underlined ion).

An exponent of two is expected if the BrO concentration of the gas phase is proportional to the Br^- injected at the beginning of the experiment (if the $\text{BrO} + \text{BrO}$ reaction is rate limiting, leading to 2Br which destroys ozone again). A smaller value of the exponent means further sinks of BrO , e.g. reactions of BrO with HO_2 , forming HOBr .

Upon addition of I^- to such aerosol (triangles in fig. 4), the decay of ozone becomes larger than in the absence of I^- . The additional ozone decay caused by iodide in the absence of bromide (squares in fig. 4) is less than 10% of that caused by bromide. Investigating the aerosol composition by ion chromatography we found a very fast transformation of I^- to IO_3^- after the illumination of the Teflon bag. This transformation may be responsible for the low ozone destruction potential of iodide in comparison with bromide. The mechanism of the transformation of I^- to IO_3^- has been described in detail by Vogt et al. (1999). Either HOI_{aq} is transformed by the reactions with $\text{Cl}_{2\text{aq}}$, $\text{Br}_{2\text{aq}}$, BrCl_{aq} , HOCl_{aq} or HOBr_{aq} to IO_2^- or by the reaction of 2IO^- and in a second step to IO_3^- .

The influence of externally mixed aerosols

In the presence of NaCl/NaBr-aerosol and SiO₂-, Fe₂O₃- or Al₂O₃- aerosol the production rate of atomic Cl is increased. This is shown in fig. 5. The results of all our experiments in the presence of these metal oxide aerosols and pure NaCl- or mixed salt aerosols are summarised in fig. 6. In both cases the amount of atomic Cl produced during the first 4 hours of the experiments increases in a linear fashion with the Br⁻ content of the aerosol, and the straight lines in fig. 6 are parallel.

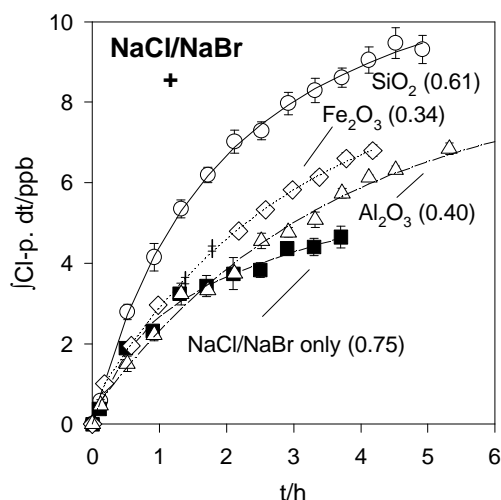


Fig. 5: In the presence of other mineral aerosols an additional production of atomic Cl was observed but several times smaller than in the presence of TiO₂. The numbers in parentheses are the initial NaBr-concentration of each experiment (in $\mu\text{g}/\text{m}^3$), contained in the NaCl. The concentrations (again $\mu\text{g}/\text{m}^3$) of the metal oxides are 176 (SiO₂), 347 (Fe₂O₃) and 153 (Al₂O₃) in the presence and 238 (SiO₂), 107 (Fe₂O₃) and 178 (Al₂O₃) in the absence of Br⁻

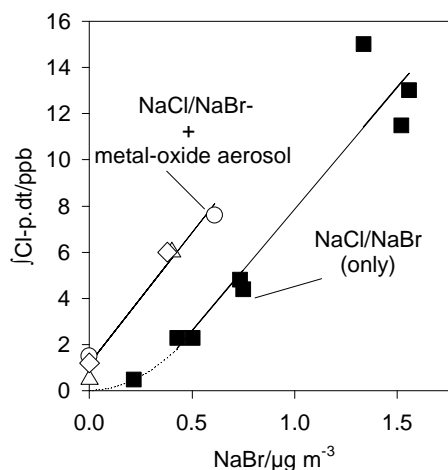


Fig. 6: With the exception of TiO₂ aerosol the production of atomic Cl (here integrated over 4 hours) of all experiments is proportional to the initial Br⁻-concentration with a positive intercept in the presence of metal oxide aerosols and a negative one in the absence.

But in the presence of the metal oxide aerosols a small positive offset is observed in the absence of Br⁻ (much smaller than in the presence of TiO₂-aerosol). Remarkable is the fact that the production rate of atomic Cl in the presence of the metal oxide aerosols is independent of the aerosol or its specific surface (the aerosol surface area varies by more than a factor of 2, see Behnke *et al.*, 1987). In the absence of metal oxide aerosols the straight line seems to have a negative offset. Obviously a small amount of the precursors of atomic Cl (HOBr, BrCl or Br₂) is consumed by oxidation reactions e.g. with acids (that of oxalic acid with Br₂ is described by Behnke *et al.* (1999)).

Conclusions

- Br₂ and BrCl are produced in the presence of NaCl/NaBr-aerosol, hydrocarbons, ozone and light. NaBr is necessary to activate Cl under environmental ozone concentrations.
- An additional activation of Br⁻ or Cl⁻ from iodide at typical marine ratios of I/Cl⁻ = 1/10⁶ is insignificant. Enriching I⁻ drastically to concentrations levels which would be more typical of Br⁻ in the aerosol, the influence of iodide remains small in comparison to bromide. No additional decay of ozone was found, the additional production rate of atomic Cl is about one third of that produced by bromide at similar concentrations. The small influence of

iodide is caused by fast transformations to iodate. A reduction of iodate to I^- may be responsible for the remaining small but constant production rate of atomic Cl.

- The presence of metal oxide aerosols increases the production rate of atomic Cl, especially at low Br^- -concentrations. This may be important during dust outbursts from deserts.
- Though the observed, very high production rates of atomic Cl in the presence of TiO_2 -aerosol are not expected to be relevant under environmental conditions, the potential impact of a photocatalytic activation is demonstrated.

References

- Behnke, W., F. Nolting and C. Zetzsch, The atmospheric fate of di(2-ethylhexyl)-phthalate, adsorbed on various metal oxide aerosols and on coal fly ash, *J. Aerosol. Sci.* **18** (1987) 849-852.
- Behnke, W., M. Elend, U. Krüger, and C. Zetzsch, The influence of pH and NaBr/NaCl ratio on the Br^- -catalysed production of halogenated radicals *J. Atmos. Chem.* **34** (1999) 87-99.
- Jobson, B.T., H. Niki, Y. Yokouchi, J. Bottenheim, F. Hopper and R. Leaitch, Measurements of C_2 - C_6 hydrocarbons during the Polar Sunrise 92 Experiment: Evidence for Cl-atom and Br-atom chemistry, *J. Geophys. Res.* **D99** (1994), 25355-25368.
- Mozurkewich, M. (1995) Mechanisms for the release of halogens from sea-salt particles by free radical reactions, *J. Geophys. Res.*, **D100**, 14199-14207.
- Oum, K.W., M.J. Lakin, D.O. DeHaan, T. Brauers, and B.J. Finlayson-Pitts; Formation of molecular chlorine from the photolysis of ozone and aqueous sea-salt particles, *Science* **279** (1998) 74-77.
- Pszenny, A.A.P., W.C. Keene, D.J. Jacob, S. Fan, J.R. Maben, M.P. Zetwo, M. Springer-Young, and J.N. Galloway, Evidence of inorganic chlorine gases other than hydrogen chloride in marine surface air, *Geophys. Res. Lett.* **20** (1993) 699-702.
- Sander, R. and P. Crutzen, Model study indicating halogen activation and ozone destruction in polluted air masses transported to the sea, *J. Geophys. Res.* **D101** (1996) 9121-9138.
- Singh, H.B., G.L. Gregory, B. Anderson, E. Browell, G.W. Sachse, D.D. Davis, J. Crawford, J.D. Bradshaw, R. Talbot, D.R. Blake, D. Thornton, R. Newell, J. Merrill; Low ozone in the marine boundary layer of the tropical Pacific Ocean, *J. Geophys. Res.* **D101** (1996) 1907-1917.
- Vogt, R., P.J. Crutzen and R. Sander, A mechanism for halogen release from sea-salt aerosol in the remote marine boundary layer, *Nature* **383** (1996) 327-330.
- Vogt, R., R. Sander, R. von Glasow, and P.J. Crutzen, Iodine chemistry and its role in halogen activation and ozone loss in the marine boundary layer: A model study, *J. Atmos. Chem.* **32** (1999) 375-395.
- Wingenter, O.W., M.K. Kubo, N.J. Blake, T.W. Smith Jr., D.R. Blake, and F.S. Rowland; Hydrocarbon and halocarbon measurements as photochemical and dynamical indicators of atmospheric hydroxyl, atomic chlorine, and vertical mixing obtained during Lagrangian flights, *J. Geophys. Res.* **D101** (1996) 4331-4340.

Interaction of Trace Gases with Water-ice Surfaces (HEP4)

A. K. Winkler, N. S. Holmes and J. N. Crowley

Max-Planck-Institut für Chemie

Division of Atmospheric Chemistry,

P.O.Box 3060, 55020 Mainz, Germany

Introduction

Cirrus ice in the upper troposphere can potentially play an important role in modifying photochemical cycles by providing a surface for heterogeneous processes. Reversible processes that influence the partitioning of trace gases between the gas and ice phase, and reactive processes that influence e.g. the NO_x to NO_y ratio are both likely to take place in cirrus clouds. Ozone production in the upper troposphere depends on levels of NO_x and the NO / NO₂ ratio, which is strongly perturbed by the presence of peroxy radicals, e.g. HO₂. As the major source of HO₂ in the upper troposphere is now believed to be the degradation of partially oxidized hydrocarbons (POH) [Singh *et al.*, 1995; Jaeglé *et al.*, 1998; Folkins and Chatfield, 2000], factors influencing both NO_x and POH need to be understood.

Experimental

A coated wall flow tube (CWFT) was coupled to a quadrupole mass spectrometer (QMS) to investigate the interaction of trace gases with the ice surface (Fig. 1). The walls of the flow tube were covered with a polycrystalline ice film after purified deionized water was frozen at T = 258 K. The films were 60 - 200 nm thick. The experiments were conducted at temperatures between 198 K and 218 K at a total pressure of Helium between 1 - 3 Torr. The trace gas was diluted in helium and flowed along a sliding injector in the centre of the insert.

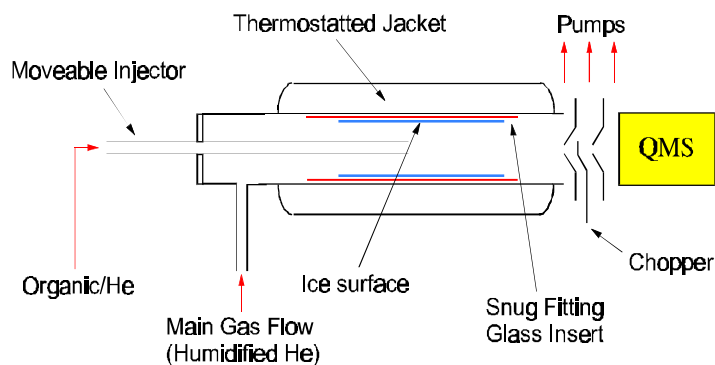


Figure 1: Experimental set-up

Acetone and formaldehyde were measured using electron impact ionization (acetone at the CH₃CO⁺ fragment ion with $m/z = 43$, formaldehyde at $m/z = 30$), methanol was measured using electron impact and chemical ionization (at $m/z = 31$). HNO₃ and N₂O₅ were measured using chemical ionization mass spectrometry (CIMS).

In all experiments on POH, the injector was first pulled back to expose the trace gas to the ice surface. A drop in the signal is observed when the trace gas is taken up by the ice. This uptake is time-dependent and the signal returns to the original value. When the injector is pushed in the desorption process is observed as an increased signal. The number of molecules taken up by the ice was calculated from the integrated area of the adsorption and desorption peaks. We observed a completely reversible uptake as the areas of the adsorption and desorption peaks are the same.

The surface coverage (number of molecules taken up per cm² of ice surface) as a function of the concentration is well described by the Langmuir equation (eq. 1).

Langmuir Isotherms

Assuming less than a monolayer of trace gas covering the ice surface, the surface coverage sc was fitted to obtain the Langmuir constant $K_L(T)$ according to the following equation:

$$sc = sc_{\text{sat}} K_L(T) c / (1 + K_L(T)c) \quad (\text{equation 1})$$

where c is the concentration and sc_{sat} the maximum surface coverage.

For low concentrations the Langmuir equation can be approximated by the linear equation

$$sc = sc_{\text{sat}} K_L(T) c = K^\#(T) c \quad (\text{equation 2})$$

$K^\#(T)$ shows an Arrhenius-like temperature dependence which is displayed in figure 3.

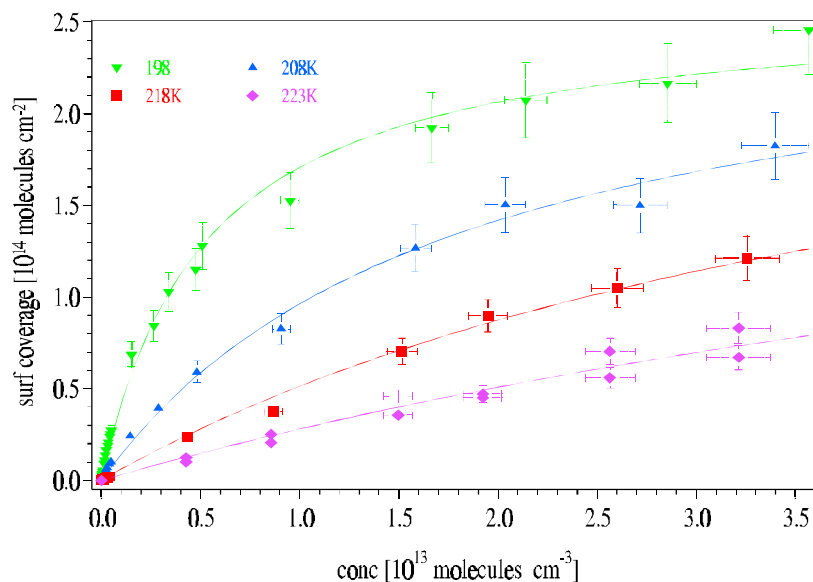


Figure 2: Langmuir plot of surface coverage (molecules/cm²) of acetone versus acetone concentration (molecules/cm³)

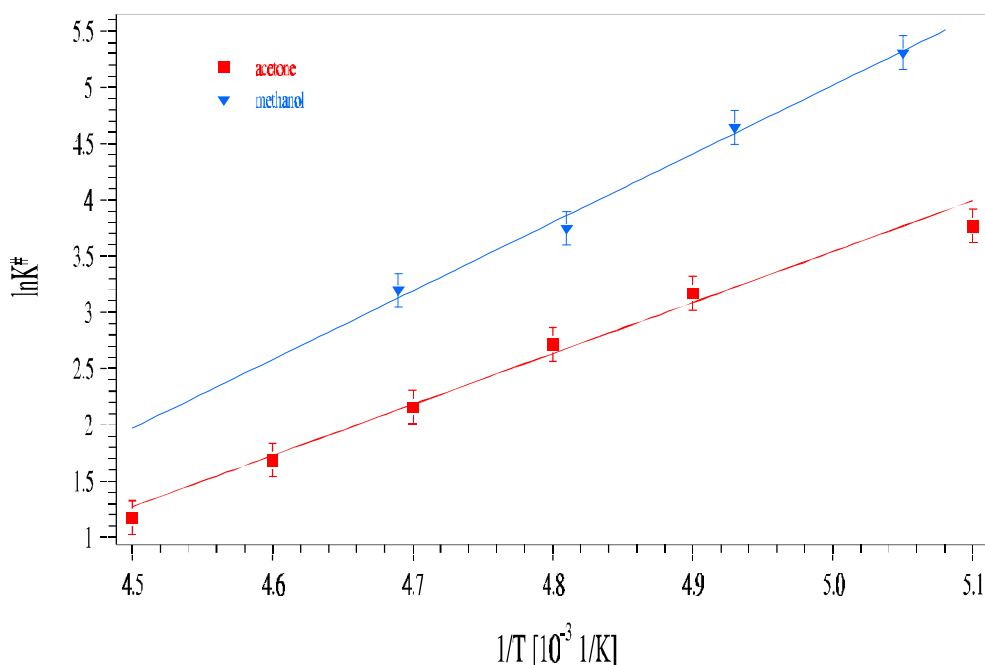


Figure 3: Temperature dependence of $K^\#$. The lines are least square fits to equation 3

Interaction of POH with ice

The adsorption of POH on ice at temperatures between 198 K and 223 K is completely reversible. Adsorption isotherms fitting the low concentration data according to equation 2 were used to derive $K^\#(T)$ for different temperatures T . $\ln K^\#(T)$ and $1/T$ display a linear relationship according to:

$$K^\#(T) = A \exp(-\Delta H_{\text{ads}}/RT) \quad (\text{equation 3})$$

where A is a constant, ΔH_{ads} the enthalpy of adsorption and R the gas constant. Enthalpies of adsorption for methanol $\Delta H_{\text{ads}} = -51(10)$ kJ/mol and acetone $\Delta H_{\text{ads}} = -46(7)$ kJ/mol were derived (fig. 3). For formaldehyde the partitioning coefficient $K^\# = 0.7$ cm showed no temperature dependence. From the Langmuir isotherms a maximum surface coverage $sc_{\text{sat}} = 2.7(7) \times 10^{14}$ molecules/cm² for acetone and $sc_{\text{sat}} = 3.2 \times 10^{14}$ molecules/cm² were derived, which correspond approximately to complete surface coverages derived from calculations assuming spherical geometry of the molecules. At high concentrations there were indications that adsorbate - adsorbate - interactions violate the assumptions made in the Langmuir analysis. Thus only low concentration data was used to derive the enthalpies of adsorption. The presence of O₃ has no influence on the methanol - ice interaction.

CIMS Detection of N₂O₅ and HNO₃

A chemical ionization detection scheme was developed to improve the sensitivity and selectivity of the experiment. H₃O⁺ - ions are produced in a discharge which is created in a N₂/H₂O - mixture at 1 Torr. HNO₃ and N₂O₅ can be detected using H₃O⁺ - ions ($m = 46$). A mass spectrum of N₂O₅ at $c = 2 \times 10^{10}$ molecules/cm³ is shown in figure 4.

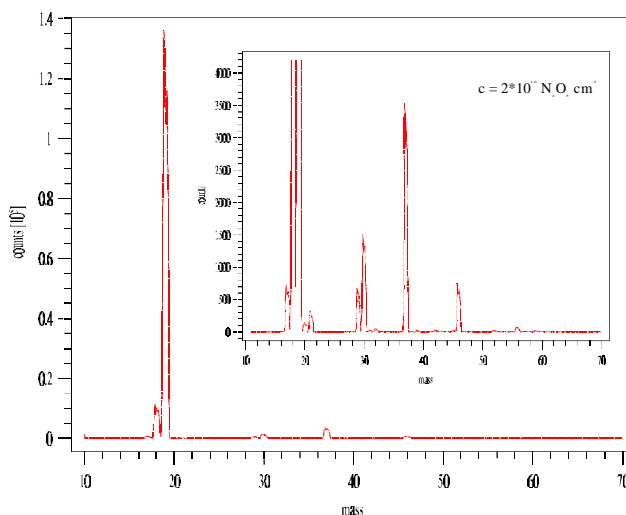


Figure 4: Mass spectrum of N₂O₅ using chemical ionization with H₃O⁺ ions

Atmospheric Implications

Our data allow us to investigate whether the adsorption of POHs on ice surfaces, e.g. cirrus clouds, is a relevant process for its removal from the upper troposphere. We note that the rate of trace gas adsorption on ice depends on the uptake coefficient γ (fraction of collisions of a trace gas with a surface that results in removal from the gas phase). From our data, we derive a lower limit of $\gamma = 1 \times 10^{-2}$ for both acetone and methanol. Assuming ice surface area densities A of up to 10^{-4} cm²/cm³, lifetimes of only a few hours are obtained. However, a further important consideration is the capacity of the ice to significantly influence the concentrations in the gas-phase. Under conditions which are typical for the upper troposphere ($T = 203$ K, $A = 10^{-4}$ cm²/cm³), the ratio $R = K^\#(T)A$ of POH molecules adsorbed by the ice surface to the number of POH molecules in the gas phase is 2.4×10^{-3} , 1.2×10^{-2} and 7×10^{-5} for acetone, methanol and formaldehyde, respectively. This implies that the gas phase concentration of POH is not significantly perturbed by the presence of cirrus

clouds. In addition, the equilibrium surface coverage of about 10^{-4} (4×10^{-4}) of a monolayer (for methanol and acetone, respectively) is not likely to significantly modify the physical and chemical properties of cirrus ice.

References

1. Singh, H.B., Kanakidou, M.;Crutzen, P.J., Jacob, D.J. *Nature* 378, 50-54 (1995).
2. Folkins, I.; Chatfield, R., J. *Geophys. Res.*, 105, 11585-11599 (2000)
3. Jaegle, L. et al., *Geophys. Res. Lett.*, 25, 1709-1712 (1998)
4. Adams, J.W., Holmes, N.S., Crowley, J.N., *Atmos. Chem. Phys.*, 2, 79-91 (2002)
5. Winkler, A. K., Holmes, N.S., Crowley, J.N., *Phys. Chem. Chem. Phys.*, 4, 5270-5275 (2002)

Aerosol flow tube studies of trace gas uptake to mineral dust (HEP4)

Friedrich Hanisch, Heleen de Coninck and John N. Crowley

Max-Planck-Institut für Chemie

Division of Atmospheric Chemistry

P.O.Box 3060, 55020 Mainz, Germany

Introduction

The ratio of NO_x to NO_y in the troposphere is correlated to O_3 concentrations. The ratio of HNO_3 to NO_x is frequently overestimated in photochemical models (e.g. Hauglustaine *et al.*, 1996). Mineral aerosol is an important constituent of the tropospheric particulate phase, and estimates suggest that between 1600 and 2000 Tg of mineral aerosol are uplifted annually into the mid troposphere by surface winds from dry soils in arid regions (Ginoux *et al.*, 2001), especially in East Asia (Tarim basin) and North Africa (Sahara). Mineral aerosol may play a role in influencing the NO_y/NO_x ratio by providing a surface for heterogenous reactions (Tabazadeh *et al.*, 1998).

Recent modelling studies (Zhang *et al.*, 1994; Dentener *et al.*, 1996) have predicted that heterogenous reactions on mineral dust can reduce NO_x levels by 50% and that HNO_3 uptake could remove all HNO_3 from the gas-phase. In vast regions of the northern and southern hemisphere at least 40% of the total nitrate was predicted to be bound to mineral aerosol. Recently, a 50% reduction of tropospheric ozone has been observed in the presence of mineral aerosol. The effect was attributed to 50% to HNO_3 uptake onto the mineral surface (De Reus *et al.*, 2000).

So far, only little attention has been paid to the role of mineral aerosol in heterogenous chemistry. Presently, there are only a few investigations that define the heterogenous reactivity of HNO_3 on mineral dust. These investigations were based on the Knudsen reactor technique and yielded uptake coefficients that differed between 10^{-1} (Hanisch and Crowley, 2001) and 10^{-5} (Underwood *et al.*, 2001). In this study we use an aerosol flow reactor to determine the uptake coefficient for uptake of HNO_3 onto mineral aerosol. This technique has some advantages over the Knudsen reactor technique because mineral aerosol surface presentation is similar to the one in the atmosphere, and relative humidities can be adjusted.

Experimental

The experiments to investigate the reactivity of HNO_3 towards mineral aerosol were carried out at ambient pressure and temperature in a glass flow reactor ($l = 140$ cm). Saharan dust, mobilised by a commercial rotating brush generator, and gas-phase nitric acid, mixed into an N_2 flow, were fed into a laminar N_2 flow ($Re = 275$) at concentrations of $\sim 10^3 \text{ cm}^{-3}$ and $\sim 10^{13} \text{ cm}^{-3}$, respectively. Dust particles were counted by an optical particle counter sizer, and HNO_3 was measured by chemiluminescence. Particles bigger than $10 \mu\text{m}$ in diameter were removed by an impactor. The number density and surface area distributions of the dust particles are shown in Figure 1. The reaction time inside the aerosol flow reactor was 7-10 sec.

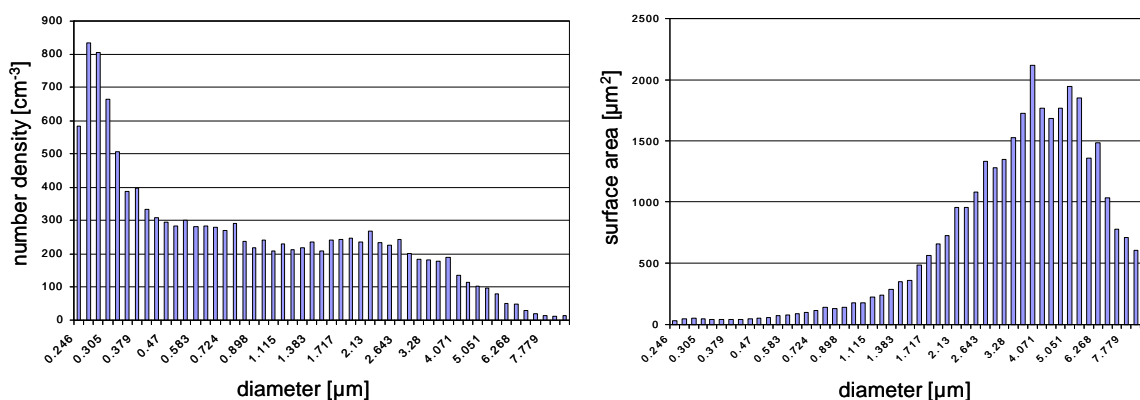


Figure 1. Number density and surface area distributions of Saharan dust particles after passage through the impactor.

Results

Experiments were performed using dust pulses of 10 to 60 sec duration in order to reduce loss of particles to the reactor walls. A reduction of the HNO_3 concentration in the presence of dust is clearly visible (Figure 2). Since HNO_3 loss is a pseudo-first order process:

$$\frac{d}{dt}[\text{HNO}_3] = -k^{\text{II}}[\text{HNO}_3][\text{dust}] ,$$

the rate constant k^{II} can be calculated from a plot of the logarithm of the relative HNO_3 loss versus dust concentration times reaction time (Figure 3). Imperfect mixing was observed for reaction lengths shorter than 80 cm; therefore, data at 60 cm reaction length were not used for the determination of k^{II} (open triangles).

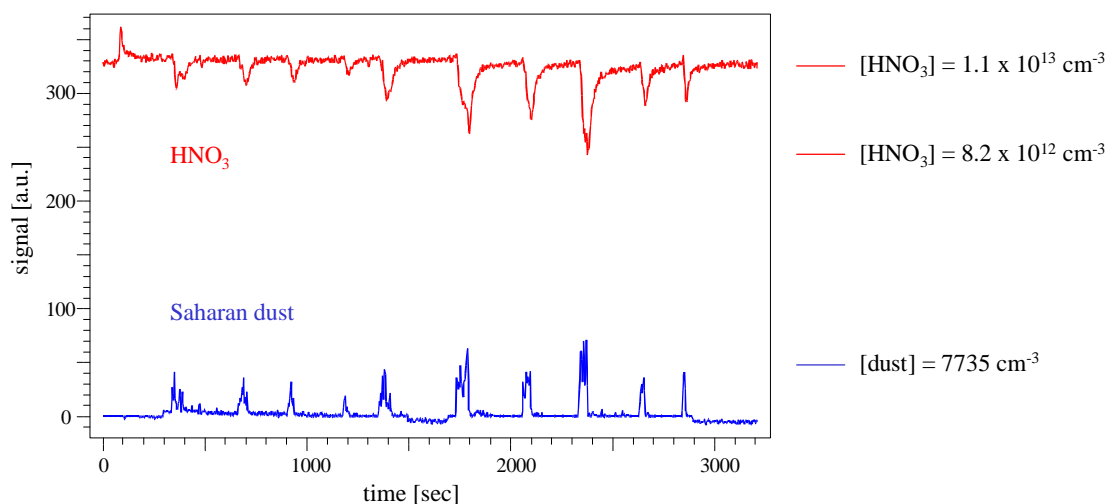


Figure 2: Uptake of HNO_3 onto Saharan dust particles. Dust pulse duration was between 10 and 60 seconds.

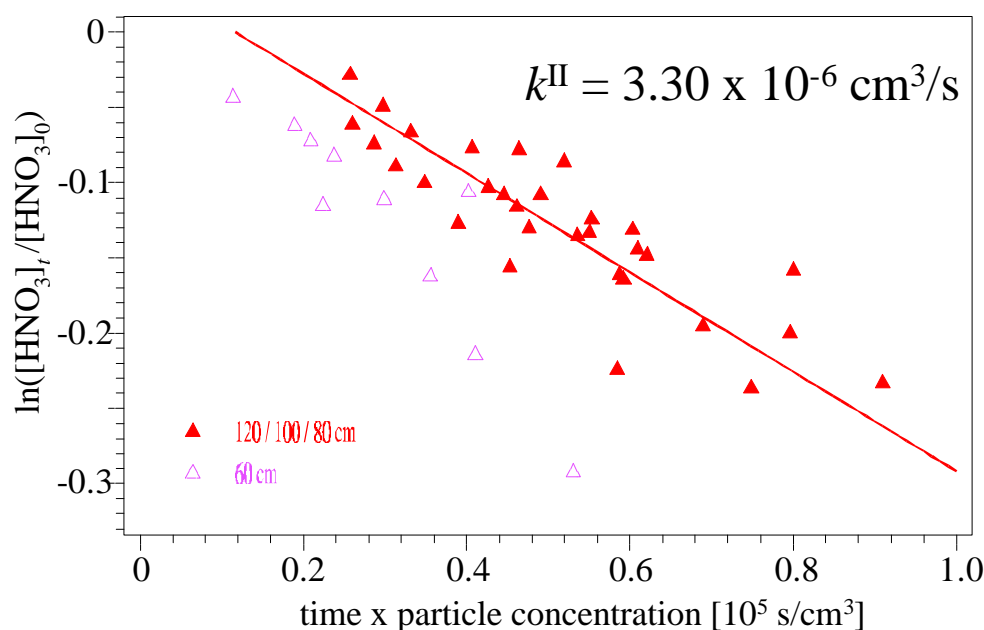


Figure 3: Plot of the logarithm of the relative HNO_3 loss versus dust concentration times reaction time. Only data from experiments with reaction length 80, 100 and 120 cm are used for the calculation of k^{II} .

The fit of the uptake data yields $k^{\text{II}} = 3.3 \times 10^{-6} \text{ cm}^3/\text{s}$ ($\pm 12\%$). The average surface area was determined by the particle counter size to be $A = 2 \mu\text{m}^2$ per dust particle ($\pm 15\%$). From these values, the uptake coefficient γ can be calculated according to $\gamma = 4 k^{\text{II}} [\text{dust}] / \bar{c} A [\text{dust}]$, where \bar{c} ($= 3.16 \times 10^4 \text{ cm/s}$) is the molecular velocity of HNO_3 at 296 K.

Our result for the uptake of HNO_3 onto airborne Saharan dust particles is $\gamma = 0.016 \pm 0.003$. This value should be regarded as a lower limit of γ because of HNO_3 -reactor wall effects and because fine particles coated with nitrate enter the chemiluminescence detector. Effects due to diffusion limitation should be negligible at a surface averaged particle radius of $0.4 \mu\text{m}$.

The atmospheric lifetime τ of HNO_3 with respect to uptake by mineral aerosol can be estimated according to $\tau = 4 / (\gamma \bar{c} A)$. A is the aerosol surface area density which is on the order $10^{-7} \text{ cm}^2/\text{cm}^3$ for a moderately high dust loading of $5 \mu\text{g}/\text{m}^3$. $\gamma = 0.016$ results in an atmospheric lifetime of 22 hours which is high enough for uptake onto mineral aerosol to compete with the photolytic lifetime of HNO_3 .

Acknowledgements

We acknowledge financial support from the European community (Minatroc).

References

- Dentener, F.J., Carmichael, G.R., Zhang, Y., Lelieveld, J., and Crutzen, P.J.; *J. Geophys. Res.* **101** (1996) 22869-22889.
- Fenter, F.F., Caloz, F., and Rossi, M.J.; *Atmos. Environ.* **29** (1995) 3365-3372.
- Ginoux, P., Chin, M., Tegen, I., Prospero, J.M., Holben, B., Dubovik, O., and Lin, S.-J.; *J. Geophys. Res.* **106** (2001) 20255-20273.
- Hanisch, F. and Crowley, J.; *Phys. Chem. Chem. Phys.* **3** (2001) 2474-2482.
- Hauglustaine, D.A., Ridley, B.A., Solomon, S., Hess, P.G., and Madronich, S.; *Geophys. Res. Lett.* **23** (1996) 2609-2612.

- Reus, M. de, Dentener, F., Thomas, A., Borrmann, S., Ström, J., Lelieveld, J.; *J. Geophys. Res.* **105** (2000) 15263-15275.
- Tabazadeh, A., Jacobson, M.Z., Singh, H.B., Toon, O.B., Lin, J.S., Chatfield, R.B., Thakur, A.N., Talbot, R.W., and Dibb, J.E.; *Geophys. Res. Lett.* **25** (1998) 4185-5188.
- Underwood, G.M., Li, P., Al-Abadleh, H., and Grassian, V.; *J. Phys. Chem.* **105** (2001) 6609-6620.
- Zhang, Y., Sunwoo, Y., Kotamarthi, V., and Carmichael, G.R.; *J. Appl. Meteorol.* **33** (1994) 813-824.

Mechanism leading to SOA-particle formation in the oxidation of biogenic alkenes (HEP7)

Boris Bonn and Geert K. Moortgat

Max-Planck-Institut für Chemie, Atmospheric Chemistry Division, D-55099 Mainz, Germany

bonn@mpch-mainz.mpg.de

Abstract

It is established that secondary organic aerosol (SOA) is formed during the reaction of ozone with biogenic alkenes. However, it has not been established if both other atmospherically important reactions of alkenes, i.e. the OH- and the NO₃-oxidation reaction, contribute to the SOA formation. Moreover, the nucleating species as well as their formation mechanisms are still topics of discussion.

This laboratory study on the SOA particle size distribution tries to compare all the three possible oxidation reactions of a single monoterpene with respect to aerosol formation, as well as to describe the mechanism for the homogeneous particle formation during the ozonolysis of these terpenes. Therefore, experiments were performed in a spherical glass vessel of 570 L volume, as well as in a flow reactor at atmospheric pressure. The particle size distribution was measured by a scanning mobility particle sizer, including a long DMA and an ultra-fine particle counter, with a time resolution of two minutes. All reactions were conducted using initial monoterpene mixing ratios of 500 ppbv as well as 50 ppbv. Different concentrations of substances such as water vapour, acids and carbonyl compounds were occasionally added. In addition, *cyclo*-hexane was present during the ozonolysis experiments to prevent interfering reactions of the produced OH-radicals with the alkene (Bonn and Moortgat, 2002). The results indicate that the homogeneous nucleation process during the ozonolysis of terpenes is controlled by the formation of large secondary ozonides, whose formation can be suppressed by the addition of water vapour. These nucleating secondary ozonides are formed differently in endo- and exocyclic reactions: *intramolecularly* in endocyclic and *intermolecularly* in exocyclic monoterpene ozonolyses (Bonn et al., 2002a). Consequently, the nucleation during endocyclic monoterpene reactions is found to be less pronounced than during exocyclic ozonolyses due to the smaller secondary ozonides formed.

Finally, studies on the nucleation threshold of monoterpene and sesquiterpene-ozone reactions (Koch et al., 2000; Bonn et al. 2002b) lead to the conclusion that homogeneous particle formation in the atmosphere is induced by secondary ozonides produced during the ozonolysis of sesquiterpenes, whereas both monoterpene and sesquiterpene reaction products contribute to heterogeneous aerosol (volume) formation.

Experimental

All experiments were performed in a static glass vessel of 570 L volume at a temperature of 295 ± 2 K and a pressure of 730 ± 1 Torr. Two selected monoterpenes, i.e. α - and β -pinene, were diluted in synthetic air, both in two different initial mixing ratios of 500 and 50 ppbv, and reacted further with either O₃, OH or NO₃. During the reaction the aerosol formed inside the reactor was physically characterised with a scanning mobility particle sizer (SMPS, TSI 3936) consisting of a long differential mobility particle analyser (LDMA, TSI 3081) and an ultra-fine particle counter (UCPC, TSI 3025A) with a time resolution of two minutes.

In order to study the influence of water vapour, all experiments were conducted at two different dew points, a) a dew point of -80 °C (in the following referred as "dry" experiments) and b) a dew point of $+4$ °C (referred as "humid" experiment). In addition, several carbonyl compounds as well as HCOOH were added in single ozonolysis experiments to examine the nucleation mechanism in the ozone-reaction. Finally, several experiments have been conducted with the sesquiterpene β -

caryophyllene and ozone in the absence of any OH-scavenger at initial mixing ratios of 25 pptv of the alkene and 50 ppbv of ozone.

Results

Our results showed that the ozonolysis reactions produced by far the highest number concentration of new aerosol particles, whereas the OH- as well as the NO₃-reactions contributed significantly to the aerosol volume yield (see Table 1). Therein the ozonolysis formed around 50 times more new aerosol particles than the OH- and the NO₃-reactions at the maximum stage during the experiments with an initial monoterpene mixing ratio of 500 ppbv. Moreover, the ozone reaction was found to be the only particle source in the experiments with the lower initial concentration of 50 ppbv, with the exception of the reaction of β -pinene with NO₃. However, the number concentration of the latter reaction was found close to the background level. Consequently, the products of the OH- and the NO₃-reactions with the monoterpenes possess a higher volatility than the products of the ozonolysis, which are able to initiate homogeneous nucleation even at 50 ppbv initial monoterpene concentration.

The influence of water vapour on the nucleation process studied for all reactions revealed no effect on the aerosol formed by the OH- and the NO₃-reaction, but only on the aerosol produced during the ozonolysis. In this case the aerosol number as well as the aerosol volume was reduced. This effect was more pronounced for the exocyclic monoterpene reactions, but less for endocyclic reactions.

Table 1: Maximum number and volume concentration during the oxidation reaction of α - and β -pinene with 500 ppbv initial mixing ratio.

Oxidant	Maximum aerosol number concentration, N^{\max} [10 ⁵ cm ⁻³]		Maximum aerosol volume concentration, V^{\max} [10 ¹¹ nm ³ cm ⁻³]	
	β -pinene	α -pinene	β -pinene	α -pinene
O ₃	10 ± 1	4.0 ± 0.2	3.0 ± 0.2	9.6 ± 0.2
OH	0.17 ± 0.005	0.05 ± 0.004	6.7 ± 1.0	2.3 ± 0.4
NO ₃	0.2 ± 0.005	0.017 ± 0.002	4.2 ± 0.2	1.1 ± 0.1

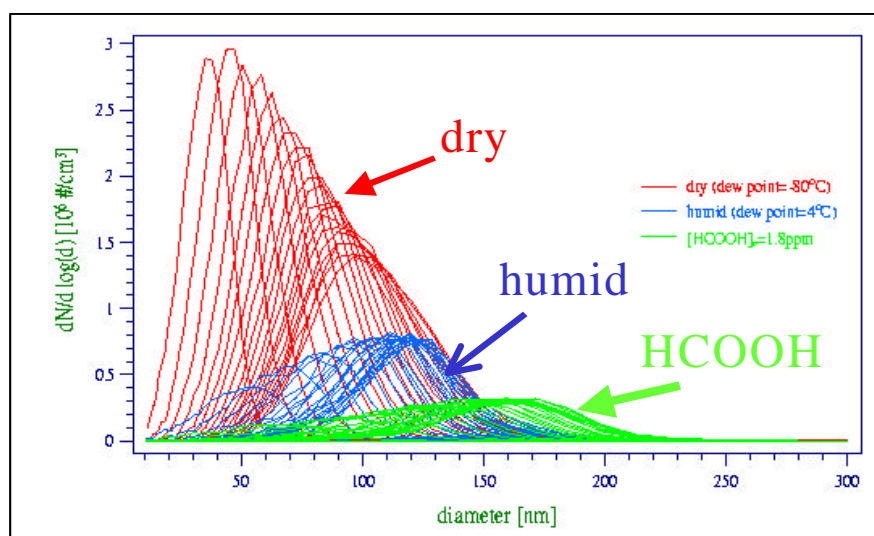


Figure 1: Particle size distribution during an ozonolysis of β -pinene at 500 ppbv initial mixing ratio: a) reference experiment (red); b) with added water vapour (blue) and c) with added HCOOH (1.8 ppmv, green)

Consequently, the formation pathway of nucleation substances proceeds via the stabilised Criegee Intermediates, which are known to react with H₂O molecules. Further experiments with added HCOOH (see Figure 1), alcohols and carbonyl compounds indicate that the produced large secondary ozonides (SOZ) may be responsible for the observed nucleation: the C₁₈-SOZ from the reaction of nopinone with the stabilised C₉-Criegee intermediate in the case of the exocyclic β -pinene and the intramolecularly formed C₁₀-SOZ in the case of the endocyclic α -pinene. Additional experiments indicated that nucleation can be suppressed by the addition of water vapour, so that this is the only channel leading to nucleation.

Atmospheric implications

The reducing effect of water vapour has also been observed in field studies (Boy and Kulmala, 2002), but the nucleation threshold, the amount of monoterpene to be reacted prior to particle formation, is too high to initiate homogeneous nucleation in the real atmosphere. Therefore, experiments with a sesquiterpene (β -caryophyllene) have been conducted at initial concentrations of 25 pptv of the terpene and 50 ppbv of ozone (Figure 2). The results indicate that most likely sesquiterpenes are responsible for the atmospherically observed homogeneous nucleation. This reaction is again affected by the presence of water vapour and a relationship between dew point and nucleation threshold have been obtained (Bonn et al., 2002b). Therefore, only ozonolysis reactions are able to initiate homogeneous particle formation in the atmosphere at concentration levels in the range of hundreds of pptv in maximum.

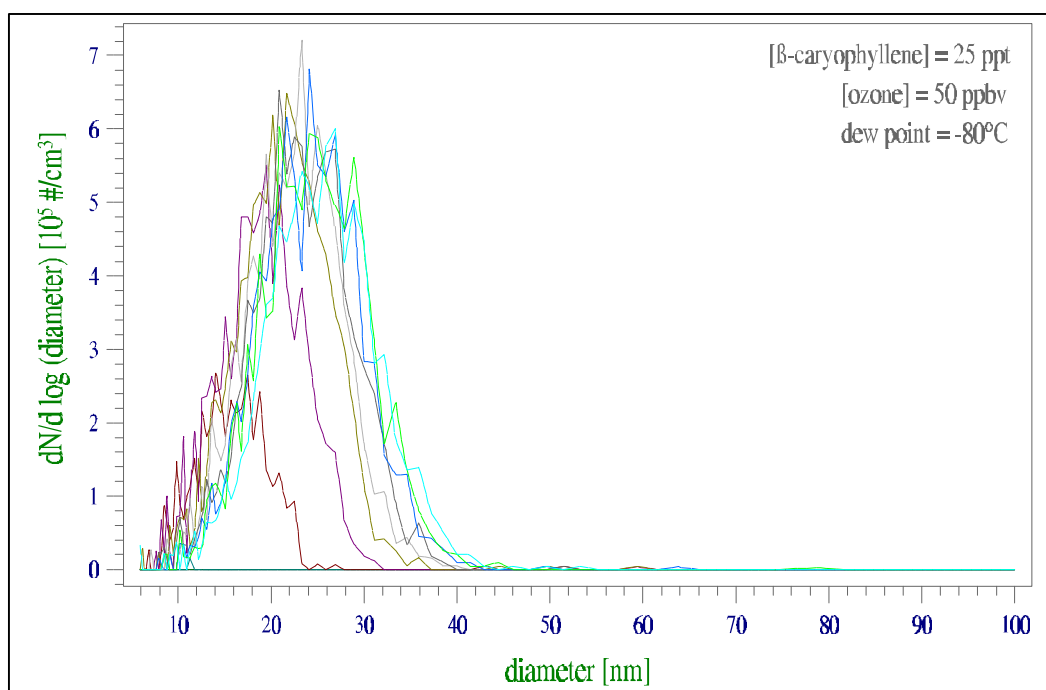


Figure 2: Particle size distribution in the "dry" ozonolysis of 25 pptv β -caryophyllene and 50 ppbv ozone.

References

- Bonn, B., G. Schuster, and G. K. Moortgat, Influence of water vapor on the process of new particle formation during monoterpene ozonolysis, *J. Phys. Chem. A*, 106, 2869-2881, 2002a.
- Bonn, B., and G. K. Moortgat, New particle formation during α - and β -pinene oxidation by O₃, OH and NO₃, and the influence of water vapour: particle size distribution studies. *Atmos. Chem. Phys.*, 2, 183-196, 2002.

- Bonn, B., A. Sadezky, and G. K. Moortgat, Importance of sesquiterpene-ozone reactions for biogenic secondary organic aerosol formation in the atmosphere. in preparation, 2002b.
- Boy, M and M. Kulmala, Nucleation events in the continental boundary layer: Influence of physical and meteorological parameters. *Atmos. Chem. Phys.*, 2, 1-16, 2002.
- Koch, St., R. Winterhalter, E. Uherek, A. Kolloff, P. Neeb, and G. K. Moortgat, Formation of new particles in the gas-phase ozonolysis of monoterpenes. *Atmos. Environ.*, 34, 4031-4042, 2000.

The characterization of surface functional groups of Secondary Organics Aerosols (SOA) generated under laboratory conditions (HEP9)

Benjamin Demirdjian and Michel J. Rossi

LPA (Laboratoire de Pollution Atmosphérique), ISTE/ENAC

EPFL (Ecole Polytechnique Fédérale de Lausanne), CH-1015 Lausanne (Switzerland)

Introduction

Today, large uncertainties persist concerning the impact of aerosols on the radiative forcing owing to the very low level of scientific understanding of the mechanisms involved. Radiative forcing due to aerosols not only depends on its spatial distribution, but also on the size, shape, and chemical composition of the particles [1]. The present work intends to characterize the surface functional groups of aerosol particles generated under well-controlled conditions as these groups primarily interact with atmospheric gases. This work is focused on Secondary Organic Aerosols (SOA) which are particulate matter formed in the atmosphere via oxidation of natural or man-made volatile organic compounds (VOC).

We have chosen toluene (C_7H_8) as an anthropogenic VOC since it is the most abundant aromatic compound in urban air. Typically, it corresponds to approximately 6 % of the concentration of the observed non-methane hydrocarbons [2]. Terpenes ($C_{10}H_{16}$) are biogenic VOC's emitted into the atmosphere in large amounts ($120\text{--}480\text{ Tg y}^{-1}$) [3]. We have used limonene as a typical example as a precursor to SOA.

Experimental Apparatus

SOA particles are generated from the (photo) oxidation of toluene or limonene in the presence of O_3 at 1 atmosphere of air using a 150W high-pressure Hg/Xe arc lamp (Figure 1). The SOA production is taking place in an atmospheric pressure flow cell whose gas phase is monitored using a differentially pumped Quadrupole Mass Spectrometer (BALZERS, QMS 200). O_3 is removed immediately after the flow reactor using a denuder tube coated with KI. Typical gas phase residence times within the flow reactor range from 0.5 to 2 minutes, and a few seconds downstream to the filter and the particle sizing equipment. Subsequently, the flow is passed across a PTFE filter (MILLIPORE, $0.2\text{ }\mu\text{m}$ pore diameter) during one to two hours at constant flow rate leading to typical collected sample masses of a few mg. The size distribution of SOA has been characterized by a Scanning Mobility Particle Sizer (TSI, 3071 A / 3022 A). Finally, FTIR Photoacoustic Spectroscopy (PAS) (MTEC, model 300) was used to identify the nature of the surface functional groups of the aerosol particles deposited onto the filter that supported the SOA samples.

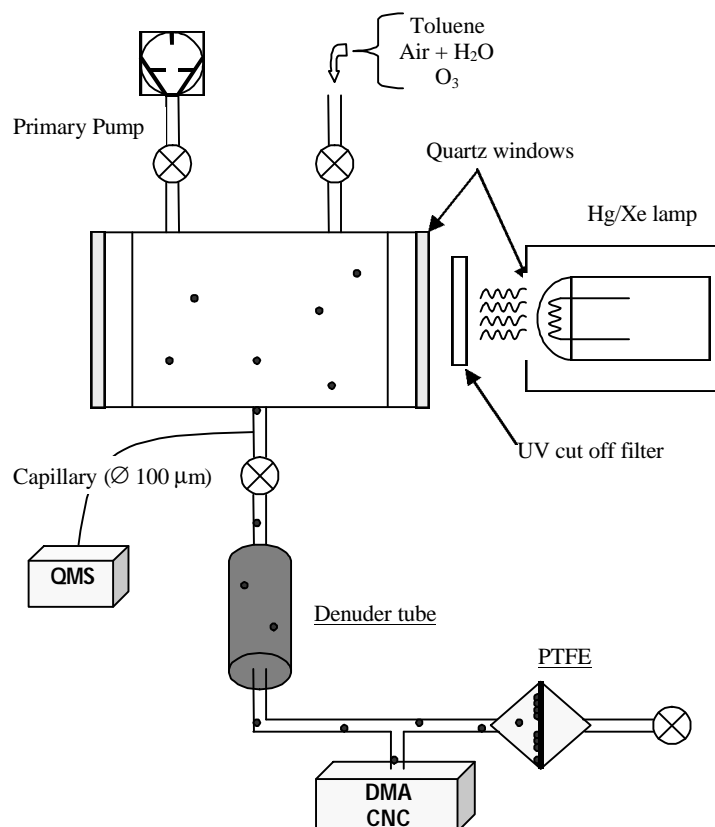


Figure 1. Experimental apparatus for the production and characterization of SOA.

Results and Discussion.

Particle size spectra of the SOA using the DMA indicate that they depend on the molecular gas residence time τ in the flow reactor.

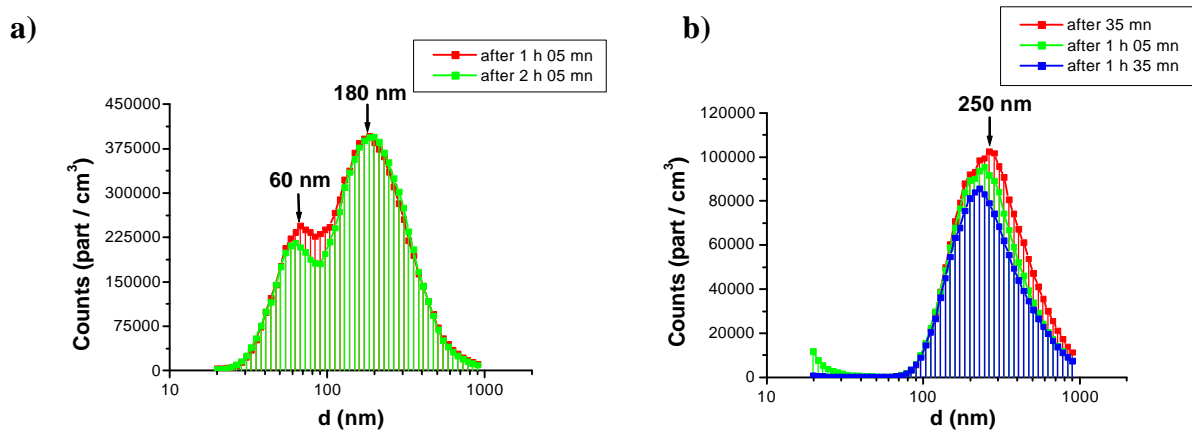


Figure 2: Size distribution of SOA generated from the photooxidation of toluene as a function of the molecular gas residence time τ ; (a) $\tau = 1$ min., (b) $\tau = 2$ min.

At $\tau = 1$ min (Figure 2a) the size distribution exhibits two modes, located at 60 and 180 nm, whereas it consists of a single peak centered at 250 nm for $\tau = 2$ min (Figure 2b). In addition, our results point towards the good stability of the particle size spectrum over the duration of the particle collection on the PTFE filter.

For SOA generated from the photooxidation of toluene the total particle concentration measured in particles cm^{-3} is about 6 times larger for $\tau = 1 \text{ min}$ compared to $\tau = 2 \text{ min}$ as shown in Table 1.

Residence time τ (min)	Total concentration part / cm^3	Total surface $\text{nm}^2 / \text{cm}^3$	Total volume $\text{nm}^3 / \text{cm}^3$
1	$6.3 \cdot 10^6$	$1.3 \cdot 10^{12}$	$9.8 \cdot 10^{13}$
2	$1.1 \cdot 10^6$	$7.0 \cdot 10^{11}$	$6.7 \cdot 10^{13}$

Table 1. Influence of the gas phase residence time τ on the total concentration of SOA generated from the photooxydation of toluene.

Despite the fact that particles from the photooxidation of toluene have a larger mean diameter for $\tau = 2 \text{ min}$ compared to $\tau = 1 \text{ min}$ (Figure 2) the difference in terms of total surface concentration ($\text{nm}^2 / \text{cm}^3$) is reduced by approximately a factor of two. The total volume concentration ($\text{nm}^3 \cdot \text{cm}^{-3}$) is smaller by only 30% which may indicate the magnitude of the loss processes in going from $\tau = 1$ to 2 minutes. Finally, analogous experiments conducted under dry conditions ($\text{rh} < 4\%$) showed that the number of particles became insignificant. This result confirms that H_2O plays a crucial role in SOA formation owing to photooxidation processes supported by the OH free radical.

For SOA generated from the ozonolysis of limonene we have observed a single peak size distribution at $\tau = 2 \text{ min}$ centered at 180 nm . The effect of the relative humidity rh on the particle size distribution is shown in Table 2.

Relative humidity	Total concentration (part / cm^3)	Total volume ($\text{nm}^3 / \text{cm}^3$)
Dry ($< 4\%$)	$1.1 \cdot 10^7$	$1.7 \cdot 10^{14}$
$\cong 90\%$	$4.5 \cdot 10^6$	$1.1 \cdot 10^{14}$

Table 2: Influence of the relative humidity on the total concentration of SOA generated from the ozonolysis of limonene.

In contrast to SOA generated from toluene photooxidation the total number concentration of SOA from limonene is about 2.4 times lower at $\text{rh}=90\%$ than at low rh which seems to indicate that water vapor inhibits SOA formation in this case. This is in agreement with the work of B. Bonn *et al.* [4].

During SOA formation we have simultaneously followed the decay of the VOC signal using on-line mass spectrometry (MS). Figure 3a and 3b display the decay of the toluene and limonene concentrations, following the MS-signal at $m/e = 92$ and $m/e = 136$, respectively, as a function of time.

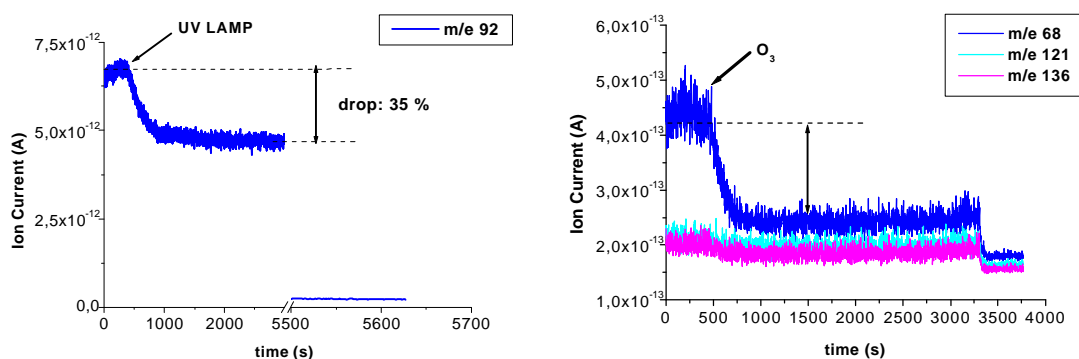


Figure 3: (a) Evolution of the toluene MS-signal ($m/e = 92$) during photooxydation; (b) Evolution of the limonene MS-signal ($m/e = 136$) during ozonolysis.

Figure 3a shows the decay of the toluene MS-signal of about 35 % as soon as the UV lamp is switched on. The integral of this MS-signal over a given time is compared to the mass of the collected SOA on the filter. It leads to an average molecular weight of the representative SOA molecular species of approximately 400 g mol^{-1} . This high molecular weight is explained by F. M. Bowman *et al.* [5] saying that organic aerosol components are sufficiently large that they can partition out of the gas phase [6]. On the other hand, the ozonolysis of limonene (Figure 3b) leads to the decay of the MS-signal at $m/e = 136$ of approximately 50 %. Therefore, the comparison with the SOA mass collected on the filter gives rise to an average molecular mass of approximately 100 g mol^{-1} .

Finally, FTIR-PAS experiments displayed in Figure 4 for the filter-supported SOA clearly show the presence of the O-H stretching vibration (large absorption between 2500 and 3650 cm^{-1}), the C-H stretching vibration (asymmetric and symmetric, respectively, at 2920 and 2850 cm^{-1}) and the carbonyl band at 1720 cm^{-1} which is broad for the SOA from toluene.

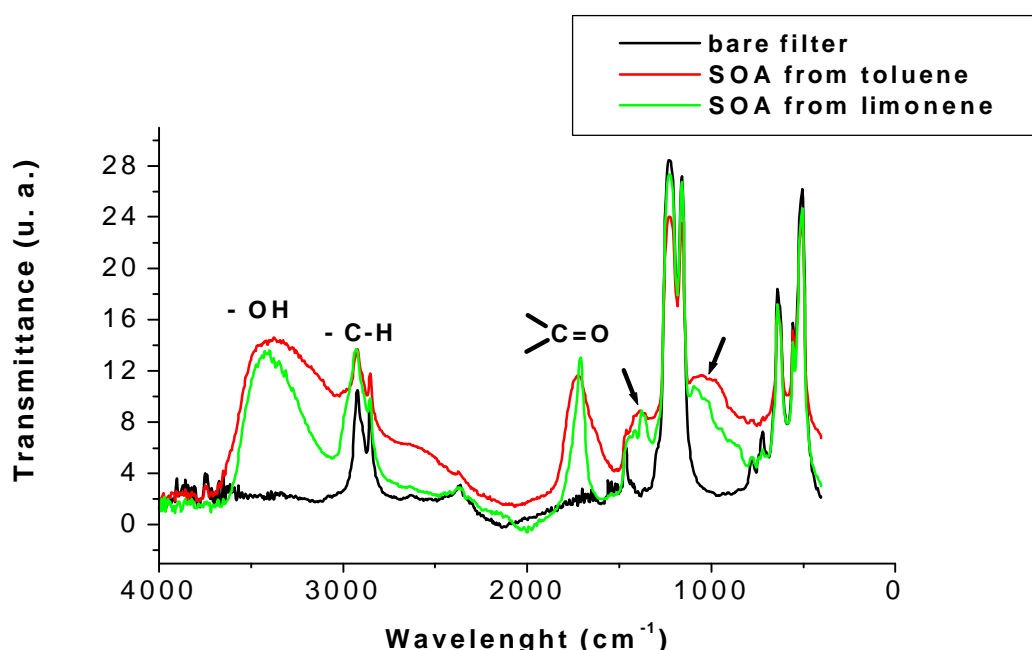


Figure 4: Comparison of spectra obtained by FTIR-PAS on SOA generated from limonene and toluene.

New absorptions in SOA samples indicated by arrows in Figure 4 correspond to not yet positively identified SOA absorptions.

Since FTIR-PAS is not a quantitative technique for the measurement of the number of functional groups, we have chosen a **titration technique** using a gas-phase probe molecule undergoing a **heterogeneous chemical reaction**. For that purpose we have used a Knudsen cell low pressure flow reactor with probe molecules whose nature determines the surface functional groups to be examined. In order to detect the quantity of oxidizable sites we have used oxidizing molecules such as O_3 or NO_2 , for the acidic sites the base $\text{N}(\text{CH}_3)_3$, and for the detection of surface carbonyl groups NH_2OH has been used. We expect that a basic probe will form a salt with SOA surface acidity, whereas NH_2OH will most likely form an oxime R-C=N-OH owing to general acid-catalyzed reaction with surface-bound carbonyl groups of the SOA sample. Unfortunately, the presently used spectroscopic technique is not sensitive enough for the identification of the reaction products of the titration reaction.

The use of the Knudsen cell flow reactor is a good method for establishing the total number of molecules lost from the gas phase because of adsorption and/or reaction [7]. The principle of our method is illustrated in Figure 5.

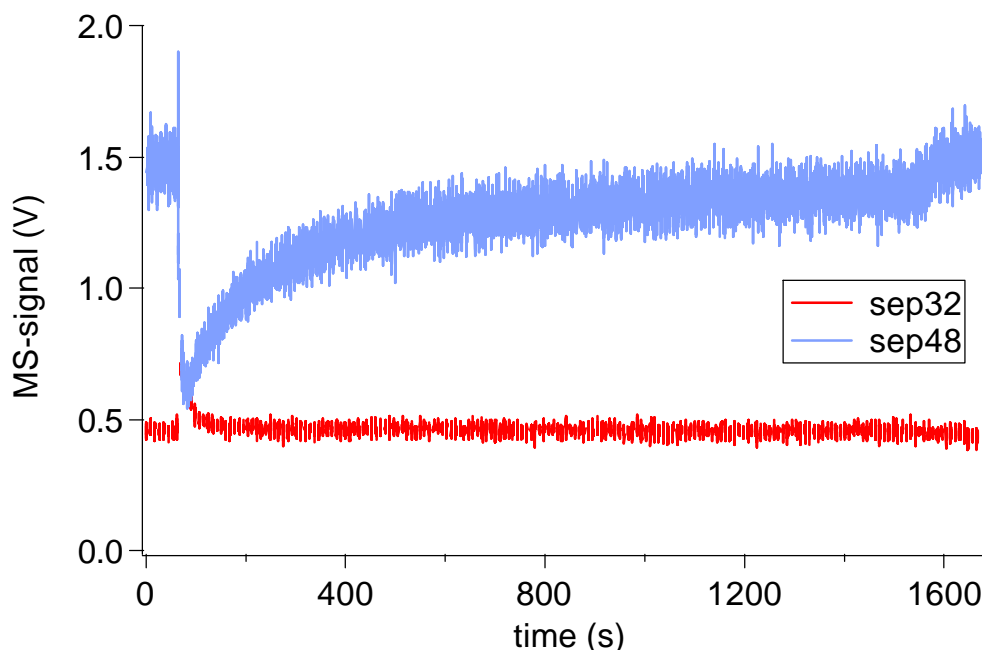


Figure 5: Typical raw data for a titration experiment using a Knudsen cell flow reactor.

The peaked curve starting at 1.5V in Figure 5 displays the MS-signal of a gas-phase probe molecule. It represents the rate of effusion of surviving probes after interaction with the supported SOA for a chosen gas phase residence time in the flow reactor. During reaction the time integration of the hatched area above the curve directly obtains the number of probe molecules lost from the gas phase once the flow has been calibrated in an absolute manner in molecules s^{-1} which corresponds to the number of sites of the SOA sample that interact with the chosen probe. Using the probe molecules NO_2 , $N(CH_3)_3$, and NH_2OH we have performed titration experiments whose results are summarized in Table 3.

VOC	NO_2		$(CH_3)_3N$		NH_2OH	
	# / mg	product	# / mg	product	# / mg	product
<i>Toluene</i>	<i>No reactivity</i>	-	$1.3 \cdot 10^{15}$	<i>salt</i>	$9.3 \cdot 10^{15}$	<i>oxime</i>
<i>Limonene</i>	<i>No reactivity</i>	-	$2.1 \cdot 10^{15}$	<i>salt</i>	$1.3 \cdot 10^{18}$	<i>oxime</i>

Table 3. Titration experiments: nature and number of SOA surface functional groups

With NO_2 we neither observed uptake nor formation of HONO. According to this result we may conclude that SOA particles are probably not responsible for the formation of HONO in the troposphere [8]. The interface of SOA from the ozonolysis of limonene contains about twice the number of acidic sites compared to the SOA interface from toluene photooxidation. According to Table 3 SOA from limonene ozonolysis strongly interacts with NH_2OH . Its interface contains more than 100 times the number of carbonyl functional groups in relation to the interface of SOA from toluene photooxidation.

Conclusion

We have shown that the heterogeneous titration is an appropriate technique to measure the nature and the number of surface functional groups using appropriately chosen probe molecules. It

allows us to characterize with great accuracy the gas-condensed phase interface by gas-phase probes rather than by chemical examination of the bulk of the particles. This study is of a fundamental nature because the functional groups distributed on the surface determine the particle reactivity towards atmospheric gases. It is the first stage necessary to understand the chemical mechanisms of transformation in the atmosphere and their consequence for the radiative forcing of these aerosol particles because the SOA particle interface is the gateway to heterogeneous chemical reactions of atmospheric trace gases.

Acknowledgments.

Generous support of Office Fédéral de l'Enseignement et de la Science (OFES) is gratefully acknowledged in the framework of the EU projects NITROCAT and THALOS.

References.

- [1] Climate Change **2001**: The scientific basis, **IPCC Third Assessment Report**.
- [2] H. E. Jeffries. Photochemical Air Pollution. In Composition, Chemistry, and Climate of the Atmosphere ; H. B Singh, Ed.; Van Nostrand Reinhold: New York, **1995**.
- [3] A. Guenther, N. C. Hewitt, D. Erickson, R. Fall, C. Geron, T. Graedel, P. Harley, L. Klinger, M. Lerdau, W. A. McKay, T. Pierce, B. Scholes, R. Steinbrecher, R. Tallamraju, J. Taylor, P. Zimmerman, J. Geophys. Res. **1995**, 100, D5, 8873-8892.
- [4] B. Bonn, G. Schuster, and, G. K. Moortgat, J. Phys. Chem. A **2002**, 106, 2869-2881
- [5] F. M. Bowman and A. M. Karamalegos, Environ. Sci. Technol. **2002**, 36, 2701-2707
- [6] J. F. Pankow, J. H. Seinfeld, W. E. Asher, G. B. Erdakos, Environ. Sci. Technol. **2001**, 35, 1806-1817
- [7] F. Caloz, F. F. Fenter, K. D. Tabor and M. J. Rossi, Rev. Sci. Instrum. **1997**, 68 (8) 3172.
- [8] B. Demirdjian and M. J. Rossi, Proceedings of the 6th International ETH Conference on Nanoparticle Measurement, 19-21 August, **2002**, Zurich, Switzerland.

The AIDA Soot Coating Campaign: Influence of Coatings on Structure and Optics of Soot Aerosol (HEP10).

Harald Saathoff, Claudia Linke, Ottmar Möhler, Karl-Heinz Naumann, Martin Schnaiter, Werner Schöck, Robert Wagner and Ulrich Schurath

Forschungszentrum Karlsruhe, Institut für Meteorologie und Klimaforschung, Postfach 3640, D-76021 Karlsruhe, Germany, Harald.Saathoff@imk.fzk.de,

Introduction

Soot particles are the most strongly absorbing aerosol particles in the atmosphere. Therefore they have a direct climatic impact by absorbing solar radiation which may also affect photochemical reaction rates. Furthermore, the absorption of radiation within the troposphere can lead to an atmospheric warming which in turn may have an impact on cloud formation. Therefore soot aerosol can have also an indirect influence on climate. During the atmospheric lifetime of soot of about one week ageing processes like coagulation and condensation change the mixing state of soot from an external mixture to an internal one. These changes can alter their dynamic, optical, and hygroscopic properties significantly. Recently the influence of coatings on the absorption properties of the soot containing composite particles has gained rising attention. This is evident in model calculations of the climatic impact of coated soot particles (Jacobson et al., 2001) but also in first laboratory investigations (Schnaiter et al., 2002; Saathoff et al., 2002) of a possible enhancement of the soot absorption upon coating with non absorbing material (e.g. secondary organic or inorganic aerosol material).

With the participation of 7 German, Swiss and Austrian institutes an intensive soot coating campaign was organised in spring 2002 at the 84 m³ large aerosol chamber AIDA of Forschungszentrum Karlsruhe. The goal of the campaign was a comprehensive investigation of the changing physical and chemical properties of spark generated (Palas) soot and soot from a commercial Diesel engine due to coating with different layers of organic material or sulphate. Organic coatings on these soot types were generated by *in situ* ozonolysis of α -pinene in the AIDA aerosol chamber in the presence of a sufficient soot surface to suppress new particle formation. With the same initial soot particles this coating procedure was repeated several times in order to address the role of increasing coating thickness. Sulphate coatings were prepared only on spark generated soot by condensing sulphuric acid on them. This was done with an oven in which the acid was evaporated and a temperature gradient tube in which the acid condensed on the aerosol surface. Subsequently this aerosol was given into the large aerosol chamber. After characterisation of the sulphuric acid coated soot its coating was transformed into ammonium sulphate by titration with ammonia. All experiments were carried out at atmospheric pressure, with a relative humidity of about 20 %, at a temperature of 296 K, and on time scales of 24 hours. With the instrumentation and expertise of the contributing scientists, the following aerosol parameters could be measured simultaneously: number and mass concentration, size distribution, chemical composition, particle morphology, single particle composition, spectrally resolved extinction (230-1000 nm and 1.7 – 13 μ m), scattering at 450, 488, 550 and 700 nm, photoelectric charging, active surface area, hygroscopic growth, and volatility. The measured optical coefficients allow the calculation of single scattering albedo as well as absorption coefficients.

Results

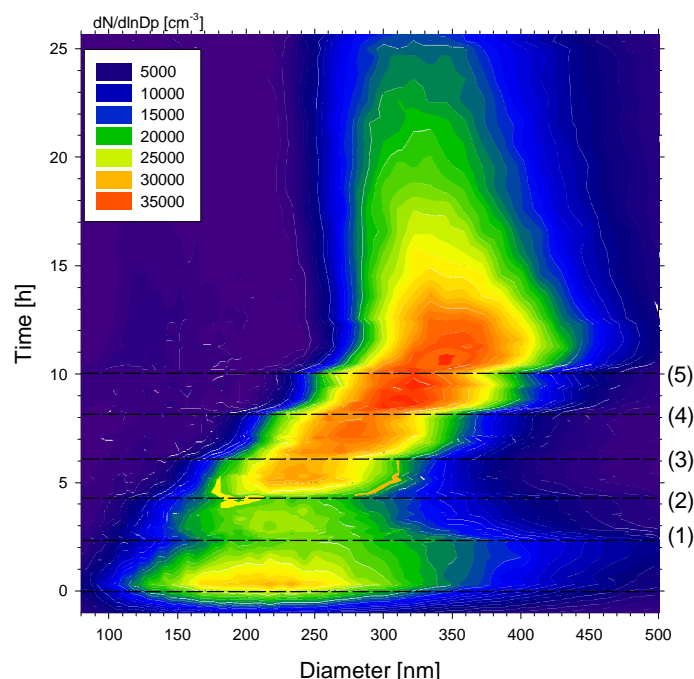


Figure 1. Temporal evolution of the mobility equivalent size distribution of Diesel soot (initially) during coating with oxidation products of the ozonolysis of α -pinene in five steps.

The ozonolysis of α -pinene was used to generate secondary organic aerosol (SOA) coating on soot particles. Initially about $100 \mu\text{g}/\text{m}^3$ of Diesel soot offer a large surface area that inhibits new particle formation almost completely during the ozonolysis of 50 ppb of α -pinene with an excess of ozone. α -pinene was added subsequently for 5 times over a period of about 8 hours. This led to a stepwise increase of the coating layer. Each coating step took about 2 hours: One hour to complete the oxidation of the α -pinene and one hour to make the necessary measurements.

Figure 1 shows the narrowing of the mobility equivalent size distribution and its shift towards smaller diameters during the first coating process (1). The initially fractal soot agglomerates were compacted. This leads to an increase of the backscatter ratio and the Angström exponent which is shown in Figure 2.

Only with the second coating the particle size starts to increase (2). With further condensation of more coating material the particles grow and become spherical, as evident by a decrease of the backscatter ratio and the Angström exponent (cf. Figure 2). Organic coating of soot aerosol leads to a strong increase of the extinction and scattering coefficients as shown in Figure 3. This is mainly due to increased scattering but partly due to increased absorption. Figure 4 shows the absorption as calculated by the difference between the measured extinction and scattering coefficients.

From the elemental (EC) and organic carbon (OC) masses measured after the final coating a coating layer thickness of about 90 nm was estimated. This coating resulted in an increase of the absorption by almost a factor of 2.

Similar findings can be reported for other soot types like spark generated 'Palas' soot. For this soot type the collapse of the fractal soot agglomerates is even more pronounced due to its small primary particles and filigree structure. The increase of the absorption seems to be in the same order but depends also on the size of the soot core compared to the non absorbing organic coating.

In further experiments spark generated soot was coated with sulphuric acid outside of the simulation chamber AIDA. After introduction of the coated aerosol into the chamber and its characterisation it was neutralised. For this purpose ammonia was added stepwise until the titration led to bi-sulphate and finally to ammonium sulphate coated particles. For this purpose the composition of the aerosol

was measured by FTIR spectroscopy. Preliminary results with inorganic coatings of spark generated soot aerosol show an increase of the extinction and scattering coefficients and indicate also a substantial increase of the absorption.

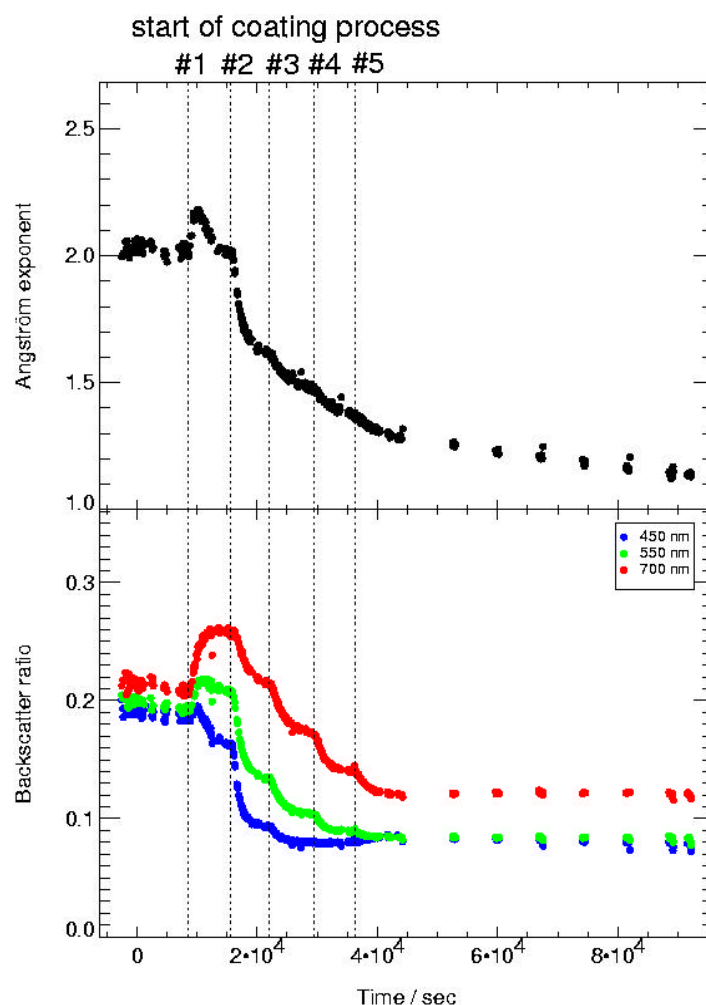


Figure 2. Temporal evolution of the calculated Angström coefficient (upper graph) and the measured backscatter ratio for 3 different wavelengths (lower graph).

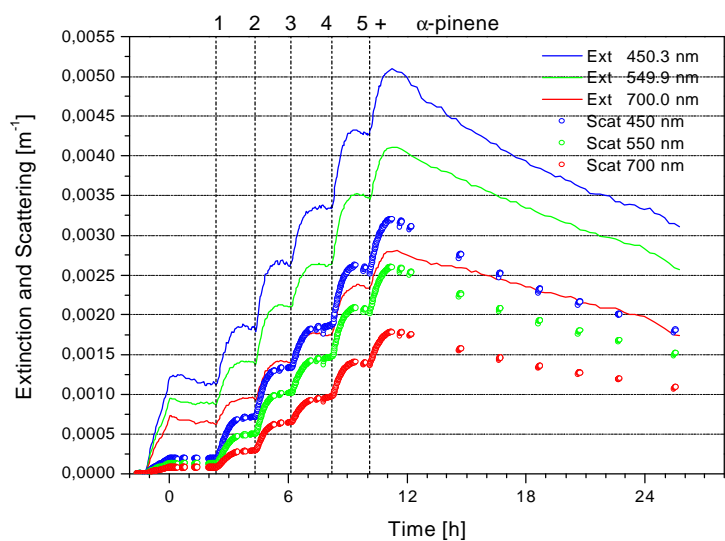


Figure 3. Temporal evolution of the measured extinction (lines) and scattering coefficients (symbols) for 3 different wavelength.

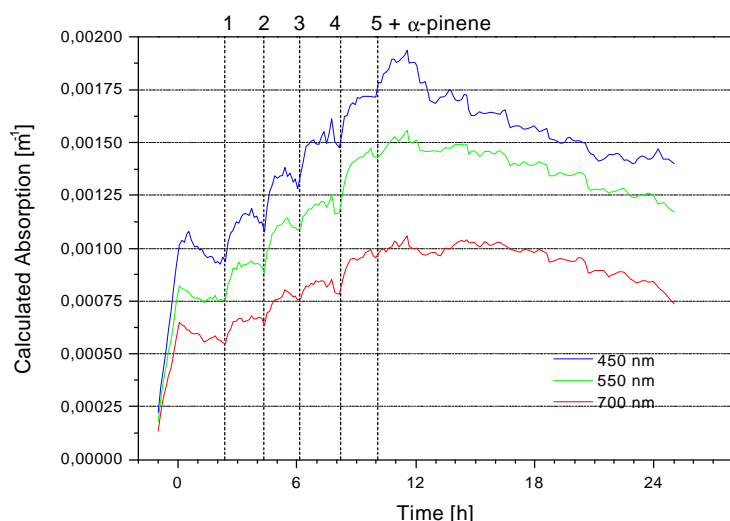


Figure 4. Temporal evolution of the calculated absorption coefficient for 3 different wavelengths.

Conclusions

To our knowledge the enhancement of the absorption coefficient of soot aerosol particles due to coating with a non absorbing coating as predicted by model calculations (Fuller et al., 1999) was verified experimentally for the first time by Schnaiter et al. (2002) and Saathoff et al. (2002). As pointed out by Jacobson (2001) this phenomenon has to be taken into account when discussing the impact of aerosols on climate. For a reliable assessment of atmospheric black carbon the evolution of its mixing state with other components of the atmospheric aerosol has to be taken into consideration.

References

- Fuller K. A., W.C. Malm, S.M. Kreidenweis, Effects of mixing on extinction by carbonaceous particles. *J. Geophys. Res.* 104 (D13) (1999) 15941-15954.
- Jacobson M. Z., Strong radiative heating due to the mixing state of black carbon in atmospheric aerosols. *Nature*, 409 (2001) 695-697.
- Saathoff H., K.-H. Naumann, M. Schnaiter, W. Schöck, O. Möhler, U. Schurath, E. Weingartner, M. Gysel, U. Baltensperger, Coating of Soot and $(\text{NH}_4)_2\text{SO}_4$ Particles by Ozonolysis Products of α -Pinene. *J. Aerosol Sci.* (2002) submitted.
- Schnaiter M., H. Horvath., O. Möhler, K.-H. Naumann, H. Saathoff, O.W. Schöck, UV-VIS-NIR spectral optical properties of soot containing aerosols. *J. Aerosol Sci.* (2002) in press.

Aerosol optical properties as a tool for studying multi-phase processes over a wide range of atmospheric conditions (HEP10)

Robert Wagner, Claudia Linke, Ottmar Möhler, Karl-Heinz Naumann, Harald Saathoff, Martin Schnaiter, Werner Schöck, and Ulrich Schurath

Forschungszentrum Karlsruhe, Institut für Meteorologie und Klimaforschung, Postfach 3640, D-76021 Karlsruhe, Germany, Robert.Wagner@imk.fzk.de

Introduction

Recent contributions from research activities at the AIDA aerosol and cloud chamber in Karlsruhe to working Group CMD-HEP mainly focussed on the optical properties of soot particles as well as the heterogeneous interaction of soot aerosol with gas molecules like O_3 und NO_2 . During an extensive measurement campaign entitled “The AIDA soot coating campaign 2002”, which took place in March/April 2002, the effect of the mixing state of soot with other aerosol particles on their optical properties was thoroughly investigated. Results from these studies are presented in the contribution by Saathoff et al. (this issue). However, being more than just a “soot chamber”, numerous other research projects make use of the unique features of the AIDA aerosol vessel. So the whole chamber (volume 84 m^3) is positioned inside a large isolating containment whose interior can be cooled to any temperature between ambient and 183 K to simulate the conditions prevailing in the upper troposphere and lower stratosphere. Furthermore, the vessel can also be evacuated down to about 0.01 mbar. In this contribution, a selected set of results from a recent AIDA Ice Nucleation/Polar Stratospheric Cloud measurement campaign (Möhler et al., 2002) is presented to give insight into current AIDA investigations besides experiments concerning soot particles and their properties. Major issues of these studies include:

- (i) the freezing behaviour of supercooled binary H_2SO_4/H_2O solution droplets in the temperature range from $-35\text{ }^\circ\text{C}$ to $-85\text{ }^\circ\text{C}$.
- (ii) the dynamical growth of ice particles upon freezing of the solution droplets.
- (iii) the optical constants of supercooled liquid aerosols.

Special attention will be drawn to results from FTIR extinction measurements as well as in situ laser light scattering – two important optical techniques to follow phase changes during freezing of supercooled liquid aerosols.

AIDA instrumentation

A sketch of the major components of the AIDA instrumentation is depicted in Figure 1 (top part). A complete description of all technical components can be found in our recent AIDA publication (Möhler et al., 2002). The bottom part of Figure 1 shows a cross sectional view of AIDA level 2 (the location of the in situ FTIR extinction measurements) and a schematic of the in situ laser scattering unit (AIDA level 1).

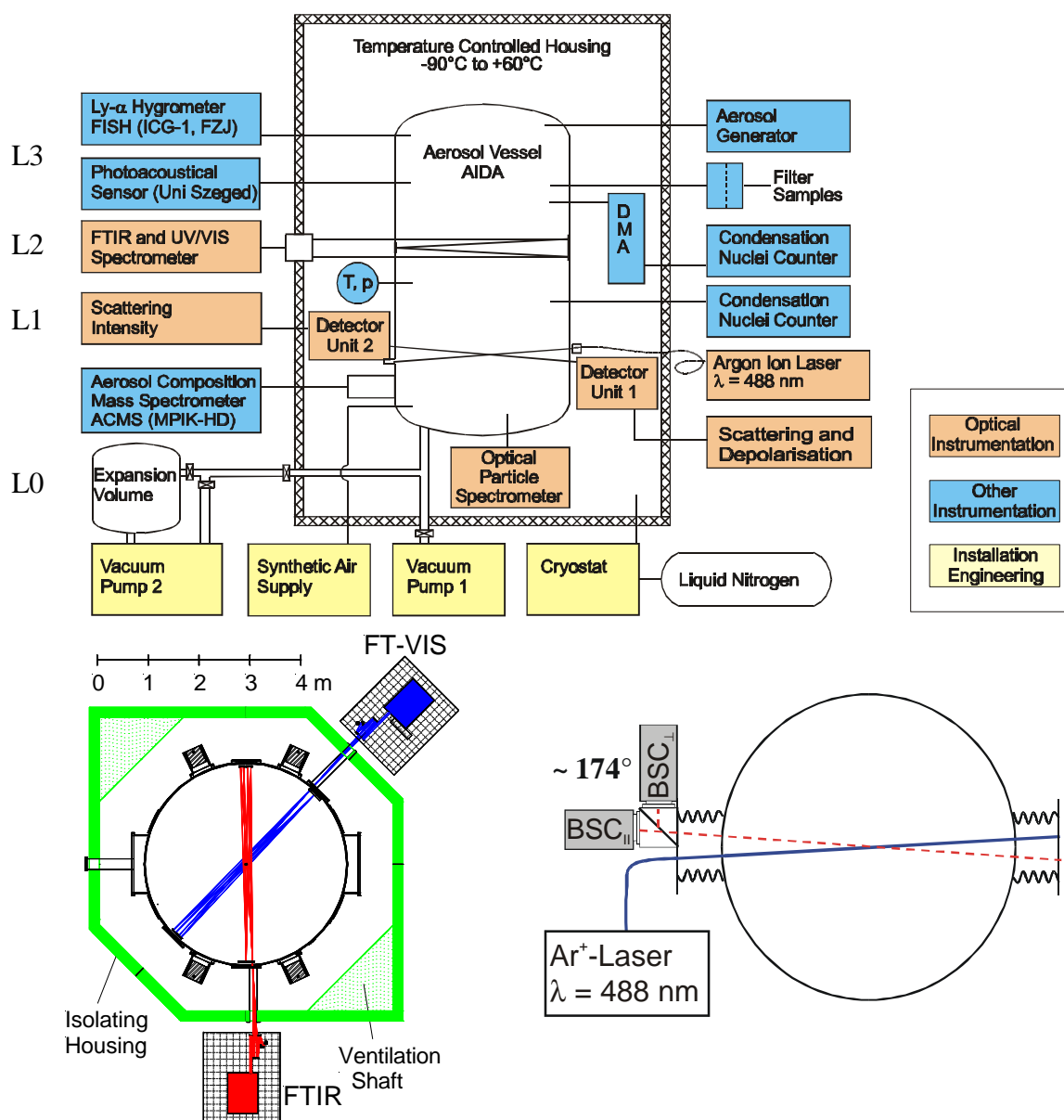


Figure 1: Schematic of the AIDA experimental facility showing the major technical components and instrumentation for the ice nucleation experiments including detailed views of the set-up for the in situ laser scattering and FTIR extinction measurements.

In situ FTIR extinction spectra of the aerosol particles were measured over a 254.3 m long optical path at medium height of the AIDA aerosol vessel using a White-type multiple reflection cell. Spectra were recorded from 800 to 6000 cm^{-1} (using barium fluoride as window material) with a resolution of 4 cm^{-1} by means of a Bruker IFS 66v FTIR spectrometer. The in situ laser scattering unit is composed of an Argon-Ion laser whose beam (99% polarised at 488 nm) is directed horizontally through the AIDA vessel. Light scattering by the aerosol particles is detected polarisation-resolved in the forward (scattering angle 4°) and backward (176°) direction. Important measured quantities are the total back-scattered intensity (BSI), i.e. the sum of the parallel and perpendicular components of the BSI , as well as the depolarisation ratio R_{Depol} , which is zero for light scattering by spherical particles but different from zero for aspherical particles.

$$R_{Depol} = \frac{BSI_{\perp}}{BSI_{\parallel} + BSI_{\perp}}$$

Results

The homogeneous freezing of H_2SO_4/H_2O aerosols

The homogeneous freezing of supercooled liquid aerosols is thought to be one of the key steps in the formation of cirrus clouds in the upper troposphere and of polar stratospheric clouds (PSC's) in the lower stratosphere. Freezing of the solution droplets only occurs when a critical supercooling is exceeded or – in other terms – when a critical saturation ratio S of the water vapour with respect to ice is exceeded, where S is defined as the ratio of the water partial pressure at the moment of ice nucleation divided by the vapour pressure over ice at the same temperature. In the real atmosphere, water vapour supersaturations are induced by an expansion cooling of up-drafting air parcels. One of the major objectives of the AIDA experiments is to mimic this atmospheric process in order to quantitatively determine the humidity conditions which are necessary for ice formation in the atmosphere. AIDA ice nucleation experiments were prepared by adding sulphuric acid droplets into the aerosol chamber at almost ice saturated conditions, achieved by coating the aluminium walls of the AIDA vessel with a thin ice film as described in detail by Möhler et al. (2002). To generate sufficiently high ice supersaturations to initiate the freezing of the aerosol particles, cloud cooling rates up to 2.8 K/min were simulated dynamically in the chamber by expansion cooling using a mechanical pump. The freezing process can be detected by various optical techniques. Figure 2 (left) shows a series of FTIR extinction spectra recorded in time steps of 40 s during a typical AIDA expansion cooling experiment. The corresponding temperature and pressure profile is plotted on the right side of Fig. 2. FTIR spectrum A was measured at static conditions before pumping. The broad extinction feature centred at around 3300 cm^{-1} is attributed to the OH stretching mode of water whereas the spectral feature at 1100 cm^{-1} denotes the SO_4^{2-}/HSO_4^- extinction regime. Spectra B – D were recorded after the onset of pumping. Due to the changing humidity conditions the sulphuric acid droplets absorb water vapour and become more dilute, which can be clearly seen by the rapid increase of the intensity of the OH extinction band relative to the intensity of the sulphate extinction band. Also, the growth of the aerosol particles due to water uptake is shown by the enhanced scattering intensity at wavenumbers $> 4000\text{ cm}^{-1}$. However, the aerosol particles still remain liquid. The onset of ice formation is apparent in spectrum E, which shows several distinct spectral changes, e.g. a band shift of the 3300 cm^{-1} extinction band and the appearance of a new absorption band around 800 cm^{-1} , which are attributable to the formation of water ice particles.

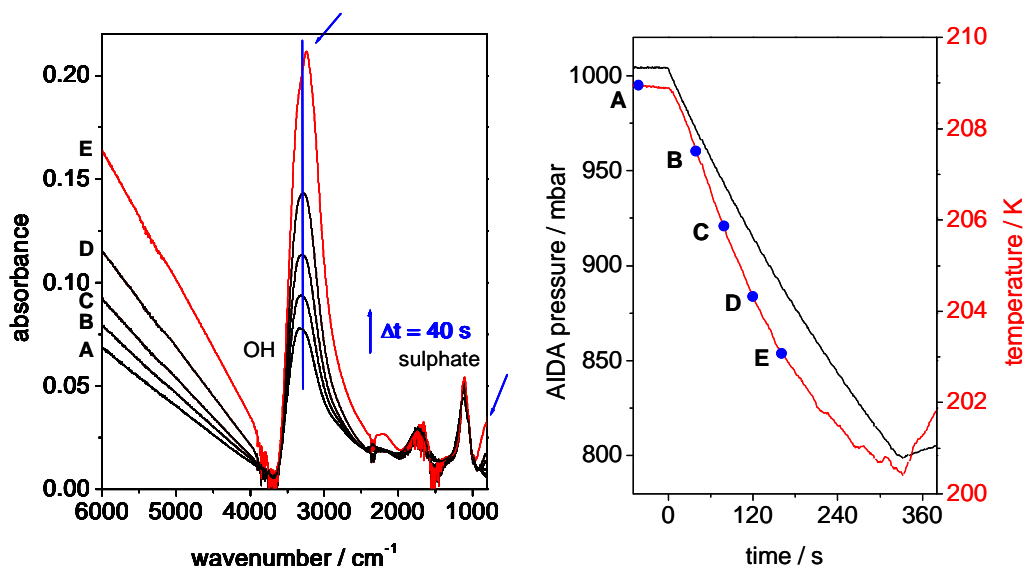


Figure 2: Freezing of sulphuric acid droplets during a typical AIDA expansion experiment, monitored by in situ FTIR extinction spectroscopy. Spectrum E (in red) marks the onset of ice formation.

In addition to FTIR extinction spectroscopy, the in situ laser scattering measurements enable us to accurately determine the onset of ice formation in the supercooled solution droplets. Typical plots of the total back-scattered intensity BSI and the depolarisation ratio R_{Depol} during an AIDA expansion experiment are shown in Figure 3. At static conditions before pumping (phase A) the two values are almost constant, the depolarisation ratio is not exactly zero due to Rayleigh scattering by air molecules. After the onset of pumping (phase B) the particles are growing due to water uptake which can be seen by an increase in the BSI signal, whereas R_{Depol} stays constant, because the aerosol particles are still liquid. The onset of ice formation (phase C) can be clearly identified by a sharp increase in the depolarisation ratio as well as the total back-scattered intensity.

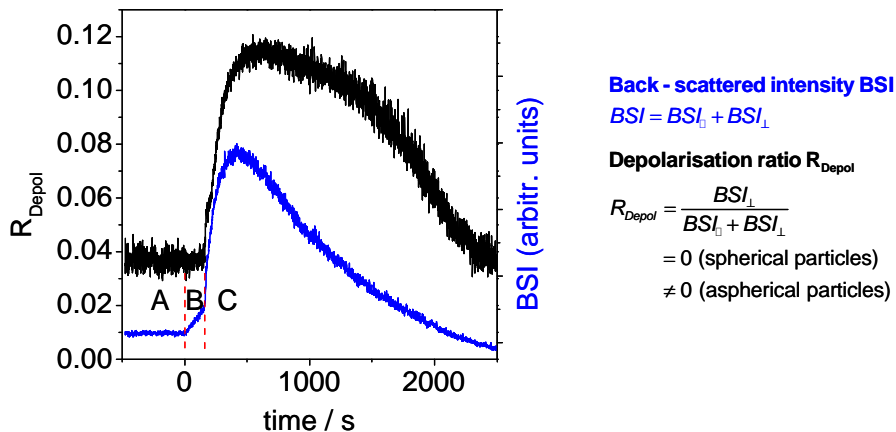


Figure 3: Time evolution of the depolarisation ratio and the total back-scattered intensity during an AIDA expansion cooling experiment.

For the overall results of the freezing experiments, i.e. a plot of the critical ice saturation ratio S measured at the onset of ice formation as a function of temperature, the reader is referred to our recent publication (Möhler et al., 2002).

Effect of the cooling rate on ice particle growth

The expansion cooling experiments carried out in the AIDA chamber are very sensitive tests for numerical models which aim to simulate these processes in the real atmosphere (Haag et al., 2002). One key question is to predict the number of ice crystals which nucleate in cirrus clouds depending on the initial temperature and the cooling rate. As the mechanical pump can be operated at variable pumping speeds, we are able to simulate different up-drafting velocities of air parcels. Figure 4 shows an example of how the number concentration and the size of the ice crystals are affected by different pumping scenarios. In case A a continuous pumping speed was applied which in turn led to a continuous decrease in the gas temperature, whereas in case B a very rapid pressure drop was induced by using an additional expansion volume (4 m^3) located next to the AIDA aerosol vessel (see Figure 1). The right panel of Figure 4 compares the FTIR spectra of the ice particles which have formed during these two different pumping scenarios (black curves). As a rough estimate for ice particle number density and size one can use Mie theory to fit these experimental spectra assuming a log-normal distribution of particles sizes (red curves). Obviously, in case A only a few ice crystals are formed which grow to very large diameters whereas in case B a large number of smaller ice crystals are produced. A main part of our ongoing work is to test the predictions of numerical models by comparing their results with the measured ice particle number densities and sizes for experiments covering different initial temperatures and cooling rates.

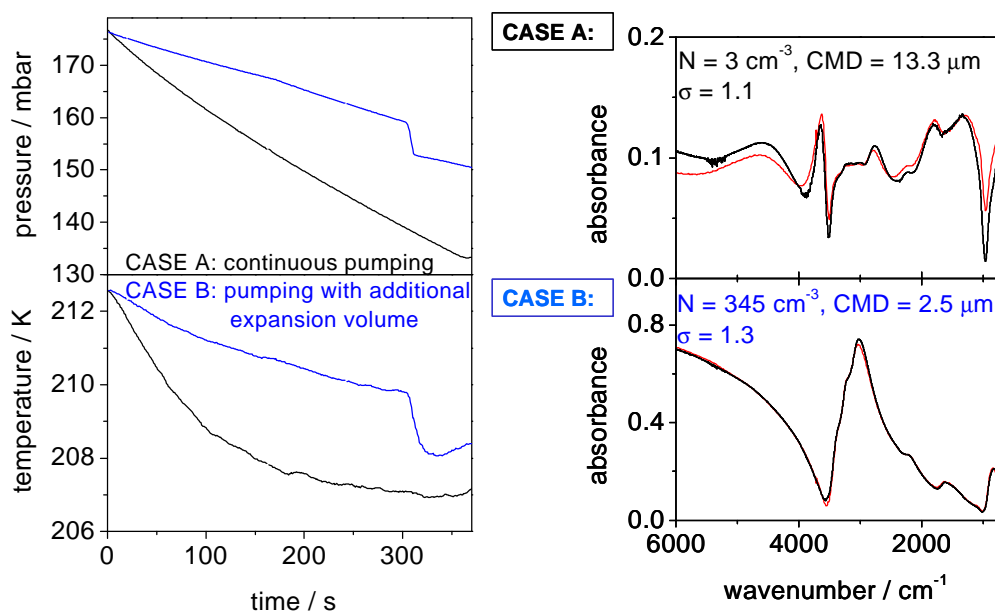


Figure 4: Dependence of ice particle number density N and size (count median diameter, CMD) on pumping speed. The experimental FTIR spectra of the ice particles are shown in black, the best fit results from the Mie calculations are plotted in red.

Optical constants of supercooled liquid aerosols

FTIR extinction spectra of supercooled liquid aerosols can be quantitatively analysed in terms of aerosol composition and mass concentration based on the frequency-dependent optical constants (i.e. the real and imaginary part of the complex refractive index) of the aerosol particles. Recently, the data base of optical constants for supercooled liquid $\text{H}_2\text{SO}_4/\text{H}_2\text{O}$ and $\text{HNO}_3/\text{H}_2\text{O}$ has been significantly improved owing to several extensive laboratory measurements which cover a wide range of aerosol compositions and temperatures (see e.g. Biermann et al., 2000; Niedziela et al., 1999). However, there still remain significant differences between the individual data sets. By comparing the retrieved aerosol parameters obtained from Mie fits to the FTIR extinction spectra with those simultaneously measured with the additional AIDA instrumentation, we are able to test the accuracy of the published low-temperature optical constants. An example of these calculations for supercooled sulphuric acid droplets is presented in Figure 5. The experimental FTIR spectrum (measured composition $56.0 \pm 0.5 \text{ wt\% H}_2\text{SO}_4$, sulphate mass concentration $470 \pm 50 \text{ }\mu\text{g/m}^3$) is nicely reproduced by the Mie fit based on the optical constants of Niedziela et al. (1999). Also, the retrieved aerosol parameters agree very well with the measured ones. On the contrary, the overall quality of the Mie fit is much poorer when using the Biermann et al. (2000) data set. In addition, the retrieved aerosol composition and mass concentration deviate substantially from the measured quantities.

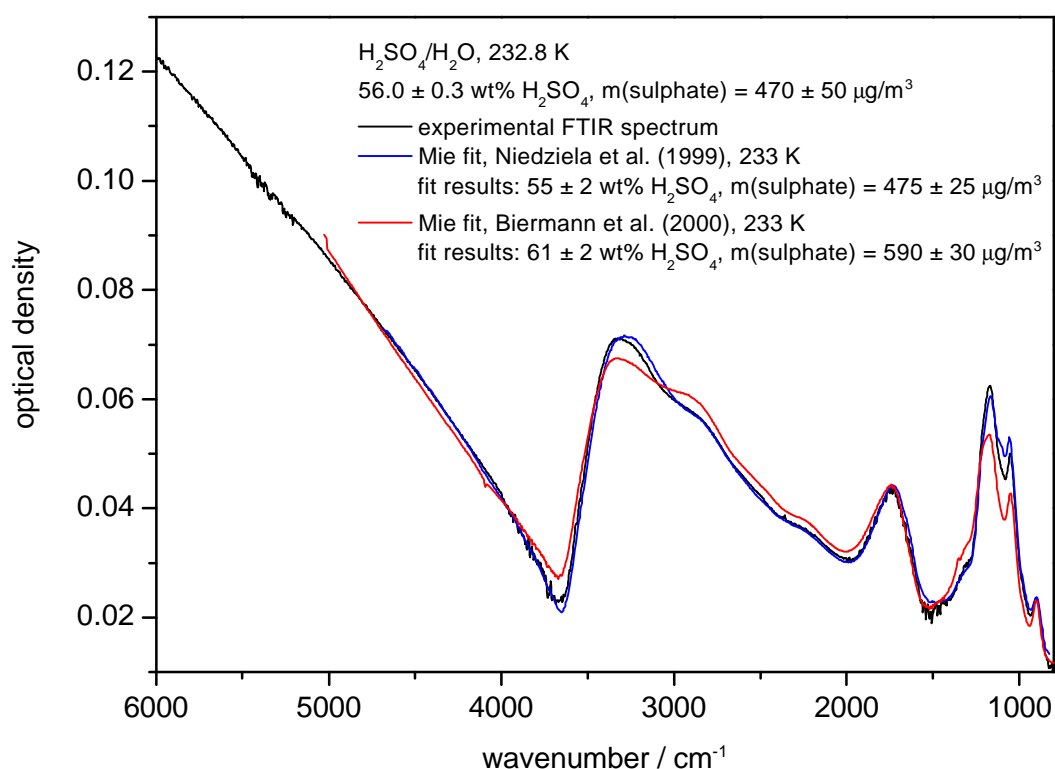


Figure 5: Experimental FTIR extinction spectra of supercooled sulphuric acid droplets and best fit results from Mie calculations using different data sets of optical constants as input values.

References

- Biermann, U. M., Luo, B. P., and Peter, T., 2000: Absorption spectra and optical constants of binary and ternary solutions of H_2SO_4 , HNO_3 , and H_2O in the mid infrared at atmospheric temperatures. *J. Phys. Chem. A*, **104**, 783-793.
- Haag, W., Kärcher, B., Schaefer, S., Stetzer, O., Möhler, O., Schurath, U., Krämer, M., and Schiller, C., 2002: Numerical simulations of homogeneous freezing processes in the aerosol chamber AIDA. *Atmos. Chem. Phys. Discuss.*, **2**, 1429-1465.
- Möhler, O., Stetzer, O., Schaefer, S., Linke, C., Schnaiter, M., Tiede, R., Saathoff, H., Krämer, M., Mangold, A., Budz, P., Zink, P., Schreiner, J., Mauersberger, K., Haag, W., Kärcher, B., and Schurath, U., 2002: Experimental investigation of homogeneous freezing of sulphuric acid particles in the aerosol chamber AIDA. *Atmos. Chem. Phys. Discuss.*, **2**, 1467-1508.
- Niedziela, R. F., Norman, M. L., DeForest, C. L., Miller, R. E., and Worsnop, D. R., 1999: A temperature- and composition-dependent study of H_2SO_4 aerosol optical constants using Fourier transform and tunable diode laser infrared spectroscopy. *J. Phys. Chem. A*, **103**, 8030-8040.

Characterization of Diesel and Synthetic Soot: a Single Particle Mass Spectrometry Investigation (HEP13)

U. Kirchner and R. Vogt

Ford Forschungszentrum Aachen GmbH, Süsterfeldstraße 200, D-52072 Aachen

Introduction

Black carbon particles are considered to serve as heterogeneous reaction sites in the atmosphere [1-2]. Their reactivity, hygroscopic behavior and potential catalytic activity are expected to depend on the nature of the functional chemical groups covering the surface of the particles. Recently diesel soot has attracted much attention due to its potential role in climate change [3]. During the AIDA II campaign physical and chemical properties of diesel soot and spark generated soot were investigated.

Soot particles were exposed to species which interact with particles in the atmosphere, such as the reaction products of α -pinene + O₃. The particles were characterized before and after the reactions and single particle mass spectrometry was used to differentiate between internal and external mixtures during the AIDA I and II campaigns.

Experimental

The portable single particle mass spectrometer LAMPAS-2 (Laser Mass Analysis of Particles in the Airborne State, Version 2) was constructed in collaboration with Spengler et al. [4] and Inbitec GmbH. It is a dual flight tube set-up for simultaneous recording of a positive and a negative mass spectrum of each particle. Particles enter through a differentially pumped inlet consisting of converging nozzle, skimmer and orifice. Transmission efficiency is optimized for particle size range 0.2 - 10 μ m.

Particles are detected by light scattering from a frequency doubled Nd:YVO₄ Laser (532 nm, 50 mW, Particle size > 0.15 μ m). Detection efficiency is 10^{-2} - 10^{-3} at 1 μ m. The sizing laser beam is split by a prism into 2 beams with 2.7 mm distance. Particle flight time is measured with 80 ns resolution to determine particle velocity which is a measure for the particle aerodynamic diameter.

Particle surface components are desorbed and ionized by a focused excimer laser of 193 nm (ArF filling) with up to 8 mJ / pulse. The instrument is also prepared for KrF, which generates 248 nm radiation. The laser is triggered by a fast calculation unit, which determines the arrival time of a particle in the focus in real time from the measured particle flight time. The mass resolution $m/\Delta m$ is ≈ 300 and spectra recording of up to 100 particles / min is allowed by data processing.

All experiments were conducted in the 84 m³ aerosol chamber AIDA at the Research Center Karlsruhe, Germany. A detailed description of the chamber and its instrumentation can be found in a paper of the first campaign [5].

Results I: Diesel soot particles

Diesel engine exhaust was passed through 3 sets of denuders filled with molecular sieve, activated charcoal and cobalt oxide to remove most of the water, hydrocarbons, and nitrogen oxides, respectively. Spectra of diesel soot particles still contain fragments of adsorbed hydrocarbons, NO_x reaction products and sulfate (Figure. 1). In former investigations [6], when a N₂ ionization laser was used soot typical C_x patterns were observed, which are not seen with the ArF ionization.

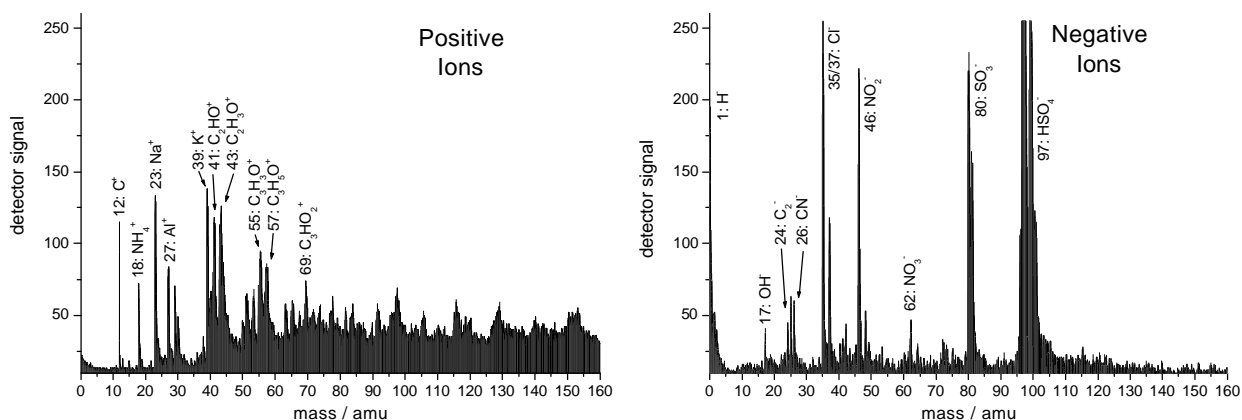


Figure. 1: Spectra of an individual diesel soot particle of approx. $0.6\ \mu\text{m}$ aerodynamic diameter sampled from the aerosol chamber. Metals, sulfate from oxidized fuel sulfur, NO_x reaction products, and oxygenated hydrocarbons which are probably adsorbed on the surface can be identified.

Single Particle Mass Spectrometry sensitively probes surface adsorbed species. Particle core characteristics such as sulfate and metals are still detected when the layer is expected thicker from α -pinene + ozone reaction products. This new layer is different from adsorbed fuel and lubricant hydrocarbons. It is detected in spectra of both polarities, but is most pronounced in the negative spectrum: $\text{C}_2\text{H}_3\text{O}^-$ at 43 amu, $\text{C}_2\text{H}_5\text{O}^-$ at 45 amu, $\text{C}_2\text{H}_3\text{O}_2^-$ at 59 amu and $\text{C}_3\text{H}_5\text{O}_2^-$ at 73 amu.

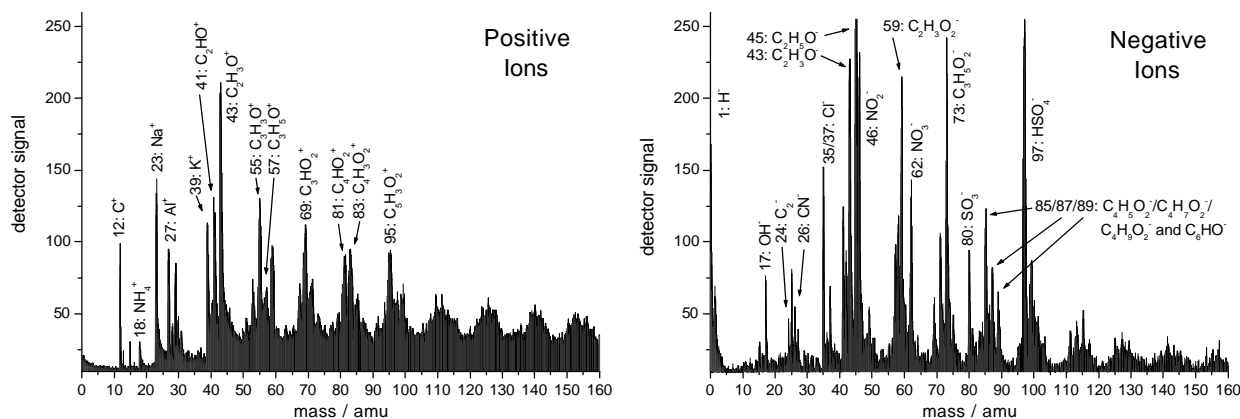


Figure. 2: Spectra of a diesel soot particle which was exposed to α -pinene and ozone reaction products. The particle core characteristics were still detected and most obvious in the negative spectrum several new peaks of oxygenated hydrocarbons were observed.

In the detectable size range no particles without a coating were observed and also no particles which consisted of α -pinene ozonolysis products only. Newly formed particles were agglomerated with soot particles or had very small sizes ($< 0.2\ \mu\text{m}$). The reaction product appears distributed among all soot particles.

Results II: Spark generated soot particles

A graphite spark generator (GfG 1000, Palas GmbH, Germany) was used to produce artificial soot with well-known physical properties and good reproducibility.

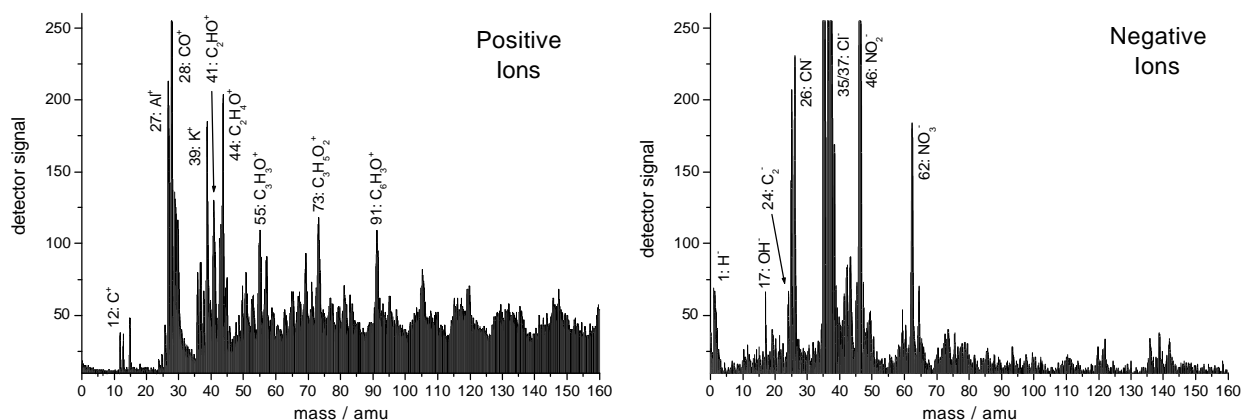


Figure. 3: Spectra of a spark generated soot particle sampled from the AIDA aerosol chamber.

In comparison to diesel soot the spark generated soot showed no sulfate, other metals or other hydrocarbons (Figure. 3). Water (OH^- at 17 amu) and adsorbed NO_x or NO_x reaction products are detected on both types of soot.

Graphite spark generated soot was exposed to α -pinene + ozone reaction products in the AIDA under the same conditions as diesel soot (Figure. 4).

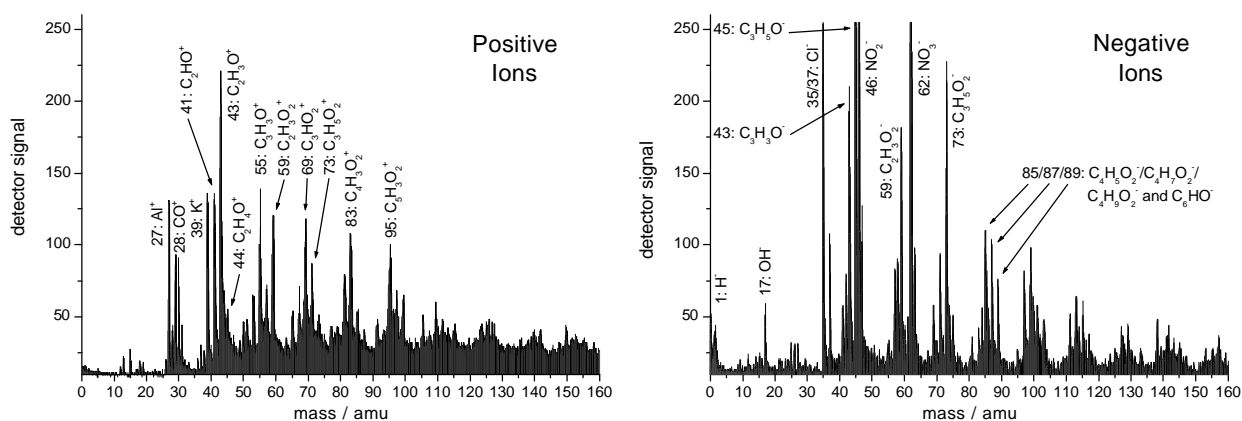


Figure. 4: Spectra of a spark generated soot particle which was exposed to α -pinene and ozone reaction products. More peaks of oxygenated hydrocarbons were observed as compared to fresh soot.

The same oxygenated hydrocarbon fragments as on diesel soot are observed in the negative spectrum: $\text{C}_2\text{H}_3\text{O}^-$ at 43 amu, $\text{C}_2\text{H}_5\text{O}^-$ at 45 amu, $\text{C}_2\text{H}_3\text{O}_2^-$ at 59 amu and $\text{C}_3\text{H}_5\text{O}_2^-$ at 73 amu. This indicates similar ionization conditions with 193 nm laser light although the soot matrices are different. When 337 nm ionization (N_2 laser) was used different fragments were observed [6].

Results III: H_2SO_4 coated spark generated soot particles

Spark generated soot particles were coated with sulfuric acid by condensation from the vapor phase in a heated flow tube with temperature gradient. In the aerosol chamber these particles were stepwise neutralized with ammonia and sampled after each step from the chamber for analysis.

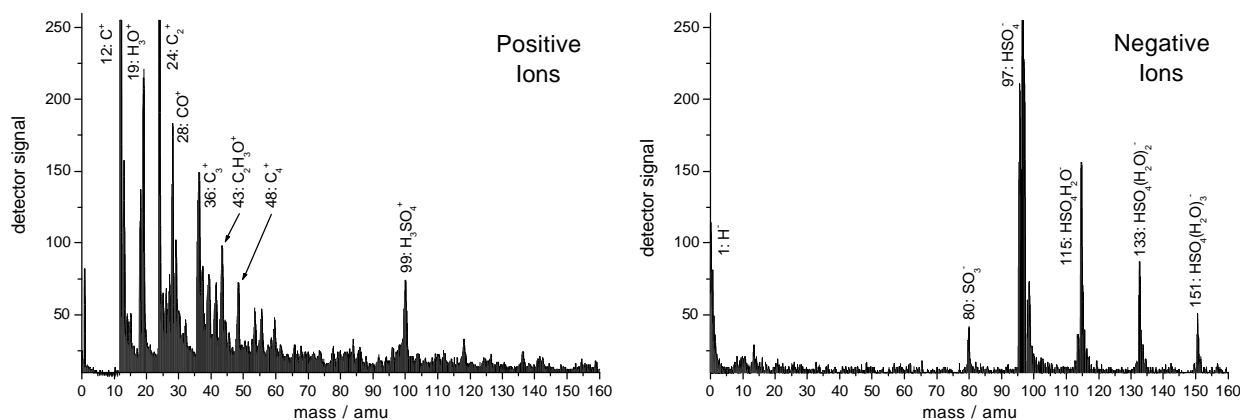


Figure 5: Spark generated soot coated with sulfuric acid.

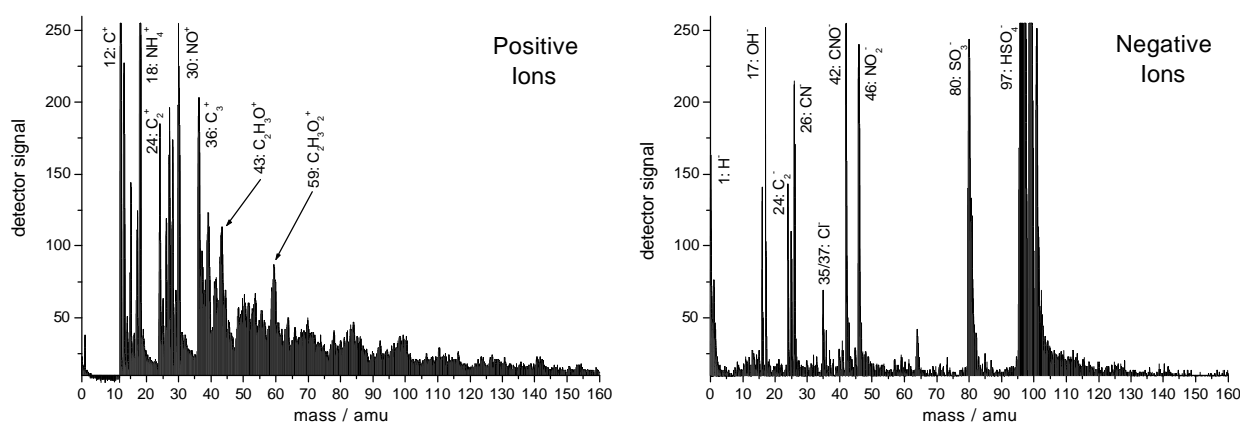


Figure 6: Particle with sulfuric acid coating after neutralization with ammonia.

The sulfuric acid layer was detected as SO_3^- and $\text{HSO}_4(\text{H}_2\text{O})_x^-$ at $m/z = 80$ and $97+18x$ ($x = 0, 1, 2, 3$, etc.). The characteristic signals of uncoated spark generated soot are obscured by these strong peaks in the negative spectrum (Figure 3 and Figure 5), but in positive mode appear carbon-containing fragments.

After neutralization ammonium ions were detected at $m/z = 18$. Other nitrogen containing species were NO^+ , CN^- , CNO^- , and NO_2^- , which were probably formed in the ionization process. All particles appeared to be coated, there was no indication for external mixing.

Conclusions and summary

- Single particle mass spectrometry gives in-situ chemical and size information of individual aerosol particles. Surface species and adsorbed reaction products are sensitively probed.
- Graphite spark generated soot (Palas GfG 1000 generator) is chemically different as compared to diesel soot and may be of limited use as general diesel soot model substance.
- Reaction products of α -pinene + O_3 condense on both types of soot and change the chemical composition significantly.
- After coating of spark generated soot with H_2SO_4 sulfate was detected, but the coated soot was still different to diesel soot, which contained sulfate. After neutralization with NH_3 beside expected NH_4^+ other nitrogen containing fragments (NO^+ , CN^- , CNO^- , NO_2^-) were detected, which were probably formed during ionization.
- Preliminary data evaluation shows no uncoated particles, all particles were internally mixed.

References

- [1] Lary, D. J.; Toumi, R.; Lee, A. M.; Newchurch, M.; Pirre, M. and Renard, J. B., *J. Geophys. Res.* **1997**, *102*, 3671 - 3682.
- [2] Hauglustaine, D. A.; Ridley, B. A.; Solomon, S.; Hess, P. G. and Madronich, S., *Geophys. Res. Lett.* **1996**, *23*, 2609 - 2612.
- [3] Jacobson, M. Z., *J. Geophys. Res.* **2002**, in press.
- [4] Hinz, K. P.; Kaufmann, R. and Spengler, B., *Aerosol Sci. Technol.* **1996**, *24*, 233 - 242.
- [5] Saathoff, H.; Moehler, O.; Schurath, U.; Kamm, S.; Dippel, B. and Mihelcic, D., *J. Aerosol Sci.* **2002**, submitted for publication.
- [6] Kirchner, U.; Vogt, R.; Natzeck, C. and Goschnick, J., *J. Aerosol Sci.* **2002**, submitted for publication.

Heterogeneous Conversion of NO₂ on Secondary Organic Aerosol Surfaces: A Possible HONO Source? (HEP15)

Jörg Kleffmann, Rolf Bröske and Peter Wiesen

Physikalische Chemie/FB 9, Bergische Universität - Gesamthochschule Wuppertal (BUGHW), D-42097 Wuppertal, Germany.

kleffman@uni-wuppertal.de

Summary

The heterogeneous conversion of NO₂ on different secondary organic aerosols was investigated with the focus on a possible formation of nitrous acid (HONO). Different organic aerosols were produced in the reactions of O₃ with α -pinene, limonene or catechol and OH radicals with toluene or limonene, respectively. In one set of experiments the aerosols were sampled on filters and exposed to humidified NO₂ mixtures under atmospheric conditions. The estimated upper limits for the uptake coefficients of NO₂ and the reactive uptake coefficients NO₂→HONO are in the range of 10⁻⁶ and 10⁻⁷, respectively. The integrated HONO formation for a reaction time 1 h was <10¹³ cm⁻² geometrical surface and <10¹⁷ g⁻¹ particle mass. In a second set of experiments the conversion of NO₂ into HONO in the presence of organic particles was carried out in an aerosol flow tube under atmospheric conditions. The aerosols were produced in the reaction of O₃ with β -pinene, limonene or catechol, respectively. The upper limits for the reactive uptake coefficients NO₂→HONO were in the range of 7×10⁻⁷-9×10⁻⁶. The results from the present study show that heterogeneous formation of nitrous acid on secondary organic aerosols (SOA) is unimportant for the atmosphere.

Introduction

HONO is an important precursor for OH radicals in the atmosphere due to the photolysis $\text{HONO} + h\nu \rightarrow \text{OH} + \text{NO}$. Different formation pathways in the atmosphere were proposed during the last decades. Recently, the heterogeneous HONO formation by the reaction of NO₂ with soot surfaces was postulated to be of importance (e.g. Ammann et al., 1998; Gerecke et al., 1998). However, more recent studies showed that the integrated HONO yield for the non-catalytic reaction is too small to explain significant HONO formation (Kleffmann et al., 1999; Arens et al., 2001). It was assumed that adsorbed organic compounds are responsible for the HONO formation on soot surfaces (Stadler and Rossi, 2000). In a recent study, significant HONO formation was observed in the reaction of NO₂ with semi-volatile hydrocarbons emitted from a diesel engine (Gutzwiller et al., 2002). Different groups of compound were postulated, although the exact nature of the hydrocarbons is still unknown. In the reaction of NO₂ with several organics such as aromatic amines (Saltzman, 1954; Huie and Neta, 1986), alcohol amines (Levaggi et al., 1974), hydroxy-substituted aromatics (Alfassi et al., 1986; Alfassi, et al., 1990; Arens et al., 2002), alkenes and polyunsaturated fatty acids (Pryor and Lightsey, 1981) nitrite formation was observed in the liquid phase, which may escape as HONO at low pH. Therefore, the formation of HONO can be expected to take place also on similar organic compounds e.g. in secondary organic particles. In the atmosphere these species are formed, at least in part, during the decomposition of volatile organic compounds with O₃ or OH radicals (Seinfeld and Pandis, 1998). Since the organic fraction of the atmospheric aerosol can significantly exceed the black carbon fraction (Raes et al., 2000), secondary organic aerosols could be an important HONO source in the atmosphere. However, the conversion of NO₂ into HONO in the presence of these particles is still unknown and was investigated in the present study using two different experimental approaches, namely in an aerosol flow tube and aerosol filter experiments.

Experimental

Two flow systems were used to generate aerosols with a constant size distribution over a long period of time. The aerosols were formed by the reaction of different hydrocarbons with O_3 or OH radicals. The experimental set-up used for the preparation and the sampling of the aerosols and the reaction of NO_2 with aerosols is shown in Figure 1.

Aerosol formation by O_3 reaction

The aerosols were produced by the reaction of O_3 with α -pinene (99%, Aldrich), limonene (99%, Aldrich) or 1,2-dihydroxibenzene (catechol, 99%, Aldrich), respectively. Ozone was prepared in pure oxygen (O_2 99.95%, Messer Griesheim) with a silent discharge generator (Figure 1, ①). The initial concentrations of the gas phase compounds were in the range of a few ppmv to get a weighable particle mass. O_3 and the different hydrocarbons were measured in a separate optical cell (optical path length 46 cm) by FTIR spectroscopy (Bruker IFS 88). All mass flows were controlled with calibrated mass flowmeters (Tylan, FM 360) and needle valves. A humidified mixture of the organic compounds in synthetic air was added to a flow of O_3 . The reaction time in the flow system could be varied between a few seconds and two minutes by the use of a movable injector. During this time a fast formation of particles took place. The particle number and the maximum of the size distribution could be varied by using different initial concentrations and reaction times. To exclude a deactivation of the freshly prepared aerosols due to a former reaction with excess O_3 , a charcoal denuder was placed behind the flow tube. The reactive gas phase compounds were captured with >90 % efficiency, whereas the particles were unaffected.

Aerosol formation by OH reaction

For generating aerosols by OH reactions a second flow system was built up (Figure 1, ②). OH radicals were produced by the UV photolysis of H_2O . A flow of $\sim 500 \text{ ml min}^{-1}$ N_2 (99.999%, Messer Griesheim) was humidified and irradiated with a Hg penray lamp (Oriol). Mixtures of toluene (99.8%, Fluka) or limonene (99%, Aldrich) in synthetic air were added behind the radiation source. By this experimental set-up the photolysis of the hydrocarbons by the penray lamp was prevented. Thus, in experiments performed with dry synthetic air no particle formation was observed.

The particle size distribution was measured by a SMPS-system (TSI 3071 electrostatic classifier and TSI 3022A condensation particle counter).

NO_2 filter experiments

The aerosols were sampled on Teflon filters (Schleicher & Schuell TE 37, $1 \mu\text{m}$ or Millipore Type FH, $0.5 \mu\text{m}$). The collected particle masses varied in the range 0.5-6 mg. After the determination of the particle mass, the filter samples were placed into a PFA filter holder and were exposed to humidified NO_2 mixtures under atmospheric conditions. HONO concentrations in the gas phase were measured using a stripping coil and ion chromatography (Shimadzu) after pre-concentration on a Dionex, TAC LP1 column. NO and NO_2 concentrations in the gas phase were determined by a luminol nitrogen oxide analyser (Unisearch, LMA-3D).

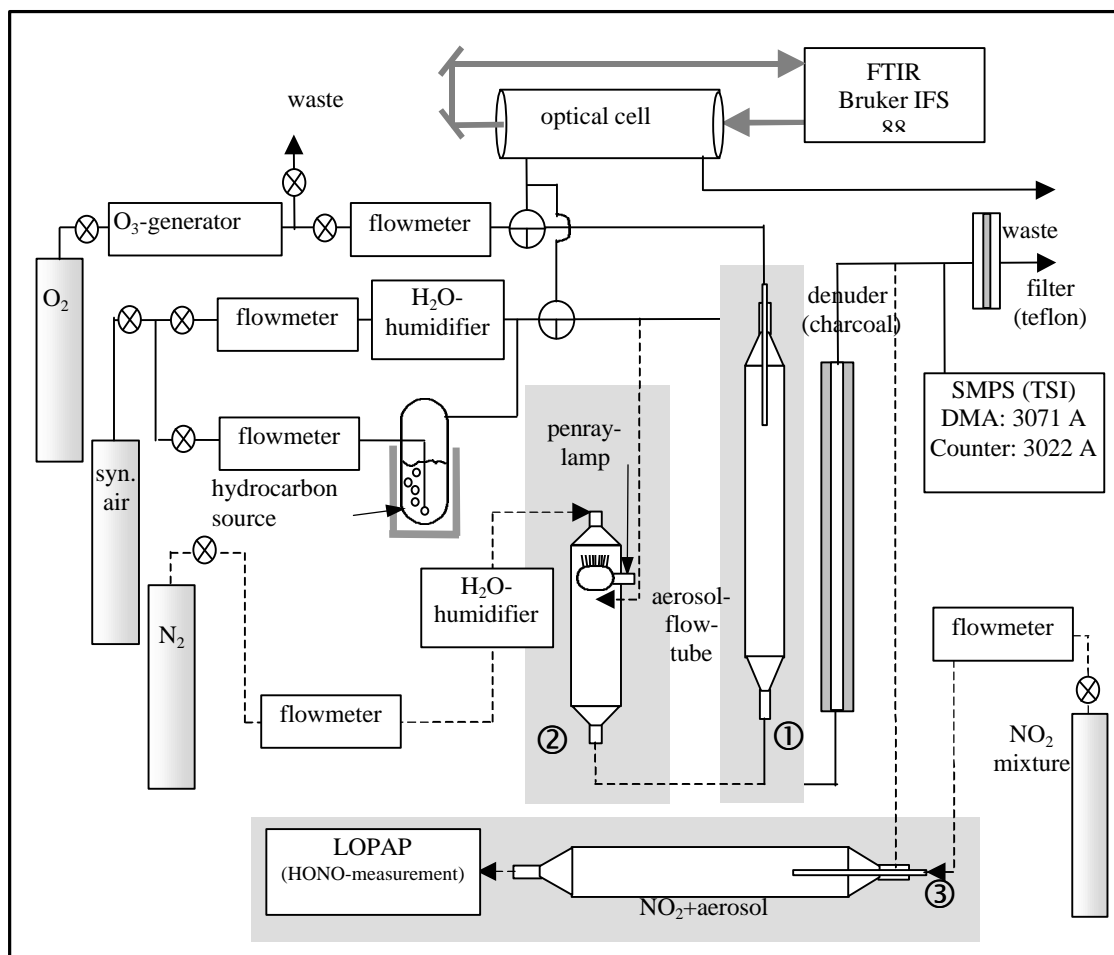


Figure 1: Experimental set-up for the generation and sampling of secondary organic particles (①: O_3 +hydrocarbon, ② OH +hydrocarbon) and for the reaction of NO_2 with organic particles in the aerosol flow tube (③).

Flow tube experiments with NO_2 :

In addition to the filter experiments, the conversion of NO_2 into HONO in the presence of organic particles was also investigated in an aerosol flow tube placed behind the charcoal denuder (Figure 1, (③)). The aerosols were generated as described above. After passing the denuder, the aerosols were exposed to 20 ppbv NO_2 (Messer Griesheim, 9.98 ppmv NO_2 in N_2) under atmospheric conditions (1 atm, 298 K, 50% r.h.). For the sensitive detection of the HONO concentration the LOPAP instrument (Heland et al., 2001; Kleffmann et al., 2002) was used with a time resolution of 1 min and a detection limit of 10 pptv. The particle size distribution was measured simultaneously as described above.

Results and discussion

Filter experiments

After the particle collection the samples were exposed to the NO_2 mixtures. Before and after the experiments blank measurements were performed to determine the NO_2 , NO and HONO background concentrations. A typical behaviour of the HONO, NO_2 and NO concentrations during the blank experiments and in the presence of the aerosol is shown in Figure 2.

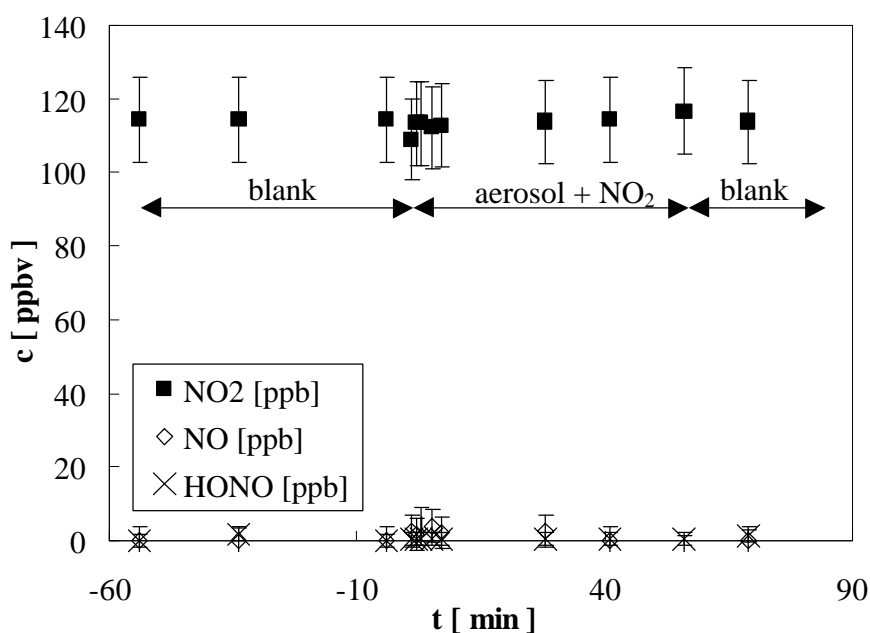


Figure 2: Example of the concentration time profiles for the conversion of NO_2 on organic particle surfaces (limonene/ O_3 , $m_{\text{aerosol}} = 2.1 \text{ mg}$, $[\text{NO}_2] = 115 \text{ ppbv}$, 57 % r.h., $T = 298 \text{ K}$).

Neither a NO_2 loss nor a HONO or NO formation was observed in any of the filter experiments. Accordingly, only upper limits for the NO_2 uptake coefficient, the reactive uptake coefficient ($\text{NO}_2 \rightarrow \text{HONO}$) and the integrated HONO formation (reaction time 1 h) could be estimated, using the following equation:

$$\gamma_{\text{geo}} = \frac{4 \times \Delta[\text{NO}_2] \times \Phi}{[\text{NO}_2]_0 \times \bar{v} \times S},$$

in which $[\text{NO}_2]_0$ and $\Delta[\text{NO}_2]$ reflect the initial and consumed NO_2 , respectively, Φ the gas flow rate, S the geometric surface of the filter and \bar{v} the mean molecular velocity of NO_2 . For the calculations, the geometric surface of the filters was taken as a lower limit leading to only upper limits of the uptake coefficients (see Table 1).

Table 1: Summary of the filter experiments with NO_2 and organic particles. The uptake coefficients were determined using the geometric filter surface.

aerosol system	uptake coefficients		integrated HONO formation ($t = 1 \text{ h}$)	
	NO_2	$\text{NO}_2 \rightarrow \text{HONO}$	cm^{-2} (geometric)	g^{-1}
α -pinene/ O_3	$<5 \times 10^{-7}$	$<1 \times 10^{-7}$	$<1.0 \times 10^{13}$	$<3.0 \times 10^{16}$
limonene/ O_3	$<1.5 \times 10^{-6}$	$<8.5 \times 10^{-8}$	$<7.7 \times 10^{12}$	$<1.3 \times 10^{17}$
catechol/ O_3	$<1.5 \times 10^{-6}$	$<8.5 \times 10^{-8}$	$<7.7 \times 10^{12}$	$<6.0 \times 10^{17}$
limonene/OH	$<1.5 \times 10^{-6}$	$<8.5 \times 10^{-8}$	$<7.7 \times 10^{12}$	$<2.8 \times 10^{17}$
tolouene/OH	$<1.5 \times 10^{-6}$	$<8.5 \times 10^{-8}$	$<7.7 \times 10^{12}$	$<6.1 \times 10^{17}$
limonen/ O_3 /OH	$<1.5 \times 10^{-6}$	$<8.5 \times 10^{-8}$	$<7.7 \times 10^{12}$	$<1.1 \times 10^{17}$

Aerosol flow tube experiments

A lower HONO formation was expected in the aerosol flow tube experiments caused by the lower total particle surface area. Therefore, the sensitive LOPAP instrument was used for HONO detection. Three different aerosols were produced as described above formed in the reaction of O_3 with limonene, catechol and β -pinene, respectively. Only O_3 aerosols were used in these experiments because the aerosol yields in the OH reactions were too low. A typical plot of the HONO concentration and the surface to volume ratio of the particles during an experiment is shown

in Figure 3. A constant flow of 19 ppbv humidified NO_2 led to the formation of ~ 800 pptv HONO, the so-called background HONO, due to the heterogeneous NO_2 conversion on the walls of the flow reactor (e. g. Kleffmann et al., 1998). The addition of ppmv levels of only O_3 led to a minor particle formation. This could be explained with the reaction of O_3 with impurities sticking on the surface of the reaction system. Only in the presence of both, O_3 and hydrocarbons a large bulk of particles was immediately formed. As shown in Figure 3 the HONO concentration is independent of the particle concentration. The upper limits for the reactive uptake coefficients $\text{NO}_2 \rightarrow \text{HONO}$ could be estimated using the following equation:

$$\gamma = \frac{4 \times \Delta[\text{HONO}]_{\text{max}}}{[\text{NO}_2] \times \bar{v} \times S/V \times \Delta t_{\text{reac}}}$$

S/V is the surface to volume ratio of the particles, $[\text{NO}_2]$ the NO_2 gas phase concentration, Δt_{reac} the reaction time of 60 s, \bar{v} the mean velocity of NO_2 . Using the upper limit of the HONO formation $\Delta[\text{HONO}]_{\text{max}}$ of <10 pptv, based on the 1 % precision of the LOPAP instrument, upper limits for the uptake coefficients in the range of 10^{-6} were estimated (see Table 2). These values are in good agreement with the upper limits from the filter experiments.

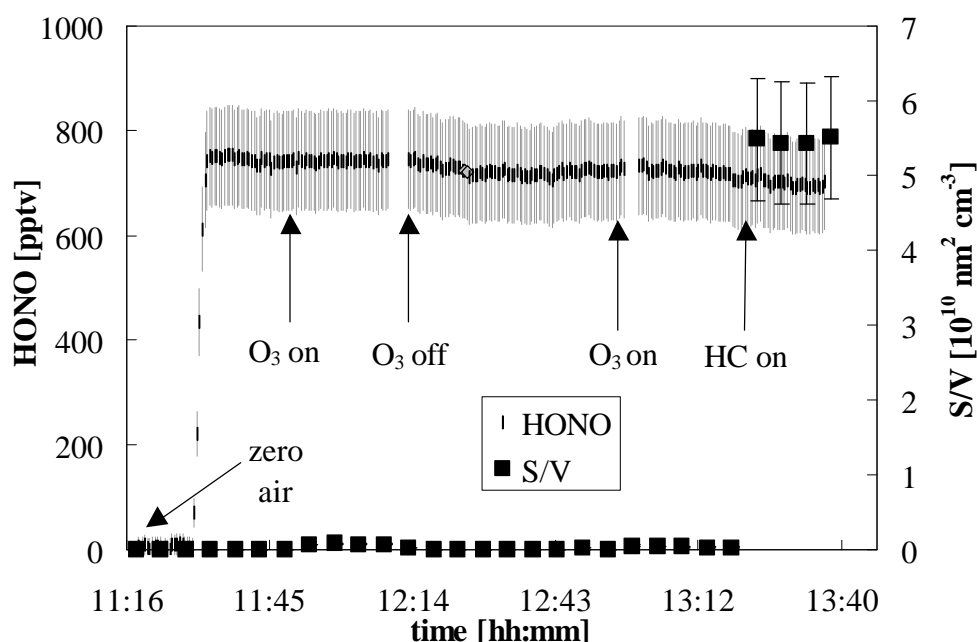


Figure 3: Example of the conversion of NO_2 on secondary organic particles in the aerosol flow tube, generated in the reaction of β -pinene with O_3 , ($[\text{NO}_2] = 19$ ppbv, 50 % r.h., $T = 298$ K, $\Delta t_{\text{reac}} = 60$ s).

Table 2: Summary of the experiments on organic particles in the aerosol flow tube ($[\text{NO}_2] = 20$ ppbv, 30-60% r. h., $T = 298$ K).

aerosol system	$\Delta S/V_{\text{max}} [\text{nm}^2 \text{cm}^{-3}]$	reactive uptake coefficients ($\text{NO}_2 \rightarrow \text{HONO}$)
β -pinene/ O_3	5.4×10^{10}	$< 2 \times 10^{-6}$
limonene/ O_3	8.5×10^{10}	$< 7 \times 10^{-7}$
catechol/ O_3	0.7×10^{10}	$< 9 \times 10^{-6}$

Implications for the atmosphere

The heterogeneous conversion of NO_2 into HONO in the presence of different organic aerosols was studied under atmospheric conditions. No NO_2 uptake and no HONO formation were observed. The upper limit for the reactive uptake was estimated to be $<10^{-7}$. For similar conditions like e.g. $[\text{NO}_2]$ and humidity, the reaction is much slower than the reaction of NO_2 with soot (e. g. Ammann et al., 1998). This leads to the conclusion that the functional groups on the surface of secondary organic

particles are different from those on soot. Accordingly, the reaction of NO₂ with secondary organic aerosols can be excluded as an important source of HONO in the atmosphere.

Acknowledgement

This work was supported by the European Commission within the NITROCAT project (contract no. EVK2-1999-00025).

References

- Alfassi, Z. B., R. E. Huie and P. Neta: Substituent Effects on Rates of One-Electron Oxidation of Phenols by the Radicals ClO₂, NO₂, and SO₃⁻, *J. Phys. Chem.*, 1986, **90**, 4156-4158.
- Alfassi, Z. B., R. E. Huie, P. Neta and L. C. T. Shoute: Temperature Dependence of the Rate Constants for Reaction of Inorganic Radicals with Organic Reductants, *J. Phys. Chem.*, 1990, **94**, 8800-8805.
- Ammann, M., M. Kalberer, D. T. Jost, L. Tobler, E. Rössler, D. Piguet, H. W. Gäggeler and U. Baltensperger: Heterogeneous Production of Nitrous Acid on Soot in Polluted Air Masses, *Nature*, 1998, **395**, 157-160.
- Arens, F., L. Gutzwiller, U. Baltensperger, H. W. Gäggeler and M. Ammann: Heterogeneous Reaction of NO₂ on Diesel Soot Particles, *Environ. Sci. Technol.*, 2001, **35**, 2191-2199.
- Arens, F., L. Gutzwiller, H. W. Gäggeler and M. Ammann: The Reaction of NO₂ with Solid Anthracene (1,2,10-trihydroxy-anthracene), *Phys. Chem. Chem Phys.*, 2002, **4**, 3684-3690.
- Gerecke, A., A. Thielmann, L. Gutzwiller and M. J. Rossi: The Chemical Kinetics of HONO Formation Resulting from Heterogeneous Interaction of NO₂ with Flame Soot, *Geophys. Res. Lett.*, 1998, **25**, 2453-2456.
- Gutzwiller, L., F. Arens, U. Baltensperger, H. W. Gäggeler and M. Ammann: Significance of Semivolatile Diesel Exhaust Organics for Secondary HONO Formation, *Environ. Sci. Technol.*, 2002, **36**, 677-682.
- Heland, J., J. Kleffmann, R. Kurtenbach and P. Wiesen: A New Instrument to Measure Gaseous Nitrous Acid (HONO) in the Atmosphere, *Environ. Sci. Technol.*, 2001, **35**, 3207 - 3212.
- Kleffmann, J., K. H. Becker and P. Wiesen: Heterogeneous NO₂ Conversion Processes on Acid Surfaces: Possible Atmospheric Implications, *Atmos. Environ.*, 1998, **32**, 2721-2729.
- Kleffmann, J., K. H. Becker, M. Lackhoff, and P. Wiesen: Heterogeneous Conversion of NO₂ and HONO on Carbonaceous Surfaces, *Phys. Chem. Chem. Phys.*, 1999, **1**, 5443-5450.
- Kleffmann, J., J. Heland, R. Kurtenbach, J. Lörzer and P. Wiesen: A New Instrument (LOPAP) for the Detection of Nitrous Acid (HONO), *Environ. Sci. Pollut. Res.*, 2002, in press.
- Huie, R. E. and P. Neta: Kinetics of One-Electron Transfer Reactions Involving ClO₂ and NO₂, *J. Phys. Chem.*, 1986, **90**, 1193-1198.
- Levaggi, D., E. L. Kothny, T. Belsky, E. DeVara and P. K. Mueller: Quantitative Analysis of Nitric Oxide in Presence of Nitrogen Dioxide at Atmospheric Concentrations: *Environ. Sci. Technol.*, 1974, **8**, 348-350.
- Pryor, W. A. and J. W. Lightsey: Mechanisms of Nitrogen Dioxide Reactions: Initiation of Lipid Peroxidation and the Production of Nitrous Acid, *Science*, 1981, **214**, 435-437.
- Raes, F., R. Van Dingenen, E. Vignati, J. Wilson, J.-P. Putaud, J. H. Seinfeld and P. Adams: Formation and Cycling of Aerosols in the Global Troposphere, *Atmos. Environ.*, 2000, **34**, 4215-4240.
- Saltzman, B. E.: Colorimetric Microdetermination of Nitrogen Dioxide in the Atmosphere, *Anal. Chem.*, 1954, **26**, 1949-1955.
- Seinfeld, J. H. and S. N. Pandis: Atmospheric Chemistry and Physics, John Wiley & Sons, 1998.
- Stadler, D. and M. J. Rossi: The Reactivity of NO₂ and HONO on Flame Soot at Ambient Temperatures: The Influence of Combustion Conditions, *Phys. Chem. Chem. Phys.*, 2000, **2**, 5420-5429.

Uptake Kinetics of Oxygenated Organics on Ice Surfaces (HEP16)

P. Behr, K. Demiral, U. Scharfenort, A. Terziyski and R. Zellner

Institut für Physikalische und Theoretische Chemie, Universität Essen, D-45117 Essen, Germany
e-mail: behr@phchem.uni-essen.de

Introduction

Trace gas measurements in the upper troposphere [Arnold et al., 1997; Singh et al., 1995] have revealed high mixing ratios of oxygenated organic species such as acetone (up to 3 ppb) and acetic acid (up to 1.9 ppb) [Jacob et al., 1996]. However, only few literature data are available on the interaction of oxygenated organic trace gases with cold ice surfaces such as on cirrus cloud particles in the upper troposphere.

The adsorption of gaseous molecules onto the ice surface is the primary step of every heterogeneous interaction. Whilst the adsorbed state represents a precursor for subsequent reactions and/or a reservoir for molecules in the gas-phase, adsorbed species can also alter the thermodynamic stability of ice by lowering its vapour pressure and allowing transport into warmer regions of the atmosphere where pure ice cannot exist [Chen and Crutzen, 1994]. The present project focuses on the experimental investigation of the kinetic, thermodynamic and mechanistic data of heterogeneous processes of oxygenated organics on ice surfaces.

In the present study we have examined the interaction of acetone and acetic acid with ice surfaces between 190 and 228 K. The results are used to derive temperature dependent adsorption constants which describe the partitioning of these species between the gas and the ice phase. Moreover, proton exchange processes of protic acetic acid molecules on D₂O-ice surfaces provide insight into the nature of the gas-ice interaction i.e. the degree of coverage and/or the degree of deactivation of active surface sites as a function of exposure time. Similarly, the desorption kinetics of isotopic labeled molecules provides information on the reactivity, residence times and thermodynamic data of adsorbed molecules.

Experimental

The heterogeneous interactions of trace gases with H₂O- or D₂O-ice surfaces have been investigated using the coated wall flow-tube technique with the detection of gaseous species and reaction products by molecular beam QMS. The reactor consists of a jacketed flow tube of 24 mm inner diameter. Its temperature is varied between 190 K and 228 K. The species were introduced by a sliding injector, a Pyrex glass tube of 6 mm outer diameter, containing a smaller glass tube surrounded by a heating wire which allowed moderate warming to prevent freezing. The carrier gas flow velocities were varied between 1 and 5 m/s at total pressures ranging from routinely 1 to 5 mbar. The gas-surface exposure time was varied by changing the position of the injector. The initial trace gas concentration was varied between 5×10^{11} and 2×10^{14} molecules cm⁻³. The ice surface was prepared by flowing water vapour with nitrogen as carrier gas through the sliding injector and moving the injector slowly until a thin uniform ice surface was formed. The flow rate of water vapour was measured by monitoring the pressure and the temperature at the water reservoir and also controlling the helium flow rate. We note that variation of the ice film thickness had no measurable influence on the amount of trace gas taken up on the surface.

Results and Discussion

Acetone

A typical example of the interaction of acetone with an ice surface at 198 K is displayed in Figure 1. Initially, a steady flow of trace gas is introduced into the flow tube with the end of the injector

located level with the end of the ice surface. This gives rise to the constant m/z signal during which there is no interaction between acetone and the ice surface. At $t = 10$ s the injector is withdrawn with a speed of 1.5 cm/s to expose 20 cm of ice coated insert to the trace gas. The profile obtained accounts for the loss of acetone until the rates of adsorption and desorption from the surface match at equilibrium and no net uptake is observed.

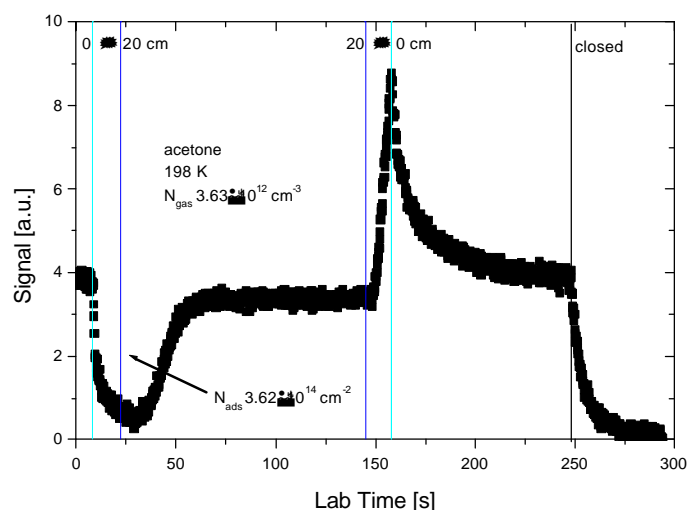


Figure 1: MS signal showing adsorption (peak at ~ 30 s) and desorption (peak at ~ 160 s) of acetone (measured at $m/z = 43$) from a ice surface at 198 K. The initial concentration of acetone was 3.6×10^{12} molecules cm^{-3} .

Once the QMS signal had been converted into a flux (in molecules s^{-1}), the total amount of gas that has been accumulated at the surface and which is required to maintain equilibrium with the gas-phase can be derived by integrating the peak area.

Within experimental error, the integrated adsorption and desorption peak areas are equal, which implies that the interaction of acetone with the ice surface is reversible.

A plot of N_{ads} versus the concentration of acetone at various temperatures is given in Figure 2.

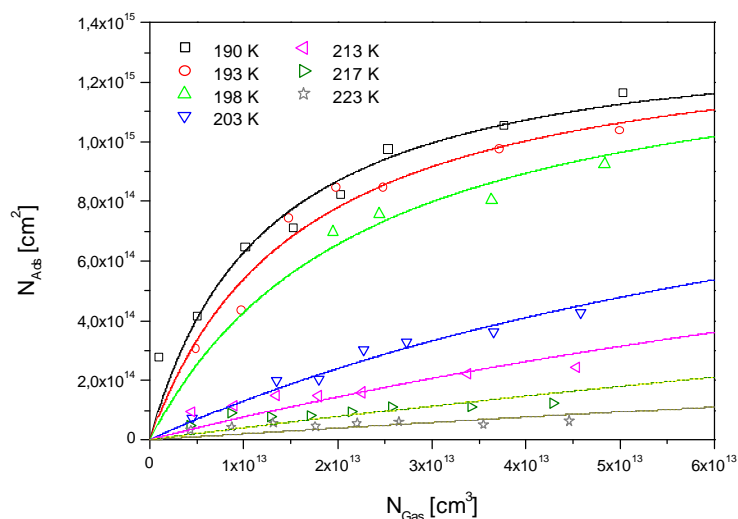


Figure. 2 Langmuir isotherms of surface coverage (N_{ads}) versus the gas phase concentration of acetone (N_{gas}) at different temperatures.

The surface coverage in figure 2 shows a monotonic dependence on the concentration of acetone which is well reproduced by a Langmuir isotherm. This suggests that multilayer adsorption is not occurring to a measurable extent. At high concentration and low temperatures the plateau in the plot of N_{ads} vs. acetone concentration indicates the approach to saturation of the surface with $N_{\text{max}} =$

$1.4(\pm 0.2) \cdot 10^{15}$ molecules cm^{-2} ($T=198$ K). Based on calculations of the liquid density and assuming spherical geometry it can be shown that $\sim 4 \cdot 10^{14}$ molecules cm^{-2} corresponds to complete surface coverage, which implies that the ice surface area under our experimental condition is at least a factor of 3 larger than the geometric surface area. Similar observations have been made by M. A. Tolbert (private communications, 2002). The isosteric adsorption enthalpy calculation at different fixed coverages yields an adsorption enthalpy of acetone on ice of $\Delta H_{\text{ads}} = 44(\pm 10)$ kJ mol^{-1} which is in good agreement with the recently published value of $\Delta H_{\text{ads}} = 46(\pm 7)$ kJ mol^{-1} [Winkler et al. 2002].

Acetic acid

i. Adsorption enthalpy

The adsorption/desorption equilibria for acetic acid on ice surfaces were also measured in a temperature range between 198 K and 228 K using initial concentration from $1.6 \cdot 10^{12}$ molecules cm^{-3} to $3.8 \cdot 10^{13}$ molecules cm^{-3} . Figure 3 shows the adsorption peaks using a initial concentration of $1 \cdot 10^{13}$ molecules cm^{-3} .

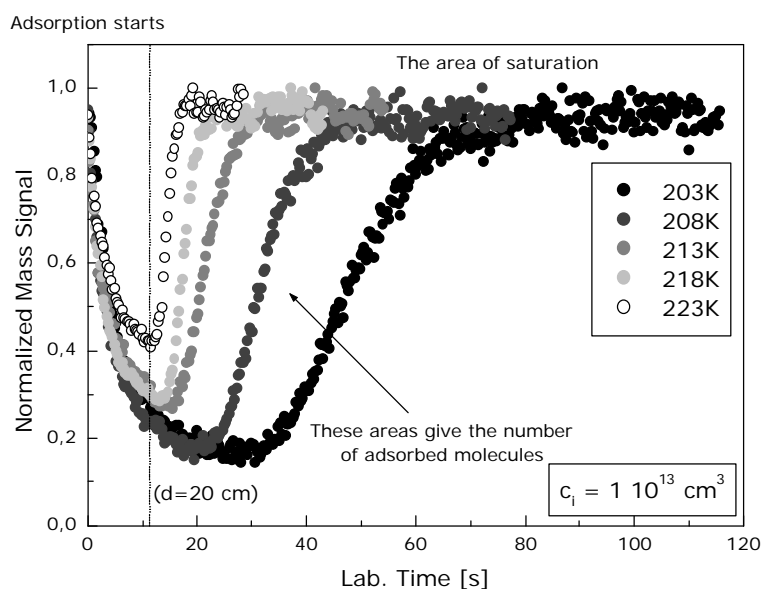


Figure 3 Normalized MS-Signal ($m/z=45$) for the temperature dependent adsorption of acetic acid on ice

The integration of the peak area gives the total number of adsorbed molecules ranging from $3.5 \cdot 10^{15}$ molecules cm^{-2} at 198 K and $4.3 \cdot 10^{14}$ molecules cm^{-2} at 223 K. The adsorption enthalpy was calculated to be $52(\pm 10)$ kJ mol^{-1} using measured Langmuir isotherms with initial concentration ranging from $1.6 \cdot 10^{12}$ molecules cm^{-2} to $3.8 \cdot 10^{13}$ molecules cm^{-2} and temperatures between 198 K and 223 K and a measured surface saturation concentration of $8 \cdot 10^{15}$ molecules cm^{-2} . As for acetone the adsorption of acetic acid was reversible after re-inserting the injector to the zero position.

ii. Desorption kinetics

Figure 4 shows the desorption kinetics of intermediately adsorbed acetic acid molecules at 198, 203 and 208 K. Displayed is the logarithmic decay of the signal intensity as a function of laboratory time.

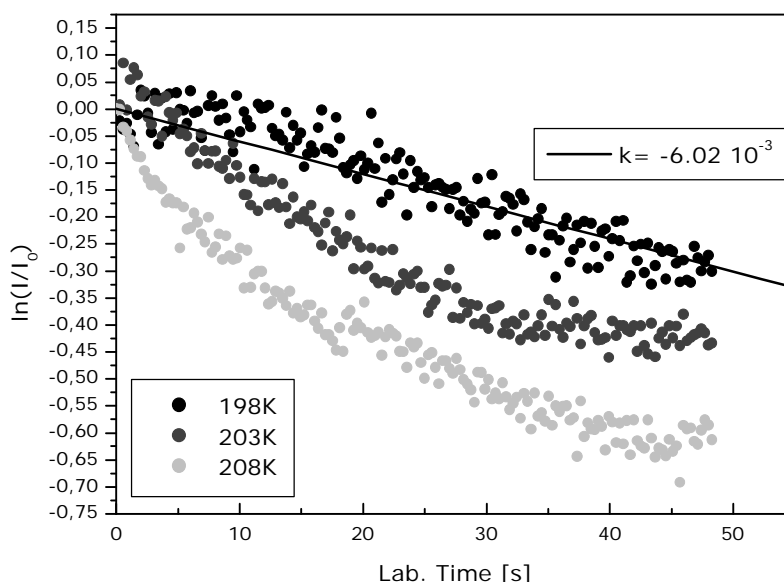


Figure 4: Desorption kinetics of adsorbed acetic acid molecules at temperatures between 198 and 208 K

At the lowest temperature (i.e. 198 K) we observed first order kinetics with a desorption rate constant of $6 \times 10^{-2} \text{ s}^{-1}$. Using this value together with the assumption of an Arrhenius like temperature dependence for desorption ($k_{\text{des}} = A_{\text{des}} \exp(-E_A/RT)$), where $k_{\text{des}} \approx 10^{13} \text{ s}^{-1}$ we obtain $E_{A,\text{des}} \approx 60 \text{ kJ mol}^{-1}$. This value is within error limit identical to the enthalpy of adsorption which indicates that there is no barrier to adsorption. At slightly higher temperatures (203 K, 208 K) an increasing deviation from first order kinetic behavior is observed. At the same time the desorption peak is broadening and shifted to longer residence times. This observation suggests an increasing mobility and a loss of the geometrical ice structure of the outer surface molecules of H_2O . This probably implies a diffusion of acetic acid molecules into the so called “quasi liquid layer” at temperatures $> 200 \text{ K}$ [Girardet and Toubin 2001].

iii. Proton exchange

To estimate the residence time, the extent of dissociation and thermodynamic data of the intermediate adsorbed acetic acid molecules we performed proton exchange experiments. During the experiments the reactor surface was coated with D_2O -ice in the same way as described previously using D_2O instead of H_2O .

Figure 5 shows the recorded concentration changes of the initial acetic acid molecules (black points) in comparison of the desorption of isotopic labeled product molecules (open circles).

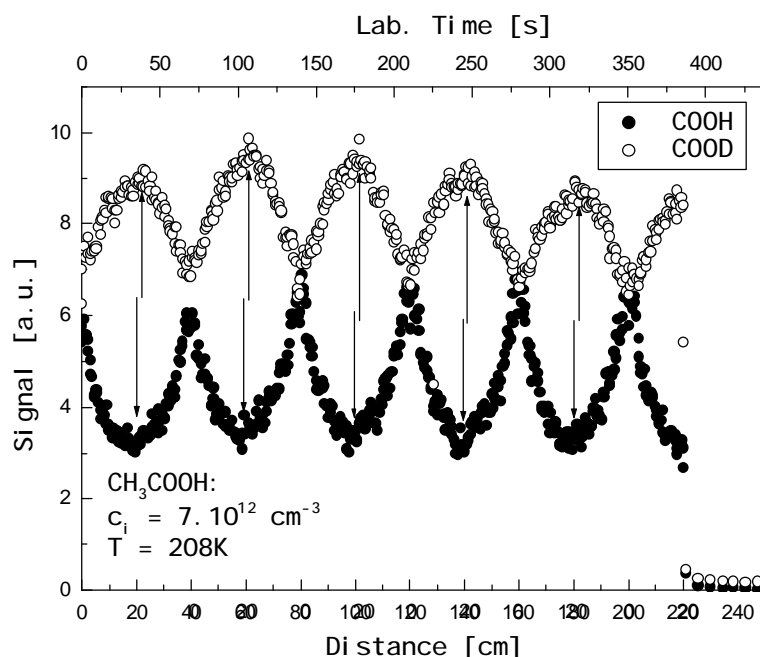


Figure 5: MS-Signal for the adsorption of CH_3COOH and desorption of CH_3COOD from a D_2O -ice surface at 208 K after changing the available surface area by moving the injector continuously between 0 and 20 cm.

The injector was moved continuously forward and backward between 0 and 20 cm with a speed of 0,7 cm/s. From the decrease of the signal intensity at $m/z = 45$ at longer contact times we calculate the proton exchange probability to be 10^{-2} .

The fact that only one molecule out of hundred, which hit the surface, dissociates and recombines with D^+ -ions leads to the assumption of a required orientation of the molecules which dissociate on the surface. With decreasing temperature we also observe an increasing time shift (τ) between the adsorption and desorption signal. At 208 K (Fig. 5) we measure $\tau = 3$ s. The measured temperature dependence of time shifts corresponds to an activation energy for desorption of $56(\pm 10)$ kJ mol^{-1} , in good agreement with direct desorption measurements. As a result proton exchanged acetic acid and primarily adsorbed acetic acid show identical surface desorption energies.

References

- Arnold, F., J. Schneider, K. Gollinger, H. Schlager, P. Schulte, D. E. Hagen, P. D. Whitefield, and P. van Velthoven, 1997: Observation of upper tropospheric sulfur dioxide and acetone pollution: potential implications for hydroxyl radical and aerosol formation. *Geophys. Res. Lett.* **24**, 57-60.
- Chen, J.-P., P. J. Crutzen, 1994: Solute effects on the evaporation of ice particles. *J. Geophys. Res.* **99**, 18847-18859.
- Winkler A. K., N. S. Holms and J. N. Crowley, 2002, Interaction of methanol, acetone and formaldehyde with ice surfaces between 198 and 223 K. *Phys. Chem. Chem. Phys.*, **4**, 5270-5275
- Giradet C., C. Toubin, 2001, Molecular atmospheric pollutant adsorption on ice: a theory survey, *Surface science reports*, **44**, 159-238
- Jacob, D. J., B. G. Heikes, S. M. Fan, J. A. Logan, D. L. Mauzerall, J. D. Bradshaw, H. B. Singh, G. L. Gregory, R. W. Talbot, D. R. Blake, and G. W. Sachse, 1996: Origin of ozone and NO_x in the tropical troposphere: a photochemical analysis of aircraft observations over the South Atlantic basin. *J. Geophys. Res.* **101 D**, 24235-24250,
- Singh, H. B., M. Kanakidou, P. J. Crutzen, D. J. Jacob, 1995: High concentrations and photochemical fate of oxygenated hydrocarbons in the global troposphere. *Nature* **378**, 50-54.

Chemical Reactivity and Transformation of Aerosol Particles: Mechanistic Description of Surface Processes Involving Reversible Adsorption and Langmuir-Hinshelwood Reactions (HEP20)

Ulrich Pöschl¹, Yinon Rudich², Markus Ammann³

¹ *Technical University of Munich, Institute of Hydrochemistry, Marchioninstr. 17, D-81377 Munich, Germany*

² *Department of Environmental Sciences, Weizmann Institute of Science, Rehovot 76100, Israel*

³ *Paul Scherrer Institute, CH-5232 Villigen PSI, Switzerland*

Introduction

Air particulate matter contains a wide range of substances, which influence the physicochemical properties of aerosol particles and thus their effects on atmospheric chemistry and physics, climate, and public health. Chemical reactions occurring on aerosol particles in the atmosphere can transform these components and change their physicochemical properties. Recent laboratory studies on a number of different solid and liquid surfaces suggest that many important heterogeneous processes progress by adsorption of the gas-phase species to the surface followed by reaction with surface-adsorbed reactants (e.g. Jayne et al., 1990; Allan et al., 1997; Chu et al., 1993; Arens et al., 2001; Pöschl et al., 2001; Clegg and Abbatt, 2001; Remorov et al., 2002; Ammann et al. 2002; and references therein). Such reactions are usually referred to as a Langmuir-Hinshelwood reactions.

Model Derivation

Here we focus on the description of surface reactions in which two species, X and Y, are adsorbed to the surface prior to reaction. More specifically, we assume that one of the species (Y) has a very long residence time on the surface and can be considered to be part of the quasi-static particle surface with a concentration $[Y]_s$ [molecule cm^{-2}]. The concentration of surface-adsorbed X molecules, $[X]_s$ [molecule cm^{-2}], is in equilibrium with the gas phase concentration in the immediate vicinity of the surface, $[X]_{gs}$ [molecule cm^{-3}] (the average concentration of X in the bulk gas phase is denoted as $[X]_g$ [molecule cm^{-3}]). The process leading to a surface reaction involves several steps. First, adsorption of the gas-phase molecule on the surface is described by defining the surface accommodation coefficient, S_0 , as the probability that X does neither immediately bounce off nor reacts upon collision with the adsorbate-free surface. S_0 has also been termed sticking coefficient, trapping probability, or adsorption coefficient by other authors. Assuming a Langmuir-type adsorption process, where collision of X with a previously adsorbed X cannot lead to adsorption, we define an adsorption rate constant,

$$k_a = S_0 \omega_x / 4 \quad (1)$$

We assume that X can also adsorb on top of Y and that S_0 describes the surface accommodation process also for this case. The adsorbed molecule can either thermally desorb back to the gas phase or undergo a reaction (including the formation of chemical adducts). Under steady-state conditions with negligible surface reaction and transport to the bulk, the rate of adsorption can be equated to the rate of desorption which leads to the well-known Langmuir equilibrium:

$$k_a [X]_{gs} (1 - \theta_x) = k_d \theta_x / \sigma_x \Leftrightarrow \theta_x = \frac{K [X]_{gs}}{1 + K [X]_{gs}} \quad (2)$$

where $\theta_x = [X]_s / \sigma_x$ denotes the fractional surface coverage of X, and σ_x [$\text{cm}^2/\text{molecule}$] is the surface area occupied by one adsorbed molecule of X. $k_d = 1/\tau$ is the first order rate coefficient for the

thermal desorption of X, which is generally described as an activated process (Masel, 1996). τ is the residence time of X on the surface. The Langmuir constant, K, in units of $\text{cm}^3/\text{molecule}$ is given by

$$K = \frac{\sigma_X k_a}{k_d} \quad (3)$$

Assuming a simple bimolecular mechanism, the rate of surface reaction R_s [$\text{molecule cm}^{-2} \text{s}^{-1}$] is expressed with a second-order rate constant k_s [$\text{cm}^2 \text{s}^{-1} \text{molecule}^{-1}$] or with an apparent first order rate constant k_s^1 as

$$R_s = k_s [Y]_s [X]_s = k_s^1 [X]_s \quad (4)$$

In cases of reversible adsorption where k_s^1 is of similar magnitude as k_d , the mass balance at the surface under steady-state conditions leads to a modified Langmuir equilibrium,

$$k_a [X]_{gs} (1 - \theta_X) = \theta_X (k_d + k_s^1) / \sigma_X \Leftrightarrow \theta_X = \frac{K' [X]_{gs}}{1 + K' [X]_{gs}} \quad (5)$$

with an effective equilibrium constant,

$$K' = \frac{\sigma_X k_a}{k_d + k_s^1} \quad (6)$$

In atmospheric chemistry models, the loss of gas phase species X by heterogeneous processes is commonly described by an uptake coefficient, γ_X , which is defined as the probability that a collision of X with the particle's surface leads to its net uptake into the condensed phase. Based on this definition the uptake coefficient can be obtained by dividing the net loss on the surface, $\theta_X k_s^1 / \sigma_X$, by the gas-kinetic collision rate, $[X]_{gs} \omega_X / 4$:

$$\gamma_X = \frac{4 k_s^1 \theta_X}{\omega_X \sigma_X [X]_{gs}} = \frac{4 k_s [Y]_s K'}{\omega_X \sigma_X (1 + K' [X]_{gs})} \quad (7)$$

Based on equations (5) and (6), Equation (7) can be rearranged to

$$\frac{1}{\gamma_X} = \frac{(k_d + k_s^1) + \sigma_X S_0 [X]_{gs} \omega_X / 4}{S_0 k_s^1} = \frac{1}{S_0} + \frac{1}{k_s^1} \left[\frac{k_d}{S_0} + \frac{\sigma_X [X]_{gs} \omega_X}{4} \right] \quad (8)$$

The uptake coefficient as described in Equation (8) can be formally separated into a resistance for mass accommodation at the surface, $1/S_0$, and a surface reaction resistance, $1/\Gamma_s$:

$$\frac{1}{\gamma_X} = \frac{1}{S_0} + \frac{1}{\Gamma_s} \quad (9)$$

$$\frac{1}{\Gamma_s} = \frac{1}{k_s^1} \left[\frac{k_d}{S_0} + \frac{\sigma_X [X]_{gs} \omega_X}{4} \right] = \frac{\omega_X \sigma_X (1 + K [X]_{gs})}{4 k_s [Y]_s K} \quad (10)$$

The resistance term $1/\Gamma_s$ can be flexibly included in the traditional resistance model for gas uptake by liquid particles driven by reactions in the particle bulk as described in detail by *Ammann et al.* (2002) and *Pöschl et al.* (2002). For $S_0 \gg \Gamma_s$ Equations (9) and (10) can be reduced to

$$\gamma_X \approx \frac{4 k_s [Y]_s K}{\omega_X \sigma_X (1 + K [X]_{gs})} \quad (11)$$

Numerical Simulations and Experimental Data

In Figures 1 and 2, the implications of the model formalism derived above on the time and concentration dependence of the uptake coefficient are explored by numerical simulations.

In Figure 1, γ_X is plotted as a function of time for different gas phase concentrations of X ($[X]_{\text{gs}} = \text{const.}$). γ_X and the concentration change of Y have been calculated iteratively for an initial concentration $[Y]_{\text{s},0} = 10^{14} \text{ cm}^2$ and $k_s = 10^{-17} \text{ cm}^2 \text{ s}^{-1}$, $S_0 = 0.01$, $\tau = 10 \text{ s}$ and $\sigma = 4 \times 10^{-15} \text{ cm}^2$. Initially, γ_X equals S_0 , until saturation coverage of X is reached. As long as the coverage is well below a monolayer, γ_X is independent of the gas phase concentration. The higher the gas-phase concentrations of X, the more rapidly saturation coverage of X is reached, and the faster γ_X decreases at short time scales. At intermediate time scales, where Y is in excess, γ_X remains constant. At low gas phase concentration of X, the magnitude of γ_X during this period is independent of the gas-phase concentration, whereas it decreases inversely proportional to it at higher concentrations, when $K[X]_{\text{gs}}$ becomes comparable to 1 (or the equilibrium coverage of X approaches a monolayer). At longer time scales, γ_X drops further due to significant depletion of Y. The higher the gas-phase concentration, the earlier this decrease sets in.

In Figure 2, a similar set of numerical simulations is shown, but here the surface reaction rate coefficient (k_s) has been varied for $[X]_{\text{gs}} = 10^{10} \text{ cm}^{-3} = \text{const.}$; the other parameters were the same as for Figure 1. For slow surface reaction ($k_s = 10^{-14} \text{ cm}^2 \text{ s}^{-1}$) we observe the plateau period where γ_X is fairly constant, as in Figure 1. However, this plateau period becomes shorter with faster surface reaction. Still, for a selected range of k_s and reaction time (around 100s in this example) γ_X scales with k_s . In the case of the fastest reaction displayed and beyond, γ_X becomes limited by the surface accommodation coefficient, S_0 , until it drops due to complete consumption of the surface reactant Y.

Figures 1 and 2 clearly illustrate that the experimental time-scale and potentially fast changes of the uptake coefficient must be taken into account in the analysis, parameterization and extrapolation of laboratory measurement results. Since individual experimental methods usually cover only a limited time range, different approaches must be combined to cover the full parameter space.

Langmuir-Hinshelwood mechanisms has been discussed since the 1990s for reactions on stratospheric ice and acid hydrate particles (e.g. Tabazadeh and Turco, 1993; Carslaw and Peter, 1997; Tabazadeh et al., 1999), but only recently they have been demonstrated to be applicable for reactions on typical tropospheric aerosols of complex chemical composition such as soot (e.g. Arens et al., 2001; Pöschl et al., 2001), condensed organics (Arens et al., 2002) or inorganic salts (Gershenson et al., 1999). As an example for the applicability to experimental data, Figure 3 displays a fit of Equation (11) to the apparent reaction probability or uptake coefficient for ozone reacting with benzo[a]pyrene on soot aerosol particles. The influence of water vapor can be attributed to competitive adsorption (Pöschl et al., 2001). More examples and general implications of the above formulations and the relations with previous modeling approaches for aerosol surface chemistry are discussed by Ammann et al. (2002).

Summary and Conclusions

The presented model formalisms provide a framework for consistent analysis and parameterization of gas-particle interactions following a Langmuir-Hinshelwood reaction mechanism. Exemplary numerical simulations and experimental data demonstrate that uptake coefficients can exhibit pronounced non-linear dependencies on gas phase and particle composition and time. The underlying parameters, S_0 , k_s , σ_X , and k_d , however, can be used in atmospheric models for the calculation of appropriate uptake coefficients under varying conditions. The presented equations have been derived for a simple model system with two species. Generalized equations for multi-component systems including other types of reaction mechanisms and mass transport processes – e.g. Eley-Rideal reactions and surface bulk exchange – will be given by Pöschl et. al. (2002).

Acknowledgements

This work was supported by the German Federal Ministry of Education and Research (AFO2000-CARBAERO), the US-Israel Binational Science Foundation (#1999134), the Minerva foundation, the European Community (Cut-Ice, EVK 1999-00005), and the Swiss Government of Education and Science.

References

- Allanic, A., R. Oppliger and M. J. Rossi, *J. Geophys. Res.*, 1997, **102**, 23529.
 Ammann, M., U. Pöschl, Y. Rudich, *Phys. Chem. Chem. Phys.*, 2002, submitted.
 Arens, F., L. Gutzwiller, U. Baltensperger, H. W. Gäggeler and M. Ammann, *Environ. Sci. Tech.*, 2001, **35**, 2191.
 Arens, F., L. Gutzwiller, H. W. Gäggeler and M. Ammann, *Phys. Chem. Chem. Phys.*, 2002, **4**, 3684.
 Carslaw, K. S., and T. Peter, *Geophys. Res. Lett.*, 1997, **24**, 1743.
 Chu, L. T., M. T. Leu and L. F. Keyser, *J. Phys. Chem.*, 1993, **97**, 12798.
 Clegg, S. M., and J. P. D. Abbatt, *Atm. Chem. Phys.*, 2001, **1**, 73.
 Gershenzon, Y. M., V. M. Grigorjeva, A. Y. Zasyplin, A. V. Ivanov, R. G. Remorov and E. L. Aptekar, *Chem. Phys. Rep.*, 1999, **18**, 79.
 Jayne, J. T., P. Davidovits, D. R. Worsnop, M. S. Zahniser and C. E. Kolb, *J. Phys. Chem.*, 1990, **94**, 6041.
 Masel, R. I., *Principles of adsorption and reaction on solid surfaces*, 1st ed.; John Wiley & Sons: New York, 1996.
 Pöschl, U., T. Letzel, C. Schauer and R. Niessner, *J. Phys. Chem. A*, 2001, **105**, 4029.
 Pöschl, U., Y. Rudich, and M. Ammann, *Atmos. Chem. Phys.*, 2002, to be submitted.
 Remorov, R. G., Y. M. Gershenzon, L. T. Molina and M. J. Molina *J. Phys. Chem.*, 2002, **106**, 4558.
 Tabazadeh, A., and R. P. Turco, *J. Geophys. Res.*, 1993, **98**, 12727.
 Tabazadeh, A., O. B. Toon and E. J. Jensen, *Geophys. Res. Lett.*, 1999, **26**, 2211

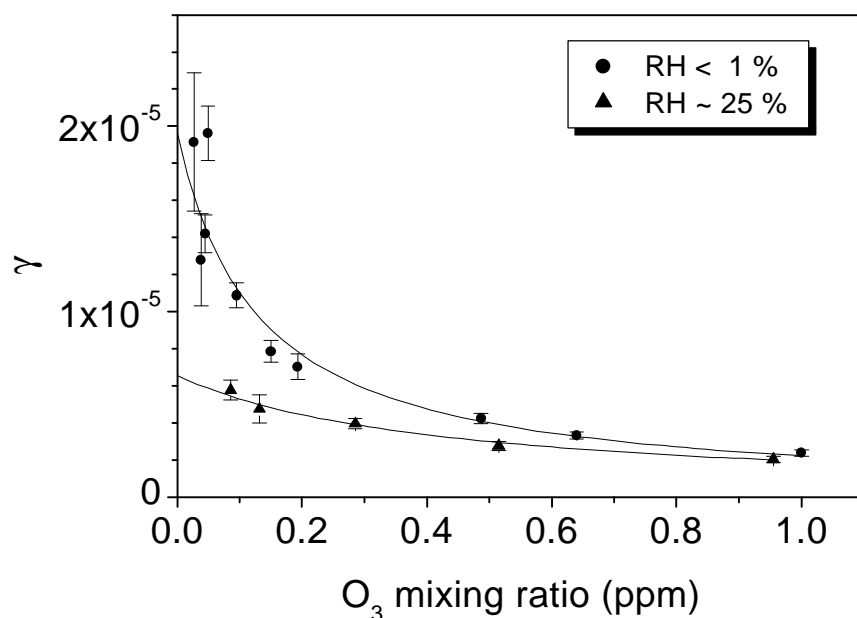


Figure 1: γ_x as a function of time for different gas-phase concentrations; numerical simulations with $[X]_{gs} = \text{const.}$, $[Y]_{s,0} = 10^{14} \text{ cm}^{-2}$, $k_s = 10^{-17} \text{ cm}^2 \text{ s}^{-1}$, $S = 0.01$, $\tau = 10 \text{ s}$, $\sigma = 4 \times 10^{-15} \text{ cm}^2$.

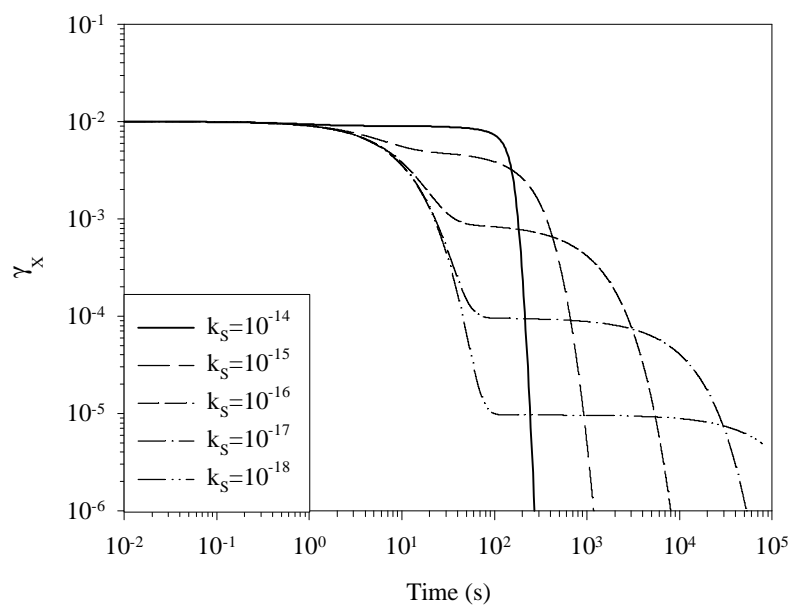


Figure 2: γ_x as a function of time for different surface reaction rate coefficients, k_s . Numerical simulations with $[X]_{gs} = 10^{10} \text{ cm}^{-3} = \text{const.}$; other parameters like in Figure 1.

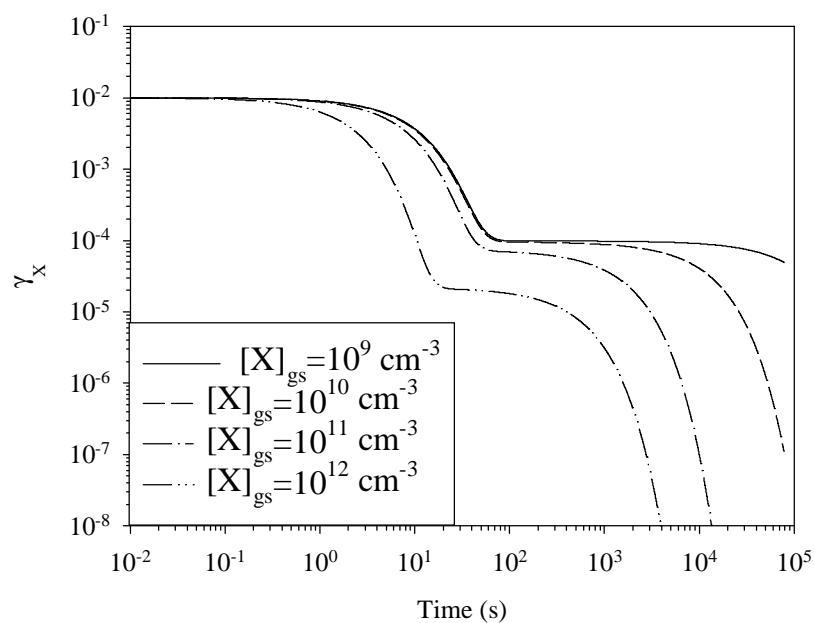


Figure 3: Uptake coefficient for ozone reacting with benzo[a]pyrene on spark-discharge soot aerosol particles at different relative humidities (296 K, 1 atm). The lines are a fits to the experimental data based on equation (11).

A New Chemical Module for Tropospheric Isoprene Degradation Applied to the RACM Mechanism (MPM2)

Harald Geiger, Ian Barnes, Iustinian Bejan, Thorsten Benter and Markus Spittler
Bergische Universität Gesamthochschule Wuppertal, FB 9 - Physikalische Chemie
D-42097 Wuppertal, Germany
E-Mail: geiger@physchem.uni-wuppertal.de

Abstract / Introduction

A highly condensed reaction scheme for the tropospheric oxidation of isoprene is presented. This mechanism was implemented into the Regional Atmospheric Chemistry Mechanism (RACM, Stockwell et al., 1997), which is an established chemical module for regional air quality modelling but contains an isoprene chemistry which is no longer state-of-the-art. The reaction scheme developed here is based on the recently published MIM ("Mainz Isoprene Mechanism", Pöschl et al., 2000) that has been constructed for application in global chemistry transport models. The MIM code was reduced to a size suitable for use in regional atmospheric chemistry models. Redundant reactions were identified and removed from the reaction scheme by means of sensitivity analyses. The revised mechanism was successfully tested against the results of smog chamber experiments carried out in the European photoreactor EUPHORE. A model intercomparison between both the original and the updated RACM mechanism was performed for a number of well-defined scenarios employing conditions ranging from very clean to highly polluted air masses. The calculations revealed large deviations in the concentration-time profiles for key species of the isoprene degradation, particularly under "low-NO_x" conditions. The new isoprene chemistry requires only a few additional reactants (7) and chemical reactions (7) and, therefore, offers the possibility for the successful application of the revised reaction scheme in chemistry-transport models (CTM) without an excessive increase in computational efforts.

Experimental / Modelling System

The smog chamber experiments were performed in the European photoreactor, EUPHORE, in Valencia, Spain. For the present study, isoprene was oxidised in the presence of NO_x in NMHC mixtures containing fractions of *n*-butane, ethene and toluene.

All the computer simulations and sensitivity analyses were carried out using the box model SBOX (Seefeld and Stockwell 1999). The same program package also allowed the performance of sensitivity analyses. The photolysis frequencies were calculated employing a suitable algorithm. For simulating the smog chamber experiments, the calculated values of J(NO₂) were fit to experimental filter radiometer or spectral radiantmeter data using scaling factors. All other J values were then calculated relative to J(NO₂).

The present work also reports modelling results for 4 well-defined cases with tropospheric conditions ranging from very clean to highly polluted air masses. The scenarios FREE, LAND, PLUME and URBAN taken from a work of Poppe et al. (2001) reflect the free troposphere, the remote planetary boundary layer and two different cases with relatively high anthropogenic VOC and NO_x contents, respectively. Additional isoprene emission rates were added. For simplification, the emission rates were kept constant over each simulation, which was run for 5 days starting at noon with photolysis conditions corresponding to July 1, 45° north.

Summary of the Results / Conclusions

A chemical module describing the tropospheric degradation of isoprene has been derived from the "Mainz Isoprene Mechanism" (MIM, Pöschl et al., 2000) and was implemented into the "Regional Atmospheric Chemistry Mechanism" (RACM, Stockwell et al., 1997). The MIM code was derived

from the highly explicit and actual Master Chemical Mechanism (MCM) and includes a number of specific isoprene reaction products and peroxy-peroxy self-reactions that were not considered in the original RACM scheme. The code of the "new" isoprene chemistry was reduced on the basis of sensitivity analysis results (see Table 1). It was shown that this reduction did not cause any significant disparities of modelling results for both full and reduced updated RACM schemes. Peroxy radical cross-reactions were not considered, since they increase the model uncertainty due to missing knowledge on their reaction products. This additional uncertainty will probably compensate a possible increase of accuracy caused by the inclusion of these reactions into the mechanism. The final revised RACM scheme is characterised by 7 additional species and 7 additional reactions compared to the original RACM. The new mechanism was tested at different VOC/NO_x ratios against smog chamber data generated in the European photoreactor EUPHORE. As illustrated in Figure 1 for an example run, these studies yielded a much better description of the experimental concentration-time profiles by the revised code in comparison to the original RACM 1.3 scheme. The plots indicate that the original RACM code clearly underpredicts the radical budget of the system. As a consequence, the NO to NO₂ conversion is too slow and ozone formation is delayed. Similar to Figure 1, a number of other runs not displayed here also showed that the formation of MACR (unsaturated carbonyl compounds) as primary oxidation products of isoprene is too small in the former RACM scheme. Since MACR reflects a group of highly reactive VOC whose photolysis or chemical oxidation will lead to additional radicals, their underprediction by the old RACM code may be one of the major reasons for the observed results.

Box model intercomparison studies for a number of well-defined scenarios representing different tropospheric conditions exhibited strong systematic deviations for a couple of reactants, due to the very different isoprene oxidation pathways in both mechanisms (see the Figures 2 and 3 as examples for the URBAN and the FREE case). Although the scenarios are fairly simple, the calculations demonstrate that particularly for clean areas, whose photochemistry is controlled by biogenic VOC emissions, the isoprene chemistry of the original RACM is too general to be able to give a representative picture of the photochemical processes. Accordingly, it is recommended here to update the original RACM mechanism by the reactions summarised in Table 2. For the CT modellers' community, the numbers of 7 additional species and 7 new elementary reactions might still appear fairly high with regard to implementation of the revised RACM scheme into CT models. However, from the chemical point of view, the mechanism provided here seems to be the most reasonable solution providing a maximum of both detail and modelling accuracy with respect to tropospheric isoprene degradation.

References

- Pöschl, U., von Kuhlmann, R., Poisson, N., Crutzen, P. J., 2000. Development and intercomparison of condensed isoprene oxidation mechanisms for global atmospheric modeling. *Journal of Atmospheric Chemistry* 37, 29-52.
- Poppe, D., Aumont, B., Ervens, B., Geiger, H., Herrmann, H., Röth, E.-P., Seidl, W., Stockwell, W. R., Vogel, B., Wagner, S., Weise, D., 2001. Scenarios for modeling multiphase tropospheric chemistry. *Journal of Atmospheric Chemistry* 40, 77-86.
- Seefeld, S., Stockwell, W. R., 1999. First-order sensitivity analysis of models with time-dependent parameters: An application to PAN and ozone. *Atmospheric Environment* 33, 2941-2953 (and references therein).
- Stockwell, W. R., Kirchner, F., Kuhn, M., Seefeld, S., 1997. A new mechanism for regional atmospheric chemistry modeling. *Journal of Geophysical Research* 102, 25847-25879.

Acknowledgements

The authors thank U. Pöschl, Technical University Munich, R. Forkel, Research Centre Karlsruhe and H.-P. Dorn, Research Centre Jülich, for very helpful discussions and L. Ruppert, Audi Motor Company, as well as K. Wirz, CEAM Valencia, for the supply of experimental data. The financial support by the German

Department of Education and Research (BMBF) within the German Atmospheric Research Programme "AFO 2000" is gratefully acknowledged.

Table 1: Numbers of species and reactions of the mechanisms applied in the present work.

mechanism	species	chemical reactions	photolysis reactions
RACM 1.3 ^{*)}	77	214	23
full updated RACM	84	222	30
reduced updated RACM	84	221	23

^{*)} Stockwell et al. (1997).

Table 2: Reactions adapted from the MIM isoprene degradation scheme, which were implemented in the updated RACM scheme. All reactants are given in RACM notation. Corresponding reactions of the original RACM were replaced by those given here.

no.	reaction	rate coefficient ^{*)}
R1	ISO + OH → ISOP	2.54E-11 exp(410/T)
R2	ISO + O3 → 0.65 MACR + 0.58 HCHO + 0.1 MACP + 0.1 ACO3 + 0.08 MO2 + 0.28 ORA1 + 0.14 CO + 0.09 H2O2 + 0.25 HO2 + 0.25 OH	7.86E-15 exp(-1913/T)
R3	ISO + NO3 → ISON	3.03E-12 exp(-446/T)
R4	ISOP + NO → MACR + NO2 + HCHO + HO2 + 0.046 ISON	2.43E-12 exp(360/T)
R5	ISOP + HO2 → ISHP	2.05E-13 exp(1300/T)
R6	ISOP + ISOP → 2 MACR + HCHO + HO2	2.0E-12
R7	ISHP + OH → MACR + OH	1.0E-10
R8	ISON + OH → HACE + NALD	1.3E-11
R9	MACR + OH → MACP	0.5 x (4.13E-12 exp(452/T) + 1.86E-11 exp(175/T))
R10	MACR + O3 → 0.9 MGLY + 0.45 ORA1 + 0.32 HO2 + 0.22 CO + 0.19 OH + 0.1 ACO3	0.5 x (1.36E-15 exp(-2112/T) + 7.51E-16 exp(-1521/T))
R11	MACP + NO → NO2 + 0.25 HACE + 0.25 CO + 0.25 ACO3 + 0.5 MGLY + 0.75 HCHO + 0.75 HO2	2.54E-12 exp(360/T)
R12	MACP + HO2 → MAHP	1.82E-13 exp(1300/T)
R13	MACP + MACP → HACE + MGLY + 0.5 HCHO + 0.5 CO + HO2	2.0E-12
R14	MACP + NO2 → MPAN	$k_0 = 9.7E-29 (T/300)^{-5.6}$ $k_\infty = 9.3E-12 (T/300)^{-1.5}$ $F_c = 0.6$
R15	MPAN → MACP + NO2	$k_{R15} = k_{R14}/(9.0E-19 \exp(14000/T))$
R16	MPAN + OH → HACE + NO2	3.6E-12
R17	MAHP + OH → MACP	3.0E-11
R18	HACE + OH → MGLY + HO2	3.0E-12
R19	NALD + OH → HCHO + CO + NO2	5.6E-12 exp(270/T)

^{*)} in molecular units, according to Pöschl et al. (2000)

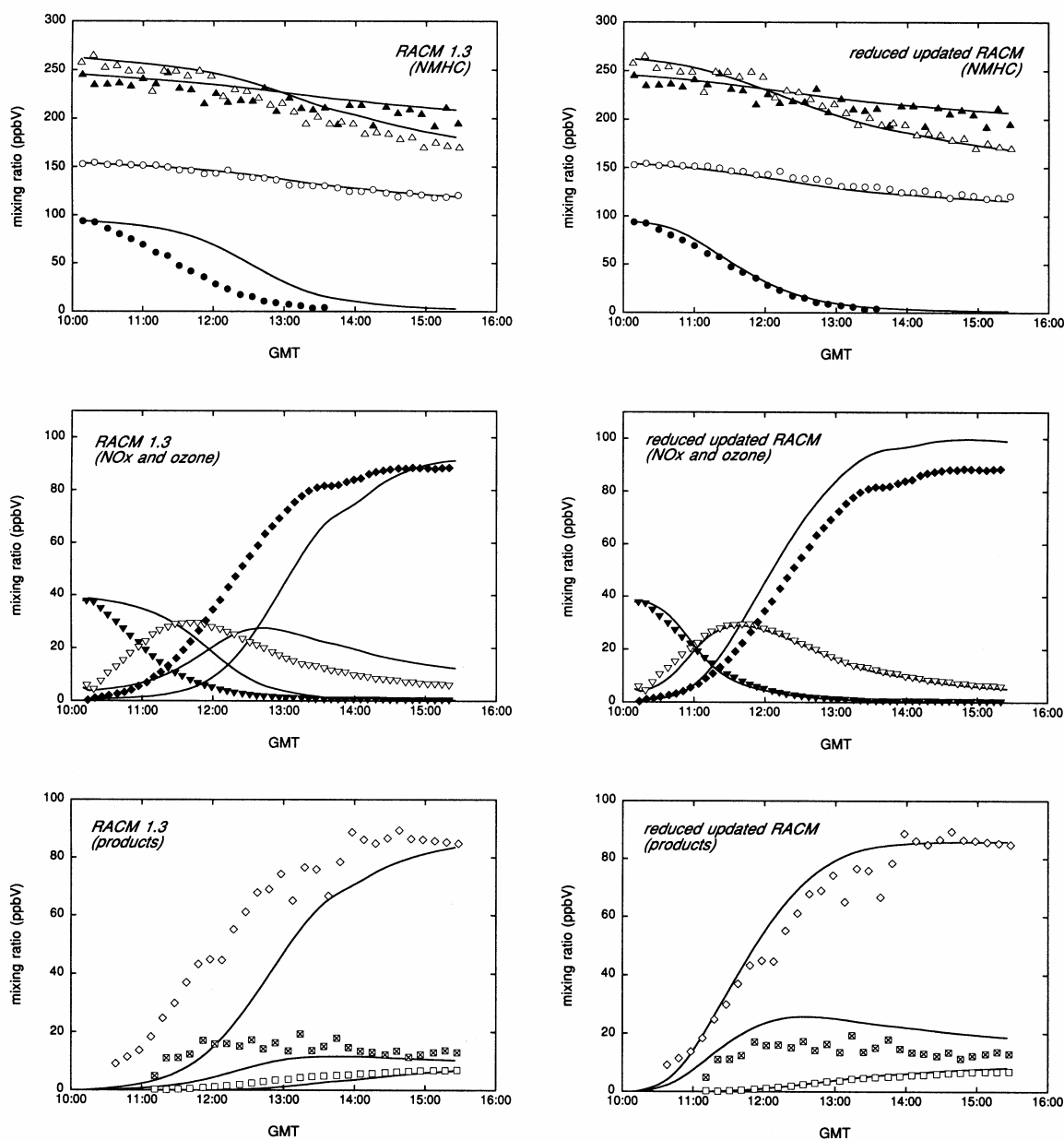


Figure 1: Comparison of experimental and simulated (RACM 1.3 and reduced updated RACM) concentration-time profiles for an example run in the EUPHORE chamber: (J) isoprene $\times 2$; (E) toluene $\times 2$; (H) *n*-butane; (C) ethene; (P) NO; (S) NO₂; (F) O₃/2; (A) HCHO; (G) PAN; (â) MACR.

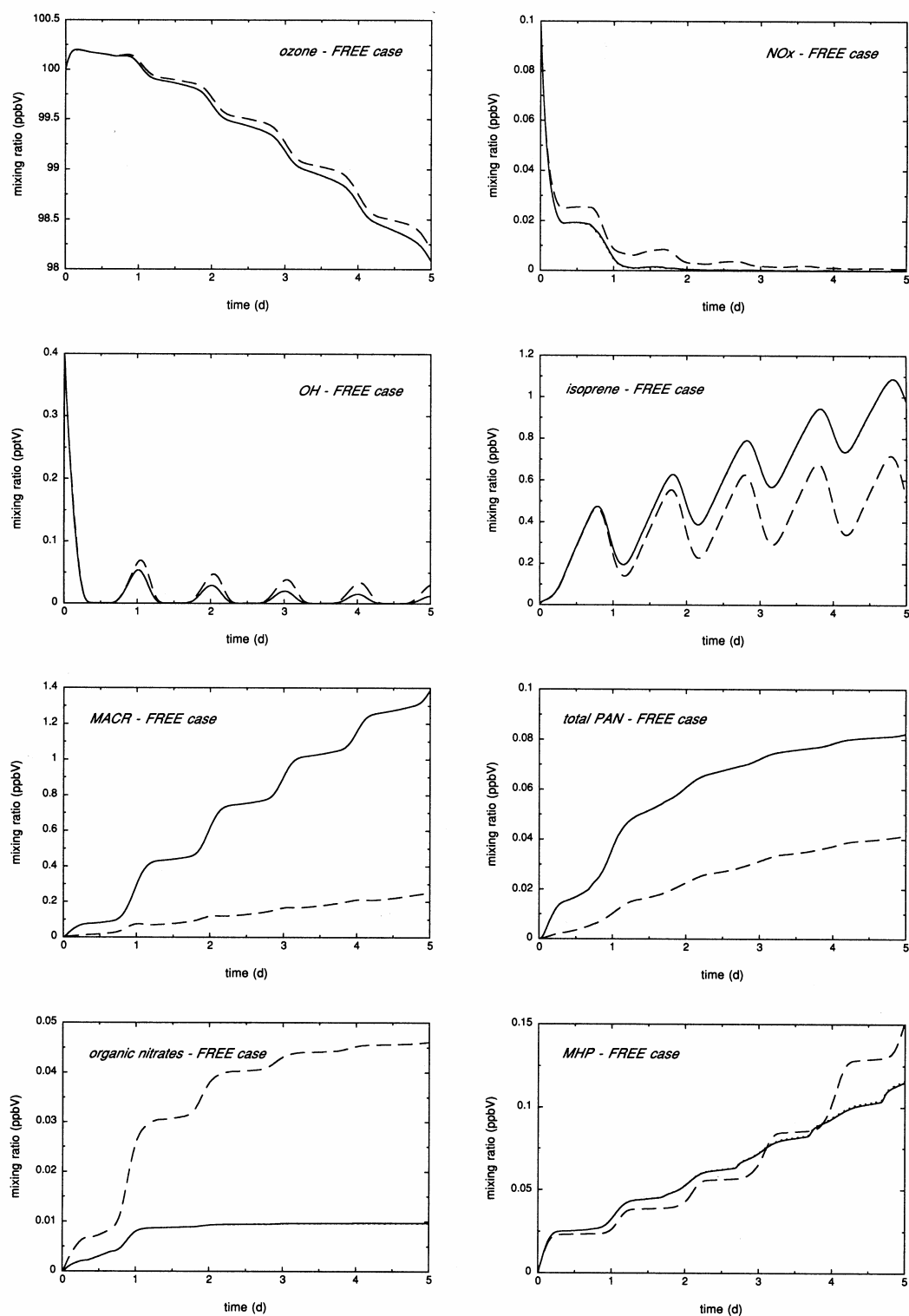


Figure 2: Mixing ratios of selected vs. versus reaction time calculated for the FREE case: (--- --) original RACM scheme; (.....) full updated RACM scheme; (—) reduced updated RACM scheme.

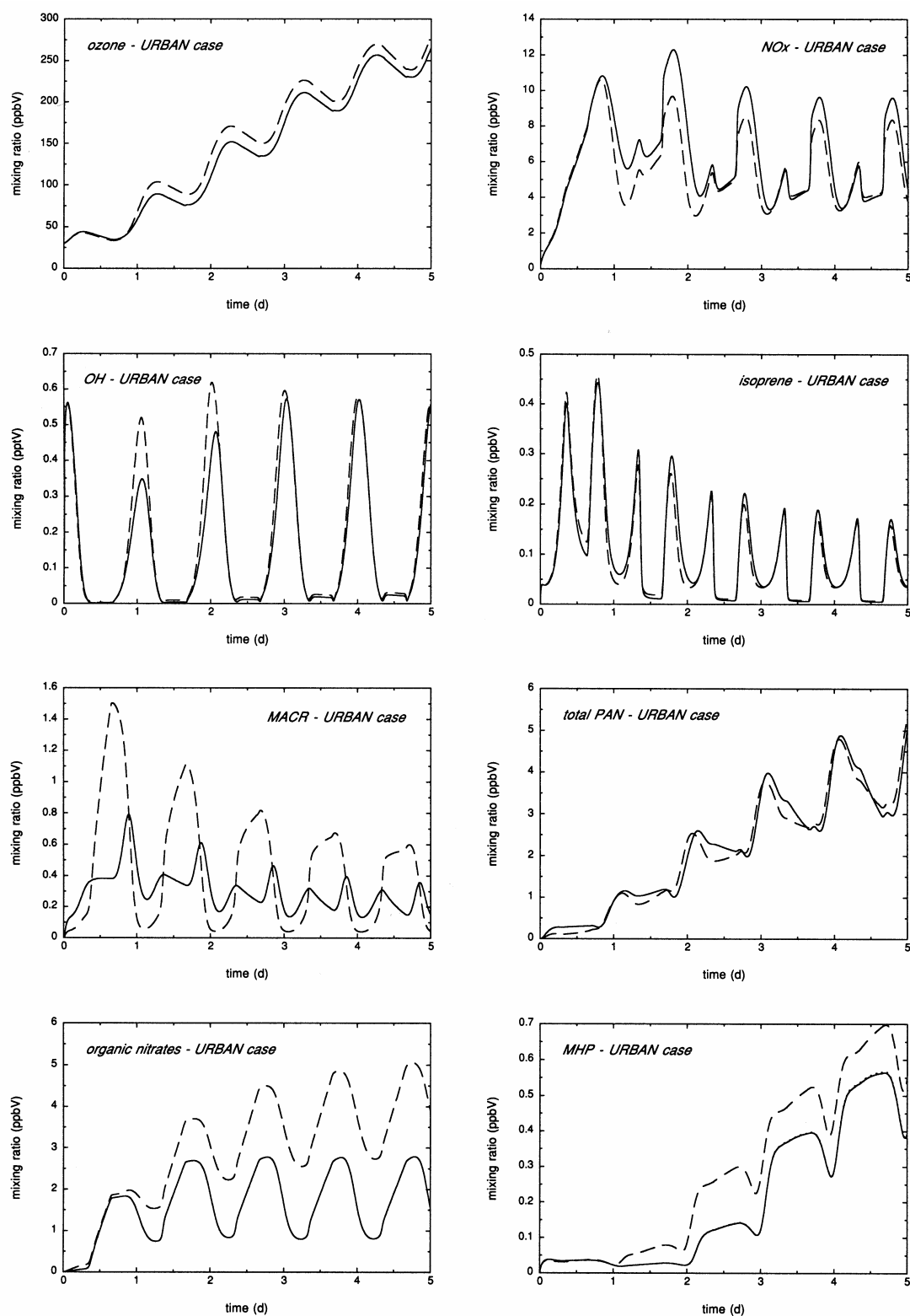


Figure 3: Mixing ratios of selected vs. versus reaction time calculated for the URBAN case:
 (----) original RACM scheme;
 (.....) full updated RACM scheme;
 (—) reduced updated RACM scheme.

Simulation of Atmospheric Photochemistry In a Large Reaction Chamber (SAPHIR): Design of Chamber Experiments using Sensitivity Analysis (MPM6).

Matthias Karl, Hans-Peter Dorn, Dirk Poppe

Institut für Chemie und Dynamik der Geosphäre II: Troposphäre

Forschungszentrum Jülich, 52425 Jülich

m.karl@fz-juelich.de

Introduction

The simulation chamber *SAPHIR* is an experimental tool which allows studying tropospheric gas-phase photochemistry under natural burdens of trace gases ranging from low concentrations typical for the background atmosphere to polluted conditions in industrialised areas. Chamber experiments have a series of advantages compared to investigations in the real atmosphere: 1.) reproducibility of experiments, 2.) independent variation of the concentrations of source gases to explore their individual influence on different parts of the chemical system, for example the radical budget, the cleaning capability of the atmosphere, and the formation of ozone, 3.) the realisation of perturbation experiments to study transient processes of the photochemical system on time scale of minutes.

The aim of this model study is to explore the potential of chamber experiments with respect to improve the kinetic database. Even rate coefficients of key reactions of tropospheric chemistry still have uncertainties ranging from 10% to 50% (e.g. [JPL, DeMore et al., 1997]).

Investigation of the photochemical OH cycle

The dominant role of the hydroxyl radical (OH) for self-cleansing of the atmosphere has been shown by model calculations and field data. In this first approach we focus on a simplified chemical system that encompasses only reactions of OH, HO₂, O₃, NO_x, HONO, CO and HCHO. This system contains already the generic features of the tropospheric gas-phase chemistry [Poppe et al., 1993]: 1.) primary production of OH, 2.) degradation of almost all reduced compounds initialized by the reaction with OH, 3.) recycling of OH to HO₂, 4.) depletion of OH and HO₂ and formation of long-lived compounds.

For this model study a subset of the latest version of Master Chemical Mechanism (MCM Version 3) [Jenkin et al., 1995] including 60 reactions is used. HONO-formation on the walls of *SAPHIR* is also accounted for as observed. During daylight the source strength for HONO depends on the relative humidity and ranges up to $3.4 \times 10^6 \text{ cm}^{-3} \text{ s}^{-1}$ scaling with the photolysis frequency of NO₂. A spatially homogeneous distribution is presumed for all compounds in the chamber.

Model tool

The strong coupling of reactions involved in the OH cycle complicates the design of experiments in *SAPHIR* for the derivation of kinetic parameters. Sensitivity analysis is used here to find experimental conditions under which the concentration of measurable trace gases (preferentially OH and HO₂) depends sensitively on an interesting part of the mechanism.

Sensitivity analysis was carried out utilizing a newly developed program package which generates scenarios in a random manner and calculates the sensitivities.

The local (logarithmic) sensitivity coefficient for a quantity *x* (here stationary concentrations of compounds or function of those) with respect to the rate parameter *k_j* of a given reaction *R_j* is used to quantify sensitivity. It is defined by:

$$s_j(x) = \frac{k_j}{x} \cdot \frac{\partial x}{\partial k_j} \quad (1)$$

A sensitivity coefficient of unity means that for example a 10% variation of the rate coefficient k_j of the given reaction R_j results in a change of 10% of the quantity x . The $s_j(x)$ are approximated by numerical differentiation with a computational error of less than 10%. Numerical studies show that $s_j(x)$ ranges between ± 2 for the simplified reaction mechanism.

Table 1: Reactions investigated in this study.

R1	$OH + O_3 \rightarrow HO_2 + O_2$
R2	$HO_2 + O_3 \rightarrow OH + 2 O_2$
R3	$OH + CO \rightarrow HO_2 + CO_2$
R4	$NO_2 + OH + M \rightarrow HNO_3 + M$
R5	$HO_2 + NO \rightarrow NO_2 + OH$
R6	$HCHO + OH + O_2 \rightarrow HO_2 + CO + H_2O$
R7	$O_3 + h\nu \rightarrow 2 OH$
R8	$HO_2 + HO_2 \rightarrow H_2O_2 + O_2$
R9	$OH + HO_2 \rightarrow H_2O + O_2$
R10	$NO_2 + h\nu (+ O_2) \rightarrow O_3 + NO$
R11	$NO + O_3 \rightarrow NO_2$
R12	$HCHO + h\nu (+ 2 O_2) \rightarrow 2 HO_2 + CO$
R13	$HCHO + h\nu \rightarrow CO + H_2$

More than 2000 scenarios with a wide range of initial concentrations of long-lived compounds, solar zenith angle and humidity sample environmentally important situations. Temperature was held constant at 298 K. Steady-state was established for short lived radicals (HO_2 , $HONO$, HO_2NO_2 , NO , NO_3 , N_2O_5 , $O(^3P)$, $O(^1D)$, OH) while the concentrations of longer lived species were held fixed during the model runs.

Table 2: Ranges of meteorological parameters and mixing ratios of long-lived compounds. Optimal choices for the proposed experiments S_i are also given. Mixing ratios in ppt if not stated otherwise. $NO_x = NO_2 + NO$. Since only small mixing ratios for H_2O_2 (≤ 1.1 ppb) and HNO_3 (≤ 7 ppb) are considered their influence is negligible.

Input Parameter	Range	$S1$	$S2$	$S3$	$S4$	$S5$	$S6$
CO [ppb]	10 – 1000	-	-	693	-	50	-
O_3 [ppb]	5 – 500	403	284	81	258	13	11
HCHO [ppb]	10 – 30	-	-	-	-	-	29
NO_2	10 ppt – 15 ppb	122	38	35	14.4 ppb	784	772
NO_x	-	123	41	42	15.3 ppb	1.8 ppb	2.0 ppb
H_2O [%]	0.04 – 3.3	2.0	3.3	1.2	0.9	2.6	0.04
Zenith angle [°]	30 – 80	80	34	46	39	44	41

From the bulk of scenarios interesting cases for experiments were chosen as follows: Firstly, concentrations of OH and HO_2 had to be above their experimental thresholds. Secondly, a scenario was selected if one or more measurable quantities displayed large sensitivities for a small number of reactions (ideally only one reaction), and at the same time very low sensitivities for the other reactions.

Six case studies

a.) Relative rate constant k_1/k_2

S1 is sensitive to the relative rate constant k_1/k_2 . The conversion of OH and HO₂ takes place only under the influence of O₃ with vanishing CO and NO_x. Ozone reacts with OH and HO₂ (R1 and R2) with nearly the same rate, yielding complete radical recycling. The HO_x-self reactions (R8 and R9) can be neglected. From the steady-state approximation it can be seen that the sensitivity of the ratio [OH]/[HO₂] does not depend on the ozone photolysis:

$$[HO_2] \cong \frac{k_1 \cdot [OH] \cdot [O_3]}{k_2 \cdot [O_3]} \quad \text{and thus} \quad \frac{[OH]}{[HO_2]} \cong \frac{k_2}{k_1} \quad (2)$$

The ratio of k_1/k_2 can be directly deduced from the measurement of OH and HO₂ within an uncertainty given by the measurement error for [OH]/[HO₂].

Table 3: Local sensitivity coefficients for [OH], [HO₂] and [OH]/[HO₂] in *S1*.

Quantity x	s₁(x)	s₂(x)	s₇(x)	s₈(x)	x
[OH]	0.6	0.5	0.3	-0.2	6.4x10 ⁶ cm ⁻³
[HO ₂]	0.4	-0.3	0.3	-0.3	1.9x10 ⁸ cm ⁻³
[OH]/[HO ₂]	-1.0	0.8	0.0	0.1	0.03

b.) Determination of k_1 : OH + O₃ reaction

The primary OH production (P_{OH}) in *S2* is strongly increased compared to *S1*, due to a very high water content and a small solar zenith angle. *S2* shows high sensitivity of [OH] for k_1 and the ozone photolysis frequency. There is only a weak dependence on k_7 . Thus k_1 can be determined in *S2*. Its error is bounded from below by the uncertainties of the P_{OH}-measurement and the measured OH-concentration. Then we obtain k_2 from *S1*. The scenario yields very high HO_x-concentrations compared to atmospheric concentrations (see table 4), and may therefore be sensitive to additional losses, for example on the wall, which are not important in the real atmosphere.

Table 4: Local sensitivity coefficients for [OH], [HO₂] and [OH]/[HO₂] in *S2*.

Quantity x	s₁(x)	s₂(x)	s₇(x)	s₈(x)	s₉(x)	x
[OH]	-0.8	0.2	0.8	0	-0.2	1.4x10 ⁸ cm ⁻³
[HO ₂]	0.33	-0.1	0.38	-0.3	-0.3	1.3x10 ⁹ cm ⁻³
[OH]/[HO ₂]	-1.1	0.3	0.4	0.3	0.1	0.11

c.) Determination of k_3 : OH + CO reaction

The reaction of CO with OH quickly forms the stable end product CO₂. Application *S3* addresses the degradation of CO in a NO_x poor scenario where the conversion of HO₂ to OH through R5 can be neglected. *S3* shows high sensitivities of OH on k_3 as well as on P_{OH}. This dependence can be derived from the steady-state approximation:

$$[OH] \approx \frac{P_{OH}(k_7, [O_3], [H_2O])}{k_3 \cdot [CO]} \quad (3)$$

Table 5: Local sensitivity coefficients for [OH], [HO₂] and [OH]/[HO₂] in *S3*.

Quantity x	s₃(x)	s₇(x)	s₂(x)	s₈(x)	x
[OH]	-0.9	0.7	0.3	-0.2	2.6x10 ⁶ cm ⁻³
[HO ₂]	0.0	0.4	0.0	-0.5	8.0x10 ⁸ cm ⁻³
[OH]/[HO ₂]	-1.0	0.2	0.3	0.3	0.03

d.) OH depletion: OH + NO₂ reaction

In *S4* the degradation of OH under formation of long lived HNO₃ is investigated, which is an important loss under NO_x rich conditions. Since cycling between OH and HO₂ will not be effected by the self-reactions of HO_x, steady-state [OH] is given by an expression earlier stated in [Poppe et al. 1993]:

$$[OH] \cong \frac{P_{OH} (k_7, [O_3], [H_2O])}{k_4 \cdot [NO_2]} \quad (4)$$

Table 6: Local sensitivity coefficients for [OH], [HO₂], [NO] and [OH]/[HO₂] in *S4*.

Quantity x	s ₄ (x)	s ₇ (x)	s ₁₀ (x)	s ₁₁ (x)	x
[OH]	-1.0	0.9	0.0	0.0	5.8x10 ⁶ cm ⁻³
[HO ₂]	-1.0	0.9	-1.0	0.9	1.3x10 ⁷ cm ⁻³
[OH]/[HO ₂]	0.0	0.0	1.0	-0.9	0.46
[NO]	0.0	0.0	1.0	-1.0	2.3x10 ¹⁰ cm ⁻³

e.) Recycling of OH to HO₂: HO₂ + NO reaction

In *S5* the reaction R5 of HO₂ with NO which plays the key role in recycling OH is studied. This reaction is known to be responsible for a large fraction of the chemical ozone production. The scenario exhibits nearly unity sensitivity of [OH]/[HO₂] on k₅. Concurrent measurement of [NO] and [OH]/[HO₂] are needed for this scenario. A difference between the measured and calculated [OH]/[HO₂], with no simultaneous disagreement in the NO concentration, can be attributed directly to k₅.

Cases *S1* to *S4* have already been discussed elsewhere ([Ehhalt, 1999; Poppe et al., 1993]) as simple limiting cases for different NO_x regimes. Scenario *S5* is not related to a simple case that can be found easily by chemical intuition. Therefore *S5* demonstrates the power of the sensitivity analysis combined with Monte-Carlo sampling technique.

Table 7: Local sensitivity coefficients of [OH], [HO₂], [NO] and [OH]/[HO₂] in *S5*.

Quantity x	s ₅ (x)	s ₇ (x)	s ₁₀ (x)	s ₁₁ (x)	x
[OH]	0.0	0.6	-0.1	0.1	1.3x10 ⁷ cm ⁻³
[HO ₂]	-1.0	0.6	-1.1	1.0	2.4x10 ⁷ cm ⁻³
[OH]/[HO ₂]	1.0	0.0	1.0	-1.0	0.54
[NO]	0.0	0.0	1.0	-1.0	2.4x10 ¹⁰ cm ⁻³

f.) Determination of k₆: HCHO + OH reaction

The photolysis of formaldehyde (HCHO) is important for the radical budget since it leads to the formation of two HO₂ radicals in subsequent reactions.

Formaldehyde acts also as a sink of HO_x since it reacts with OH (R6) with an estimated lifetime of 5.6 h (for [OH] = 5x10⁶ cm⁻³). Due to this short lifetime the rate constant k₆ can be directly determined from the measurement of the decay of [HCHO] as function of time.

The degradation of HCHO follows pseudo-first-order kinetics and may be expressed as:

$$\frac{d[HCHO]}{dt} = -(k_{12} + k_{13}) \cdot [HCHO] - k_6 \cdot [OH] \cdot [HCHO] \quad (5)$$

$$[HCHO]_t = [HCHO]_0 \cdot \exp - \int (k_{12} + k_{13} + k_6 \cdot [OH]) dt$$

Only measurements of HCHO and OH are required. The Monte Carlo method is used to find initial conditions that maximize the OH concentration under tropospheric relevant concentrations to ensure the predominance of R6 in the degradation of HCHO.

Starting at 8:20, HCHO decreases from 30 to 1 ppb within 4.7 hours (**fig. 1**). Given the small measurement uncertainties of [HCHO] as well as for the photolysis frequencies k_{12} and k_{13} , rate constant k_6 can be obtained in a SAPHIR experiment applying equation (5).

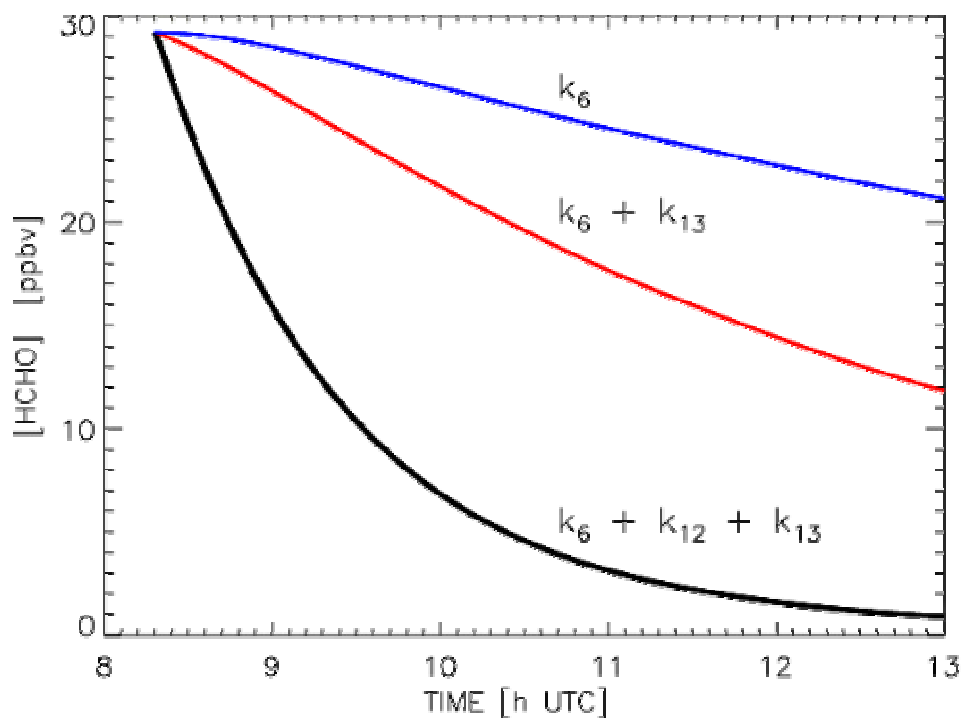


Figure 1: Contribution of the processes R6, R12 and R13 on the modelled degradation of HCHO in S6. Black line: all processes, red line: R6 and R13, blue line only R6. Measured photolysis frequencies from a typical day of the POPCORN campaign, August 1994, were used as input (Rudolph and Koppmann, 1998). Time given in UTC.

Conclusions

Sensitivity analysis combined with a Monte-Carlo based method is utilized to design experiments for the SAPHIR chamber. Sensitivity coefficients help to identify experimental conditions under which measurable quantities depend sensitively on a small number of rate coefficients. This decoupling of several parts of the chemical system allows for the application of standard kinetic techniques to improve the rate coefficients considered. In some cases (*S1...S4*) the analysis proposes experimental conditions that are already well known as limiting cases of the fast photochemistry. However in case of *S5* a promising experiment is suggested that has not been discussed so far. The considerable potential of the presented analysis is its capability to discover optimal experimental conditions. Moreover it leads to a better understanding of atmospheric chemistry in terms of a system analysis.

Acknowledgement

This work was performed within the IDEC project (Integrated Data Archive of Atmospheric Chemical Standard Scenarios for the Evaluation of Chemistry-Transport-Models) of AFO 2000, which is supported by the German Federal Ministry of Education and Research (BMBF) under grant 07ATF02.

References

- DeMore, W. B., S. P. Sander, D.M. Golden, R. F. Hampson, M. J. Kurylo, C. J. Howard, 1997: Chemical kinetics and photo-chemical data for use in stratospheric modeling. **Eval. 12, Rep. JPL 2000-1**, *Jet Propulsion Laboratory, California Institute of Technology*.
- Ehhalt, D. H., 1999: Gas phase chemistry of the troposphere, Chapter 2, in: Global aspects of Atmospheric Chemistry. Steinkopff Verlag, Darmstadt, Springer Verlag, New York, R. Zellner guest editor.
- Jenkin, M. E., S. M. Saunders, M. J. Pilling, 1995: The tropospheric degradation of volatile organic compounds; a protocol for mechanism development. *Atmospheric Environ.* **31**, 81-104, <http://chmlin9.leeds.ac.uk/MCMframe.html>.
- Poppe, D., M. Wallasch, J. Zimmermann, 1993: The dependence of the concentration of OH on its precursors under moderately polluted conditions: A model study. *J. Atm. Chem.* **16**, 61-78.
- Rudolph, J., R. Koppmann, 1998: Atmospheric measurements during POPCORN – Characterisation of the photochemistry over a rural area. Kluwer Academic Publishers, Dordrecht.

Numerical Simulations of Nitrous Acid in the Planetary Boundary Layer – Rate Constants and Unknown Sources (MPM10)

Bernhard Vogel¹, Heike Vogel¹, Jörg Kleffmann², Ralf Kurtenbach²

¹*Institut für Meteorologie und Klimaforschung, Forschungszentrum Karlsruhe/
Universität Karlsruhe, Postfach 3640, D-76021 Karlsruhe*

²*Physikalische Chemie/FB9, Bergische Universität Wuppertal, D-42097 Wuppertal*

The Problem

There is a general agreement that the photolysis of nitrous acid is an important source of OH radicals shortly after sunrise whereas the relative importance of HONO on photochemistry during the rest of the day is still an open question. Recent model simulations taken into account only gas phase reactions show large differences between observed and modelled diurnal cycles of HONO (Fig. 1, dotted line).

This study is an application of recent observational findings on HONO formation (Kurtenbach et al., 2001) using the comprehensive numerical simulation model KAMM/DRAIS (Vogel et al., 1995) and addresses the following questions: 1. What is the relative importance of a) the direct HONO emissions, b) the heterogeneous reactions at aerosol surfaces, and c) heterogeneous reactions at the ground itself for the diurnal cycle of HONO? 2. What is the relative importance of HONO as a source of the OH radical?

The Method

In order to simulate the vertical profiles of the gaseous and aerosol species a 1-D version of KAMM/DRAIS is coupled with the aerosol model MADEsoot (Ackermann et al., 1998; Riemer, 2002). In the vertical direction 45 layers are used. The vertical grid size varies from 17 m close to the surface up to 400 m at the top of the model domain which is at 12 km above sea level. The time steps are on the order of seconds. The whole model system runs in a fully coupled mode. The gas phase emissions are time dependent and represent the conditions of a moderately polluted area in Europe. Concerning HONO we included the following processes in our model.

According to Kurtenbach et al. (2001) direct HONO emission are taken into account as 0.8 % of the NO emissions.

The heterogeneous production of HONO



is included as a first order reaction with $k_{\text{het}} = 3 \cdot 10^{-3} \text{ m min}^{-1} \cdot A$ (Kurtenbach et al., 2001) where A is the surface area density.

This reaction can occur at the simulated aerosol surfaces or at the ground. For the reaction at the ground we use $A = 0.1 \text{ m}^{-1}$. The latter assumption means that air in the lowest model box is exposed to a surface of 1.7 m^2 . Finally we introduced an artificial HONO source (E_{phot}) which is proportional to the daily cycle of the photolysis rate constant of NO_2 (J_{NO_2}).

$$E_{\text{phot}} = b \cdot J_{\text{NO}_2} \quad (1)$$

Results

The daily cycles of the model simulations (Vogel et al., 2002) are compared to observational data of Kleffmann et al. (2002). The measurements were carried out during October 18-19, 2001. Figure 1 shows the results for the simulation when all processes mentioned above except the photolytic source of HONO were taken into account (reference case). During the night the simulated HONO concentrations are in agreement with the observations. However, during daytime HONO is underestimated by the model by a factor of two.

We checked the rate constant of the reaction of $\text{NO} + \text{OH} \rightarrow \text{HONO}$ which is the main gas phase source of HONO and found differences by a factor of two between the values currently used in chemical transport models and recent data published by IUPAC. Using the new kinetic data we drastically reduced the difference between the observed and the simulated HONO concentrations. However, the daytime HONO concentrations are still underestimated by the model by 30 % (Fig. 1). This implies that there is an additional source of HONO during the day.

Therefore, we introduced the artificial HONO source. After tuning this artificial source by modifying factor b in equation 1 we were able to reproduce the observed HONO concentrations during daytime (Fig. 2).

For the vertical profiles of nitrous acid we also found a better agreement between measured and simulated data when the photolytical source is taken into account.

We compared the OH production by the photolysis of HONO with the OH production due to the photolysis of ozone. For the day in October, when low ozone concentrations and low water vapour were present the photolysis of HONO was the main source of OH. Additional simulations for a summer day with high temperature, high water vapour and ozone concentrations gave a different picture. In this case and with the exception of the early morning hours the photolysis of HONO appeared to be a minor source of OH.

Summary

Taking into account direct HONO emissions and heterogeneous reactions at the surface, and applying the new rate constant for reaction R1, lead to a good agreement of observations and model results during night. The daytime concentrations of HONO are almost identical for all cases we looked at and are about 30-45 % lower than the observed ones. When we included a so far unknown photolytical HONO source we found a good agreement with the measured daytime concentrations. This additional HONO source is about 25 times higher than the direct emissions of HONO.

For the conditions in October the photolysis of HONO is the most important source of HONO whereas for the summer conditions the photolysis of ozone supplies the highest amount.

References

- Kleffmann, J., R. Kurtenbach, J. Lörzer, P. Wiesen, N. Kalthoff, B. Vogel, and H. Vogel, 2002: Measured and simulated vertical profiles of nitrous acid, Part I: Field measurements. Submitted to *Atmos. Environ.*
- Kurtenbach, R., K.H. Becker, J.A.G. Gomes, J. Kleffmann, J.C. Lörzer, M. Spittler, P. Wiesen, R. Ackermann, A. Geyer, and U. Platt, 2001: Investigations of emissions and heterogeneous formation of HONO in a road traffic tunnel, *Atmos. Environ.*, 35, 3385-3394.
- Riemer, N., 2002: Numerische Simulationen zur Wirkung des Aerosols auf die troposphärische Chemie und die Sichtweite, *Wiss. Ber. Inst. Meteorol. Klimaforsch. der Univ. Karlsruhe*, 29.
- Vogel, B., H. Vogel, J. Kleffmann, and R. Kurtenbach, 2002: Measured and simulated vertical profiles of nitrous acid, Part I: Field measurements, Part II: Model simulations and indications of a photolytic source. Submitted to *Atmos. Environ.*
- Vogel, B., F. Fiedler, and H. Vogel, 1995: Influence of topography and biogenic volatile organic compounds emission in the state of Baden-Wuerttemberg on ozone concentrations during episodes of high air temperatures, *J. Geophys. Res.*, 100, 22907-22928.

Figures

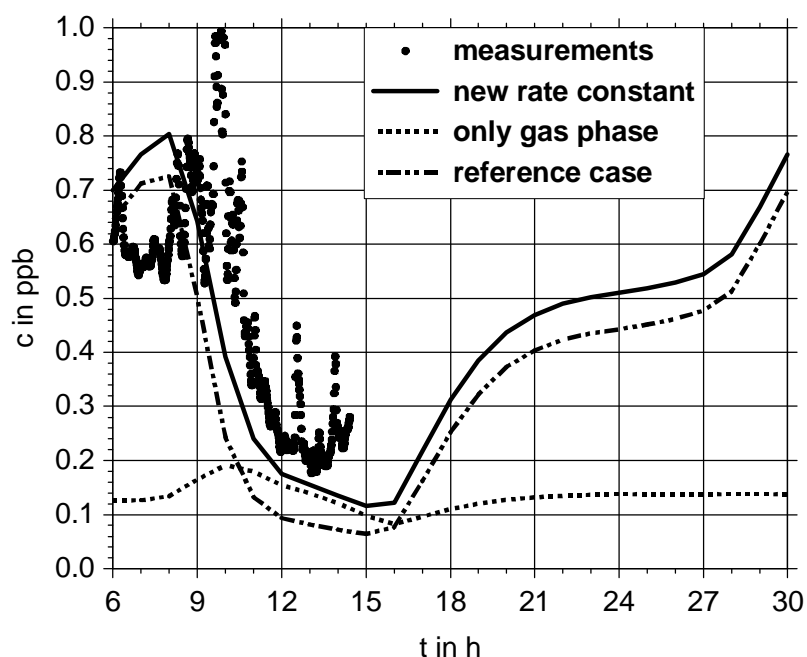


Figure 1: Daily cycles of the HONO concentration for October 18, 2001. The dots represent the observations. Hour 6 is identical to 6:00 CET at October 18, 2001.

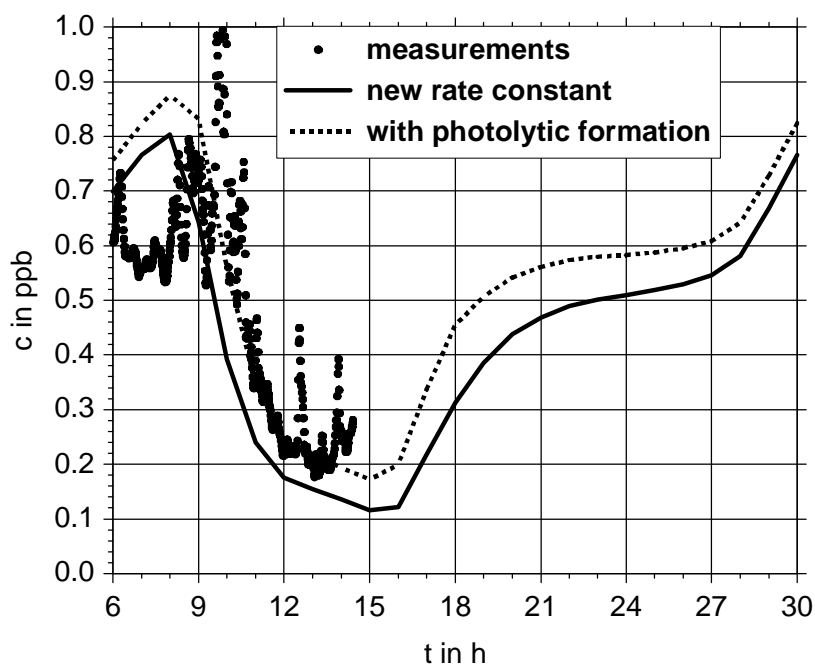


Figure 2: Same as Fig 1, but for the case with the updated rate constant (continuous line) and the simulation including the photolytic HONO source (dashed line).

Sensitivity Study on the Influence of New Kinetic Data and of Species Lumping on the Simulation Results (MPM11)

F. Kirchner, M. Junier, Y.A. Roulet, A. Clappier, and H. van den Bergh
EPFL Lausanne, DGR - LPAS, CH-1015 Lausanne, Switzerland

Summary

Models should calculate fast and precisely. Because the chemical mechanism is a very time consuming part of the model, it is important to optimise it with respect to speed and precision. One important tool for reducing the size of a mechanism is the lumping of similar chemical species into one mechanism species. To answer the question how much detailedness of a mechanism is needed and how intensive lumping can be, we performed sensitivity studies in which we changed the degree of lumping step by step. The work was done applying the mechanism generation programme CHEMATA (CHEMical MEchanism ADaptation to Tropospheric Applications) which is able to generate explicit or lumped mechanisms according to the wishes of the user. Using the RACM mechanism (Stockwell et al., 1997) as starting point we extended and reduced the number of lumping groups and evaluated the sensitivity of the model results to each variation in the mechanism. We especially tested:

- Treatment of secondary VOC species: Many mechanisms have very simple approaches of representing secondary VOC, e.g. treating all higher aldehydes as CH₃CHO. Our simulations show that this is justified for simulating ozone episodes ≤ 2 days.
- Reducing the mechanism by parameterising of the RO₂ reaction and by lowering the number of the VOC lumping groups.

The tests were done in a boxmodel as well as a 3D model which was used for simulating an ozone episode from spring 1998 in the region of Milan (Martilli et al., 2002). Simulations were also performed in order to evaluate the influence of new kinetic data and to evaluate the importance of current uncertainties in kinetic data and product yields.

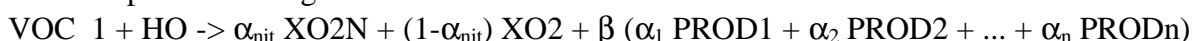
The Influence of Species Lumping: Results

Using RACM as a starting point we investigated the influence of the way of lumping on the model results. Based on identical kinetic data 3 new mechanisms were generated:

- **Mechanism 1:** The lumping groups ALD and KET of the RACM mechanism were replaced by several new lumping groups: The higher aldehydes are splitted into 7 groups: CH₃CHO, C₂H₅CHO, n-C₃H₇CHO, i-C₃H₇CHO, R'-CHO, R''CHO, R'''CHO (with: R' for a chain ≤ 4 C atoms, R'' for a chain = 5 C atoms, R''' for a chain ≥ 6 C atoms). The higher ketones are splitted into 6 groups: ketones with 3, 4, 5, 6, 7, and more than 7 carbon atoms. In the same way the RO₂ groups ACO3 and KETP from the RACM mechanism were divided into 7 and 6 groups corresponding to the new lumping of the carbonyl species.
- **Mechanism 2:** The RACM mechanism was condensed by a new parameterising of the RO₂ chemistry. Only the RO₂ species CH₃O₂ (MO2) and CH₃C(O)O₂ (ACO3) were kept, all other RO₂ species of RACM were replaced by the species XO2 and XO2N. The parameterising was made in a way that the products of the RO₂ reactions were formed at the same time as RO₂. The RACM parameterising has the form (ONIT = organic nitrates):



The new parameterising for the same reactions:



α are the product yields and β can have a value between $(1-\alpha_{\text{nit}})$ and 1. In our studies it was always $(1-\alpha_{\text{nit}})$, assuming that the reaction with NO is the by far most important loss process for RO₂.

- **Mechanism 3:** The RO₂ parameterising was the same as in Mechanism 2. The number of different VOC classes was lowered from 34 to 10 (CH₄, alkanes, alkenes, aromats, HCHO, 3 classes of higher aldehydes, ONIT, PAN). The lumping was based on the average emission values either of the boxmodel or of the Milan region. The inorganic chemistry of RACM was adopted without any changes except skipping the species H₂.

In the boxmodel 3 scenarios were used to test these mechanisms:

- Case 1 (Moderately polluted case with constant emissions): The emissions and conditions are taken from Kuhn et al., 1998. The simulation starts at noon of the first day and ends at noon of the 6th day.
- Case 2 (Highly polluted case with constant emissions): In Case 2 ten times higher VOC emissions and 30 times higher NO_x emissions than in Case 1 are applied.
- Case 3 (Highly polluted case, but no emissions): No emissions are considered in Case 3. The initial concentrations are equal to the concentrations of the RACM mechanism of Case 2 at noon of the third day.
- Case 4: Extremely polluted: 300 times more NO_x and 1000 times more VOC than in case 1. Conditions like this do not exist for a whole day in reality, but in the morning before the mixing layer increases concentrations like this are found in the centre of very polluted cities.

Comparison of different kinds of lumping in a boxmodel: The results are shown in Figure 1. Comparing the results of RACM and Mechanism 1 shows that the error made by restricting to small products (as it is done in RACM) leads for VOC sensitive conditions to an underestimation of the ozone production. This underestimation is small during the first 2 days and becomes more important for longer time scales. The ozone values calculated by RACM and Mechanism 2 are nearly identical for the Cases 1-3, suggesting that introducing this RO₂ parameterising is a good way for reducing a mechanism. Nevertheless Case 4 shows a faster increase of ozone in the morning. Therefore at 10 a.m. Mechanism 2 yields 30% more ozone than RACM. Mechanism 3 fits well to the RACM results for the cases 1 and 2 but fails for Case 3. In Case 4 we find an even faster ozone increase leading at 10 a.m. to 70% more ozone than in RACM.

3D simulations for the Milan region: Applying the model TAPOM (Transport and Air Pollution Model) for the region of Milan we found the ozone maximum at 2 p.m. in the mechanisms RACM (181 ppb), Mech 1 (183 ppb) and Mech 2 (184 ppb). Mech 3 shows the ozone maximum at 1 p.m. (189 ppb). In the whole region the mechanisms differ from RACM at 2 p.m. by less than 5 (Mech 1), less than 4 (Mech 2) and less than 7 (Mech 3) ppb ozone. Until 7 p.m. none of the mechanism differs by more than 5 ppb ozone over the whole region. After sunset larger differences are found in the center of Milan (up to 10 ppb for Mech2 and up to 25ppb for Mech 3). The largest differences are found in the morning in the Milan plume. The very rapid ozone formation in these very polluted air masses is slowed down by the increase of the mixing layer. In this situation the mechanisms with the simplified RO₂ scheme show much faster ozone formation. Whereas Mech 1 and RACM show nearly identical ozone values at 10 a.m. Mech 2 provide up to 9 ppb higher and Mech 3 up to 35 ppb higher ozone values. These deviations of Mech3 and to a smaller amount of Mech2 are in agreement with the boxmodel results of Case 4. Outside of the Milan plume in the other parts of the Milan regions the differences between RACM and the other mechanisms are much smaller (± 3 ppb for all mechanisms).

One can conclude that the error made by treating the higher carbonyl species like smaller carbonyls in RACM is small for simulating ozone episodes ≤ 2 days. Further mechanism reduction is possible by changing the parameterising of the RO₂ reactions. Reducing the VOC groups can strongly affect the morning values in very polluted areas but seems to be possible in less polluted regions.

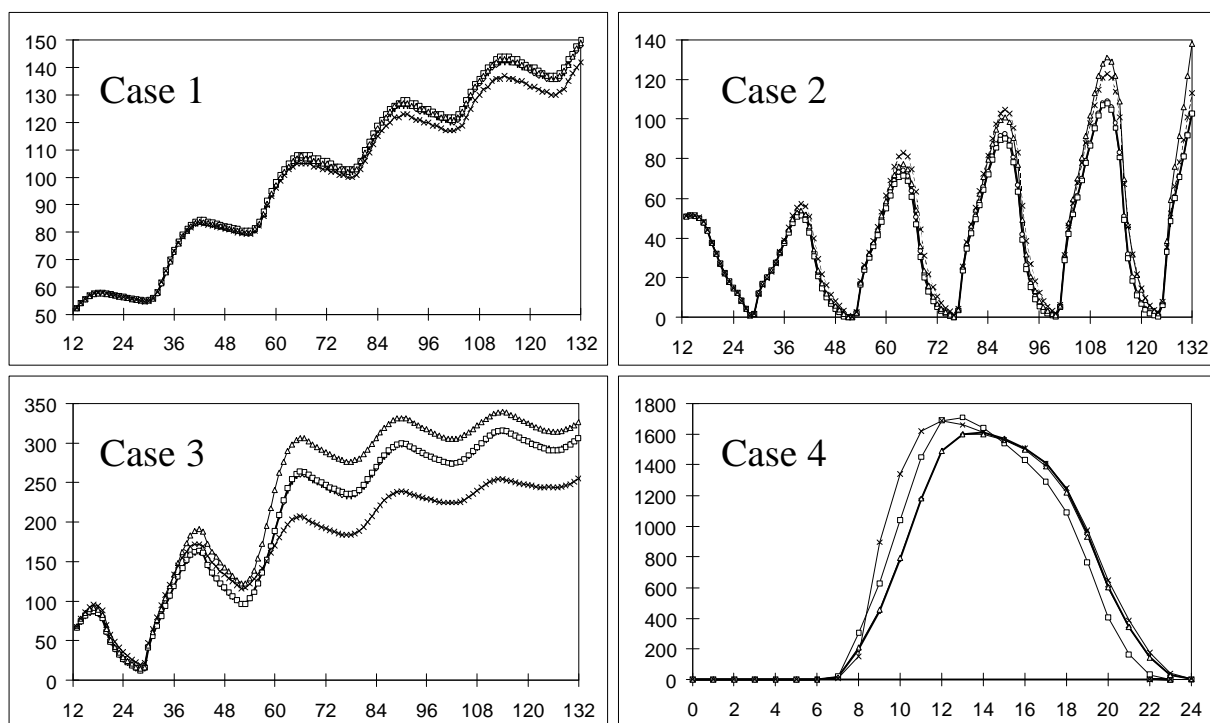


Figure 1.1: Plot of the mixing ratios of ozone (in ppb) against the time (in hours). RACM: rhombs and fat line, Mech 1: triangles, Mech 2: squares, Mech 3: crosses

New kinetic data: Results.

Higher rate constants for the decomposition reaction of RO (as measured by Zabel et al.) lead to higher aldehyde concentrations which increase the ozone production in the case of VOC sensitive conditions. We introduced the values measured by Zabel et al. and assumed according to these new measurements 5 times higher decomposition rate constants and 2 times higher isomerisation rate constants for all RO radicals which have not been measured.

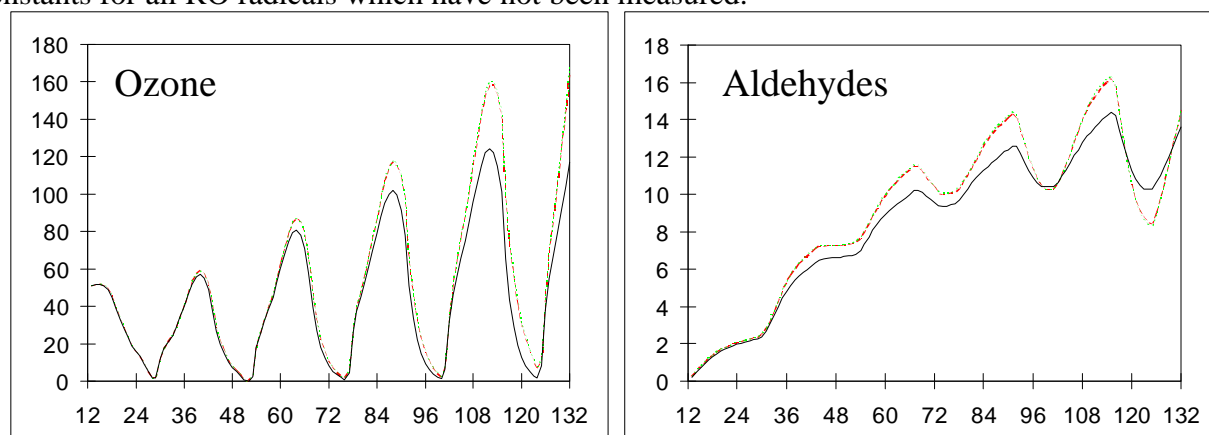


Figure 1-2: Effect of updating the RO rate constants for Case 2 on the mixing ratios of ozone and higher aldehydes (in ppb): black line: RACM, broken line: updated decomposition rate constants, dotted line: updated decomposition and isomerisation rate constants.

Updating the alkene + NO₃ kinetic based on the results of Martinez et al. leads to reduced night and daytime concentrations of terminal alkenes whereas the ozone reduction is very small.

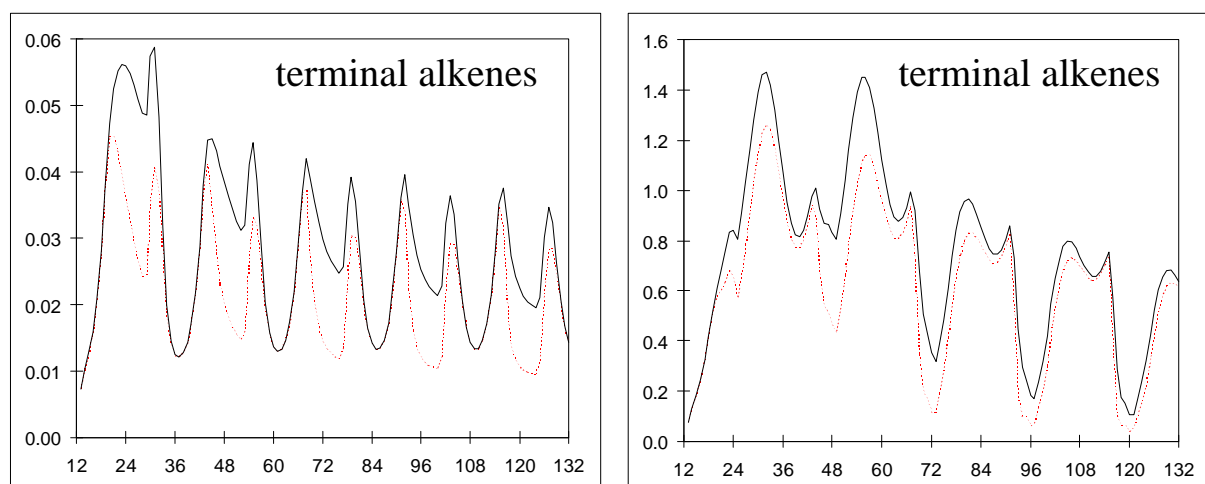


Figure 1-3: Mixing ratios (in ppb) for terminal alkenes for the Cases 1 (left) and 2 (right) with RACM (black line) and updated alkene + NO₃ chemistry (dotted line)

References

- Kuhn, M., et al., Intercomparison of the gas-phase chemistry in several chemistry and transport models, *Atmos. Environ.* **32**, 693-709 (1998)
- Martilli, A., A. Neftel, G. Favaro, F. Kirchner, S. Sillman, A. Clappier, Simulation of the ozone formation in the northern part of the Po valley with the TVM-CTM, *J. Geophys. Res.*, in press (2002)
- Martinez et al., CMD data panel
- Stockwell, W.R., F. Kirchner, M. Kuhn, and S. Seefeld, A new mechanism for regional atmospheric chemistry modeling, *J. Geophys. Res.* **102**, 25,847-25,879 (1997)
- Zabel et al., CMD data panel
- Zetzsch et al., CMD data panel